A REATTACHING, TURBULENT, THIN SHEAR LAYER

by

David Howe WOOD, B.E., M.Eng.Sc. (Sydney)

DEPARTMENT OF AERONAUTICS
IMPERIAL COLLEGE
LONDON UNIVERSITY

A thesis submitted for the degree of
Doctor of Philosophy of the University of London

January, 1980

BIBL.
LONDIN.
UNIV.

In all but the most trivial areas of enquiry, there arise questions about the extent to which events are shaped by predictable natural laws as against the accidents of initial conditions and perturbations.

Robert M. May, Nature, 7 October, 1977

First I shall test by experiment before I proceed further, because my intention is to consult experience first and then with reasoning show why such experience is bound to operate in such a way. And this is the true rule by which those who analyse the effects of nature must proceed: and although nature begins with the cause and ends with the experience, we must follow the opposite course, namely, begin with experience, and by means of it investigate the cause.

Leonardo da Vinci

I only learn from error; till lately I trusted
in the practice of my hand.

From "The Hard Way" by Robert Lowell

ABSTRACT

Single point and double point measurements have been made in a high Reynolds number, single stream turbulent mixing layer, growing to reattach to the wind tunnel floor. The flow remains a thin shear layer over the entire region of interest. Away from the influence of the wall, the conditionally sampled correlation measurements show that the turbulent large eddy structure is three-dimensional over the width of the shear layer. A theoretical analysis is described which implies that the large correlation scales measured in the potential flow are due largely to the nature of the potential flow as such, and not due to the two-dimensionality of the large turbulent eddies, as suggested by previous workers.

The large eddy structure appears to have two components. A double roller eddy, with circulation at right angles to the normal direction, exists in the "inner" region of high intensity. "Superimposed" on this structure is an outer motion responsible for the eruption of turbulent fluid into the potential flow. The outer motion dominates the turbulence structure near the high velocity edge.

The first effect of the wall is to stretch the spanwise and streamwise scales of the eddies and hence weaken the double roller eddy. The outer motion becomes dominant until it is finally limited by the wall after reattachment.

Both in the potential core and in the reattached flow, $\overline{u^2}$ is amplified significantly more than $\overline{w^2}$ by the wall, as in the measurements of grid turbulence near a moving wall by Thomas and Hancock (1977). This disparity in amplification, and the unexpected result that $\overline{v^2}$ rises across the mixing layer before reattachment due to wall effect, appear to be related to the nature of the outer motion.

ACKNOWLEDGEMENTS

Without the help of a large number of people, this thesis would not have appeared. Unfortunately, it is not possible to thank everyone personally.

I am grateful to my supervisor, Professor Peter Bradshaw, whose interest, encouragement and physical insight were invaluable. I am also grateful to all my past and present colleagues for their friendship and help. In particular, Dr. Rabi Mehta, for many discussions on mixing layer structure; Dr. Peter Hoffmann, for his practical help in preparing this thesis; Mr. Muck Kin Choong, for his help with the intermittency routine and the spectral program and Mr. David Abrahams for the work he did for Appendix B.

Professor Joel Ferziger, while on leave from Stanford University, did the important work described in Appendix C, and the many discussions I had with him considerably improved my understanding of mixing layers and potential flow. I also had valuable discussions with Dr. J. M. R. Graham, Professor A. Roshko, Dr. Neale Thomas and Professor I. Wygnanski.

Mr. Len Eals gave me considerable help with the electronic problems I encountered, and the Workship Staff, especially Messrs. John Coles and A. Gill gave me much help, both generally, and in constructing the rigs.

I thank Helen Bastin and Ros Fairhurst for their speedy and efficient typing.

I am grateful to the Science Research Council who funded this work.

To my Mother, and my late Father, for their encouragement and forbearance, and to my friends for their support go my deep thanks.

List of Contents

	Page
List of Contents	(i)
List of Figures	(iii)
Principal Notation	(xiii)
CHAPTER 1 INTRODUCTION	1
1.1 Introduction	1
1.2 Literature Review	3
1.2.1 Instability and Transition Region	3
1.2.2 Fully Developed Free Mixing Layer	5
1.2.3 Effects of Initial and Boundary Conditions	11
1.2.4 The Effect of a Solid Boundary on the Flow	15
1.3 The Present Experiment	16
CHAPTER 2 EXPERIMENTAL TECHNIQUE AND DATA REDUCTION METHODS	19
2.1 Introduction	19
2.2 Mean Velocity Measurements	22
2.3 X-wire Measurements	22
2.4 Data Analysis	27
CHAPTER 3 MEAN VELOCITY RESULTS AND TWO-DIMENSIONALITY	41
3.1 Free Shear Layer Results	41
3.2 Reattached Flow	42
3.3 Two-Dimensionality	43
CHAPTER 4 SINGLE POINT RESULTS	59
4.1 The Free Shear Layer	59
4.2 Potential Core Measurements	63
4.3 The Reattached Flow	72
4.4 The Turbulence Spectra	76

		Page
CHAPTER 5	THE POINT MEASUREMENTS AND AUTO CORRELATIONS	128
5.1	The Intermittency Scheme	128
5.2	The Correlation Measurements	132
5.3	General Discussion of the Correlations	145
5.4	The Potential Core Correlations	147
CHAPTER 6	FURTHER DISCUSSION AND CONCLUSIONS	218
6.1	Further Discussion	218
6.2	Conclusions	221
REFERENCES		224
APPENDIX A	SOME COMMENTS ON THE ACCURACY OF THE HOT WIRE RESULTS	231
APPENDIX B	DERIVATION OF SHEAR STRESS AND NORMAL MEAN VELOCITY PROFILES FROM THE CONTINUITY AND MOMENTUM EQUATIONS	238
APPENDIX C	AN ANALYSIS OF THE IRROTATIONAL NEAR FIELD	249

LIST OF FIGURES

Fig.		Page
2.1a	Schematic diagram of first test section.	34
2.1b	Schematic diagram of final test section.	34
2.2	Working section floor.	35
2.3	Effect of the floor on correlation "tails".	36
2.4	Floor static pressure distribution.	36
2.5	Block diagram for the mean velocity measurements.	37
2.6	Block diagram for cross wire measurements.	38
2.7	King's law calibrations for $x - x_o = 62.32$ cm. (a) x, z plane calibrations; (b) x, y plane calibrations.	39
2.8	Yaw calibrations for $x - x_o = 62.32$ cm.	40
3.1	Determination of effective origin, x_o.	47
3.2a	Mean velocity in the initial region.	48
3.2b	Mean velocity in the fully developed flow.	49
3.3	Initial and floor boundary layer velocity profiles.	50
3.4	Mixing layer, boundary layer and potential core thicknesses.	51
3.5	Mean velocity in the reattached flow.	52
3.6	Clauser charts for the wall boundary layers.	53
3.7	Spanwise uniformity of mean velocity profiles.	54
3.8a	Spanwise uniformity of the initial boundary layer.	55
3.8b	Spanwise mean velocity traverse, $x - x_o = 39.03$ cm.	56
3.8c	Spanwise mean velocity traverse, $x - x_o = 77.29$ cm.	57
3.8d	Spanwise mean velocity traverse, $x - x_o = 155.64$ cm.	58

Fig.		Page
4.1	$\overline{u^2}$ in the free shear layer (a) x, y plane results; (b) x, z plane results.	80
4.2	$\overline{v^2}$ in the free shear layer.	81
4.3	$\overline{w^2}$ in the free shear layer.	82
4.4	$\overline{uv}$ in the free shear layer.	82
4.5	$\overline{uw}$ in the free shear layer.	82
4.6	R_{uv} in the free shear layer.	83
4.7	$\overline{u^3}$ in the free shear layer (a) x, y plane results; (b) x, z plane results.	84
4.8	$\overline{v^3}$ in the free shear layer.	85
4.9	$\overline{w^3}$ in the free shear layer.	85
4.10	$\overline{u^2v}$ in the free shear layer.	86
4.11	$\overline{uv^2}$ in the free shear layer.	86
4.12	$\overline{u^2w}$ in the free shear layer.	87
4.13	$\overline{uw^2}$ in the free shear layer.	87
4.14	S_u in the free shear layer (a) x, y plane results; (b) x, z plane results.	88
4.15	S_v in the free shear layer.	89
4.16	S_w in the free shear layer.	89
4.17	F_u in the free shear layer.	90
4.18	F_v in the free shear layer.	90
4.19	F_w in the free shear layer.	91
4.20	V_q' in the free shear layer.	92
4.21	V_τ in the free shear layer.	92
4.22	Mean square intensities in potential flow, $x - x_o$ = 24.05 cm.	93
4.23	Streamwise development of $\overline{v^2}$ in the potential core.	94
4.24	Streamwise development of $\overline{u^2}$ in the potential core.	95
4.25	Streamwise development of $\overline{w^2}$ in the potential core.	96

Fig.		Page
4.26a	R_{uv} in the potential core.	97
4.26b	R_{uw} in the potential core.	97
4.27	$(\overline{u^2} + \overline{w^2}) / \overline{v^2}$ in the potential core.	98
4.28	$\overline{u^2}/\overline{w^2}$ in the potential core.	98
4.29	$\ell n\ \overline{u^2}$ vs. η in potential core, $x - x_o = 24.05$ cm.	99
4.30	$\ell n\ \overline{u^2}$ vs. $\ell n\ (\eta_o - \eta)$ in the potential core, $x - x_o = 24.05$ cm.	99
4.31	Spectra of v in the unaffected potential flow.	100
4.32	Spectra of u in the unaffected potential flow.	101
4.33	Spectra of w in the unaffected potential flow.	102
4.34	Spectra of v in the wall affected potential flow.	103
4.35	Spectra of u in the wall affected potential flow.	104
4.36	Spectra of w in the wall affected potential flow.	105
4.37	$\overline{u^2}$ in the reattached flow (a) x, y plane results; (b) x, z plane results.	106
4.38	$\overline{v^2}$ in the reattached flow.	107
4.39	$\overline{w^2}$ in the reattached flow.	107
4.40	$\overline{uv}$ in the reattached flow.	108
4.41	$\overline{uw}$ in the reattached flow.	108
4.42	R_{uv} in the reattached flow.	109
4.43	$\overline{u^3}$ in the reattached flow (a) x, y plane results; (b) x, z plane results.	110
4.44	$\overline{v^3}$ in the reattached flow.	111
4.45	$\overline{w^3}$ in the reattached flow.	111
4.46	$\overline{u^2v}$ in the reattached flow.	112
4.47	$\overline{uv^2}$ in the reattached flow.	112
4.48	$\overline{u^2w}$ in the reattached flow.	113
4.49	$\overline{uw^2}$ in the reattached flow.	113
4.50	S_u in the reattached flow (a) x, y plane results; (b) x, z plane results.	114

Fig.		Page
4.51	S_v in the reattached flow.	115
4.52	S_w in the reattached flow.	115
4.53	F_u in the reattached flow (a) x, y plane results;	
	(b) x, z plane results.	116
4.54	F_v in the reattached flow.	117
4.55	F_w in the reattached flow.	117
4.56	V_q' in the reattached flow.	118
4.57	V_τ in the reattached flow.	118
4.58	u spectra, $x - x_o = 36.89$ cm.	119
4.59	v spectra, $x - x_o = 36.89$ cm.	120
4.60	w spectra, $x - x_o = 36.89$ cm.	121
4.61	u spectra, $x - x_o = 75.06$ cm.	122
4.62	v spectra, $x - x_o = 75.06$ cm.	123
4.63	w spectra, $x - x_o = 75.06$ cm.	124
4.64	u spectra, $x - x_o = 151.51$ cm.	125
4.65	v spectra, $x - x_o = 151.51$ cm.	126
4.66	w spectra, $x - x_o = 151.51$ cm.	127
5.1	Streamwise development of γ.	153
5.2	Convergence of γ, $x - x_o = 36.41$ cm.	153
5.3 (a-f)	Typical plots from the correlation analysis.	154-159
5.4	$R_{11}(0, 0, r)$, $x - x_o = 24.14$ cm.	160
5.5	$R_{22}(0, 0, r)$, $x - x_o = 24.14$ cm.	160
5.6	$R_{33}(0, 0, r)$, $x - x_o = 24.14$ cm.	161
5.7	$R_{12}(0, 0, r)$, $x - x_o = 24.14$ cm.	161
5.8	$R_{11}(0, r, 0)$, $x - x_o = 24.02$ cm.	162
5.9	$R_{22}(0, r, 0)$, $x - x_o = 24.02$ cm.	162
5.10	$R_{33}(0, r, 0)$, $x - x_o = 24.09$ cm.	163
5.11	$R_{21}(0, r, 0)$, $x - x_o = 24.02$ cm.	163

Fig.		Page
5.12	$R_{II}(0, 0, r)$, $x - x_o = 24.14$ cm.	164
5.13	Variation of γ_A, γ_B; $x - x_o = 24.14$ cm.	164
5.14	Conditionally sampled $R_{11}(0, 0, r)$, $x - x_o =$ 24.14 cm, $\eta = - 0.074$.	165
5.15	Conditionally sampled $R_{22}(0, 0, r)$, $x - x_o =$ 24.14 cm, $\eta = - 0.074$.	165
5.16	Conditionally sampled $R_{12}(0, 0, r)$, $x - x_o =$ 24.14 cm, $\eta = - 0.074$.	166
5.17	Conditionally sampled $R_{12}(0, 0, r)$, $x - x_o =$ 24.14 cm, $\eta = + 0.024$.	166
5.18	Conditionally sampled $R_{11}(0, r, 0)$, $x - x_o =$ 24.02 cm, $\eta = + 0.003$.	167
5.19	Conditionally sampled $R_{22}(0, r, 0)$, $x - x_o =$ 24.02 cm, $\eta = + 0.003$.	167
5.20	$R_{11}(0, 0, r)$, $x - x_o = 36.41$ cm.	168
5.21	$R_{22}(0, 0, r)$, $x - x_o = 36.41$ cm.	168
5.22	$R_{33}(0, 0, r)$, $x - x_o = 36.41$ cm.	169
5.23	$R_{12}(0, 0, r)$, $x - x_o = 36.41$ cm.	169
5.24	$R_{11}(0, r, 0)$, $x - x_o = 36.89$ cm.	170
5.25	$R_{22}(0, r, 0)$, $x - x_o = 36.89$ cm.	170
5.26	$R_{33}(0, r, 0)$, $x - x_o = 36.89$ cm.	171
5.27	$R_{21}(0, r, 0)$, $x - x_o = 36.89$ cm.	171
5.28	Autocorrelation of u, $x - x_o = 36.89$ cm.	172
5.29	Autocorrelation of v, $x - x_o = 36.89$ cm.	173
5.30	Autocorrelation of w, $x - x_o = 36.89$ cm.	174
5.31	$R_{II}(0, 0, r)$ and $R_{II}(0, r, 0)$, $x - x_o = 36.41$ cm.	175
5.32	Variation of γ_A and γ_B, $x - x_o = 36.41$ cm.	175
5.33	Conditionally sampled $R_{11}(0, 0, r)$, $x - x_o =$ 36.41 cm, $\eta = - 0.075$.	176

Fig.		Page
5.34	Conditionally sampled $R_{22}(0, 0, r)$, $x - x_o$ = 36.41 cm, η = - 0.075.	176
5.35	Conditionally sampled $R_{11}(0, 0, r)$, $x - x_o$ = 36.41 cm, η = - 0.051.	177
5.36	Conditionally sampled $R_{22}(0, 0, r)$, $x - x_o$ = 36.41 cm, η = - 0.051.	177
5.37	Conditionally sampled $R_{11}(0, 0, r)$, $x - x_o$ = 36.41 cm, η = - 0.026.	178
5.38	Conditionally sampled $R_{22}(0, 0, r)$, $x - x_o$ = 36.41 cm, η = - 0.026.	178
5.39	Conditionally sampled $R_{11}(0, 0, r)$, $x - x_o$ = 36.41 cm, η = - 0.001.	179
5.40	Conditionally sampled $R_{22}(0, 0, r)$, $x - x_o$ = 36.41 cm, η = - 0.001.	179
5.41	Conditionally sampled $R_{11}(0, 0, r)$, $x - x_o$ = 36.41 cm, η = + 0.023.	180
5.42	Conditionally sampled $R_{22}(0, 0, r)$, $x - x_o$ = 36.41 cm, η = + 0.023.	180
5.43	Conditionally sampled $R_{12}(0, 0, r)$, $x - x_o$ = 36.41 cm, η = - 0.051.	181
5.44	Conditionally sampled $R_{12}(0, 0, r)$, $x - x_o$ = 36.41 cm, η = - 0.026.	181
5.45	Conditionally sampled $R_{12}(0, 0, r)$, $x - x_o$ = 36.41 cm, η = - 0.001.	182
5.46	Conditionally sampled $R_{12}(0, 0, r)$, $x - x_o$ = 36.41 cm, η = + 0.023.	182
5.47	Conditionally sampled $R_{11}(0, r, 0)$, $x - x_o$ = 36.89 cm, η = + 0.002.	183

Fig.		Page
5.48	Conditionally sampled $R_{22}(0, r, 0)$, $x - x_o$ = 36.89 cm, η = + 0.002.	183
5.49a	Sketch of proposed large eddy structure.	184
5.49b	Sketch of the effect of a large eddy on the potential flow.	184
5.50	$R_{11}(0, 0, r)$, $x - x_o$ = 77.64 cm.	185
5.51	$R_{22}(0, 0, r)$, $x - x_o$ = 77.64 cm.	185
5.52	$R_{33}(0, 0, r)$, $x - x_o$ = 77.64 cm.	186
5.53	$R_{12}(0, 0, r)$, $x - x_o$ = 77.64 cm.	186
5.54	$R_{11}(0, r, 0)$, $x - x_o$ = 75.14 cm, and conditionally sampled results at η = + 0.003.	187
5.55	$R_{22}(0, r, 0)$, $x - x_o$ = 75.14 cm, and conditionally sampled results at η = + 0.003.	187
5.56	$R_{33}(0, r, 0)$, $x - x_o$ = 75.06 cm.	188
5.57	$R_{21}(0, r, 0)$, $x - x_o$ = 75.14 cm.	188
5.58	Autocorrelation of u, $x - x_o$ = 75.06 cm.	189
5.59	Autocorrelation of v, $x - x_o$ = 75.06 cm.	190
5.60	Autocorrelation of w, $x - x_o$ = 75.06 cm.	191
5.61	Variation of γ_A, γ_B; $x - x_o$ = 77.64 cm.	192
5.62	$R_{II}(0, 0, r)$, $x - x_o$ = 77.64 cm, $R_{II}(0, 0, r)$, $x - x_o$ = 75.14 cm.	192
5.63	Conditionally sampled $R_{11}(0, 0, r)$, $x - x_o$ = 77.64 cm, η = - 0.074.	193
5.64	Conditionally sampled $R_{22}(0, 0, r)$, $x - x_o$ = 77.64 cm, η = - 0.074.	193
5.65	Conditionally sampled $R_{11}(0, 0, r)$, $x - x_o$ = 77.64 cm, η = - 0.025.	194
5.66	Conditionally sampled $R_{22}(0, 0, r)$, $x - x_o$ = 77.64 cm, η = - 0.025.	194

Fig.		Page
5.67	Conditionally sampled $R_{11}(0, 0, r)$, $x - x_o$ = 77.64 cm, η = + 0.025.	195
5.68	Conditionally sampled $R_{22}(0, 0, r)$, $x - x_o$ = 77.64 cm, η = + 0.025.	195
5.69	Conditionally sampled $R_{12}(0, 0, r)$, $x - x_o$ = 77.64 cm, η = - 0.025.	196
5.70	Conditionally sampled $R_{12}(0, 0, r)$, $x - x_o$ = 77.64 cm, η = + 0.025.	196
5.71	Conditionally sampled $R_{11}(0, r, 0)$, $x - x_o$ = 75.14 cm, η = - 0.051.	197
5.72	Conditionally sampled $R_{22}(0, r, 0)$, $x - x_o$ = 75.14 cm, η = - 0.051.	197
5.73	Conditionally sampled $R_{21}(0, r, 0)$, $x - x_o$ = 75.14 cm, η = + 0.002.	197
5.74	$R_{11}(0, 0, r)$, $x - x_o$ = 151.11 cm.	198
5.75	$R_{22}(0, 0, r)$, $x - x_o$ = 151.11 cm.	198
5.76	$R_{33}(0, 0, r)$, $x - x_o$ = 151.11 cm.	199
5.77	$R_{12}(0, 0, r)$, $x - x_o$ = 151.11 cm.	199
5.78	$R_{11}(0, r, 0)$, $x - x_o$ = 151.11 cm.	200
5.79	$R_{22}(0, r, 0)$, $x - x_o$ = 151.11 cm.	200
5.80	$R_{33}(0, r, 0)$, $x - x_o$ = 151.11 cm.	201
5.81	$R_{21}(0, r, 0)$, $x - x_o$ = 151.11 cm.	201
5.82	Autocorrelation of u, $x - x_o$ = 151.11 cm.	202
5.83	Autocorrelation of v, $x - x_o$ = 151.11 cm.	203
5.84	Autocorrelation of w, $x - x_o$ = 151.11 cm.	204
5.85	$R_{II}(0, 0, r)$ and $R_{II}(0, r, 0)$, $x - x_o$ = 151.11 cm.	205
5.86	Variation of γ_A and γ_B, $x - x_o$ = 151.11 cm.	205
5.87	Conditionally sampled $R_{11}(0, 0, r)$, $x - x_o$ = 151.11 cm, η = - 0.050.	206

Fig.		Page
5.88	Conditionally sampled $R_{22}(0, 0, r)$, $x - x_o$ = 151.11 cm, η = - 0.050.	206
5.89	Conditionally sampled $R_{11}(0, 0, r)$, $x - x_o$ = 151.11 cm, η = - 0.025.	207
5.90	Conditionally sampled $R_{22}(0, 0, r)$, $x - x_o$ = 151.11 cm, η = - 0.025.	207
5.91	Conditionally sampled $R_{11}(0, 0, r)$, $x - x_o$ = 151.11 cm, η = + 0.025.	208
5.92	Conditionally sampled $R_{22}(0, 0, r)$, $x - x_o$ = 151.11 cm, η = + 0.025.	208
5.93	Conditionally sampled $R_{12}(0, 0, r)$, $x - x_o$ = 151.11 cm, η = - 0.050.	209
5.94	Conditionally sampled $R_{12}(0, 0, r)$, $x - x_o$ = 151.11 cm, η = + 0.025.	209
5.95	Conditionally sampled normal correlations, $x - x_o$ = 151.11 cm (a) $R_{11}(0, r, 0)$; (b) $R_{22}(0, r, 0)$; (c) $R_{21}(0, r, 0)$.	210
5.96	Conditionally sampled $R_{11}(0, r, 0)$, $x - x_o$ = 151.11 cm, η = + 0.003.	210
5.97	Conditionally sampled $R_{22}(0, r, 0)$, $x - x_o$ = 151.11 cm, η = + 0.003.	211
5.98	Conditionally sampled $R_{21}(0, r, 0)$, $x - x_o$ = 151.11 cm, η = + 0.003.	211
5.99	Autocorrelation of u in the unaffected potential flow.	212
5.100	Autocorrelation of v in the unaffected potential flow.	213
5.101	Autocorrelation of w in the unaffected potential flow.	214

Fig.		Page
5.102	$R_{11}(0, 0, r)$ in the unaffected potential flow.	215
5.103	$R_{22}(0, 0, r)$ in the unaffected potential flow.	215
5.104	$R_{33}(0, 0, r)$ in the unaffected potential flow.	216
5.105	$R_{11}(0, r, 0)$, $R_{22}(0, r, 0)$ and $R_{33}(0, r, 0)$ in the unaffected potential flow.	217
A.1	Transverse component effect on ψ_{eff}.	236
A.2	Cosine law at large $\Delta\psi$.	237
B.1	Calculated V and $\overline{uv}$ in free shear layer, ϵ dependence included.	244
B.2	Calculated V and $\overline{uv}$ in free shear layer, no ϵ dependence.	245
B.3	$\overline{u^2} - \overline{v^2}$ in the reattached flow.	246
B.4	Calculated V and $\overline{uv}$ in reattached flow, without normal stress term.	247
B.5	Calculated V and $\overline{uv}$ in reattached flow with normal stress term.	248
C.1	Homogeneous unbounded potential flow for Phillips' theory.	261
C.2	Coordinates for potential flow outside linearly growing shear layers.	261
C.3	Solid wall and image layer.	262
C.4	Effect of the wall on $\overline{v^2}$, $\overline{u^2}$ and $\overline{w^2}$.	262
C.5	Effect of the wall on calculated $R_{11}(0, 0, r)$ and $R_{33}(0, 0, r)$.	263

PRINCIPAL NOTATION

A	Hot wire calibration constant, Eqn. (2.2) or fixed probe in correlation measurements.
B	Hot wire calibration constant, Eqn. (2.2) or moving probe in correlation measurements.
B'	Hot wire calibration constant, Eqn. (2.3).
c_f	$\equiv 2\tau_w/U_1^2$, skin friction coefficient.
E	Anemometer output voltage, Eqn. (2.2).
F_u, F_v, F_w	Flatness factor of u, v and w respectively.
h	Distance from lip to wind tunnel floor, fig. 2.1b.
I(t)	Intermittency function.
k	Wave-number.
$\underset{\sim}{k}$	Vector wave-number.
k_1, k_3	Streamwise and spanwise components, respectively, of k.
P	Total pressure.
p	Static pressure.
p'	Fluctuating static pressure.
q^2	$\equiv u^2 + v^2 + w^2$, twice the turbulent kinetic energy.
R_{ij}	Correlation of u_i at probe A and u_j at probe B; direction of separation unspecified.
$R_{ij}(0, 0, r)$	Spanwise correlation of u_i and u_j.
$R_{ij}(0, r, 0)$	Normal correlation of u_i and u_j.
$R_{ij}(r, 0, 0)$	Streamwise correlation of u_i and u_j.
R_{uv}	$\equiv \overline{uv}/\sqrt{\overline{u^2}}\sqrt{\overline{v^2}}$, correlation coefficient of $\overline{uv}$.
R_{uw}	$\equiv \overline{uw}/\sqrt{\overline{u^2}}\sqrt{\overline{w^2}}$, correlation coefficient of $\overline{uw}$.
r	Probe separation.
r'	$\equiv U_c t$.
S_u, S_v, S_w	Skewness of u, v and w respectively.
t	Time or time delay.

U, V, W	Total velocity in the x, y, z directions, respectively, Sections 2.3 and 2.4 and Appendix A, <u>otherwise</u> mean velocity.
U_c	Convection velocity.
U_{eff}	Effective velocity, Eqn. (2.6).
U_1	Free stream velocity.
U_2	Secondary stream velocity.
u, v, w	Fluctuating velocity in the x, y, z directions.
u_i	Fluctuating velocity; $u_1 = u$, $u_2 = v$, $u_3 = w$; similarly for j.
V_q	$\equiv (\overline{p'v} + \frac{1}{2}\overline{q^2 v}) / \overline{q^2}$, convection velocity of the turbulent kinetic energy.
V_q'	$\equiv (\overline{v^3} + \overline{uv^2}) / (\overline{u^2} + \overline{v^2})$, the measurable approximation to V_q.
V_τ	$\equiv \overline{uv^2} / \overline{uv}$, convection velocity of the shear stress.
x, y, z	Coordinates, defined in figs. 2.1b and 2.2.
x_o	Effective origin of mixing layer.
$\underset{\sim}{x}$	Vector position.
y_o	Effective origin of potential motion.

<u>Greek Symbols</u>

β	Correction factor for hot wire calibration constant, B, Eqn. (A.3).
γ	Intermittency factor <u>or</u> inclination of plane of cross wires to the x axis.
Δ	Denotes difference.
ΔU	$\equiv U_1 - U_2$.
Δt	"Hold time", Section 5.1.
$\Delta\psi$	Angle increment for yaw calibration, Eqn. (2.4).
$\Delta\gamma_{cm}$	Change in γ between calibration and measurement.

$\Delta\psi_{cm}$	Change in ψ_{eff} between calibration and measurement.
δ	Shear layer thickness or delta function.
δ^*	Boundary layer displacement thickness.
δ_p	Potential core thickness, fig. 3.5.
ε	Denotes $x - x_0$, Appendix A, otherwise dissipation rate of turbulent kinetic energy.
η	$\equiv y/(x - x_0)$, normalized vertical distance in mixing layer similarity form.
η_0	Effective origin for potential motion.
η_{u0}, $\eta_{\tau 0}$	Position near the wall where $\partial U/\partial y = 0$ and $\tau = 0$, respectively, in reattached flow.
η_w	$\equiv h/(x - x_0)$, position of the wall in mixing layer similarity form.
θ_0	Initial boundary layer momentum thickness.
$\theta(\underset{\sim}{k})$	Forcing spectrum for potential motion, Eqn. (C.3).
θ_{11}, θ_{33}	Spectrum constants, Eqn. (C.9).
i	$\equiv \sqrt{-1}$.
ν	Kinematic viscosity.
τ	$\equiv -\overline{uv}$, kinematic shear stress.
τ_w	Wall shear stress.
Φ	Unnormalized spectral density.
ϕ	Velocity potential, Appendix A, otherwise normalized spectral density, Eqn. (4.8).
χ_{11}, χ_{33}	Spectrum constants in mixing layer similarity form.
ψ_{eff}	Effective angle for cosine law.
ω	Circular frequency.

Subscripts

A, B	Fixed and moving probe respectively, in correlation measurements.

bℓ	Boundary layer.
c	Calibration position value, except for U_c.
m	Measurement position value.
mℓ	Mixing layer.
N	Non-turbulent.
T	Turbulent.

Overbar	Denotes time average.

CHAPTER 1

INTRODUCTION

It is well known that the presence of a solid surface has a large effect on turbulent shear layer structure and it is often convenient to distinguish between unbounded free shear layers, far away from a solid wall, and wall-bounded flows, or wall layers for short (Townsend, 1976, p. 105). This division is very important in considering closure assumptions for calculation methods which are gross simplifications of, and hence are less general than, the Navier-Stokes equations. For example, any representative turbulence length scale varies as the distance from the wall near a solid surface but is roughly constant in a free shear layer. Many current models for the pressure-strain term in the shear stress transport equation must also be altered significantly in the presence of a solid surface (e.g. Launder, Reece and Rodi, 1975). The major aim of this work is to document the changes in turbulence structure as a free shear layer becomes a wall bounded flow in the hope that the results may help to unify the modelling of turbulent shear layers.

The primary motivation for the present work was the finding by Castro (1973), in a highly distorted free shear layer, and Chandrsuda (1975), in a flow over a backward facing step, that the third order moments in a free mixing layer were significantly altered as the flow approached the wind tunnel floor. It was felt that a more detailed study of this transformation in the absence of other distortions would be worthwhile. The simple case of a turbulent mixing layer growing to reattach to the wind tunnel floor on the high speed side (see fig. 2.1) was chosen. The results of Chapters 3 and 4 show that the flow remains a thin shear layer (TSL) over the region of interest.

The wall alters the flow in two ways. Provided that the floor boundary layer thickness is only a small fraction of the thickness of the potential core, the wall can be replaced conceptually by the instantaneous mirror image of the free shear layer in the wall, so that the "image constraint" boundary condition, i.e. $v = 0$ at the wall is satisfied. Obviously, the "no slip constraint" boundary condition $u = w = 0$ at the wall also applies in a real fluid, hence the need to keep the floor boundary layer thickness small. Fig. 3.4 shows this was achieved for most of the length of the potential core in the present experiment. Note that here, and throughout this thesis the term "free shear layer" denotes a flow that is unaffected by the no slip constraint rather than a flow that is not influenced by a wall (called an unbounded flow). This usage has a practical justification as it will be shown that at least some previous plane mixing layer experiments were influenced by image constraint. Once the flow has reattached (or equivalently the potential core has been absorbed) the shear layer structure will be directly influenced by the no slip constraint. The theoretical work of Hunt and Graham (1978) and the experimental studies of Uzkan and Reynolds (1967) and Thomas and Hancock (1977) which are reviewed in Section 1.2.4 and discussed further in Chapters 4 and 6 have clarified the different effects of these two constraints.

If the working section had been sufficiently long the present flow would have become a fully developed wall jet. However, most practical wall jets can be more usefully considered as an interaction (in the sense of Dean and Bradshaw, 1976) of a turbulent boundary layer and a mixing layer of comparable size. Although such a flow is considerably more complicated than that studied here, the present results should be useful in understanding aspects of the interaction.

The secondary motivation of this study was to further investigate the free mixing layer structure, which is the subject of much controversy, principally over the two dimensionality or otherwise of the large structure. Conditionally sampled spanwise and normal correlation measurements presented in Chapter 5 show that the turbulent motion is essentially three-dimensional, while the corresponding scales of the potential motion are much larger. Using the theoretical analysis described in Appendix C this result is plausibly attributed to the nature of the potential flow as such, and hence is not due to the basic two-dimensionality of the large eddies as has been suggested by previous workers.

1.2 Literature Review

For reasons that should become obvious it is no longer possible to ignore the influence of initial and boundary conditions on turbulent free shear layer structure, even if attention is to be focussed primarily on the "fully developed" region, and a review of current knowledge of all parts of the flow is necessary.

1.2.1 Instability and Transition Region

Of most importance are the theoretical works of Michalke (for example Michalke, 1972 and references therein) and the combined theoretical and experimental studies of Freymuth (1966) and Miksad (1970, 1972 and 1973). Perhaps unfortunately, the bulk of their experimental results were taken for the conceptually easier case of transition forced by sound at a constant frequency. However, Browand (1966) and Miksad suggest that there are qualitative similarities with unforced transition. Freymuth concluded from his experimental results that instability is independent of Mach number and axisymmetry: the latter result is useful since many mixing layer studies have been

made in the initial regions of axisymmetric jets. He divided the mixing layer into four regions:-

(i) the "transformation region" very close to the lip where there is a single maximum in the disturbance amplitude at the forcing frequency.

(ii) the "linear region" where the phase and disturbance amplitude are well predicted by the two-dimensional, linear, inviscid, spatial stability analysis developed principally by Michalke.

(iii) the "non linear region" of vortex roll up and pairing, and,

(iv) the fully turbulent region.

This division can be seen clearly in Yule (1978, fig. 11).

Free shear layers are inviscidly unstable, i.e. as the Reynolds number increases, the viscous solution to the disturbance equation asymptotes to the inviscid solution (see Michalke, 1972, pp. 217-218). This simplification, which only occurs in flows that have an inflexion point in the mean velocity profile, means that regions (I) and (II) are reasonably well understood. Region (III) is not, for several related reasons. The now dominant non-linear terms have yet to be satisfactorily analysed. Furthermore the randomness in initial and boundary conditions now strongly influence the flow, even for the simpler case of forced transition.

It is now that differences between plane and axisymmetric mixing layers appear. In contrast to wall flows it appears (Miksad, 1970) that the secondary instability may first reinforce the two-

dimensionality of the plane mixing layer before amplifying the three-dimensional disturbances. In axisymmetric flow the secondary instability appears to be of the Widnall-Sullivan type (Yule, 1978; Chandrsuda, Mehta, Weir and Bradshaw, 1978) dependent on the ratio of the vortex ring radius to vortex core radius, by which the mutual interation of the vortex rings quickly produces a three-dimensional large structure.

The difficulties mentioned above have meant that most information on the influence of the transition region is empirical. This is reviewed in Section 1.2.3.

1.2.2 Fully Developed Free Mixing Layer

Free turbulent mixing between uniform streams may be one class of self-preserving flows in that a single length and velocity scale are sufficient to collapse the distribution of mean quantities at any downstream station (Townsend, 1976, pp. 195-198). This possible simplification has greatly influenced studies of turbulent flows especially in the division between the flow influenced by initial conditions (regions (I), (II), possibly (III)) and the fully developed flow. For genuine self-preservation the former must not influence the latter. However, the mixing layer literature is dominated by cases where this influence is not negligible.

Self-preservation analysis is a special case of the statistical theory of turbulence, which in itself has many drawbacks, the most important being the closure problem. Any system of time-averaged equations derived from the Navier-Stokes equations contains more unknowns than equations to solve. This has prompted many workers to search for a more satisfactory description of turbulence. The dominant approach at present is to search for coherent structures; identifiable and repeatable motions whose randomness in size and

phase is sufficient to give the flow a statistical appearance, but whose dynamics, it is hoped, is crucial. The biggest impetus to this approach came from the work of Brown and Roshko (1974) in mixing layers.

Prior to their work the accepted view was that the mixing layer is dominated by very strong but highly three-dimensional large eddies. These eddies, whose scales are comparable to the shear layer thickness (in this thesis the term "large structure" implies a scale of at least the shear layer thickness) dominate the entrainment process, bear most of the shear stress and are responsible for the extraction of energy from the mean flow by the turbulence (Townsend, 1976, Chapter 4, Section 6.11ff; Tennekes and Lumley, 1972, Chapters 1 and 2). An understanding of their role is crucial since at sufficiently high Reynolds number the small scale motion, responsible for nearly all of the dissipation into thermal internal energy, simply adjusts to the energy transfer from low wave-numbers.

Several good reviews of mixing layer data are already available (Murthy, 1975; Rodi, 1973; Brown and Roshko, 1974 and Batt, 1977) so the task of reviewing the literature in detail will not be attempted here. Rodi (1973) compared the reliability of turbulence measurements in mixing layers and concluded that the measurements of Castro (1973) made in the present rig are among the best available.

Spatial correlation measurements are a good way of determining the average large eddy structure because the correlation between two signals separated by a distance r can only have contributions from eddies whose scale is the same order as or larger r_Λ. The technique is not free from ambiguity (Townsend, 1976, pp. 118-120), but it is a sufficiently powerful tool that one of the aims of the present study is to extend the number of available correlation measurements. The interpretation of correlations is largely kinematic because the equations for the velocity covariances (the unnormalized

correlations) are very complicated, while there exist simple kinematic constraints on the behaviour of correlations. For example from the continuity equation there can be no net flow of the fluctuating normal component v across the x, y plane, thus R_{22} $(r_1, 0, r_3)$ must have a negative loop (Tennekes and Lumley, pp. 252-253 and Townsend, 1976, pp. 16-17 for a more general discussion). From a set of correlation measurements a large eddy structure can be found to account for the sign of the correlations at large r. Usually only a few simple eddy forms yield the correct signs. The method is well described by Grant (1958) who made extensive correlation measurements in the wake of a circular cylinder. A simple calculation of the large eddy structure showed that the contribution to the correlations R_{11} (0, 0, r), R_{11} (r, 0, 0), R_{33} (0, 0, r) and R_{33} (r, 0, 0) were appreciable (about 13%) even at small separation (see his fig. 4). Thus the large eddies have appreciable energy. Grant's proposed large eddy structure, a vortex pair eddy had no vertical component so he suggested the R_{22} results arose from another structure which he termed "mixing jets". They originate in the centre of the wake at roughly regular intervals. Bradshaw, Ferriss and Johnson (1964) made fairly extensive spatial correlation measurements in the initial region of an axisymmetric jet which were satisfactorily repeated by Weber (1974). They concluded "that the large eddy structure in the mixing layer consists of a series of mixing jets which instead of lying in the x, y-plane as in the wake, move at an angle of about 45° to this plane". The latter conclusion was based on some not very accurate fourth order measurements. They found that the large eddy motion was strongly periodic in the x direction; a new mixing jet "is triggered by the preceding one at a late stage in the life of the latter". This conclusion is similar to Bruun's (1979) description of eddy behaviour. Bradshaw et al (1964) estimated that the large eddies in the mixing layer bear about one

quarter of the shear stress.

Brown and Roshko's (1974) flow visualizations of high pressure two stream mixing layers with varying U_2/U_1 show clearly two-dimensional large structures. Their mixing layer grew linearly by the process of vortex pairing, the mechanism also observed by Winant and Browand (1974) at low Reynolds numbers. Since the growth rate of Brown and Roshko's mixing layer was close to a consensus of previous measurements implying that the shear stress distribution was also normal, they suggested that the two-dimensional large structure was also normal. This conclusion was challenged by Chandrsuda et al (1978) who suggested that what will be called Brown-Roshko structures (B-R for short) persist only in the absence of mechanisms that cause the flow to go from Stage (III) to Stage (IV) in Freymuth's division. Specifically they suggested that B-R structures would not be formed if the initial boundary layer was turbulent or if the free stream turbulence level was sufficiently high; the latter is almost inevitable in a single stream mixing layer with a nominally zero secondary stream. In this flow Chandrsuda et al observed that the breakdown mechanism involved helical pairing of the initially "straight" vortex lines - see their figs. 2 and 3 which were taken in the present rig.

The strongest quantitative evidence claimed for the B-R interpretation have been measurements made outside the shear layer. Dimotakis and Brown (1976) found a strong periodicity in their u-component autocorrelation measurements outside a two stream mixing layer. In a similar flow Jones, Planchon and Hammersley (1973) found that R_{11} (r, 0, 0) has a negative peak of - 0.57 at a separation of about the shear layer thickness. Their R_{11} (0, 0, r) measurements as well as those of Browand and Troutt (1979) have integral scales, defined as $\int_0^\infty R_{11}$ (0, 0, r) dr, of about ten shear layer thicknesses which is considerably higher than the integral scale measured near

maximum γ. Wygnanski, Oster, Fiedler and Dziomba (1979) disputed the claims of Chandrsuda et al largely on the basis of R_{11} (0, 0, r) measured just outside their two stream mixing layers. The scale of R_{11} (0, 0, r) was not significantly changed by making the initial boundary layer turbulent using vortex generators or trip wires or by making the free stream highly turbulent using a grid placed well upstream. They concluded that the large structure remained basically two-dimensional despite these strong perturbations.

Thus there is fundamental disagreement over the large structure in the turbulent mixing layer; B-R structures are found in some flows, e.g. Dimotakis and Brown, Fiedler (1975) but not in others (e.g. Batt, 1977; Bates, 1977). Statements of opposing views can be found in Roshko (1976) and Bradshaw (1980, from which many of the present ideas are drawn). Wygnanski et al interpreted their R_{11} (0, 0, r) measurements within the shear layer which show small non-zero "tails" at large r as indicating that the large eddies are weak in the sense of Townsend's now abandoned "large eddy equilibrium hypothesis". The difficulty with this interpretation is the difficulty of imagining a structure that contributes to turbulent diffusion, which is affected by the large eddies and is of the same order as the dissipation, ε, while not contributing to $\overline{q^2}$ itself which is of the order of $(\varepsilon\delta)^{2/3}$ where δ is the shear layer thickness. Furthermore, the conditionally sampled correlations presented in Chapter 5 show that very little of the "tail" in R_{11} (0, 0, r) is due to the turbulent motion. An alternative explanation is that the large structures are not perfectly aligned in the spanwise direction so that statistical measures such as correlations are sufficiently degraded to suggest three-dimensionality. However, the random departures from two-dimensionality must be of the order of the shear layer thickness to explain the correlations in the fully turbulent region. Even if a line vortex could be contorted so violently and not lose its basic

structure it is hard to see such a structure giving large scales of R_{11} (0, 0, r) in the potential flow. Two probes separated by a distance of the order of the wrinkling would then be, for considerable periods of time, in regions that are strongly anticorrelated because of the large negative loop in R_{11} (r, 0, 0) mentioned earlier. Thus it is unlikely that the spanwise integral scale in the potential flow would be an order of magnitude greater than δ. A similar conclusion based on different arguments is given by Pui and Gartshore (1979).

The most plausible explanation for the large scales in the potential flow is that they are due partly to the nature of the potential flow itself. The analysis of Appendix C shows that the relevant scale for the potential flow is the distance from the shear layer and this is strongly supported by the results of Chapter 5. Thus it is possible to measure arbitrarily large scales relative to the shear layer thickness simply by measuring sufficiently far from the turbulence. The present work extends the number of available correlation measurements in the potential flow and it is shown in Chapter 5 that a three-dimensional large structure is necessary to explain all the correlations.

It should be realised that discussion of flow structure is inevitably circular and conclusions are not independent of initial assumptions. This makes it difficult to discuss both sides of a controversy fairly and to use terms and concepts unambiguously. There is a consequent need for care and clarity in the use of terminology; this was pointed out for the present case by Yule (1978, 1979)*.

---

* Turbulence research is not unique in this regard. It is common and perhaps inevitable that problems like these arise in scientific research particularly during times of controversy - see T. S. Kuhn "The Structure of Scientific Revolutions", Chicago U.P., 1969 and Paul Feyerabend "Against Method", NLB 1975 and the discussion of these views and related matters in A. Musgrove (Ed.) "Criticism and the Growth of Knowledge", C.U.P., 1970.

Unfortunately, little will be said about the more general question of whether turbulence is a statistical process (do we accept defeat in the face of the enormous complexity of initial and boundary conditions?) or whether the search for coherent structures will lead to a more complete understanding of the dynamics. If the large eddies in a mixing layer are two-dimensional and hence coherent, then the implications for classical concepts like vortex stretching and the energy cascade are enormous. But coherent structures do not have to be two-dimensional; certainly they cannot be in a boundary layer. That there is controversy over one aspect suggests that solutions to these questions will take a long time.

1.2.3 The Effects of Initial and Boundary Conditions

For the reasons given in Section 1.2.1 most work on the effects of initial conditions has been experimental. In the absence of imposed length scales any length such as x_d, the distance to full development, must scale as:-

$$\frac{x_d}{\theta_o} = f\left(\frac{\Delta U \theta_o}{\nu}\right)$$

where θ_o is the initial boundary layer momentum thickness, ΔU is the velocity difference across the shear layer and f denotes functional dependence. Since the instability is "inviscid" the Reynolds number dependence should be weak (Bradshaw, 1966). However, this simple scaling does not work in general, suggesting the importance of secondary instabilities related to imposed length scales such as the scale of the free stream turbulence or the nozzle radius for vortex ring type instabilities. Bradshaw (1966) and Husain and Hussain (1978) found that the approach to full development was faster if the initial

boundary layer was laminar. Typically $\overline{u^2}$, $\overline{v^2}$ and $\overline{uv}$ overshoot their asymptotic values before returning to them, showing that vortex pairing produces a high shear stress, while $\overline{w^2}$ rises monotonically (Yule, 1978). For a turbulent initial boundary layer the corresponding behaviour is monotonic. Typically the origin for the fully developed flow is upstream of the lip for a laminar initial boundary layer and downstream for a turbulent initial boundary layer. Thus the growth rate of the shear layer close to the lip must be higher than the asymptotic value in the former case, hence so must $\overline{uv}$; the two quantities are directly related in self-preserving flows (see Appendix B). Bradshaw (1966) suggested that full development is not reached until a distance of about 1000 θ_o or until $x \simeq \nu/\Delta u \times 10^6$. The latter value gives a higher Reynolds number than the critical Reynolds number, Re_{cr}, given by Bernal, Breidenthal, Brown, Konrad and Roshko (1979) for the appearance of streamwise "streaks" in their chemically reacting two stream mixing layers. The streaks are associated with a rapid increase in mixing within the shear layer and are remarkably persistent even in long exposure photographs. Their value for $Re_{cr} \sim 10^5$ is consistent with the observations of Clark and Markland (1973).

Batt's (1975) measurements suggest that the high spreading rate found by Wygnanski and Fiedler (1970) for a single stream mixing layer was due to a trip wire placed at the tip. However, Oster et al (1978) show that the effect of the trip at the lip when $U_2 = 0.4\ U_1$ is to decrease the spreading rate. Hussain and Zedan (1978a, 1978b) found that varying the fluctuation level in the initial boundary layer could alter the spreading rate by 20%. These fluctuations in a "laminar" boundary layer were attributed to "sloshing" of the flow probably caused by acoustic resonance in the settling chamber and contraction (see Hussain and Clark, 1977). This alteration was much larger than could be obtained by varying θ_o. They also suggested that Bradshaw's

criterion of $10^3\ \theta_o$ is conservative. However, as they point out, it is impossible to vary the initial conditions independently (even if all the important ones could be identified!) so the only satisfactory test for full development is the collapse of measured quantities using the relevant velocity and length scales (ΔU and $x - x_o$ - see Townsend, 1976, p. 198) rather than in satisfying criteria measured in another flow. Hussain and Zaman (1978) found that the variation of fluctuating strain rates, etc. is more violent in a developing axisymmetric mixing layer than in a plane mixing layer and that large fluctuations in uv occur during vortex pairing.

Oster et al (1978) found that forcing the mixing layer by flapping the trailing edge or by using sound at a constant frequency could drastically alter the spreading rate*. In the latter case, flow visualization showed the large structure to be obviously two-dimensional, but there was no tendency for the vortices to pair (see also Fiedler and Thies, 1978, and Fiedler, Korschelt and Mensing, 1978). Since the growth of Brown and Roshko's mixing layer was due to vortex pairing, this suggests that studying vortices isolated by acoustic forcing to gain an insight into mixing layer structure is bad methodology.

Chandrsuda et al (1978) suggest that B-R structures will not form if the initial boundary layer is turbulent and interpret the results of Pui and Gartshore (1979) and Sabin (1963) in two stream mixing layers as showing that the inevitable splitter plate wake can also break down B-R structures. Browand and Latigo (1979), Foss (1977)

---

* It was suggested to me by Professor Bradshaw that this could be due to the mixing layer bodily flapping in order to conserve the v-component momentum imparted by the trailing edge vibrating on a scale too large for the near field turbulence field to absorb. Once the shear layer has grown to a sufficient scale the spreading rate should decrease, as was found in the measurements.

and Husain and Hussain (1978) found that the spreading rate depends on whether the initial boundary layer is turbulent or laminar, while Birch (1977) suggests that at sufficiently high Reynolds number there is a single spreading rate independent of initial conditions. However, it would take a rig much larger than any used previously to definitely settle this important question.

The boundary conditions also have a striking effect on the flow. If the arguments of Chandrsuda et al are correct, the free stream turbulence level is very important and there are many cases where some sort of feedback mechanism is important. There are two possibilities. Feedback may be caused by the growth of the mixing layer to reattach to the wall so that the reattachment length becomes an important parameter (Dimotakis and Brown, 1976; see also Yu and Tam, 1978). Presumably the upstream effects will be qualitatively similar to those in a mixing layer over a cavity of finite length (Rockwell and Naudascher, 1979). The second possibility is acoustic disturbance dependent on wind tunnel geometry. Fiedler, Korschelt and Mensing (1978) found a dominant frequency related to the working section length and not $x - x_o$ in their spanwise temperature correlations across a slightly heated mixing layer. Fiedler and Thies (1978) show how "weak dynamic disturbances from tunnel vibrations, acoustic characteristics, etc." can "drastically influence" the flow. Pui and Gartshore (1979) found a dominant frequency in their normal correlation measurements in a two stream mixing layer which they attributed to a standing acoustic wave. They eliminated it by stiffening the trailing edge. Perhaps the most striking example is the correlation by Fiedler and Thies (1978) of spreading rate against Re_L where L is the working section length; this could only be successful if feedback was occurring.

1.2.4 The Effect of a Solid Boundary on the Flow

There are three important aspects here:-

(i) the effect of the image constraint on the potential flow;

(ii) the effect of the image on the turbulence structure of the free shear layer, and,

(iii) the combined effect of the no slip and image constraints after reattachment.

The effect of the image constraint on an eddy is easy to visualize. Consider a spherical eddy approaching the wall. The wall inhibits the vertical motion so that the sphere roughly becomes a pancake as the streamwise and spanwise scales increase relative to the normal scale. This will be called the "splat" effect.

The present work on (i) extends the analysis of Phillips (1955) who studied the unbounded potential flow above an homogeneous sheet of turbulence. The important results of Phillips' analysis are that for large y:-

$$\overline{v^2} = \overline{u^2} + \overline{w^2} \tag{1.1}$$

and:-

$$\overline{u^2}, \overline{v^2}, \overline{w^2} \sim (y - y_o)^{-4} \tag{1.2}$$

where y_o is the effective origin for the potential motion. Eqn. (1.2) has wide experimental support at least for the more easily measured $\overline{u^2}$

while the results of Townsend (see Phillips, 1955) and Sunyach and Mathieu (1969), the latter outside a mixing layer, suggest that both Eqns. (1.1) and (1.2) are valid remarkably close even to inhomogeneous shear layers.

The effect of the imposition of a solid boundary moving at the free stream speed on grid turbulence was studied experimentally by Uzkan and Reynolds (1967) and Thomas and Hancock (1977) who found reasonable agreement with the linearized "rapid-distortion" theory of Hunt and Graham (1978). The large eddy simulation of Biringen, Reynolds, Moin and Ferziger (1979) was also in reasonable quantitative agreement with the experimental results. Outside a thin viscosity dominated region, corresponding roughly to the thin floor boundary layer under the potential core in the present experiment, the effect of the image constraint on $\overline{v^2}$ extended further into the flow, about two integral length scales, than did the no slip constraint on $\overline{u^2}$ and $\overline{w^2}$. As the wall is approached $\overline{v^2}$ tends to zero with fluctuations at low wave-number decreasing first. Some low frequency energy is transferred to $\overline{u^2}$ and $\overline{w^2}$ which, theoretically, are amplified equally without a large change to the shape of their spectra. Experimentally $\overline{w^2}$ is not amplified significantly. The amplification of $\overline{u^2}$ increases downstream which is also in disagreement with the theory.

1.3 The Present Experiment

The short length of the previous section indicates how little has been done on the important problem of how an initially unbounded thin shear layer changes structure as it becomes wall bounded. The present experiment is probably the simplest realization of such a flow. Even so, the controversy over mixing layer structure necessitated detailed measurements well before reattachment, in

particular it was felt that further correlation measurements especially in the spanwise direction were necessary to gain a better understanding of the large eddy structure. The correlation measurements were continued downstream to investigate how the structure changes due to the influence of the wall. The large scales of the potential flow correlation suggest that significant contributions to the correlations within the intermittent region may come from non-turbulent fluid. The spanwise correlations of u and v therefore, were conditionally sampled in order to find the contributions from the turbulent and potential motion.

The discussion in the previous section indicates that it is necessary to measure w as well as u and v. Consequently, single probe measurements were made in the x, y and x, z planes at nominal $x - x_o$ stations of 25, 37, 50, 62, 75 and 100 cm in the free shear layer and at 125 and 150 cm in the reattached layer. Normal and spanwise correlations and autocorrelations of u, v and w were measured at 25, 37, 75 and 150 cm. Chapter 2 describes the experimental methods and Chapter 3 the mean velocity results. The single point measurements are presented in Chapter 4 and the correlations and autocorrelations in Chapter 5. Chapter 6 contains a general discussion and conclusions. Appendix A discusses the accuracy of the hot wire measurements and Appendix B describes the derivation of the normal velocity and shear stress distributions from the measured streamwise velocity using the continuity and momentum equations. The extension of Phillips (1955) analysis to compute potential correlations and to account for the presence of the wall is given in Appendix C.

This work is a comparison study to the work of Weir, Wood and Bradshaw (1980) who measured the interaction of two real mixing layers to form a two-dimensional plane jet. One of the mixing layers was heated slightly and conditionally sampled measurements were made.

The interaction altered the turbulence structure but not sufficiently to preclude a simple and reasonably accurate calculation of the flow using the superposition principle of Bradshaw, Dean and McEligot (1973) with closure assumptions strictly applicable to a single mixing layer only.

CHAPTER 2

EXPERIMENTAL TECHNIQUE AND DATA REDUCTION METHODS

2.1 Introduction

All the measurements were made in the no. 1 30" x 5" (76.2 cm x 12.7 cm) blower tunnel in the Turbulence Laboratory. The tunnel is described by Bradshaw (1972) and Shabaka (1979) so only the working section used here will be described.

As shown in fig. 2.1 a single stream mixing layer is formed at the contraction exit and grows to reattach to the wind tunnel floor. For all the measurements presented here the free stream velocity, U_1 was 16.4 ± 0.1 ms^{-1}. With the working section roof in position the free stream turbulence level, $\sqrt{\overline{u^2}}/U_1$, is about 0.1%. The level was not measured for the present configuration but a value of about 0.1% is consistent with the results of fig. 4.22 as explained in Chapter 4.

The work was done in two stages. Before the preliminary measurements were made it was felt that the floor boundary layer should be removed through a bleed slot prior to reattachment. Thus the mixing layer would interact only with a very thin boundary layer as well as the image shear layer. However, with the first rig (fig. 2.1a) we could only achieve a reduction in boundary layer thickness near reattachment of about 50%, at the cost of a fairly large step change in wall height at the slot. The main reason for this is the effect of the increasing free stream turbulence level induced in the diminishing potential core which caused rapid transition of the floor boundary layer; it was, of course, necessary to locate the step well before the reattachment point. In view of the early effect of the wall on the mixing layer structure this seemed an excessive price to pay. Any alternative arrangement for boundary layer control would also

influence the image flow. The final rig, shown in figs. 2.1b and 2.2 had no boundary layer control; the results presented in the next chapter strongly suggest that the overall effect of the floor boundary layer was small.

The early influence of the wall on the mixing layer structure was first shown by the appearance of non-zero asymptotic "tails" in the preliminary, analog, R_{11} (0, 0, r) measurements, some of which were reported by Chandrsuda et al (1978, fig. 4). The first rig was used to investigate the causes of these tails. It was found that the results were insensitive to the insertion of a vertical backplate placed above the contraction exit to form a "semi-infinite" wall, to alteration of the height of the side walls from 60 cm to 30 cm and to the use of bellmouth fairings on the top of the side walls, to improve the flow as used by Wygnanski and Fiedler (1970).

If the tail in the correlation measurements is the result of wall interference the only possible scaling for the size of the tails is:-

$$R_{11}\ (0,\ 0,\ r \to \infty) = f\ (\eta,\ \eta_w) \qquad (2.1)$$

where f denotes functional dependence and $\eta_w \equiv - h/(x - x_o)$ is the value of η at the wall. This was tested by inserting a false floor (fig. 2.1a) from x = 0 to well past the bleed slot. The results shown in fig. 2.3 support Eqn. (2.1). The second rig was built from three 30" x 72" x 1" aluminium faced blockboard panels with 1 cm wide transverse slots cut as shown in fig. 2.2. For the spanwise correlation measurements a slide was screwed to the underneath of the floor to take the department's standard traverse gear (Shabaka, 1979, fig. 2.4). For the single X probe and pitot tube measurements the slider was replaced by a disc support ring, also mounted on the

underneath of the floor, to hold the 3½" diameter disc holding the traverse gear and the yaw calibration saddle for the X probe calibrations (Section 2.3.1). For the measurements at $x - x_0 \leq 75$ cm nominally, the unused slots were taped over. Once these measurements had been completed the upstream slots were carefully refilled with Polyfilla to form a smooth surface. Static pressure tappings of 1 mm inside diameter were inserted at each station at $z = 0$, and a 1.5 cm diameter hole was drilled at $x - x_0 = 50$ cm nominally, $z = -14$ cm, for probe calibration for the downstream stations. When the measurements at successive downstream slots had been completed they, in turn, were refilled. The working section floor was carefully checked for straightness in the streamwise and spanwise direction before the measurements were started and again before the rig was taken apart, since it was necessary to climb onto the working section to mount the probes. No significant departures were found. Several traverse gears with linear potentiometer outputs monitored by a Solatron LM1420 digital voltmeter (DVM) were used. Before any traverse the initial height of the probe was set using a Vernier height gauge accurate to 0.001" and the DVM output was initialized. The probe height was then measured at the maximum distance from the floor, and usually at one or two other positions as well, and the potentiometer calibration determined. The repeatability of this method was always within 0.5%.

The reference pressure P_{ref}, the difference between the total head and the wall static pressure, p_{ref}, at $x = -6.2$ cm located on the contraction side wall, was continuously monitored using a Betz Projection Manometer. The resulting velocity is hereafter denoted U_{ref}. Δp_s, the difference between the wall static pressure at each x and the atmospheric static pressure is shown in fig. 2.4 to be small especially as the large size of the static pressure tappings relative to the boundary layer thickness will overestimate

Δp_s (see Shaw, 1960).

2.2 Mean Velocity Measurements

The mean velocity profiles were measured in the free shear layer using a 1.2 mm O.D. pitot tube and in the initial and floor boundary layers and in the reattached flow using a 1 mm O.D. pitot tube. Unless otherwise stated, the measurements were made at z = 0. The pitot tubes were connected to a Furness Controls Limited Type MDC capacitance manometer. The block diagram for these measurements is shown in fig. 2.5. By calibrating the manometer at each x against P_{ref} it was found that U_1 decreased by less than 0.5% between x = 0 and x = 75 cm. From fig. 3.2 the repeatability of the mean velocity measurements is seen to be about 1% of U_1.

No attempt was made to map the outer flow in detail, anticipating the difficulties of using an X probe accurately in regions of high V/U and high local intensities, when most of the interesting changes occurred in more accessible regions. Furthermore, it would have required significant modifications to the traverse gear to measure the outer flow at large x.

Extensive checks of the uniformity of the potential flow were made in both the normal (y) and spanwise (z) directions, some of which are shown in Chapter 3. In agreement with the measurements of Wong (1970) in the same tunnel the variation of U_1 in either direction was always within ± 0.2% which is within the uncertainty of the micro-manometer calibration.

2.3 X-Wire Measurements

All the probes used in these experiments were made by the author by soft soldering platinum cored, silver coated Wollaston wire onto DISA 55P51 X-probes. A central portion of around 1 mm was then

etched leaving an active wire 5 μm in diameter with a length to diameter ratio of between 200 - 250. All the probes were operated by DISA 55D01 constant temperature bridges. The frequency response was tested regularly by the standard square wave method and adjusted if necessary so that all wires used had a - 3 db point of about 50 kHz.

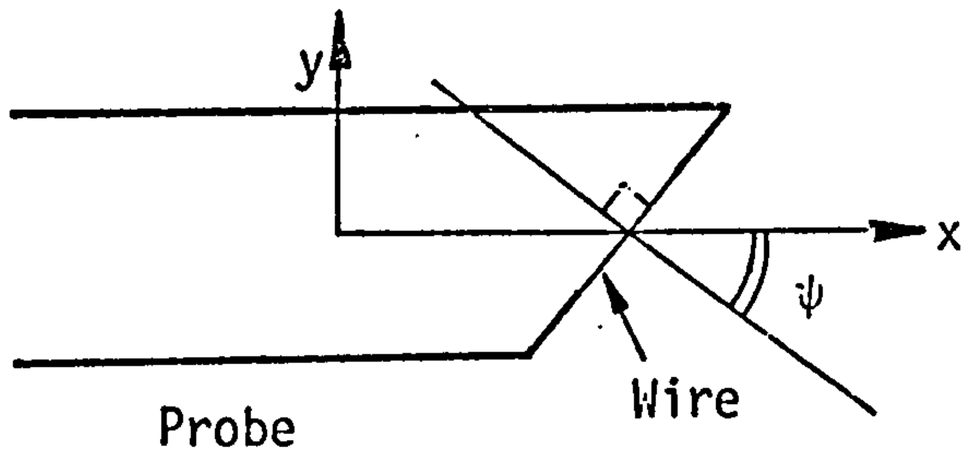
The anemometer outputs for the single probe and for the moving probe in the correlation measurements were passed through PSI 6141 signal conditioners set to a bandwidth of 1 Hz - 10 kHz. These signal conditioners have adjustable gains which were used in measuring the potential flow; gains of up to 75 were used. The signal conditioner gains were calibrated and found to be within specification. If the outputs from the other probe used in the correlation traverses had to be amplified, standard departmental PHI operational amplifiers were used. These were checked regularly for noise level, distortion and DC offsets. For each traverse the overall system gain between measurement and digitizing was found by recording sine waves of known rms voltage through the signal conditioners set to the gains used for most of the traverse. The gains for the other settings were found from the calibration mentioned above. Before digitizing the output rms voltage was measured at the entry point to the analog-to-digital converter (ADC) and the overall gain determined. The block diagram for the X-probe measurements is shown in fig. 2.6.

2.3.1 Calibration Procedure

For the single probe and normal correlation measurements the probes were calibrated at the measuring station for $x - x_o \leq 75$ cm nominally. Thereafter, the potential core fluctuations were either too intense or there was no potential core, so the probes were calibrated at $x - x_o = 75$ cm nominally. The use of the slider for the spanwise correlation measurements also necessitated upstream

calibration.

The X-probes were calibrated statically using King's law and by assuming each wire responds only to velocity fluctuations normal to it (called the "cosine law assumption").



The response equation for the wire measuring u + v, for example (see the sketch above), is then:-

$$E^2 = A + B' (U \cos \psi + V \sin \psi)^{0.45} \qquad (2.2)$$

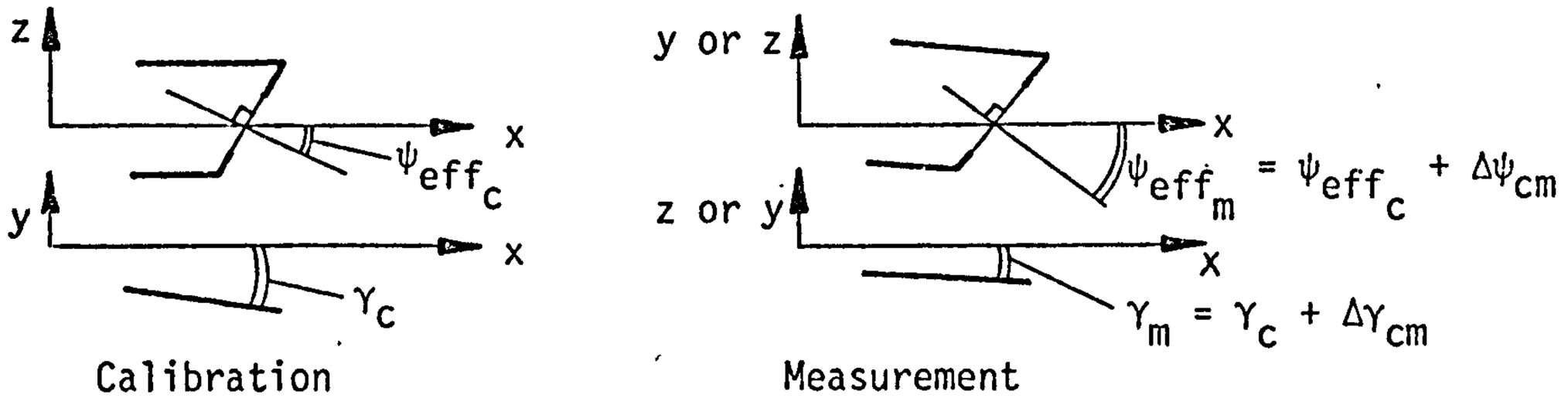
However, the difficulties in measuring ψ accurately and the uncertainty of interpreting the cosine law too literally suggest that ψ in Eqn. (2.2) should be replaced by ψ_{eff}, an effective angle determined experimentally once A and B′ in Eqn. (2.2) are known. This was done using the method described by Bradshaw (1971) and Shabaka (1979). This had to be done in the x, z plane due to the small height of the potential core and traverse gear limitations. V = 0 in the potential core so Eqn. (2.2) reduces to:-

$$E_c^2 = A + B_c U^{0.45} \quad , \quad B_c = B' \cos^{0.45} \psi_{eff_c} \qquad (2.3)$$

where the subscript c denotes the calibration (x, z) plane. Once A and B_c were found a yaw calibration was performed. Briefly this consists of yawing the probe by a known amount $\Delta\psi$ and plotting:-

$$\alpha \equiv \left(\frac{E^2_{\Delta\psi} - A}{E^2_{\Delta\psi=0} - A} \right)^{2\cdot222} - \cos \Delta\psi \quad \text{against} \quad \sin \Delta\psi \tag{2.4}$$

for several values of $\Delta\psi$. The resulting straight line of best fit has a slope of $\tan \psi_{eff}$. The results of fig. 2.7 show that the cosine law works well for $-14 \leq \Delta\psi \leq 14^{o}$ and the results presented in Appendix A show that, for the probes used here, it is a surprisingly good first approximation for double this range of $\Delta\psi$. If the probe then had to be moved downstream or turned through 90° to measure in the x, y plane there was no guarantee that ψ_{eff} or γ, the inclination of the plane of the wires to the x-axis, remains unchanged (see sketch



above). It is shown in Appendix A that for typical values of $\Delta\gamma_{cm}$, which were likely to be the same order as $\Delta\psi_{cm}$, i.e. less than 2°, the effect on the calibrations is negligibly small. However, this is not so for small changes in ψ_{eff}. From Eqn. (2.3) we expect only B_c to change due to a change in ψ_{eff}, as A and B′ are independent of ψ_{eff}. After the probe was repositioned, $\Delta\psi_{cm}$ was found using $\Delta\psi_{cm}$ for wire 1 measuring $u + v = -\Delta\psi_{cm}$ for wire 2 measuring $u - v$ and:-

$$E^2 = A + B_m U^{0\cdot45} \quad , \quad B_m = B_c \left[\frac{\cos (\psi_{eff_c} + \Delta\psi_{cm})}{\cos \psi_{eff_c}} \right]^{0\cdot45} \tag{2.5}$$

for both wires., where the subscript m denotes measuring position.

To save computer time the calibrations are used in the data reduction programs (see Section 2.4) in the form:-

$$E^2 = A + BU_1^{0.45} \left(\frac{U}{U_1} + \frac{V}{U_1} \tan \psi_{eff} \right)^{0.45} \qquad (2.6)$$

where $U + V \tan \psi_{eff}$ is called the effective velocity, U_{eff}, and it is shown in Appendix A that significant errors can occur if the change in ψ_{eff} and B are not included. This procedure could not be used for the reattached flow and consequently the errors in these measurements are larger than those for the free shear layer measurements (Appendix A).

The procedure worked well for most of the calibrations such as for wire 2 in figs. 2.7a and 2.7b, but for some it did not. An example is the behaviour of wire 1 in figs. 2.7a and 2.7b which shows the calibrations for the x, z and x, y plane traverses at $x - x_o =$ 62.32 cm. After a King's law and yaw calibration (calibration No. 1 and the O and X points in fig. 2.8) the u, w measurements were made and the probe recalibrated (calibration No. 2). After turning through 90°, fig. 2.5 could only be used if A was altered from 6.277 to 6.163 in volts^2 and finding $\Delta\psi_{cm}$ from wire 2 only. This happened apparently randomly and the cause was never satisfactorily located. By plotting the mean voltages against y for each traverse it was found that A never jumped during a traverse. After the u, v measurements the probe was recalibrated (calibration No. 4) and then turned through 90° for a further King's law and yaw calibration (calibration No. 5 and the + and x points in fig. 2.8). This time A for wire 1 did not change while for wire 2 it did, slightly. The repeatability of B for both wires indicates that ψ_{eff} did not change between calibration 1 and 5 and the repeatability of the yaw calibrations supports this conclusion. The repeatability of the yaw calibrations is typical but often the King's law calibrations altered during a traverse due to slight temperature changes and dirt accumulation on the wire. To a good first approximation this was accounted for by a change in A only. If

the change was larger than 3% the traverse was repeated, while for smaller changes values for each point in the traverse were linearly interpolated between the calibrations in the measuring plane before and after the traverse. If the jump in A between the calibration and measurement position was large or if A for both wires appeared to jump the traverse was also repeated. A appears in the yaw calibration, Eqn. (2.4), and since these calibrations were repeatable it was felt that the jumps were not significant. The accuracy of the measurements is estimated in Appendix A to be about 10% for second order quantities and about 20% for the third order results in the free shear layer and about 15% and 30% respectively in the attached flow.

2.4 Data Analysis

The AC coupled signals were recorded on an Ampex FR1300 analog tape recorder at 30 inches per second (ips). At this speed the tape recorder bandwidth is the same as that of the signal conditioners. The signals were later played back (reproduced) at 15 ips and using the departmental ADC system described by Bradshaw (1979) the data was transcribed onto digital tapes. The real time sampling frequency was 20 kHz per channel and the reproduced signals were low pass filtered at 10 kHz to prevent aliasing. The four channel data could only be digitized at 8 kHz real time per channel and were low pass filtered at 6.67 kHz. The autocorrelations and spectra were all computed from the two channel (single point) data. The spectral program, written by the author with help from Messrs. Muck Kin Choong and Peter Cheung, called Electrical Engineering Department routines to fast Fourier transform the data in blocks of 2048 or 4096 points. The total number of blocks processed corresponded closely to the averaging time used for the time domain results presented in Chapter 5. The spectra were then averaged and the autocorrelation was found as the inverse

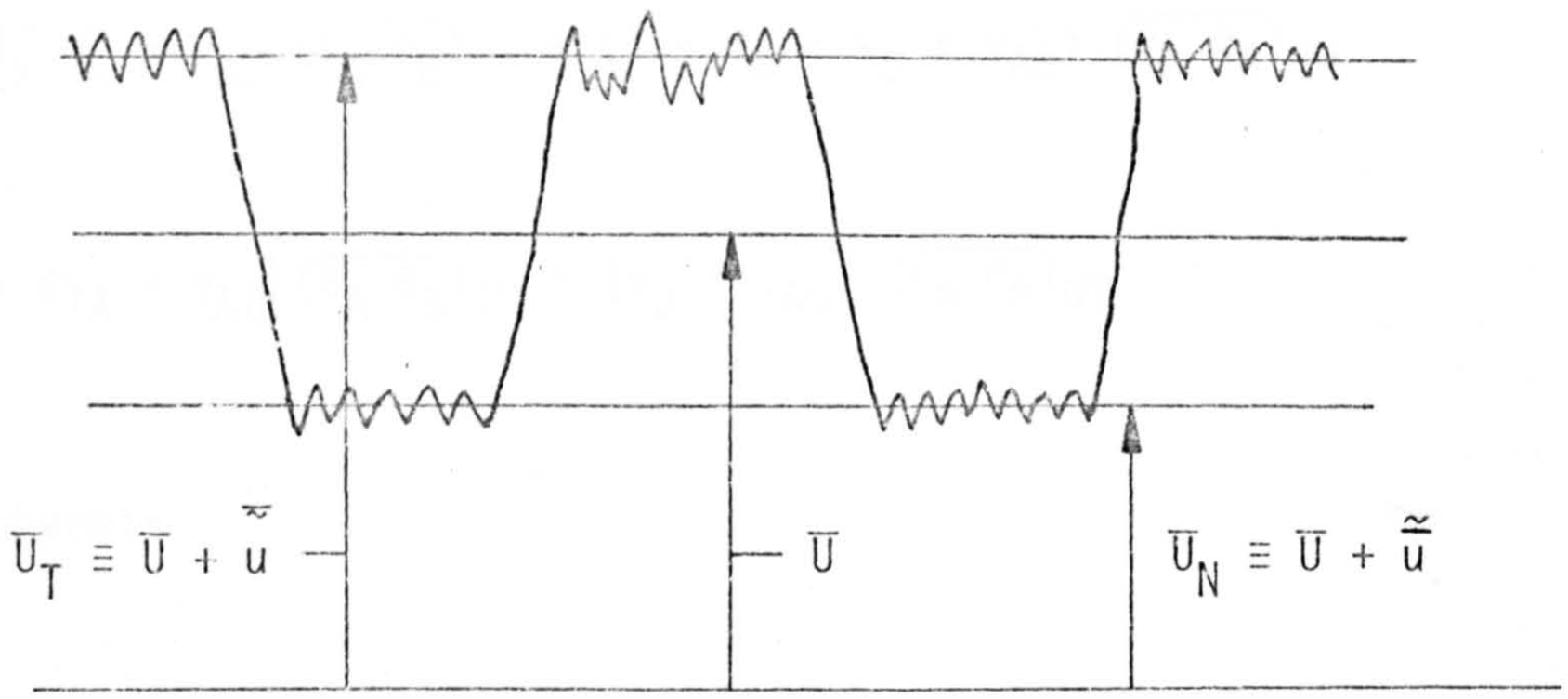
transform of the averaged spectra, again using an Electrical Engineering Department routine.

The time domain results were obtained by analysing the digital tapes on the College CDC 6500 computer using the standard two channel program DIG2MK6, or DIG4MK1 written by the author to analyse the four channel (correlation) data. Both these programs set up calibration arrays to effectively linearize the signal (Weir and Bradshaw, 1974). DIG4MK1 was checked by using the same input to channels 1 and 3 (the u + v channels) and different but equal inputs to channels 2 and 4 (the u - v channels). The expected results $R_{11} = R_{22} = 1.0$ were obtained. The large amount of data reduction precluded the use of wholly satisfactory averaging times. Typical averaging times varied from 15 seconds to 22 seconds of real time between $x - x_o = 24$ and 151 cm nominally for the single probe measurements and about 60% of these times for the correlation measurements. The effects on the results are discussed in Appendix A,

The most important features of DIG4MK1 are the conditional sampling routines. A routine discussed in Chapter 5 generates the intermittency function I(t) which has a value of 1 if the flow is turbulent at time t and is zero otherwise. The two channel program computes zone averages relative to the mean of the quantity which allows the addition law:-

$$\gamma\overline{\theta}_T + (1 - \gamma)\,\overline{\theta}_N = \overline{\theta} \qquad (2.7)$$

where the suffixes T and N denote turbulent and non-turbulent respectively, to be applied to any quantity $\theta(t)$. For example the program computes the average of U over those points for which I(t) = 1,



denoted by $(\widetilde{\quad})$ using the notation of Kovasznay et al (1970). As can be seen from the sketch (taken from Dean and Bradshaw, 1976):-

$$\overline{\widetilde{U + u(t)}} = \overline{U} + \tilde{u} \equiv \overline{U}_T$$

where $\overline{U}$ and $u(t)$ are the conventional mean and fluctuating components respectively, of the total signal U. Since I(t) is either 1 or 0:-

$$\overline{I(t)\ \theta} = \gamma\ \overline{\widetilde{(\overline{\theta} + \theta)}} \qquad \text{and} \qquad (2.8)$$

$$\overline{\left[1 - I(t)\right]\ \theta} = (1 - \gamma)\ \overline{\widetilde{(\overline{\theta} + \theta)}}$$ where $(\widetilde{\quad})$ is the non-turbulent zone average. For $\overline{u^2}$ the result is:-

$$\overline{\widetilde{(\overline{U} + u)^2}} = \overline{U}^2 + 2\overline{U}\ \tilde{u} + \tilde{u}^2 \quad , \quad \tilde{u}^2 \equiv \overline{u_T^2}$$

$$= \overline{U}^2 + 2\overline{U}\ (\overline{U}_T - \overline{U}) + \overline{u_T^2} \qquad (2.9)$$

so that $\overline{u_T^2}$ can be found once $\overline{U}$, $\overline{U}_T$ are known. The turbulence quantities are calculated in increasing order as $(\overline{u^{m-1}\ v^{n-1}})_T$ is needed to evaluate $(\overline{u^m\ v^n})_T$. For two point measurements the addition law becomes:-

$$\overline{\theta_A\ \theta_B} = \gamma_{AB}\ (\overline{\theta_A\ \theta_B})_{TT} + (1 - \gamma_A - \gamma_B + \gamma_{AB})\ (\overline{\theta_A\ \theta_B})_{NN}$$

$$+ (\gamma_A - \gamma_{AB})(\overline{\theta_A\ \theta_B})_{TN} + (\gamma_B - \gamma_{AB})\ (\overline{\theta_A\ \theta_B})_{NT} \qquad (2.10)$$

where:-

$$\gamma_{AB} = \overline{I_A(t)\ I_B(t)}$$

The first term on the right hand side is the product of θ at point A and θ at B averaged only over the time when A is turbulent and B is turbulent and similarly for the other terms. The first subscript always refers to point A. For the results presented in Chapter 5, A is always the fixed probe.

Unless otherwise stated the correlations are normalized so that $R_{ii} = R_{ij} = 1$ at zero separation. Thus:-

$$R_{11} \equiv \frac{\overline{u_A\ u_B}}{(\overline{u_A^2} \cdot \overline{u_B^2})^{1/2}}\ , \quad R_{12} \equiv \frac{\overline{u_A\ v_B}}{\left[(\overline{uv_A}) \cdot (\overline{uv_B})\right]^{1/2}}\ , \quad R_{22} \equiv \frac{\overline{v_A\ v_B}}{(\overline{v_A^2} \cdot \overline{v_B^2})^{1/2}} \qquad (2.11)$$

and similarly for R_{33}. The major reason for using these definitions is that to first order any small calibration errors will cancel out of Eqn. (2.11). Now the addition laws, Eqns. (2.7) and (2.10), do not apply to terms like $\overline{u^m}/\overline{v^n}$ or to those in Eqn. (2.11) so the only way to use the addition law, Eqn. (2.10), to find the contributions to R_{ij} is to apply it to the numerator only. Before zone averaging this is:-

$$U_i(t)\ U_j(t) = \left[\{\overline{U}_i + u_i(t)\}\ I_A(t) + \{1 - I_A(t)\}\ \{\overline{U}_i + u_i(t)\}\right]$$

$$\times \left[\{\bar{U}_j + u_j(t)\}\ I_B(t) + \{1 - I_B(t)\}\ \{\bar{U}_j + u_j(t)\}\right]$$

where $U_i(t)$ is measured by probe A, $U_j(t)$ by B.

Using Eqn. (2.10) and taking the four possibilities in turn; the ATBT (A turbulent, B turbulent) zone average is:-

$$\gamma_{AB}\left[\bar{U}_i\bar{U}_j + \bar{U}_i\tilde{u}_j + \bar{U}_j\tilde{u}_i + (\overline{u_iu_j})_{TT}\right]$$

where ($\tilde{}$) now denotes a turbulent/turbulent zone average,

$$= \gamma_{AB}\left[\bar{U}_i\bar{U}_j + \bar{U}_i\ (\bar{U}_{j,TT} - \bar{U}_j) + \bar{U}_j\ (\bar{U}_{i,TT} - \bar{U}_i) + (\overline{u_iu_j})_{TT}\right] \qquad (2.12)$$

which reduces to Eqn. (2.9) if A = B and i = j. ATBN reduces to:-

$$(\gamma_A - \gamma_{AB})\left[\bar{U}_i\bar{U}_{j,TN} + \bar{U}_j\bar{U}_{i,TN} - \bar{U}_i\bar{U}_j + (\overline{u_iu_j})_{TN}\right]. \qquad (2.13)$$

ANBT reduces to:-

$$(\gamma_B - \gamma_{AB})\left[\bar{U}_i\bar{U}_{j,NT} + \bar{U}_j\bar{U}_{i,NT} - \bar{U}_i\bar{U}_j + (\overline{u_iu_j})_{TN}\right] \qquad (2.14)$$

and ANBN reduces to:-

$$(1 - \gamma_A - \gamma_B + \gamma_{AB})\left[\bar{U}_i\bar{U}_{j.NN} + \bar{U}_j\bar{U}_{i,NN} - \bar{U}_i\bar{U}_j + (\overline{u_iu_j})_{NN}\right]. \qquad (2.15)$$

The four channel program evaluates Eqns. (2.12) - (2.15) to find $\gamma_{AB}\ (\overline{u_iu_j})_{TT}$, etc. and divides each by the denominator of Eqn. (2.10) so that:-

$$R_{ij} = R_{iTjT} + R_{iTjN} + R_{iNjT} + R_{iNjN} \qquad (2.16)$$

Thus the contributions to the total correlations as defined by Eqns. (2.12) - (2.16) were found. As the separation between the probes decreases the turbulent/turbulent and non-turbulent/non-turbulent contributions to R_{ij} must asymptote to the single point results for probe A. These results are plotted in Chapter 5 and serve as a check on the conditional correlations. The turbulent/non-turbulent and non-turbulent/turbulent contributions asymptote to zero since they are mutually exclusive in the limit; compare Eqn. (2.10) to (2.7). Thus as the probe separation decreases:-

$$R_{iTjT} \to \frac{\gamma_A \, (\overline{u_i u_j})_T}{\overline{u_i u_j}} \quad , \quad R_{iNjN} \to \frac{(1 - \gamma_A) \, (\overline{u_i u_j})_N}{\overline{u_i u_j}} \qquad (2.17a)$$

$$R_{iNjT} \ , \ R_{iTjN} \to 0 \qquad (2.17b)$$

and:-

$$R_{iTjT} + R_{iNjN} \to 1 \qquad (2.17c)$$

where u_i, u_j are now measured by probe A. Eqns. (2.17a) - (2.17c) were used to find the contributions at zero separation. Note that Eqn. (2.17a) is just the single point addition law, Eqn. (2.7), divided through by $\overline{\theta} = \overline{u_i u_j}$.

The correlation of the intermittency functions:-

$$R_{II} = \frac{\overline{\{I_A(t) - \gamma_A\} \{I_B(t) - \gamma_B\}}}{\left[\overline{\{I_A(t) - \gamma_A\}^2} \cdot \overline{\{I_B(t) - \gamma_B\}^2}\right]^{1/2}} = \frac{\gamma_{AB} - \gamma_A \gamma_B}{(\gamma_A - \gamma_A^2)^{1/2} (\gamma_B - \gamma_B^2)^{1/2}} \qquad (2.18)$$

was also found. Eqn. (2.17) has the same form as Eqn. (2.11) and is one if $I_A(t) = I_B(t)$ and zero if $I_A(t)$ and $I_B(t)$ are uncorrelated. The definition, Eqn. (2.18), is the same as that used by Kovasznay et al (1970, Eqn. 20).

All the single point and normal correlation measurements were made at z = 0, while the positions of the fixed probes for the spanwise correlations are shown in fig. 2.2.

No experimental results have been tabulated as they have been stored on two archive files SPLAT1 for the single point measurements and SPLAT2 for the two point and autocorrelation measurements. Copies are available from Professor Bradshaw.

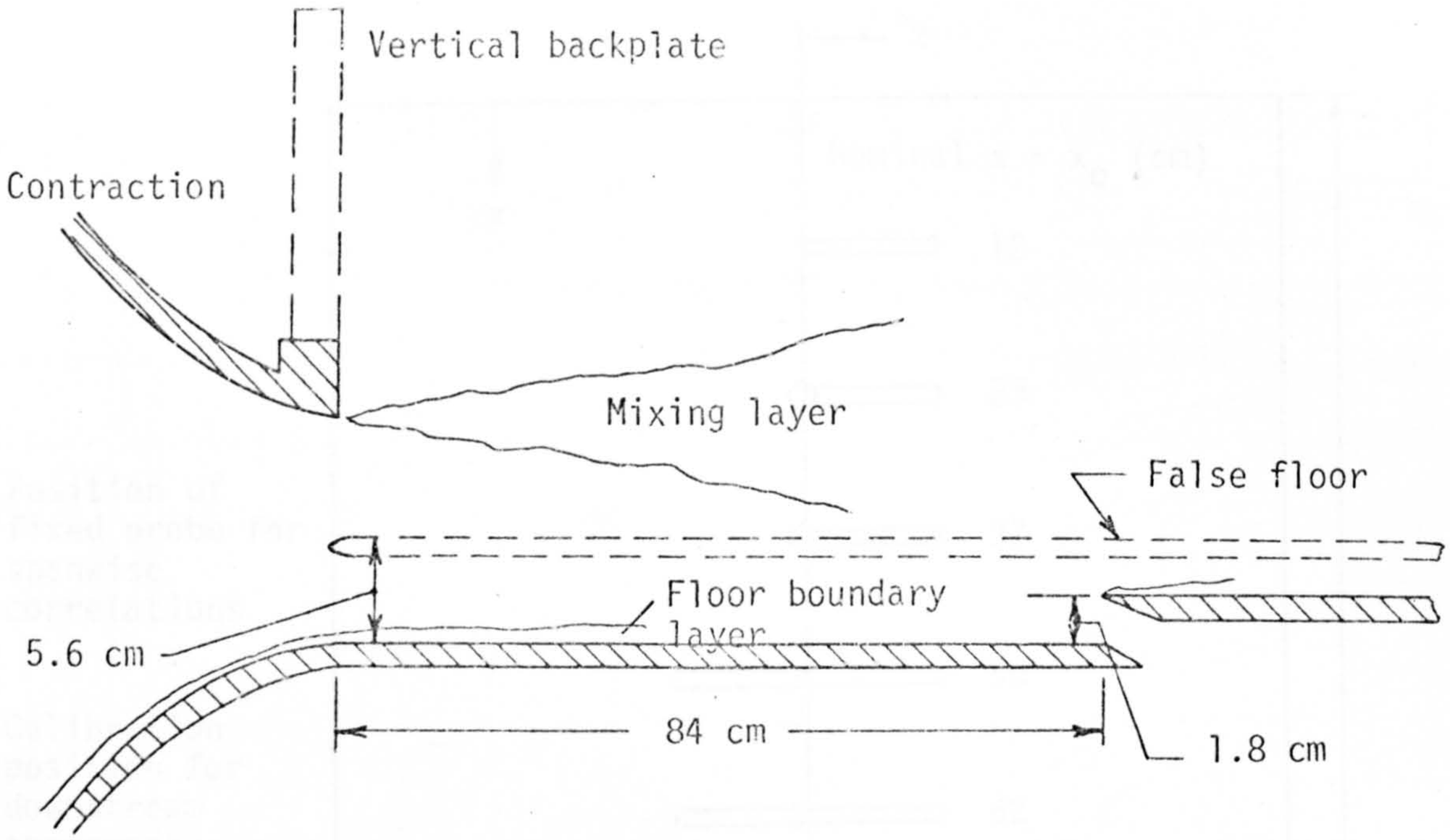


Fig. 2.1a Schematic diagram of first test section

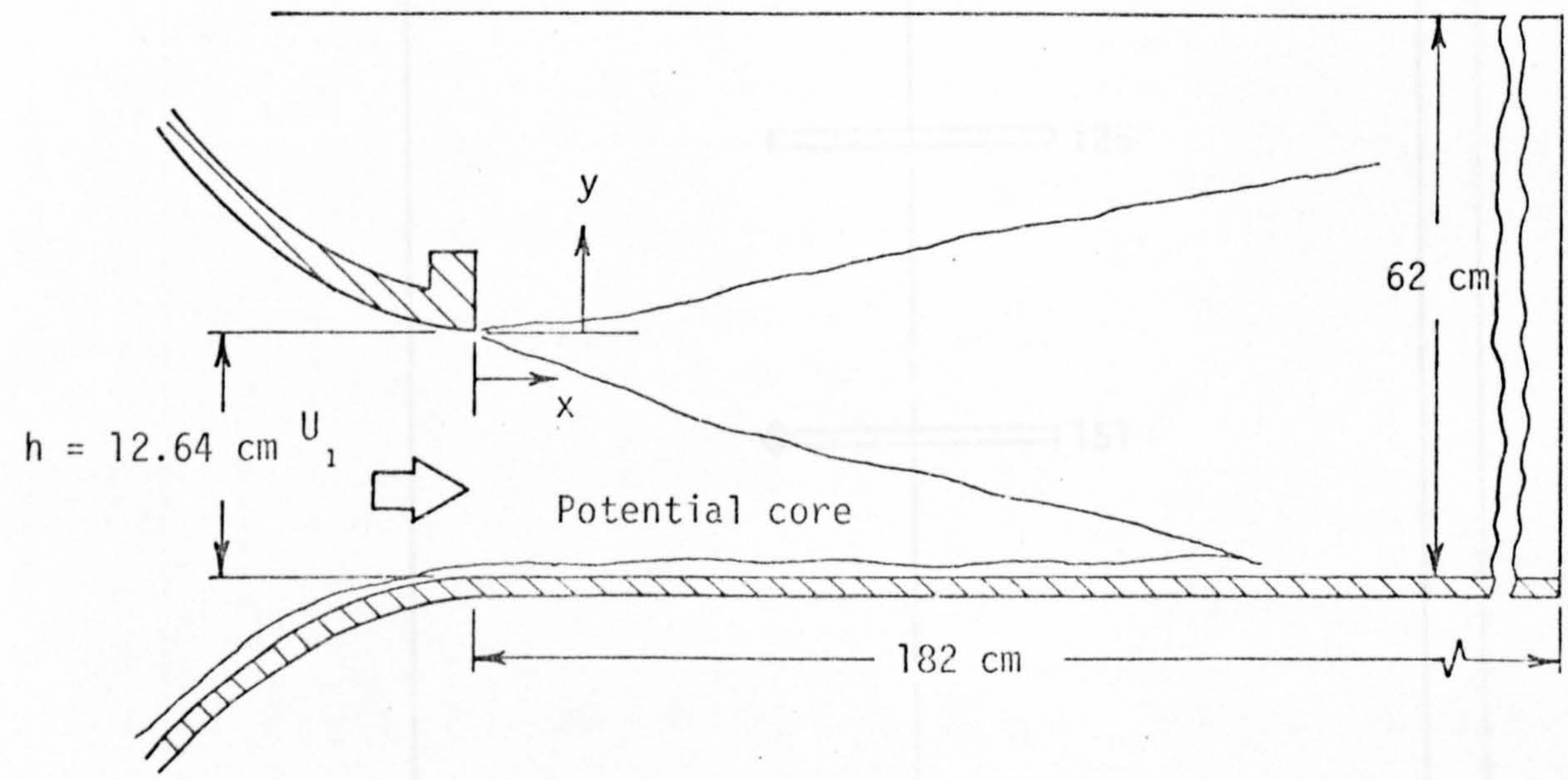


Fig. 2.1b Schematic diagram of final test section

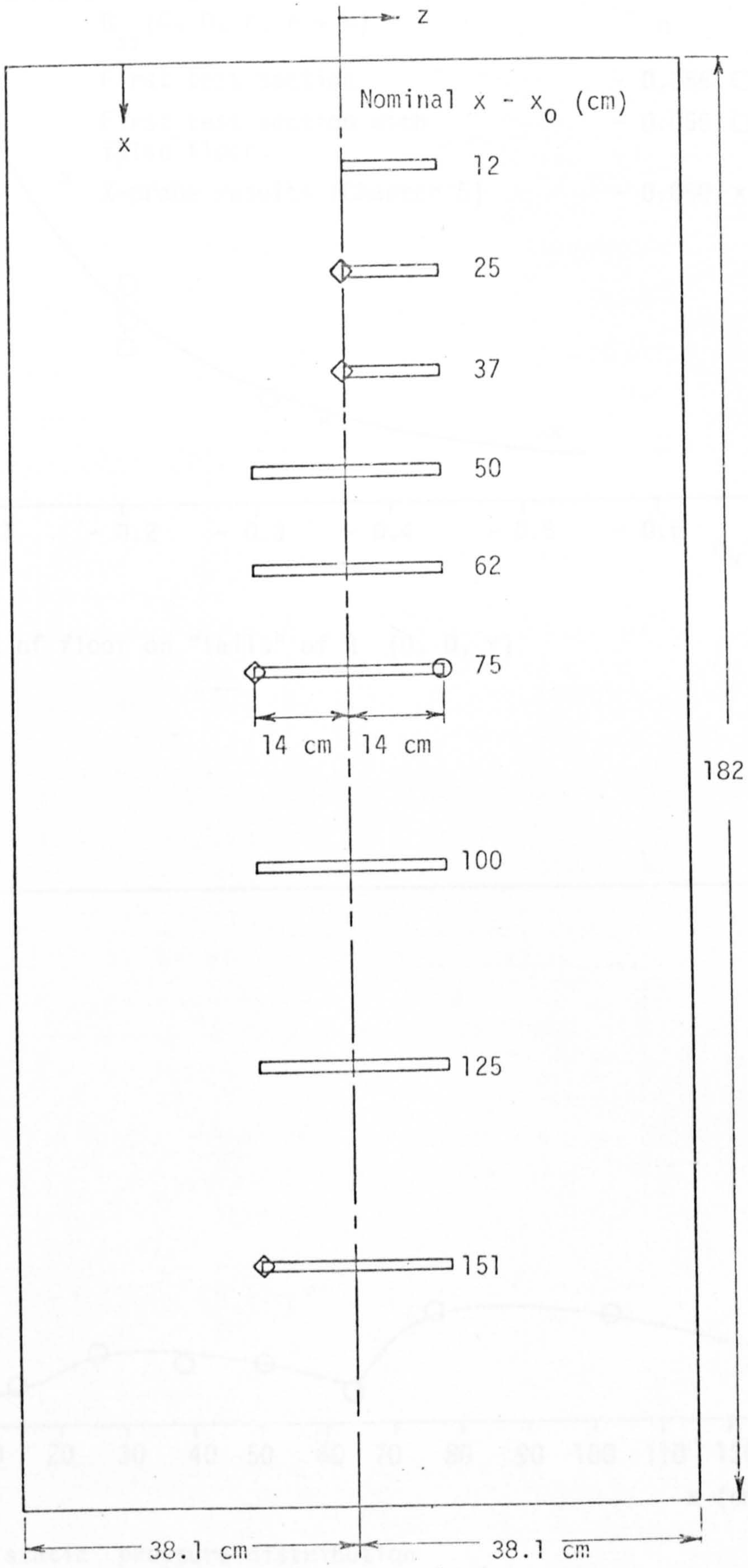


Fig. 2.2 Working section floor

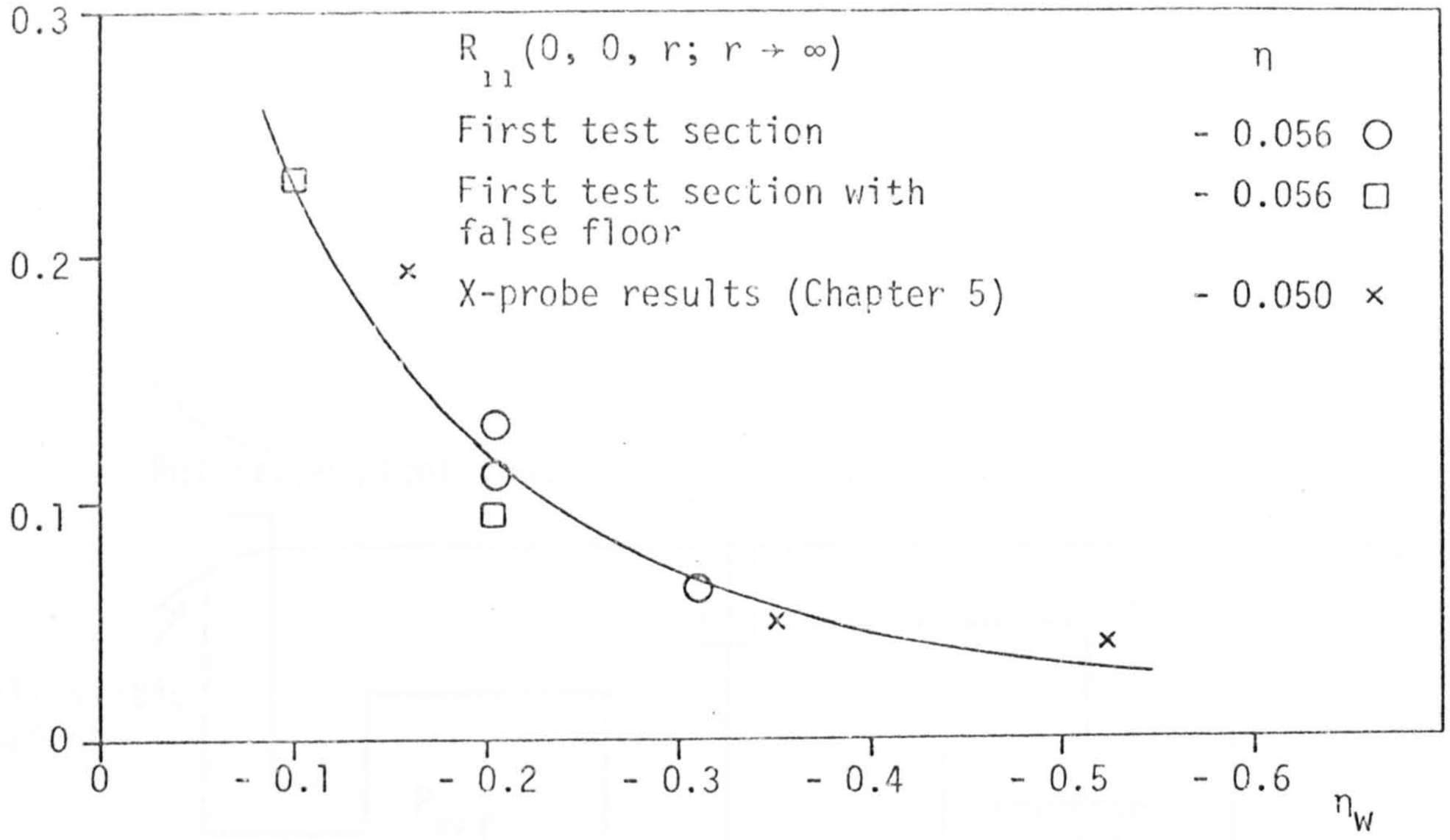


Fig. 2.3 Effect of floor on "tails" of $R_{11}(0, 0, r)$

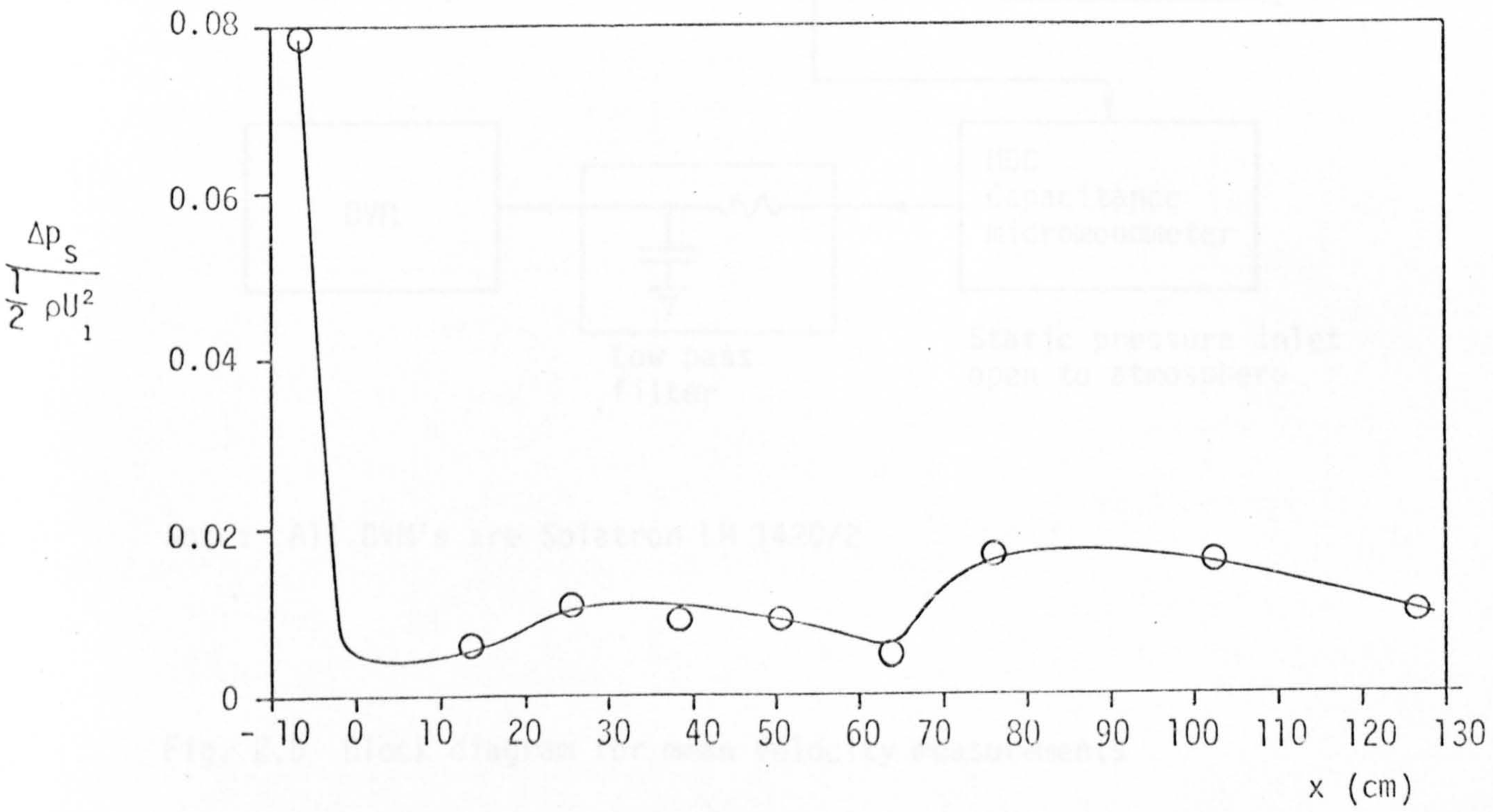
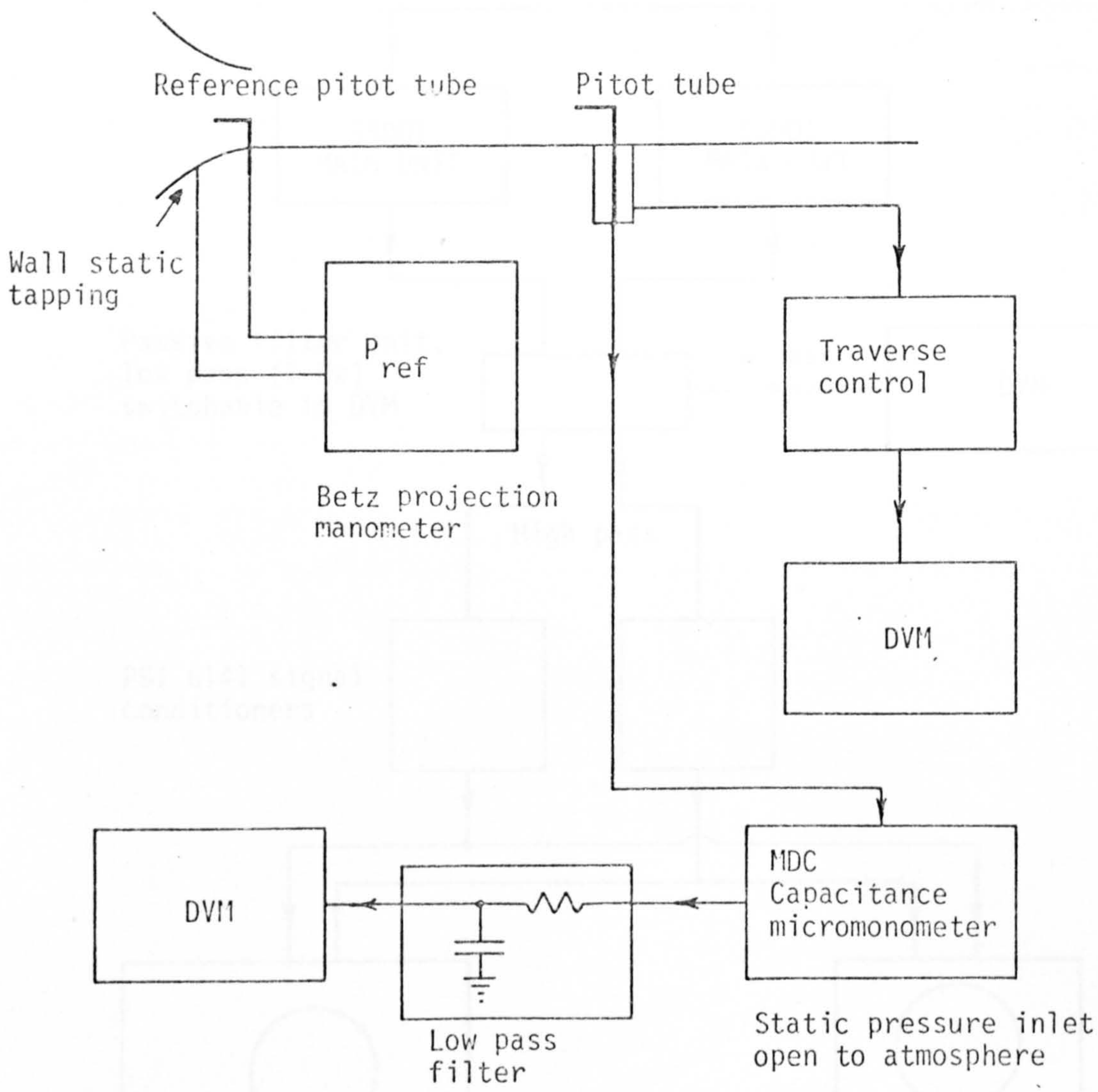


Fig. 2.4 Floor static pressure distribution



Note: All DVM's are Solatron LM 1420/2

Fig. 2.5 Block diagram for mean velocity measurements

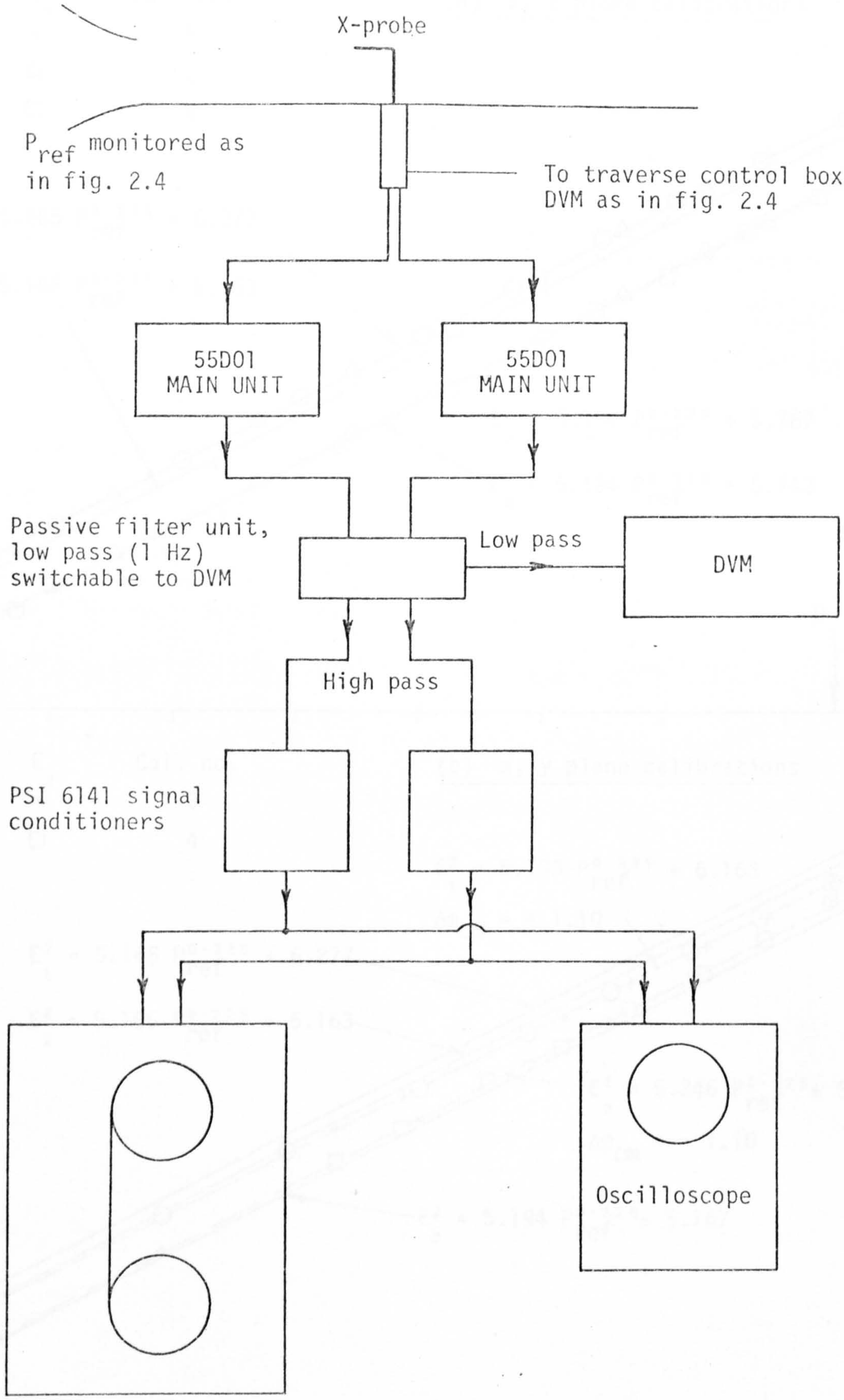


Fig. 2.6 Block diagram for cross wire measurements

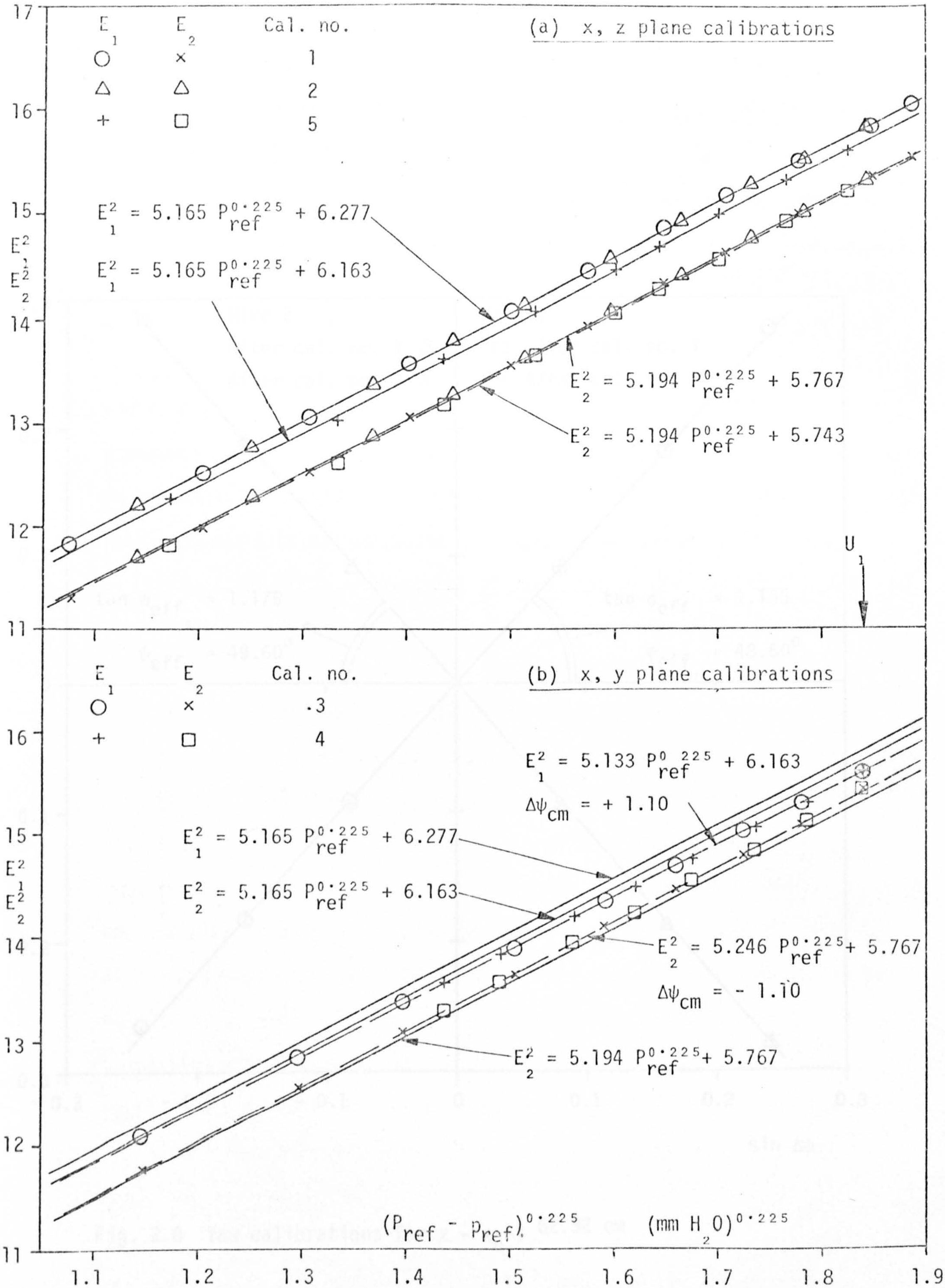


Fig. 2.7 King's Law calibrations for $x - x_o = 62.32$ cm

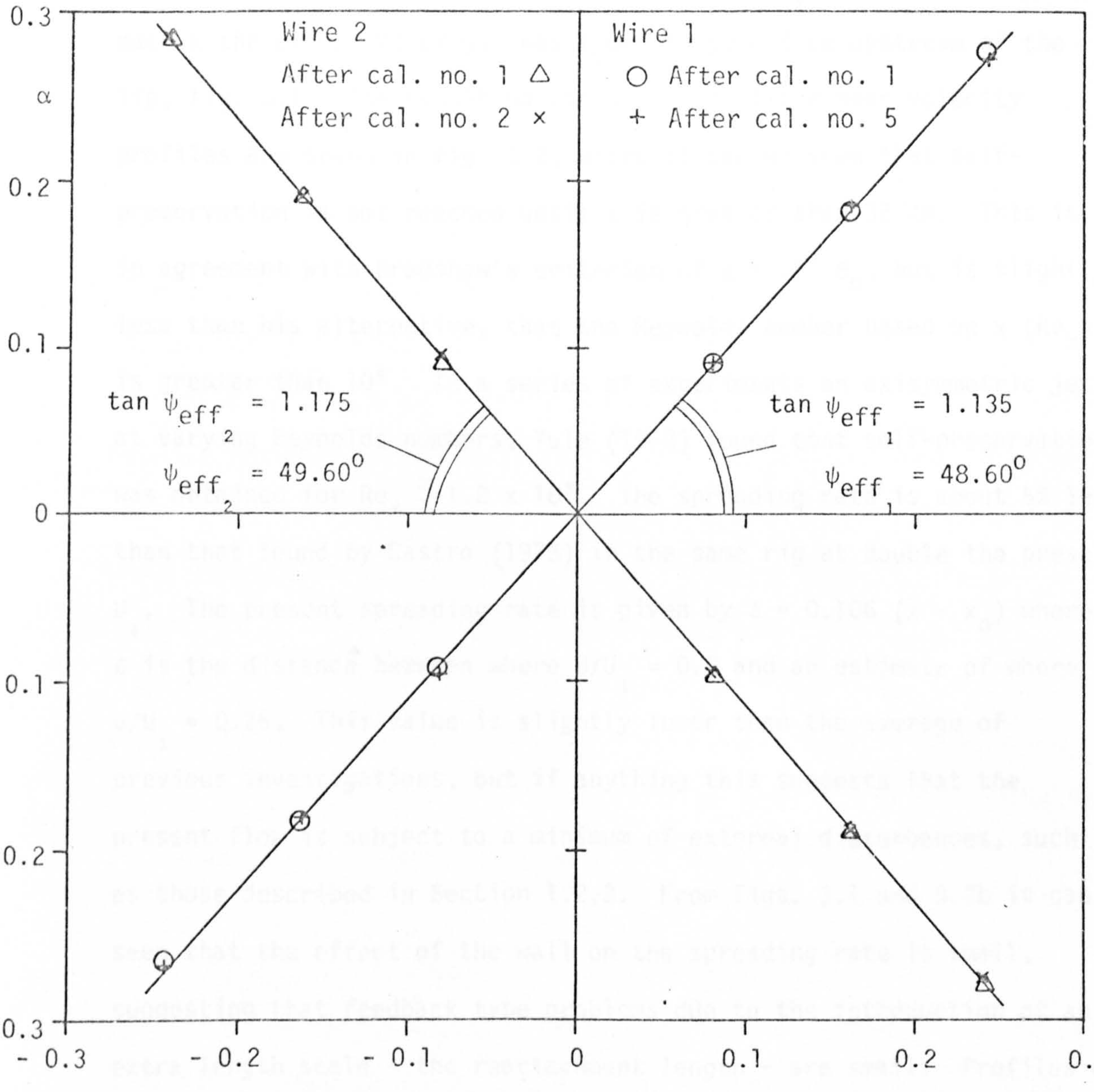


Fig. 2.8 Yaw calibrations for $x - x_o = 62.32$ cm

CHAPTER 3

MEAN VELOCITY RESULTS AND TWO-DIMENSIONALITY

3.1 Free Shear Layer Results

By plotting the values of y where $U/U_1 = 0.9$ and 0.4 for each x the effective origin was found to be 6.8 cm upstream of the lip, fig. 3.1. The resulting non-dimensionalized mean velocity profiles are shown in fig. 3.2, where it can be seen that self-preservation is not reached until x is greater than 32 cm. This is in agreement with Bradshaw's criterion of $x > 10^3\ \theta_0$, but is slightly less than his alternative, that the Reynolds number based on x (Re_x) is greater than 10^6. In a series of experiments on axisymmetric jets at varying Reynolds numbers, Yule (1978) found that self-preservation was obtained for $Re_x \gtrsim 1.2 \times 10^5$. The spreading rate is about 5% less than that found by Castro (1973) in the same rig at double the present U_1. The present spreading rate is given by $\delta = 0.106\ (x - x_0)$ where δ is the distance between where $U/U_1 = 0.9$ and an estimate of where $U/U_1 = 0.25$. This value is slightly lower than the average of previous investigations, but if anything this suggests that the present flow is subject to a minimum of external disturbances, such as those described in Section 1.2.3. From figs. 3.1 and 3.2b it can be seen that the effect of the wall on the spreading rate is small, suggesting that feedback type problems due to the introduction of an extra length scale - the reattachment length - are small. Profiles of the normal mean velocity V calculated using the continuity equation are given in Appendix B.

The initial boundary layer was measured at x = - 0.12 cm and the results are shown in fig. 3.3. The manometer was calibrated against P_{ref} and no correction was made for the difference in static

pressure (see fig. 2.4). A correction would increase the measured values. Given the small thickness of the initial boundary layer and the large size of the total head tube ($\sim 0.45\ \delta$) all that can be said is that the initial boundary layer is reasonably approximated by the Blasius profile. Also shown in fig. 3.3 are the measurements of the floor boundary layer and the values of $\delta_{b\ell}$ the 99.5% thickness are given. These values are plotted in fig. 3.4 together with the laminar boundary layer growth rate calculated assuming the floor boundary layer at x = 0 has the same thickness as the initial boundary layer. The floor boundary layer grows rapidly after x = 80 cm due to the increase in the free stream turbulence level induced in the diminishing potential core (figs. 4.23 - 4.25). Fig. 3.4 also shows the ratio of mixing layer thickness ($\delta_{m\ell}$) to $\delta_{b\ell}$; $\delta_{m\ell}$ is the distance between the value of y where $U/U_1 = 0.995$ and the estimated position where $U/U_1 = 0.005$. For the reattached flow $\delta_{b\ell}$ is the distance to where U/U_1 is a maximum. For the entire region measured the mixing layer thickness is an order of magnitude greater than $\delta_{b\ell}$. The comparison between the ratio of potential core thickness, δ_p, the distance between the high speed edge of the mixing layer defined above to $\delta_{b\ell}$, and $(\delta_p + \delta_{b\ell})/\delta_{m\ell}$ (fig. 3.4) shows that for most of the free shear layer $\delta_{b\ell}$ can be ignored in considering image effects.

3.2 Reattached Flow

The mean velocity profiles for the reattached flow, plotted with the profile at $x - x_0 = 104.69$ cm in fig. 3.5 again show that the wall hardly, if at all, alters the spreading rate on the low velocity side. The dip below the free shear layer profile around the maximum of U/U_1 particularly noticeable at $x - x_0 = 155.64$ cm is most likely due to the negative $\partial U/\partial x$ induced by the relatively high $\partial V/\partial y$ in the rapidly growing floor boundary layer and not to a change in

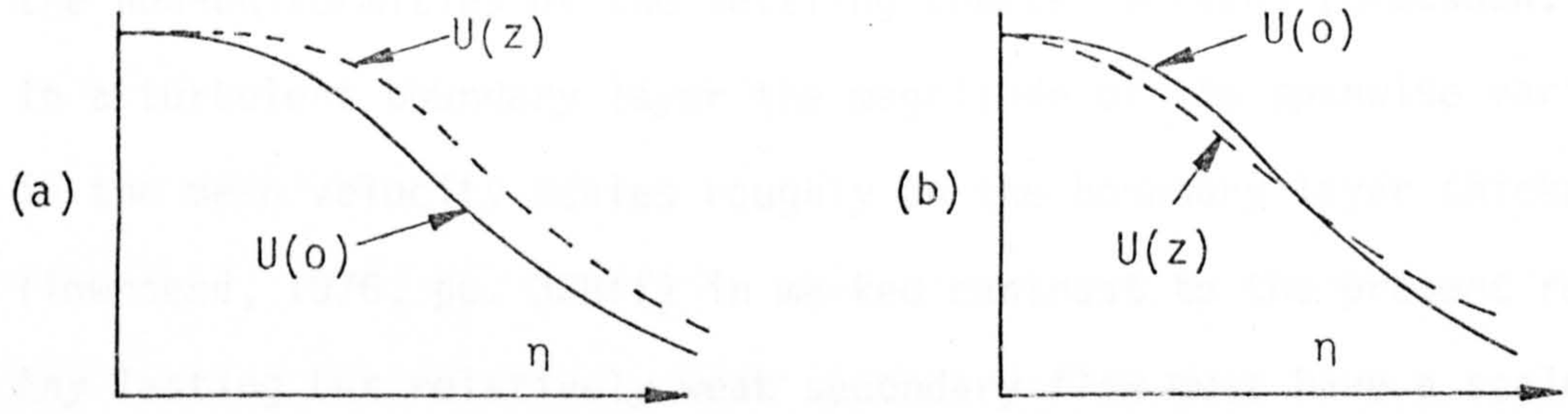
spreading rate. The wall region profiles are shown on a Clauser chart in fig. 3.6, from which the values of wall shear stress, τ_w, used in fig. 4.4 were found. The results in fig. 3.6 are quite different from fully developed wall jet profiles, see for example fig. 6 of Bradshaw and Gee (1960); of course, it would take a much longer downstream distance to achieve a fully developed wall jet than was possible in the present rig.

3.3 Two-Dimensionality

While measuring the spanwise correlations presented in Chapter 5 it was noticed that the mean voltages from the moving probe varied considerably with spanwise position. Partly to check on anemometer behaviour and partly due to awareness of possible secondary flows (largely due to the work of the author's colleagues, Drs. P. H. Hoffmann, R. D. Mehta and I. M. Shabaka) checks on the two-dimensionality of the mean flow were made. During the preliminary mean velocity measurements (which are not as accurate as those shown in figs. 3.2 - 3.6) several traverses were made near the extremes of the range of the spanwise correlation, fig. 3.7. Apart from those at $x - x_0 = 39.35$ cm the scatter is small, and the results are consistent with the later, spanwise traverses at constant height shown in figs. 3.8b - 3.8d. The 39.35 cm results from two independent traverses at each z show a considerable change in the mean velocity profile, and the results in fig. 3.8b near $z = 13.02$ cm are in reasonable agreement with fig. 3.7. An estimate of the spanwise variation of the initial boundary layer is shown in fig. 3.8a. A total head tube of 1 mm O.D. was used and the dynamic head ($P' \equiv P(z) - p_{ref}$ where $P(z)$ is the total head) is plotted normalized by $P'_0 \equiv P(z=0) - p_{ref}$. The results, which are nearly proportional to τ_w^2 since $u \simeq \tau_w/\mu\, y$ in the inner part of laminar boundary layer, show considerable

variation as was found by Foss (1977). Also shown in figs. 3.8b - 3.8d are the results of fig. 3.8a with the small scale variations smoothed by averaging each point with those on either side. It is not impossible that the spanwise variations of mean velocity in the mixing layer are related to the spanwise non-uniformity of the initial boundary layer.

Since the shape of the variations at constant $x - x_o$ is nearly independent of η the most likely explanation is that the mixing layer



is bodily wrinkled in the spanwise direction with nearly constant spreading rate, see sketch (a) above. If the spreading rate changed significantly with z (sketch b) the shape of the spanwise variations would vary significantly with η and the magnitude of the maximum variation would be constant and not decreasing as roughly $(x - x_o)^{-1}$ as in fig. 3.8. If x_o was a strong function of z the results would be qualitatively similar to sketch (b), hence this is not a possibility, but in this case the maximum variation would also decrease as $(x - x_o)^{-1}$. This latter result implies that the scale of the bodily wrinkling is nearly constant with x. However, there are slight changes in spreading rate; the 39.35 cm results in fig. 3.7 collapse at positive η but not near the high speed edge. Furthermore, estimating the size of the wrinkling, $\Delta\eta$, using:-

$$\Delta\left(\frac{U}{U_1}\right) \equiv \frac{U(z)}{U_1} - \frac{U(o)}{U_1} \approx \Delta\eta \left.\frac{\partial U/U_1}{\partial \eta}\right|_{z=0}$$

gives values of $\Delta\eta$ varying with η.

By the time the flow has reattached the mean velocity is almost constant, fig. 3.8d, implying that the side wall influences at this the last measuring station were negligible.

The mechanisms by which the initial non-uniformities effect the mixing layer are not understood. The initial variations are most likely due to longitudinal vortices arising from the Taylor-Görtler instability in the contraction boundary layer locking into the non-uniformities of the settling chamber screens (Bradshaw, 1965). In a turbulent boundary layer the magnitude of the spanwise variation in the mean velocity scales roughly on the boundary layer thickness (Townsend, 1976, pp. 328ff) in marked contrast to the present results. Any lasting but relatively weak secondary flow must have a scale of at least the shear layer thickness in order not to be absorbed by the turbulence, so presumably the difference is related to the much higher growth rate of the mixing layer. The spanwise scale of the non-uniformity increases with $x - x_o$ (compare figs. 3.8b and 3.8c) again in contrast to the boundary layer results suggesting a longitudinal vortex of, at most, constant circulation imbedded in the flow, which eventually becomes too weak to be noticeable as it grows in size.

It is tempting to further speculate that the streamwise "stripes" obvious in nearly all photographs of the initial regions of a circular jet and found by Clark and Markland (1973) in a plane mixing layer are locked into the non-uniformities of the initial boundary layer. The long-time exposure photograph in Bernal et al (1979) shows stripes of longitudinal vorticity that are very steady as is the secondary motion shown in fig. 3.8.

It would have been interesting to use the point measurements from the moving probe used in the spanwise correlation measurements to further study the secondary flow. However, the large amount of

digital data reduction needed to analyse the correlation measurements together with the low sampling rate used (see Chapter 2) resulted in insufficient real time to obtain convergence in the single point measurements. The repeatability of the correlation measurements, Chapter 5, suggests that they were not significantly affected.

To the author's knowledge there have been no previous detailed studies of the spanwise behaviour of mixing layers. The present cursory study suggests that spanwise non-uniformities in the initial boundary layer should be added to the plethora of important initial conditions. It would be interesting to study an artificially induced secondary motion, say by placing a vortex generator in the wind tunnel contraction. The results of such a study would directly support or disprove most of the above speculations.

Some further comments on secondary flow are made in the next chapter when discussing the single point measurements.

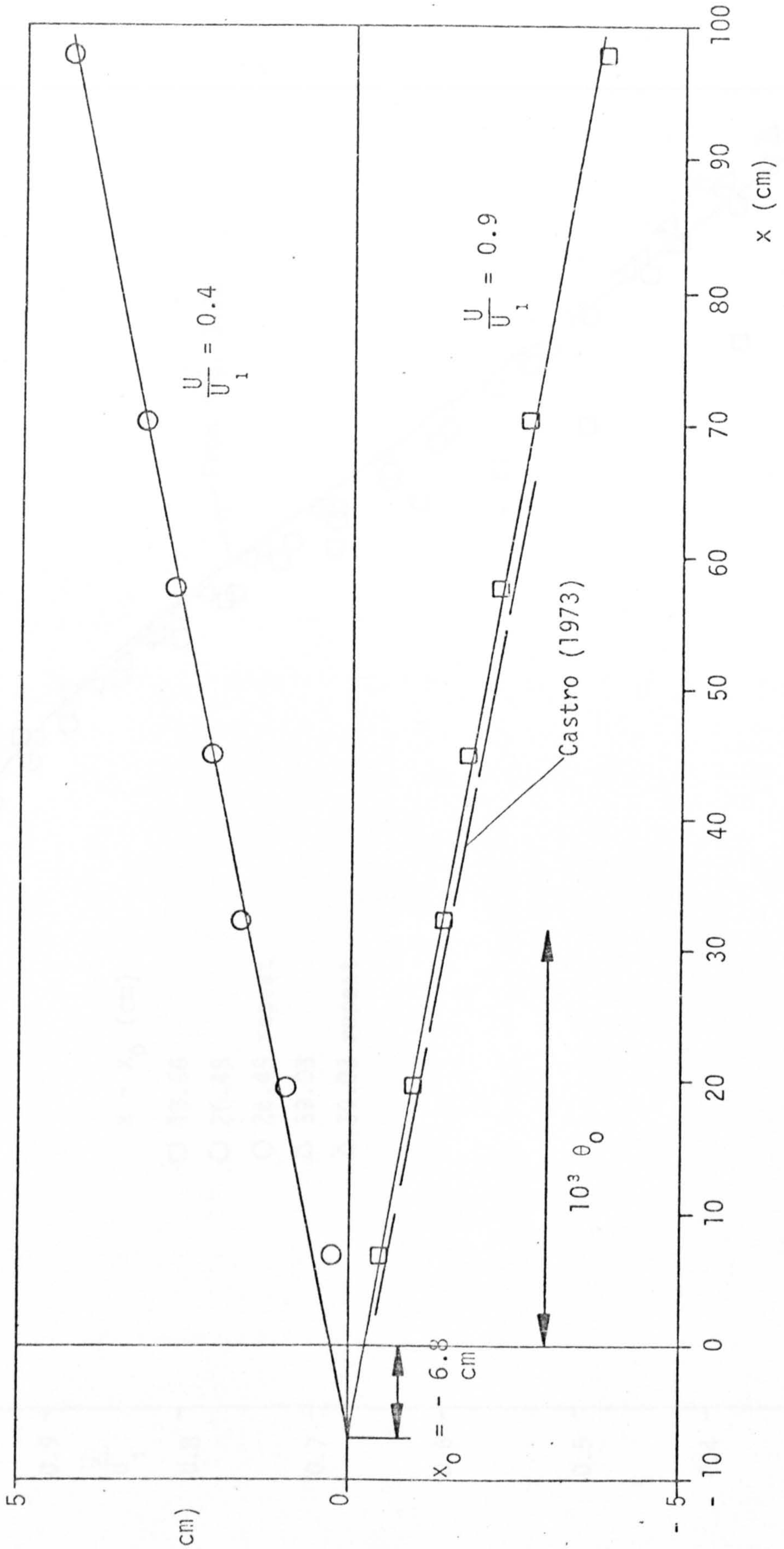


Fig. 3.1 Determination of effective origin

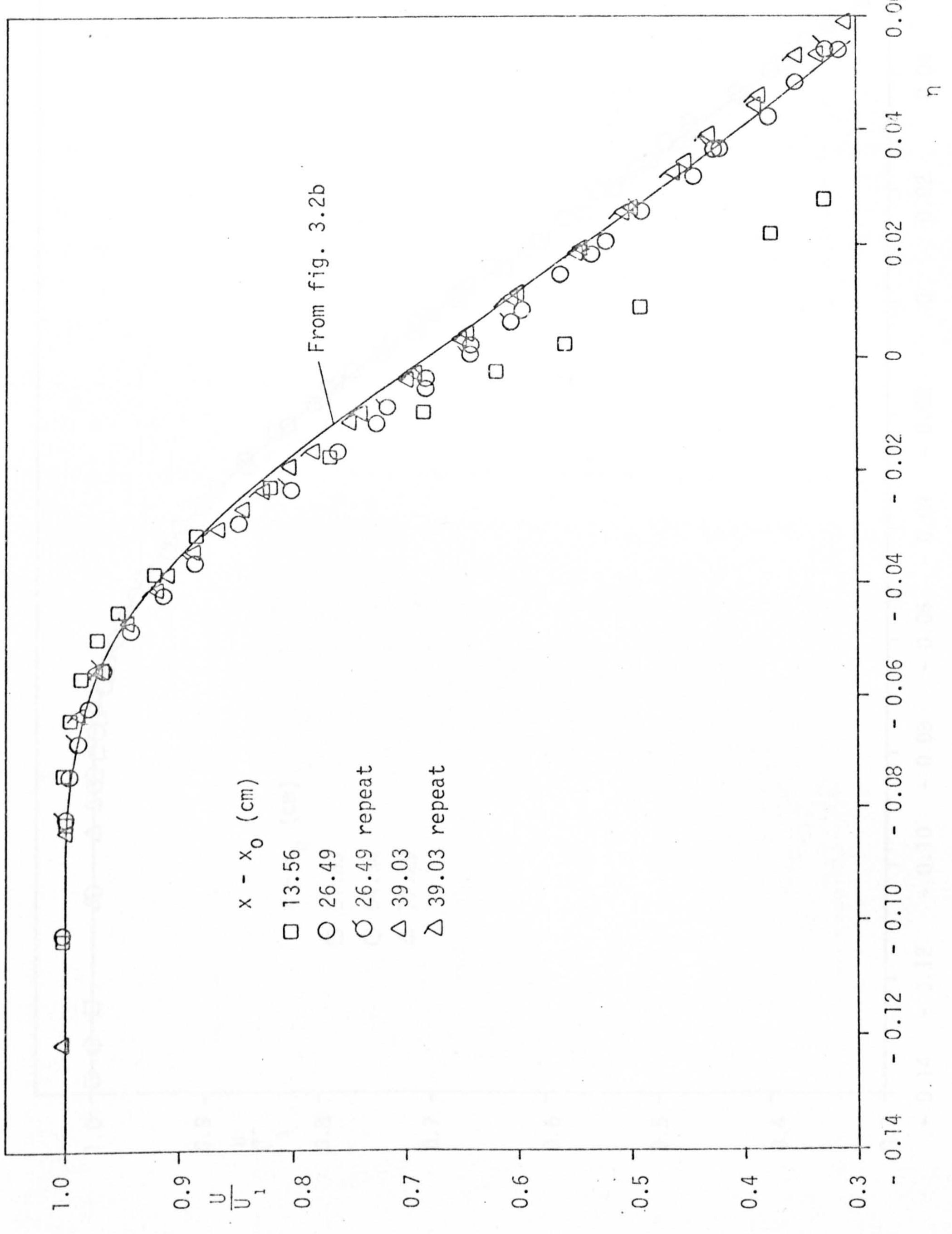


Fig. 3.2a Mean velocity profile in the initial region

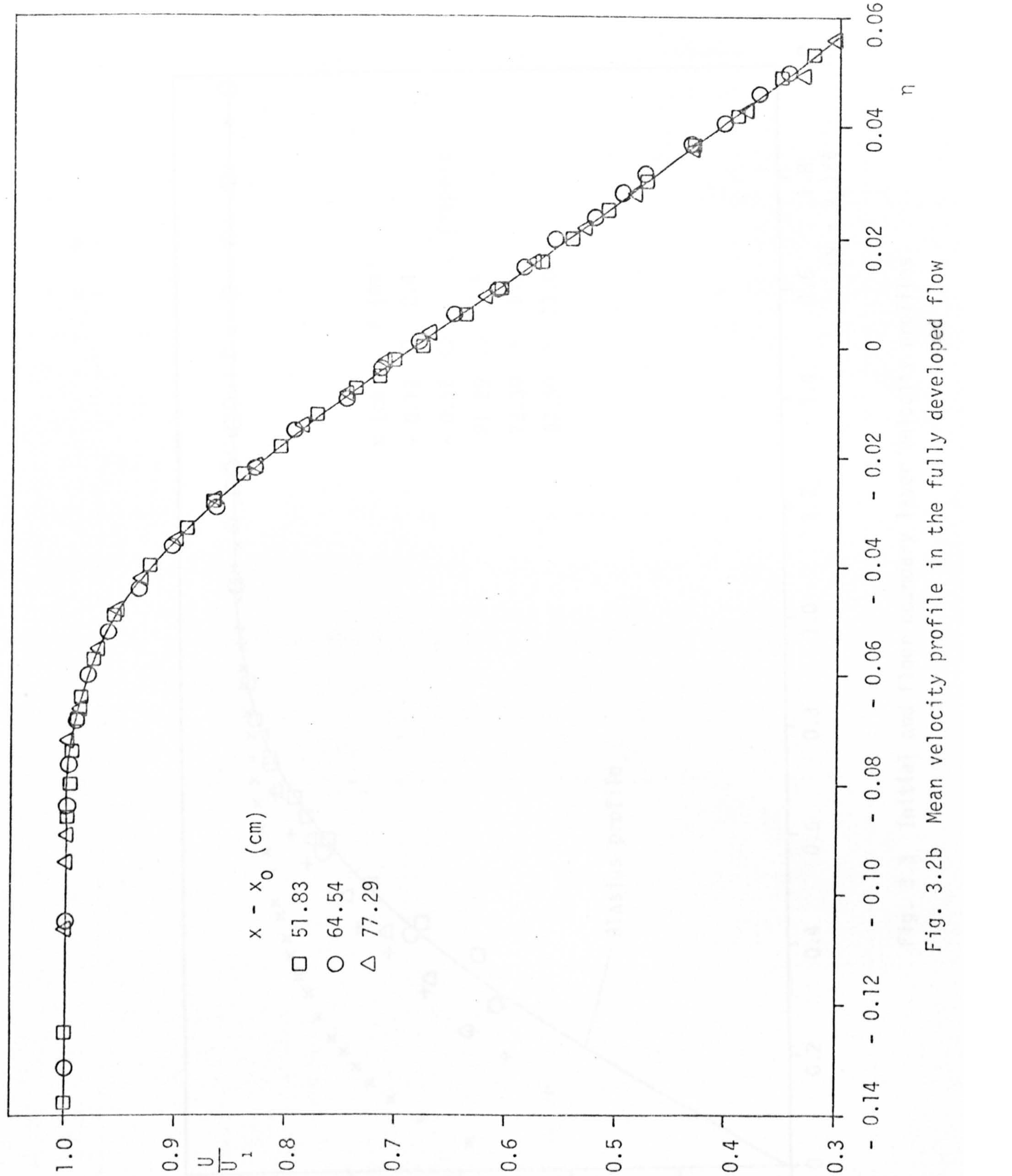


Fig. 3.2b Mean velocity profile in the fully developed flow

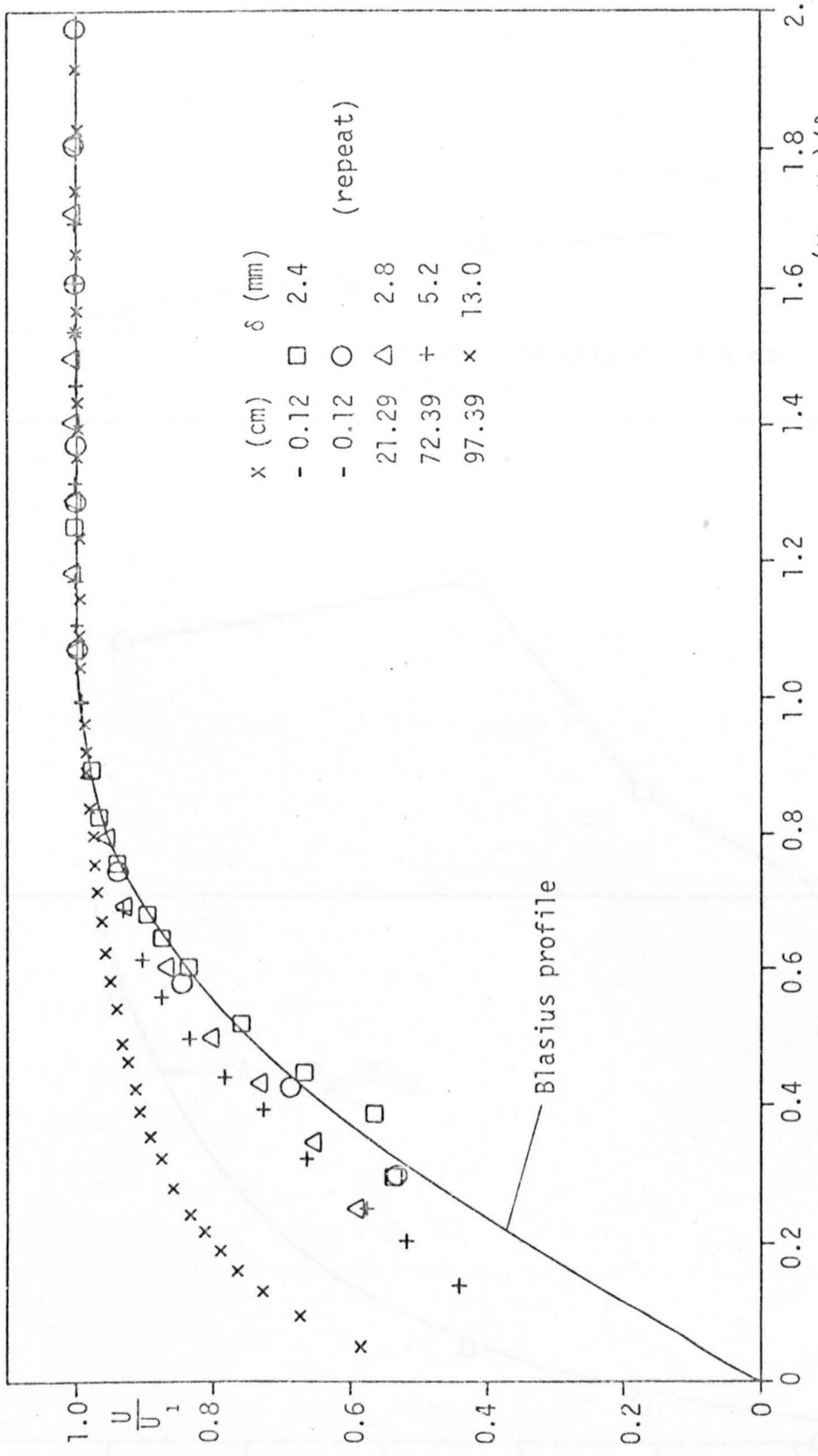


Fig. 3.3 Initial and floor boundary layer velocity profiles

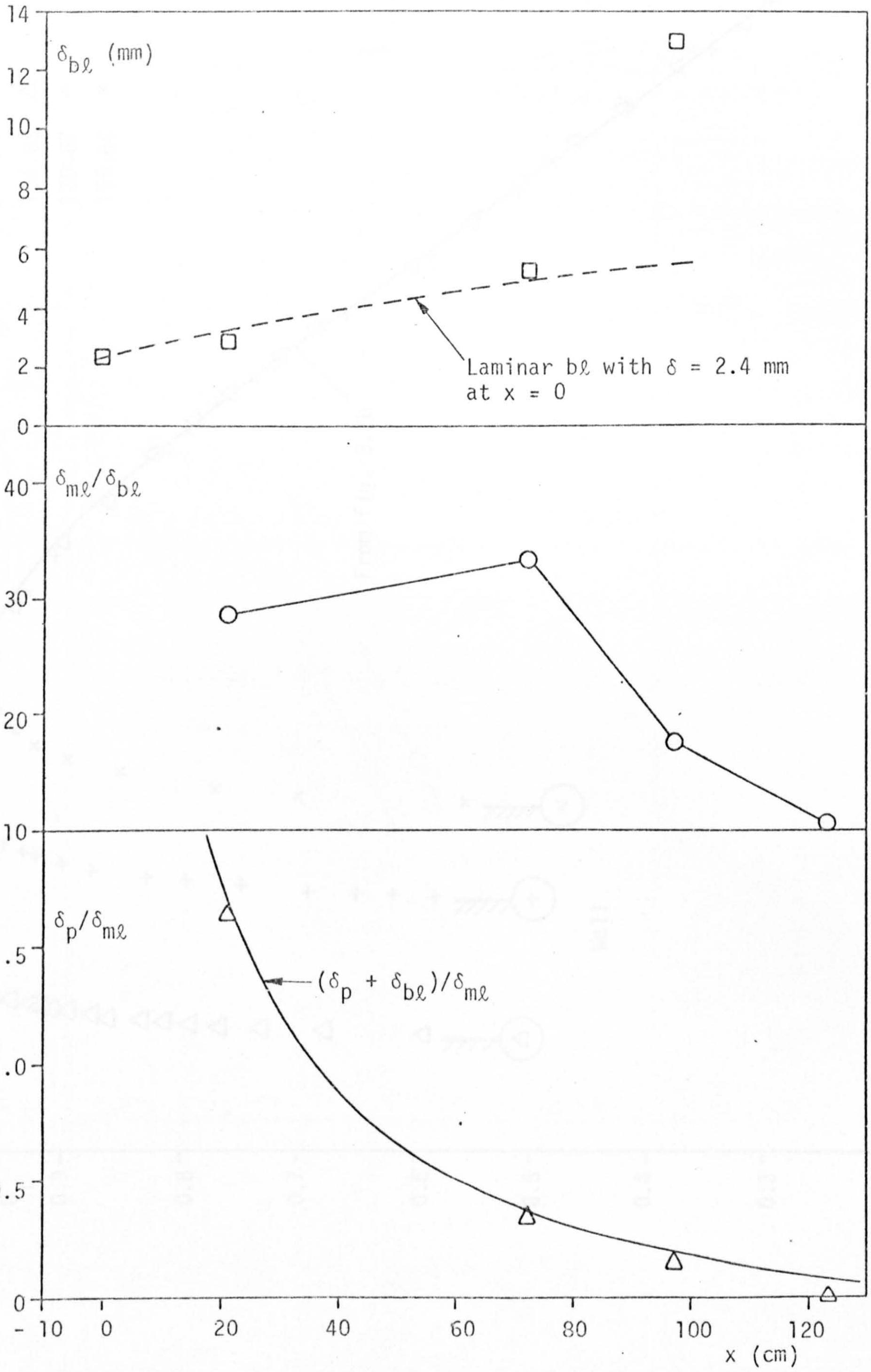


Fig. 3.4 Mixing layer, boundary layer and potential core thicknesses

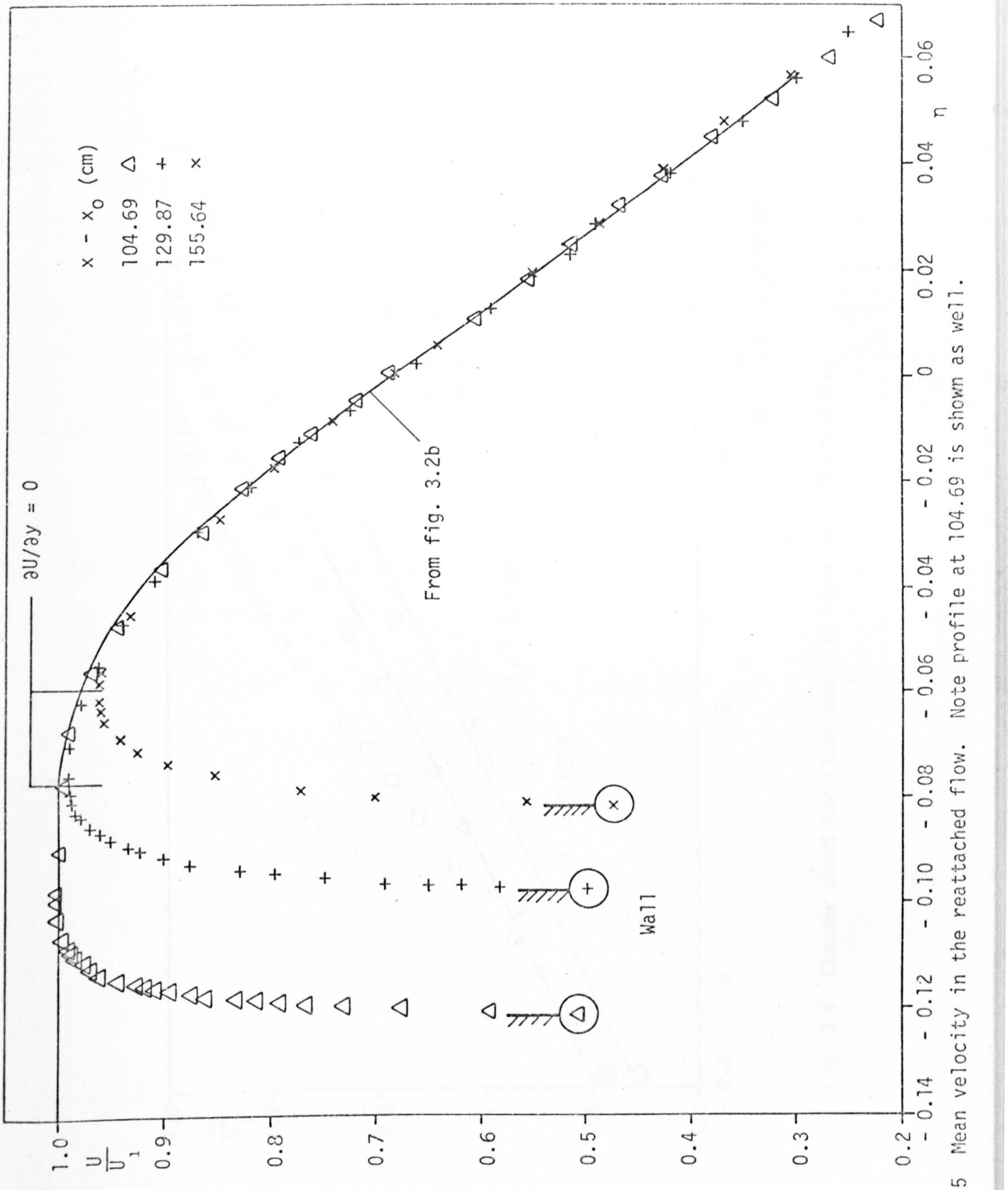


Fig. 3.5 Mean velocity in the reattached flow. Note profile at 104.69 is shown as well.

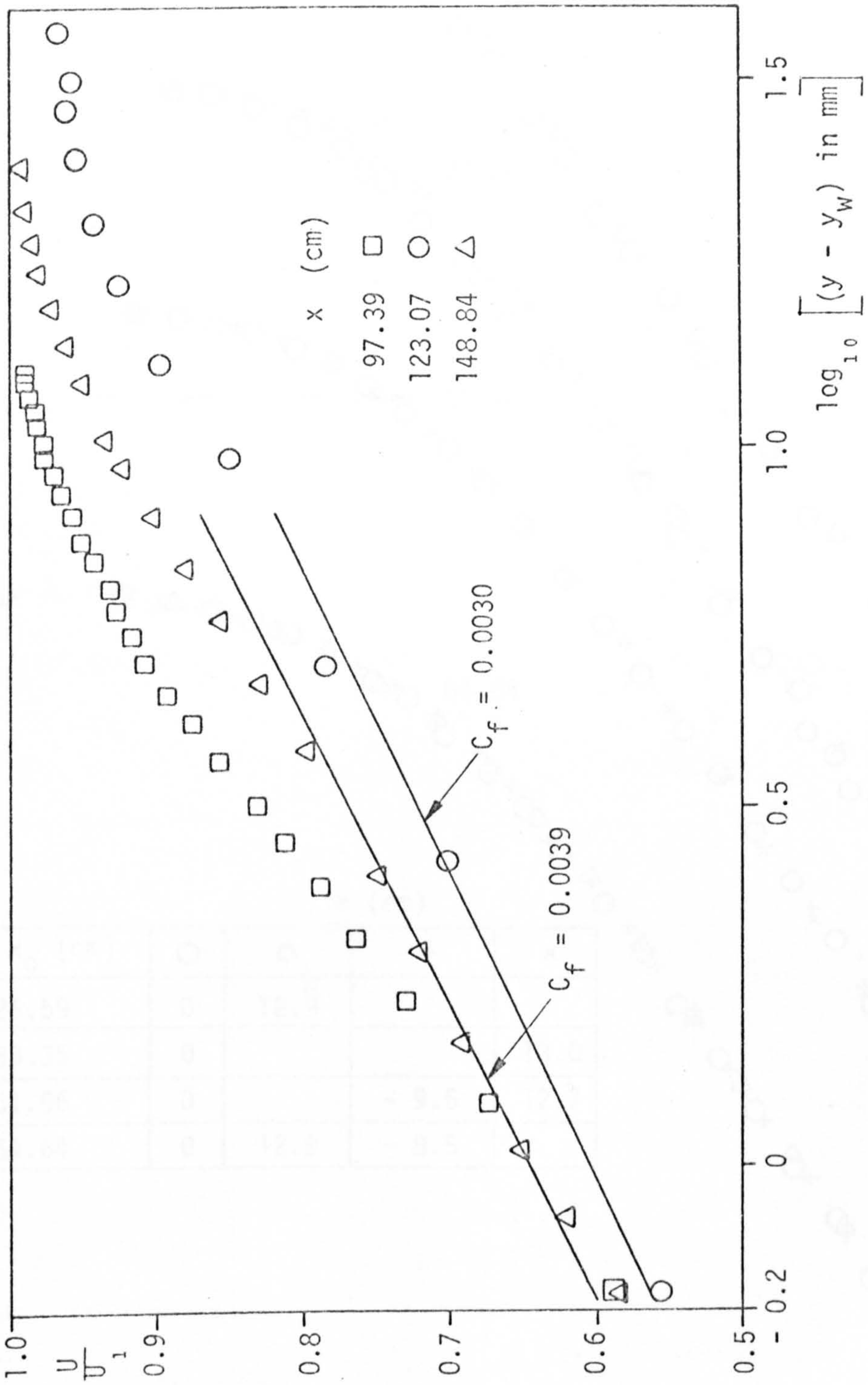
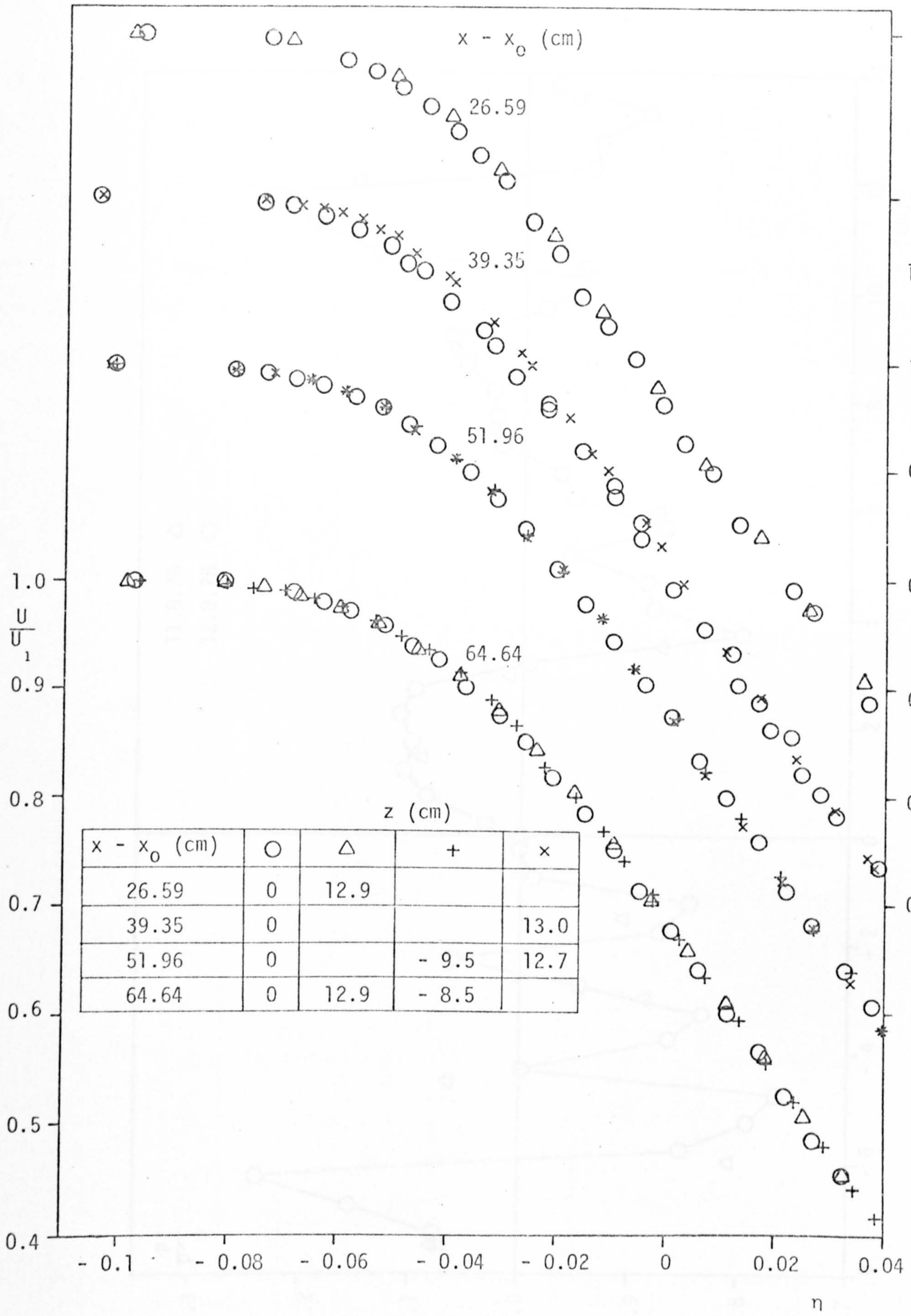


Fig. 3.6 Clauser chart for floor boundary layer velocity profiles



x - x_o (cm)	○	△	+	×
26.59	0	12.9		
39.35	0			13.0
51.96	0		- 9.5	12.7
64.64	0	12.9	- 8.5	

Fig. 3.7 Spanwise uniformity of mean velocity profiles

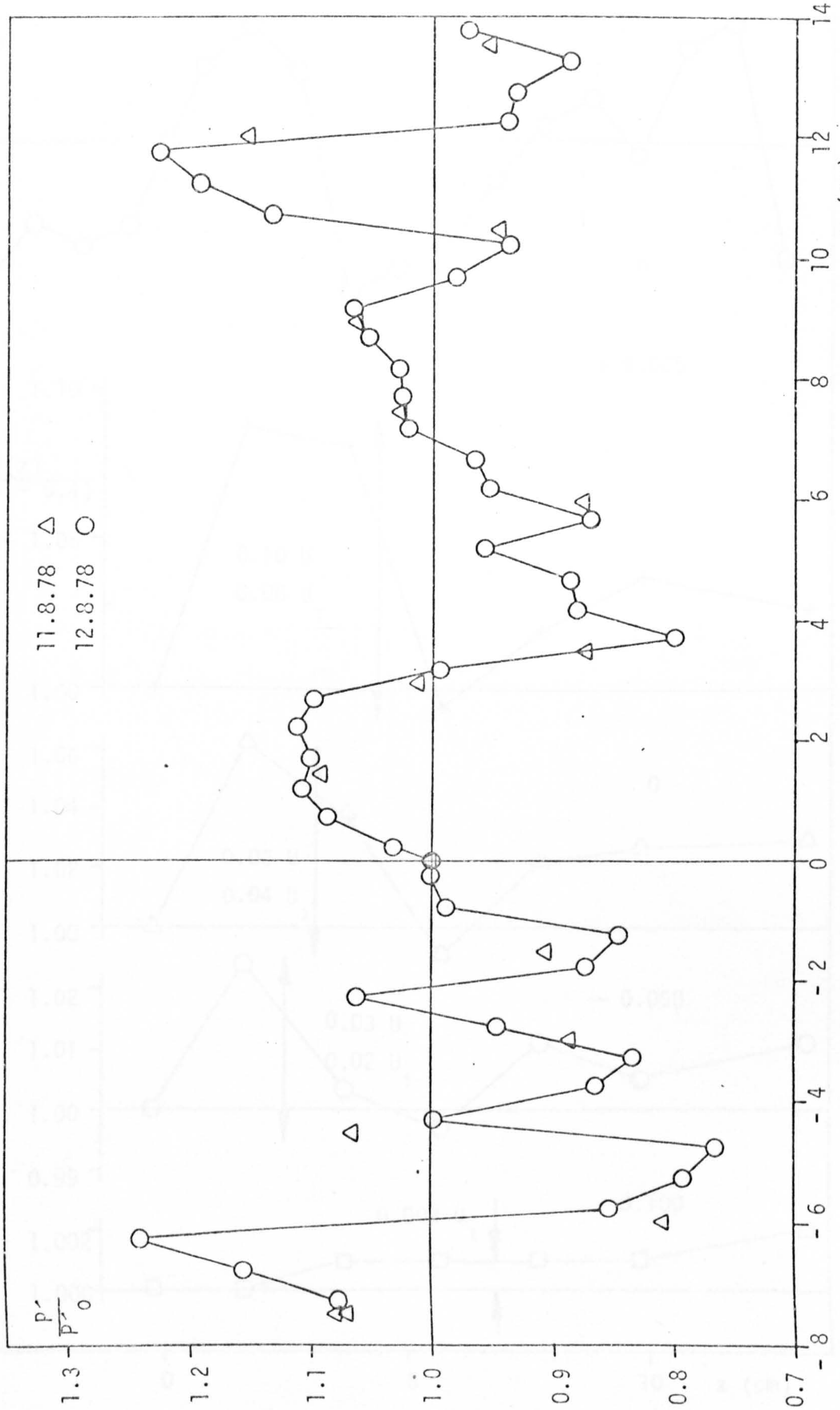


Fig. 3.8a Spanwise uniformity of the initial boundary layer

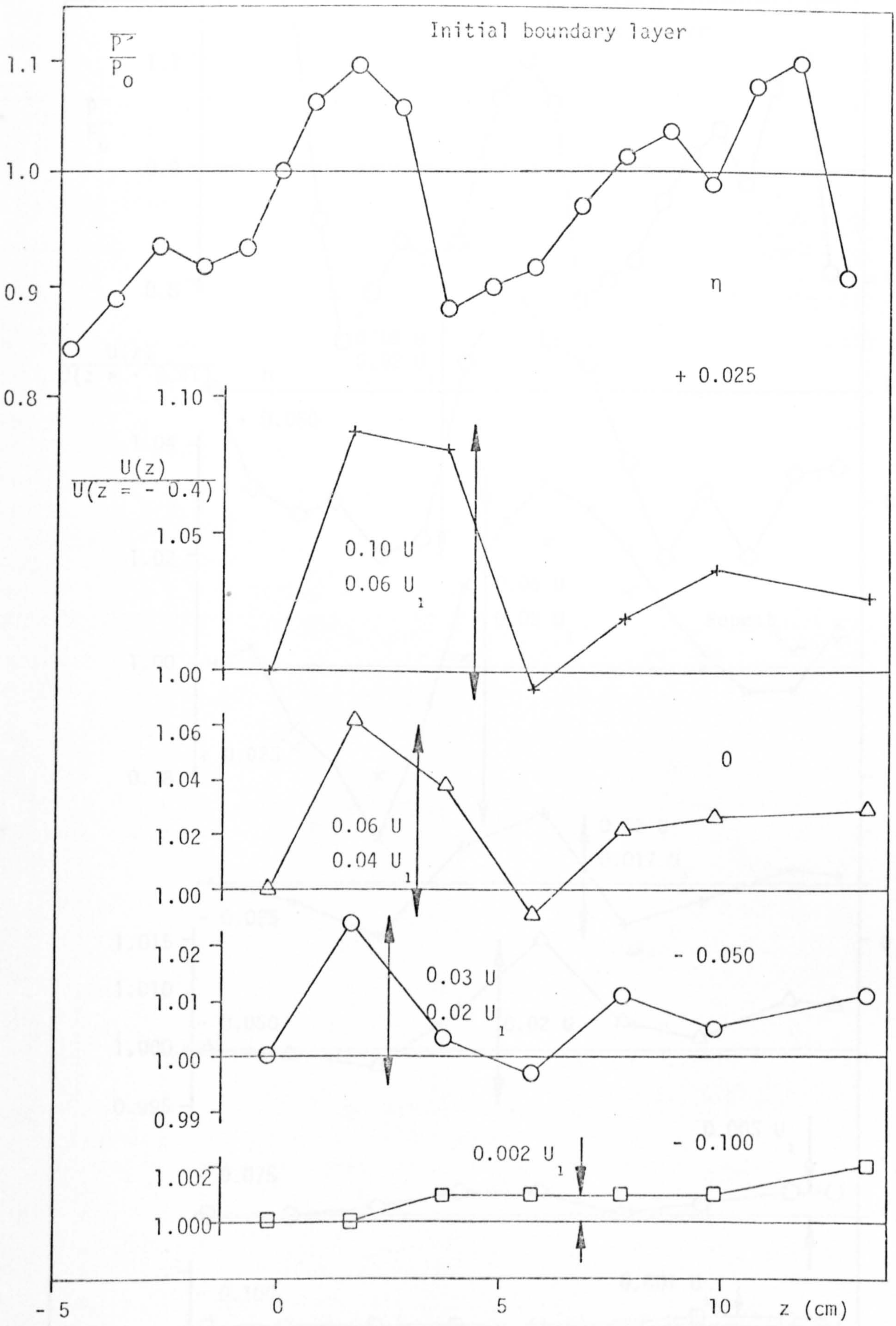


Fig. 3.8b Spanwise mean velocity traverse, $x - x_o = 39.03$ cm

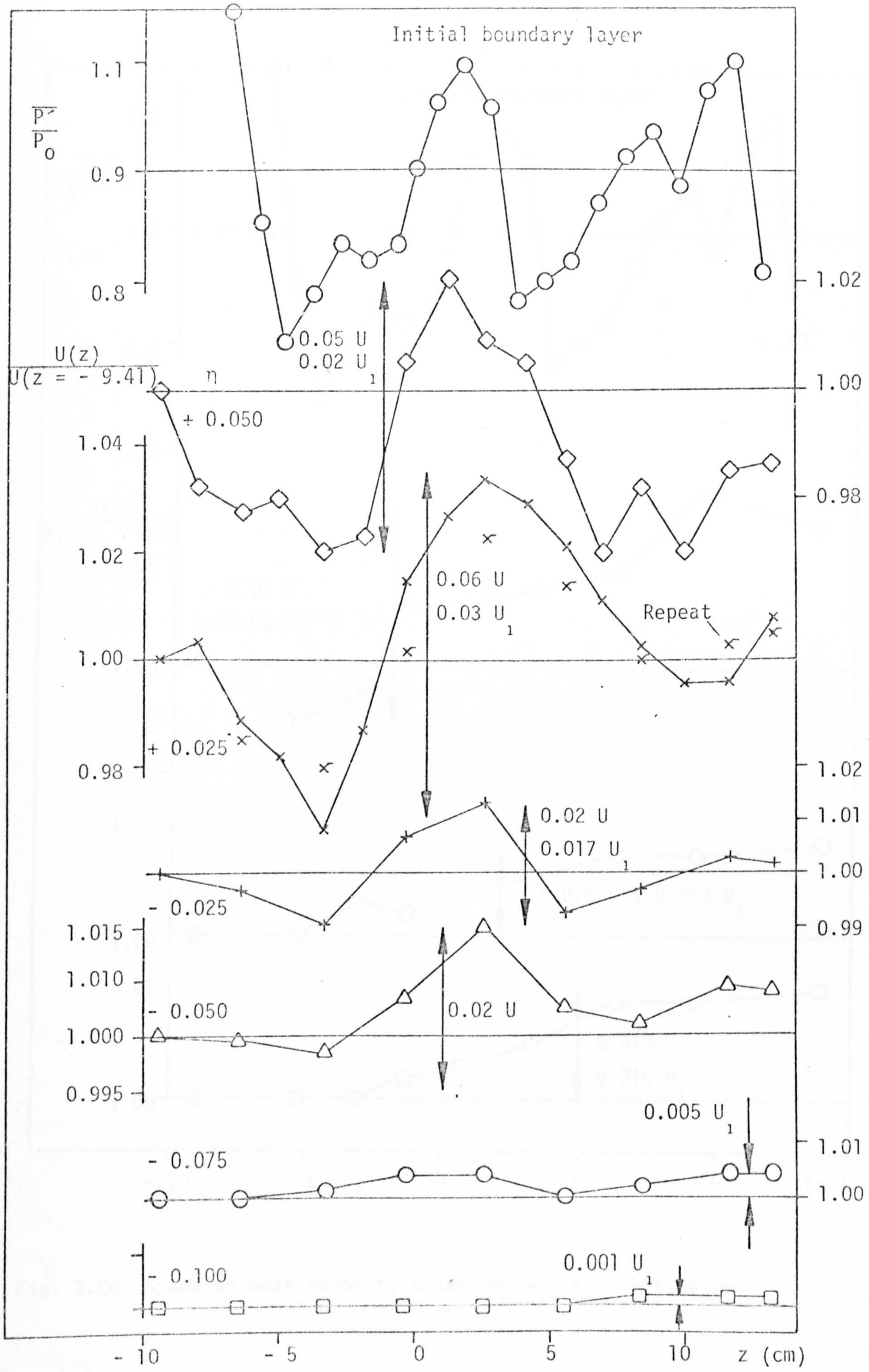


Fig. 3.8c Spanwise mean velocity traverse, $x - x_o = 77.29$ cm

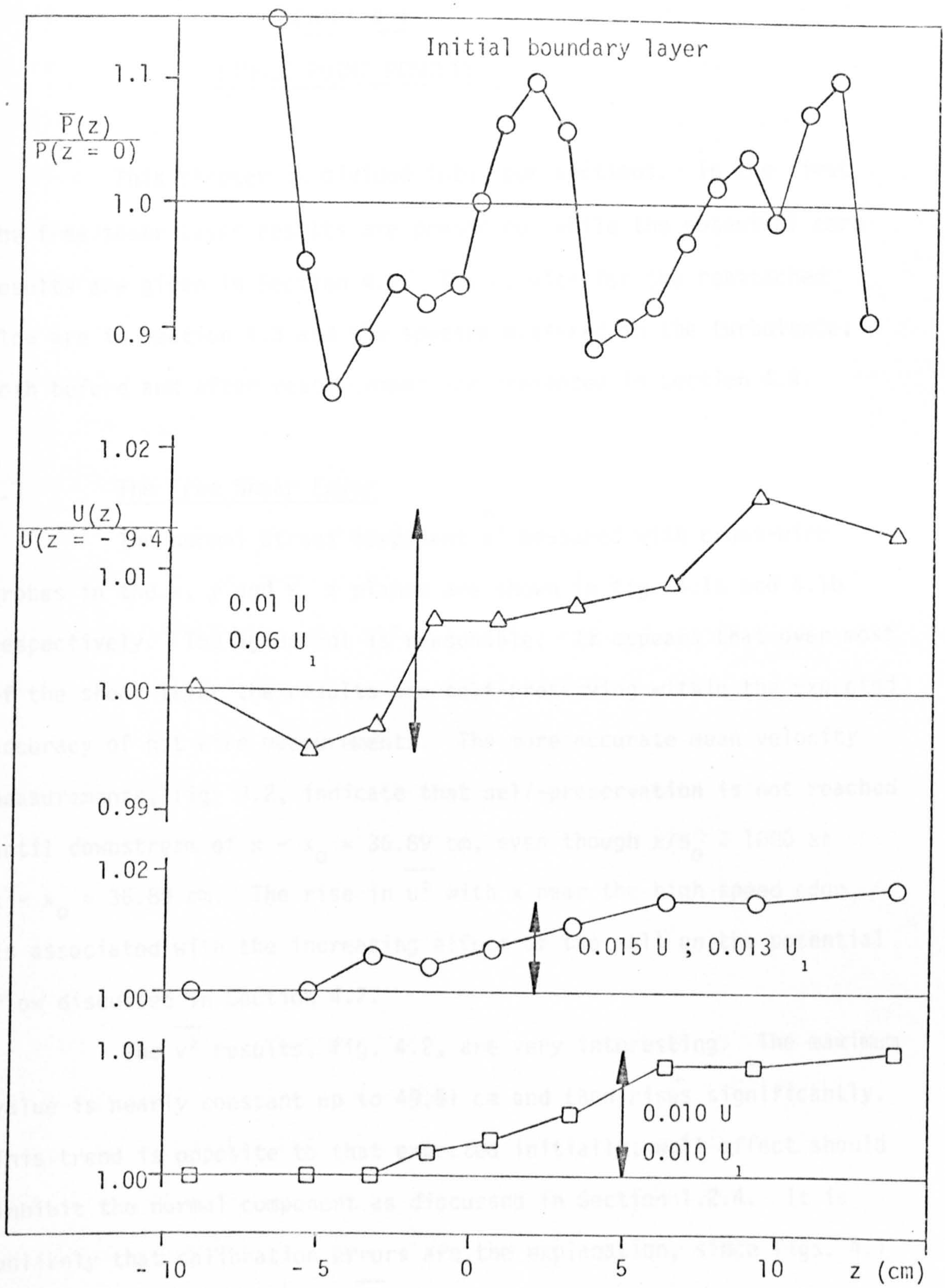


Fig. 3.8d Spanwise mean velocity traverse, $x - x_o = 155.64$ cm

CHAPTER 4

SINGLE POINT RESULTS

This chapter is divided into four sections. In the first the free shear layer results are presented, while the potential core results are given in Section 4.2. The results for the reattached flow are in Section 4.3 and the spectra measured in the turbulence, both before and after reattachment are presented in Section 4.4.

4.1 The Free Shear Layer

The normal stress component $\overline{u^2}$ measured with cross-wire probes in the x, y and x, z planes are shown in fig. 4.1a and 4.1b respectively. The agreement is reasonable. It appears that over most of the shear layer the results are self-preserving within the expected accuracy of hot wire measurements. The more accurate mean velocity measurements, fig. 3.2, indicate that self-preservation is not reached until downstream of $x - x_o = 36.89$ cm, even though $x/\theta_o \simeq 1000$ at $x - x_o = 36.89$ cm. The rise in $\overline{u^2}$ with x near the high speed edge is associated with the increasing effect of the wall on the potential flow discussed in Section 4.2.

The $\overline{v^2}$ results, fig. 4.2, are very interesting. The maximum value is nearly constant up to 49.51 cm and then rises significantly. This trend is opposite to that expected initially; wall effect should inhibit the normal component as discussed in Section 1.2.4. It is unlikely that calibration errors are the explanation, since figs. 4.1 and 4.3, the latter showing $\overline{w^2}$, do not display this trend. All the traverses were done independently with the x, y plane measurements done after those in the x, z plane. The behaviour of $\overline{v^2}$ is discussed further in Section 4.4.

The shear stress $\overline{uv}$ is shown in fig. 4.4. Although the

maximum value is roughly constant with x, the values near the high velocity edge for the first two stations are generally low. The agreement between the measured $\overline{uv}$ and that calculated from the momentum equation (Appendix B) for the self-preserving region is generally within 10%. This is encouraging agreement for a highly turbulent flow.

Figs. 4.1 - 4.4 show that the approach to similarity is quite different in a plane mixing layer as compared to an axisymmetric mixing layer of comparable Reynolds number (Bradshaw, 1966; Yule, 1978). In the latter $\overline{u^2}$, $\overline{v^2}$ and $\overline{uv}$ all overshoot their asymptotic levels in the initial region while $\overline{w^2}$ rises monotonically to its fully developed value. There is no hint of similar behaviour here. Perhaps the explanation lies in fig. 4.5 which indicates appreciable secondary motion in the initial region which then decreases before rising again at the last station before reattachment. The calculations of shear stress in Appendix B based on the two-dimensional equations of motion show the overshoot found experimentally in axisymmetric mixing layers but absent from fig. 4.4.

The shear stress correlation coefficient, R_{uv}, fig. 4.6, reaches a maximum value of 0.52 at 49.51 cm before falling again as $\overline{v^2}$ increases. The distribution at 49.51 cm is in good agreement with the axisymmetric results of Bradshaw et al (1964).

The results for $\overline{u^3}$ in the two measuring planes are shown in figs. 4.7a and 4.7b. The agreement is reasonable and shows a significant increase (decrease in magnitude) with x on the high velocity side, while $\overline{v^3}$, fig. 4.8, decreases with x. The magnitude of $\overline{v^3}$ increases over the whole layer after 49.51 cm as in the case of $\overline{v^2}$.

The distribution of $\overline{w^3}$, which like $\overline{uw}$ is zero in a strictly two-dimensional flow, is given in fig. 4.9. On the high velocity side $\overline{w^3}$ decreases in magnitude with x as does $\overline{uw}$ and as would be expected

from the spanwise mean velocity measurements of Chapter 3. However, at the last measuring station both $\overline{uw}$ and $\overline{w^3}$ have increased.

On the high velocity side neither $\overline{u^2v}$ nor $\overline{uv^2}$ show any consistent trend with x, figs. 4.10 and 4.11, while on the low velocity side there is a general increase with x.

Fig. 4.12 shows that $\overline{u^2w}$ is almost zero on the high velocity side while the behaviour on the low velocity side is more similar to that of $\overline{uw}$ than $\overline{w^3}$. The $\overline{uw^2}$ results, fig. 4.13, show similarity over the entire range of x.

The skewness of the u component fluctuations, defined as $S_u \equiv \overline{u^3}/(\overline{u^2})^{3/2}$ is shown in figs. 4.14a and 4.14b for both measuring planes. The agreement is good and the collapse of the results for $\eta > 0$ is better than that for $\overline{u^2}$ and $\overline{u^3}$ individually, indicating that some of the scatter in the individual results is due to the averaging-time problems discussed in Appendix A. The skewness is a measure of the asymmetry of a probability distribution function (pdf). Thus the results show that the pdf of u becomes more nearly symmetric with x. However S_v is almost unchanged, fig. 4.15, while S_w which again should be zero in a strictly two-dimensional flow is markedly asymmetric near the high speed edge. With increasing negative η, $\overline{w^3}$ and $\overline{w^2}$ both go to zero more quickly than do the corresponding quantities for the other components so S_w will become increasingly inaccurate. A similar result applies to the potential core $\overline{uw}$ measurements discussed in the next section.

The flatness factor of u, defined as $F_u \equiv \overline{u^4}/(\overline{u^2})^2$ is shown in fig. 4.17. The flatness factor is an indication of the size of the tails of a pdf. For a Gaussian distribution F = 3, as shown in fig. 4.17. In agreement with the x, z plane results (which are not shown) the maximum value of F_u drops remarkably from around 15 at 24.05 cm to just over 4 at 100.36 cm. Between these stations $\overline{u^2}$ and $\overline{u^4}$ rise more

than the turbulent zone contributions $\overline{u_T^2}$, $\overline{u_T^4}$. For example at $\eta = -0.050$ $\overline{u^2}$ increases by a factor of 1.8 while $\overline{u_T^2}$ increases by a factor of 1.43. For $\overline{u^4}$ the corresponding factors are 1.55 and 1.30. Since γ does not alter appreciably with x, fig. 6.1, the trend in fig. 4.17 is due to the increasing level of the potential fluctuations which have an F_u close to 3 (the results are not shown here) since this is also the approximate value near maximum γ. The results for F_v, fig. 4.18, and F_w, fig. 4.19, are consistent with this explanation. The level of $\overline{v^2}$ in the potential flow, fig. 4.23, increases with x, but much less so than $\overline{u^2}$, fig. 4.24, while the decrease in F_v is significantly less than the decrease in F_u. In the potential flow $\overline{w^2}$ increases with x, more than $\overline{v^2}$ but less than $\overline{u^2}$, fig. 4.25, while the behaviour of F_w is intermediate between that of F_u and F_v. Note that the relationship $F \sim 3/\gamma$ where $F = F_u$, F_v or F_w assumes that the level of the potential fluctuations is significantly less than that of the turbulent fluctuations (Corrsin and Kistler, 1954) and so is inapplicable to the present case.

The bulk convection velocity of the turbulent kinetic energy is defined as:-

$$V_q \equiv \frac{\overline{p'v'} + \frac{1}{2}\overline{q^2 v}}{\overline{q^2}} .$$

It is the average velocity of transport of q^2 by the v component fluctuations. Since $\overline{p'v'}$ should be negligible, at least well away from wall influence the measurable approximation to V_q:-

$$V_q' \equiv \frac{\overline{v^3} + \overline{uv^2}}{\overline{u^2} + \overline{v^2}}$$

is shown in fig. 4.20. Near the high velocity edge the turbulent

energy equation reduces to advection $\tilde{\sim}$ turbulent transport, or in similarity form:-

$$(V - \eta U) \frac{\partial \frac{1}{2} \overline{q^2}}{\partial \eta} = \frac{\partial}{\partial \eta} \left(\overline{p'v} + \frac{1}{2} \overline{q^2 v} \right) . \qquad (4.1a)$$

In this region $U \simeq U_1$ and $V << \eta U$ so that Eqn. (4.1a) implies:-

$$V_q \sim - \eta U_1 \qquad (4.1b)$$

as shown in fig. 4.20 $V_q'/U_1 \sim - \eta U_1$ for all x, suggesting that $\overline{p'v}$ remains unimportant. The effect of the wall appears to shift V_q' bodily upwards, but only at the last measuring station. The analagous transport velocity for the shear stress is $V_\tau \equiv \overline{uv^2}/\overline{uv}$. Near the high speed edge, V_τ, fig. 4.21, is similar to V_q'. In this region the ratio V_q'/V_τ is nearly constant at about 2.5, which is lower than that found by Weir et al (1980) in their mixing layer before interaction.

4.2 Potential Core Measurements

These measurements are essential in two ways to the determination of the theoretical correlations for the potential flow derived in Appendix C. Firstly they are a check on the validity of Phillips' (1955) analysis for a strongly inhomogeneous shear layer and secondly they are needed to find the parameters χ_{11}, χ_{33} and η_0 which are the only "adjustable constants" in Eqns. (C.21 - C.25) for the potential flow correlations. Furthermore some of the features of wall influence on the potential flow is similar to the effects on the reattached flow, Section 4.3.

The only station for which all the potential flow measured is uninfluenced by the wall and by streamwise inhomogeneity is 24.05 cm,

see below, even though the turbulence is not self-preserving there. The results are compared to Phillips' theory, Eqn. (C.15) in fig. 4.22. It can be seen that the relationship between the components, Eqn. (1.1), is verified to within experimental error. As shown in Appendix C this result follows from irrotationality and homogeneity (i.e. $\overline{uv} = \overline{uw} = 0$) of the potential flow and is not a test of Phillips' formulation of the inner boundary condition, Eqn. (C.2). The individual mean square intensities decay in apparent agreement with Phillips' - 4 power law; the deviation in $\overline{u^2}$ at large negative η is consistent with a free stream turbulence intensity of about 0.1%. No corrections for free stream levels were applied to any of the results presented in this thesis. The agreement between $\overline{u^2}$ measured in the x, y and y, z plane is encouraging but it appears that the effective origin for the three components is different. The lines of best fit to the results are:-

$$\left[\frac{\overline{v^2}}{U_1^2}\right]^{-1/4} = 60.0\ (0.005 - \eta) \qquad (4.2a)$$

$$\left[\frac{\overline{u^2}}{U_1^2}\right]^{-1/4} = 62.4\ (0.014 - \eta) \qquad (4.2b)$$

and:-

$$\left[\frac{\overline{w^2}}{U_1^2}\right]^{-1/4} = 107.0\ (-0.016 - \eta) \qquad (4.2c)$$

The downstream development of $\overline{v^2}$, $\overline{u^2}$ and $\overline{w^2}$ is shown in figs. 4.23 - 4.25 together with the predictions of Eqn. (C.19) using χ_{11}, χ_{33} and η_0 from Eqns. (4.2a) - (4.2c). Thus both the streamwise inhomogeneity and the structural changes within the turbulence, due to the approach to full development and then to the wall effect, are

ignored in using Eqn. (C.19). From Eqn. (C.19) the maximum wall influence on $\left[\overline{u^2}/U_1\right]^{-1/4}$, at $\eta = -0.273$, is less than 3% at 24.05 cm, so this is the only station where wall effect is negligible for all the potential flow measured. The results of Section 4.1 show that the structural differences between the mixing layer at 24.05 cm and the fully developed flow are fairly small, so the approach to full development should not affect the potential flow significantly. The theory predicts the shape but not the magnitude of the $\overline{v^2}$ distributions, fig. 4.23. Both $\overline{u^2}$ and $\overline{w^2}$ are amplified significantly more than predicted, with the amplification of $\overline{u^2}$ being considerably larger than that of $\overline{w^2}$, figs. 4.24 and 4.25. The latter result is similar to the behaviour of grid turbulence near a moving floor (Thomas and Hancock, 1977). Some of the discrepancy between the theory and the results must be due to the streamwise inhomogeneity and to the anisotropy of the turbulence (compare fig. 2.1 with fig. C.3). Fig. 4.26a shows that R_{uv} in the potential flow is nearly zero at 24.05 cm but becomes negative for larger x. The denominator of R_{uv} increases with x so that the increase in magnitude of $\overline{uv}$ itself, the results are not shown here, is large. The results of fig. 4.26a are in qualitative agreement with the results of figs. 4.23 - 4.25. The non-homogeneous form of Eqn. (C.14) for $\underset{\sim}{x}_1 = \underset{\sim}{x}_2$ in mixing layer coordinates (see Eqns. (B.3) and (B.4)) is:-

$$\frac{\partial}{\partial \eta}\left(\overline{u^2} + \overline{w^2} - \overline{v^2}\right) = \left(x\frac{\partial}{\partial x} - \frac{\partial}{\partial \eta}\right)\overline{uv}$$

if $\overline{uw}$ is unimportant. From fig. 4.26a:-

$$x\frac{\partial}{\partial x} >> \frac{\partial}{\partial \eta}$$

emphasizing the importance of the inhomogeneity and from fig. 4.27:-

$$\frac{\partial}{\partial \eta}\left(\overline{u^2} + \overline{w^2} - \overline{v^2}\right) < 0. \qquad \text{Thus } \frac{\partial \overline{uv}}{\partial x} < 0$$

in agreement with the results of fig. 4.26a. The behaviour of R_{uw}, fig. 4.26b, is somewhat puzzling. It is initially high, but at large x there appears no consistent trend in the results. Although the denominator of R_{uw} is significantly less than that of R_{uv} the x, z plane results should be the more accurate, since there will be no change in ψ_{eff} between calibration and measurement (Chapter 2). However, Eqn. (A.6) shows that a smaller error in ψ_{eff}, usually less than 1°, is required to make R_{uw} non-zero than is needed to make R_{uv} non-zero, about 2° at the smallest.

The downstream development of $(\overline{u^2} + \overline{w^2})/\overline{v^2}$, fig. 4.27, clearly shows the importance of wall effect. The ratio $\overline{u^2}/\overline{w^2}$ is shown in fig. 4.28. Both Eqn. (C.15) and Eqn. (C.19) predict that the ratio is constant, whereas even in the unaffected flow it is clearly not constant. The important implication for the analysis in Appendix C is that for $\overline{u^2} > 3\,\overline{w^2}$, χ_{33} in Eqn (C.10) becomes negative. This result is unphysical since a turbulence spectrum can only be positive. Both within and outside a turbulent wake behind a cylinder Townsend (see Phillips, 1955) and Fabris (1979) found that $\overline{u^2}/\overline{w^2}$ is much smaller than the present values. Bradshaw (1967a) found a value of $\overline{u^2}/\overline{w^2}$ of about 2.6 at a position corresponding roughly to $\eta = -0.100$ outside a retarded equilibrium boundary layer. Sunyach and Mathieu (1969) found $\overline{u^2}/\overline{w^2} = 2.5$ on average outside a mixing layer. However, the ratio of $\overline{u^2}/\overline{w^2}$ within their mixing layer was significantly less than in the present flow (see Sunyach, 1971). Thus it appears that $\overline{u^2}/\overline{w^2}$ outside a shear layer is a function of the ratio within the turbulence, but this does not explain why $\overline{u^2}/\overline{w^2}$ is also a function of distance from the shear layer. As x increases $\overline{u^2}/\overline{w^2}$ increases, fig. 4.28, as

was found by Thomas and Hancock (1977). Thus the results of fig. 4.28 are due to some presently unexplainable features of both the unaffected flow and the influence of the wall.

The results of fig. 4.28 cast severe doubts on the adequacy of the severely truncated Taylor series, Eqn. (C.9), used in Appendix C. This is not the only possible low wave-number representation of the spectrum forcing the potential flow. If the shear layer was composed of essentially two-dimensional large structures then $\theta(\underset{\sim}{k})$ could be written as:-

$$\theta(k_1, k_3) = \delta(k_3)\ \theta(k_1) \tag{4.3}$$

which gives, in mixing layer similarity form:-

$$\overline{u^2} = \overline{v^2} = \int_{-\infty}^{\infty} \theta(k_1^*)\, e^{-2|k_1^*|(\eta_o - \eta)}\, dk_1^*,\ \overline{w^2} = 0 \tag{4.4}$$

where integration is over all values of $k_1^* \equiv (x - x_o)\ k_1$, as in Appendix C. If $\theta(k_1) = \delta(k_1 - k_f)$ represents a forcing function at the large eddy wave-number k_f then:-

$$\overline{u^2} = \overline{v^2} \sim e^{-2k_f^*(\eta_o - \eta)},\ \overline{w^2} = 0 \tag{4.5}$$

Fig. 4.29 shows $\ell n\ (\overline{u^2}/U_1^2)$ plotted against η. The resulting line of best fit has a slope corresponding fairly closely with the peak in the potential flow spectra, figs. 4.31 - 4.33. Eqn. (4.5) is the familiar result for potential fluctuations above a two-dimensional "wavy wall" as discussed by Kibens and Kovasznay (1969) who found reasonable agreement between an equation similar to Eqn. (4.5) and their measurements outside a turbulent boundary layer, where the large

eddies are undoubtedly three-dimensional.

Another possibility is that spanwise fluctuations do not contribute to the low wave-number end of $\theta(\underset{\sim}{k})$ so that:-

$$\theta(\underset{\sim}{k}) \sim \theta_{11}\ k_1^2 \qquad (4.6)$$

In this case:-

$$\overline{u^2},\ \overline{v^2} \sim (\eta - \eta_0)^{-3} \quad , \quad \overline{w^2} = 0^*. \qquad (4.7)$$

An attempt to find the optimum exponent was made by plotting $\ell n\ \overline{u^2}$ against $\ell n\ (\eta_0 - \eta)$, fig. 4.30. As there are now two adjustable constants, η_0 and the exponent, the method is not accurate. However, the optimum exponent appears to be nearly - 4, fig. 4.30.

The difficulty in assessing the relative merits of Eqns. (C.10), (4.5) and (4.7) is that over the measurable range, η varies by a factor of 2, fig. 4.22, while Eqn. (4.5) increases by a factor of 12.18 between η = - 0.100 and - 0.200, a difference of only 30% from the corresponding increase, 16, in Eqn. (C.10). The most convincing reason for rejecting Eqns. (4.5) and (4.7) is that the behaviour of the spanwise potential correlations at large separation is crucially dependent on the small, but not negligible, w component fluctuations as discussed in Chapter 5.

Spectra of u, v and w in the unaffected potential flow are shown in figs. 4.31 - 4.33 normalized as required by the analysis of Appendix C, or by Eqns. (4.5) or (4.7). That is:-

---

* Eqns. (4.5) and (4.7) were derived by Professor Ferziger.

$$\phi^*_{ii} = \frac{U_1}{y - y_o}\,\phi_{ii} \quad , \quad \text{where } \phi_{ii} = \frac{\overline{u_i^2\ (\omega)}}{\overline{u_i^2}\ \Delta\omega} \quad \text{for } i = 1,\ 2,\ 3 \tag{4.8}$$

is plotted against:-

$$\omega^* = \frac{(y - y_o)}{U_1}\,\omega \tag{4.9}$$

where ω is the circular frequency and $\Delta\omega$ is the frequency window centred on w and given in Table 4.1. From Eqns. (4.8) and (4.9):-

$$\int_0^\infty \phi^*_{ii}\ (\omega^*)\ d\omega^* = 1$$

The spectra of all components (as are the correlations presented in Chapter 5) are a function of χ_{11} and χ_{33} so that a general effective origin, y_o, is needed. Since χ_{11} is considerably larger than χ_{33} the choice of y_o should be biased in favour of the effective origin for the potential flow $\overline{u^2}$ distribution, Eqn. (4.2b). In view of the uncertainty of determining the general effective origin in the unaffected flow and the impossibility of determining y_o in the wall affected region from the mean square intensities (due to the inaccuracy of Eqn. (C.19)) the effective origin for all the spectra, figs. 4.31 - 4.36, was taken as $y_o = + 0.014\ (x - x_o)$. Using arguments similar to those used in deriving Eqn. (C.15) it can be shown easily that Eqns. (4.8) and (4.9) do not conflict with mixing layer scaling requirements. For the spectra where there is little or no wall influence, figs. 4.31 - 4.33, the collapse is reasonable, and certainly better than if $x - x_o$ was used instead of $y - y_o$ in Eqns. (4.8) and (4.9). There is considerable scatter at low ω^*, more so

in ϕ_{11}^* than in the others and it is particularly noticeable at η = - 0.209. From fig. 4.22 free stream effects are starting to be important at this η. The fact that the ϕ_{11}^* results are the most scattered suggests that wind tunnel unsteadiness which will not contribute to v and w is the most likely cause. The lack of collapse at high wave-number for the positions closer to the shear layer is most likely due to small contributions from the turbulence, at least for η = - 0.103.

Bradshaw (1967a, Eqn. (14a)) shows that for the special case of turbulence homogeneous in the x, z plane, the low wave-number end of the potential spectra is given by:-

$$\phi_{22}(\omega^*) \quad , \quad \phi_{11}(\omega^*) \quad , \quad \phi_{33}(\omega^*) \sim \omega^{*2} \tag{4.10}$$

and as shown in figs. 4.31 - 4.33 this result is not inconsistent with the present data. A plausible corresponding result for large ω^* (Bradshaw, 1967a, Eqn. (14b)) is:-

$$\phi_{22}^*(\omega^*) \quad , \quad \phi_{11}^*(\omega^*) \sim \omega^{*5/2}\, U_c^{*-5/2}\, e^{-2\omega^* U_c^*} \tag{4.11}$$

where $U_c^* \equiv U_c/U_1$ and U_c is the convection velocity. This allows the convection velocity of the potential motion to be determined from the $y - y_0$ dependence of the spectra since the measurements of $\phi_{ii}(\omega^*)$ at varying $y - y_0$ "amount to a degenerate filtered space correlation" (Bradshaw, 1967a). Relaxing the constraint of homogeneity would seriously complicate the mathematics but is unlikely to alter Eqn. (4.11) significantly. An attempt was made to find U_c using Eqn. (4.11) but the fairly small scatter in figs. 4.31 and 4.32 for $\log_{10} \omega^* > 0.25$ precluded an accurate determination of U_c, as the slope of Eqn. (4.11)

on a log scale is not a strong function of U_c. Tolerable fits to the data were obtained for $0.6 < U_c/U_1 < 1$. However, the collapse of the spectra in figs. 4.31 - 4.33 implies that the convection velocity in the potential flow is constant, at least to a good first approximation.

Corresponding spectra for the strongly wall affected potential flow at 75.06 cm are shown in figs. 4.34 - 4.36. The scaling of Eqns. (4.8) and (4.9) is used but this should not collapse the data as there is now an important new length scale, $y - y_w$, where y_w is the position of the wall. Qualitatively the wall attenuates vertical motion of scale large compared to $y - y_w$, for partly the same reasons that the length scale in the inner region of wall bounded flows is proportional to the distance from the wall. Thus the peak in ϕ^*_{22} should move outwards with increasing negative η (decreasing $y - y_w$) as it does in fig. 4.34.

The effect of a wall on the spectra in grid turbulence (Thomas and Hancock, 1977; Hunt and Graham, 1978) is to attenuate Φ_{22} ($\equiv \overline{v^2}\,\phi_{22}$) at low wave-numbers only. This low wave-number energy is transferred to Φ_{33} ($\equiv \overline{w^2}\,\phi_{33}$) at low wave-numbers while Φ_{11} ($\equiv \overline{u^2}\,\phi_{11}$) is increased mostly at high wave-number. A comparison with the present results at $\eta = -0.130$ for ϕ_{11} and ϕ_{22} and $\eta = -0.129$ for ϕ_{33} was made by plotting faired curves for the data of figs. 4.31 - 4.33 on figs. 4.34 - 4.36. The faired curves were shifted down by:-

$$\log_{10}\left[\frac{\overline{u_i^2}\ (x - x_o = 75.06)}{\overline{u_i^2}\ (x - x_o = 24.05)}\right] \quad \begin{array}{l} \eta = -0.130 \text{ for } i = 1, 2 \\ \eta = -0.129 \text{ for } i = 3 \end{array}$$

so that the effects of the wall on Φ_{ii} can be seen. There is attenuation of Φ_{22} at low wave-numbers, fig. 4.34, as expected, but there is also significant loss for $0.25 < \log_{10} \omega^* < 0.5$. Generally

Φ_{11} is amplified, fig. 4.35, but in contradistinction to the grid turbulence results most of the amplification occurs for low wave-numbers, $\log_{10} \omega^* < 0.25$. The behaviour of Φ_{33} is the most similar to the grid turbulence results; nearly all the amplification occurs at low wave-numbers.

4.3 The Reattached Flow

The single point results for the reattached flow, together with those for the last measuring station in the free shear layer, are shown in figs. 4.37 - 4.57. The results are normalized using U_1 and η to emphasize the changes from the free mixing layer structure. The position of the wall, η_w, is - 0.100 and - 0.0834 for 125.86 and 151.51 cm respectively.

The x, y and x, z plane measurements of $\overline{u^2}$ are shown in fig. 4.37. Note the change in scale from fig. 4.1. There is a huge rise in $\overline{u^2}$ near the wall, while $\overline{v^2}$, fig. 4.38, is hardly affected. Fig. 4.39 shows that $\overline{w^2}$ is amplified but, as in the potential core and in the measurements of Thomas and Hancock (1977), the amplification is less than that of $\overline{u^2}$. Generally there is a rise in $\overline{u^2}$ and $\overline{w^2}$ with x, while $\overline{v^2}$ first decreases and then increases, although the increased scatter due to increased uncertainty of measurement and averaging time problems would account for at least some of the differences. In agreement with the momentum equation calculation of Appendix B, the measured shear stress, $\overline{uv}$, fig. 4.40, has increased significantly from the free shear layer value by 151.51 cm and the peak has moved closer to the wall. The calculations also indicate that $\overline{uv}$ at 125.86 cm is above the free shear layer values, but the expected change is within experimental uncertainty. The Clauser charts, fig. 3.6, indicate a wall shear stress, τ_w, of 0.00195 U_1^2 and 0.0015 U_1^2 at 125.86 cm and 151.51 cm respectively and the measurements are

consistent with these values. The maximum negative η results were obtained with the probe resting on the floor. Both the measured and calculated results show that the position where $\overline{uv} = 0$, denoted $\eta_{\tau o}$, is significantly different from the position of zero $\partial U/\partial y$, η_{uo}, which occurs at $\eta = -0.077$ and $\eta = -0.059$ near 125.86 and 151.15 cm respectively, fig. 3.5. The difference between $\eta_{\tau o}$ and η_{uo} is even greater than in a fully developed wall jet (Bradshaw and Gee, 1960) and indicates that a turbulence model in which $\overline{uv}$ is directly related to $\partial U/\partial y$, such as by an eddy viscosity, would be incapable of predicting the present results.

Comparing fig. 4.41 with fig. 4.5 shows that $\overline{uw}$ increases as the flow reattaches. This may be a further reason for the discrepancy between the calculated and measured shear stresses for reasons similar to those given in Section 4.1 for the behaviour of $\overline{uv}$ in the initial region of the free shear layer. However, the spanwise variation in mean velocity at the last measuring station, fig. 3.8d, is comparatively small so the effects of the secondary motion on $\overline{uv}$ are likely to be smaller in the reattached flow than in the free shear layer.

The shear stress correlation coefficient R_{uv} is plotted in fig. 4.42. The magnitude generally increases with x, firstly due to the decrease in $\overline{v^2}$ and then to the increase in $\overline{uv}$.

The x, y and x, z plane measurements of $\overline{u^3}$, figs. 4.43a and 4.43b, show a continuation of the trend of fig. 4.7. On the high velocity side $\overline{u^3}$ decreases in magnitude and finally becomes positive, while there is a general increase on the low velocity side. The trend of $\overline{v^3}$ is opposite to that in the free shear layer, fig. 4.8, as the magnitude has decreased on the high speed side. This result is consistent with initial ideas about the "splat effect" although it is puzzling that $\overline{v^2}$ does not show the same trend.

Figs. 4.45 and 4.48 show that $\overline{w^3}$ and $\overline{u^2w}$ have increased slightly, again indicating renewed secondary motion.

Both $\overline{u^2v}$ and $\overline{uv^2}$, figs. 4.46 and 4.47, which were unaffected on the high speed side in the free shear layer, figs. 4.10 and 4.11, have now changed significantly, with $\overline{u^2v}$ even going positive near the wall at 151.51 cm. In the free shear layer, $\overline{uw^2}$ was the most closely self-preserving quantity, fig. 4.13, while in the reattached flow it has changed significantly, fig. 4.49. The maximum value has increased and the results around $\eta = 0$ have the appearance of being bodily shifted towards the wall.

Again the agreement between $\underline{S_u}$ measured in the x, y and y, z planes is better than that for $\overline{u^2}$ and $\underline{u^3}$ individually, figs. 4.50a and 4.50b. The general decrease on the high speed side evident in the free shear layer, fig. 4.14, continues. S_v is now dramatically affected by the wall, fig. 4.51, in contrast to the free shear layer results, fig. 4.15. S_v goes positive near the wall for both the reattached flow stations, while S_u does so only for the last station. The crossover point at the last station is nearly equal for S_u and S_v and is considerably different from the crossover point of $\overline{uv}$. In equilibrium shear layers the sign of S_uS_v is generally the sign of $\overline{uv}$ so the present results suggest that the motion near the wall is composed of two widely different scales. These are the large scale motion of the mixing layer and the "small scale" motion, originating in the upstream boundary layer, that is responsible for the negative shear stress. From fig. 3.4 the large eddies in the mixing layer are an order of magnitude larger than those in the boundary layer, which in turn are larger than the shear-stress-bearing eddies in the wall region. The wall affected mixing layer eddies are responsible for the high levels of $\overline{u^2}$ and $\overline{w^2}$ (see below) and for the behaviour of S_u and S_v. Of course, this argument is merely transposing the concept of

"inactive" motion (Townsend, 1961; Bradshaw, 1967b) to the present situation.

In contrast to the $\overline{w^3}$ results, fig. 4.52 shows that S_w decreases with x in the reattached flow. This is probably partly due to the large increase in $\overline{w^2}$ near the wall which should make the results of fig. 4.52 more accurate than those in the free shear layer.

The agreement between the x, y and x, z plane measurements of F_u is good, fig. 4.53. There is little apparent difference between the three stations, showing that the large decrease with x in the free shear layer, fig. 4.17, has ceased. The reduction in F_v, fig. 4.54, is confined to the region close to the wall, while F_w, fig. 4.55, is reduced in the region of large amplification of $\overline{w^2}$ showing that the amplification of $\overline{w^2}$ in the potential flow, fig. 4.25, continues. From the normal correlation traverse at 151.51 cm (fig. 5.78) with the moving probe at η = - 0.075 the turbulent contributions to $\overline{u^2}$ and $\overline{v^2}$ were 84 and 88% respectively. Neither the single point x, y plane measurements at 151.51 cm nor any of the x, z plane measurements were conditionally sampled, but it is unlikely that the turbulent contribution to $\overline{w^2}$ would be significantly less than that to $\overline{u^2}$ and $\overline{v^2}$. Thus most of the amplification in $\overline{u^2}$ and $\overline{w^2}$, figs. 4.37 and 4.39, is due to the turbulent motion. A plot of u; v and uv at η = - 0.075 is given in fig. 6.1f.

The upward shift in V_q evident at the last station in the unattached flow, fig. 4.20, continues in the reattached flow, fig. 4.56. The present results are qualitatively similar to the hot-zone measurements of Weir et al (1980, fig. 14) in the interaction region of two real mixing layers. In a zero pressure gradient boundary layer the equivalent form of Eqn. (4.1b) is:-

$$\frac{V_q}{U_1} = \frac{d}{dx}(\delta - \delta^*). \qquad (4.12)$$

V_q' increases nearly linearly with distance from the wall until it reaches a constant value; in their undisturbed boundary layer Smits et al (1979) measured $V_q' = + 0.016\ U_1$ at the outer edge. There cannot be any direct comparison with the present situation and, in any case, Eqn. (4.12) is not strictly applicable here. However, the small positive values of V_q in the wall region are most likely due to what was the upstream boundary layer. This conclusion is supported by the order of magnitude disparity between the scales of the large eddies in the boundary layer and the mixing layer; it is these eddies which affect most of the turbulent diffusion and hence V_q'. This also implies that the effect on V_q' of the boundary layer, as such, will be negligible away from the region of positive V_q'.

V_τ, fig. 4.57, is more difficult to interpret since it goes to infinity as $\overline{uv} \to 0$. In their undisturbed boundary layer Smits et al (1979) found $V_\tau \simeq + 0.04\ U_1$. This is in reasonable agreement with the point closest to the wall at 125.86 cm but then V_τ appears to oscillate around zero before becoming negative on the high speed side. At the last station there are no positive values of V_τ near the wall.

4.4 The Turbulence Spectra

The spectra of u, v and w were computed near maximum γ and the half intermittency point for 36.89 cm, figs. 4.58 - 4.60; 75.06 cm, figs. 4.61 - 4.63 and 151.51 cm, figs. 4.64 - 4.66. For comparison, potential flow spectra are included for the first two stations. The spectral analysis was done separately from the time domain analysis which always used a bandwidth of 1 Hz - 10 kHz as mentioned in Chapter 2. Since the interesting aspects of wall effect occur at relatively

low frequencies, the folding frequency was limited to 5 kHz, after 37 cm to avoid excessive computing. The effect of cutting off the high frequency end of the spectra was determined by comparing the area under the unnormalized spectra with the time domain mean square intensity which the spectral program also calculated. In all cases the difference was less than 0.5%. Details of the folding frequency, block lengths and frequency windows used in determining the spectra are given in Table 4.1. All the spectra presented in this section have been normalized using mixing layer similarity scales, so the vertical scale is:-

$$\log_{10} \phi'_{ii} = \log_{10} \left[\frac{U_1}{x - x_o} \phi_{ii} \right]$$

where ϕ_{ii} is defined by Eqn. (4.8), and the abscissa is:-

$$\log_{10} \omega' = \log_{10} \left[\frac{\omega (x - x_o)}{U_1} \right]$$

The spectra at 36.89 cm, figs. 4.58 - 4.60, are unremarkable. Near maximum γ they all display an extensive inertial subrange over which the - 5/3 rds law holds. ϕ'_{11} at η = + 0.018, fig. 4.58, is in good agreement with Castro's (1973, fig. 4.11) analog spectra at η = 0, which is a useful test of the digital program. ϕ'_{22} has a slight peak at $\omega' \simeq 7.5$, fig. 4.58. For comparison the maximum γ results at 36.89 cm are replotted in figs. 4.61 onwards; without any corrections for change in mean square intensity.

At 75.06 cm, the peaks in all the spectra, figs. 4.61 - 4.63, have moved to lower ω' as the streamwise (and spanwise) scales of the motion are increased by wall effect. The peak in ϕ'_{11}, fig. 4.61, has sharpened slightly around ω' = 3.6, while the peak in ϕ'_{22}, fig. 4.62,

at this frequency has been amplified considerably. This is the most likely cause of the increase in $\overline{v^2}$ with x, fig. 4.2. The peak in ϕ'_{33}, fig. 4.63, has not been sharpened.

At 151.51 cm the peaks in all the spectra, figs. 4.64 - 4.66, have moved outwards by almost the ratio 151.51/75.06, which might suggest that a feedback mechanism, independent of mixing layer scaling, was responsible. However, the peaks occur at nearly the same ω' as at 36.89 cm, while the effect of the wall, and the consequent rise in $\overline{v^2}$ after 50 cm, has not altered either the spreading rate of the free shear layer or the mean velocity profile over most of the reattached flow. The most likely explanation is that at 151.51 cm, the stretching of the streamwise scales by the wall (which cannot proceed indefinitely) has been finally limited.

The reattached flow spectra closest to the wall show the large disparity in scale between the mixing layer and the floor boundary layer, mentioned in the previous section. In a turbulent boundary layer, the (broad) peak in ϕ_{ii} occurs at a frequency of about $U_1\ \delta_{b\ell}^{-1}$. Taking $(\eta_{uo} - \eta_w)\ (x - x_o)$ as an overestimate of $\delta_{b\ell}$ (since using $\eta_{\tau o}$ would give a smaller value) $U_1\ \delta_{b\ell}^{-1}$ corresponds to $\log_{10} \omega' \simeq 1.6$. The spectra near the wall have the appearance of consisting of two widely different frequency bands. In the first band, containing the peak around $\log_{10} \omega' \simeq 0.8$, the spectral density falls rapidly until around $\log_{10} \omega' \simeq 1.6$ where the shape changes as the "boundary layer" turbulence becomes dominant.

TABLE 2.1

PARAMETERS FOR SPECTRA

$x - x_o$ (cm)	Digitizing rate (Hz)	Low pass filter frequency (Hz)	No. points per block
	Turbulence Spectra		
36.89	20000.0	10000.0	2048
75.06	10000.0	5000.0	4096
151.51	9090.9	5000.0	4096
	Potential Spectra		
24.05 and 36.89	9090.9	3333.3	2048
75.06	4545.5	1667.7	2048

Notes

1. Parameters were equal for u, v and w spectra.
2. All frequencies in real time.
3. Folding frequency = $\frac{1}{2}$ x digitizing rate.
4. Frequency window = $\frac{\text{digitizing rate}}{\text{no. points per block}}$

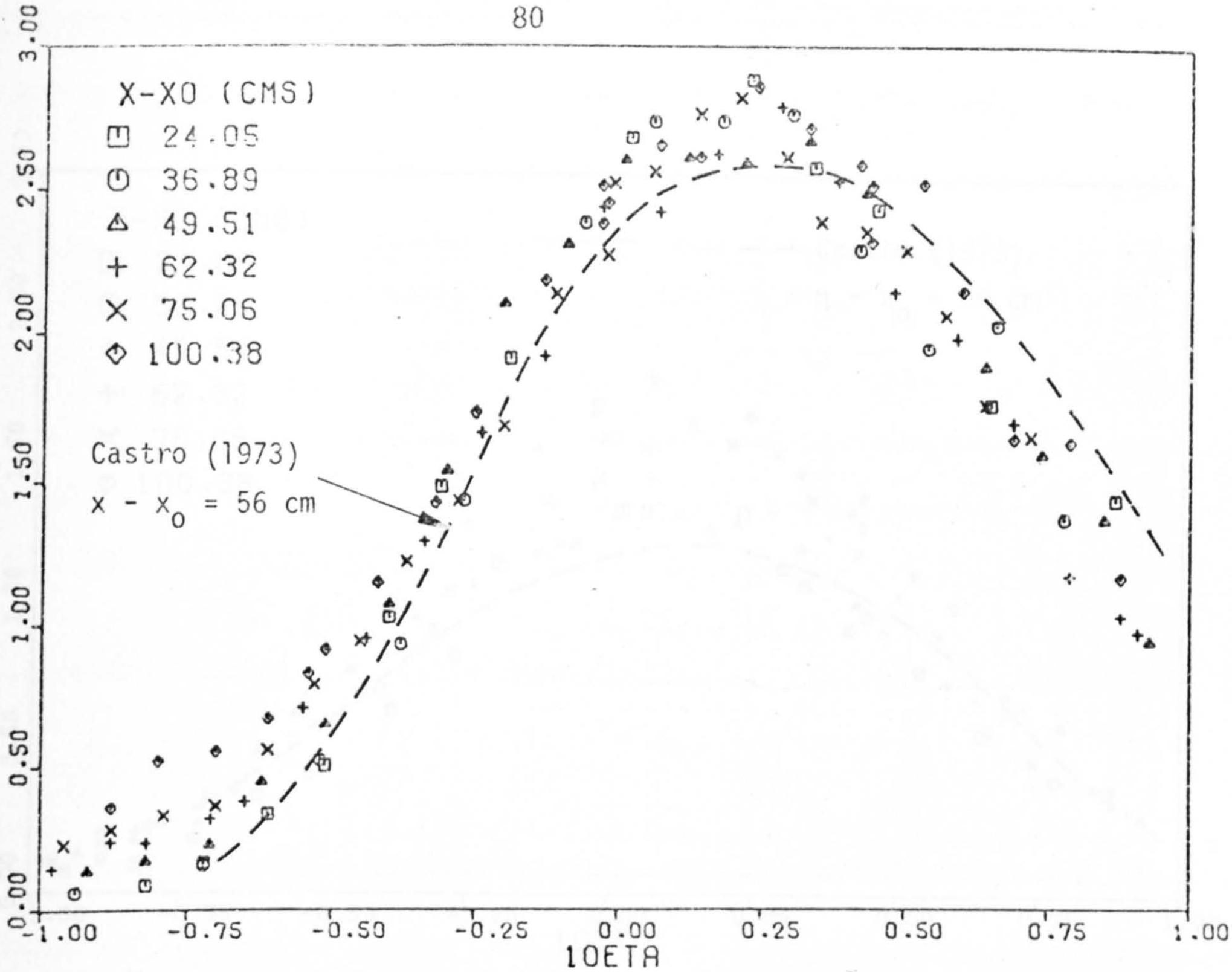


Fig. 4.1a $10^2\ \overline{u^2}/U_1^2$ in the free shear layer; x, y plane results

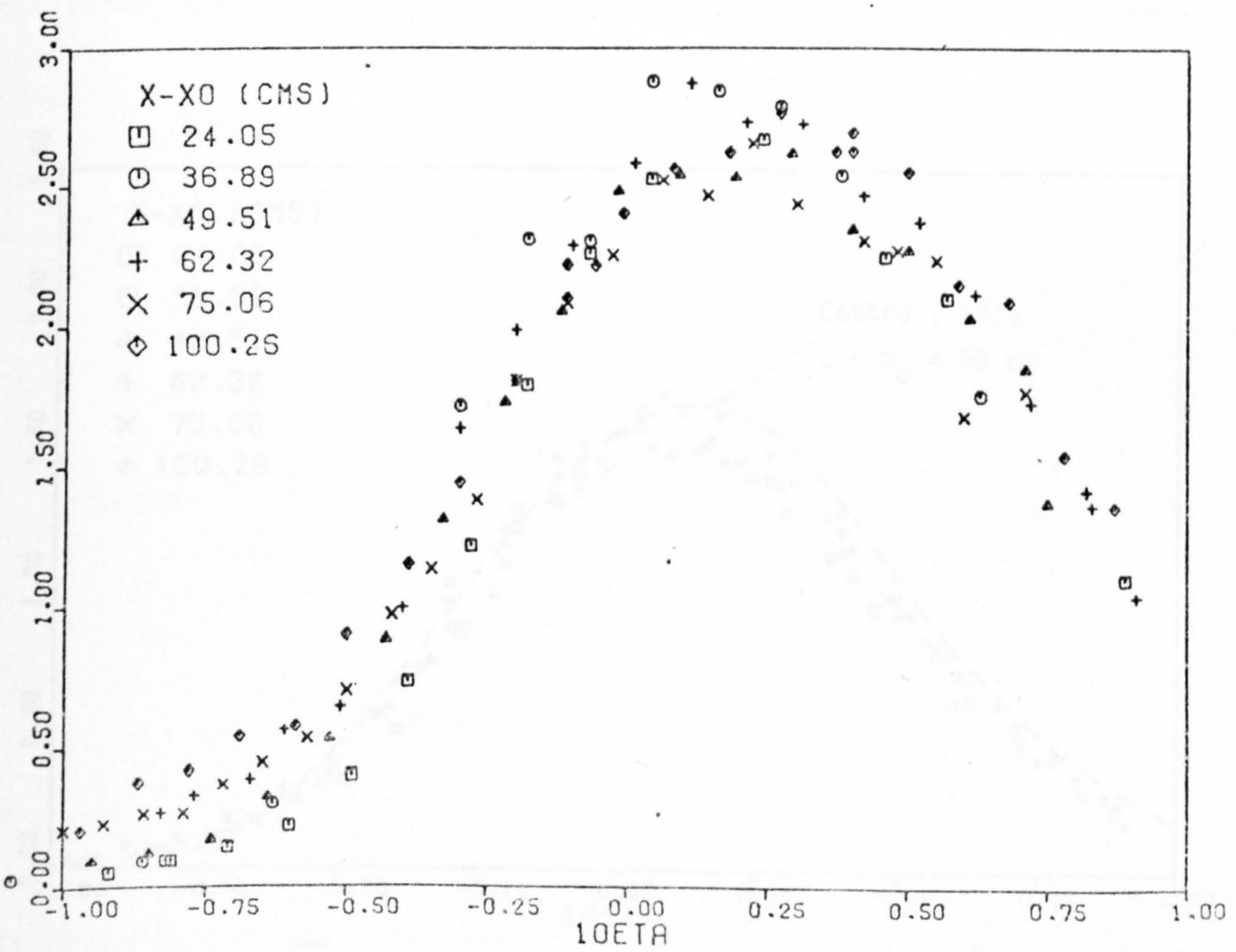


Fig. 4.1b $10^2\ \overline{u^2}/U_1^2$ in the free shear layer; x, z plane results

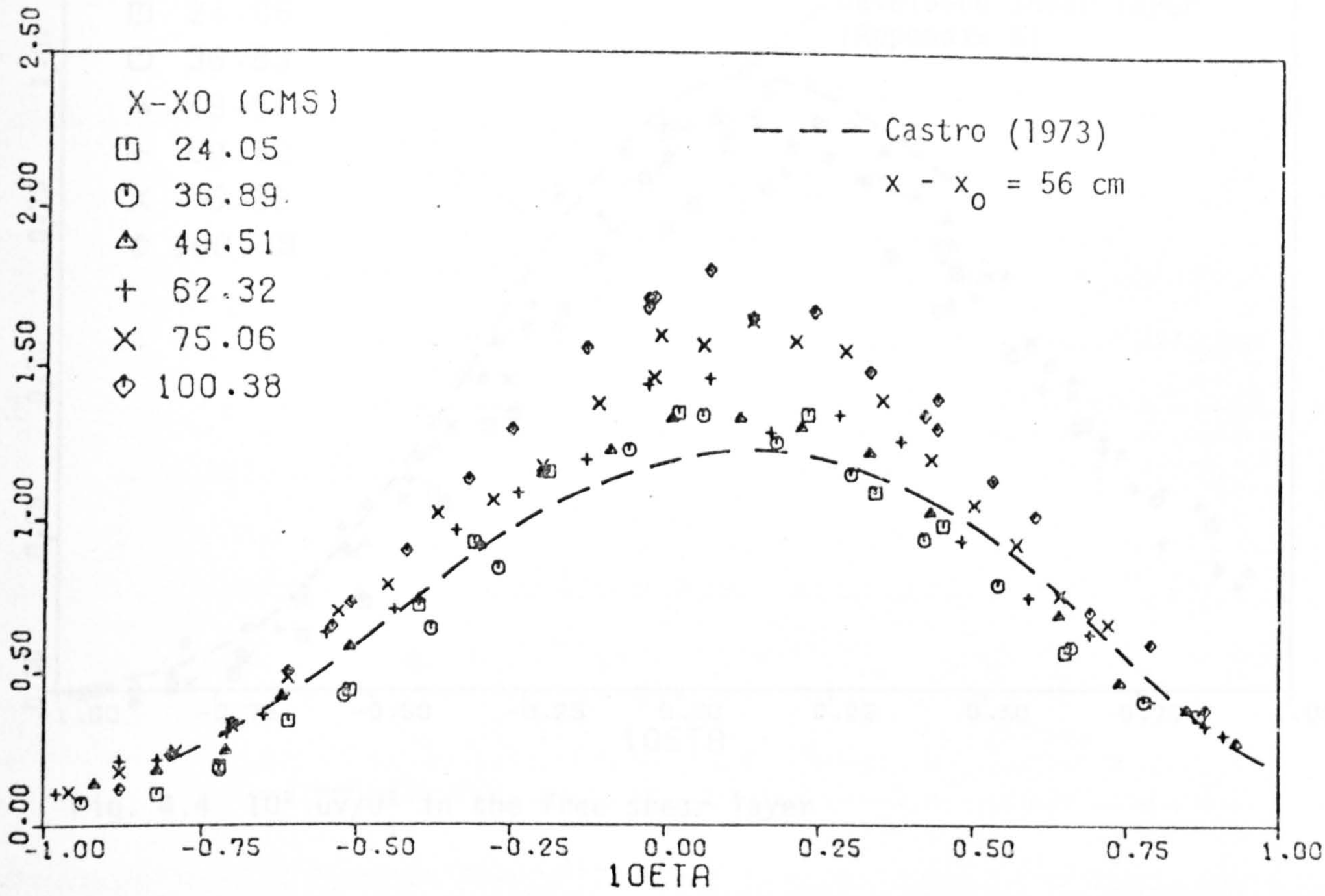


Fig. 4.2 $10^2\ v^2/U_1^2$ in the free shear layer

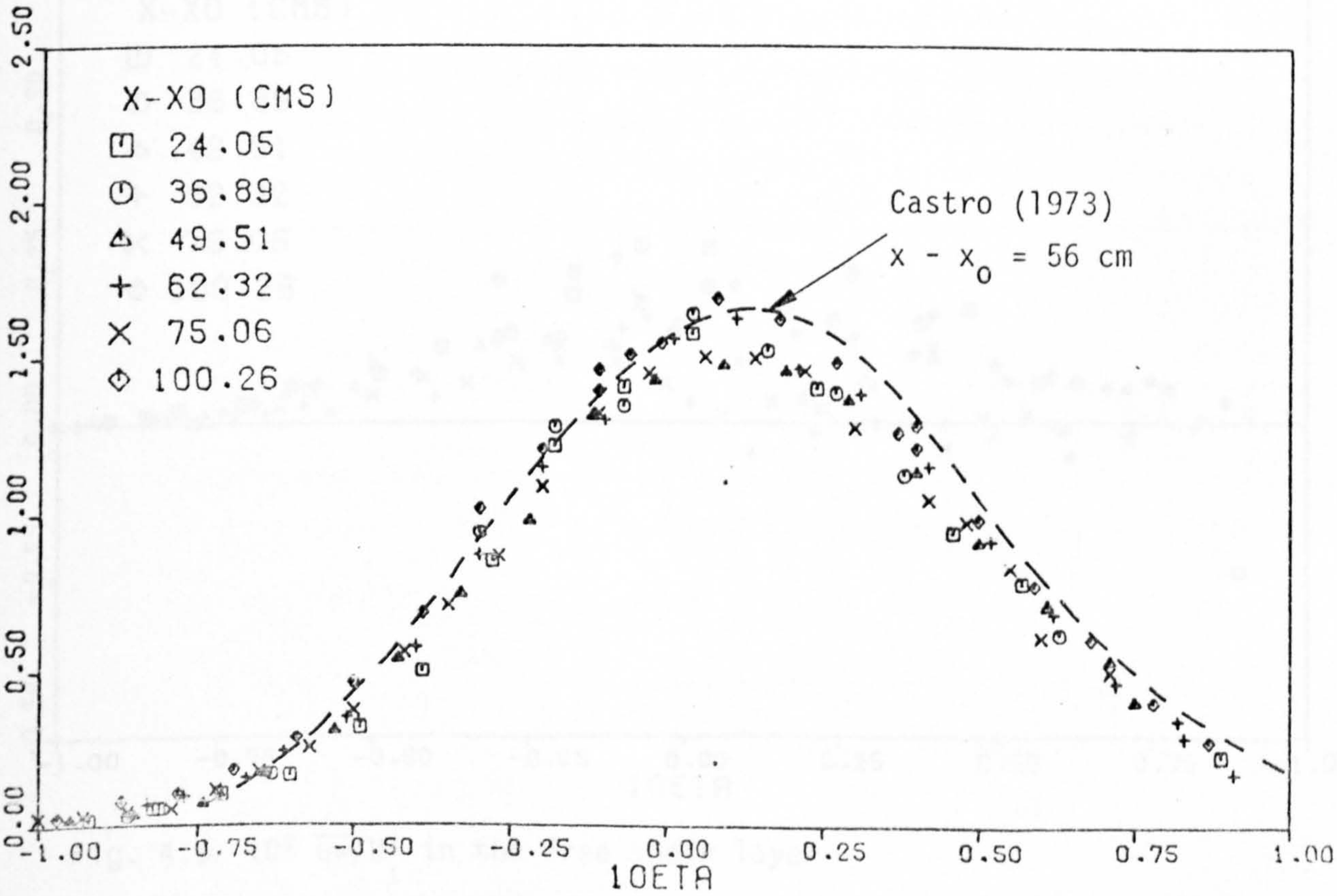


Fig. 4.3 $10^2\ \overline{w^2}/U_1^2$ in the free shear layer

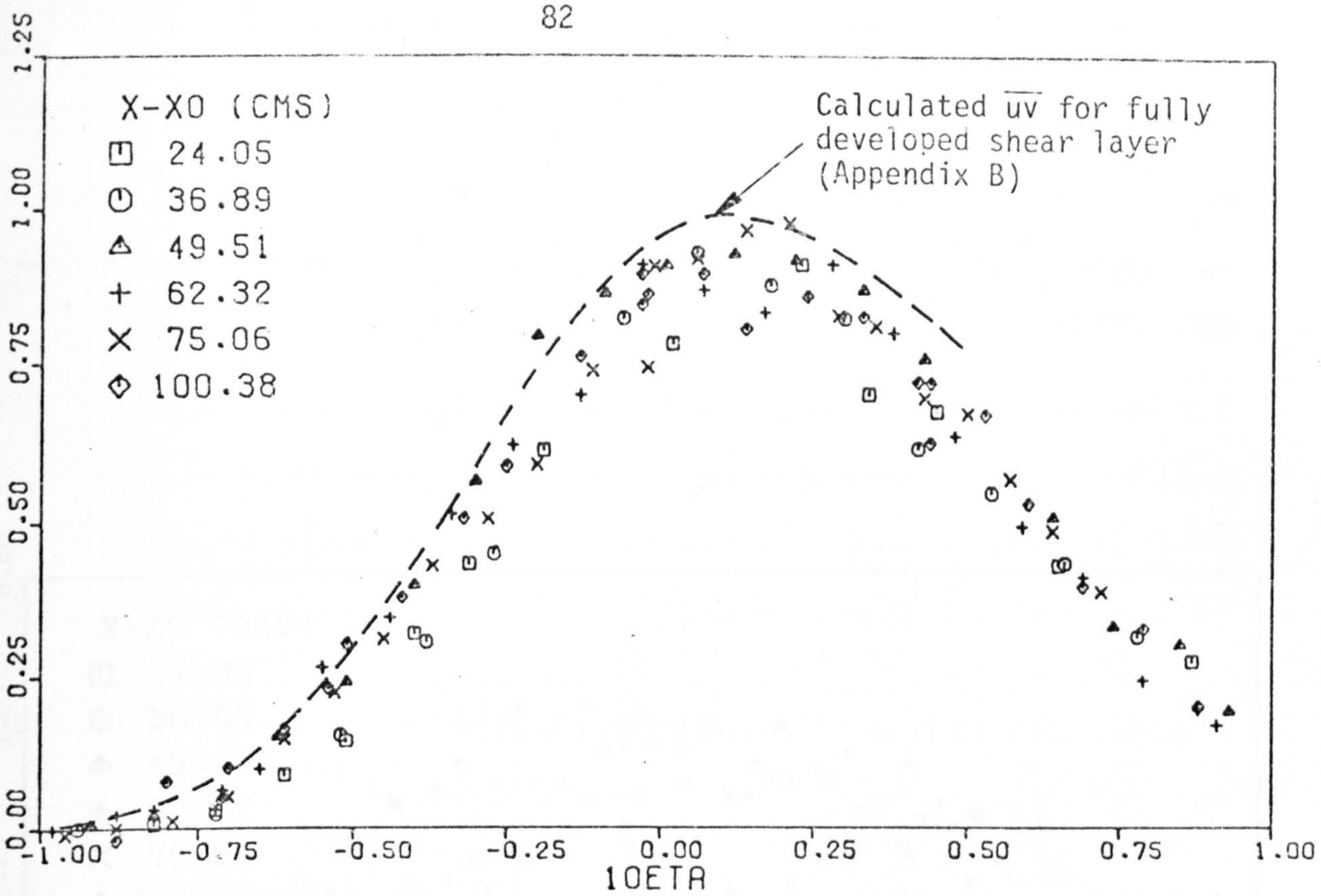


Fig. 4.4 $10^2\ \overline{uv}/U_1^2$ in the free shear layer

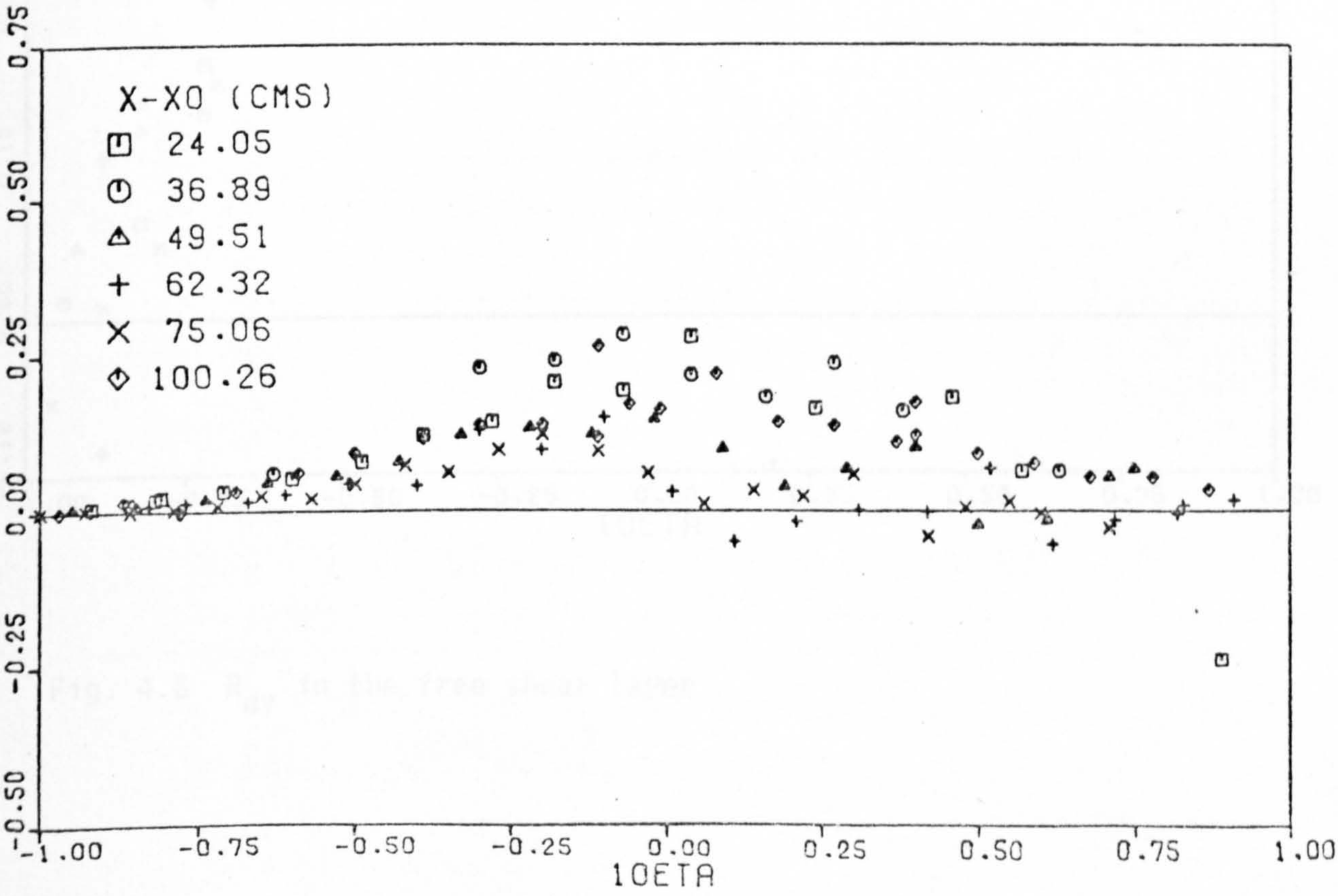


Fig. 4.5 $10^2\ \overline{uw}/U_1^2$ in the free shear layer

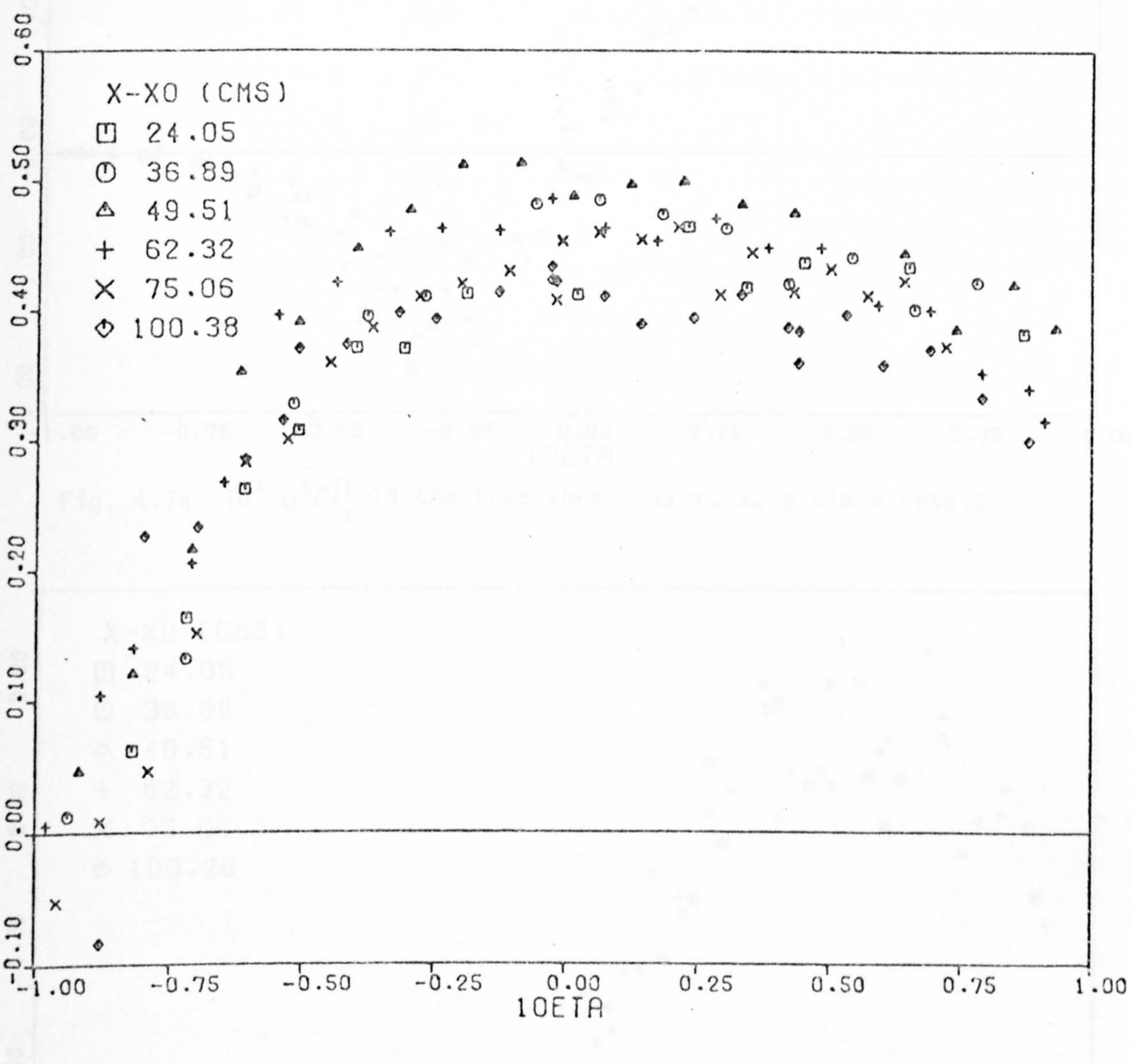


Fig. 4.6 R_{uv} in the free shear layer

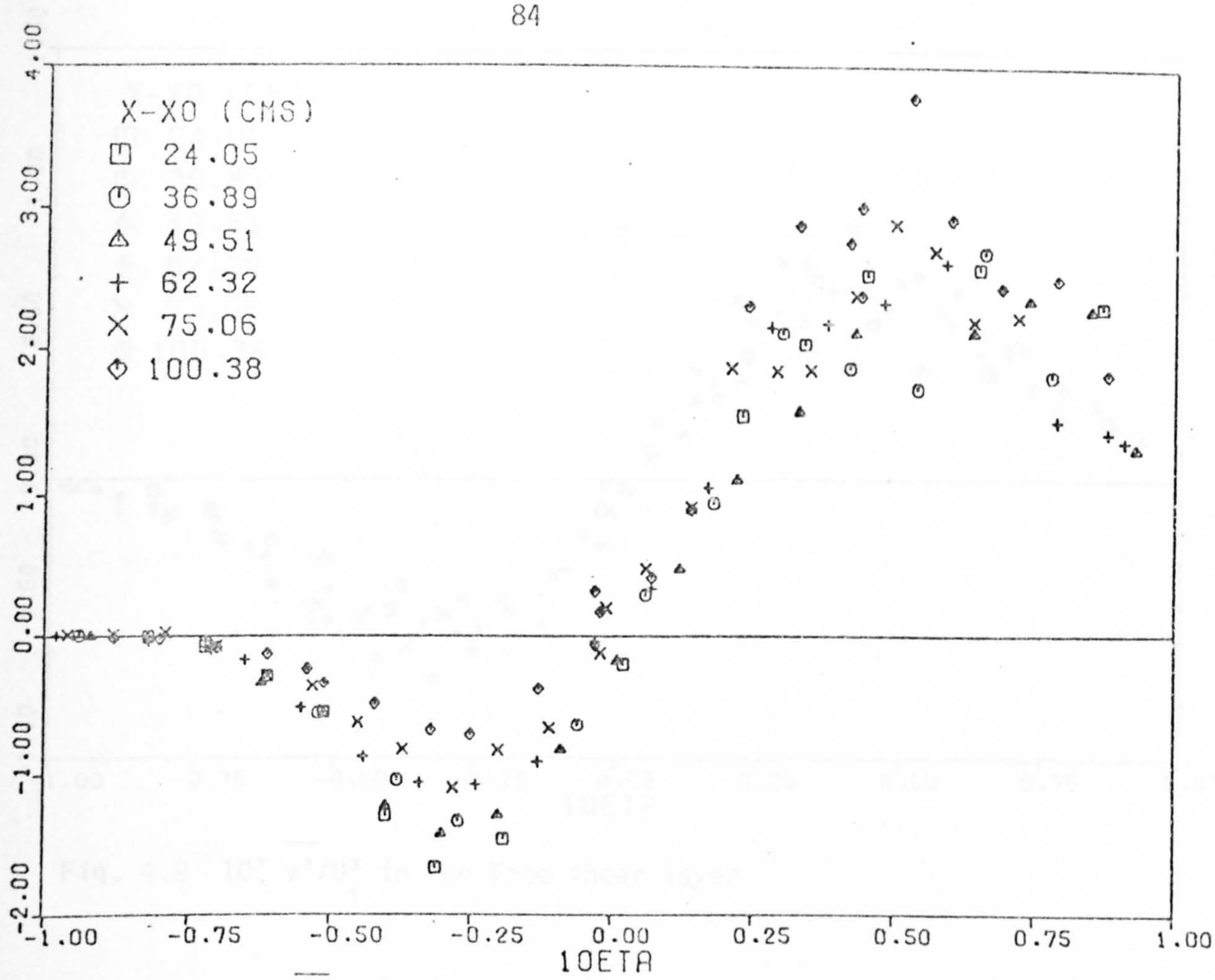


Fig. 4.7a 10^3 u^3/U_1^3 in the free shear layer; x, y plane results

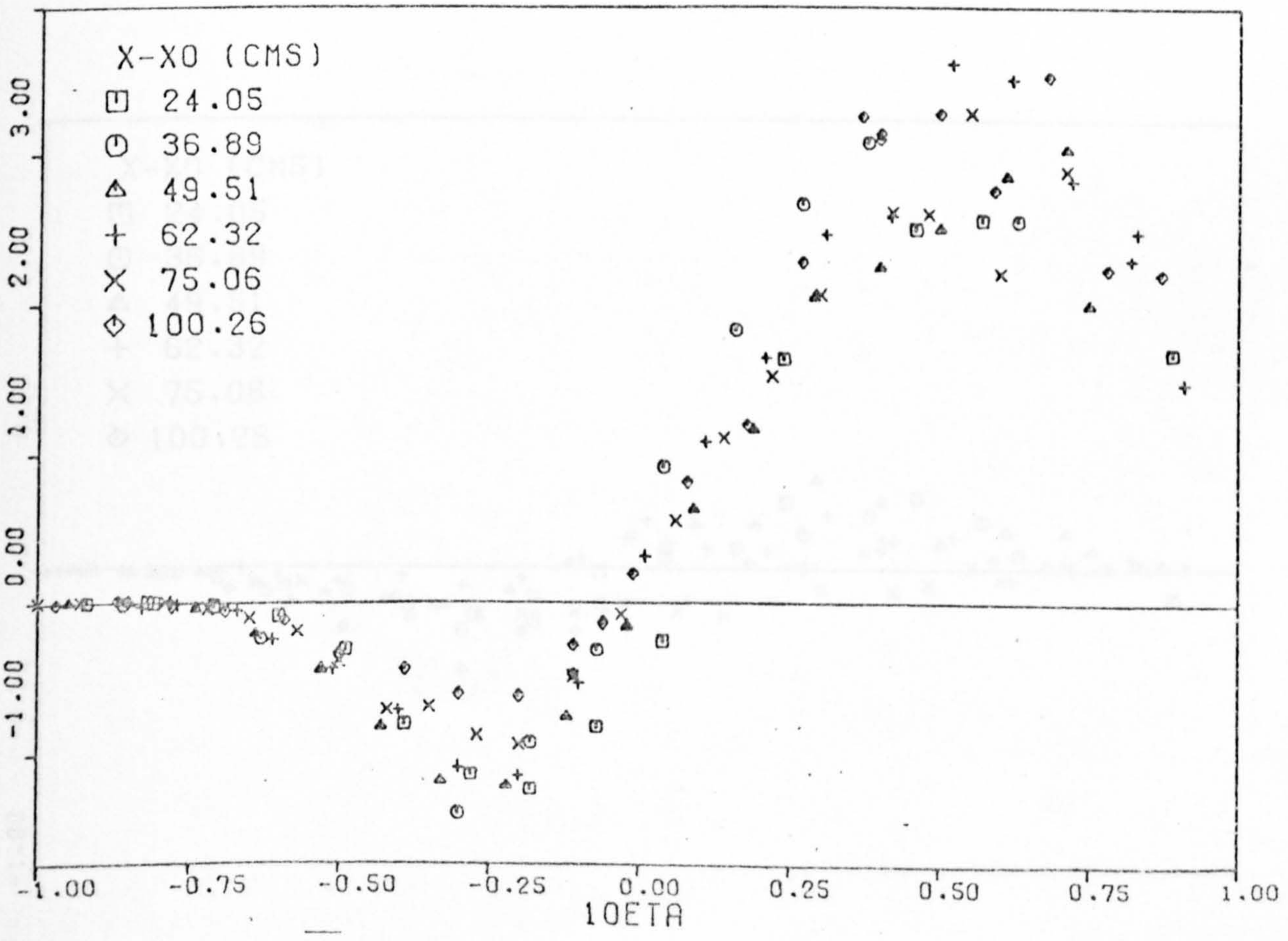


Fig. 4.7b 10^3 u^3/U_1^3 in the free shear layer; x, z plane results

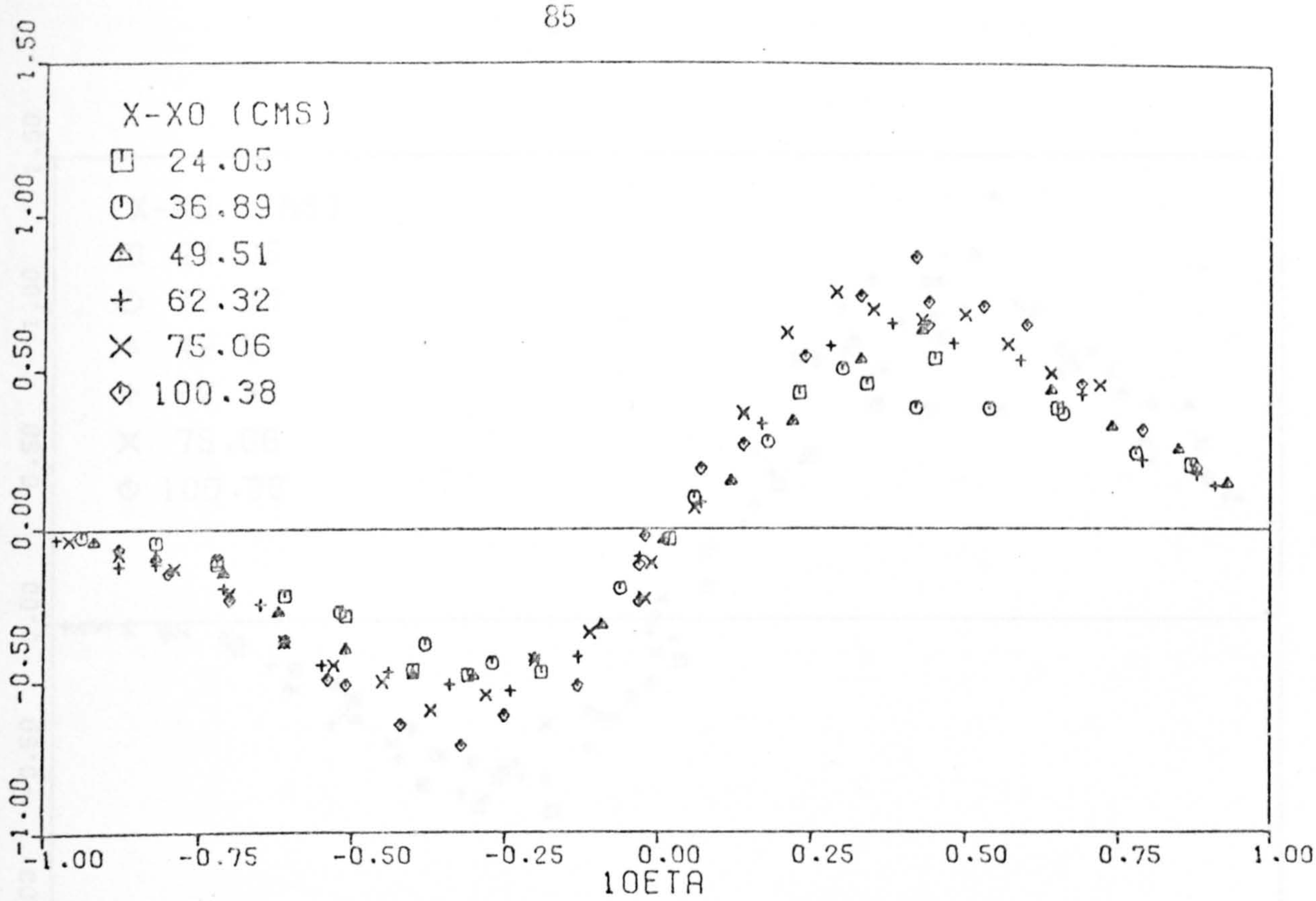


Fig. 4.8 $10^3 \overline{v^3}/U_1^3$ in the free shear layer

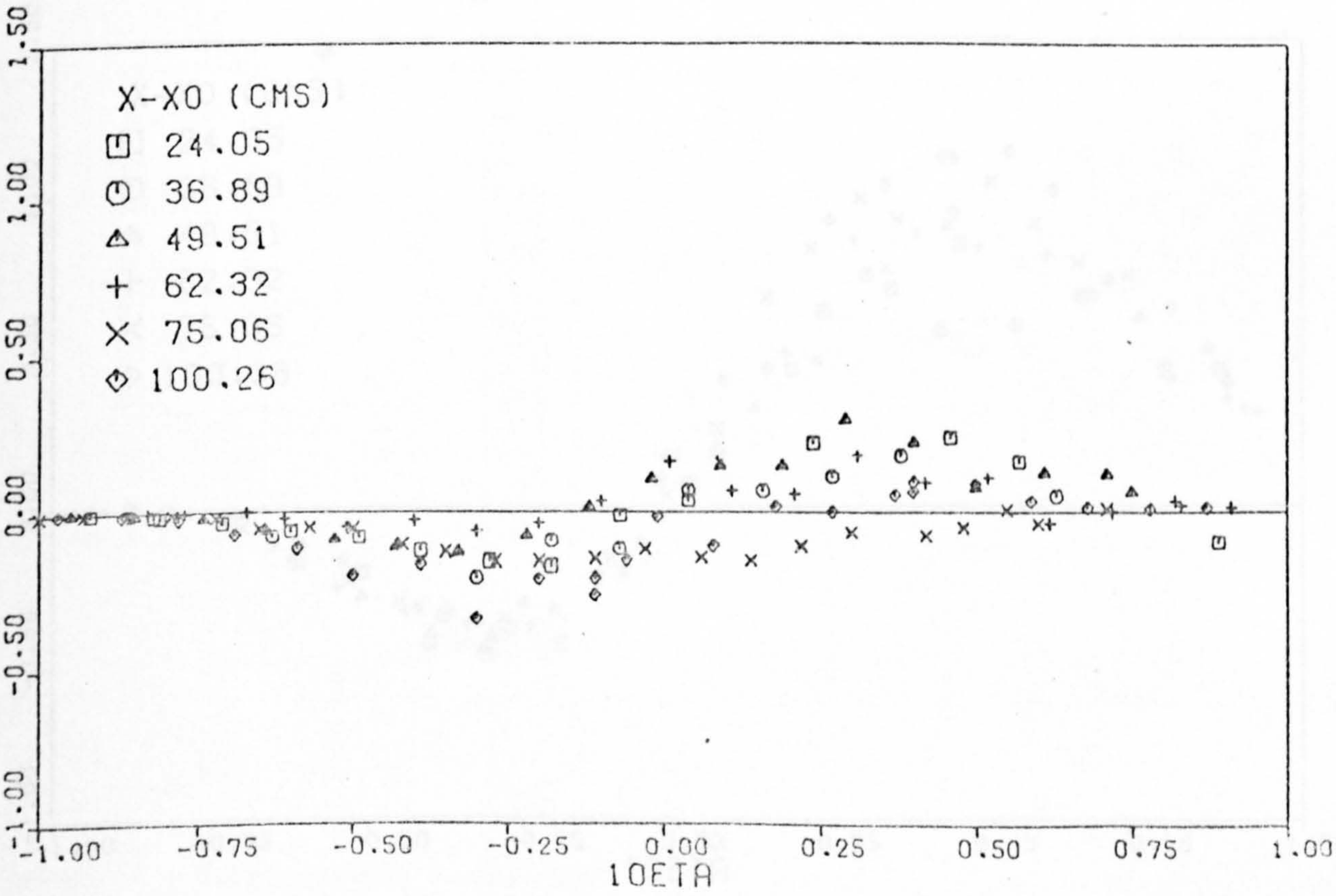


Fig. 4.9 $10^3 \overline{w^3}/U_1^3$ in the free shear layer

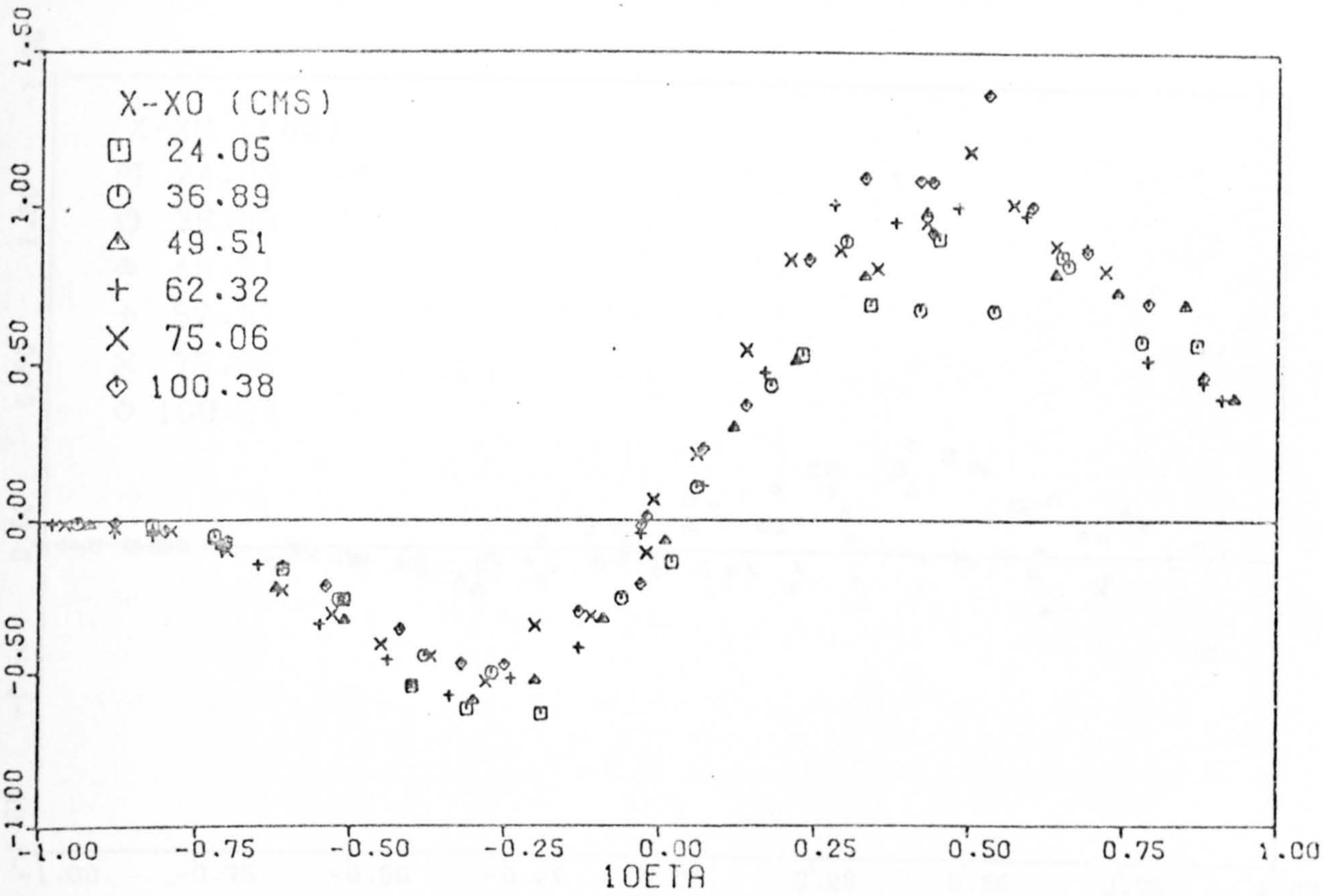


Fig. 4.10 $10^3\ \overline{u^2v}/U_1^3$ in the free shear layer

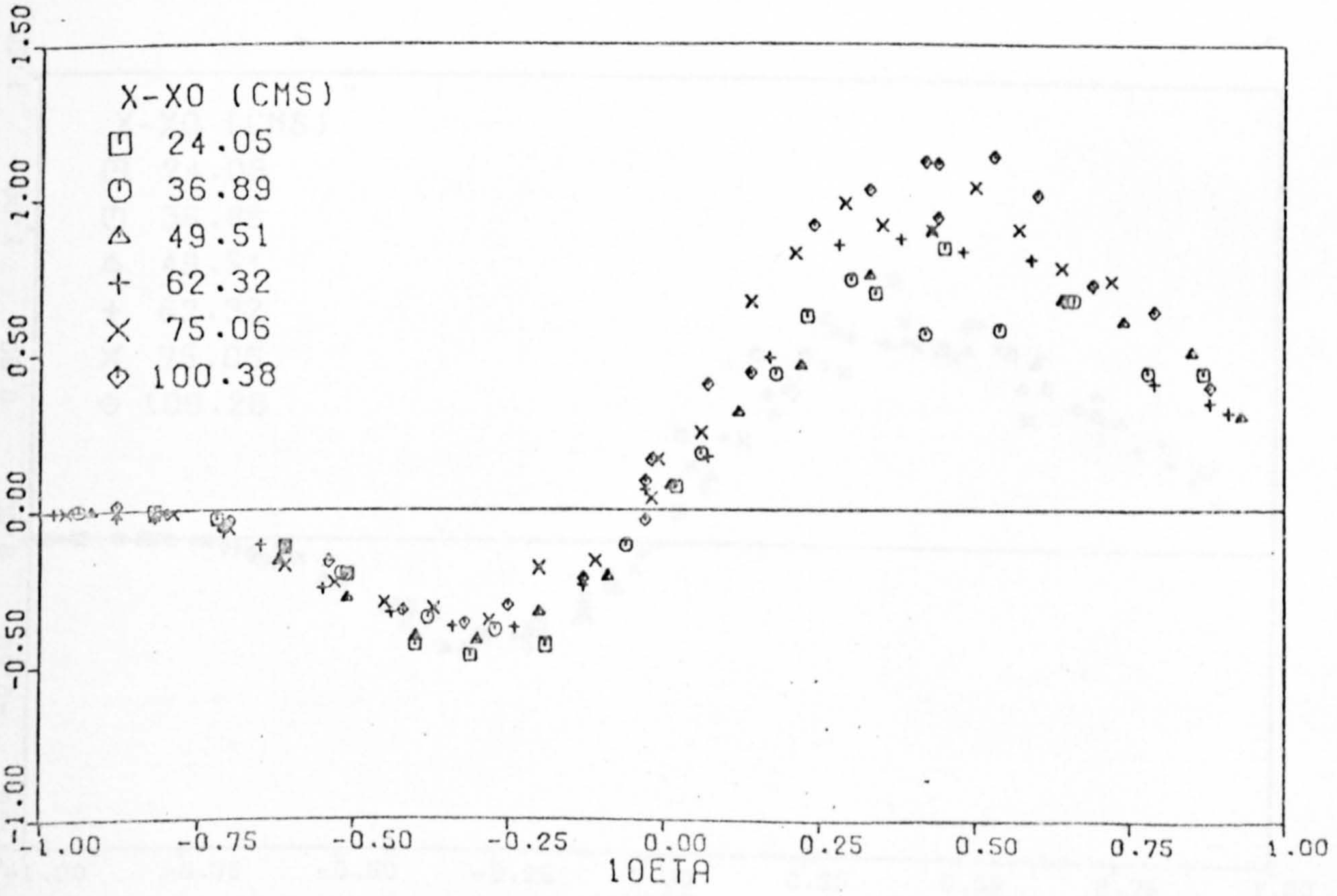


Fig. 4.11 $10^3\ \overline{uv^2}/U_1^3$ in the free shear layer

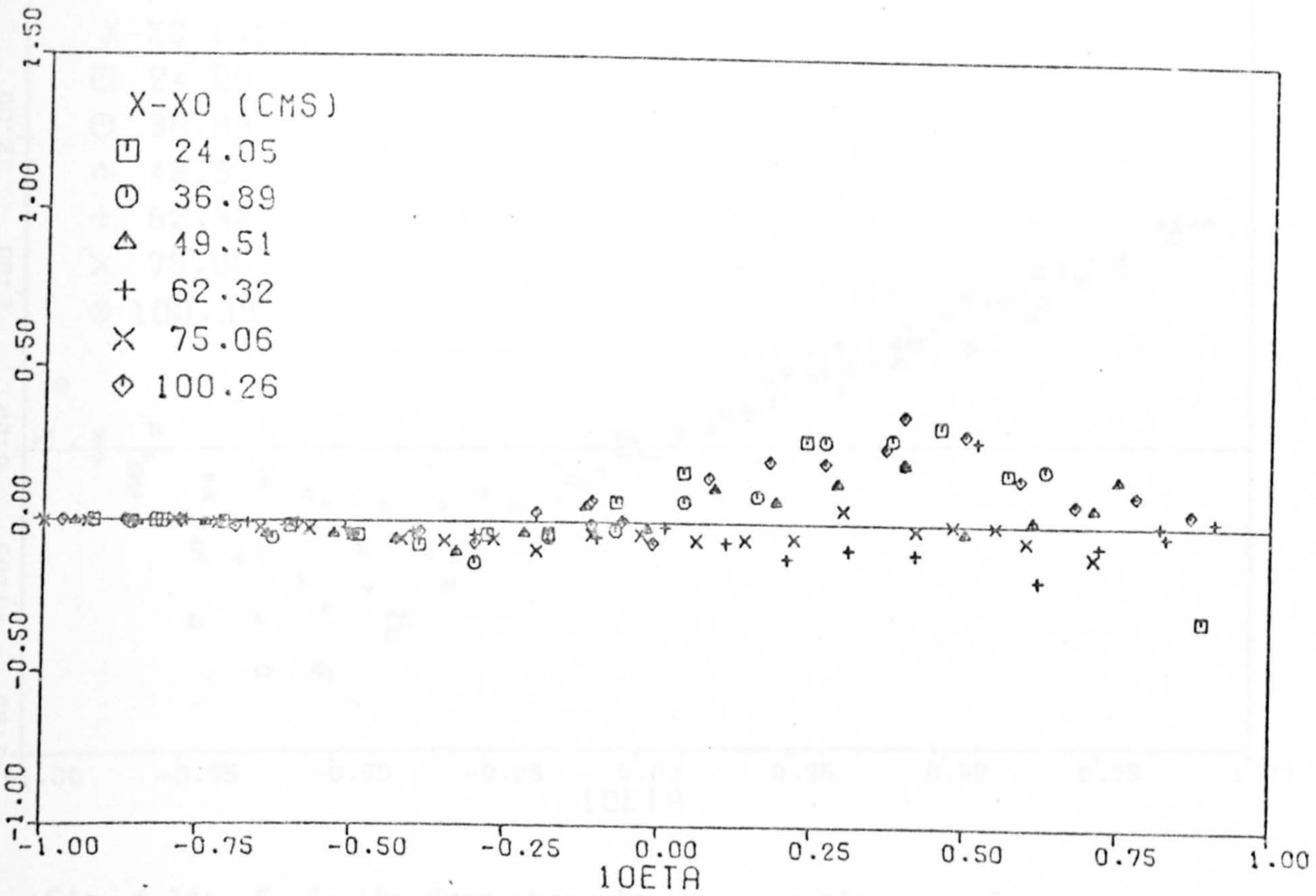
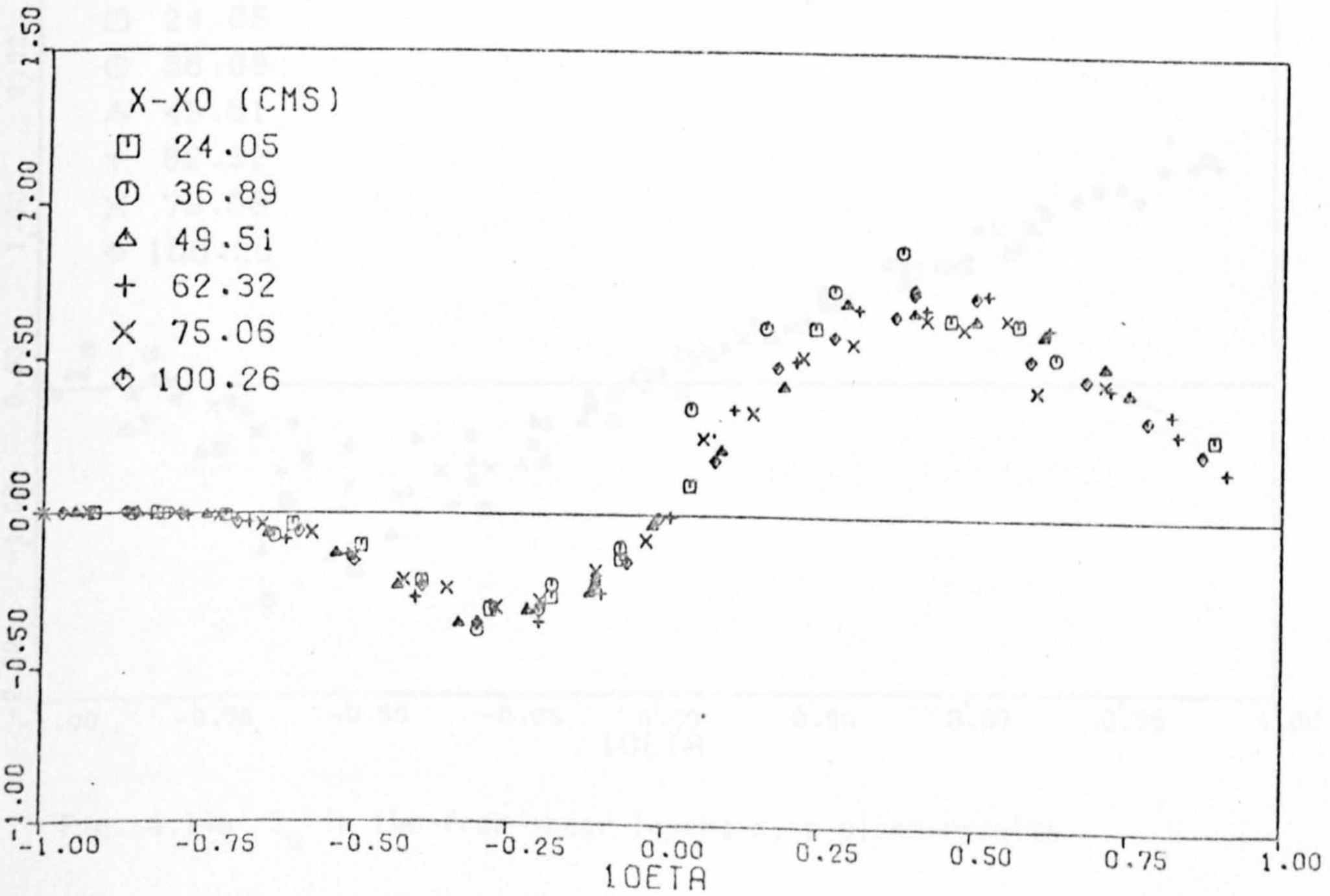


Fig. 4.12 $10^3\ \overline{u^2 w}/U_1^3$ in the free shear layer



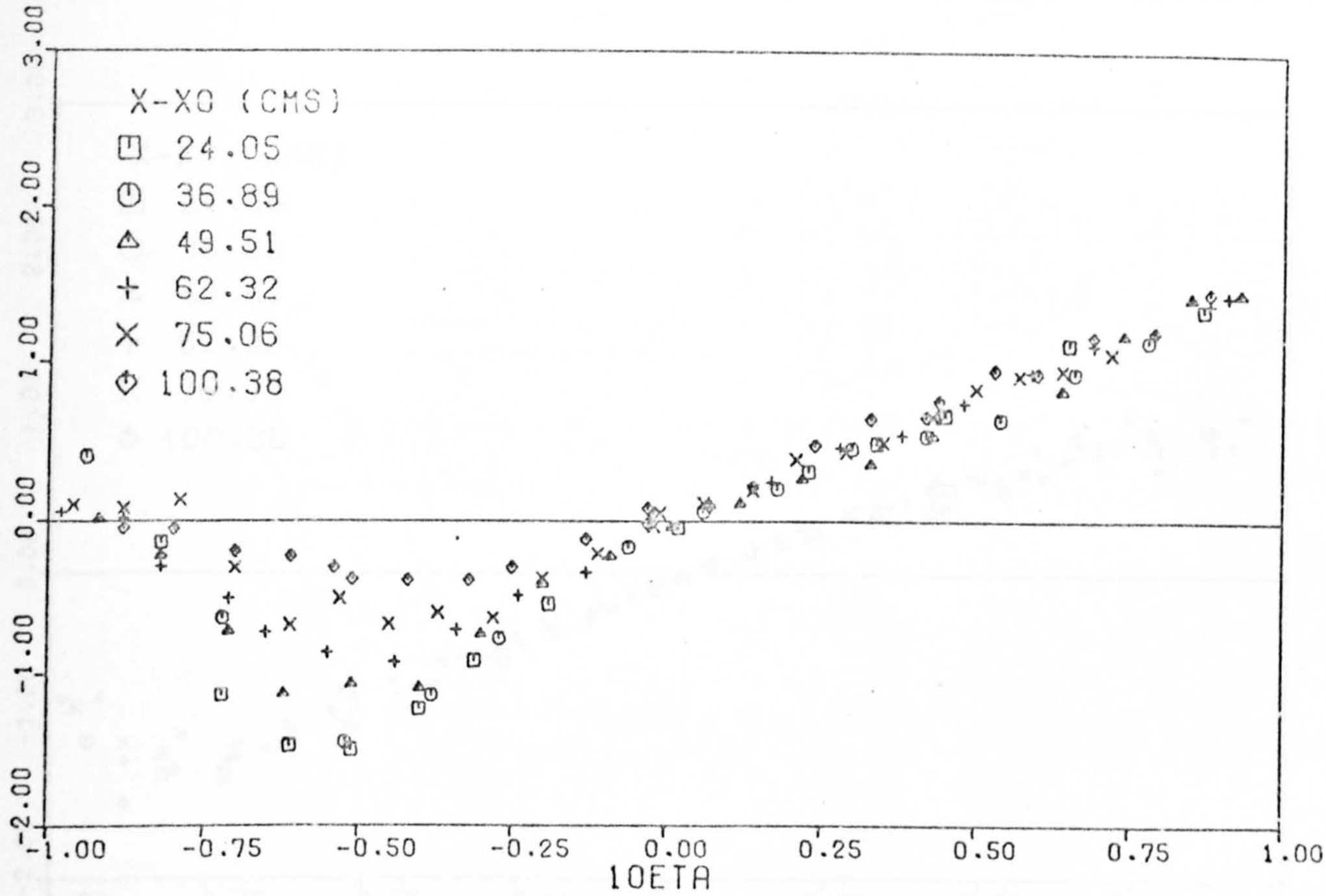


Fig. 4.14a S_u in the free shear layer; x, y plane results

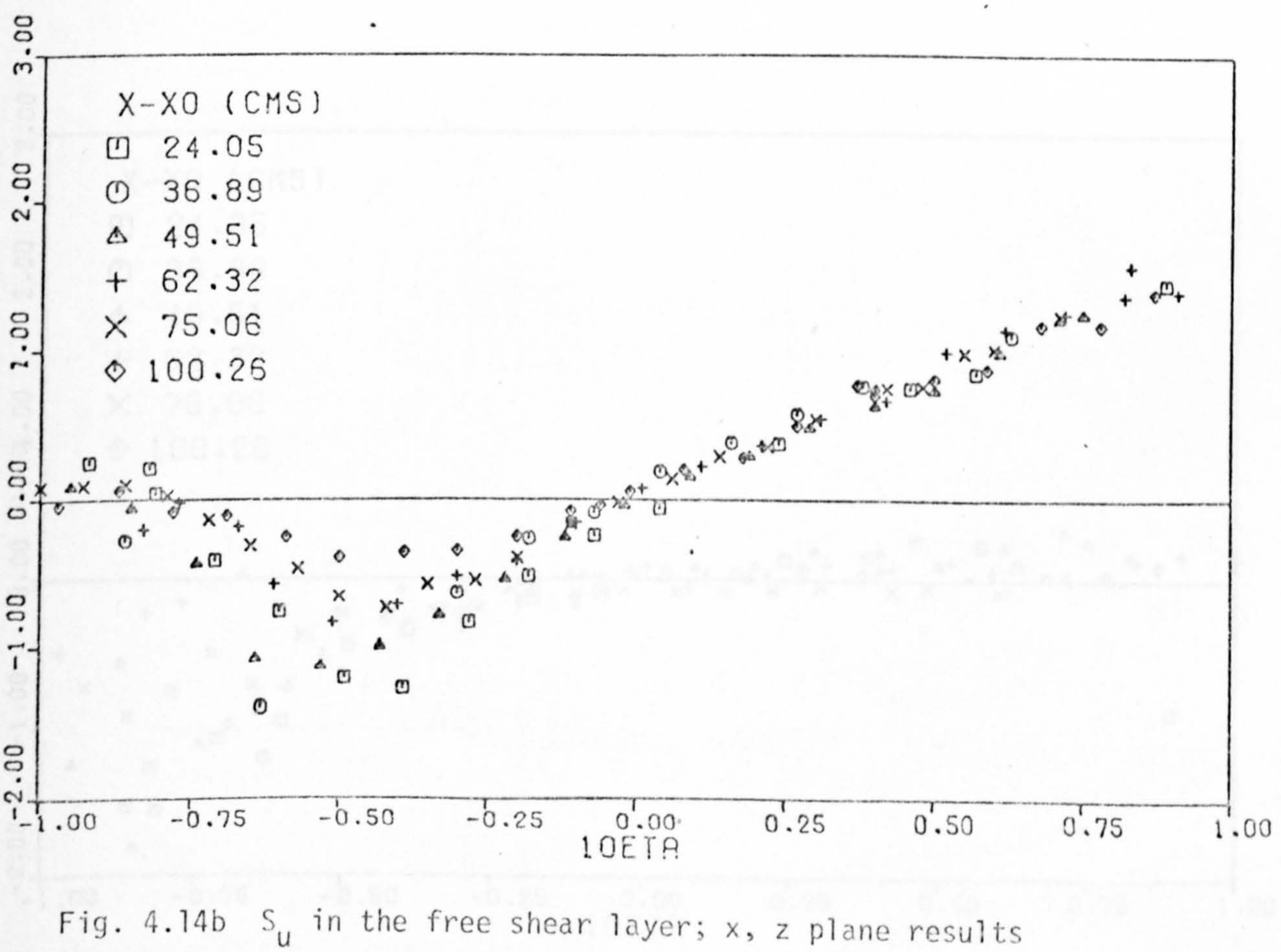


Fig. 4.14b S_u in the free shear layer; x, z plane results

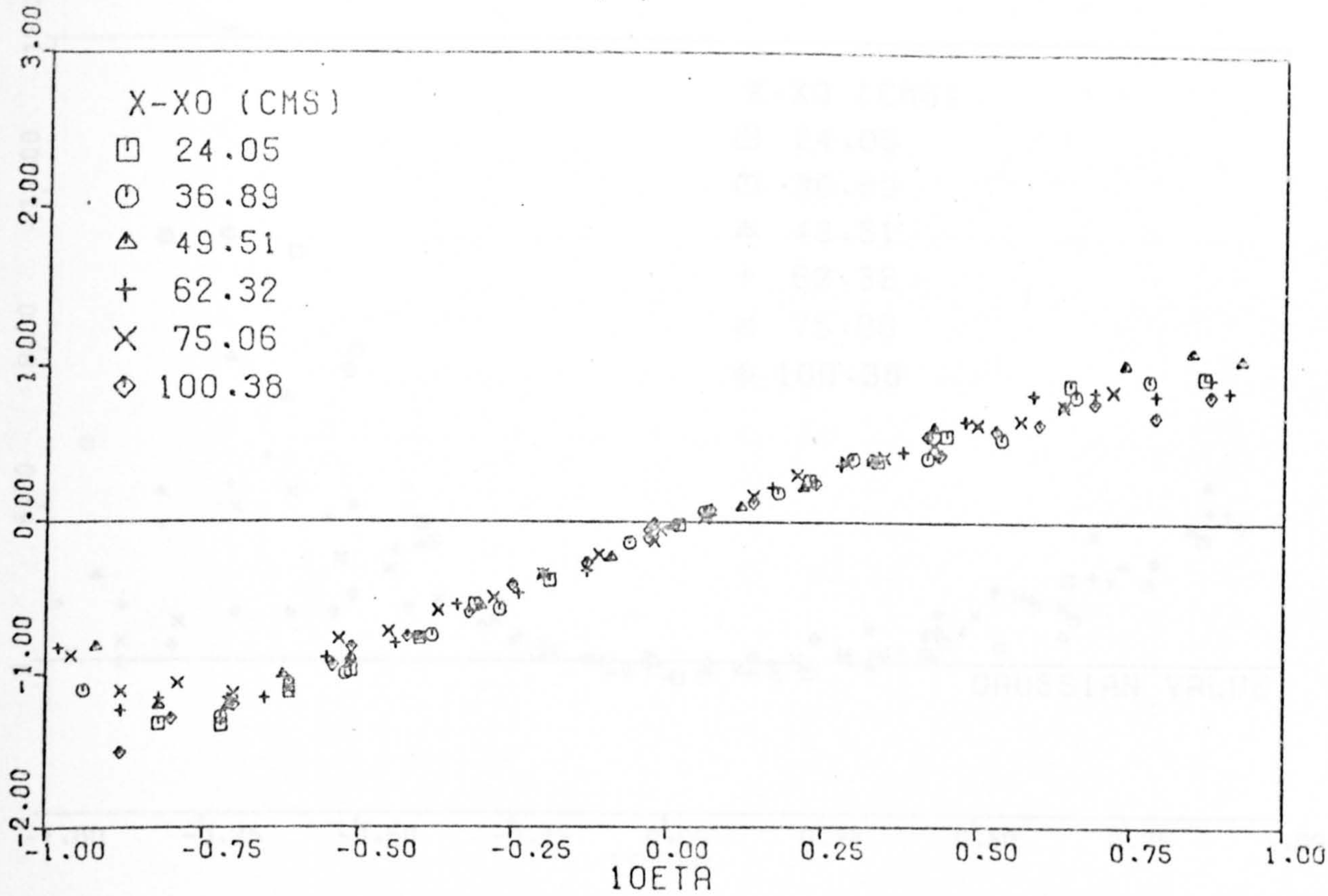


Fig. 4.15 S_V in the free shear layer

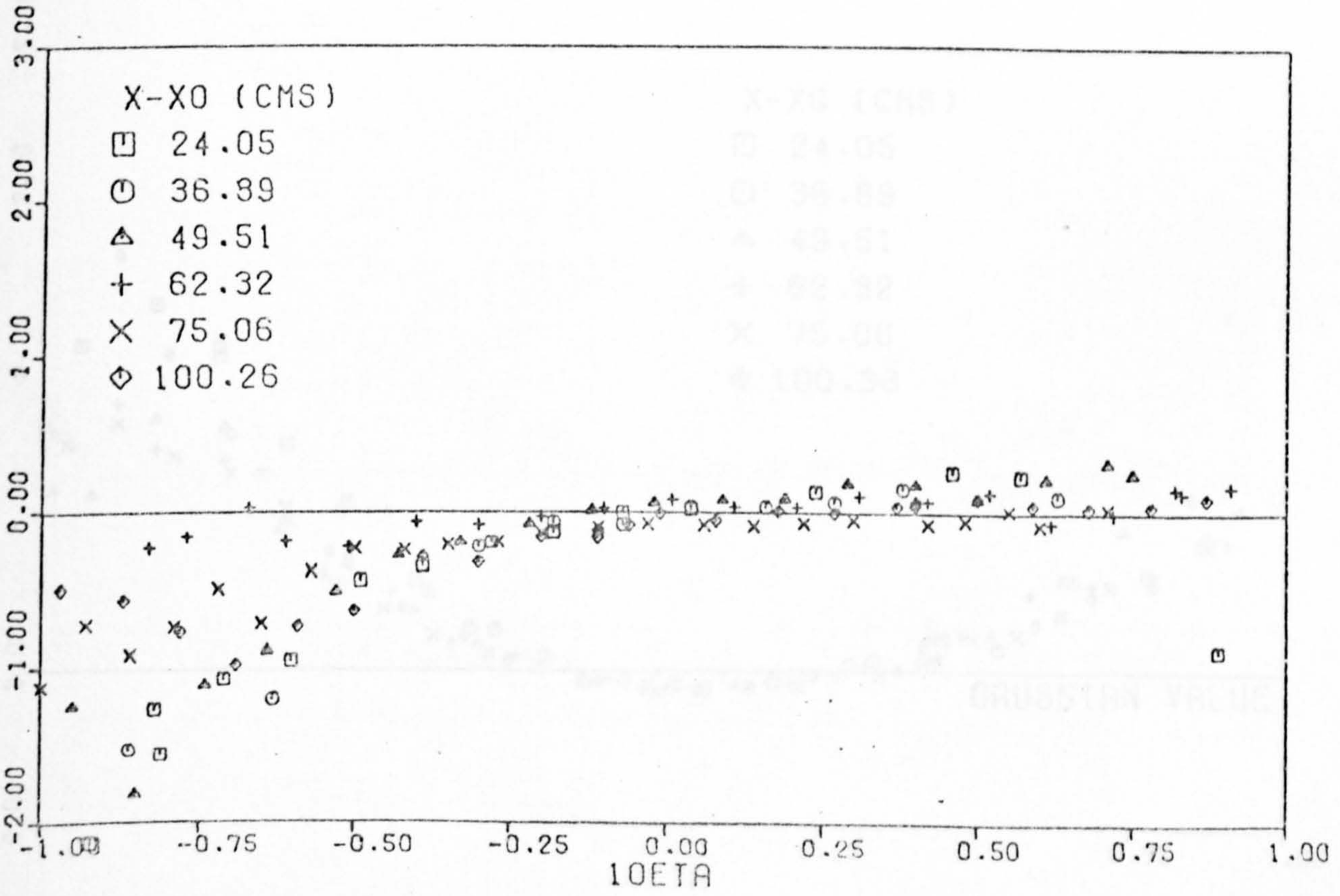


Fig. 4.16 S_W in the free shear layer

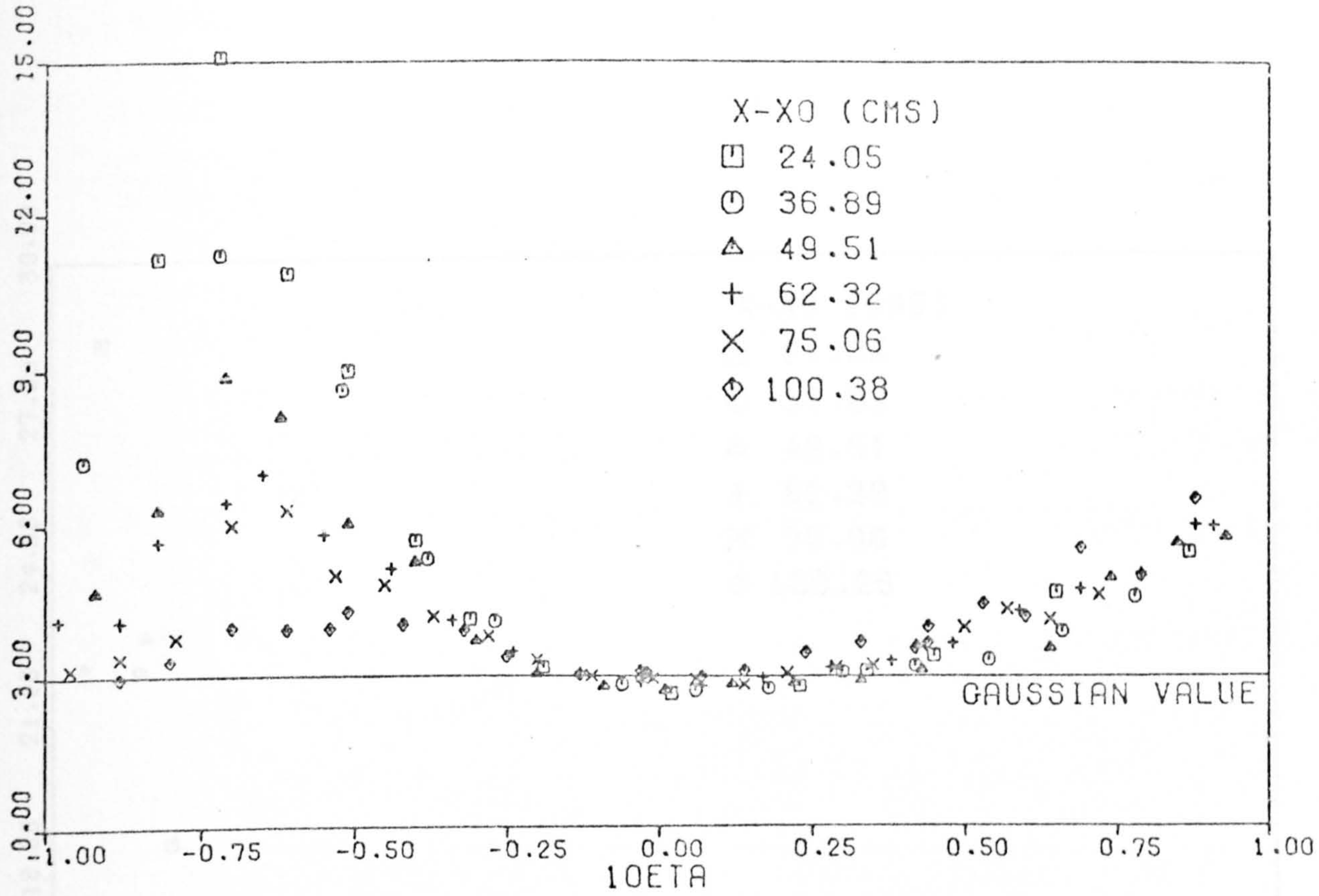


Fig. 4.17 F_u in the free shear layer

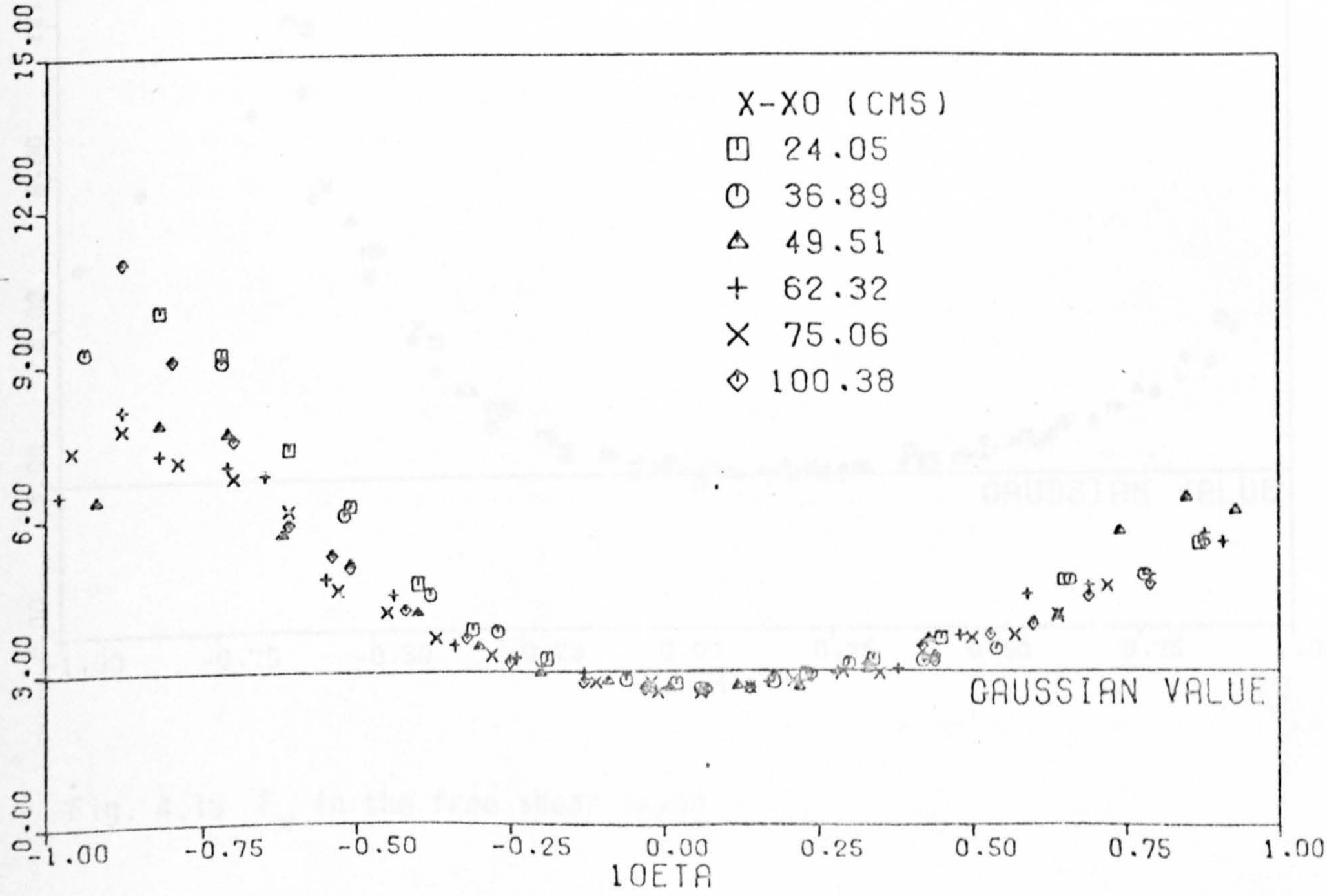


Fig. 4.18 F_v in the free shear layer

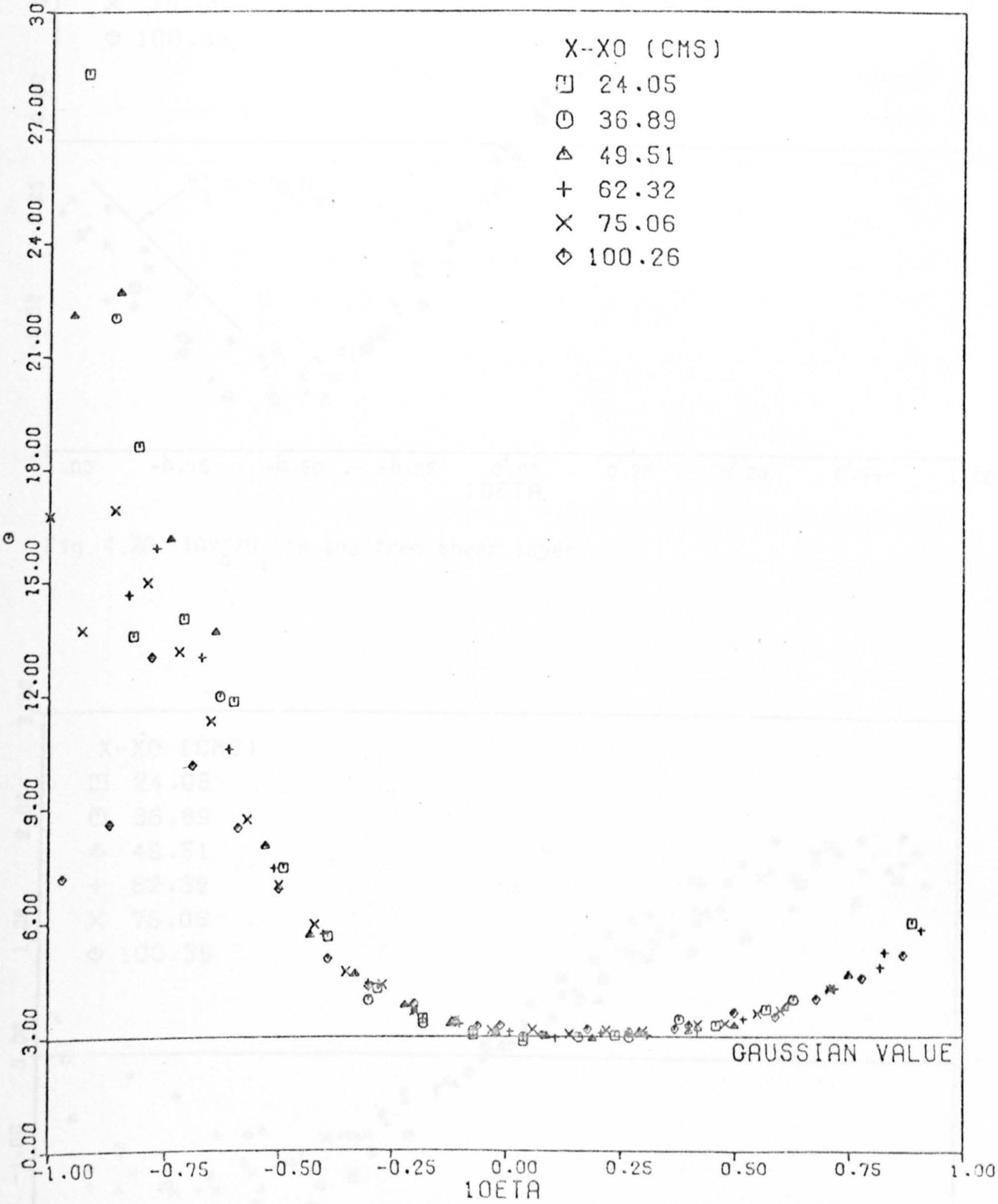


Fig. 4.19 F_w in the free shear layer

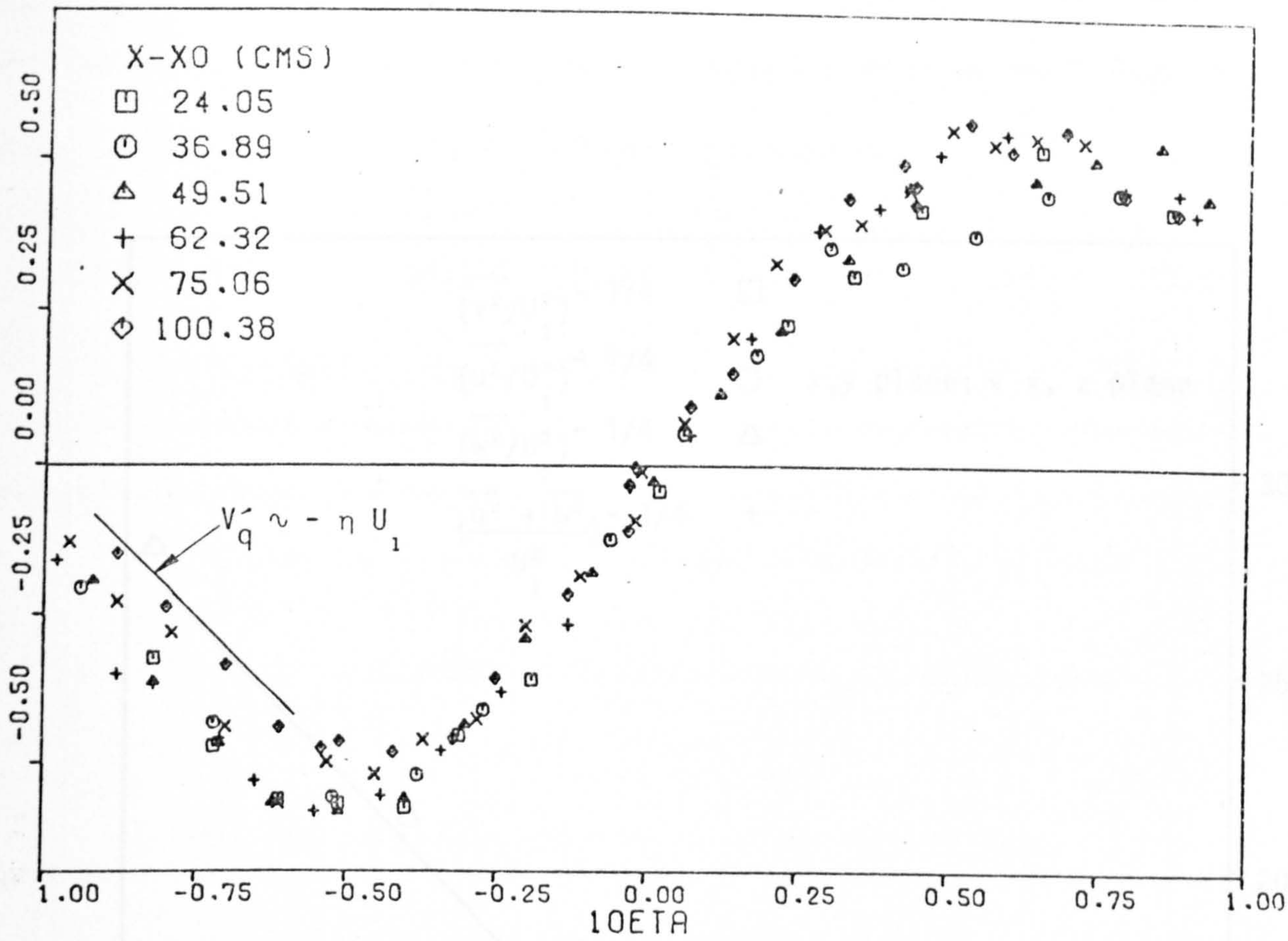


Fig. 4.20 $10V_q'/U_1$ in the free shear layer

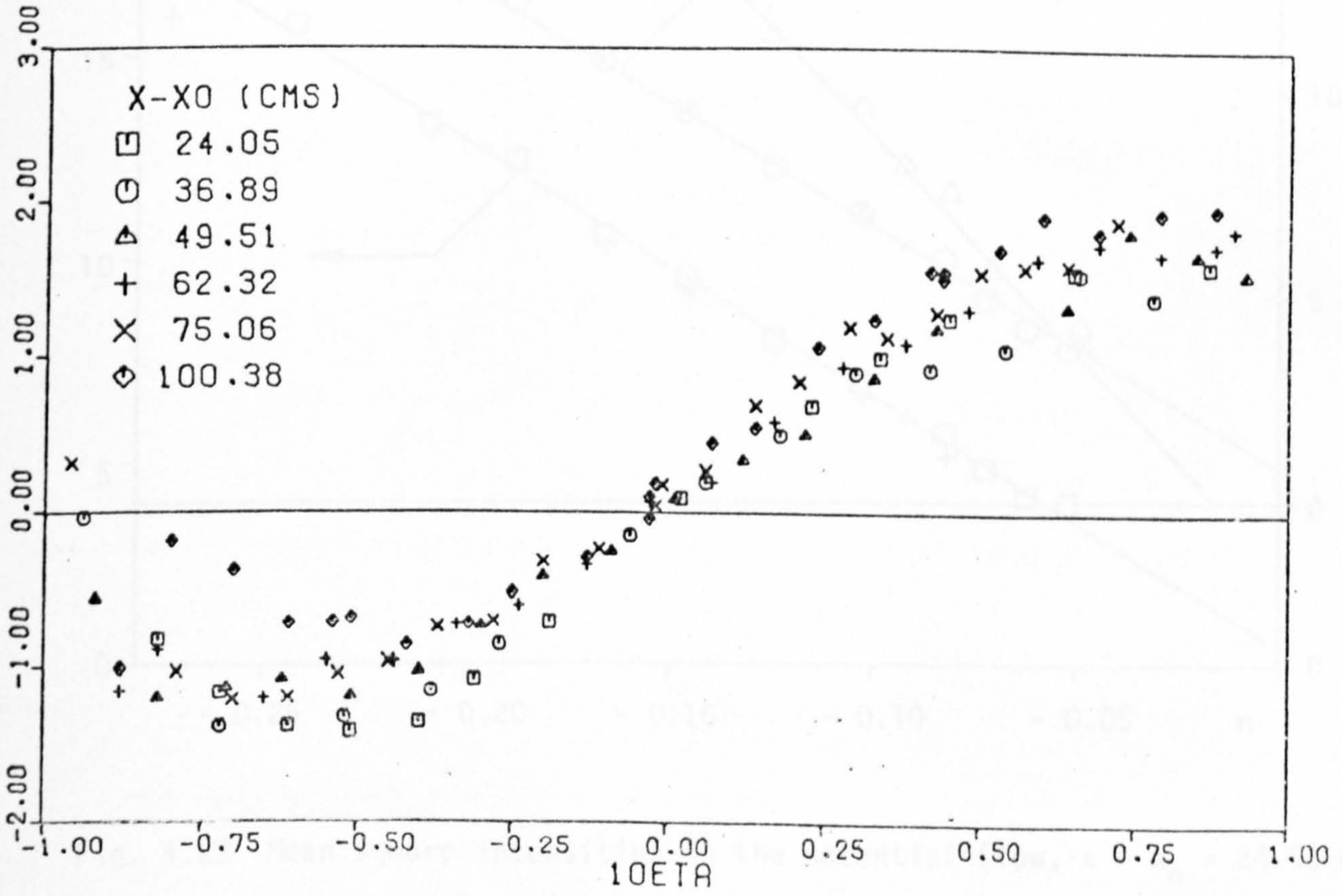


Fig. 4.21 $10V_\tau/U_1$ in the free shear layer

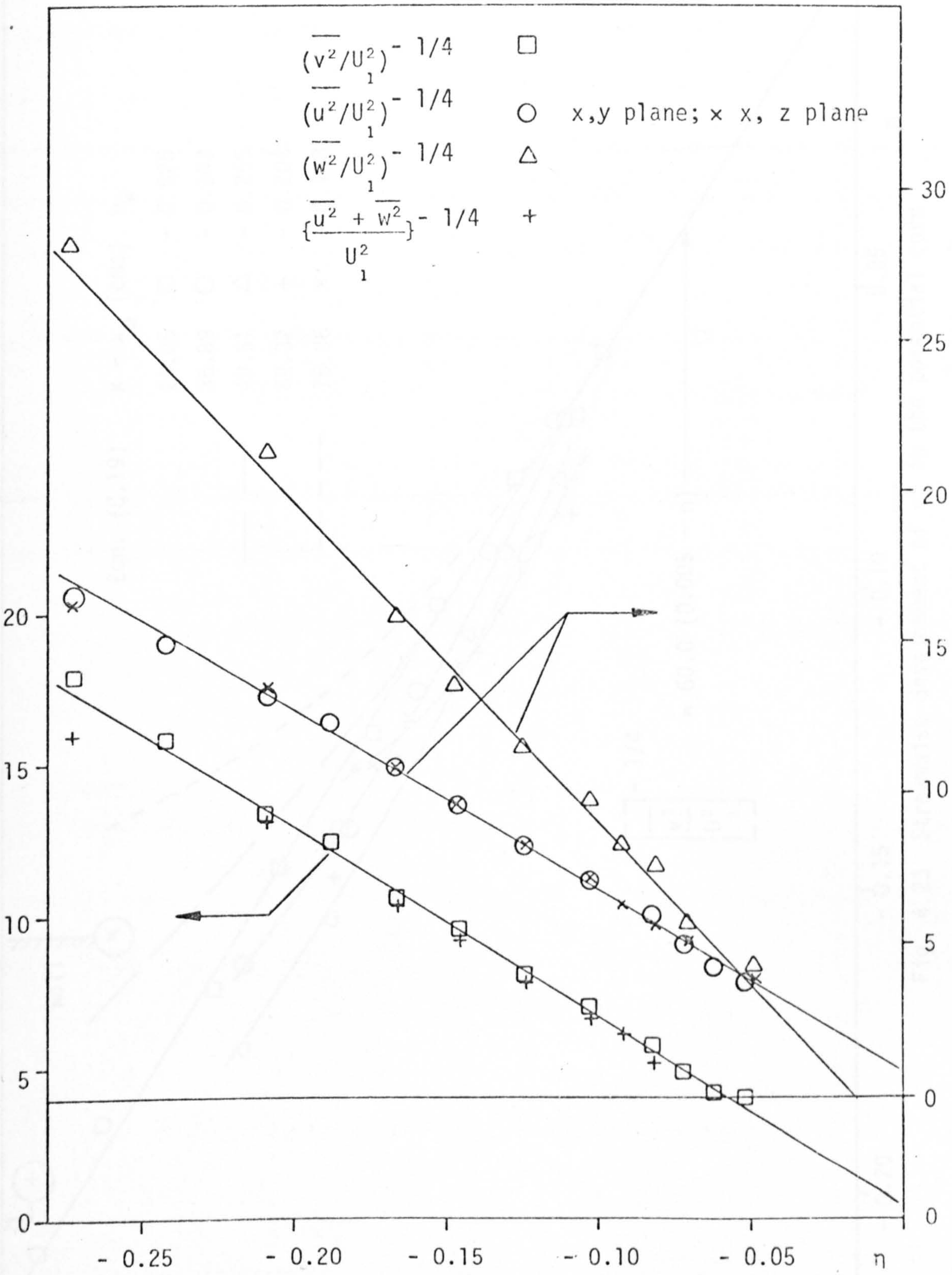


Fig. 4.22 Mean square intensities in the potential flow, $x - x_o = 24.05$ cm

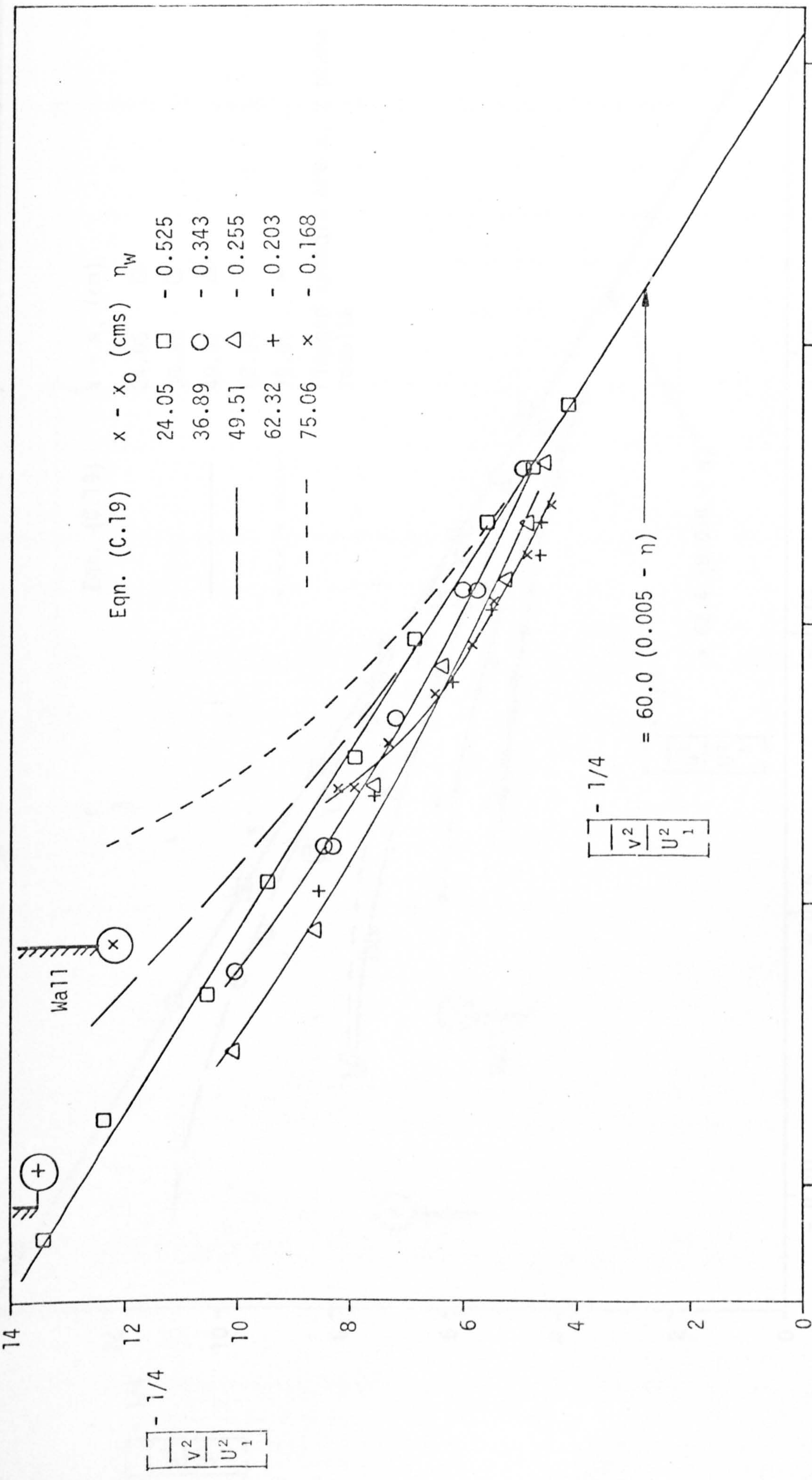


Fig. 4.23 Streamwise development of v^2 in the potential core

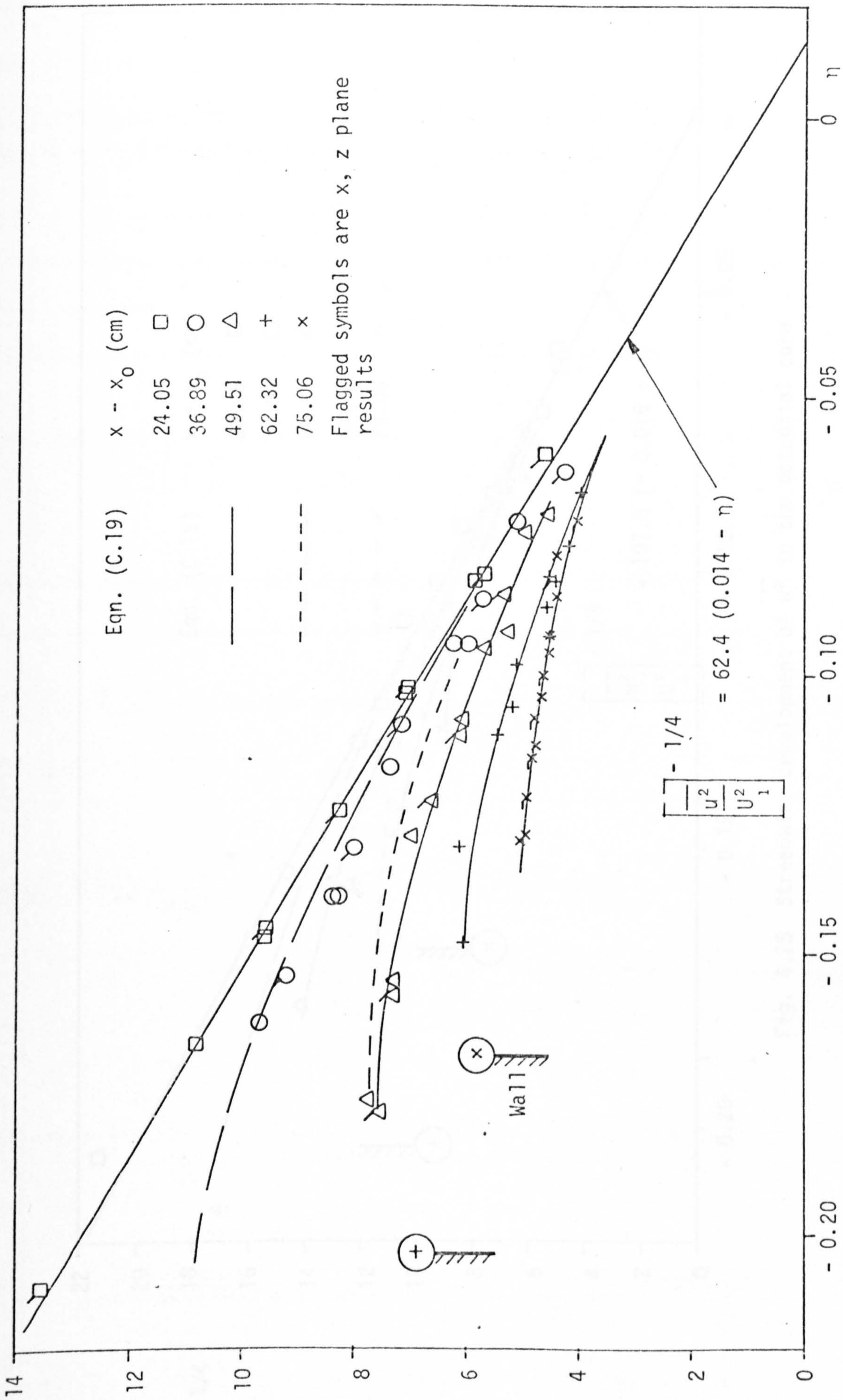


Fig. 4.24 Streamwise development of $\overline{u^2}$ in the potential core

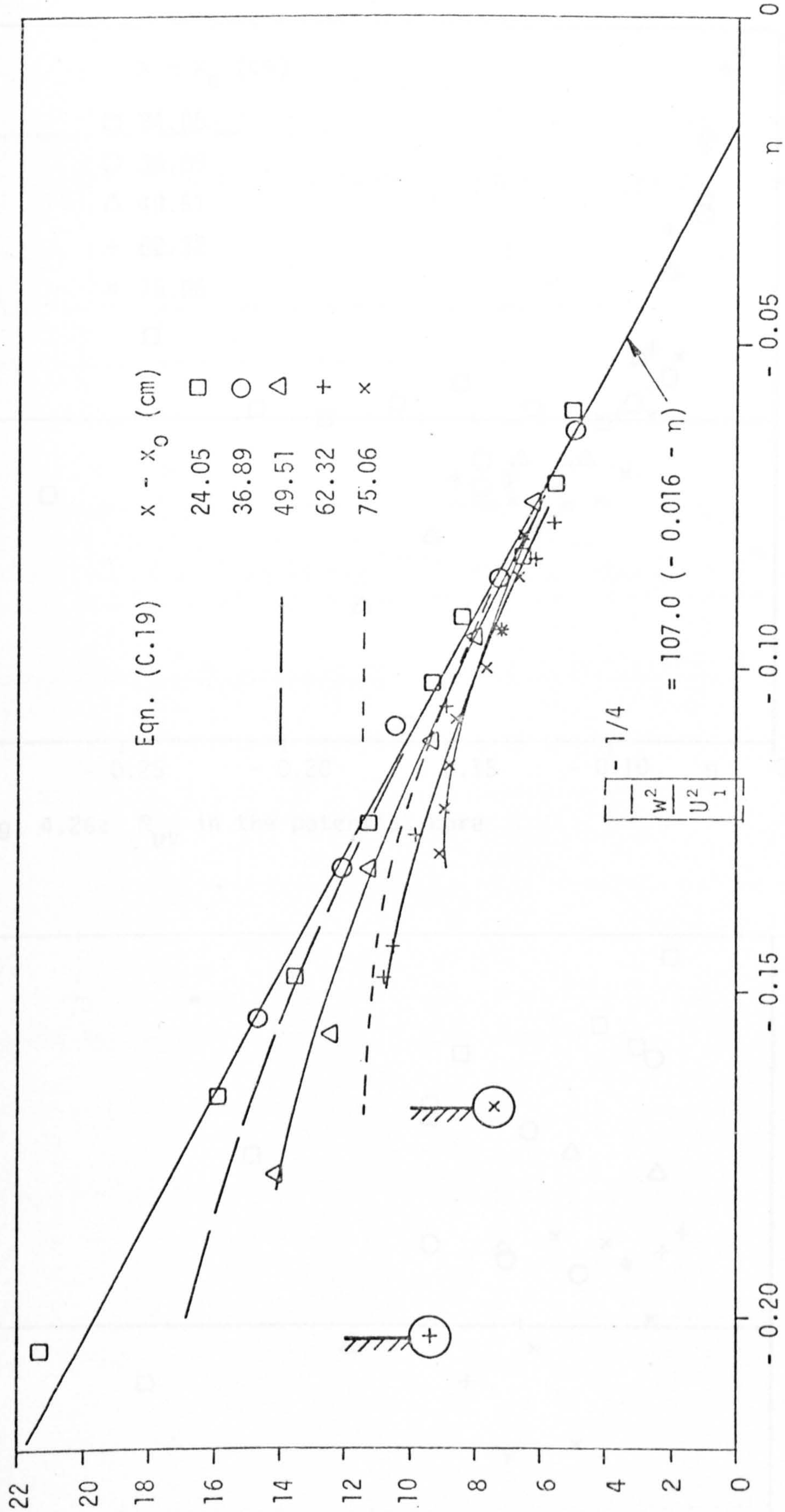


Fig. 4.25 Streamwise development of w^2 in the potential core

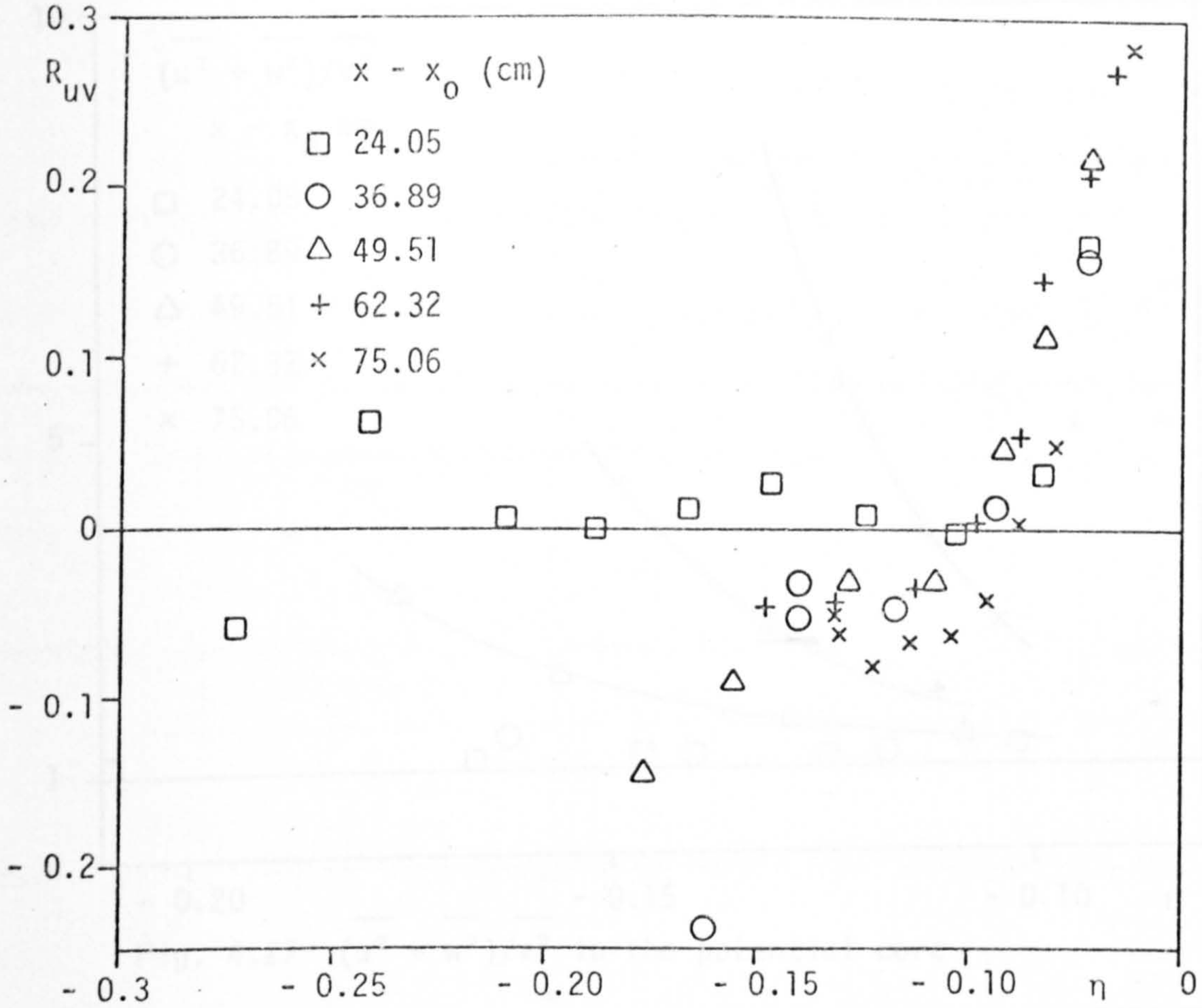


Fig. 4.26a R_{uv} in the potential core

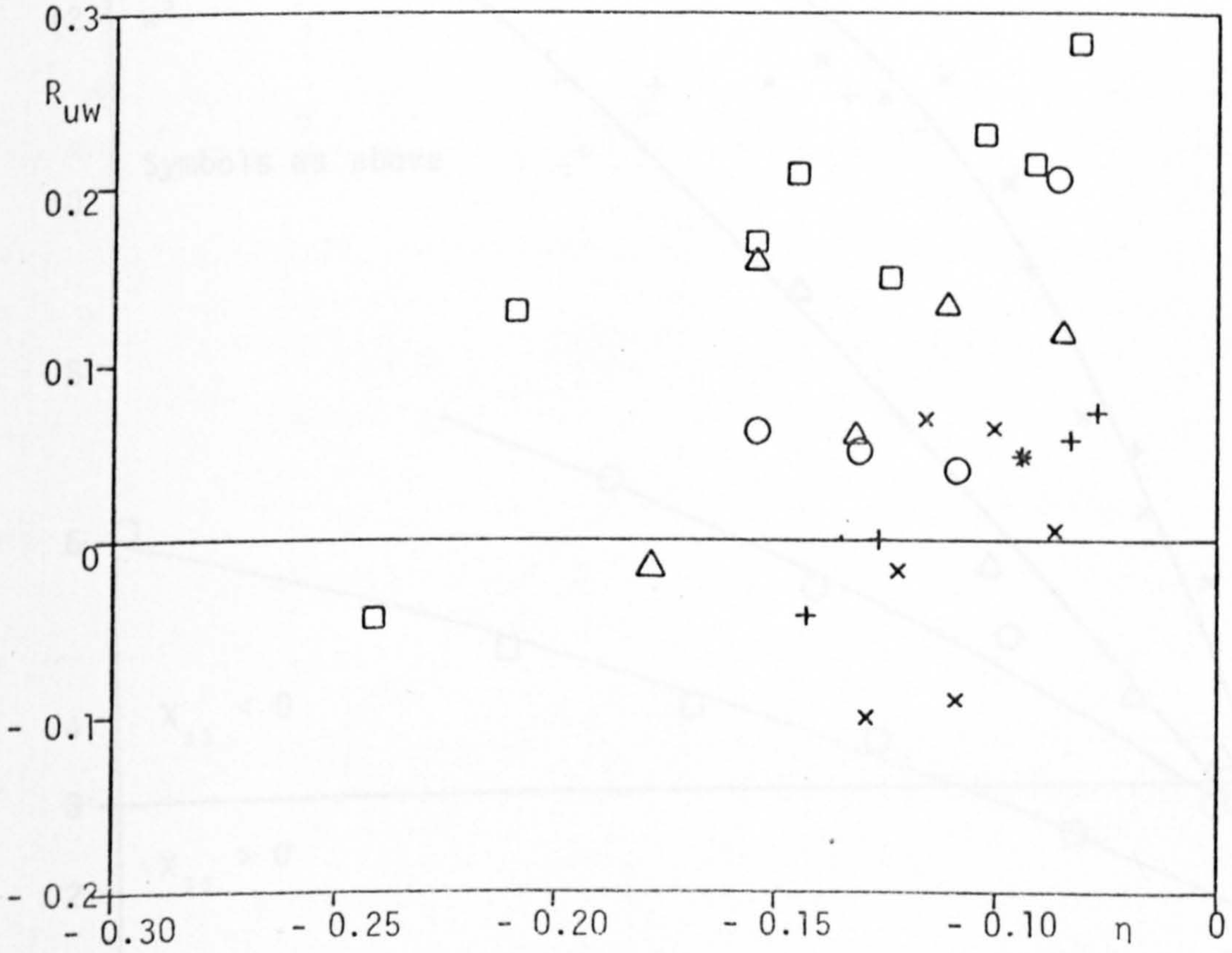


Fig. 4.26b R_{uw} in the potential core. Symbols as in fig. 4.26a.

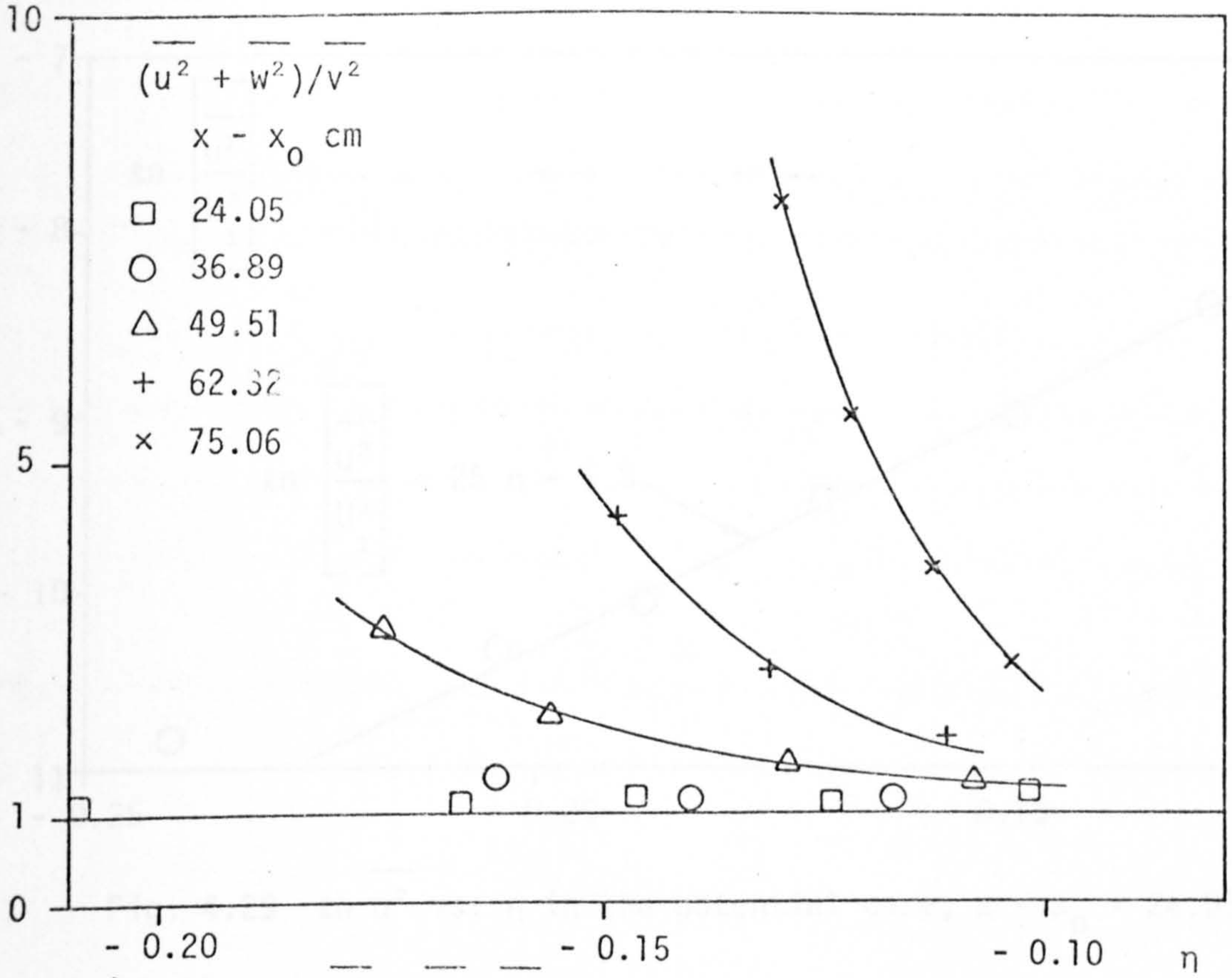


Fig. 4.27 $\overline{(u^2 + w^2)/v^2}$ in the potential core

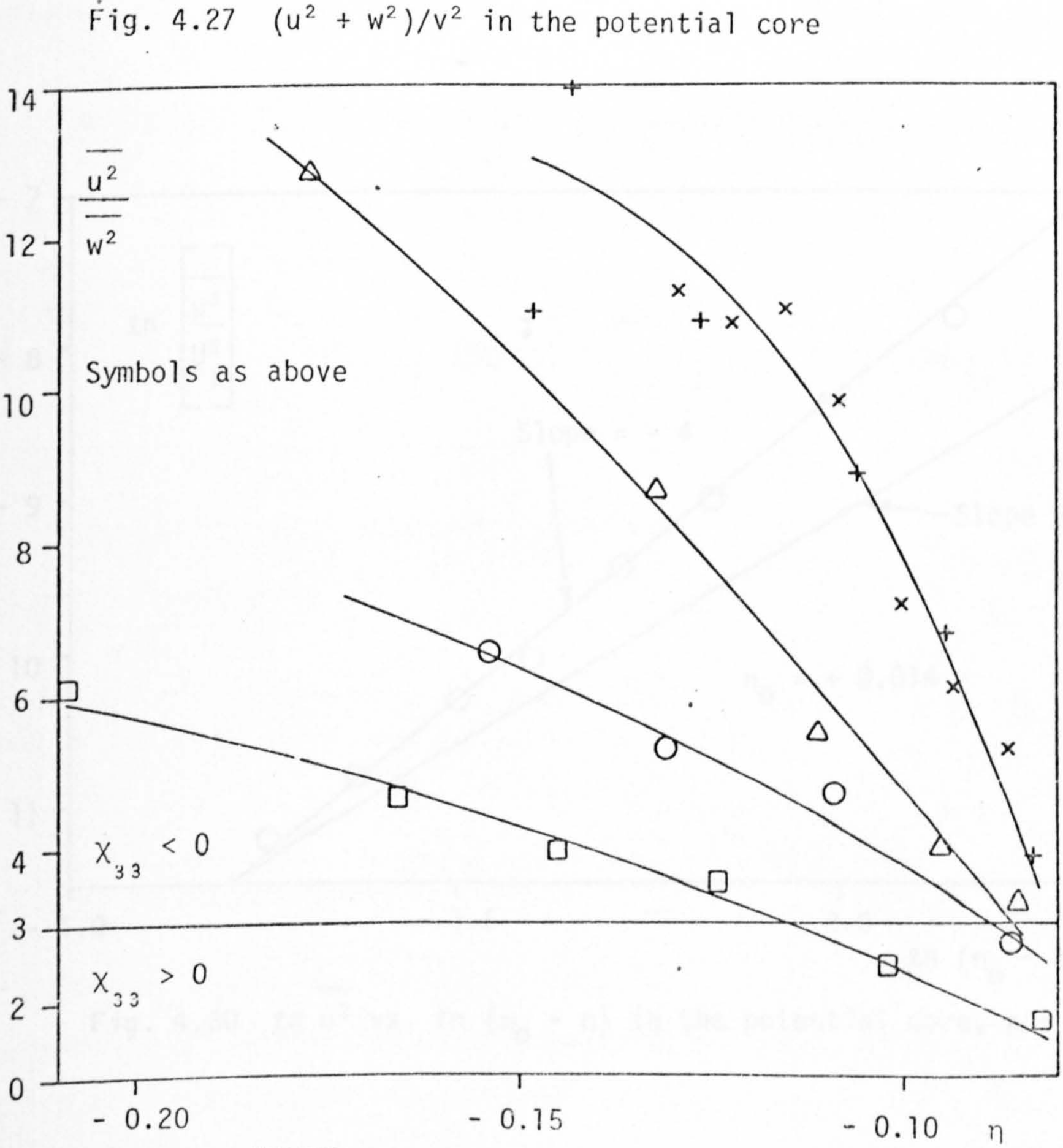


Fig. 4.28 $\overline{u^2}/\overline{w^2}$ in the potential core

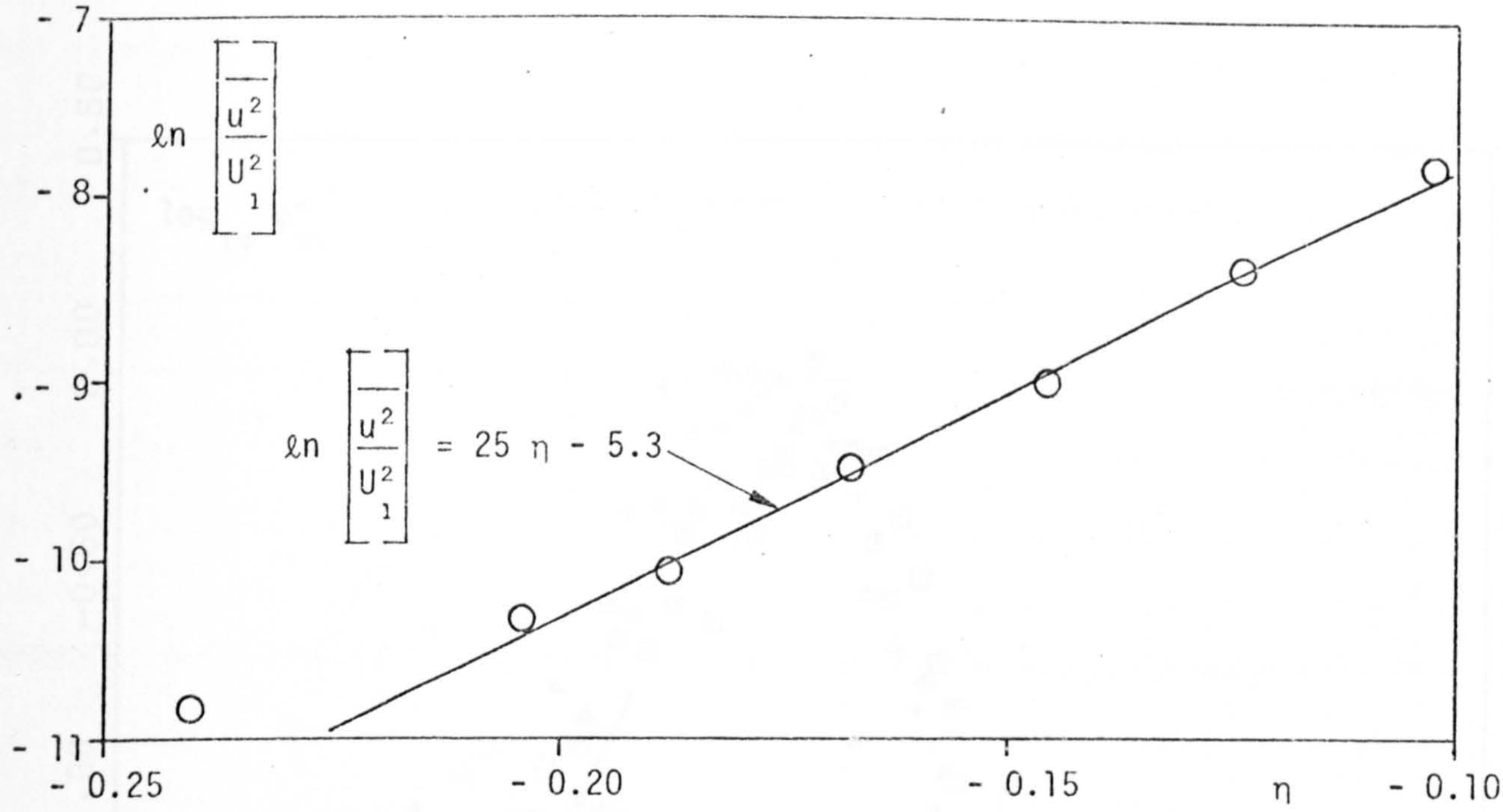


Fig. 4.29 $\ell n\ \overline{u^2}$ vs. η in the potential core, $x - x_o = 24.05$ cm

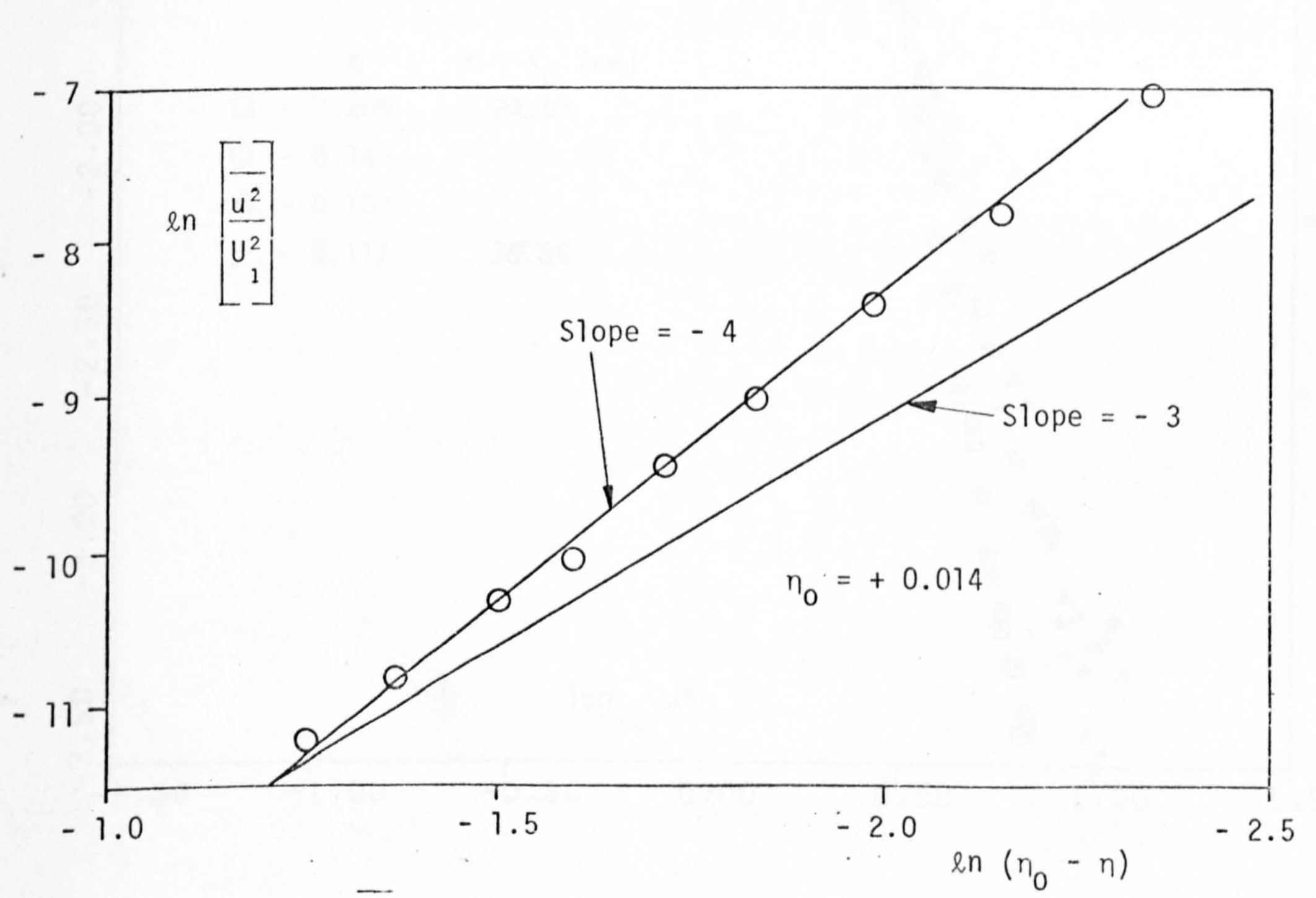


Fig. 4.30 $\ell n\ \overline{u^2}$ vs. $\ell n\ (\eta_o - \eta)$ in the potential core, $x - x_o = 24.05$ cm

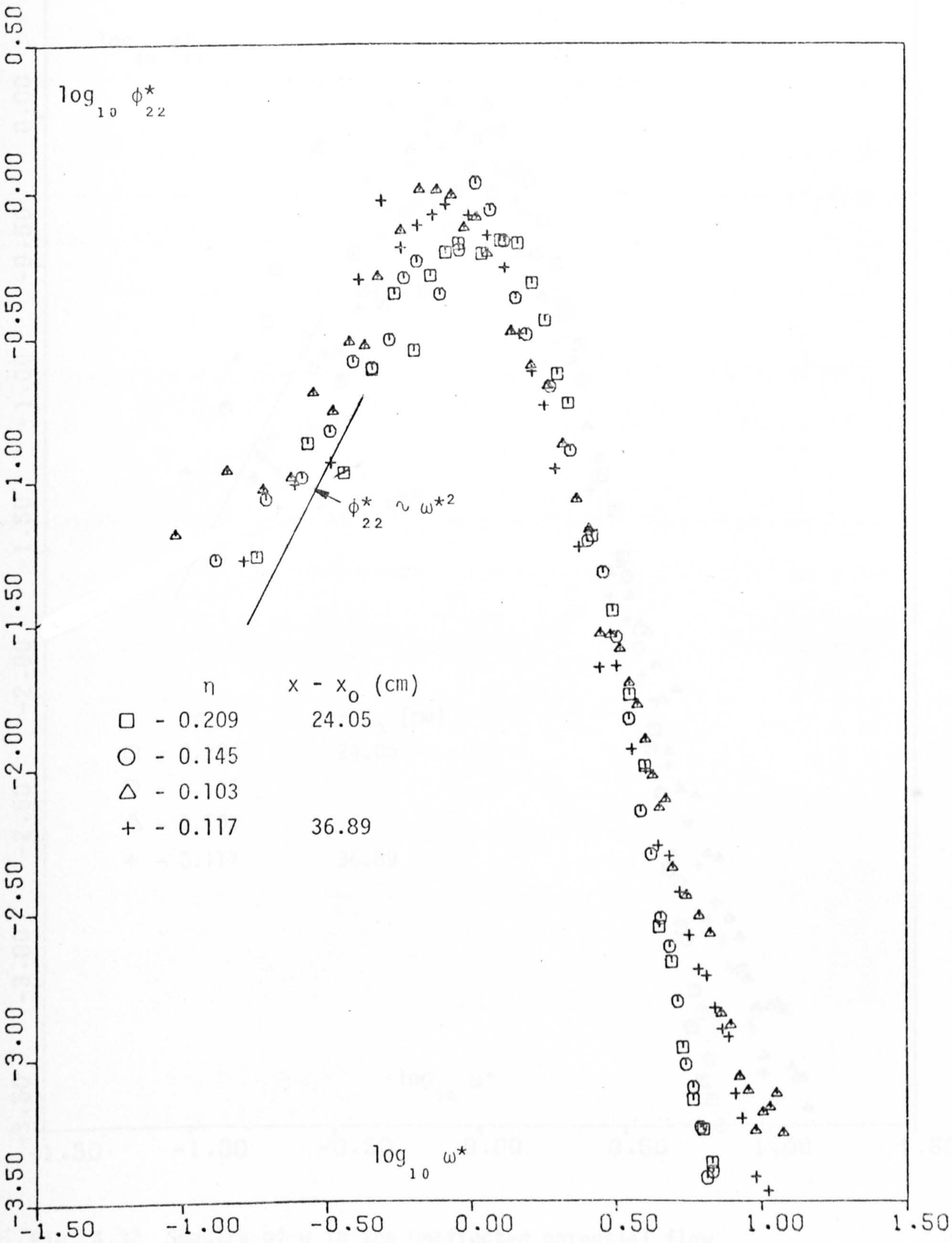


Fig. 4.31 Spectra of v in the unaffected potential flow

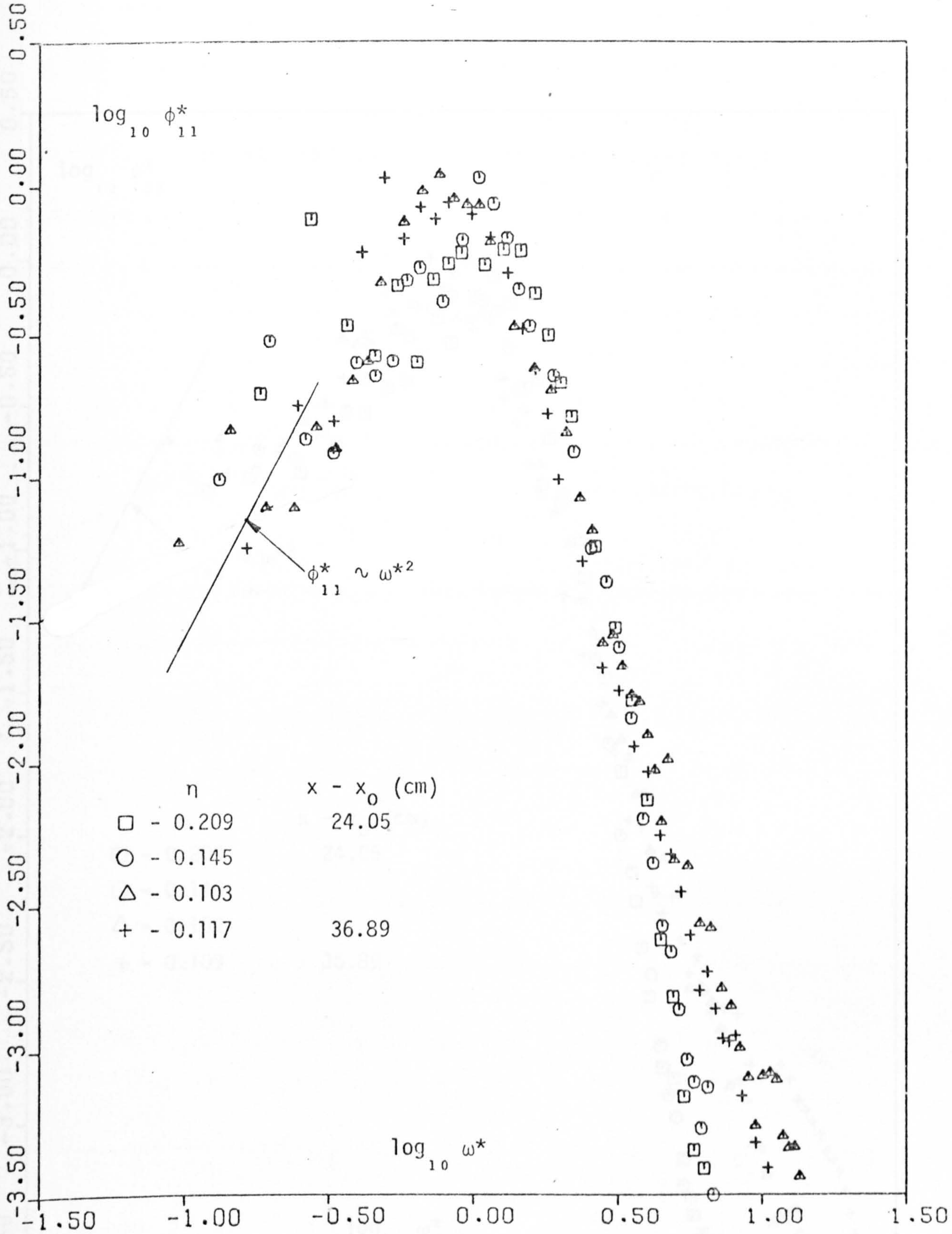


Fig. 4.32 Spectra of u in the unaffected potential flow

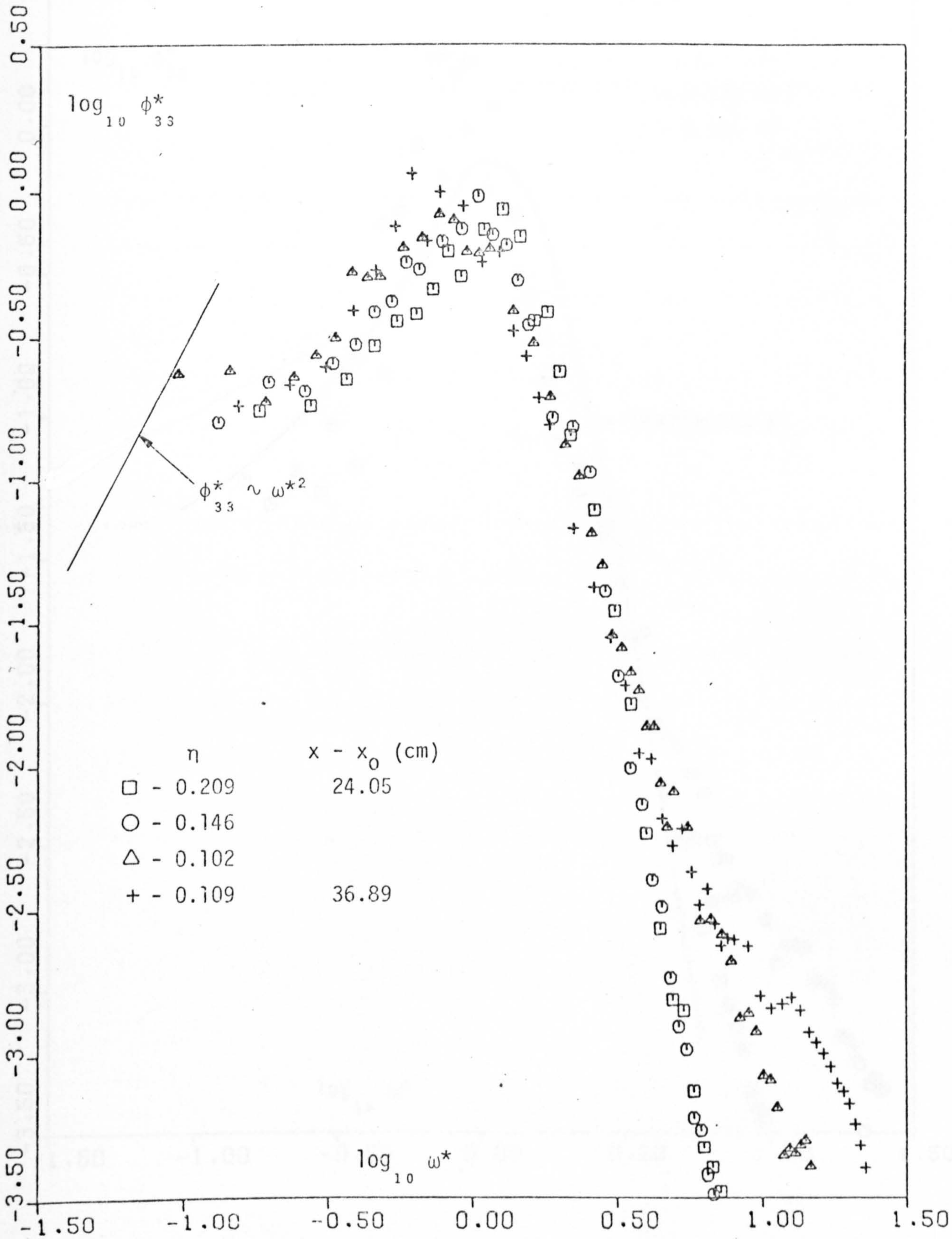


Fig. 4.33 Spectra of w in the unaffected potential flow

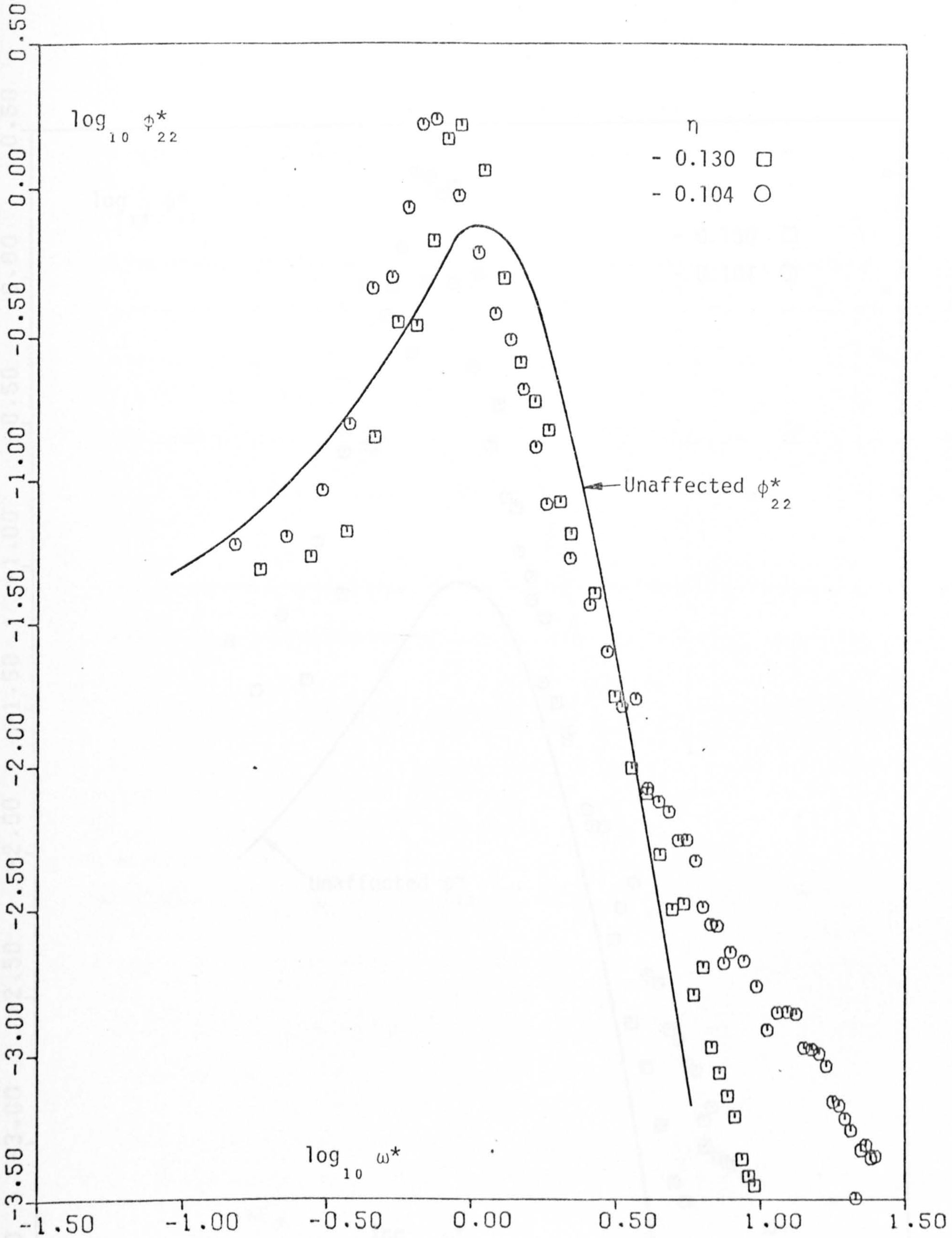


Fig. 4.34 Spectra of v in the wall effected potential flow, $x - x_o = 75.06$ cm

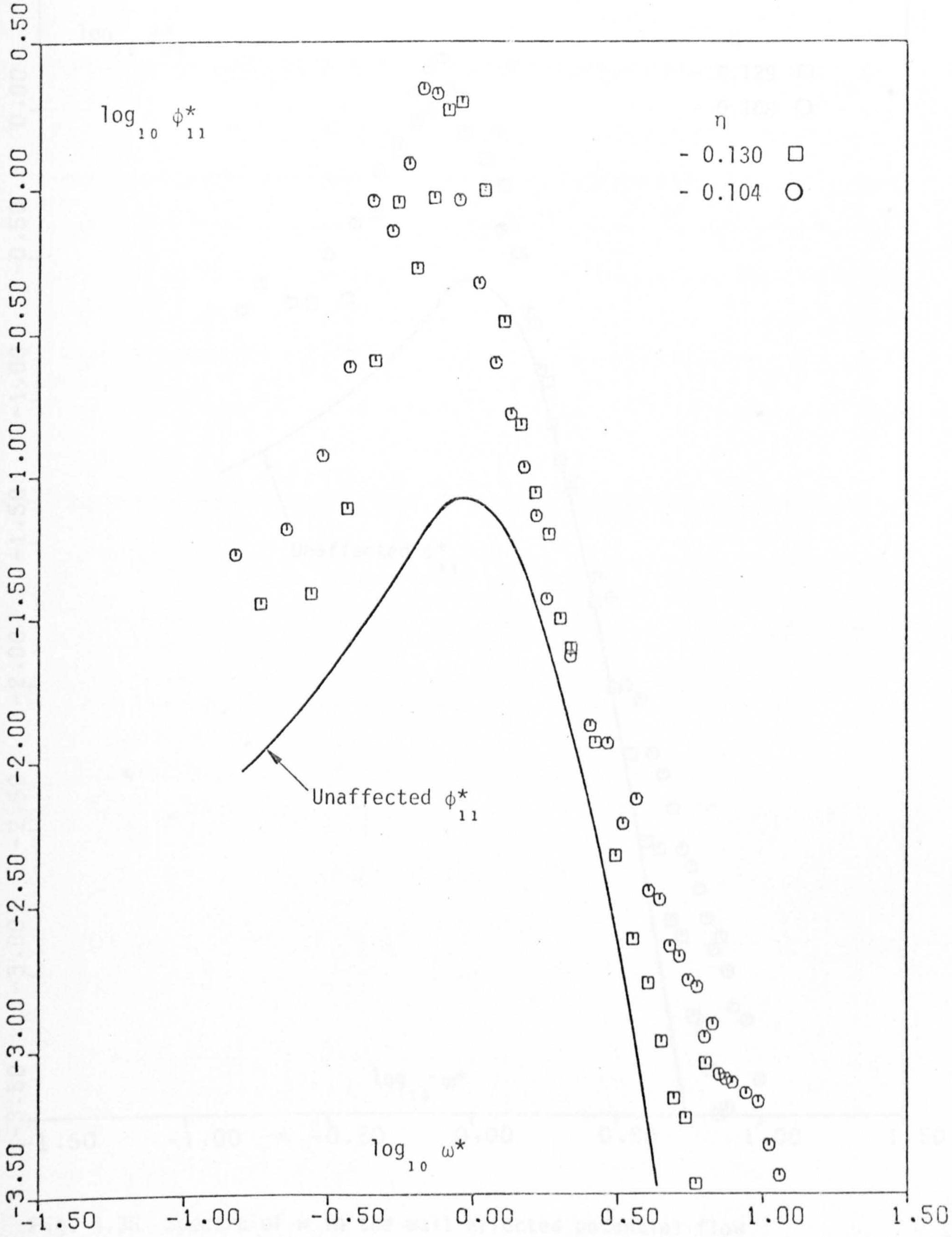


Fig. 4.35 Spectra of u in the wall effected potential flow, $x - x_o = 75.06$ cm

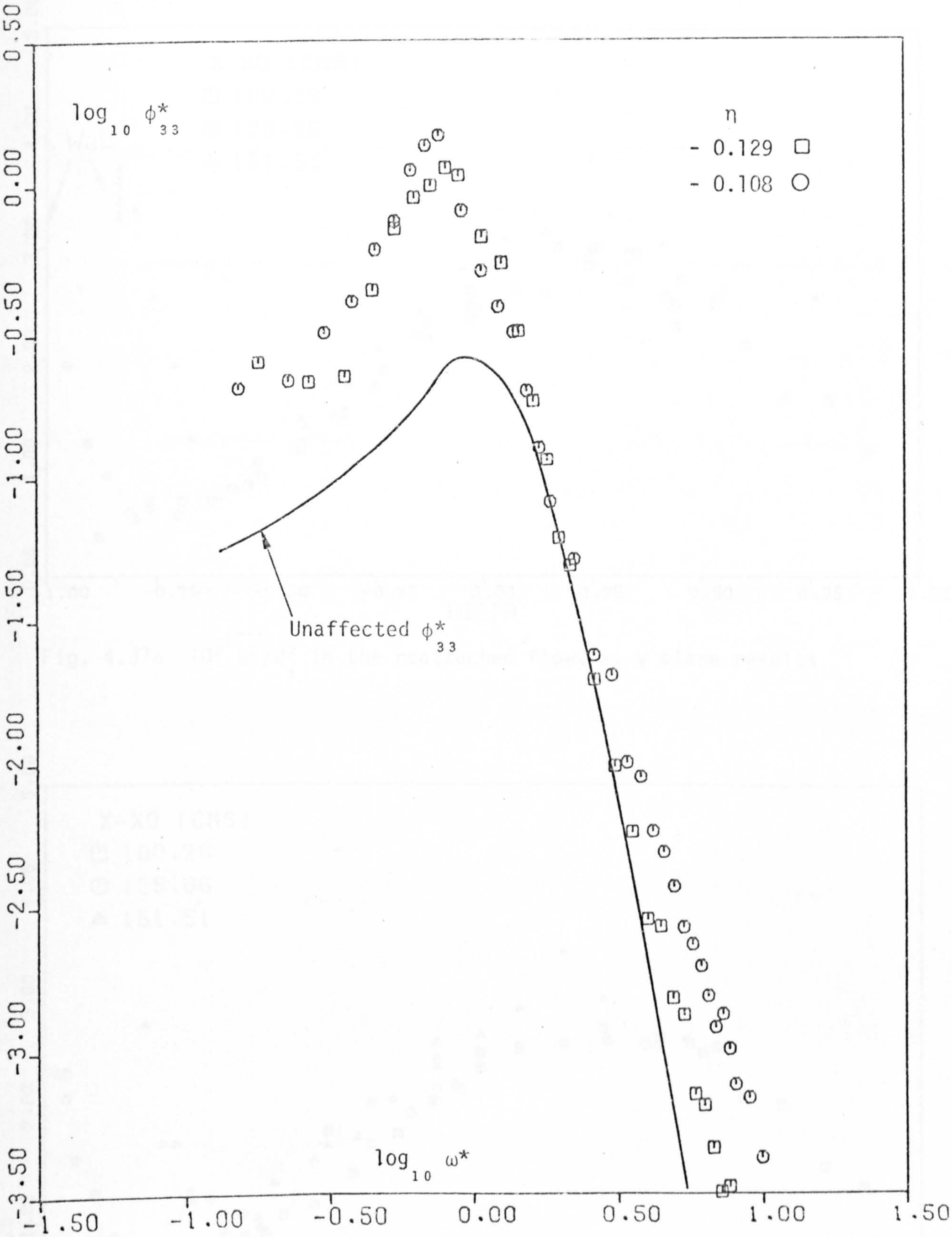


Fig. 4.36 Spectra of w in the wall effected potential flow

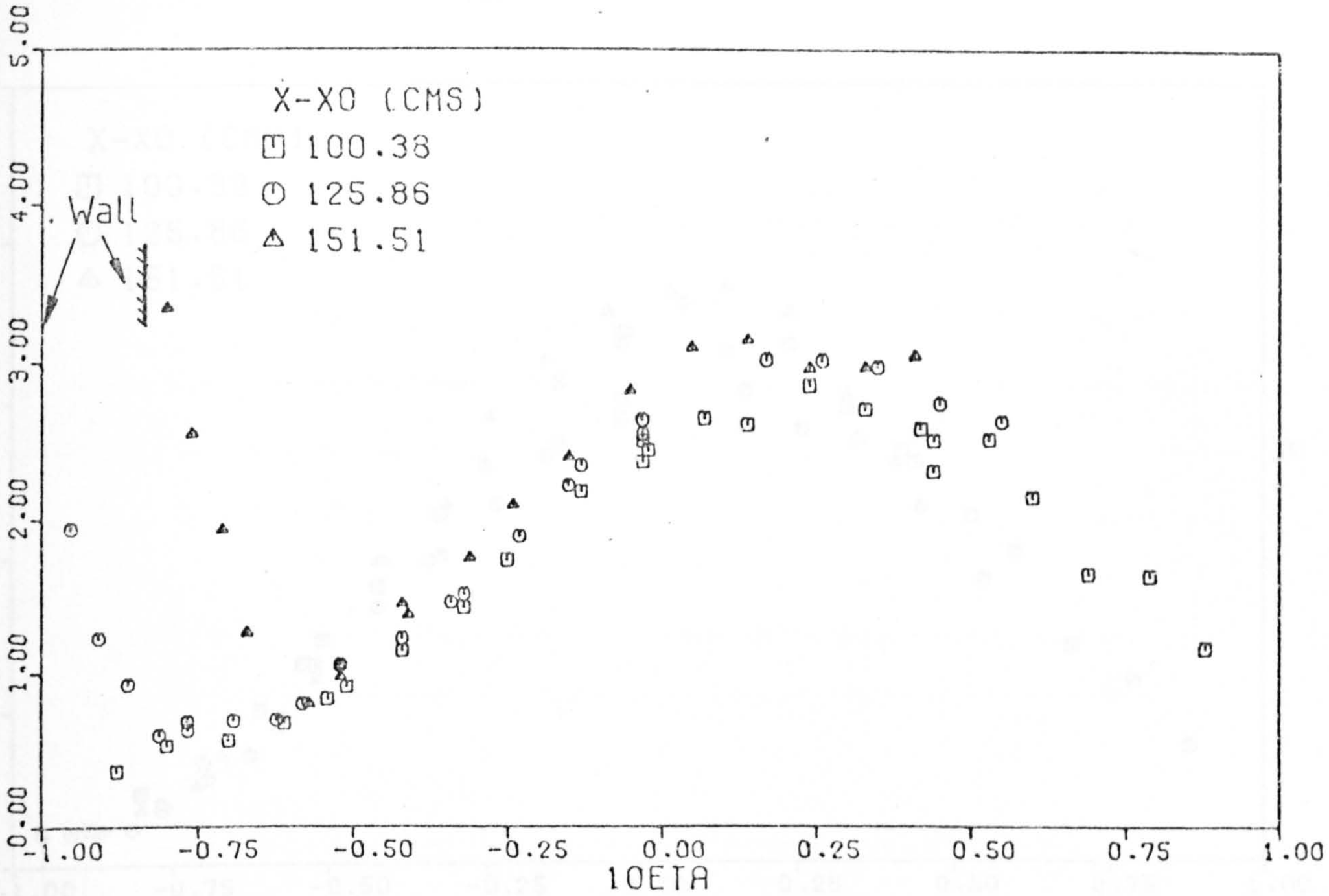


Fig. 4.37a $10^2 \overline{u^2}/U_1^2$ in the reattached flow; x, y plane results

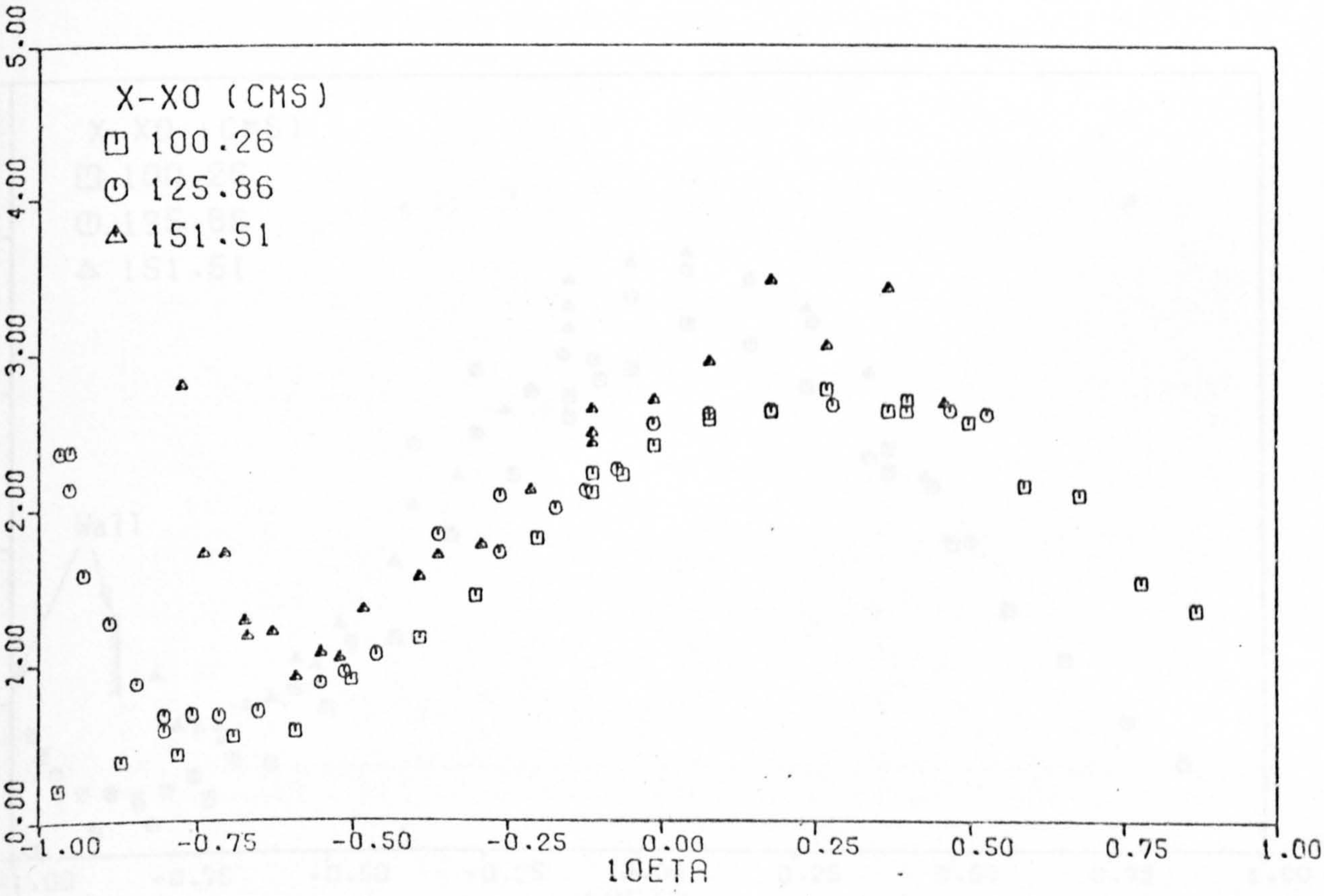


Fig. 4.37b $10^2 \overline{u^2}/U_1^2$ in the reattached flow; x, z plane results

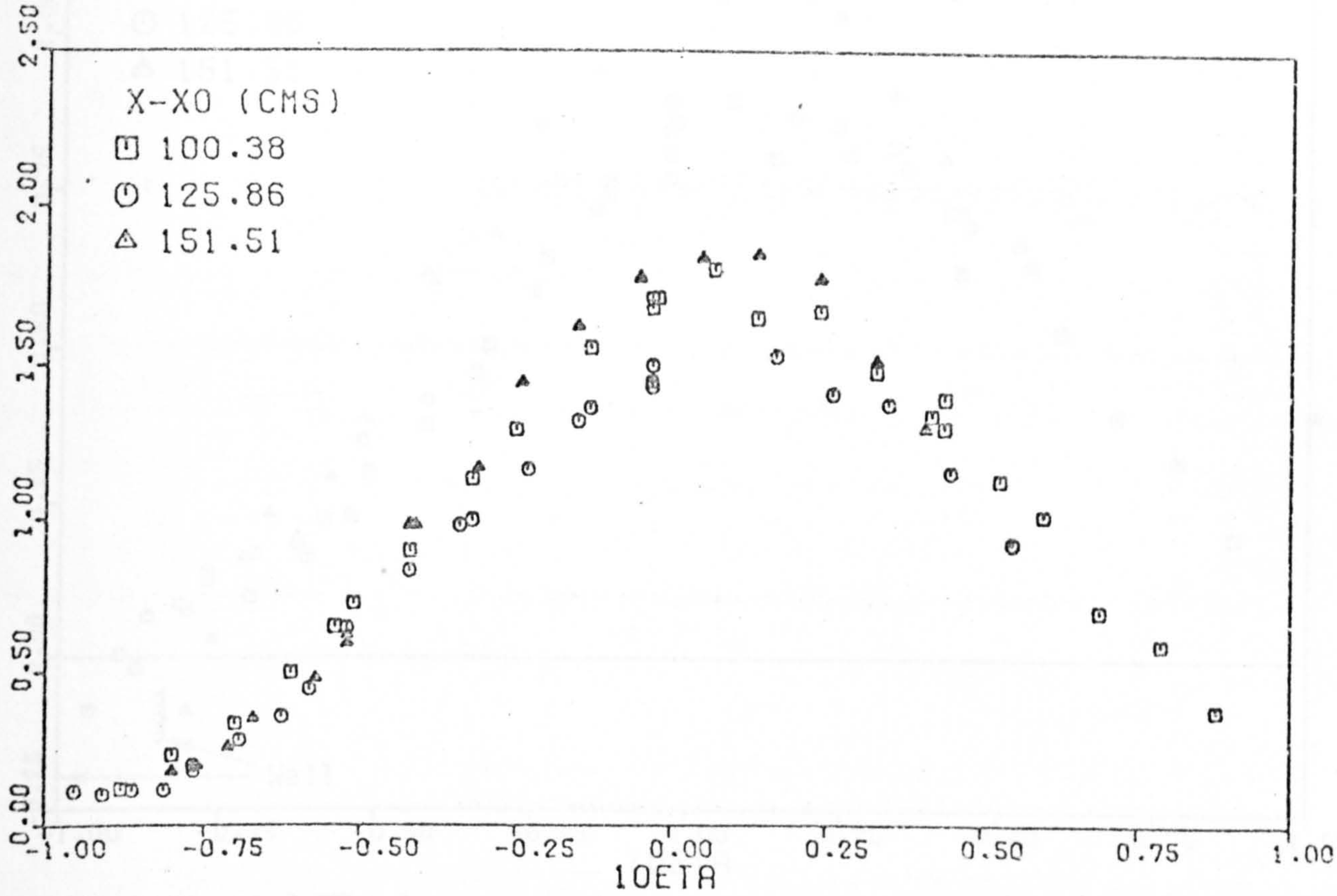


Fig. 4.38 $10^2\ \overline{v^2}/U_1^2$ in the reattached flow

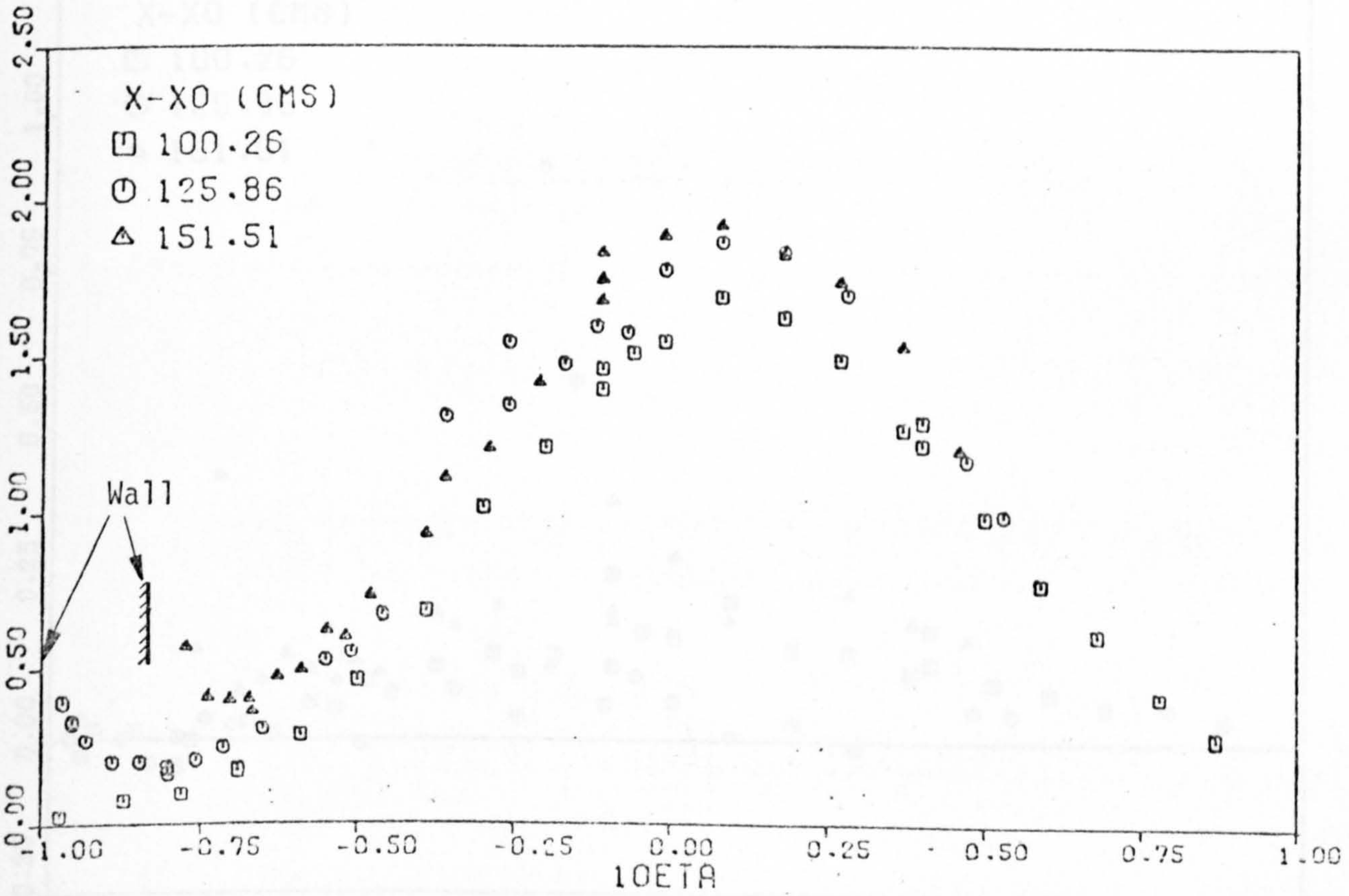


Fig. 4.39 $10^2\ \overline{w^2}/U_1^2$ in the reattached flow

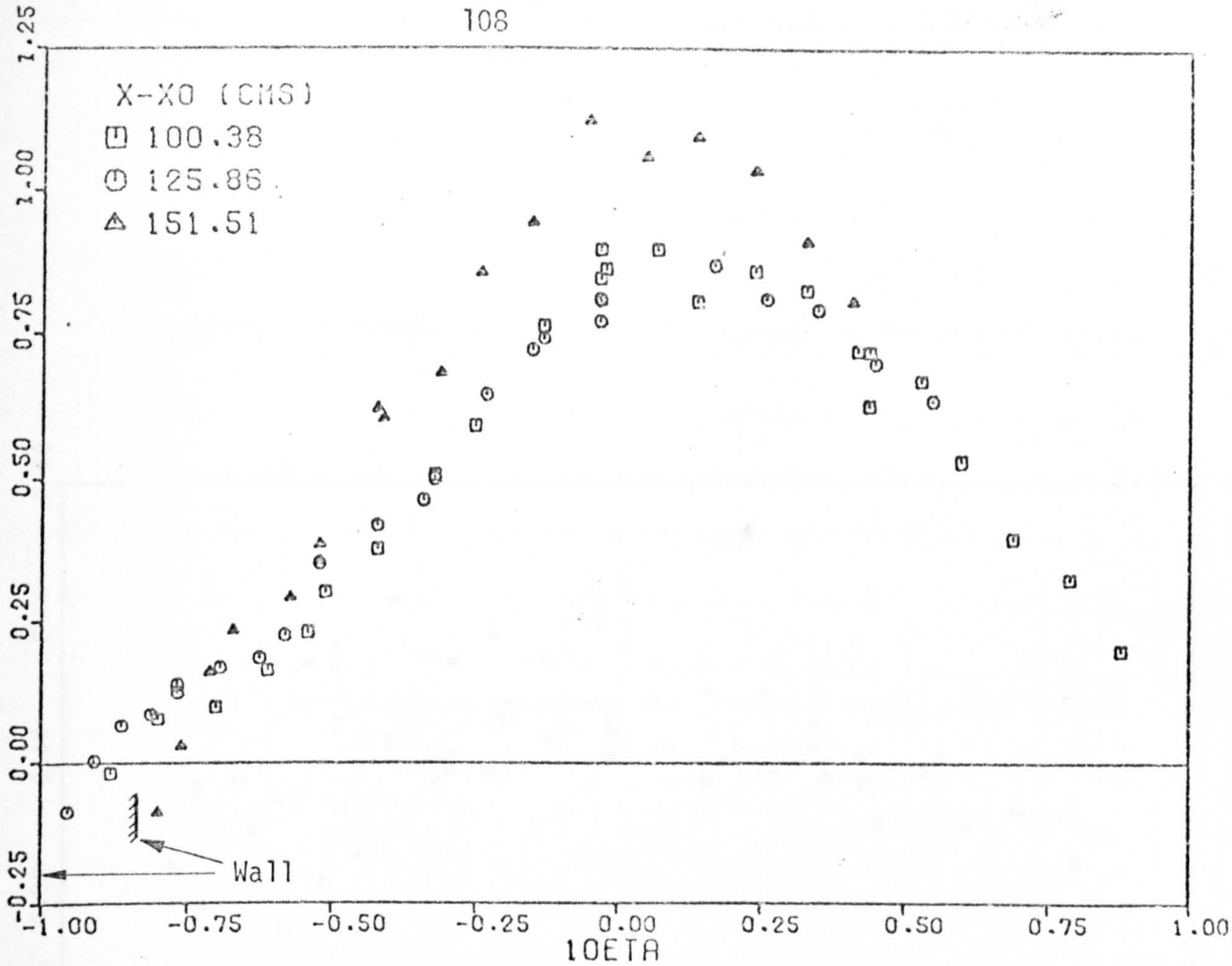


Fig. 4.40 $10^2\ \overline{uv}/U_1^2$ in the reattached flow

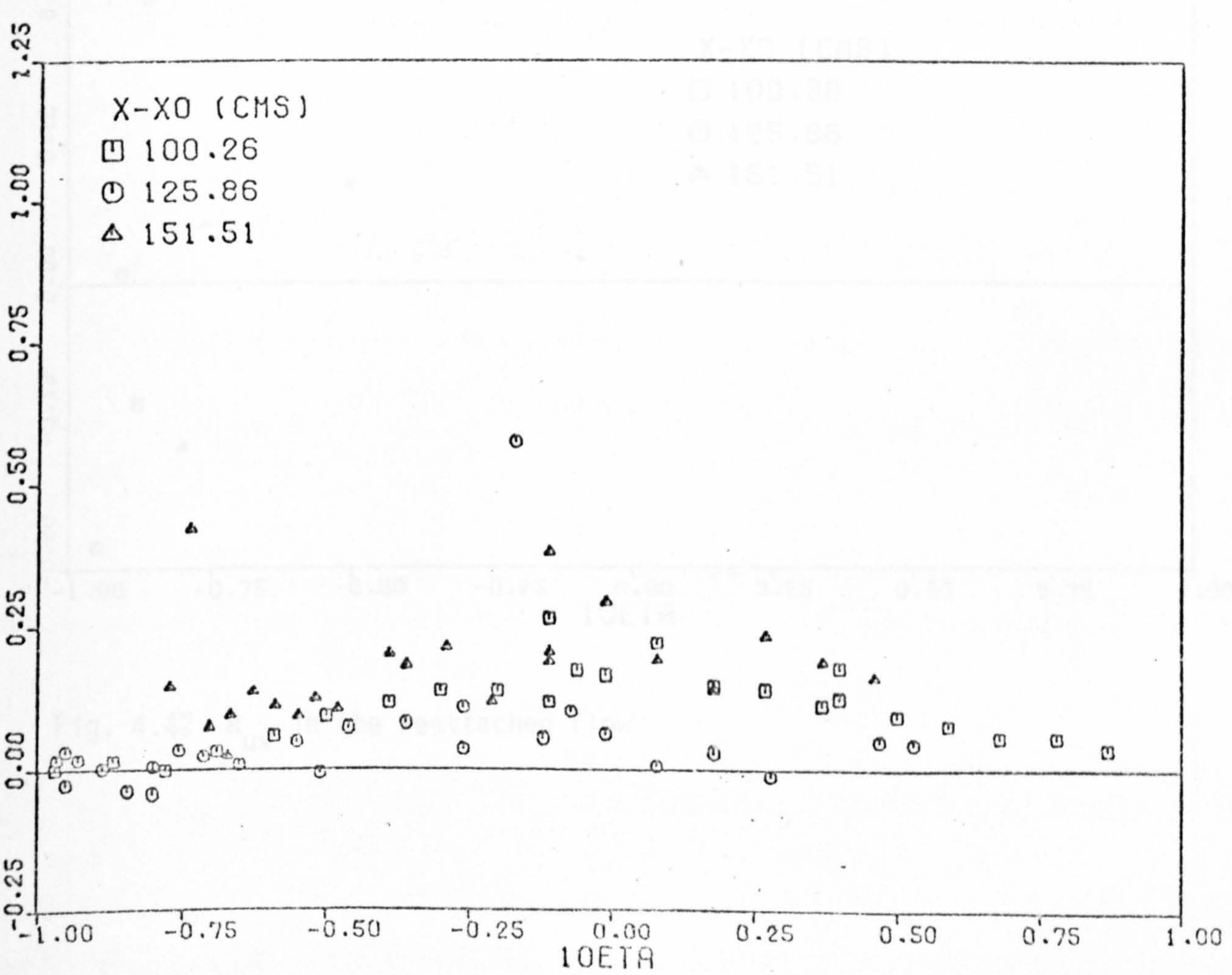


Fig. 4.41 $10^2\ \overline{uw}/U_1^2$ in the reattached flow

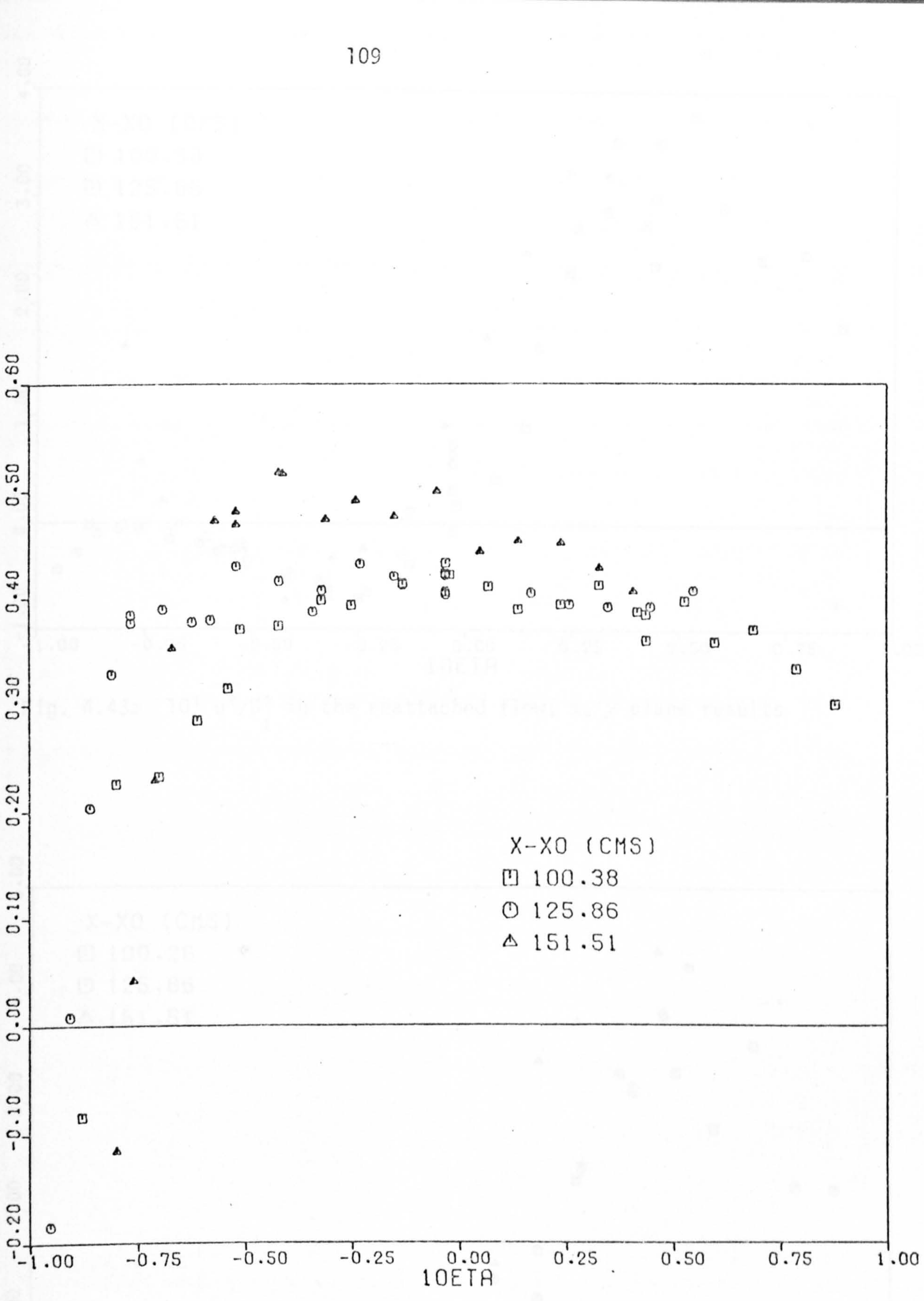


Fig. 4.42 R_{uv} in the reattached flow

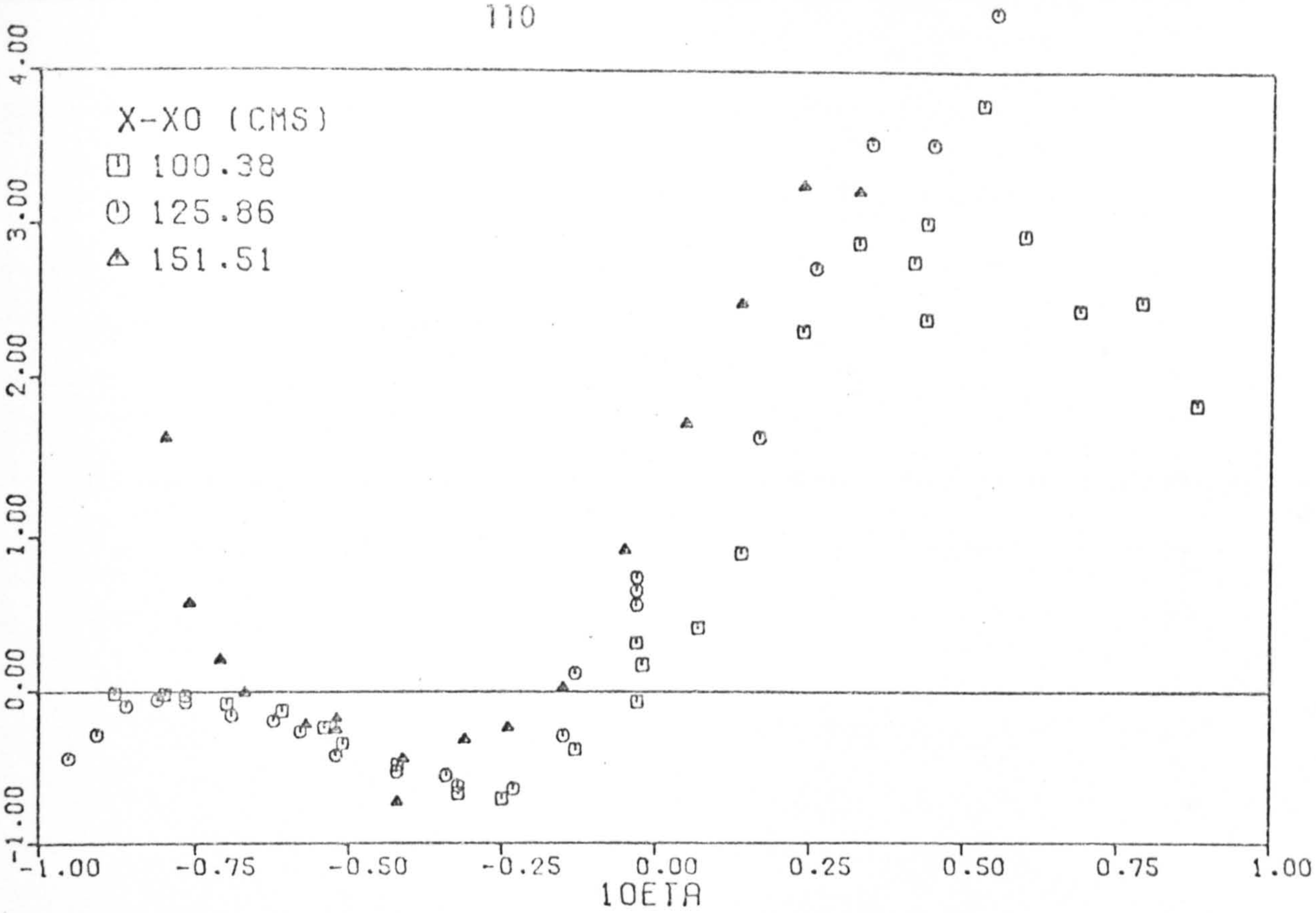


Fig. 4.43a $10^3 \overline{u^3}/U_1^3$ in the reattached flow; x, y plane results

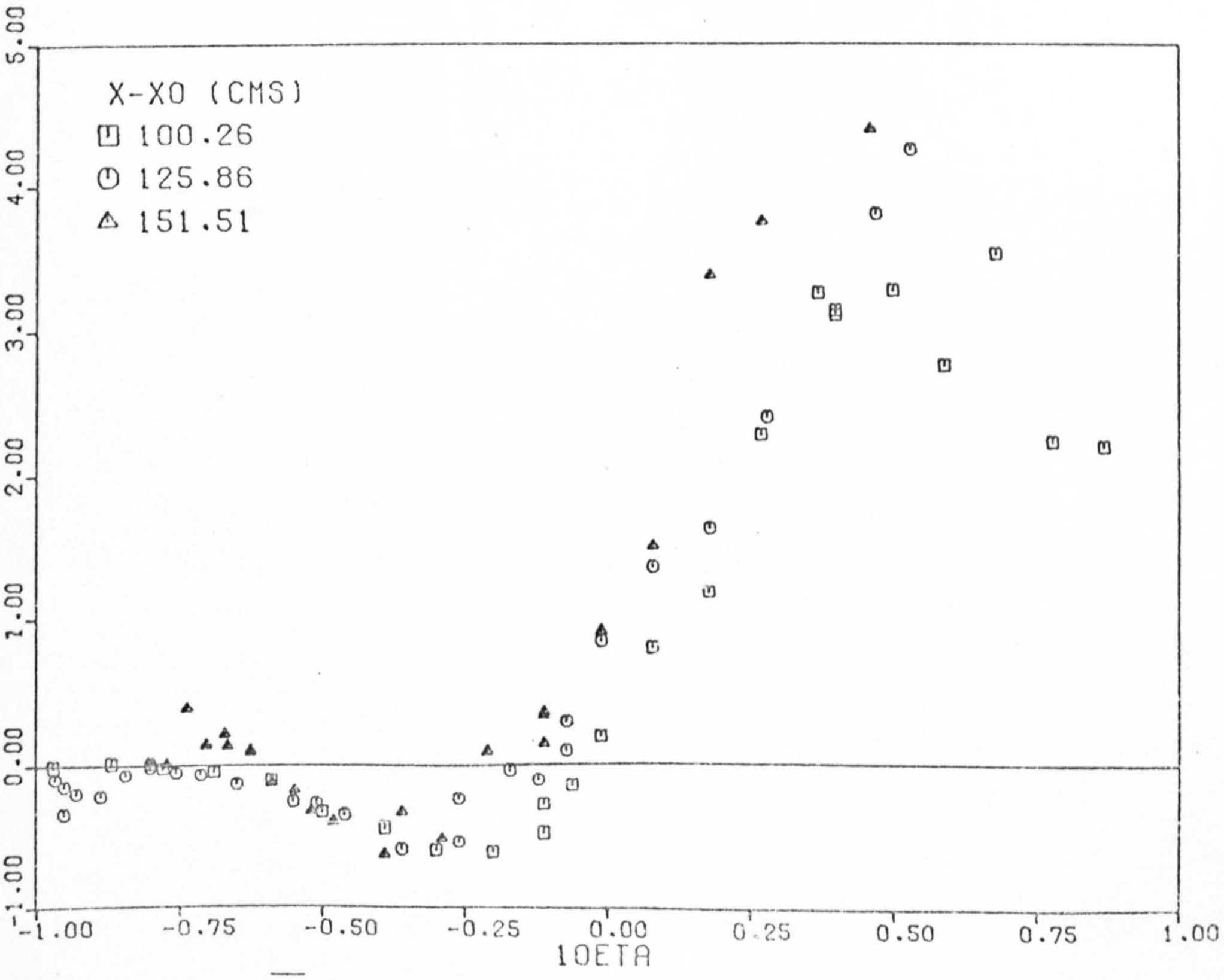


Fig. 4.43b $10^3 \overline{u^3}/U_1^3$ in the reattached flow; x, z plane results

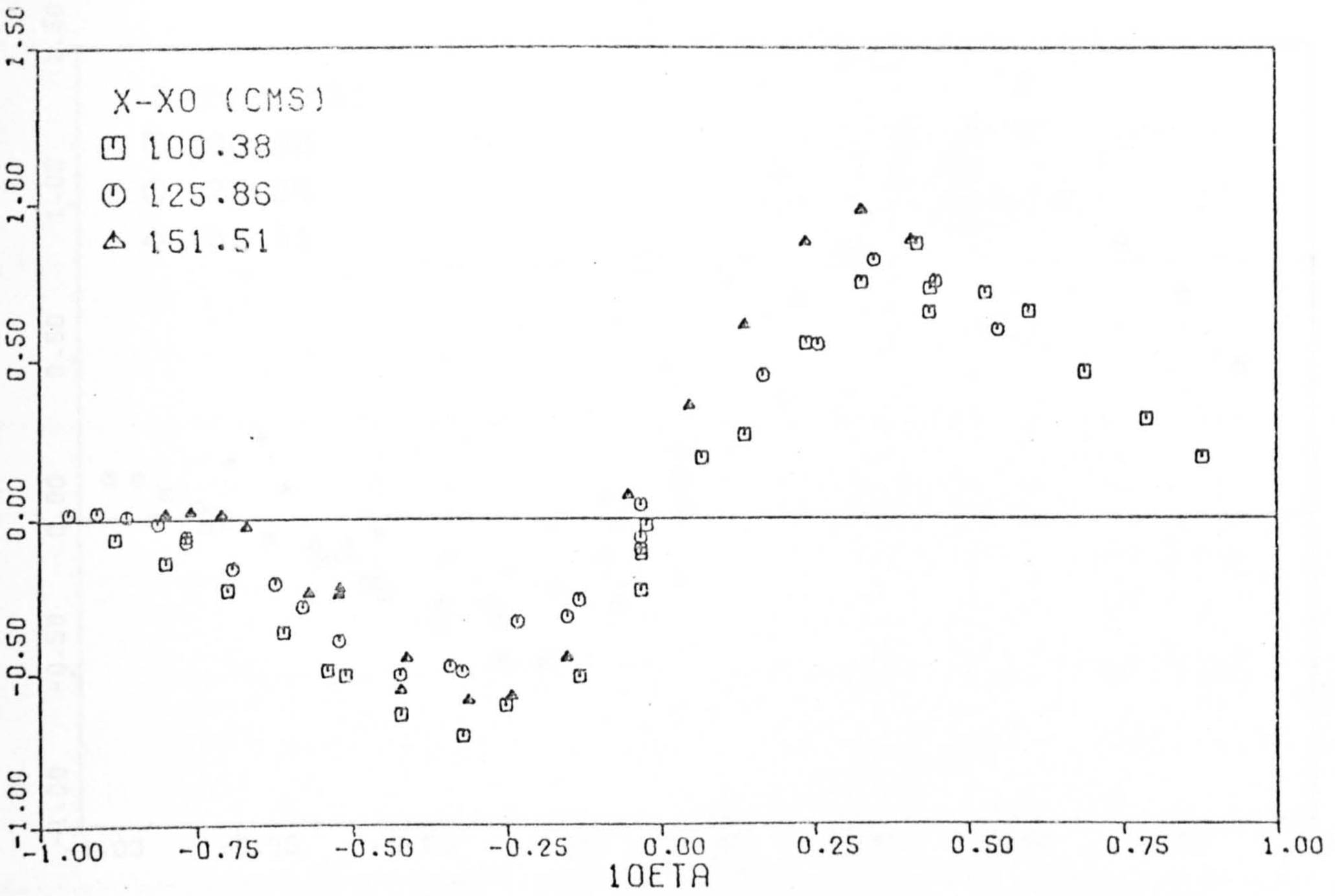


Fig. 4.44 $10^3 \overline{v^3}/U_1^3$ in the reattached flow

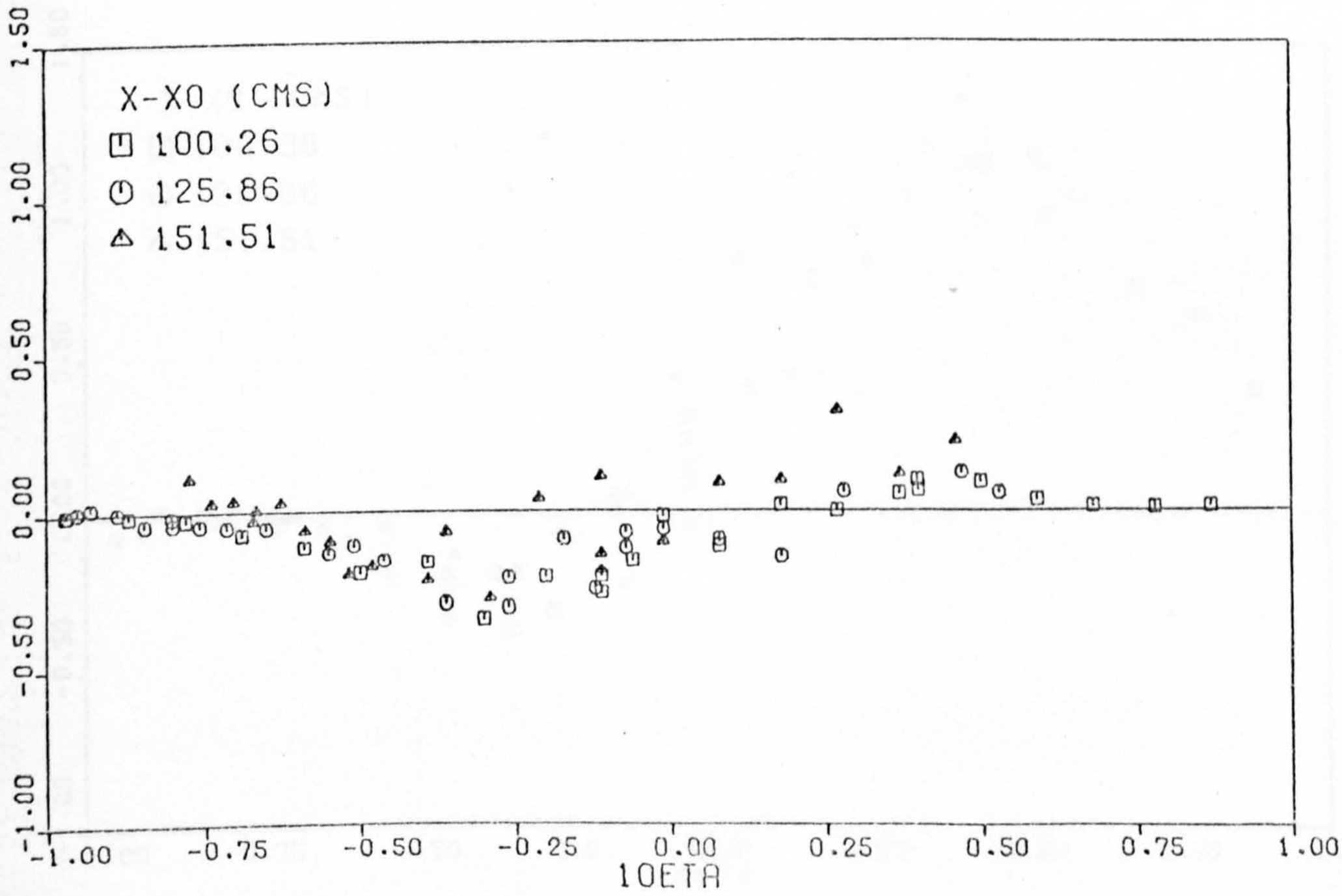


Fig. 4.45 $10^3 \overline{w^3}/U_1^3$ in the reattached flow

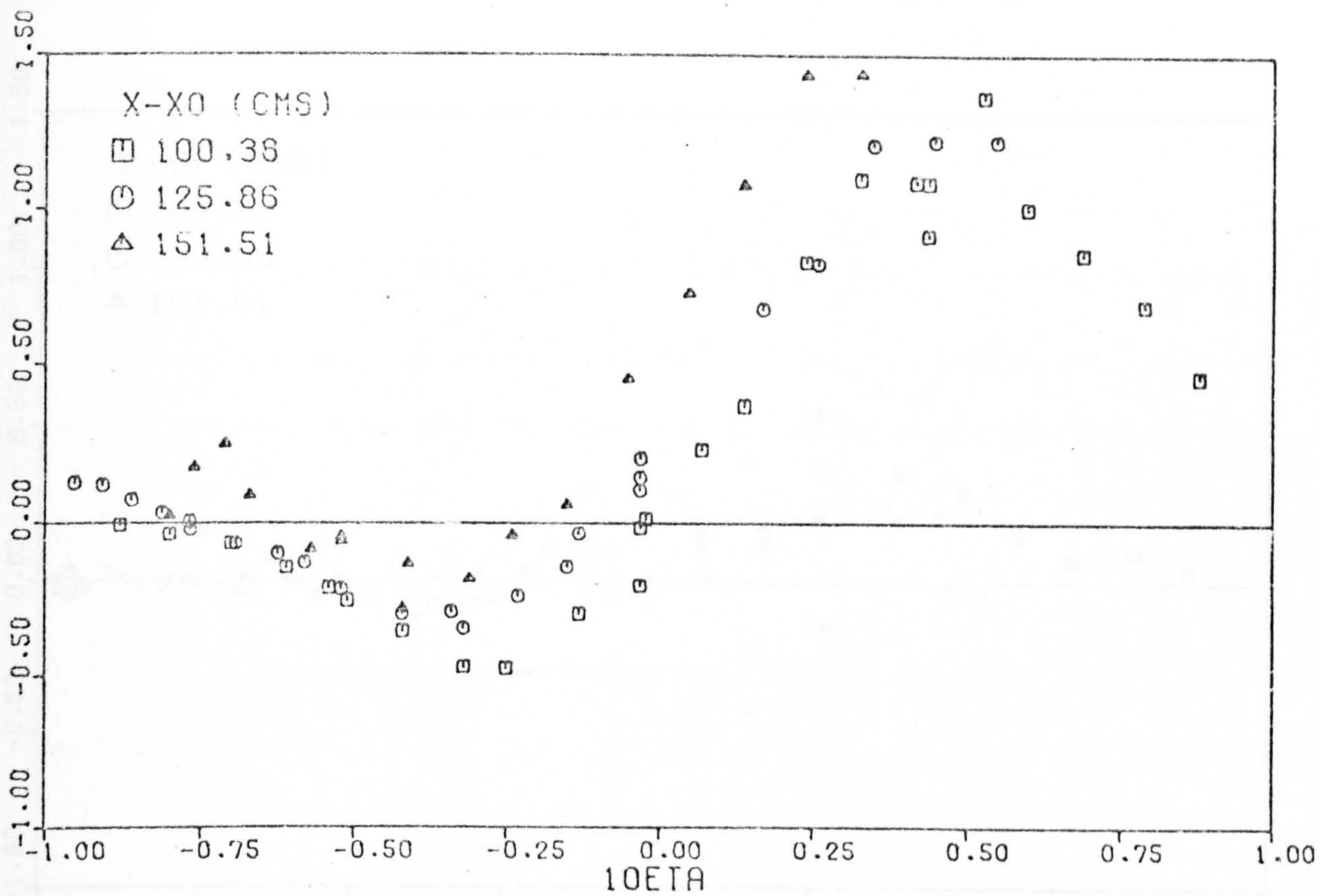


Fig. 4.46 $10^3 \overline{u^2v}/U_1^3$ in the reattached flow

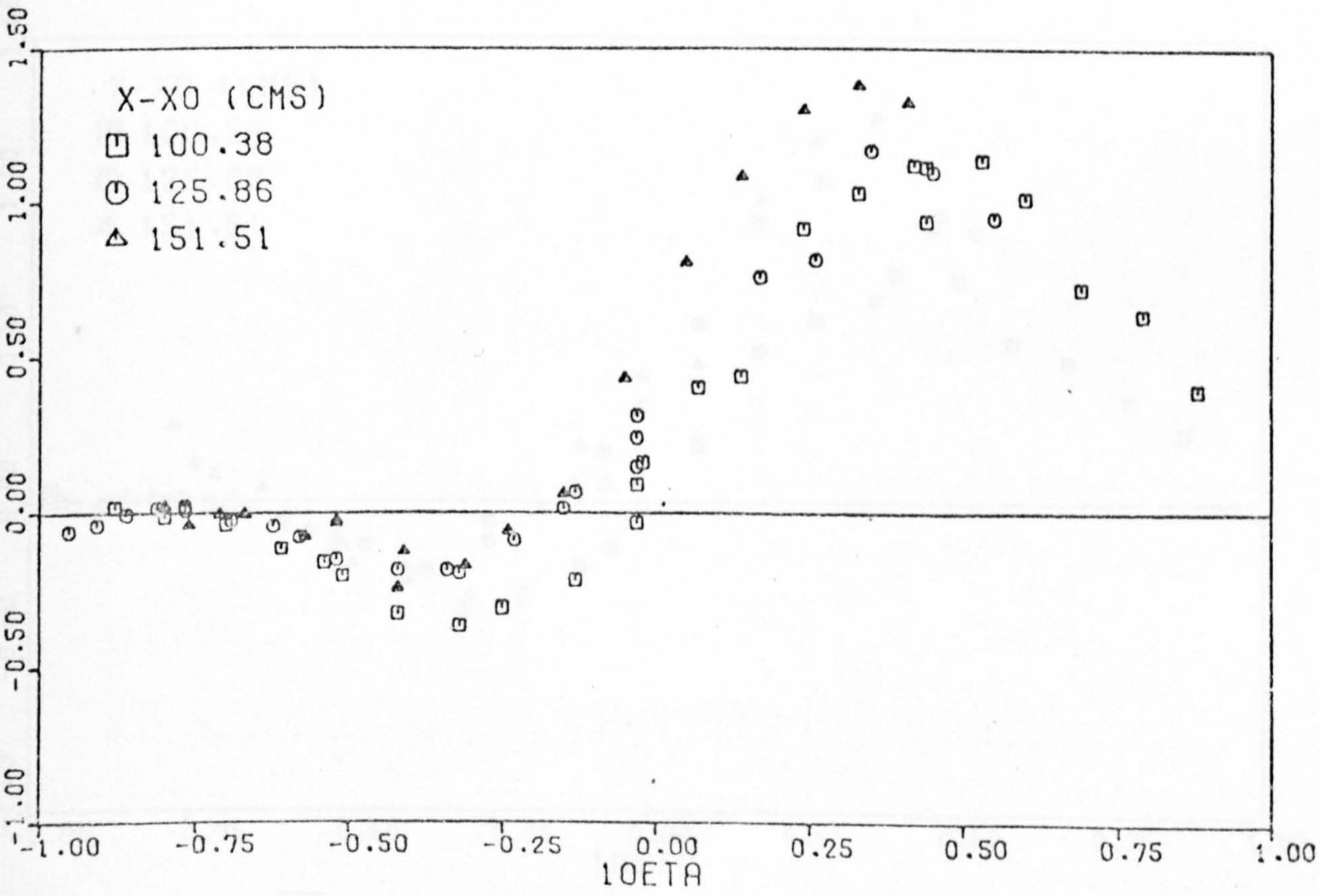


Fig. 4.47 $10^3 \overline{uv^2}/U_1^3$ in the reattached flow

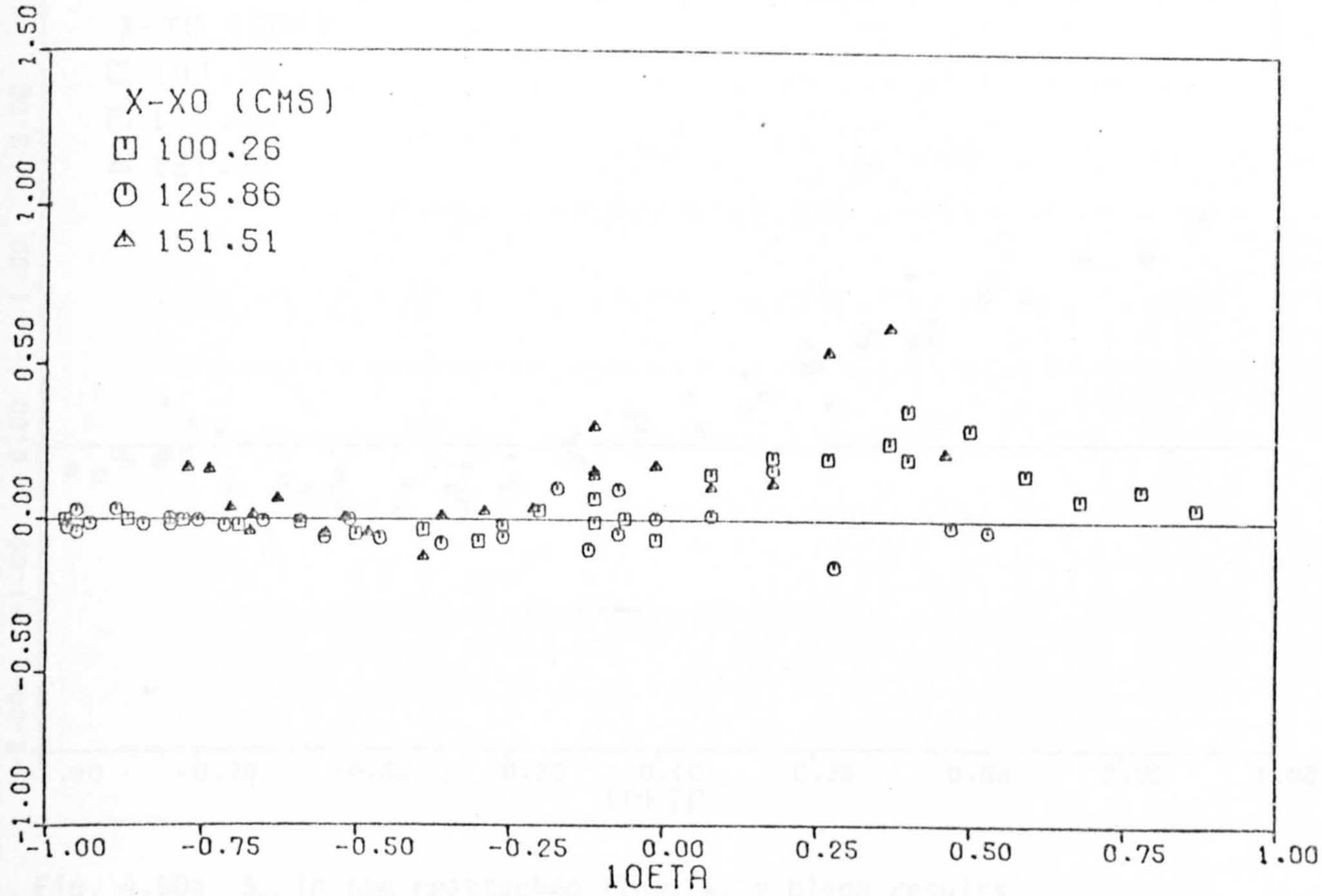


Fig. 4.48 $10^3\ \overline{u^2w}/U_1^3$ in the reattached flow

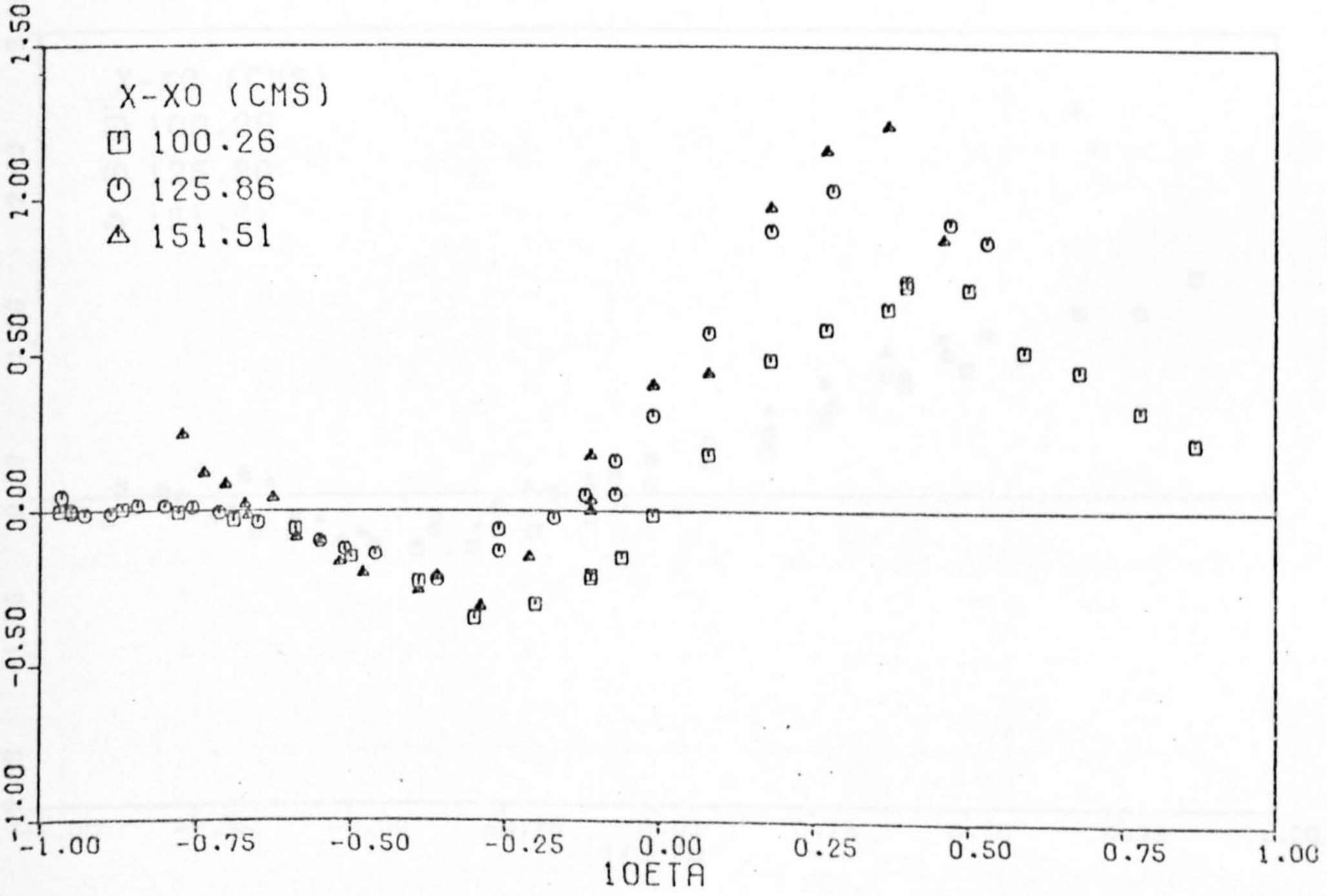


Fig. 4.49 $10^3\ \overline{uw^2}/U_1^3$ in the reattached flow

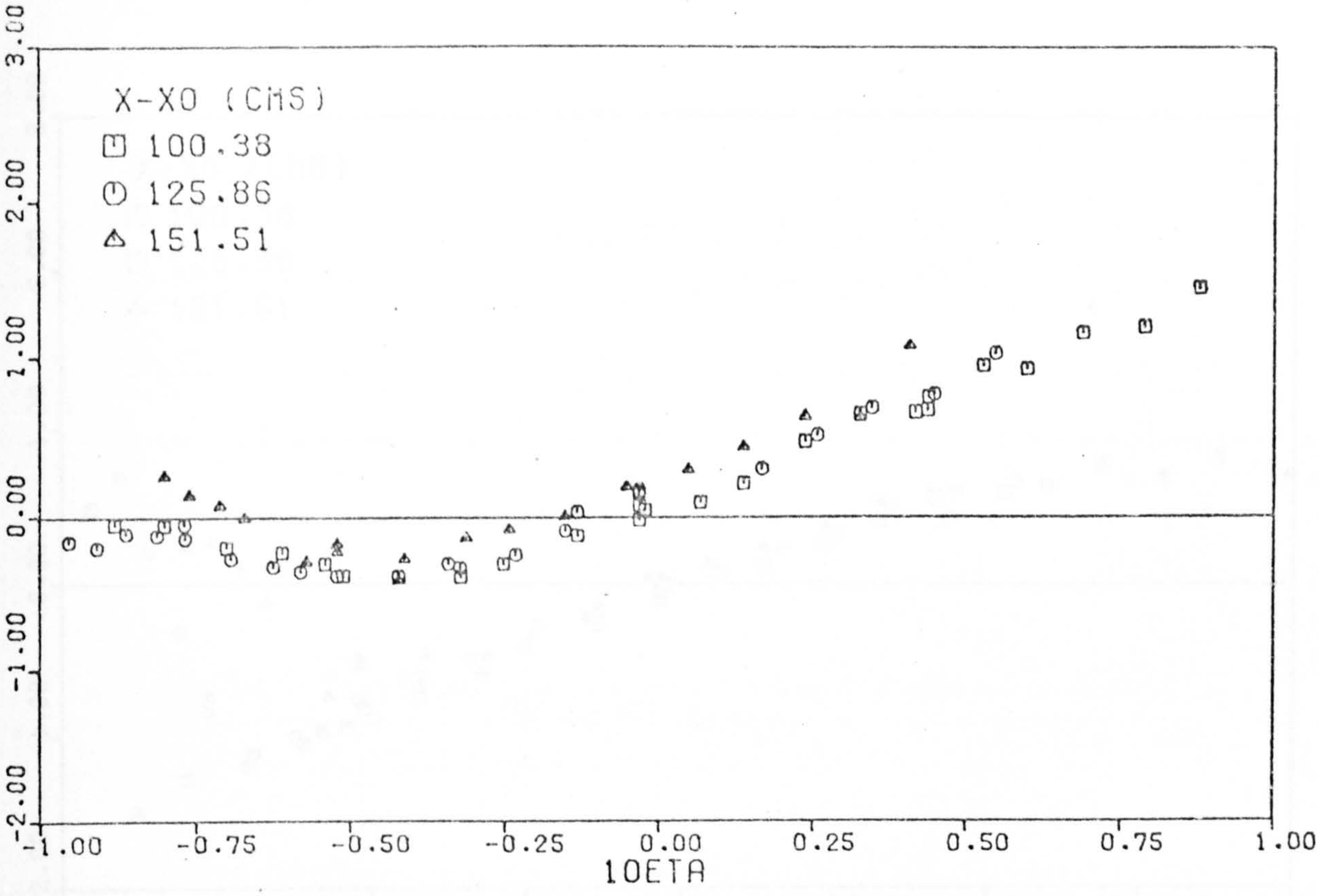


Fig. 4.50a S_u in the reattached flow; x, y plane results

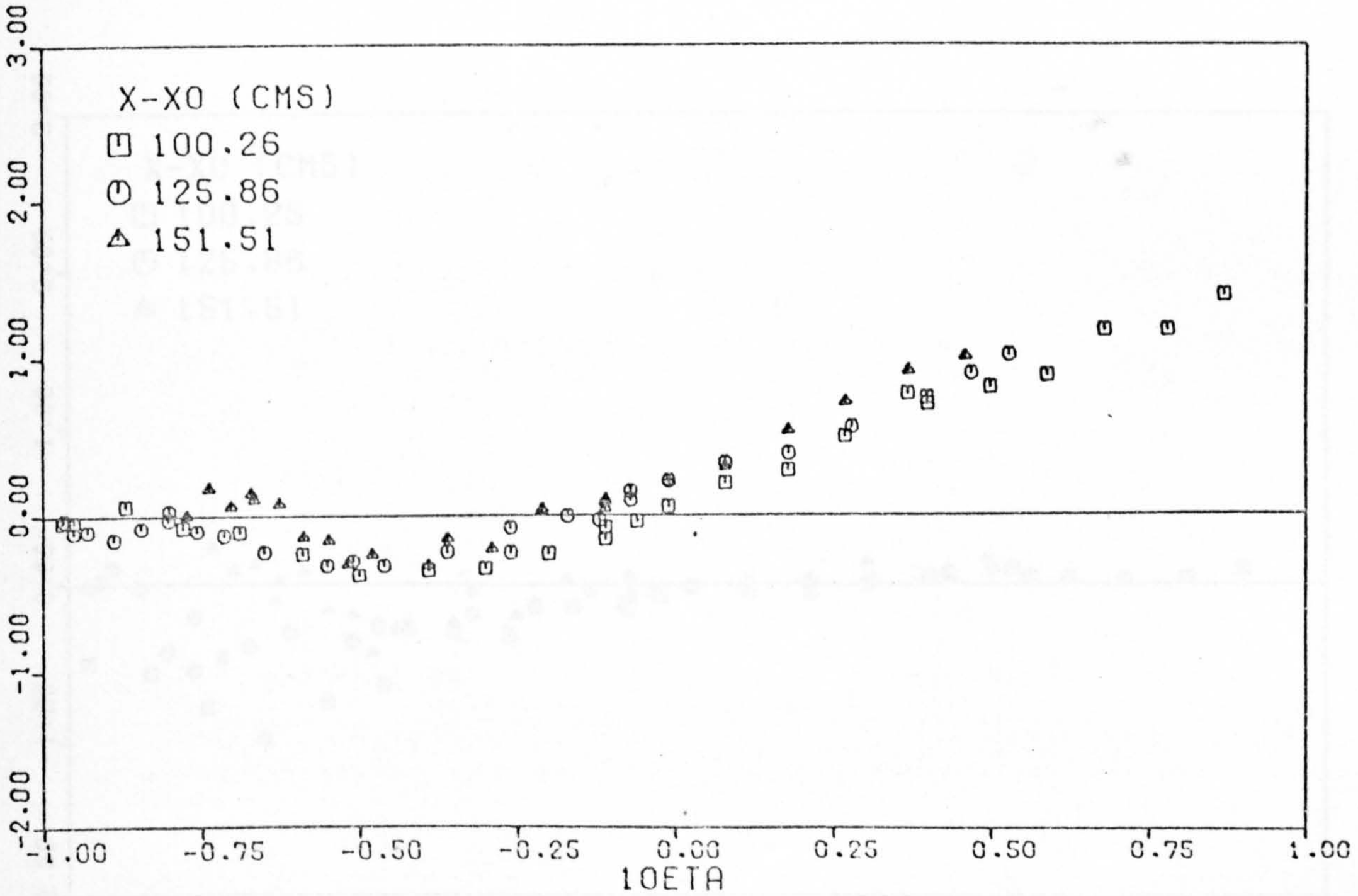


Fig. 4.50b S_u in the reattached flow; x, z plane results

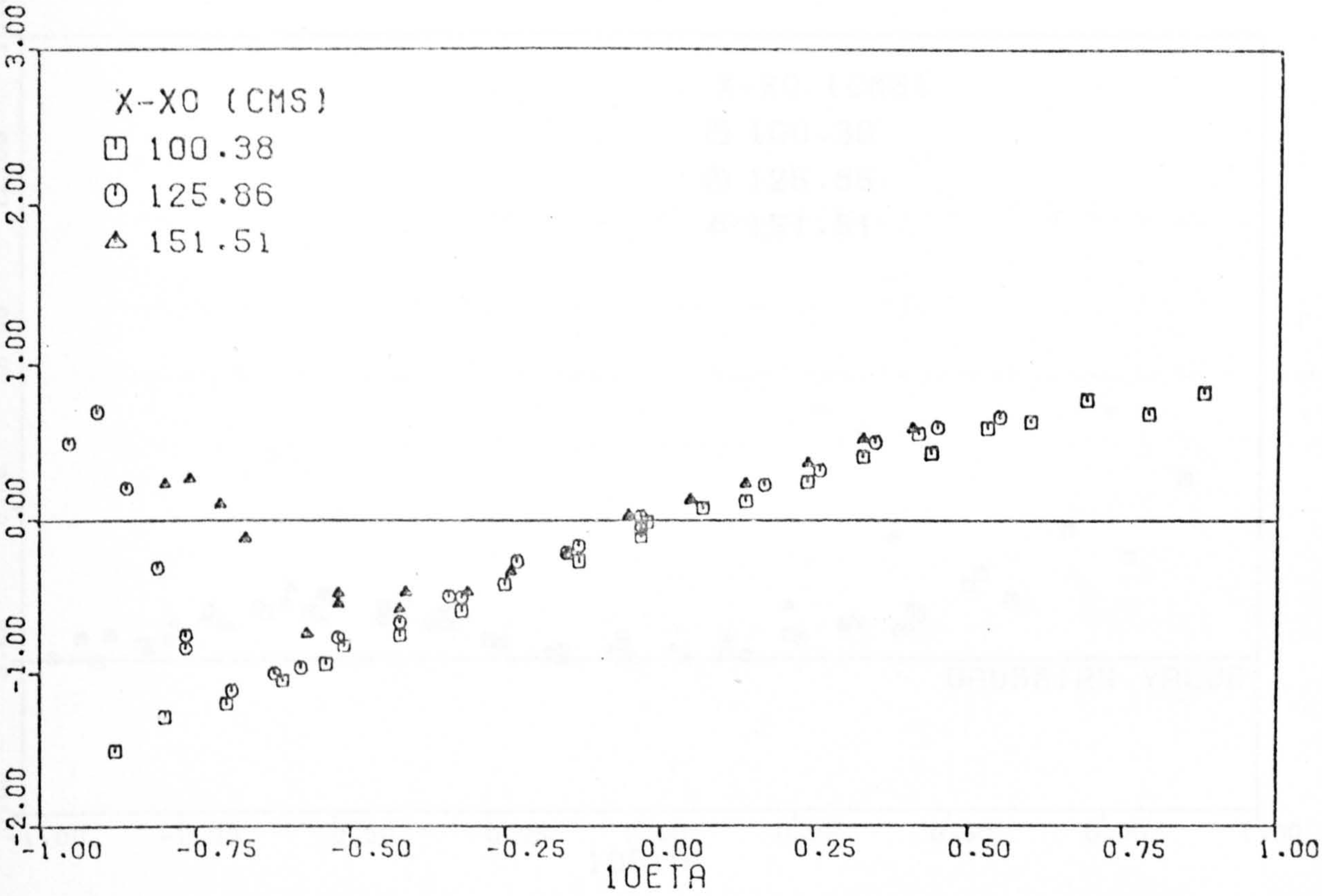


Fig. 4.51 S_v in the reattached flow

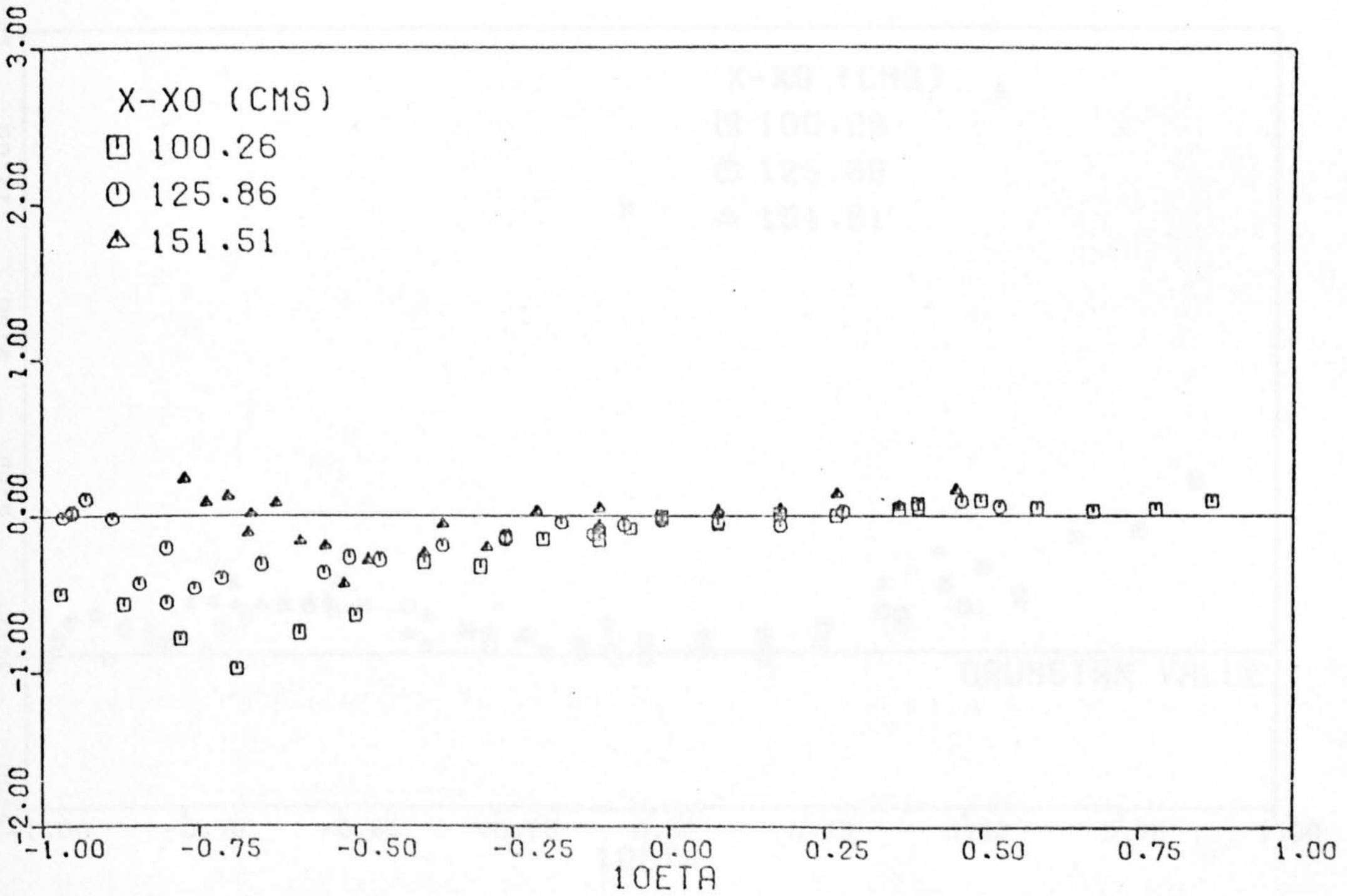


Fig. 4.52 S_w in the reattached flow

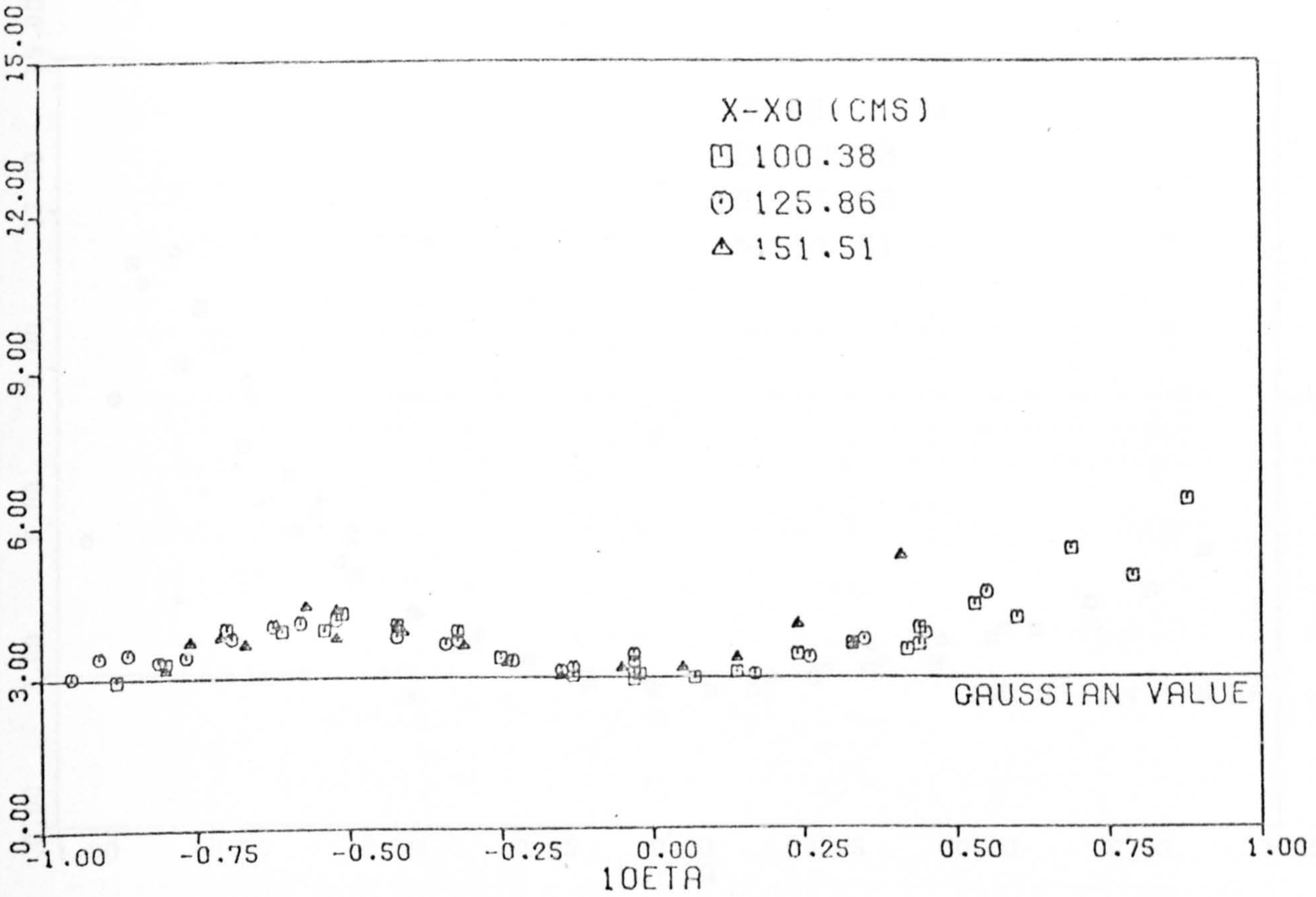


Fig. 4.53a F_u in the reattached flow, x, y plane results

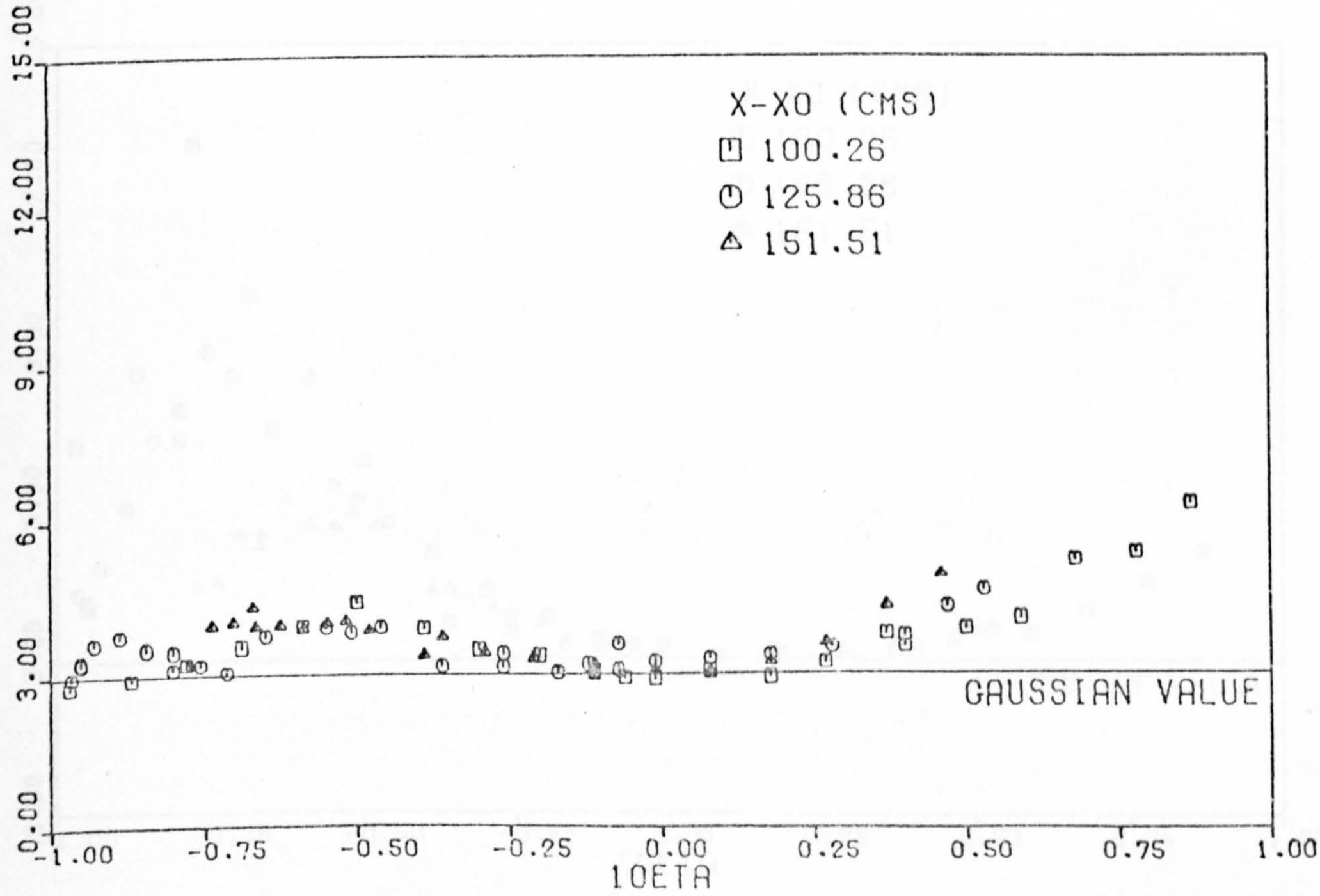


Fig. 4.53b F_u in the reattached flow; x, z plane results

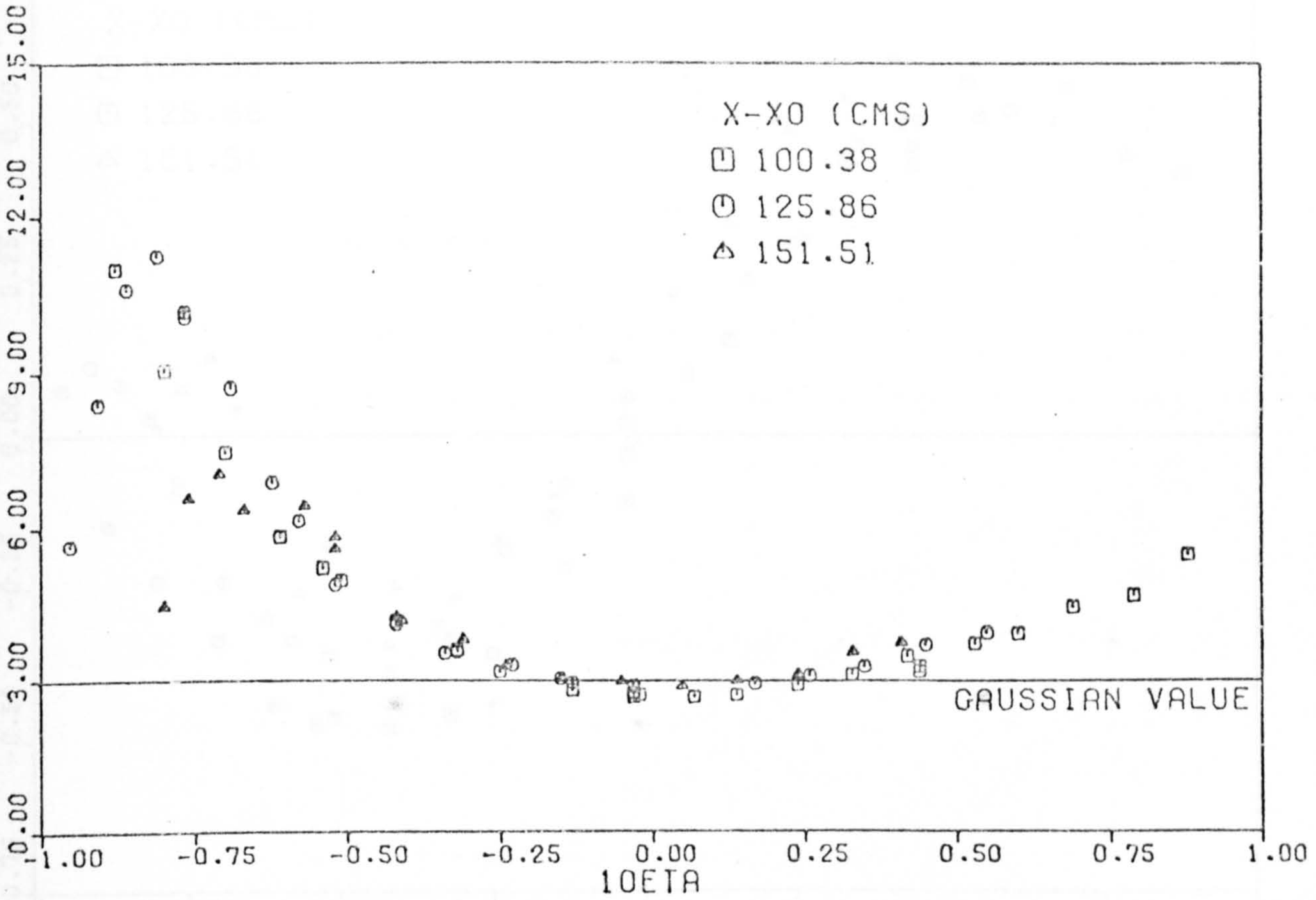


Fig. 4.54 F_v in the reattached flow

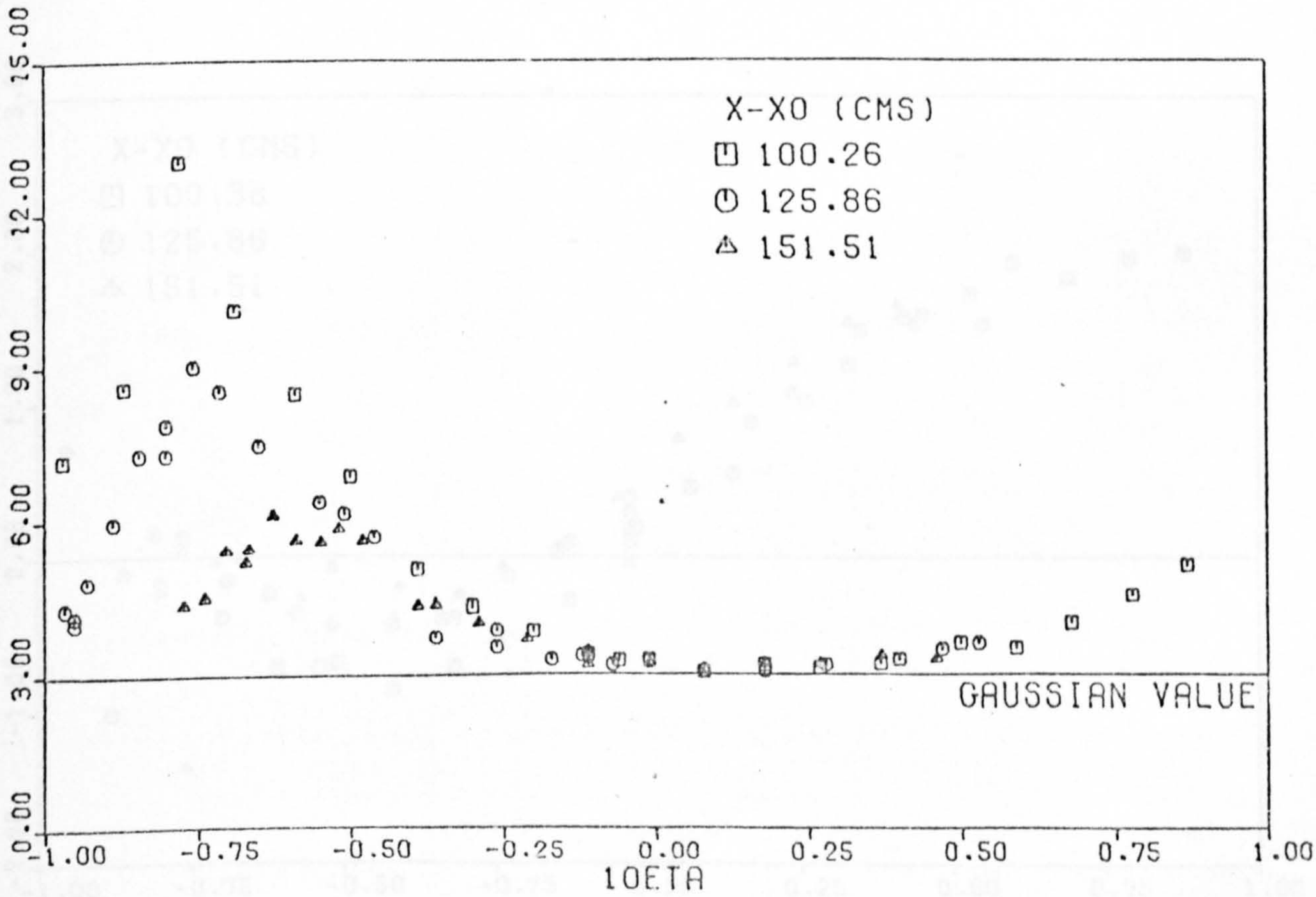


Fig. 4.55 F_w in the reattached flow

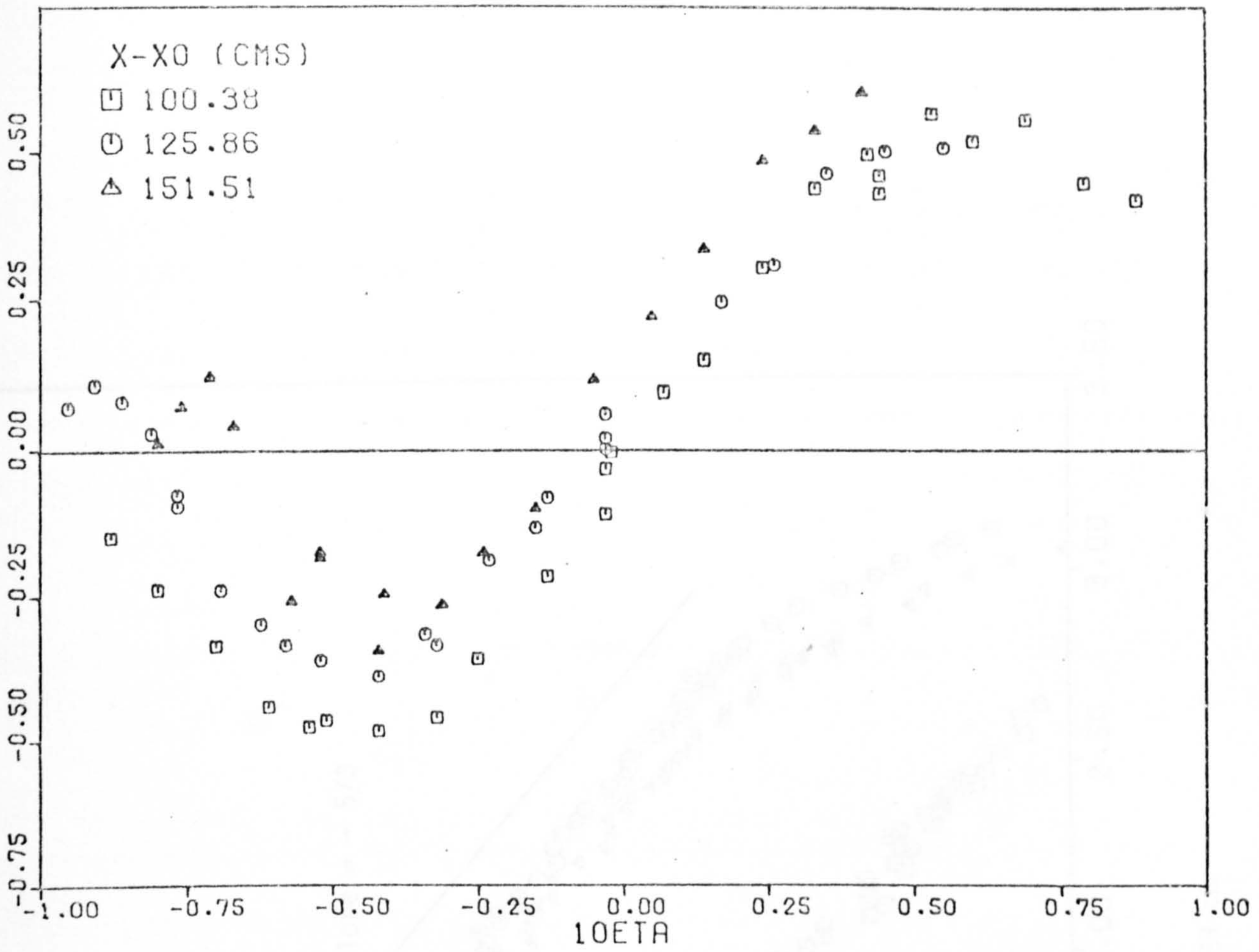


Fig. 4.56 10 V_q'/U_1 in the reattached flow

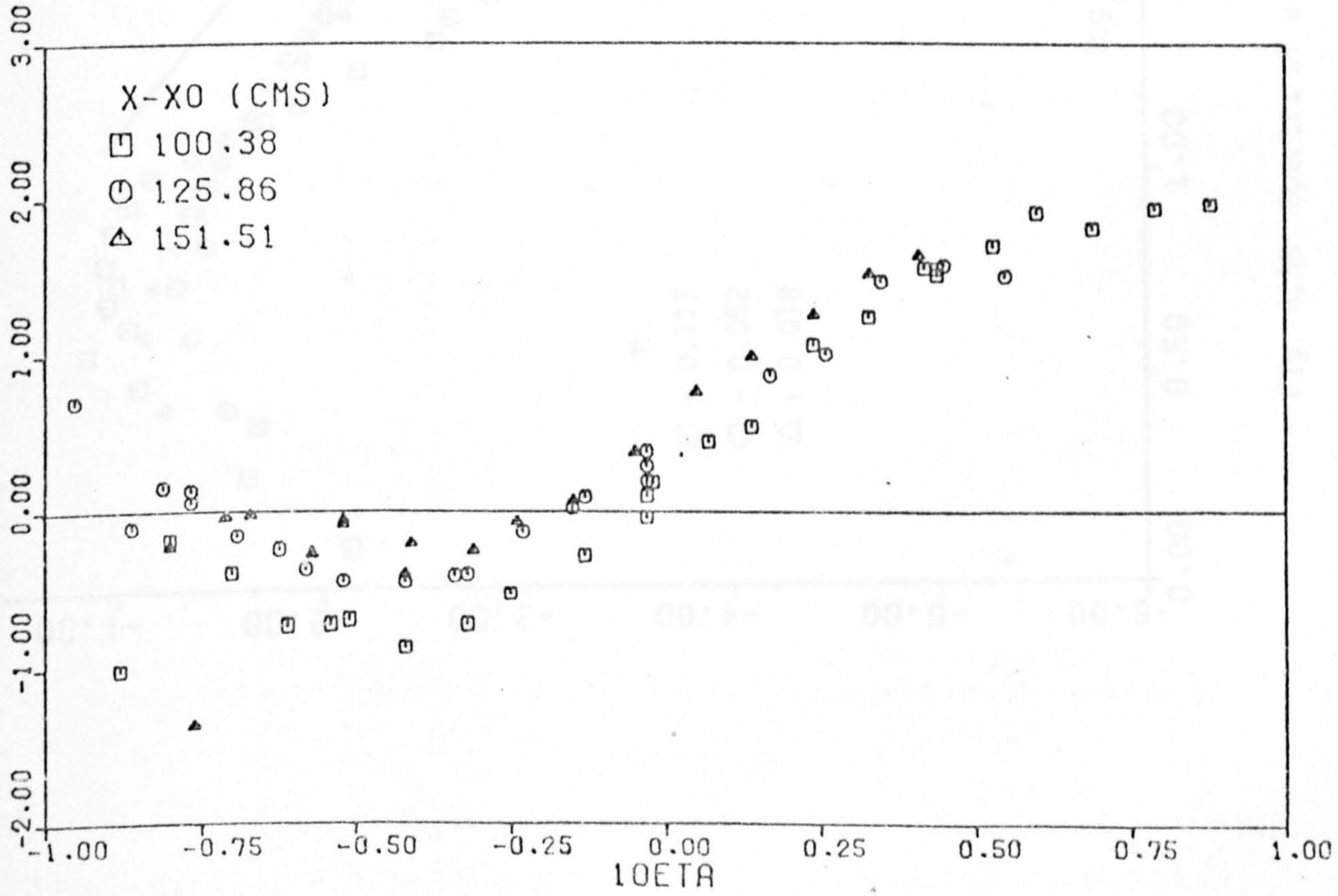


Fig. 4.57 10 V_τ/U_1 in the reattached flow

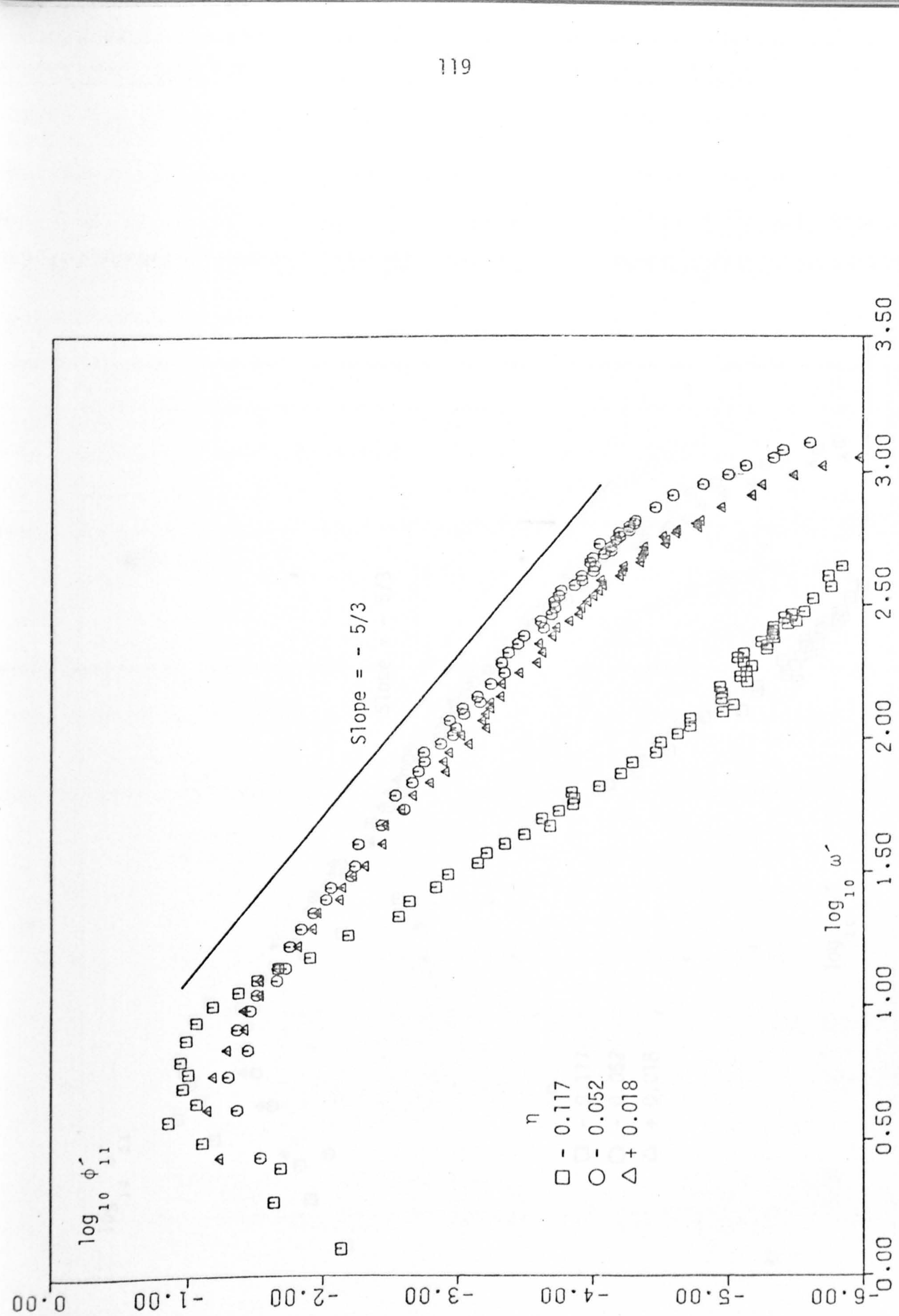


Fig. 4.58 Spectra of u, x - x_o

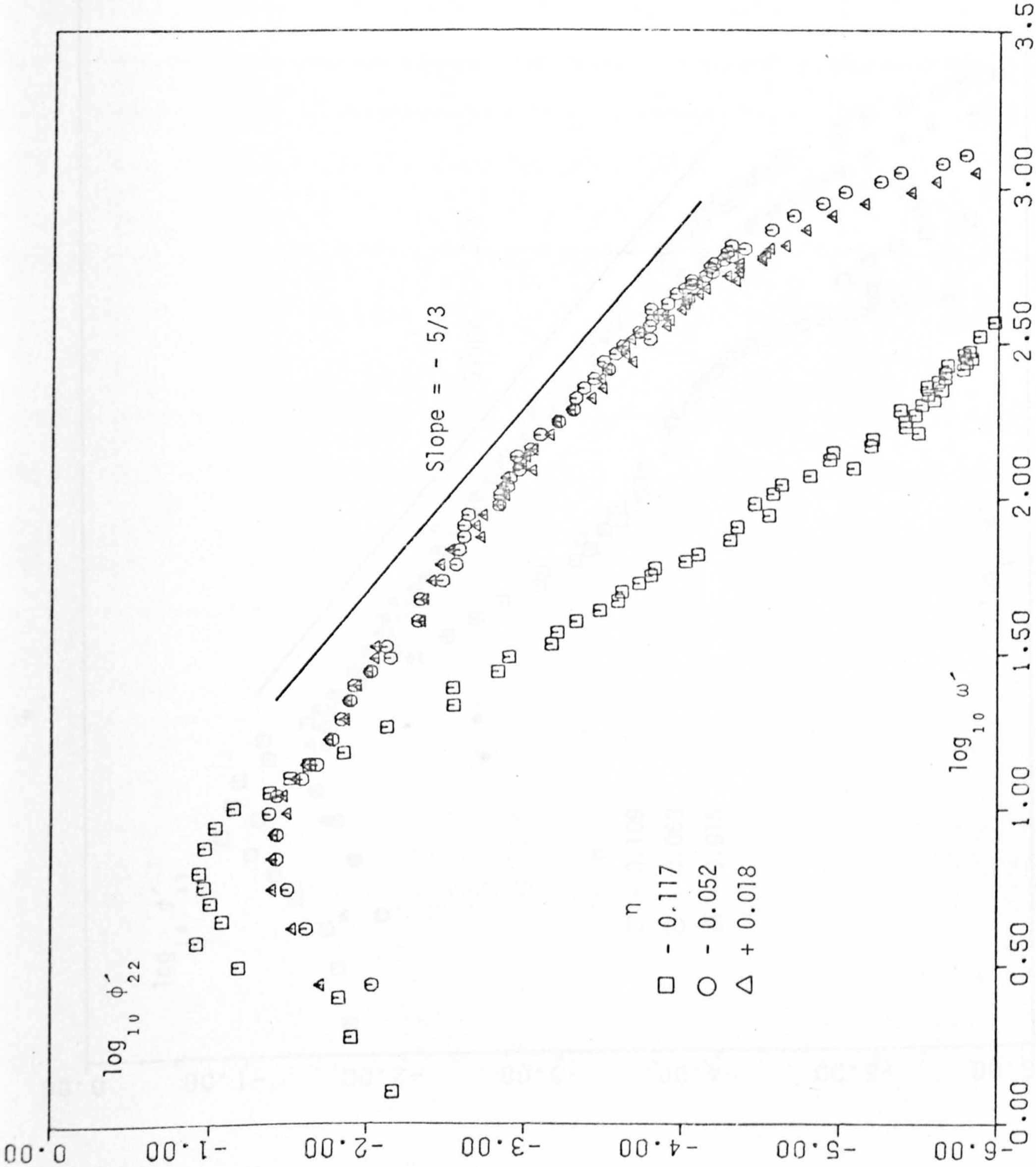


Fig. 4.59 Spectra of v, x - x_0 = 36.89 cm

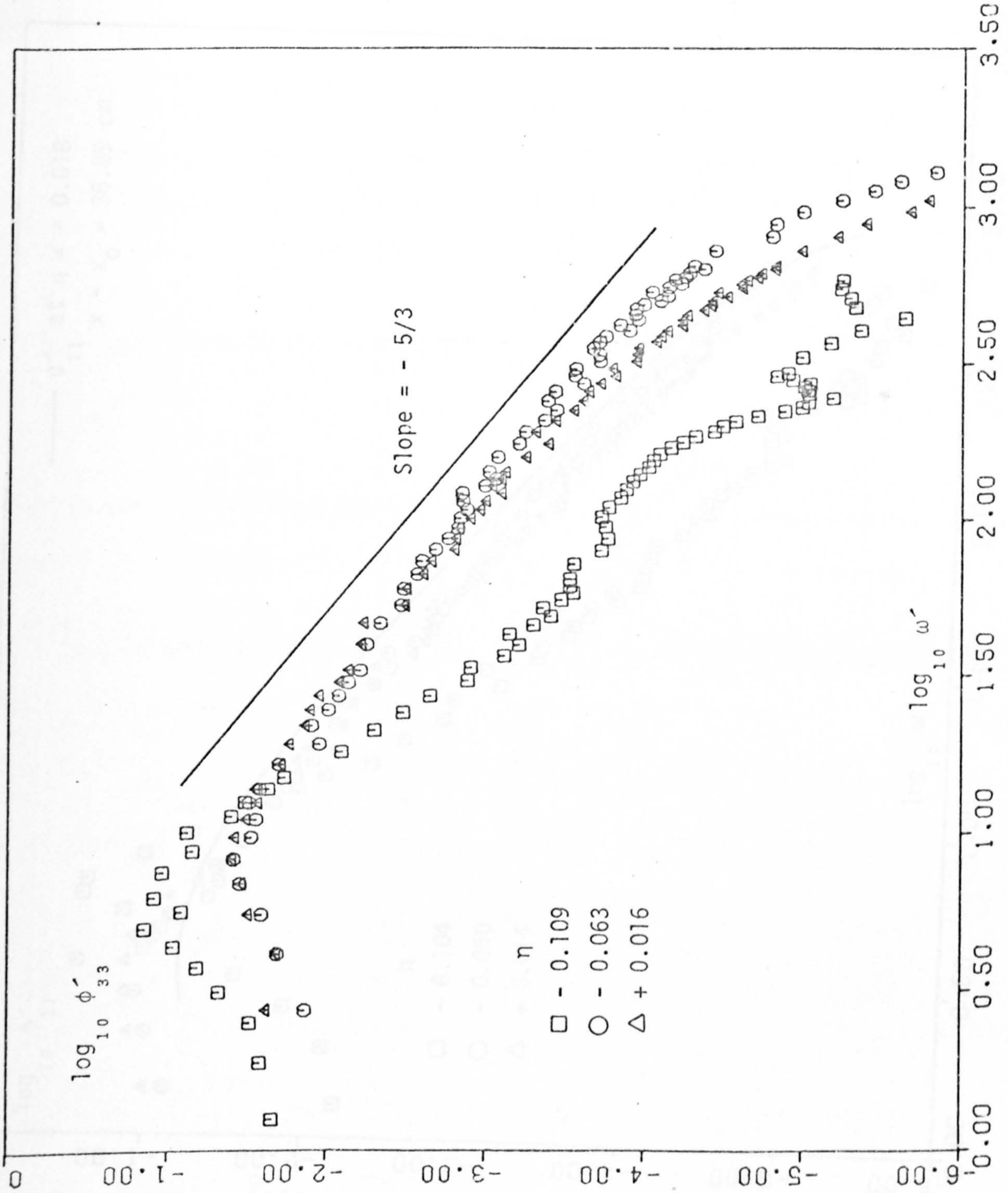


Fig. 4.60 Spectra of w, x - x_o = 36.89 cm

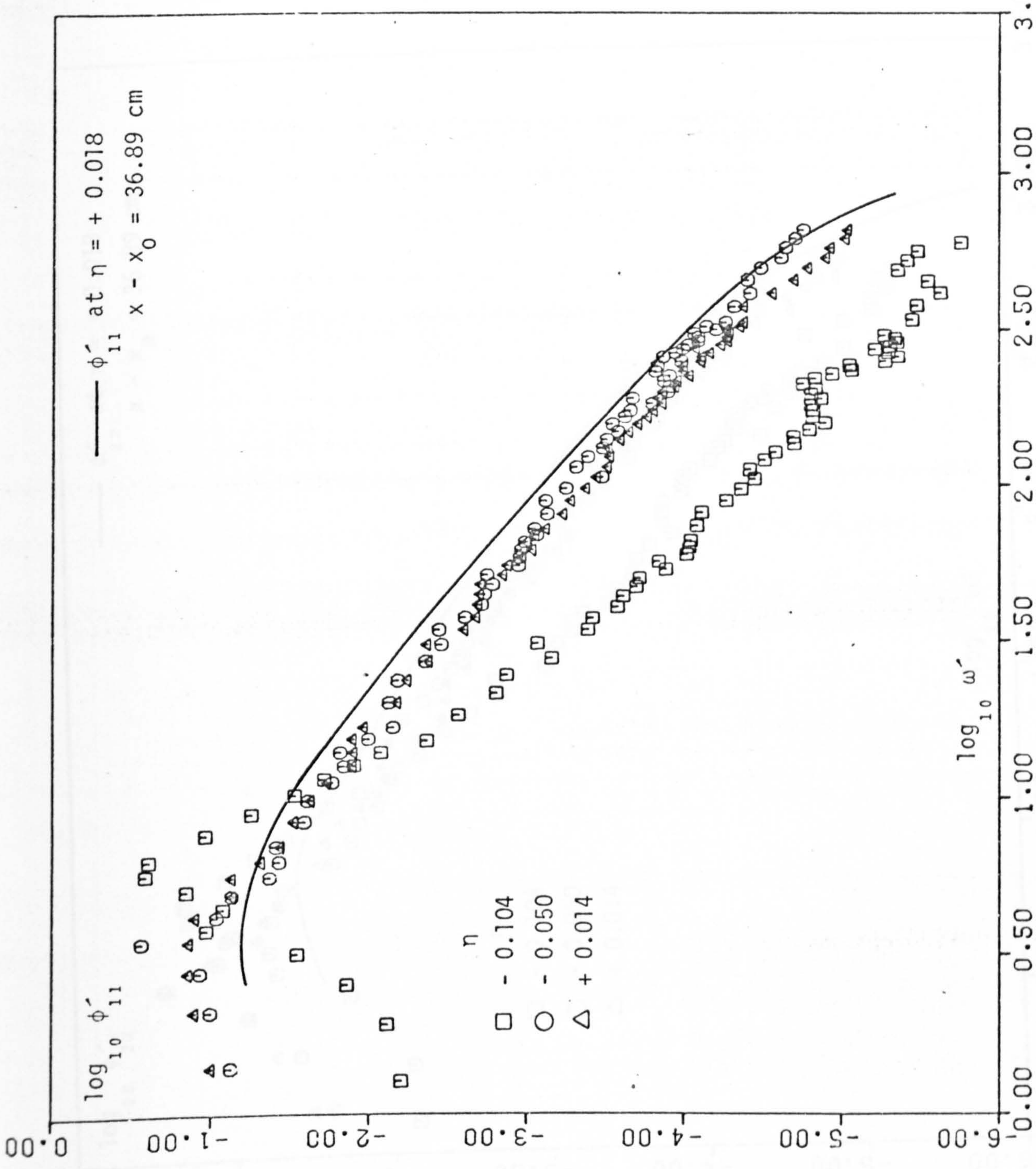


Fig. 4.61 Spectra of u, x

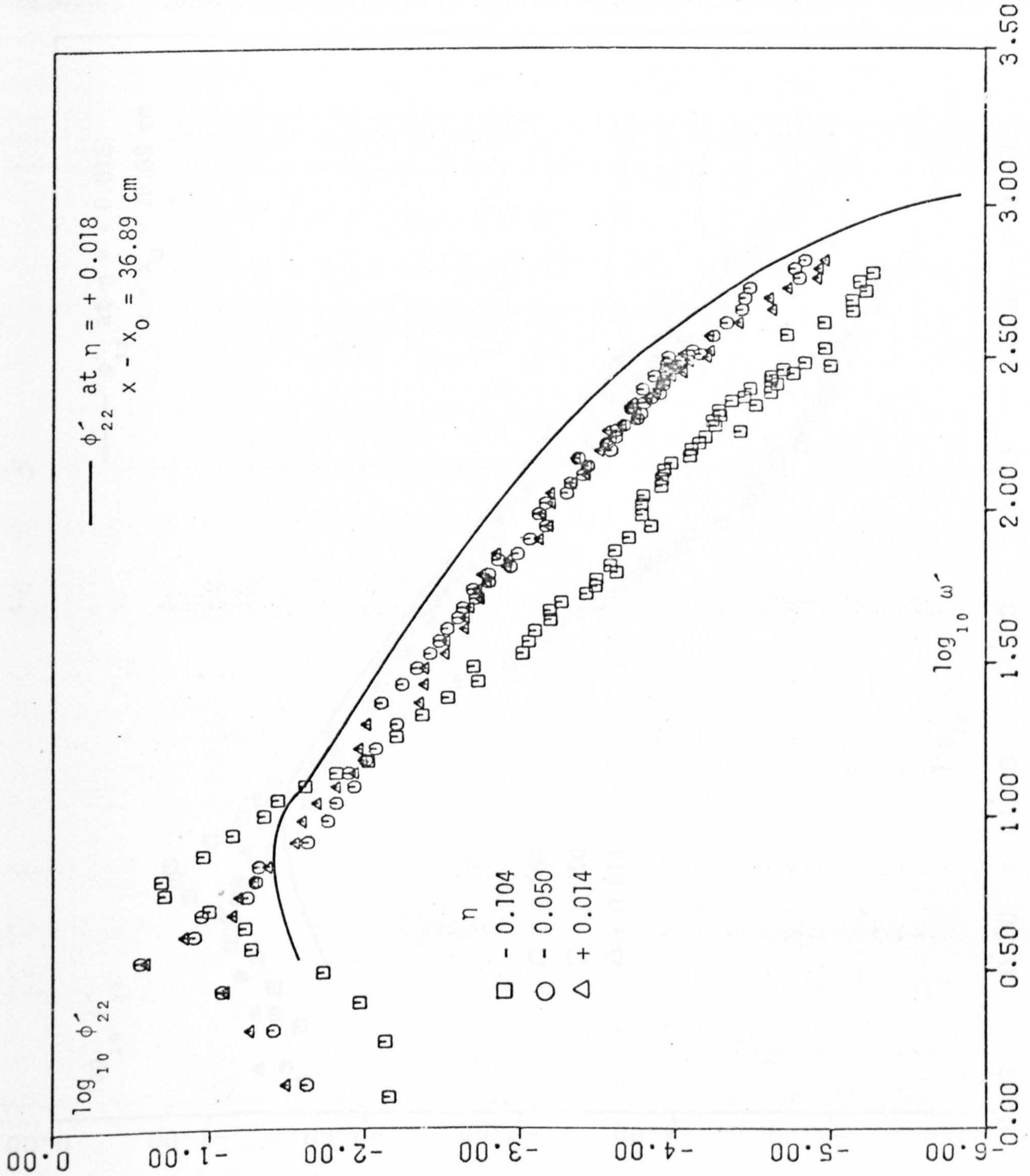


Fig. 4.62 Spectra of v, x - x_o = 75.06 cm

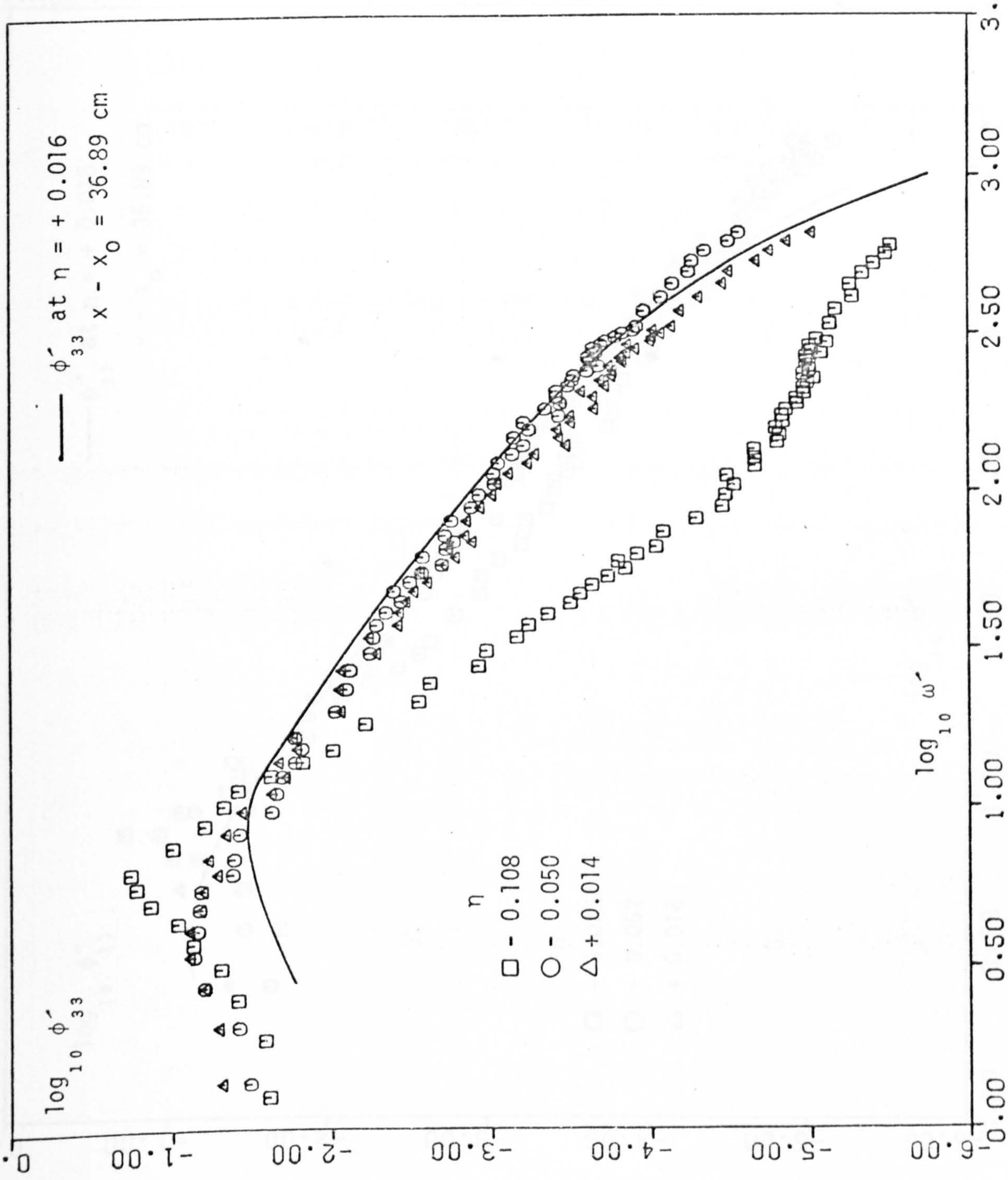


Fig. 4.63 Spectra of w, x - x_o = 75.06 cm

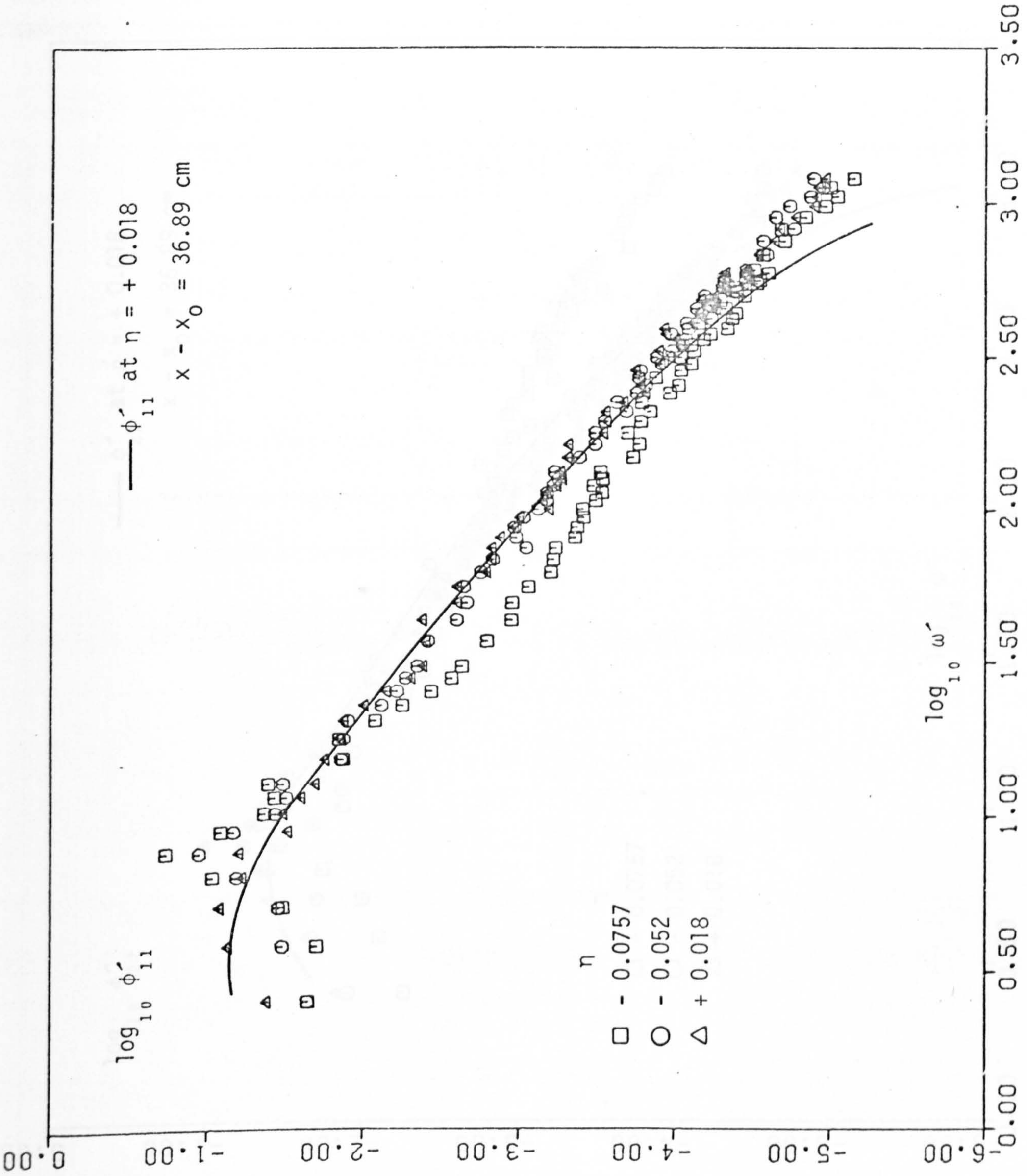


Fig. 4.64 Spectra of u, $x - x_o$ = 151.

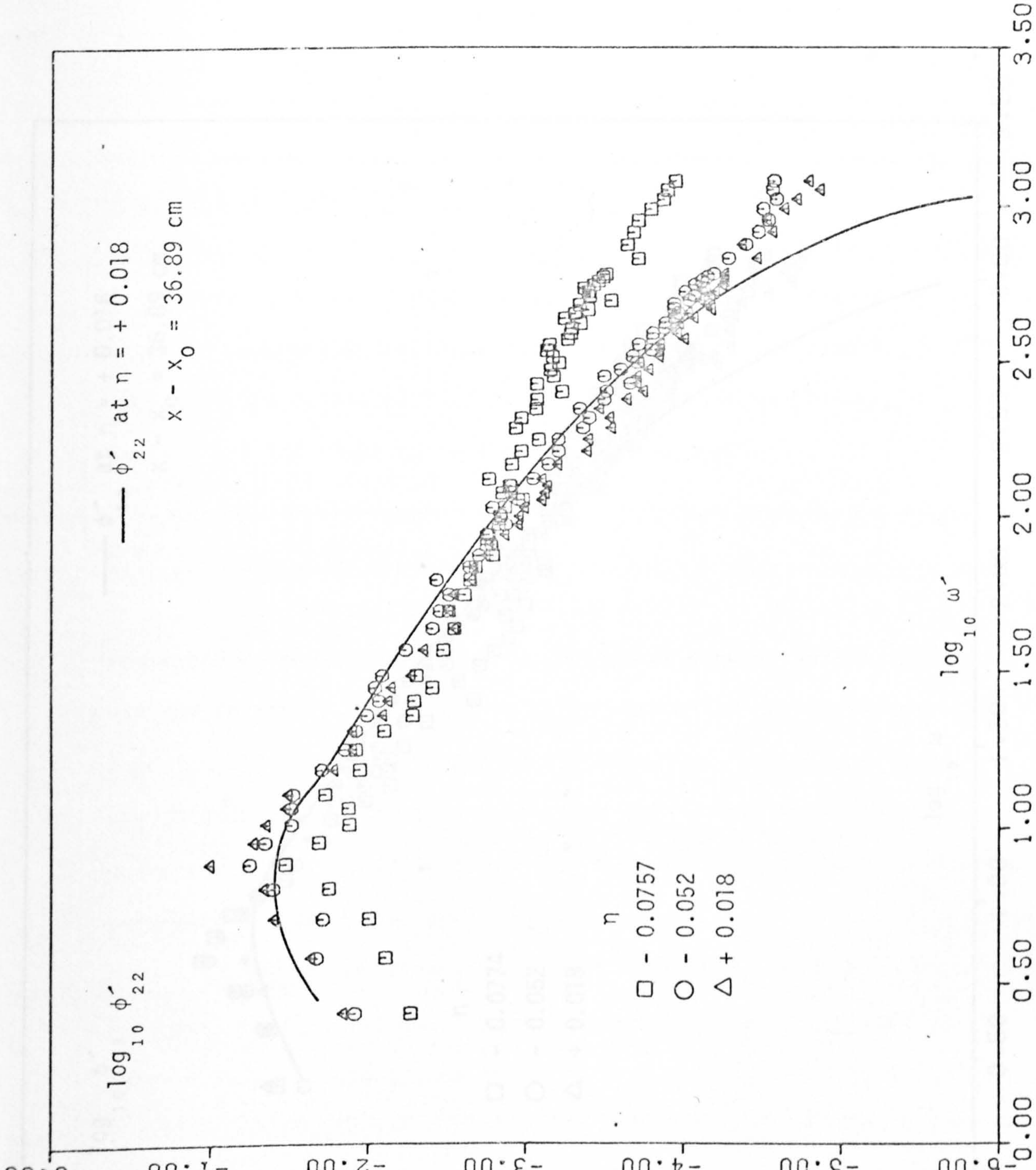


Fig. 4.65 Spectra of v, x - x_o = 151.51 cm

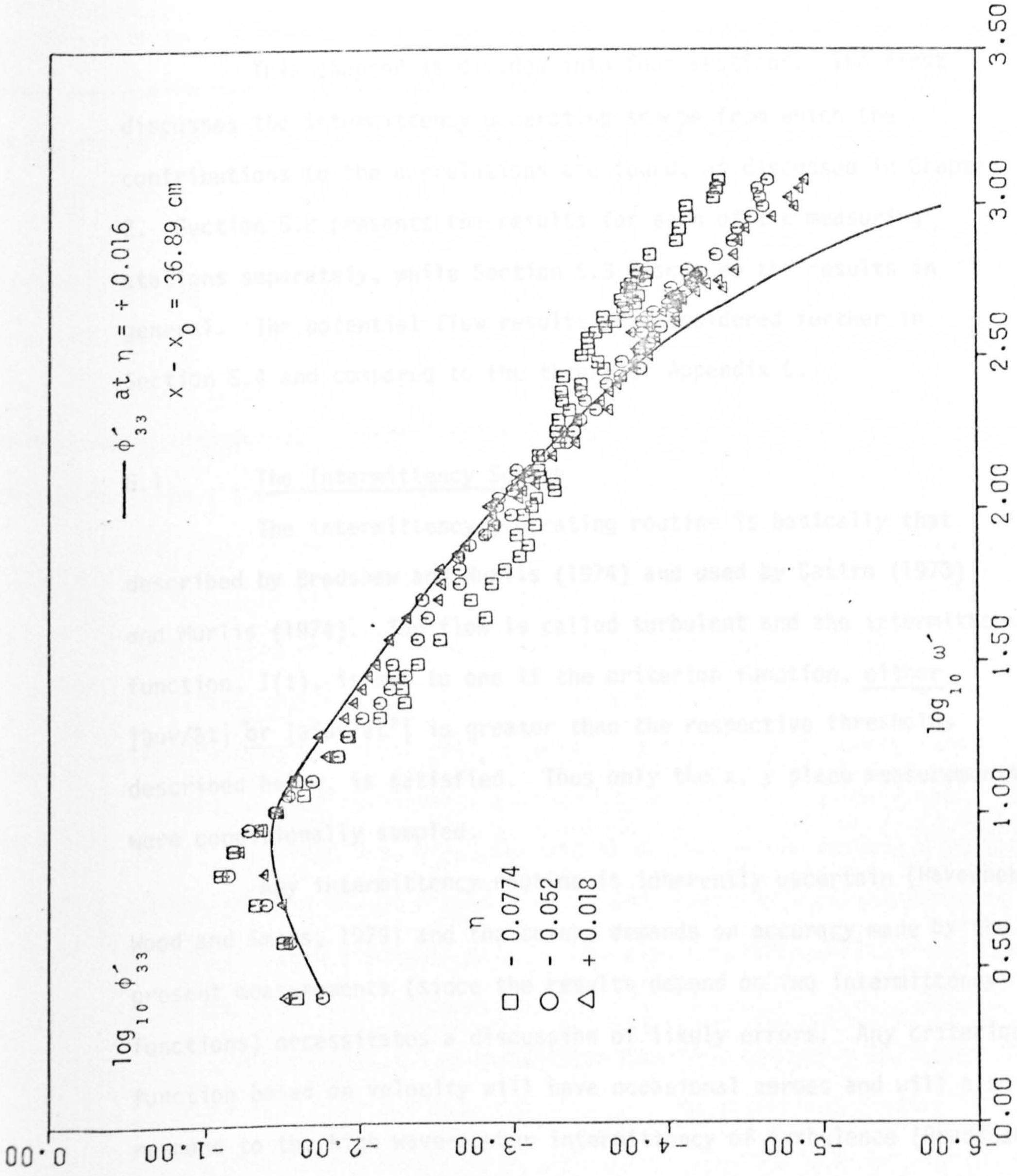


Fig. 4.66 Spectra of w, $x - x_0$

CHAPTER 5

TWO POINT MEASUREMENTS AND AUTOCORRELATIONS

This chapter is divided into four sections. The first discusses the intermittency generating scheme from which the contributions to the correlations are found, as discussed in Chapter 2. Section 5.2 presents the results for each of the measuring stations separately, while Section 5.3 discusses the results in general. The potential flow results are considered further in Section 5.4 and compared to the theory of Appendix C.

5.1 The Intermittency Scheme

The intermittency generating routine is basically that described by Bradshaw and Murlis (1974) and used by Castro (1973) and Murlis (1974). The flow is called turbulent and the intermittency function, I(t), is set to one if the criterion function, either $|\partial uv/\partial t|$ or $|\partial^2 uv/\partial t^2|$ is greater than the respective thresholds described below, is satisfied. Thus only the x, y plane measurements were conditionally sampled.

Any intermittency routine is inherently uncertain (Haverbeke, Wood and Smits, 1979) and the severe demands on accuracy made by the present measurements (since the results depend on two intermittency functions) necessitates a discussion of likely errors. Any criterion function based on velocity will have occasional zeroes and will also respond to the high wave-number intermittency of turbulence (Bradshaw and Murlis, 1974) causing signal "dropouts". The usual method of preventing dropouts is to introduce a hold time, the minimum period over which the intermittency function is not allowed to alter. Bradshaw and Murlis show that, in practice, the use of a hold time

obscures the fine structure of the interface. The alternative is to use the "signal or derivative" method, as is done here, in the hope that if the magnitude of the signal, $|\partial uv/\partial t|$ in the present case, is below its threshold then the derivative, $|\partial^2 uv/\partial t^2|$, will be sufficiently large to prevent a dropout. These matters are discussed more fully by Muck (1980) who justifies the use of the present criterion function. It is sufficient to note here that dropouts still occurred; see the downward facing arrows in fig. 5.3. The present scheme effectively uses a hold time of two digital time increments, except at the beginning and end of each record, see below. In non-dimensional form the hold time, Δt, in the present experiment is in the range $0.08 \geq U_1 \Delta t/\delta \geq 0.013$, with the upper limit occurring at 24 cm. The hold time was constant for all x, while the Kolmogorov frequency increases with x so that the ratio of hold time to Kolmogorov frequency decreases with x. At 24 cm the ratio is about six and so, at best, the resolution of the present intermittency scheme is of the order of the fine scale structure of the interface. Thus, removing the dropouts by increasing the hold time would also remove genuine features of the turbulence, such as those indicated by the upward facing arrows in fig. 5.3. For signal or derivative methods Muck (1980) recommends the use of a hold time of the order of that used here, to obtain the best trade-off between reducing dropouts and observing the fine detail of the interface.

From fig. 5.1, the maximum measured value of γ is 0.92. This is lower than previous measurements, e.g. Wygnanski and Fiedler (1970), and is most likely caused by signal dropouts, which will be most important near high γ (Muck, 1980). The single point results, which were digitized at over twice the real time frequency of the double point measurements, are generally lower. Since $\Delta t = 2 \times (\text{digitizing frequency})^{-1}$ this result is most likely due to a decrease in dropouts

as Δt increases. The maximum measured value of γ decreases with x. Since the number of dropouts should also decrease with x this result is probably genuine. As the high velocity edge is approached the intermittency scheme first becomes sensitive to the starting values of the thresholds, described below, and then becomes completely unreliable, largely because of difficulties associated with finding the turbulent zone averages for the criterion function.

For all the measurements presented in this thesis the values of the thresholds for $|\partial uv/\partial t|$ and $|\partial^2 uv/\partial t^2|$ were 0.25 and 0.35 of the turbulent zone averages of these quantities respectively. These thresholds were found by Muck (1980) to give the best agreement with the temperature intermittency scheme described by Weir et al (1980) over a variety of flows. The turbulent zone averages were updated at the end of each digital record consisting of 246 points; six records are shown in each part of fig. 5.3. This updating caused the single sided spikes in I(t), figs. 5.3b and 5.3c, in those plots taken from near the start of the digitized data. The turbulent zone averages were not known initially, so for the first five records starting thresholds were used. These were usually set so high that, initially, γ was low, but fig. 5.2 shows that except for $\eta = -0.075$ and -0.051 to a lesser extent, γ quickly becomes independent of the starting thesholds. About 10% of the $\eta \simeq -0.075$ results were rerun because the final γ was not reliable. For rerunning, the starting thresholds were set to the final turbulent zone averages of the previous run. No rerunning was considered necessary for the other results. The conditionally sampled contributions to the correlations are smooth and repeatable, except for figs. 5.63 and 5.64 where the effects of the starting thresholds are apparent. Therefore, the choice of starting thresholds was not important, in general.

Since signal dropouts are due to low values of uv, and hence

low values of u and/or v, within the turbulence, several conclusions can be tentatively drawn. If anything, dropouts will cause an over-estimate of the turbulent/turbulent (t/t) contribution since the reduction in γ_{AB}, defined in Eqn. (2.10), will be outweighed by the increase in the t/t zone average. Near the high velocity edge, this will be at the expense of the non-turbulent/non-turbulent (nt/nt) contribution, otherwise the turbulent/non-turbulent (t/nt) and non-turbulent/turbulent (nt/t) contributions will be reduced. However, there is no way to check these assertions independently. The normal correlation results, e.g. figs. 5.18 and 5.19, show that the t/t contributions go to zero as γ goes to zero, as expected, so the errors cannot be large.

The effects of dropouts on $R_{II}(0, 0, r)$ can be estimated by writing Eqn. (2.18) as:-

$$R_{II}(0, 0, r) \simeq \frac{\gamma_{AB} - \gamma_A^2}{\gamma_A(1 - \gamma_A)} \tag{5.1}$$

for the purposes of discussion. γ_A^2 is always underestimated, but less so for low γ. The denominator will be overestimated for $\gamma > 0.5$ and underestimated otherwise. If γ is high, dropouts will reduce γ_{AB} since most dropouts in $I_A(t)$ say, will occur while $I_B(t) = 1$. This effect should decrease with decreasing γ, unless $I_A(t)$ and $I_B(t)$ are always well correlated, which the present results show is very unlikely. Thus $R_{II}(0, 0, r)$ will be underestimated at high γ and at small separation and probably overestimated otherwise. Furthermore at high γ both the numerator and denominator of Eqn. (5.1) are small differences, making the results even more uncertain.

Fig. 5.3 shows digital plots taken at random from the data analysed, covering the range of x, η and probe separation of the present

experiment.

5.2 The Correlation Measurements

From Chapter 4, most of the interesting changes in the turbulence structure induced by the wall occur on the high speed side, so the correlation measurements were restricted to $\eta \leq + 0.025$. As mentioned in Chapter 2, all the normal correlations were measured at $z = 0$ and the separation, r, is always negative. The positions of the fixed probes for the spanwise measurements are shown in fig. 2.2. The separation was always in the positive z direction. The small differences in $x - x_o$ for each nominal station are due to the different traverse arrangements for the spanwise and normal correlations. All the probe separations are normalized by $x - x_o$ to emphasize any structural changes caused first by the approach to full development and then by the effect of the wall. These changes should cause departure from similarity scaling in the measurements.

For the single component correlations, R_{ii} where i = 1, 2 or 3, it is useful to distinguish between longitudinal and transverse separations. In the former the separation is in the direction of the component measured while in the latter the separation is in the plane normal to the component (note that in presenting the results, the terms "streamwise" and "spanwise" are used exclusively for separations in the x and z directions respectively). From continuity there can be no net flux of a fluctuating velocity component across any plane normal to the component, so its covariance, the unnormalized correlation, must integrate to zero over this plane. Hence the correlation must have a negative region somewhere in this plane. This negative region, which indicates "backflow", need not occur along the coordinate axes, which were the only directions of separation measured here, but the result is useful in deducing eddy structure. There is

no such constraint on longitudinal correlations, so any negative loops in these are particularly important.

Before the analysis was started it was decided that the spatial cross correlation between u and v should be computed from the digitized data. Generally R_{12} and R_{21} are similar (Kovasznay et al, 1970; Tritton, 1967), while two-dimensionality in the mean, makes $R_{12}(0, 0, r)$ and $R_{21}(0, 0, r)$ equal. For economy, R_{12} was chosen. the normal correlations were analysed in inverse order to the spanwise correlations; i.e. the fixed probe and moving probe input signals to DIG4MK1 (Chapter 2) were inverted in the former. Due to an oversight, that was not realised until after the analysis was completed, the conditional sampling routines were not altered for the normal correlations, so $R_{21}(0, r, 0)$ was computed; the R_{ii} correlations were unaffected by the inversion. For correlations between the turbulence and the potential flow, this has the a posteriori justification that it is the turbulent v motion that forces the potential flow, Appendix. C.

The most extensive measurements were made at 37 cm nominally, as this position was considered to be a compromise between the approach to full development and the onset of wall effect. Except near the high velocity edge the 25 cm results, figs. 5.4 - 5.19, are similar to those at 37 cm. From Section 4.1 the difference can be attributed to the development of the mixing layer. Since the potential flow at 25 cm is almost entirely free of wall influence, Section 4.2, the turbulence structure will be as well. Although the mixing layer at 37 cm is not quite fully developed, fig. 3.2a, it is safe to conclude that the 37 cm results, within the turbulence, are reasonably representative of a fully developed plane mixing layer in the absence of wall effect.

The spanwise correlations of u, $R_{11}(0, 0, r)$, and v,

$R_{22}(0, 0, r)$, are shown in figs. 5.20 and 5.21. The measurements were made in two separate traverses and included a repeat at $\eta = -0.075$, from which the accuracy of the R_{11}, R_{22} and R_{33} correlations is estimated to be better than $\pm$ 0.05. From the definition, Eqn. 2.11, accuracy of the R_{12} and R_{21} measurements in regions where $\overline{uv}$ is small is considerably less than the single component correlations. The agreement between x, y and x, z plane measurements of $R_{11}(0, 0, r)$ and $R_{11}(0, r, 0)$ was always within these limits for all x and so no direct comparisons are shown. In particular the x, z plane measurements alter none of the conclusions based on the appearance of negative loops in R_{11}, even though the behaviour of R_{22} and R_{33} is, in general, quite different. In most traverses one point, usually at minimum r, was repeated. The repeatability was always within the accuracy given above, showing that the relatively short averaging times, Chapter 2, did not seriously affect the correlations.

For $\eta \geq -0.026$, $R_{11}(0, 0, r)$, fig. 5.20, has a negative loop that does not alter in size or position with η. For $\eta < -0.026$ the scale increases monotonically with decreasing η. Townsend's (1976) definition of scale is used here; it is either the position where $R_{ii} = 0.05$ if R_{ii} is always positive, or the crossover point after the negative loop. The 99% mixing layer thickness, δ, is approximately $0.22\ (x - x_o)$ so that the scales in the high intensity region are 0.6δ for $R_{11}(0, 0, r)$ and 1.5δ for $R_{22}(0, 0, r)$, fig. 5.21. The latter is always positive, but the increase in scale with decreasing γ is less than that of $R_{11}(0, 0, r)$.

$R_{33}(0, 0, r)$, fig. 5.22, always has a small, but consistently repeatable negative loop (see also fig. 5.6), even though $R_{33}(0, 0, r)$ is a longitudinal correlation. The crossover point is nearly constant for $\eta > -0.026$, but then moves outward with decreasing γ. The behaviour of $R_{12}(0, 0, r)$, fig. 5.23, is similar to that of $R_{11}(0, 0, r)$.

For the region of small $\overline{uv}$ the results become unreliable and are included only to give an indication of the behaviour. In this region the computed magnitudes of R_{12} were sometimes greater than one; these points were not plotted.

The normal correlations of u, v and w, that is $R_{11}(0, r, 0)$, $R_{22}(0, r, 0)$ and $R_{33}(0, r, 0)$ respectively, are shown in figs. 5.24 - 5.26, with an indication of the distance from the fixed probe, to the edge of the shear layer, defined as the position where $U = 0.995\ U_1$. With the fixed probe in the high intensity region, $R_{11}(0, r, 0)$ is persistently negative well into the potential flow, while the other components are positively correlated. These results are very similar to those of Bradshaw et al (1964) in an axisymmetric mixing layer. As the position of the fixed probe is moved toward the potential core the scales of all three correlations increase significantly, even though the normal direction scale of the large eddies can only be of order δ. Although the results are very unreliable, $R_{21}(0, r, 0)$, fig. 5.27, appears to take large negative values when the moving probe is in the potential core. This is consistent with the change in sign of $\overline{uv}$ between the shear layer and the potential core, figs. 4.6 and 4.26a, for 37 cm, while the 24 cm results, fig. 5.11, are puzzling since there R_{uv} is almost zero in the potential core.

The autocorrelations, generated from the spectra shown in figs. 4.58 - 4.60, have been turned into pseudo-streamwise correlations, figs. 5.28 - 5.30, by using $r' \equiv U_c t$ where t is the time delay and U_c, the convection velocity, was assumed to be $0.65\ U_1$ for <u>all</u> the results presented in this chapter. This is the convection velocity of the high intensity region measured by Bradshaw et al (1964) and Wills (1964). They found the variation of U_c with η to be small relative to the variation in mean velocity, so the uncertainty in choosing U_c should not be too serious. Except for $R_{11}(r', 0, 0)$ at $\eta = + 0.018$, all the

autocorrelations have persistent negative regions, which are particularly strong in the potential flow. These results emphasize the strong streamwise periodicity of the large eddies.

The spanwise correlation of the intermittency function, $R_{II}(0, 0, r)$, fig. 5.31, is remarkably constant with η, in view of the discussion of likely errors in Section 5.1. The scale is comparable to that of $R_{22}(0, 0, r)$ near maximum γ, and suggests that the scale of the turbulent motion does not vary significantly with η. The available $R_{II}(0, r, 0)$ results, also plotted in fig. 5.31, show a large increase as the fixed probe is moved towards the potential core, due partly to the concurrent improvement in accuracy of the intermittency scheme. However, it is improbable that this could account for all the large difference (see also fig. 5.62) which suggests a change in the turbulence structure. The variation of γ_A, for the fixed probe, and γ_B is shown in fig. 5.32. The former indicates the scatter in the measurements; as expected the scatter decreases with increasing γ. The latter give a further indication of the spanwise uniformity of the flow. The results are in general agreement with those of fig. 3.8b which show that the velocity at probe B is nearly always higher than at probe A so that γ_B should be less than γ_A.

The conditionally sampled $R_{11}(0, 0, r)$ and $R_{22}(0, 0, r)$ results are shown in figs. 5.33 - 5.42. The symbols are derived from those used by Weir et al (1980) for their single point measurements, conditionally sampled using temperature. The circles are the total measurement, the inverted triangles the t/t contribution (mnemonic-hot plume) and the triangles are the nt/nt contribution (mnemonic-iceberg). The t/nt and nt/t contributions, the squares, are shown together, simply for clarity. For the spanwise correlations the t/nt and nt/t contributions are nominally equal. No significant differences between these usually small contributions were found. Note that the

addition law, Eqn. (2.16), applies and that the results for zero separation are just the single point results for probe A, see Eqn. (2.17a). They provide a check on the consistency of the double point conditional sampling routines but not on the accuracy of the intermittency scheme itself.

Near the high velocity edge, figs. 5.33 and 5.34, the dominant contribution to $R_{11}(0, 0, r)$ and $R_{22}(0, 0, r)$ is from potential fluid, while the scales of the turbulent motion are no larger than the scales of the total correlations near maximum γ. There is no sign of a negative loop in the t/t contribution to $R_{11}(0, 0, r)$. The smoothness of the total correlation and the shape of $R_{11}(0, 0, r)$ in the purely potential flow, fig. 5.20, make it most unlikely that this result is due to an artifact of the intermittency scheme. The t/t contribution to $R_{22}(0, 0, r)$ is always positive at $\eta = -0.051$, the t/t contribution to $R_{11}(0, 0, r)$, fig. 5.35, has a small, local minimum near the negative peak in the high intensity region measurements, but is still always positive, as is the t/t contribution to $R_{22}(0, 0, r)$, fig. 5.36.

At $\eta = -0.026$, the negative loop in $R_{11}(0, 0, r)$, fig. 5.37, is due partly to turbulent fluid while the t/nt contribution to $R_{11}(0, 0, r)$ and to $R_{22}(0, 0, r)$, fig. 5.38, is small. For $\eta > -0.026$, figs. 5.39 - 5.42, the nt/nt contribution is negligible, and nearly all the correlation, including the negative loop in $R_{11}(0, 0, r)$, is due to the turbulent motion. The conditionally sampled measurements strongly emphasize the conclusion drawn from fig. 5.31, that the spanwise scale of the turbulent motion is independent of η. Since this scale is of the order of the shear layer thickness the large eddies are essentially three-dimensional.

The η dependence of the conditionally sampled $R_{12}(0, 0, r)$ measurements, figs. 5.43 - 5.46, shows that the similarity of the

total correlation to $R_{11}(0, 0, r)$ extends to the contributions as well. In particular the negative loop in $R_{12}(0, 0, r)$ for $\eta \geq - 0.026$ arises almost entirely from the turbulent motion.

The conditionally sampled measurements of $R_{11}(0, r, 0)$, fig. 5.47, and $R_{22}(0, r, 0)$, fig. 5.48, with the fixed probe at $\eta = + 0.003$, are a useful check on the intermittency scheme since the vertical scale of the large eddies can only be of order δ. As mentioned in Section 5.1, the intermittency scheme breaks down for very low values of γ, but the extrapolations of the t/t contributions are plausible and suggest that the intermittency scheme works reasonably well. The scale of the t/t contribution to $R_{22}(0, r, 0)$ is larger than that to $R_{11}(0, r, 0)$ as in the spanwise correlations. The squares in figs. 5.47 and 5.48, are, almost exclusively, the correlation between the turbulent motion at the fixed probe and the potential motion at the moving probe. At large separation this contribution is negative for $R_{11}(0, r, 0)$ and strongly positive for $R_{22}(0, r, 0)$. The latter correlation shows a two component structure with the local minimum in the total correlation occurring at the crossover point of the t/t and t/nt contributions. The strong correlation between the turbulent and potential v motion suggests that errors in the intermittency scheme are more likely to affect the conditionally sampled measurements of R_{22}, in general, rather than the measurements of R_{11}.

The major difference between the present spatial correlations and the axisymmetric results of Bradshaw et al (1964) and Weber (1974) is the negative loop in the present $R_{33}(0, 0, r)$ results. This loop appears even in the high intensity region where the nt/nt contributions to $R_{11}(0, 0, r)$ and $R_{22}(0, 0, r)$ are negligible, and so is associated with the turbulent motion. Away from this inner region the crossover point in $R_{33}(0, 0, r)$ moves outward, fig. 5.22, suggesting that there the negative region is due to the potential

motion since the scales of the turbulent motion are independent of η. Bradshaw et al (1964) suggested that the negative loop in $R_{11}(0, 0, r)$ "is connected with the v motion rather than the w motion" largely because the negative peak in $R_{11}(0, 0, r)$ decreased by a similar amount to the decrease in the peak of ϕ_{22} as x increased. In the present flow the opposite occurs. Near maximum γ the negative peak in $R_{11}(0, 0, r)$ has decreased and moved outward as x increases - compare figs. 5.20 and 5.50 - while ϕ_{22} has developed a peak - compare figs. 4.59 and 4.62 and the resulting autocorrelations, figs. 5.29 and 5.59. Thus an interpretation of the present results exclusively in terms of Grant's (1958) mixing jets, which Bradshaw et al considered were the dominant large eddy structure in their flow, see Chapter 1, is untenable.

The easiest interpretation of the present results is that the large eddy structure has two basic components and two basic regions. In the "inner region", defined as the region where $R_{11}(0, 0, r)$ has a negative loop, that is $\eta > 0.050$, approximately, the spanwise correlations of u and w arise from a structure very similar to Grant's (1958) double roller eddy, fig. 5.49a. From his off-axis correlations Grant concluded that the double roller eddy is inclined, in the x, y plane, in the direction of the mean velocity gradient, as shown in fig. 5.49a. The scales of this "inner motion" are remarkably constant with η and presumably the double roller eddy extends further into the low velocity side than was measured. Superimposed on this motion is an "outward (meaning away from the high intensity region) motion" responsible for the always positive spanwise v correlations. The strongest evidence for the superposition is the striking similarity between $R_{12}(0, 0, r)$ and $R_{11}(0, 0, r)$ and the fact that the scale of $R_{11}(0, 0, r)$ is nearly half that of $R_{22}(0, 0, r)$ in the inner region. This "outer motion" becomes completely dominant in the "outer region",

$\eta < -0.050$ approximately, on the high velocity side. On the basis of the similarity of $R_{22}(0, 0, r)$ and $R_{22}(r, 0, 0)$ between the different flows the present outer motion is probably the periodic mixing jets found by Grant (1958) in a wake and Bradshaw et al (1964), throughout their axisymmetric mixing layer. Apart from the unchanged $R_{33}(r', 0, 0)$, there is no trace of the double roller eddy in the outer region; there the t/t contribution to $R_{11}(0, 0, r)$ is always positive and $R_{11}(r', 0, 0)$ has a negative loop. The normal correlation between w in the inner region r corresponding to the outer region is zero, fig. 5.26, while the t/t contribution to $R_{11}(0, r, 0)$ is almost zero, fig. 5.47. The mixing jets are likely to be much more symmetric in the y, z plane in the present flow than in the axisymmetric mixing layer since the ratio $\overline{v^2}/\overline{w^2}$ is much higher in the former, compare fig. 4.28 with fig. 4 of Bradshaw et al (1964). Thus the outer motion in a plane mixing layer transports significantly less w component momentum.

In the inner region most of the backflow in u occurs along the z axis within the double roller eddy, with a much smaller amount occurring along the y axis in the potential flow. The backflow in w occurs almost exclusively along the x axis, hence the crossover point in $R_{33}(r', 0, 0)$, fig. 5.30, is closer to the origin than for the other autocorrelations. Grant's double roller eddy requires $R_{11}(0, 0, r)$ to be always positive, so the negative $R_{11}(r', 0, 0)$ after the large value of the crossover point for $\eta = +0.018$, fig. 5.28, is more difficult to interpret as are u component correlations in general. The reason is that "flapping" of the mixing layer by the low wave-number v motion will contribute to u through the mean velocity gradient, and $\partial U/\partial y$ reaches its maximum near $\eta = +0.018$. This would explain the eventual negative region if $R_{11}(r', 0, 0)$ but would not explain the negative loop in $R_{11}(0, 0, r)$. The present results suggest that the backflow in v is almost entirely restricted to the x

axis, for all η. Near the centre of the inner region, around the position of maximum γ, this could be achieved by the alternate dispatch of turbulent fluid to the outer regions on the high and low velocity sides.

In the outer region both $R_{11}(0, 0, r)$ and $R_{11}(0, r, 0)$ are always positive so the backflow in u presumably comes from separations oblique to the y and z axes. The most reasonable explanation is that it occurs at those parts of the double roller eddy that must be auto-correlated with the outer motion, since the double roller eddy contains u component motion of both signs. Note that it is the covariance that must integrate to zero over the transverse plane by continuity, so this explanation is not in conflict with the conclusion that the backflow in the inner region is largely confined to separation along the z axis. The backflow occurring at positions oblique to the y and z axes within the double roller eddy can be negligible for the inner motion but be significant for the outer motion because of the large change in $\overline{u^2}$ across the shear layer, fig. 4.1. Two-dimensionality, in the mean, requires that the effect of this backflow will be to make the t/t contribution to $R_{11}(0, r, 0)$, between the inner and outer regions, zero which is nearly the result of fig. 5.47.

The effect of the proposed eddy structure on the potential motion is shown schematically in fig. 5.49b. This explanation is crude, as can be seen by comparing the plot in fig. 5.3e with the following. The $R_{II}(0, 0, r)$ results show no indication of spanwise periodicity in the large eddy structure so an explanation in terms of one large eddy alone, is justified. In the y, z plane the outer motion can be viewed as an eruption from the centre of the shear layer into the potential core. This "pushes" the potential motion away from the shear layer in the y direction, and away from the

centre of the eddy in the z direction, so that $R_{22}(0, 0, r)$ is always positive in the potential flow while $R_{33}(0, 0, r)$ will have a negative loop dependent on the spanwise scale of the large eddy, and on the distance from the shear layer, see Section 5.4. This is also consistent with the strong positive correlation between v in the inner region and in the potential flow, fig. 5.25. The corresponding, but smaller, w correlation arises because at the downstream end of the large eddy (called the "front") the w motion is away from the centre of the eddy, in the z direction, as is the potential motion, while at the "back" the turbulent w motion is toward the eddy centre ($R_{33}(r', 0, 0)$ always has a negative loop, fig. 5.30) as is the potential w motion by continuity. The convection velocity of the large eddy is less than U_1; hence it represents a blockage to the free stream, causing u to be everywhere increased in the y, z plane, so $R_{11}(0, 0, r)$ is positive and of large scale in the potential motion. Once the back of the large eddy has moved downstream of the y, z plane considered, u will decrease everywhere in the plane and the potential flow will move inward (towards what was the centre of the large eddy) in the y and z directions, by continuity. Thus it is likely that nearly all the backflow for v and some of that for w in the outer motion occurs in the potential motion.

This crude model also suggests that positive u and negative v motion in the potential flow are related, as is negative u and positive v in agreement with the results of fig. 4.26a that $\overline{uv} < 0$ in the potential flow, at least for $x - x_0 > 25$ cm.

The correlations at 75 cm are presented in the same order in figs. 5.50 - 5.62 (note the change in scales). In general, the spanwise and streamwise scales of all the measured correlations have increased, as would be expected from wall effect. In particular, the negative loops in $R_{11}(0, 0, r)$ and $R_{33}(0, 0, r)$, figs. 5.50 and 5.52,

have moved outward, while the size of the negative peak in the former has decreased. This is consistent with the inner motion being a double roller eddy; as its x and z scales are stretched by wall effect and in the absence of viscous effects the normal direction vorticity must decrease. $R_{12}(0, 0, r)$, fig. 5.53, is no longer similar to $R_{11}(0, 0, r)$, and the scales of the normal correlations, figs. 5.54 - 5.56 have increased. The conditionally sampled measurements for $\eta = + 0.003$ are included in figs. 5.54 and 5.55 for economy. There is no longer a negative correlation between the u motion in the inner region and the potential flow, but $R_{21}(0, r, 0)$ has not changed significantly.

The change in the autocorrelations, figs. 5.58 - 5.60 (note the change in scale), for the potential flow are directly related to the discussion of the spectra in Section 4.2. Within the turbulence, all the autocorrelations now have strong negative loops.

Except for the minimum separation, where the errors are likely to be the greatest, $R_{II}(0, 0, r)$ at $\eta = + 0.025$, fig. 5.62 (which also show the $R_{II}(0, r, 0)$ results), closely follows the 37 cm results; while on the high speed side there is a general increase. The conditionally sampled $R_{11}(0, 0, r)$ and $R_{22}(0, 0, r)$ are shown in figs. 5.63 - 5.68, with the relevant t/t contribution at 37 cm shown for comparison. All the t/t scales have increased. The conditionally sampled $R_{12}(0, 0, r)$, figs. 5.69 - 5.70, emphasize the change in structure; now there is no evidence of superposition of the inner and outer motion. With the weakening of the y direction vorticity the outer motion has become dominant over the range of η measured. From fig. 4.2 $\overline{v^2}$ has increased and fig. 4.62 shows that this increase is associated with a narrow frequency band whose central frequency corresponds to a streamwise distance of about 2δ, fig. 5.59. By continuity, this organization of the v motion must be related to the other components. The appearance of a less defined peak in ϕ_{11},

fig. 4.61, while the peak in ϕ'_{33}, fig. 4.63, has not sharpened, show that this organization is limited to the x, y plane motion.

The correlations for 151 cm, again in the same order, are presented in figs. 5.74 - 5.98. The crossover point in $R_{11}(0, 0, r)$ at $\eta = + 0.025$, fig. 5.74, has moved inward and generally the scale of $R_{11}(0, 0, r)$ has decreased from 75 cm. $R_{22}(0, 0, r)$, fig. 5.75, shows no significant trend with η and the scale is less than for any $R_{22}(0, 0, r)$ at 75 cm. $R_{33}(0, 0, r)$, fig. 5.76, is also constant with η and is similar to the 75 cm results for $\eta = - 0.050$ and 0. The similarity between $R_{12}(0, 0, r)$, fig. 5.77, and $R_{11}(0, 0, r)$ seems to be re-established while the major difference in the normal correlations, figs. 5.78 - 5.81, is the disappearance of the positive correlation with the potential motion; $\eta_w = - 0.084$ at 151.15 cm. For $\eta < 0$, $R_{11}(r', 0, 0)$, fig. 5.82, shows strong periodicity as do $R_{22}(r', 0, 0)$, fig. 5.83, and $R_{33}(r', 0, 0)$, fig. 5.84, for all η.

$R_{II}(0, 0, r)$, fig. 5.85, has the same η dependence as at 75 cm, while the spanwise variation of γ_B is much less than in the free shear layer, in agreement with the results of fig. 3.8d. The conditionally sampled $R_{11}(0, 0, r)$ and $R_{22}(0, 0, r)$ show that the spanwise scale of the turbulent u motion has increased from that of the unbounded free shear layer, fig. 5.87, while the spanwise scale of the turbulent v motion has decreased, presumably because the wall has finally limited the outward eruption of the large eddies, whose main feature is the relatively large spanwise scale of v. Compared to the wall affected free shear layer, the spanwise scales of the turbulent u motion, figs. 5.89 and 5.91, and the turbulent v motion, figs. 5.90 and 5.92, have decreased.

The conditionally sampled $R_{12}(0, 0, r)$ results, figs. 5.93 and 5.94, show, that as at 37 cm, the similarity with $R_{11}(0, 0, r)$ extends to the contributions as well. In spite of the persisting

negative region in $R_{11}(r', 0, 0)$ for $\eta = + 0.014$, fig. 5.82, this similarity together with the persistence of the negative loop in $R_{33}(0, 0, r)$, fig. 5.76, suggests that the double roller eddy is again becoming dominant in the inner region as the wall now inhibits the outward motion. This is not particularly surprising in view of Townsend's (1976, p. 120) statement "it is probable that the dominant eddies of shear flow [in general] are double-roller eddies". Townsend (1976, p. 156ff) postulates that the effect of the wall on a double roller eddy is to produce a double cone eddy attached to the wall. The main differences between the two are that, in the latter, $R_{22}(0, 0, r)$ has a negative loop, while $R_{33}(0, 0, r)$ and all the streamwise correlations are always positive. If such a large eddy structure is the asymptotic form for the present flow, then there must be considerable further development after this, the last measurement station.

The conditionally sampled normal correlations are shown in figs. 5.95 - 5.98, together with the position of the wall and $\eta_{\tau 0}$, from fig. 4.40. $R_{22}(0, r, 0)$ is always positive while $R_{11}(0, r, 0)$ and $R_{21}(0, r, 0)$ go negative after $\eta_{\tau 01}$ approximately. This is further evidence that the wall region motion is dominated by the mixing layer structure, since if the outer motion of the floor boundary layer was important it should produce a negative $R_{22}(0, r, 0)$ near the wall as it is of opposite sign to the outer motion of the mixing layer.

5.3 General Discussion of the Correlations

It was shown that the large eddy structure in the unbounded free shear layer could be discussed without recourse to the possibility of basically two-dimensional large eddies. In fact, the measurements preclude the possibility. In particular, the negative loops in $R_{11}(0, 0, r)$, $R_{12}(0, 0, r)$ and $R_{33}(0, 0, r)$ - the latter being the

"correlation that is most representative of the [double roller eddies], i.e. the one most unlikely to arise from some other kind of eddy" (Grant, 1958) - are incompatible with the existence of B-R structures in the present flow. A simple physical reason was given for the large scales of $R_{11}(0, 0, r)$ and, to a lesser extent $R_{22}(0, 0, r)$, in the potential flow; the mathematics are considered in the next section.

It is interesting that the correlation measurements show no evidence of the secondary motion responsible for the spanwise non-uniformity in the mean velocity profiles which is most pronounced at 37 cm, figs. 3.7 and 3.8. An embedded longitudinal vortex of the type postulated in Chapter 3 would cause negative regions in $R_{22}(0, 0, r)$. That this does not occur, even at 37 cm, is further evidence that the secondary motion is relatively weak.

The first effect of the wall is to augment the outer motion, even though the spanwise and streamwise scales of all the motion have increased due to the "splat effect". Since the outer motion is almost entirely responsible for the v motion this augmentation is related to the increase in $\overline{v^2}$, fig. 4.2. Consideration of the equations for the normal stress components is unlikely to help. Since $\overline{uv}\ \partial U/\partial y$ is unchanged at 75 cm there is no extra production of $\overline{u^2}$. Since $\overline{u^2}$ and $\overline{w^2}$ are unchanged there is no preferred energy transfer to $\overline{v^2}$ via $\overline{p'\partial v/\partial y}$. Since the peak in ϕ_{22}, figs. 4.62 and 4.65, indicate that the increase in $\overline{v^2}$ is a local phenomenon, it is unlikely to be caused by streamwise diffusion, while the fact that $\overline{v^2}$ increases over the whole shear layer precludes the possibility of cross stream diffusion being responsible. In absence of definite knowledge of the behaviour of $\overline{p'v}$ this leaves two alternatives. The first is that the dissipation term in the equation for $\overline{v^2}$ is reduced, which is unlikely because the effect of the wall is, primarily, on the large scale structure. The second, more reasonable, alternative is that the single point measure-

ments are not sufficiently accurate to justify the statements above. Apparently, the periodic outer motion is "bouncing" off the wall, at a strongly preferred frequency that is too high to significantly amplify $\overline{u^2}$ through the mean velocity gradient. The conclusion that the augmentation of the outer motion is largely confined to the x, y plane motion is consistent with the increase in u^2/w^2 with x near the high velocity edge, fig. 4.28.

By 151 cm the situation is quite different. The imposition of the no slip constraint has altered the growth of the shear layer and $\overline{uv}\ \partial U/\partial y$ has increased significantly over most of the layer while the image constraint has prevented the extra available energy from going into $\overline{v^2}$. This has reduced the importance of the outer motion and there is some evidence that the double roller eddy is becoming important again. The outer motion has not disappeared however; it still transports momentum down from the centre of the shear layer since the production of turbulent energy near the wall is relatively small; it is zero at η_{uo} and $\eta_{\tau o}$ and negative between these two positions. It is probably for this reason that the energy transfer, caused by the wall, that is responsible for the huge rise in $\overline{u^2}$, fig. 4.37, and the less spectacular rise in $\overline{w^2}$, fig. 4.39, occurs in the region where the outer motion dominated the free shear layer.

5.4 The Potential Core Correlations

Equations for the correlations in the potential core are derived in Appendix C. The purpose of this section is to compare the theoretical results with the measurements and to discuss the implications for the large eddy structure of the mixing layer.

The most important result of Appendix C is the prediction that the correct scale for the potential flow correlations is the normal distance from the effective origin of the potential motion.

To test this prediction, the non-dimensional probe separation for the results, figs. 5.99 - 5.105, is:-

$$\xi \equiv r\,(y - y_0)^{-1} = r\,(\eta_0 - \eta)\,(x - x_0)^{-1}$$

where η_0 was set to + 0.014, as in Section 4.2.

On the basis of the reasonable collapse of the unaffected potential flow spectra, figs. 4.31 - 4.36, at frequencies greater than the peak position, it was argued in Section 4.2 that the convection velocity in the potential core was sensibly constant. The autocorrelations, generated from these spectra, have been turned into pseudo-streamwise correlations using $r' \equiv U_c t$, where U_c was again taken as 0.65 U_1, figs. 5.99 - 5.101. "Streamwise" correlations are the most likely to be affected by the streamwise inhomogeneity and this effect will increase with increasing $\eta_0 - \eta$. No corrections were applied to the data, in particular $\eta_0 - \eta$ was assumed to be independent of the time delay t. Generally, the negative peak in figs. 5.99 - 5.101, moves outward, as would be expected if scaling on $\eta_0 - \eta$ was incorrect. However, the change is less than half that needed to make the results independent of $\eta_0 - \eta$ which changes by nearly a factor of two over the range of the measurements. Furthermore, the negative peak for the single measurement at 36.89 cm, when compared to the result at closest η for 24.05 cm, has not moved outward by anything like the ratio 36.89/24.05 which would occur if the potential correlations scaled on $x - x_0$ alone, as do the turbulence results.

The x, y plane spatial correlations are shown in figs. 5.102 - 5.105. The results at 36.89 cm are included, since from figs. 4.23 - 4.25, the effect of the wall on these measurements should be small. Also included in figs. 5.102 and 5.103 are the nt/nt zone averaged

correlations from the outer layer conditionally sampled measurements. The results for the unaffected potential flow are consistent with the scaling law of Appendix C and with the expectation, Section 5.1, that the nt/nt zone averaged correlations will be underestimated by the present intermittency routine. The present scaling collapses the data better than the scaling used for the measurements in the previous section as η_o - η changes by almost 60% in figs. 5.102 and 5.103.

The results of figs. 5.102 - 5.104 are qualitatively consistent with the relation between the irrotational covariances, Eqn. (C.7). Since the spanwise scale of $R_{22}(0, 0, r)$ is less than that of $R_{11}(0, 0, r)$, $R_{33}(0, 0, r)$ must go negative for Eqn. (C.7) to remain valid. This demonstrates the importance of the relatively small w motion in the potential flow; the negative loop in $R_{33}(0, 0, r)$, fig. 5.104, could only arise if the forcing spectrum for the potential motion has significant contributions from low wave-numbers in the spanwise direction. Together with the success of the scaling in fig. 5.104 this is further evidence against the interpretation that the large eddies in the mixing layer are essentially two-dimensional.

Fig. 5.99 also shows Professor Ferziger's numerical calculation of Eqn. (C.21) using χ_{11}/χ_{33} = - 8.65 obtained from Eqns. (4.2) and (C.15). The calculation for $R_{11}(0, 0, r)$ is shown in fig. 5.102, together with the simple analytic form, Eqn. (C.24) for the special case of homogeneous (in the x, z plane) turbulence. The corresponding result for $R_{33}(0, 0, r)$, Eqn. (C.25), is shown in fig. 5.104. No great significance can be attributed to these results, since the numerical calculation implies an unphysical, negative spectrum constant and the assumption of homogeneity is plainly unjustified for the present flow. In view of these limitations it is surprising that the theory gives, at least, the

correct shapes for the correlations shown. However, as noted in Appendix C, Eqn. (C.24) is also the homogeneous equation for $R_{33}(r, 0, 0)$ and is always positive while $R_{33}(r', 0, 0)$ has a pronounced negative loop. This further suggests that some of the discrepancies between the theory and the measurements is due to the streamwise inhomogeneity of the shear layer.

The effect of the wall on the potential flow correlations is to increase the spanwise scale of $R_{11}(0, 0, r)$, fig. 5.102, and $R_{22}(0, 0, r)$, fig. 5.103, and to move the crossover point in $R_{33}(0, 0, r)$ outwards. As wall effect has also increased the spanwise scales of the turbulent motion this result is consistent with the simple physical model of fig. 5.49b. $R_{11}(0, 0, r)$ increases because the cross-sectional area of the potential flow is now finite so the blockage effect of the large eddies will be greater. This should also enhance the relation between the potential u and v motion, explaining the increase in $-\overline{uv}$, fig. 4.26a. The incorporation of wall effect into the equations for the correlations was done only for the simpler, homogeneous case. Comparison with fig. C.5 shows that, as for the mean square intensity results of Section 4.2, the theory gives the correct trend for $R_{11}(0, 0, r)$ and $R_{33}(0, 0, r)$ with wall effect, but considerably underestimates the magnitude of the changes, probably for the reasons given in Section 4.2 for the behaviour of the single point measurements.

The normal correlations at 24.05 cm with the fixed probe at $\eta = -0.100$ are compared with Eqn. (C.23) in fig. 5.105. For $\xi \lesssim 1$ (i.e. $\eta \lesssim 0.2$) the effects of free stream turbulence and the wall are negligible, Section 4.2. Over this range of ξ the agreement between the theory and $R_{11}(0, r, 0)$ is good, while the agreement with $R_{22}(0, r, 0)$ is good over the entire range measured. $R_{33}(0, r, 0)$ is consistently overpredicted. The interesting feature of Eqn. (C.23)

is that it is independent of the ratio χ_{11}/χ_{33} and is also the theoretical result in best agreement with the measurements. No normal correlation measurements were made in the wall affected potential flow.

The results presented in this section strongly suggest that the nature of the potential flow partially determines the potential correlations. Very crudely, the shapes of the correlations are determined by the turbulence, fig. 5.49b, but the scales are determined by the nature of forced potential flow. Thus it is possible to measure an arbitrarily large scale of $R_{11}(0, 0, r)$, relative to the shear layer thickness, simply by measuring sufficiently far from the effective origin of the potential motion. It is unfortunate that previous workers did not determine this effective origin and measured only $R_{11}(0, 0, r)$; as argued above the only possible interpretation of the present $R_{33}(0, 0, r)$ results is that the large eddies in the present mixing layer are three-dimensional.

Browand and Troutt (1979) found that the spanwise scale of their potential flow $R_{11}(0, 0, r)$ measurements, at constant η, increased linearly with $x - x_0$, in agreement with the scaling used in this section. The importance of the nature of the potential flow to the potential correlations is well demonstrated by the measurements of $R_{11}(0, 0, r)$ by Wygnanski et al (1970), discussed in Chapter 1. The changes induced in the potential flow correlations by using vortex generators or trip wires in the upstream initial boundary layers were insignificant compared to the change induced by making the potential flow highly turbulent, see their fig. 2. (For the reasons given in the footnote to Section 1.2.3, it is more difficult to interpret the effect of vibrating the trailing edge, which Wygnanski et al showed also significantly affected the potential correlations.)

The scaling law of Appendix C also indicates the reason for the greater importance of potential flow effects outside mixing layers than outside other shear layers in general. In free shear layers, generally, the effective origin for the potential motion is likely to be near the position of maximum $\overline{v^2}$, since by Eqn. (C.3), the potential motion is forced by the turbulent v motion. Outside wall bounded flows the effective origin is constrained by the wall to be closer to the half intermittency point (Bradshaw, 1967a). Thus the high velocity edge of the present, asymmetric free shear layer is further from the effective origin of the potential motion than is the corresponding edge of symmetric free shear layers and wall bounded flows.

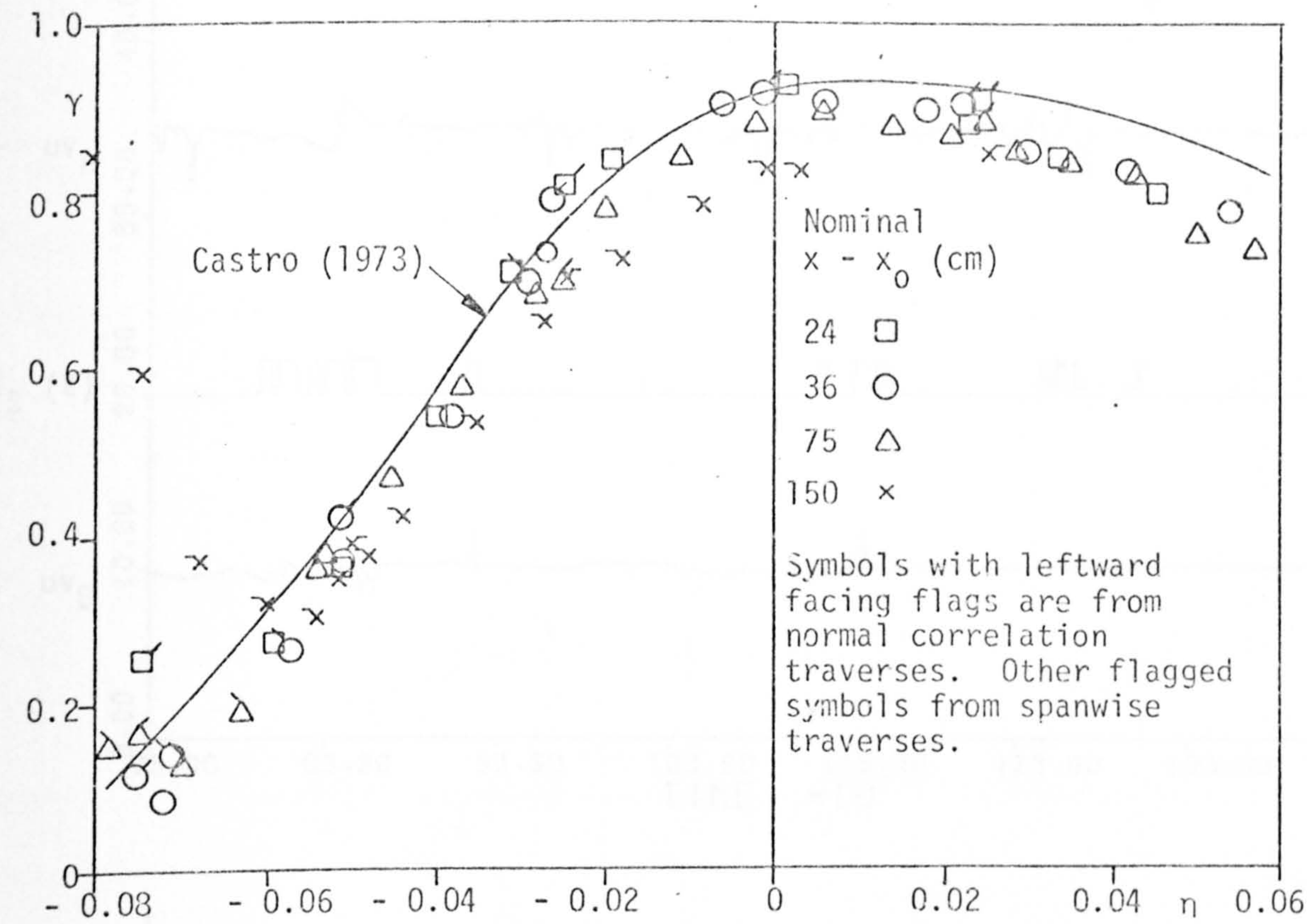


Fig. 5.1 Streamwise development of γ. Unflagged symbols are single point results

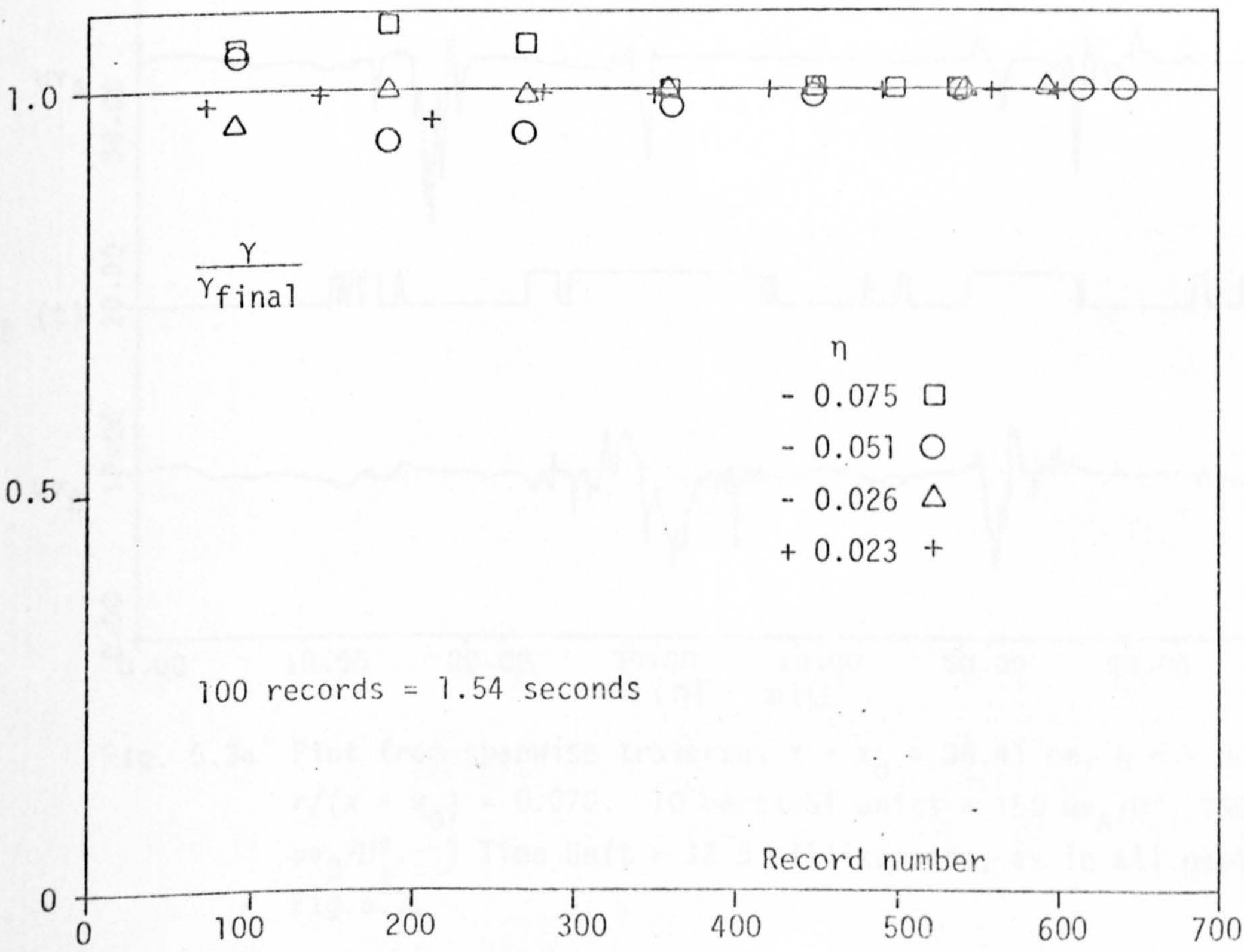


Fig. 5.2 Convergence of γ, $x - x_o$ = 36.41 cm

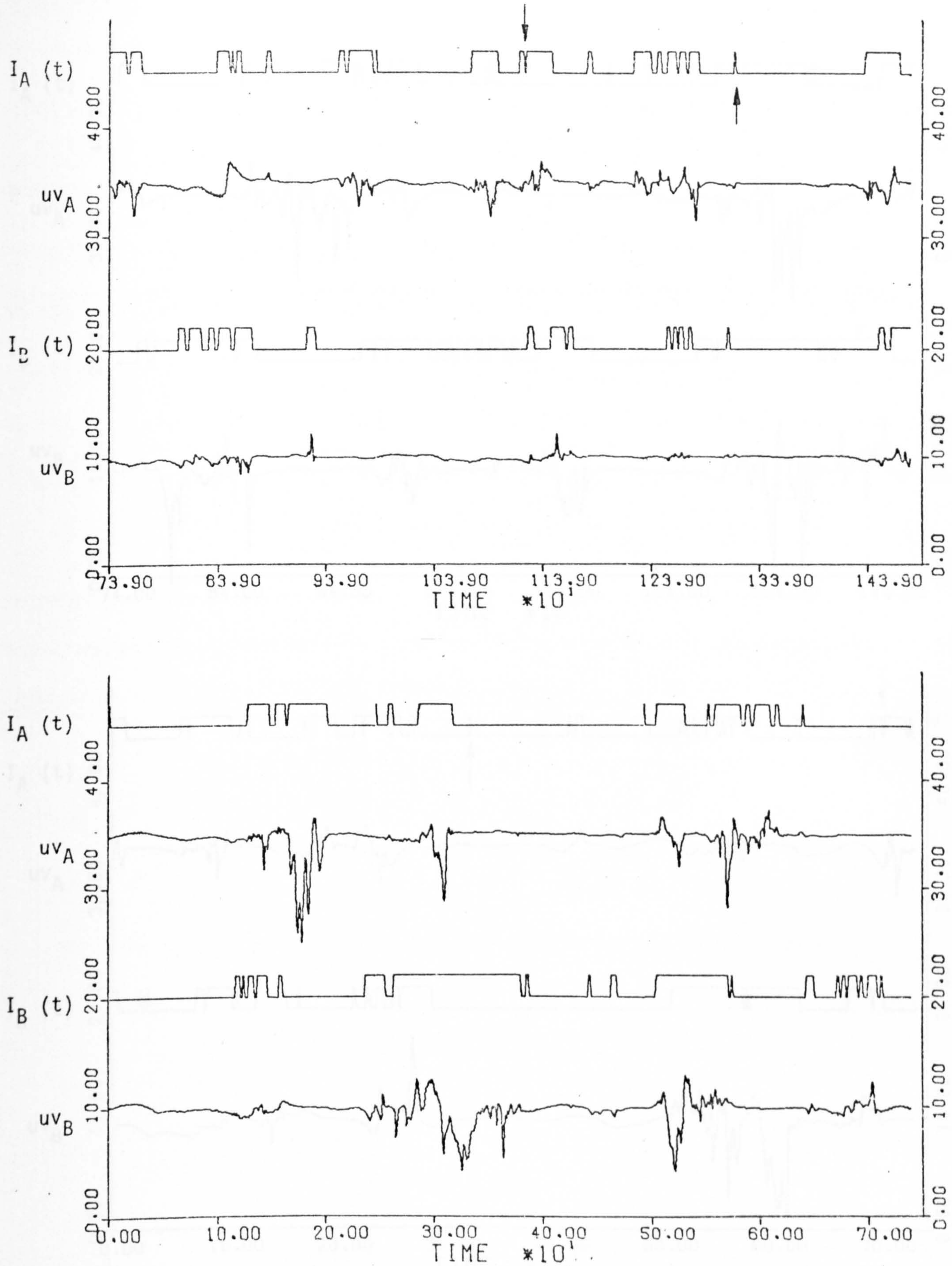


Fig. 5.3a Plot from spanwise traverse; $x - x_0 = 36.41$ cm, $\eta = -0.051$, $r/(x - x_0) = 0.070$. 10 vertical units = 150 uv_A/U_1^2, 150 uv_B/U_1^2. 1 Time Unit = 12.5 milliseconds, as in all parts of Fig.5.3.

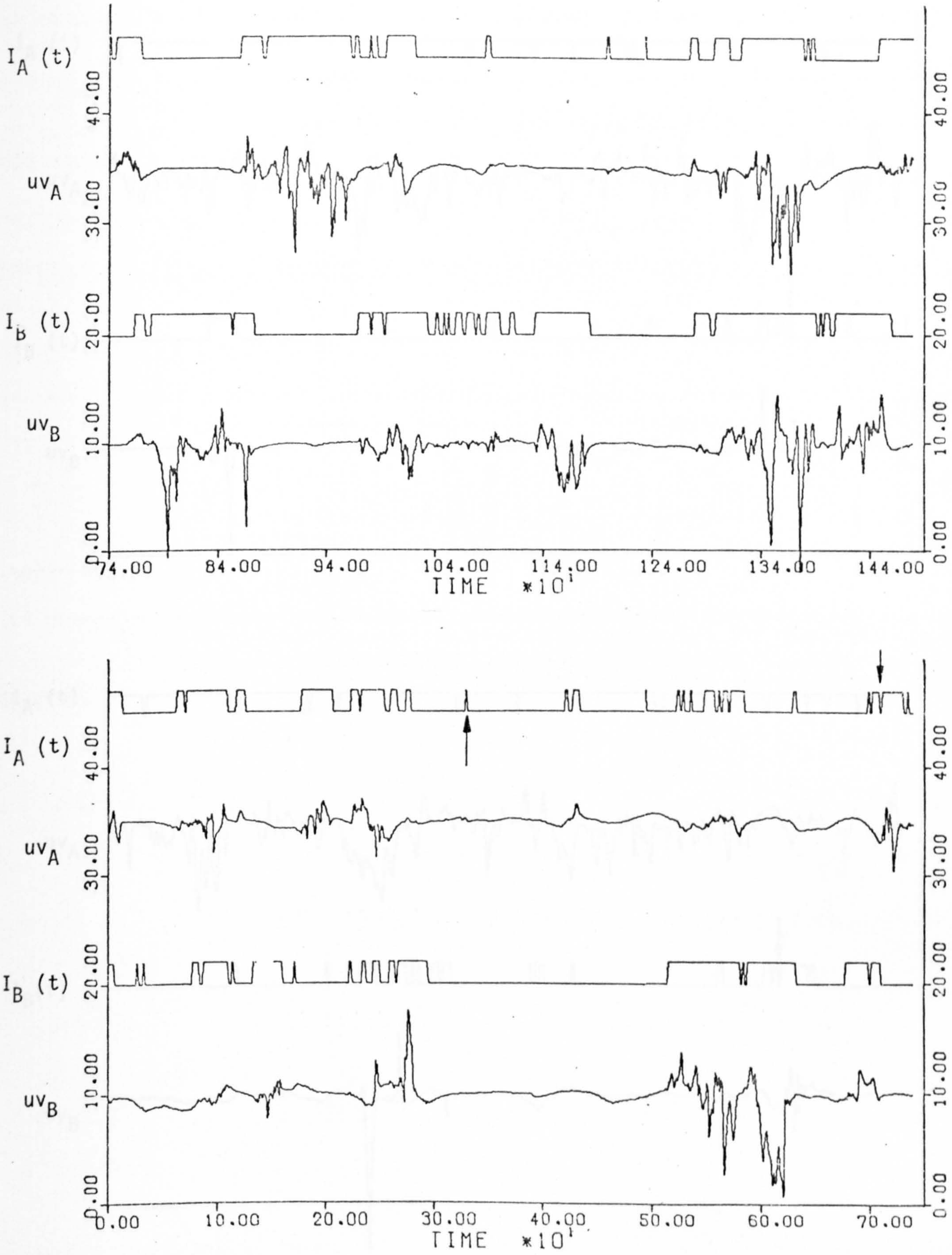


Fig. 5.3b Plot from spanwise traverse; $x - x_o = 36.41$ cm, $\eta = -0.051$, $r/(x - x_o) = 0.349$. Scales as for fig. 5.3a.

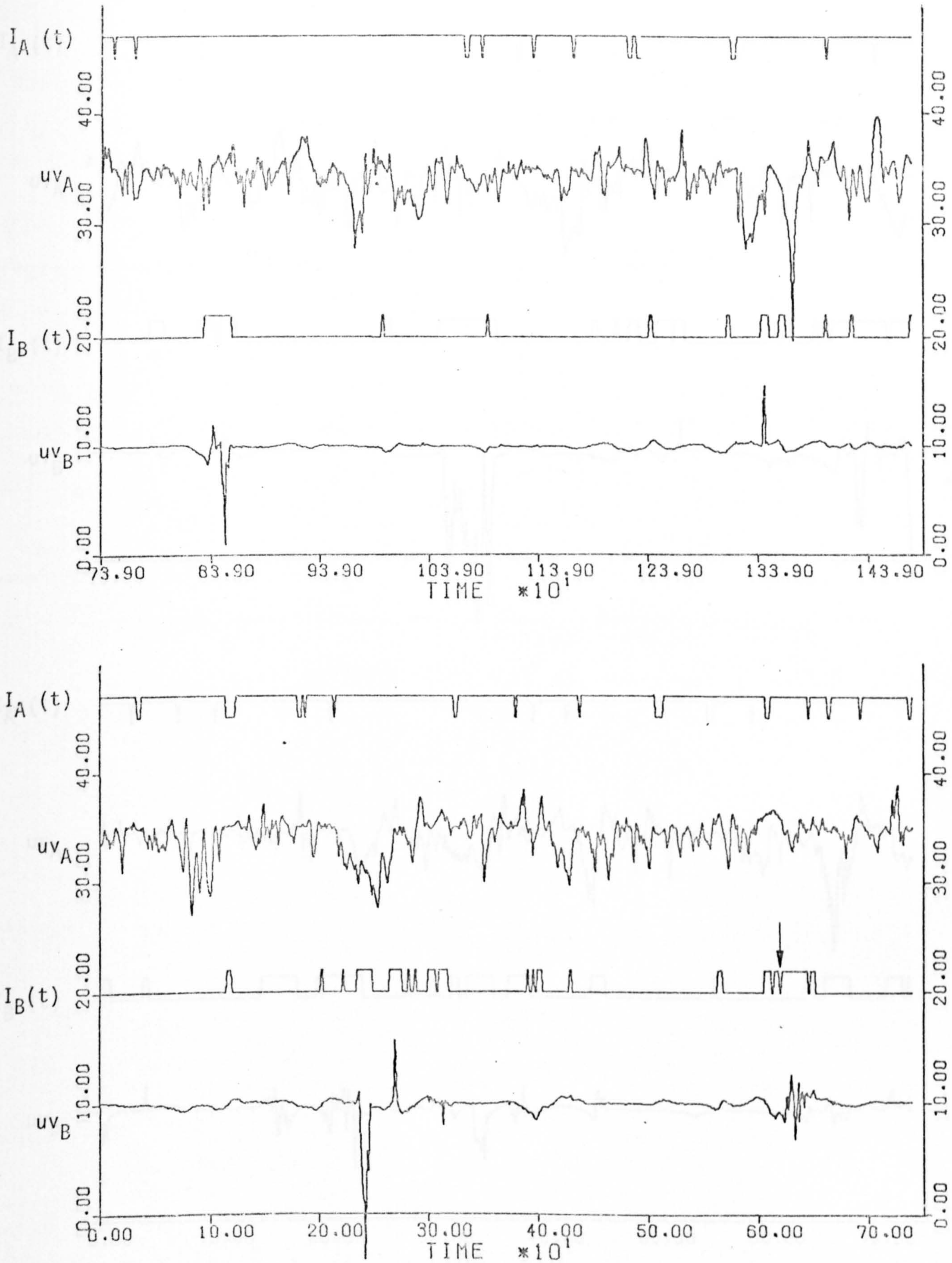


Fig. 5.3c Plot from normal traverse; $x - x_o$ = 24.02 cm, η = + 0.003, $r/(x - x_o)$ = - 0.076. 10 vertical units = 100 uv_A/U_1^2, 400 uv_B/U_1^2.

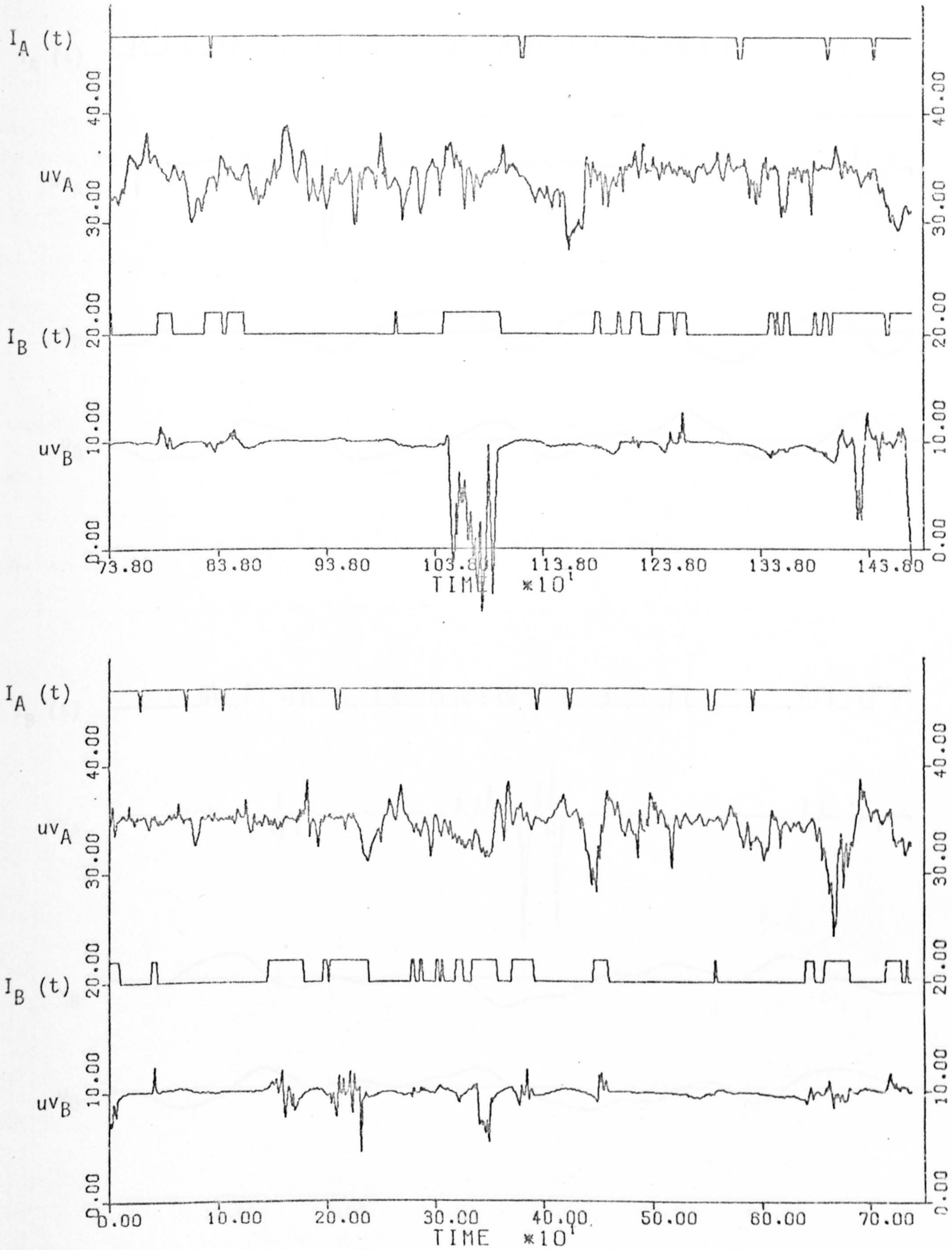


Fig. 5.3d Plot from normal traverse; $x - x_o = 36.89$ cm, $\eta = + 0.002$, $r/(x - x_o) = - 0.059$. 10 vertical units = 1000 uv_A/U_1^2, 240 uv_B/U_1^2

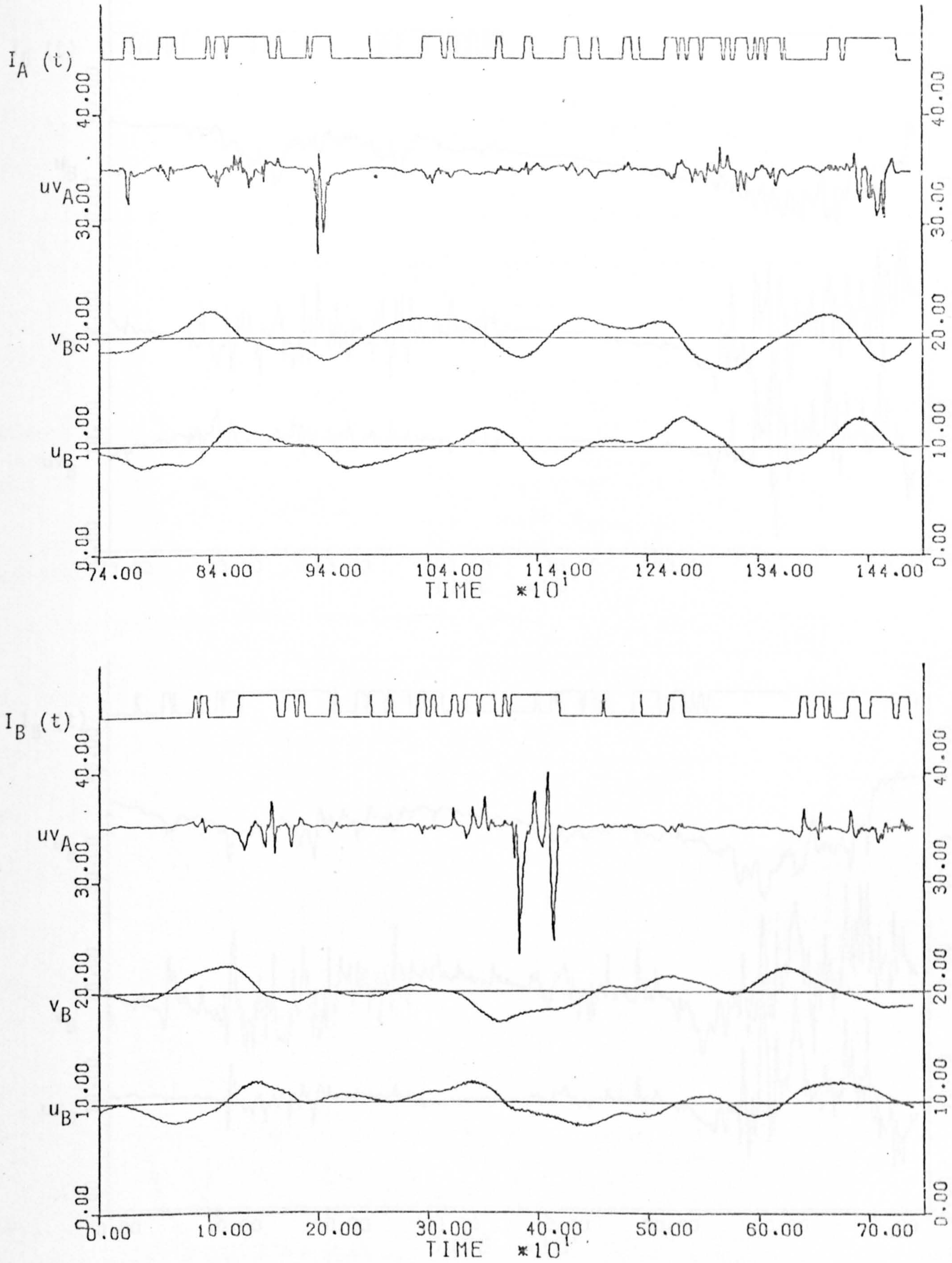


Fig. 5.3e Plot from normal traverse; $x - x_o = 24.02$ cm, $\eta = -0.050$, $r/(x - x_o) = -0.075$. 10 vertical units = 150 uv_A/U_1^2, 100 u_B/U_1, 100 v_B/U_1

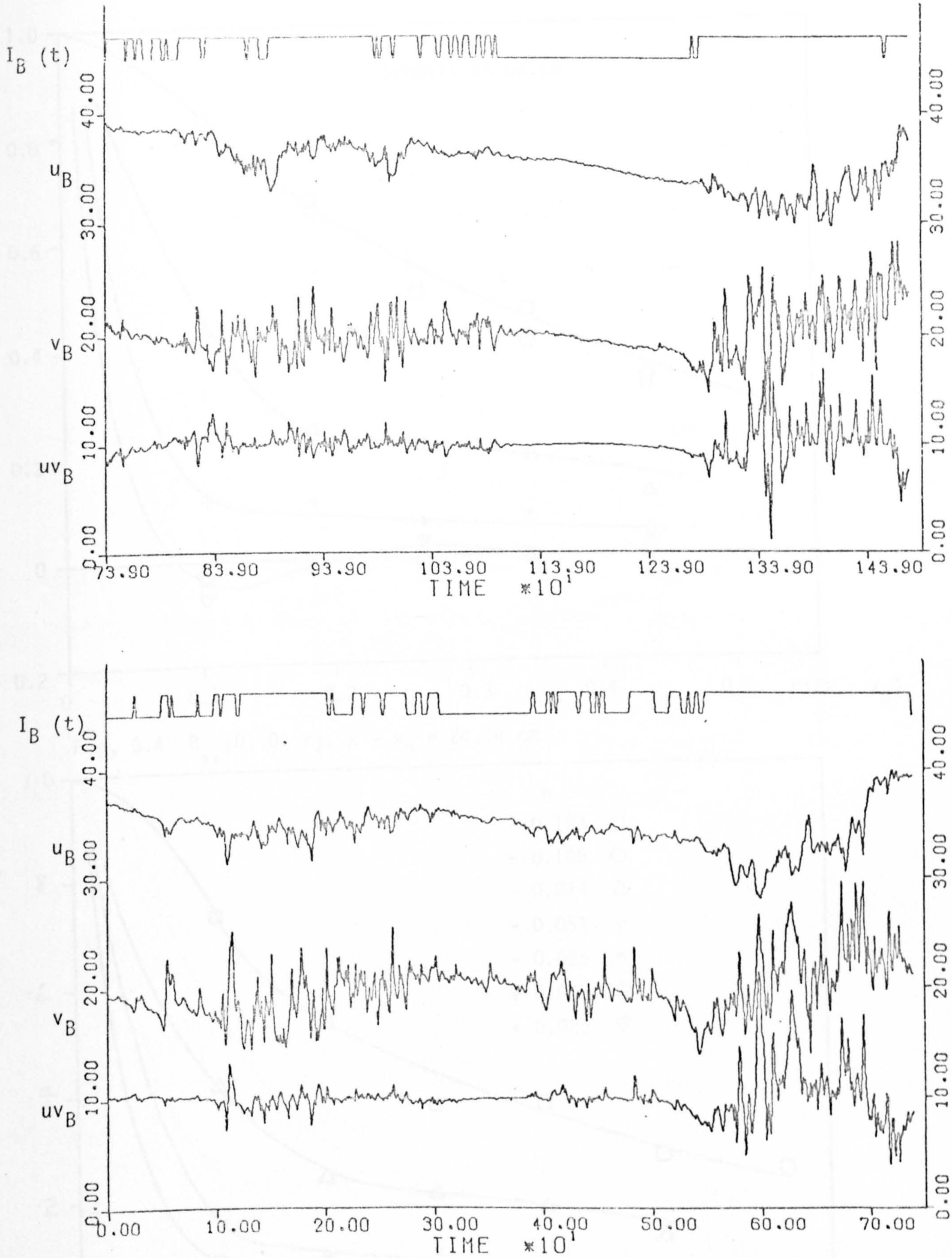


Fig. 5.3f Plot from normal traverse; $x - x_o = 151.11$ cm, probe B at $\eta = -0.075$. 10 vertical units = 15 u_B/U_1, 50 v_B/U_1, 200 uv_B/U_1^2

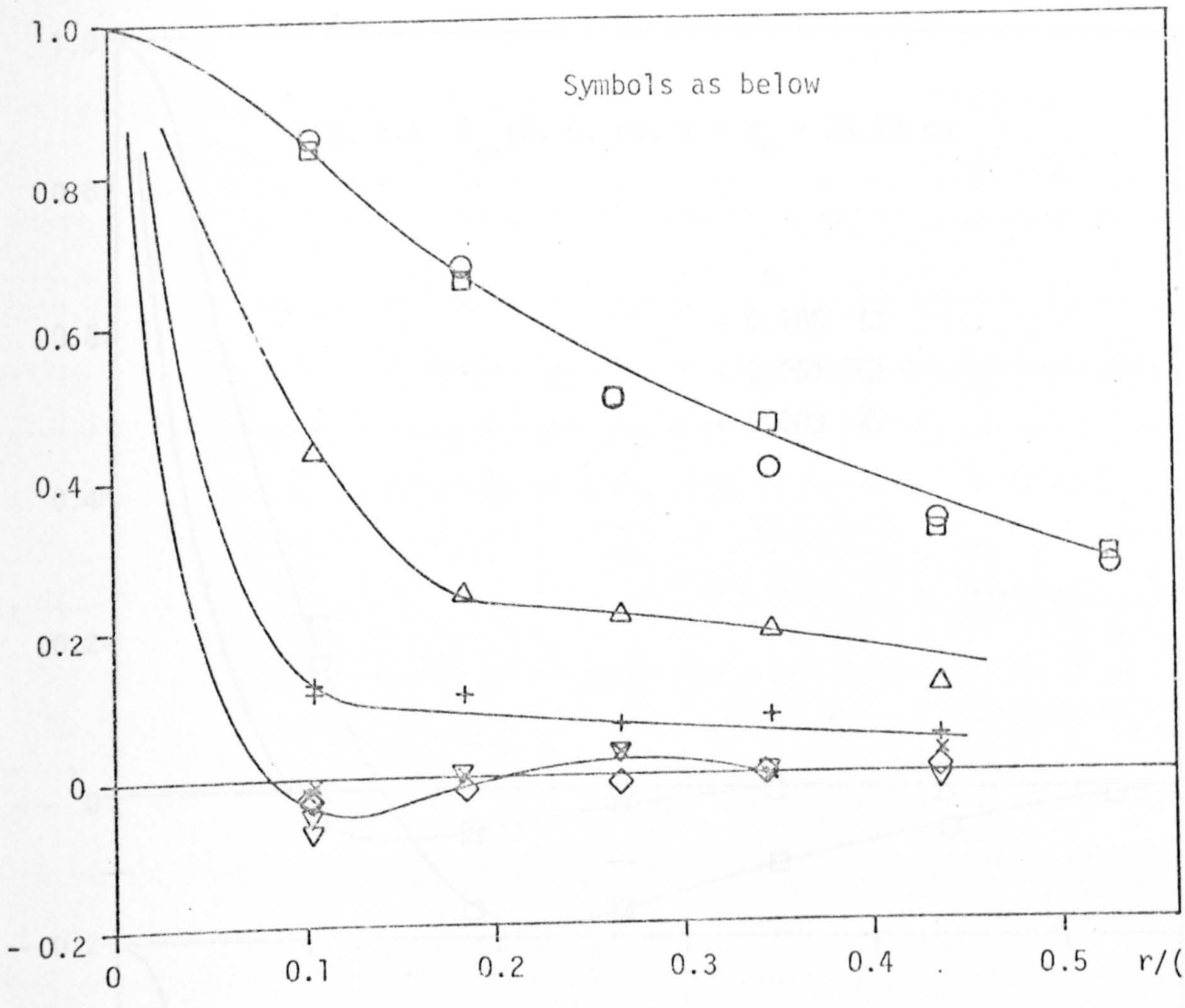


Fig. 5.4 $R_{11}(0, 0, r)$, $x - x_o = 24.14$ cm

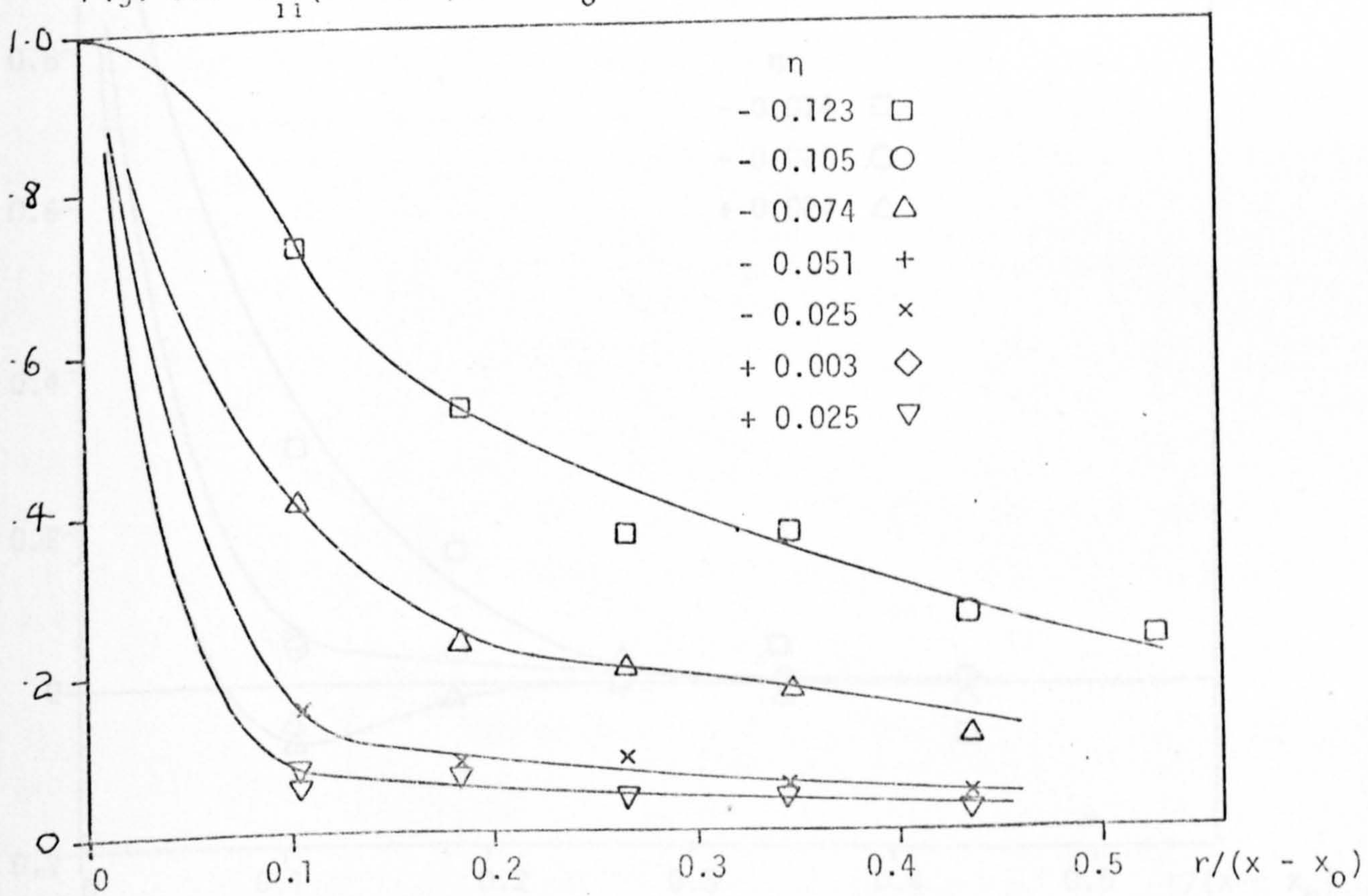


Fig. 5.5 $R_{22}(0, 0, r)$, $x - x_o = 24.14$ cm

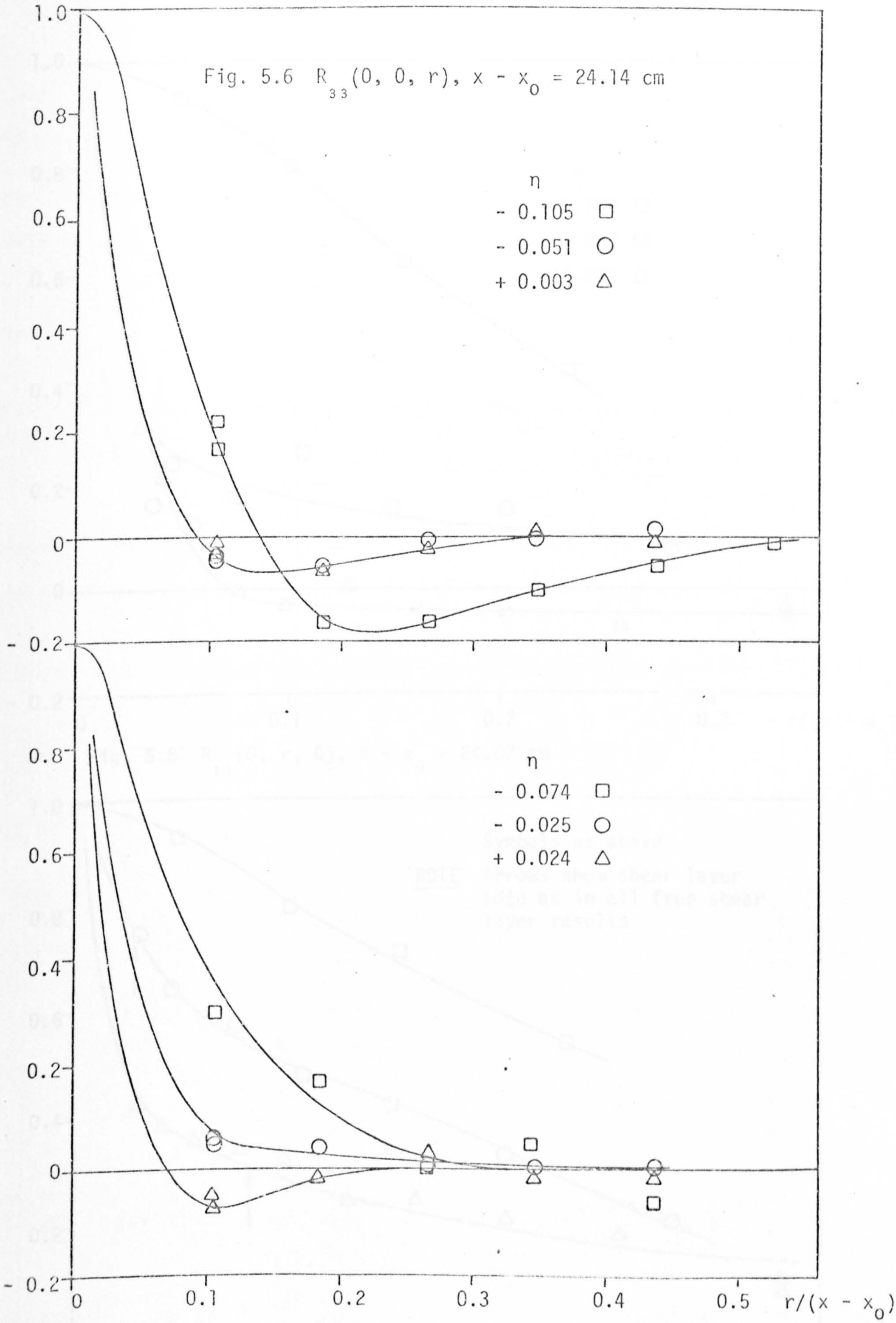


Fig. 5.6 $R_{33}(0, 0, r)$, $x - x_o = 24.14$ cm

Fig. 5.7 $R_{12}(0, 0, r)$, $x - x_o = 24.14$ cm

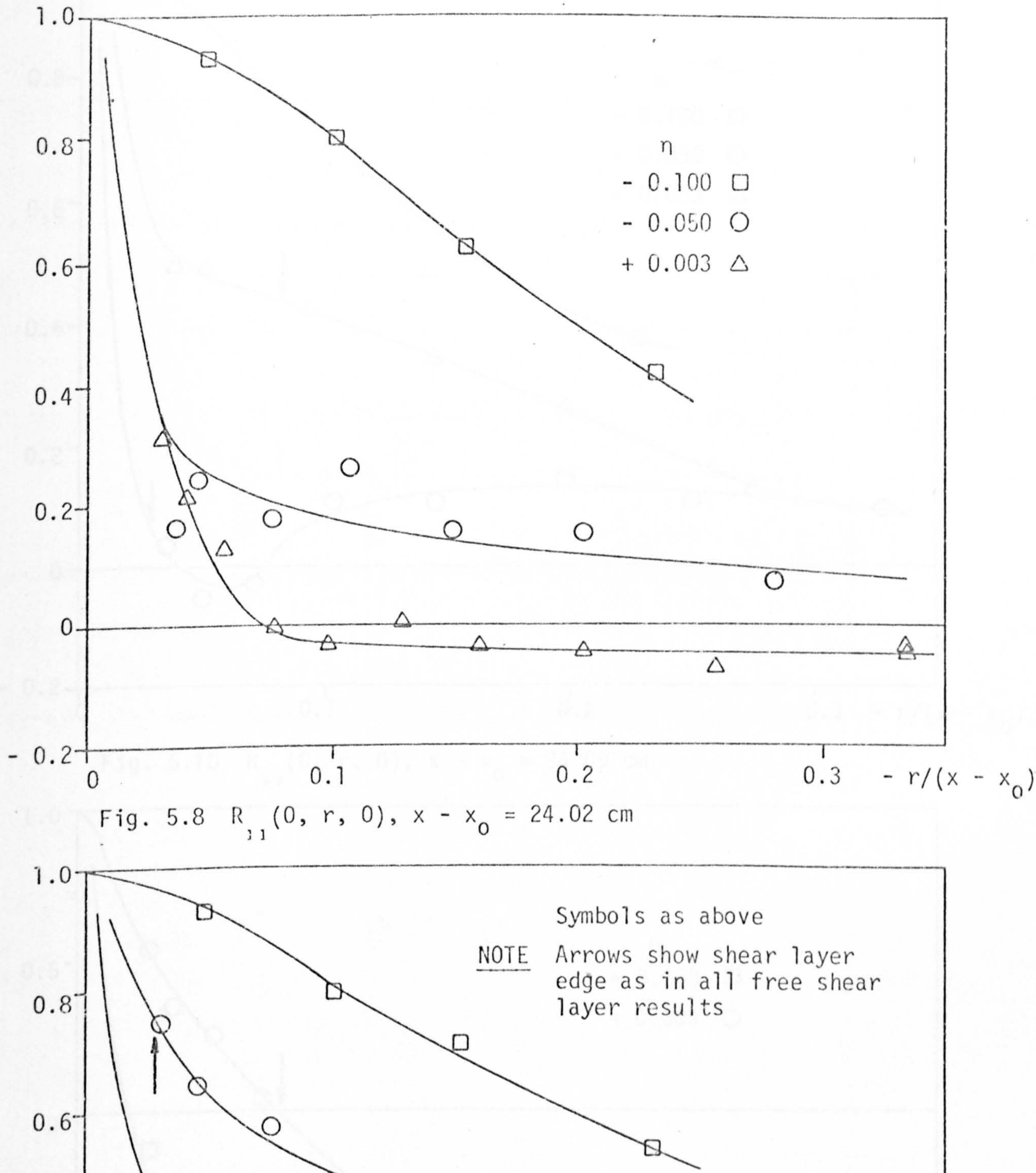


Fig. 5.8 $R_{11}(0, r, 0)$, $x - x_0 = 24.02$ cm

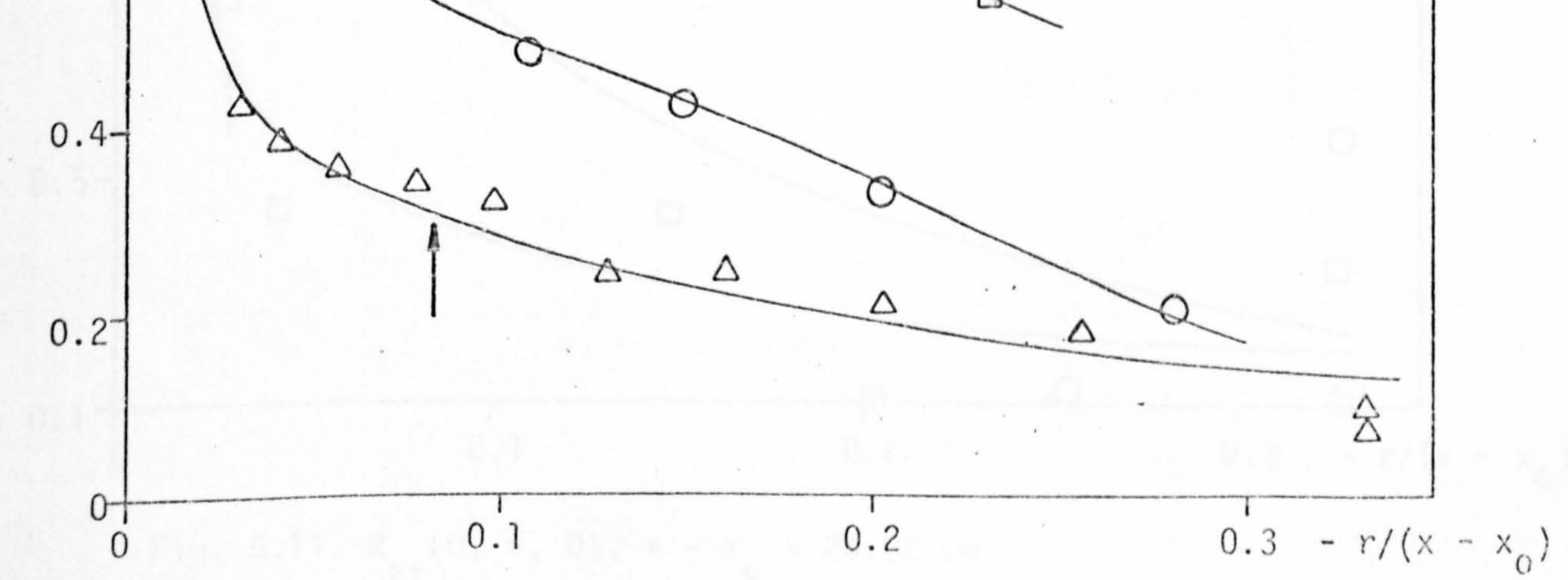


Fig. 5.9 $R_{22}(0, r, 0)$, $x - x_0 = 24.02$ cm

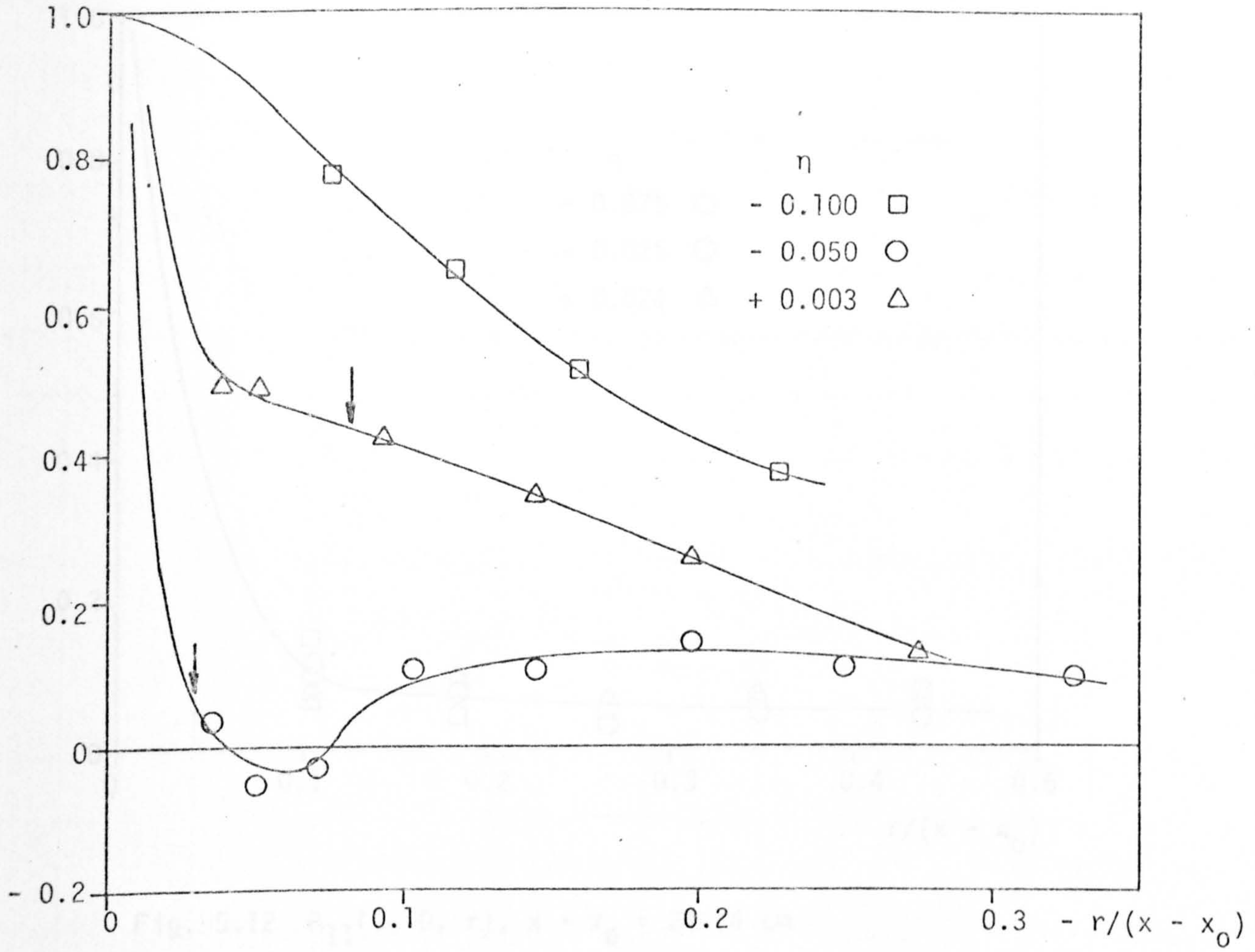


Fig. 5.10 $R_{33}(0, r, 0)$, $x - x_0 = 24.09$ cm

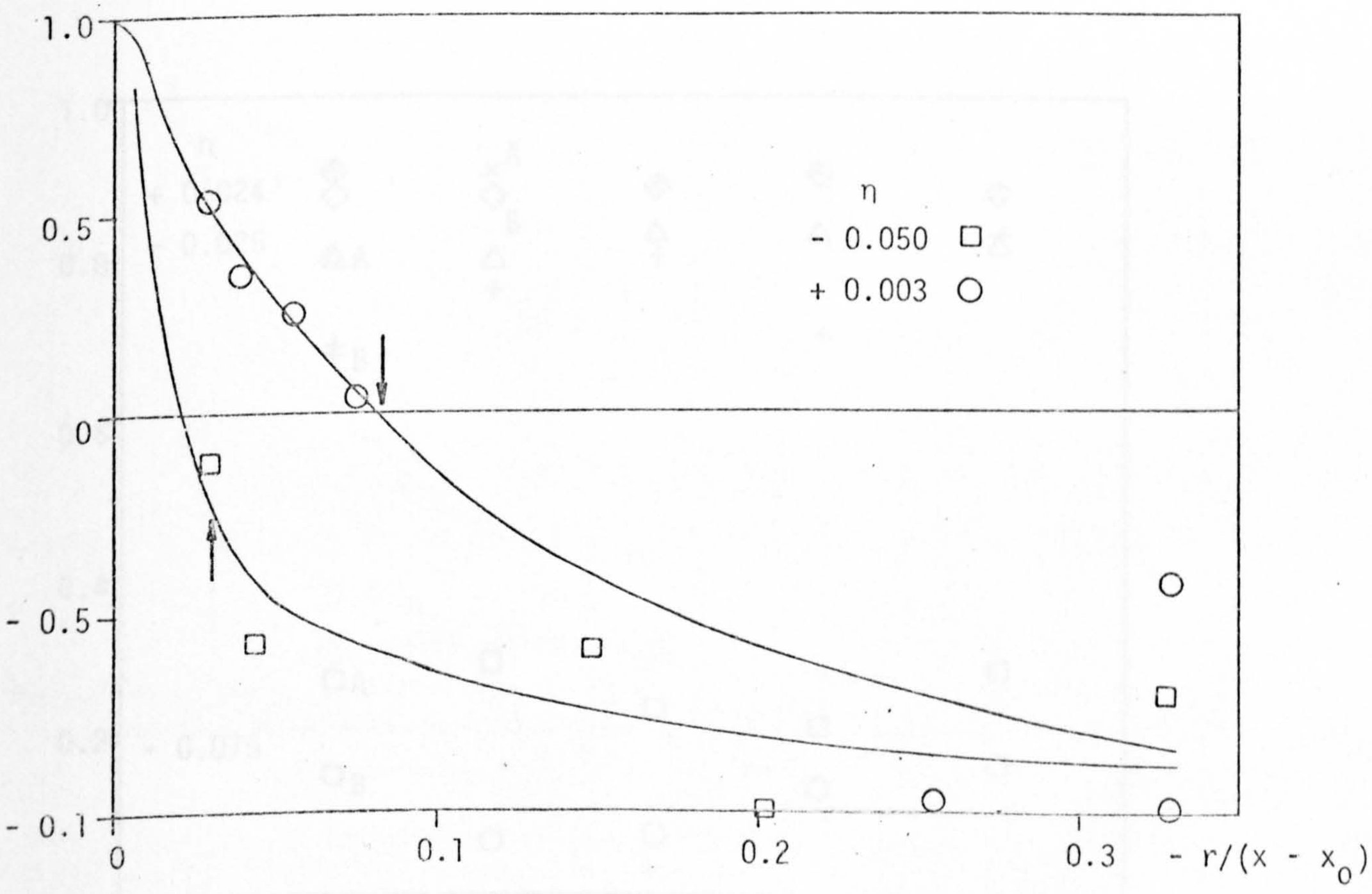


Fig. 5.11 $R_{21}(0, r, 0)$, $x - x_0 = 24.02$ cm

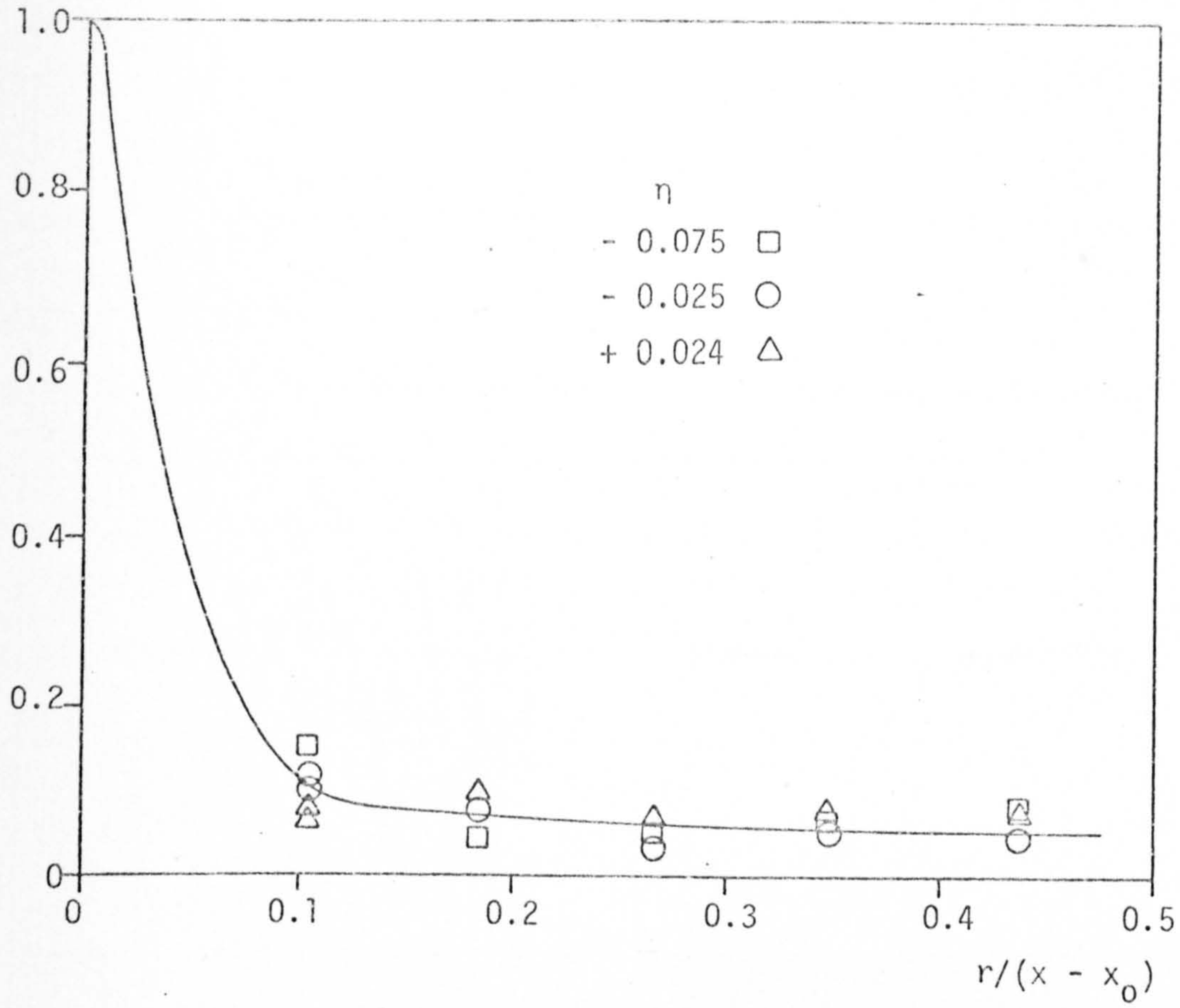


Fig. 5.12 $R_{II}(0, 0, r)$, $x - x_o$ = 24.14 cm

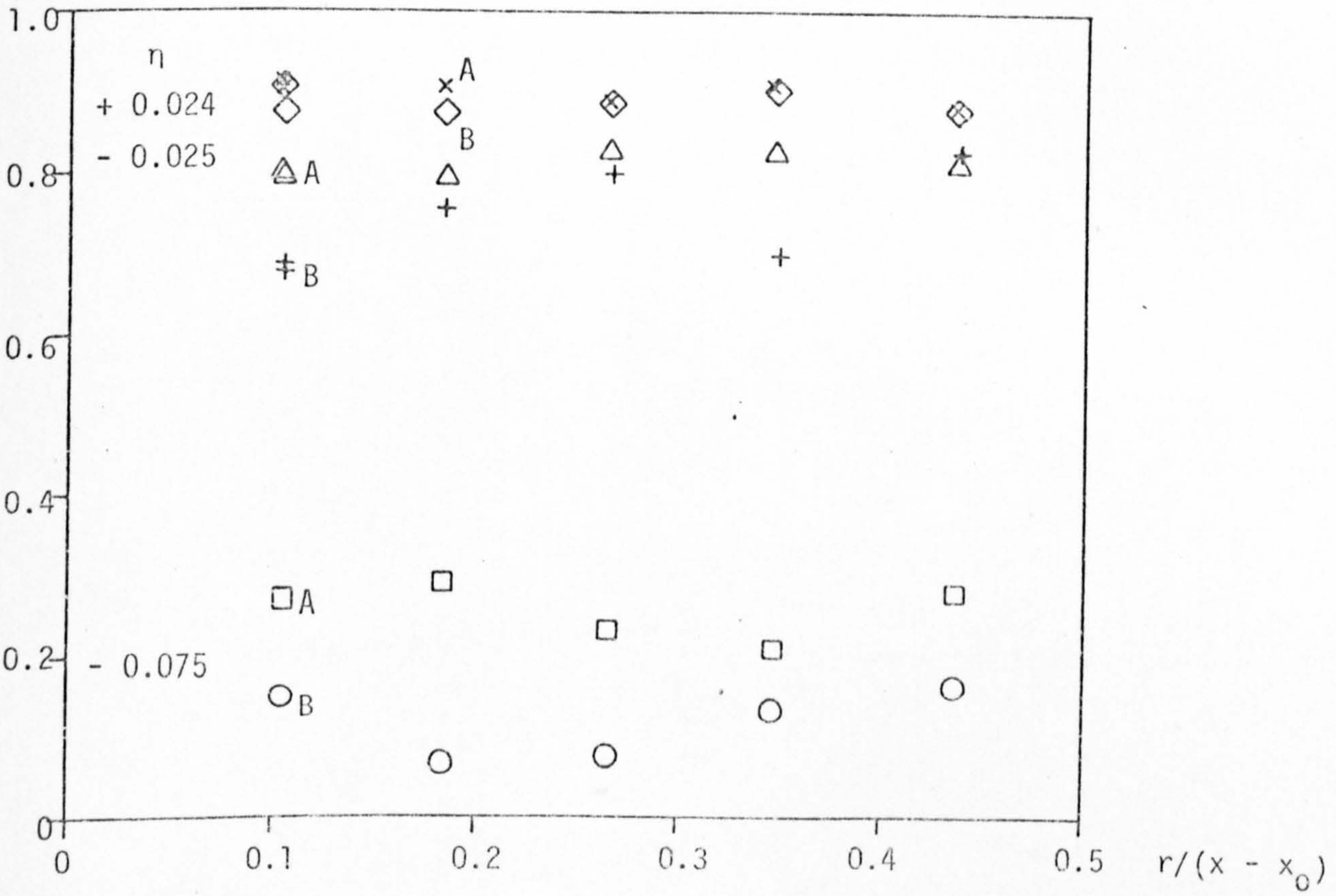


Fig. 5.13 Variation of γ_A, γ_B; $x - x_o$ = 24.14 cm

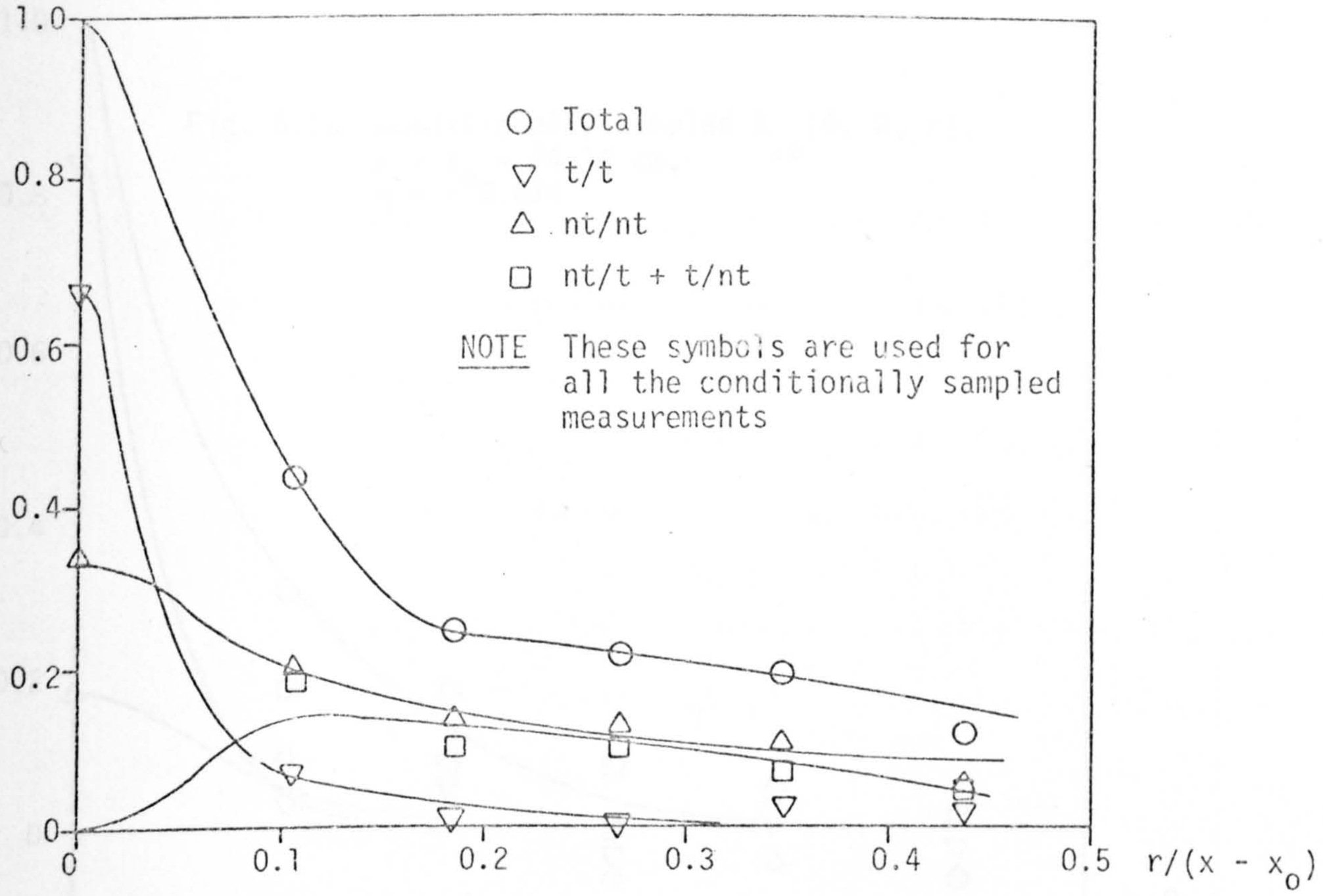


Fig. 5.14 Conditionally sampled $R_{11}(0, 0, r)$, $x - x_o = 24.14$ cm, $\eta = -0.074$

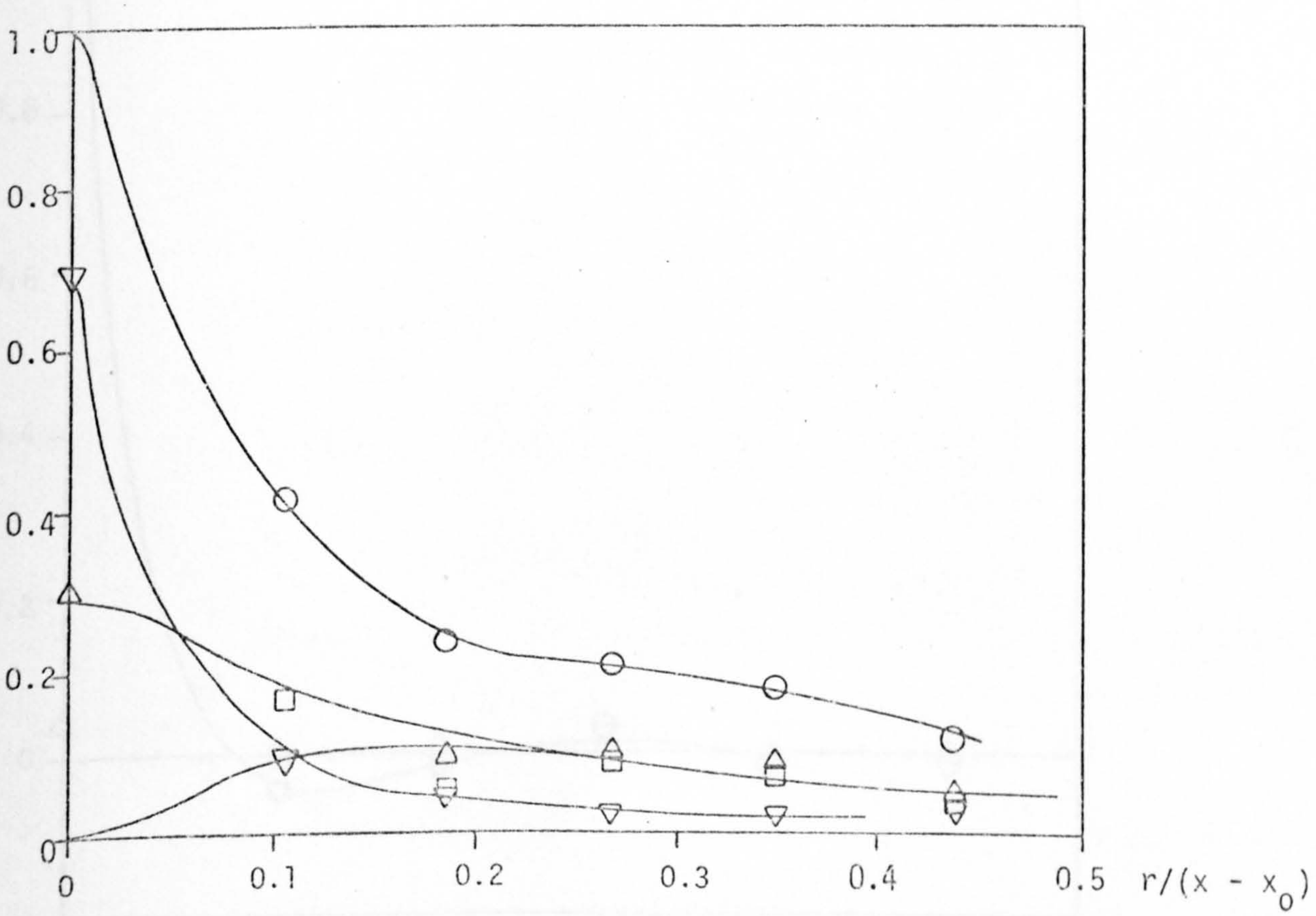


Fig. 5.15 Conditionally sampled $R_{22}(0, 0, r)$, $x - x_o = 24.14$ cm, $\eta = -0.074$

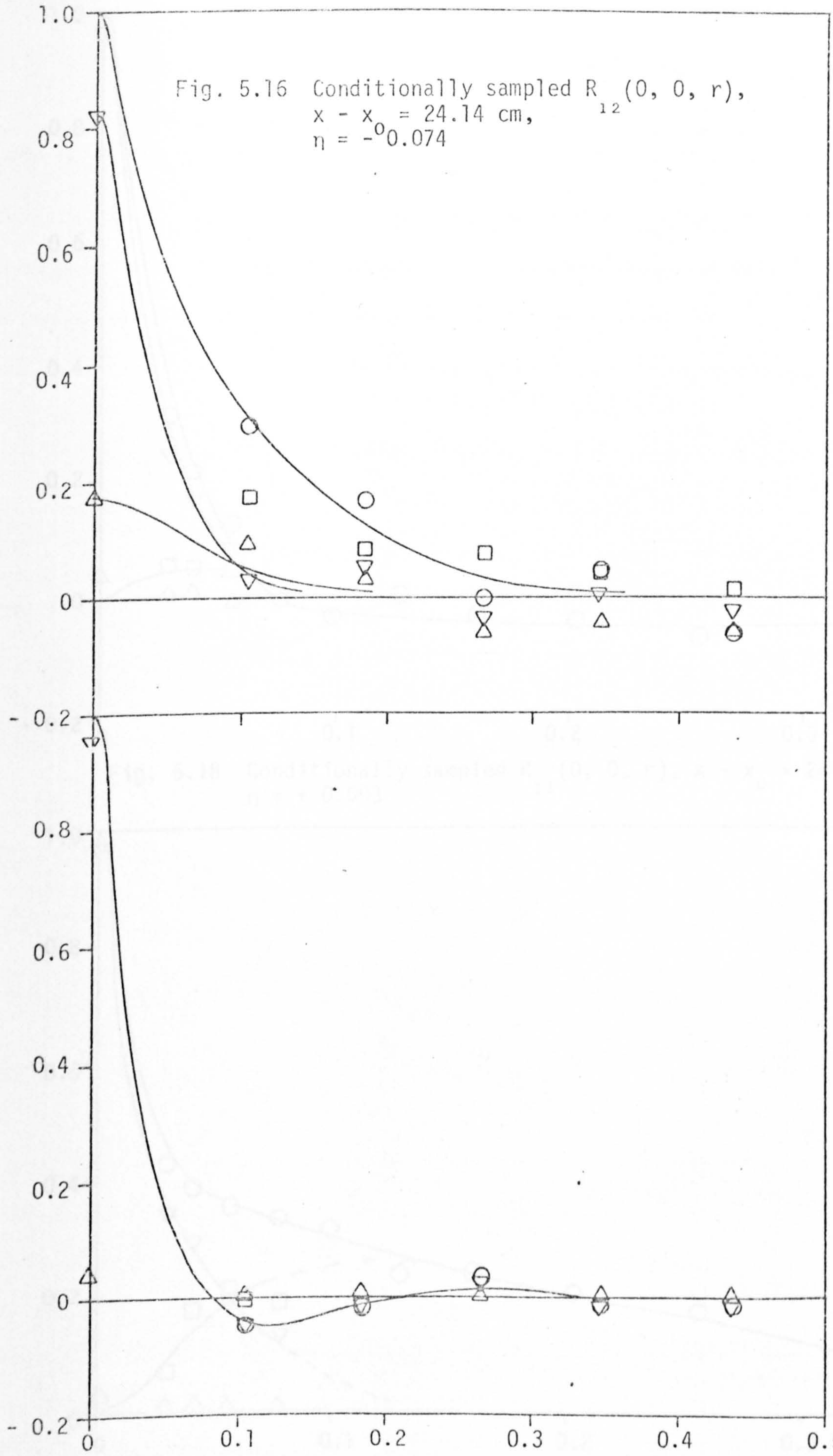


Fig. 5.16 Conditionally sampled $R_{12}(0, 0, r)$, $x - x_o = 24.14$ cm, $\eta = -0.074$

Fig. 5.17 Conditionally sampled $R_{12}(0, 0, r)$, $x - x_o = 24.14$ cm, $\eta = +0.024$

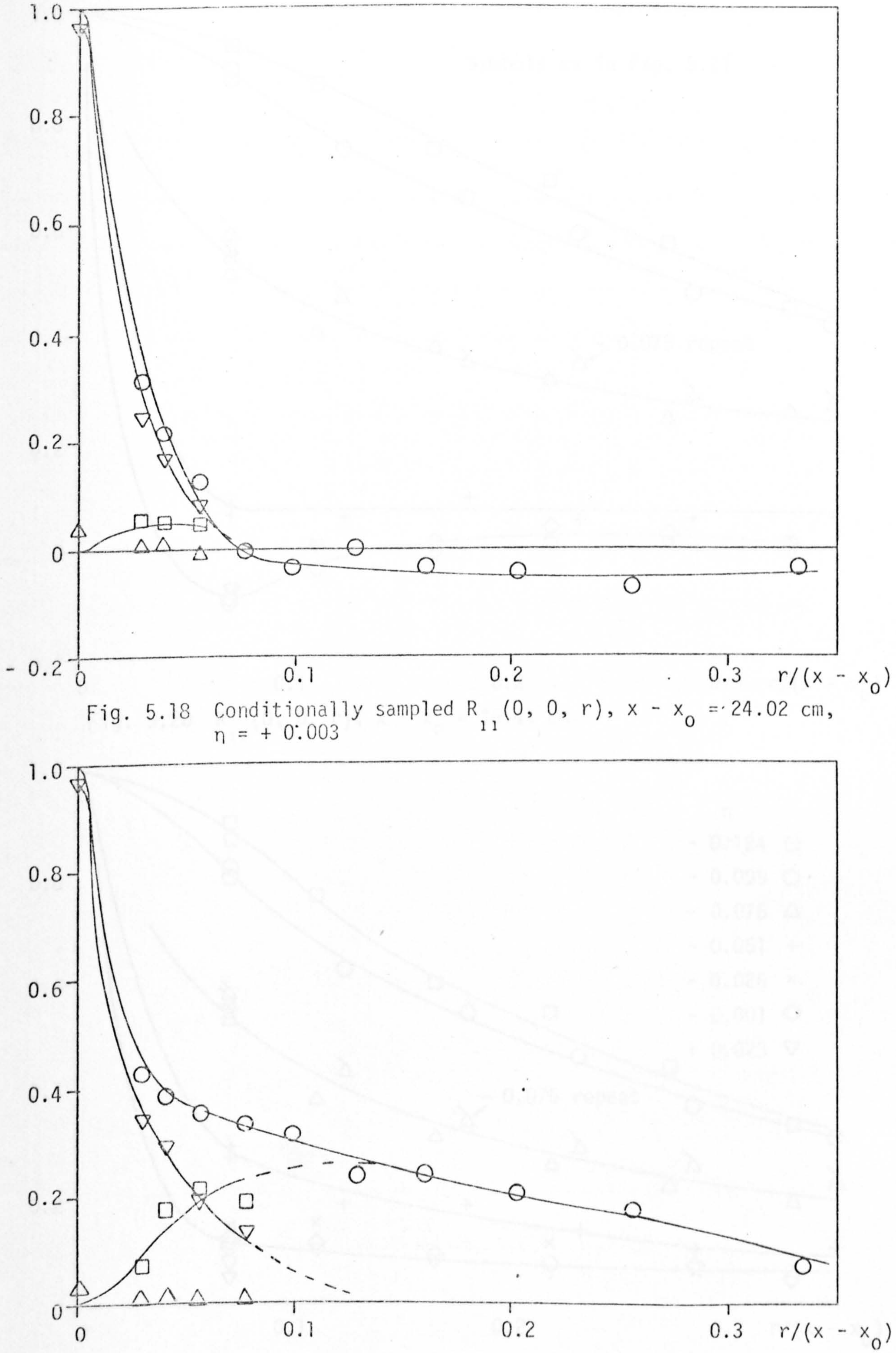


Fig. 5.18 Conditionally sampled $R_{11}(0, 0, r)$, $x - x_o = 24.02$ cm, $\eta = + 0.003$

Fig. 5.19 Conditionally sampled $R_{22}(0, r, 0)$, $x - x_o = 24.02$ cm, $\eta = + 0.003$

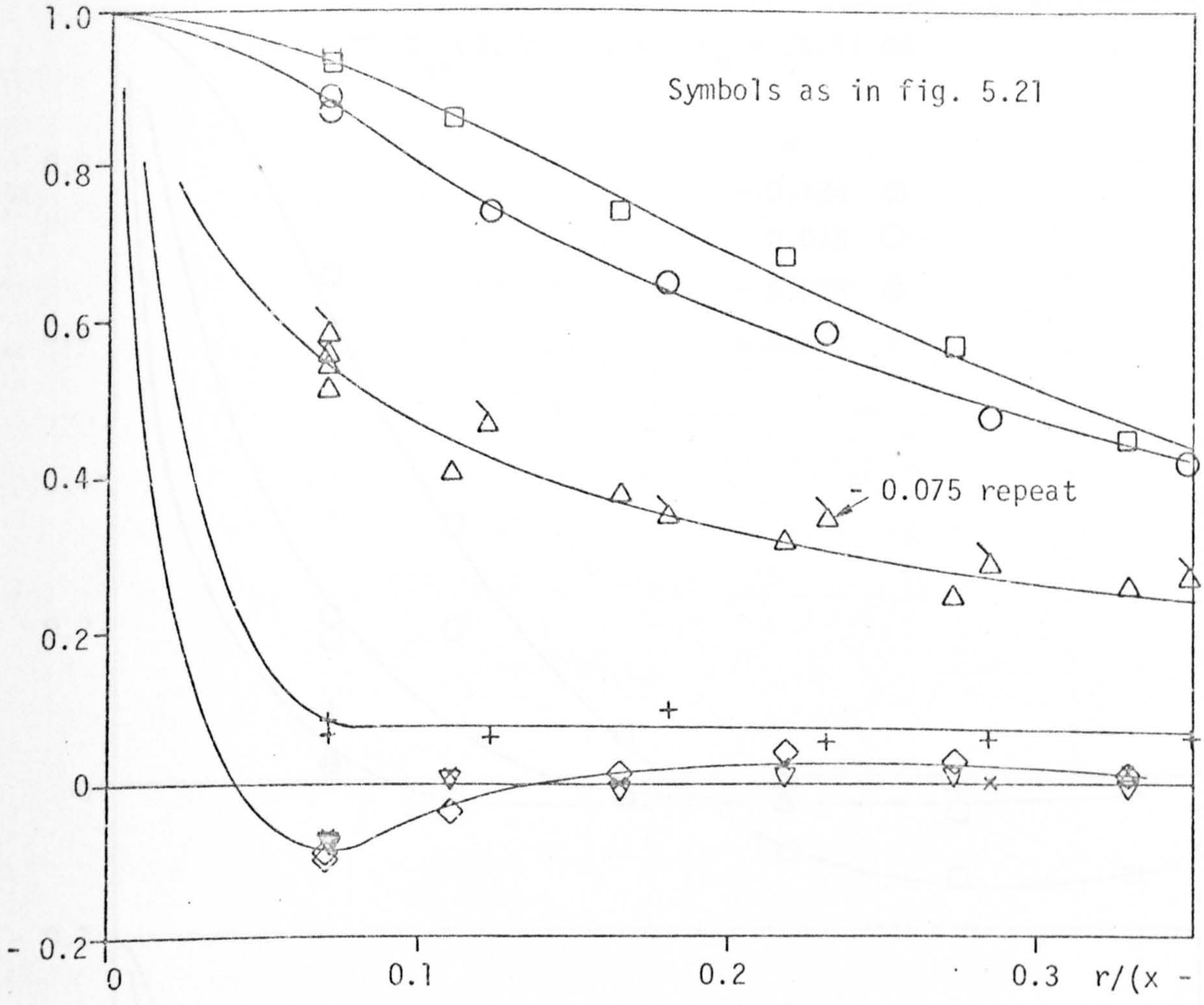


Fig. 5.20 $R_{11}(0, 0, r)$, $x - x_o = 36.41$ cm

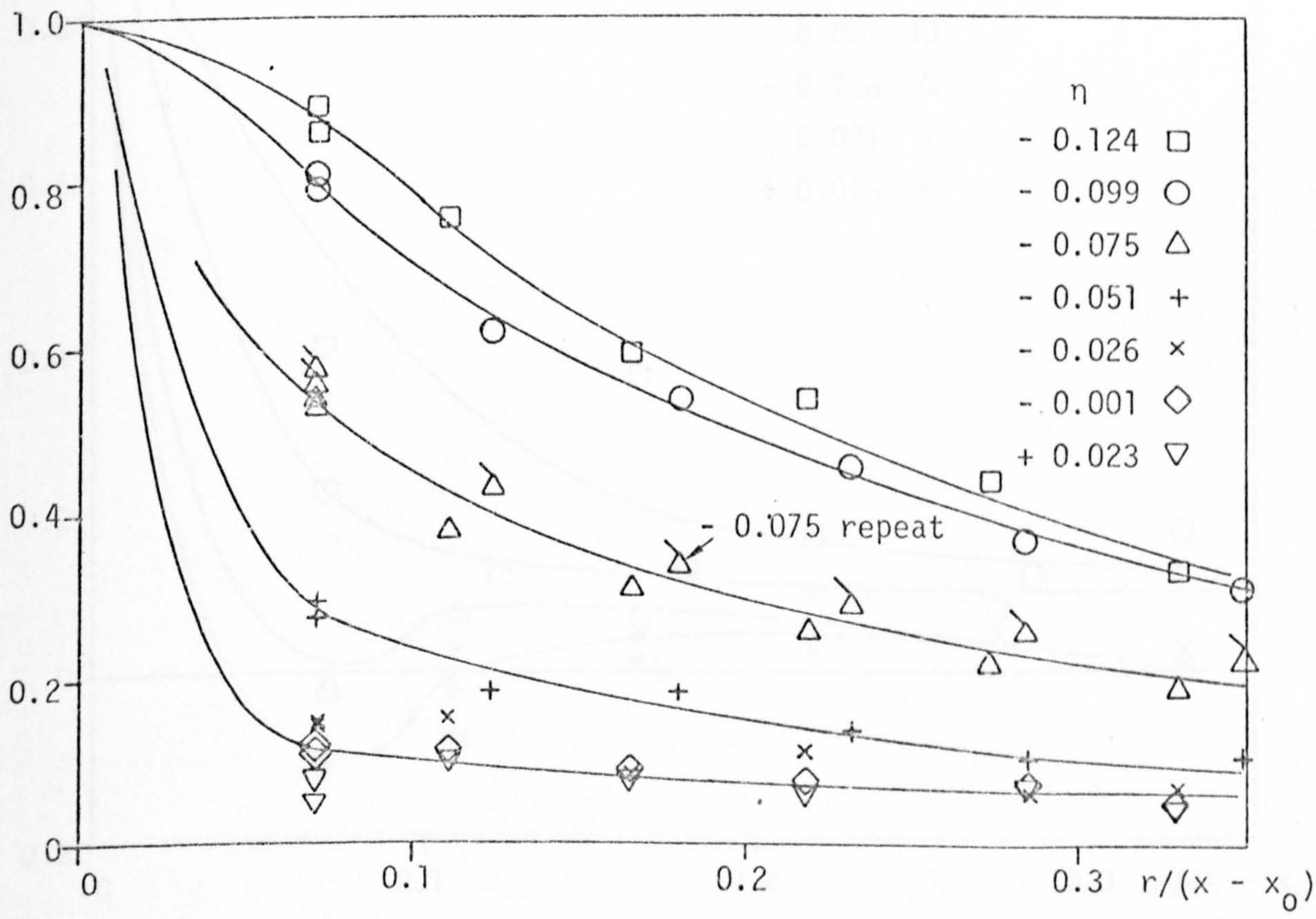


Fig. 5.21 $R_{22}(0, 0, r)$, $x - x_o = 36.41$ cm

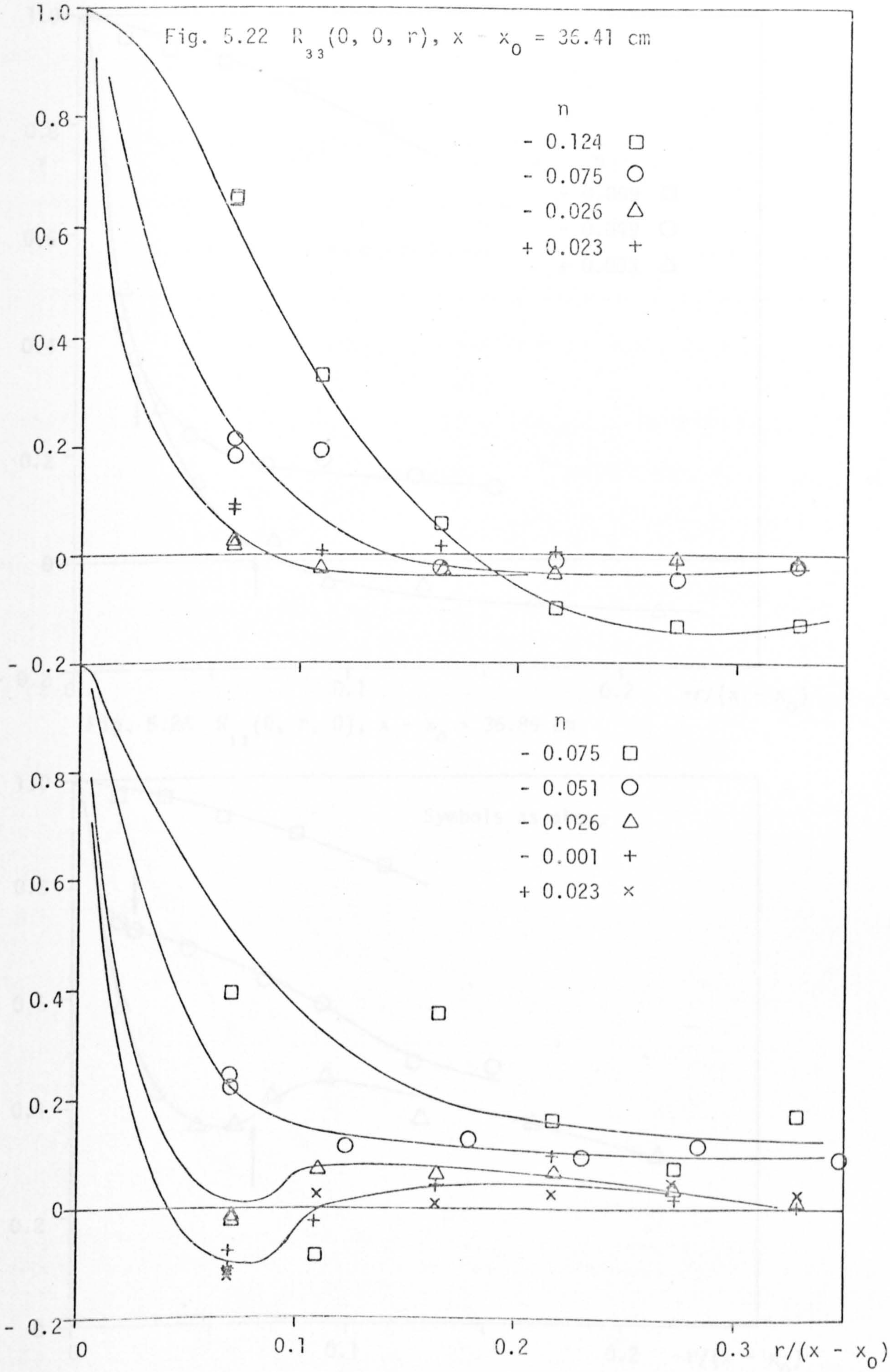


Fig. 5.22 $R_{33}(0, 0, r)$, $x - x_0 = 36.41$ cm

Fig. 5.23 $R_{12}(0, 0, r)$, $x - x_0 = 36.41$ cm

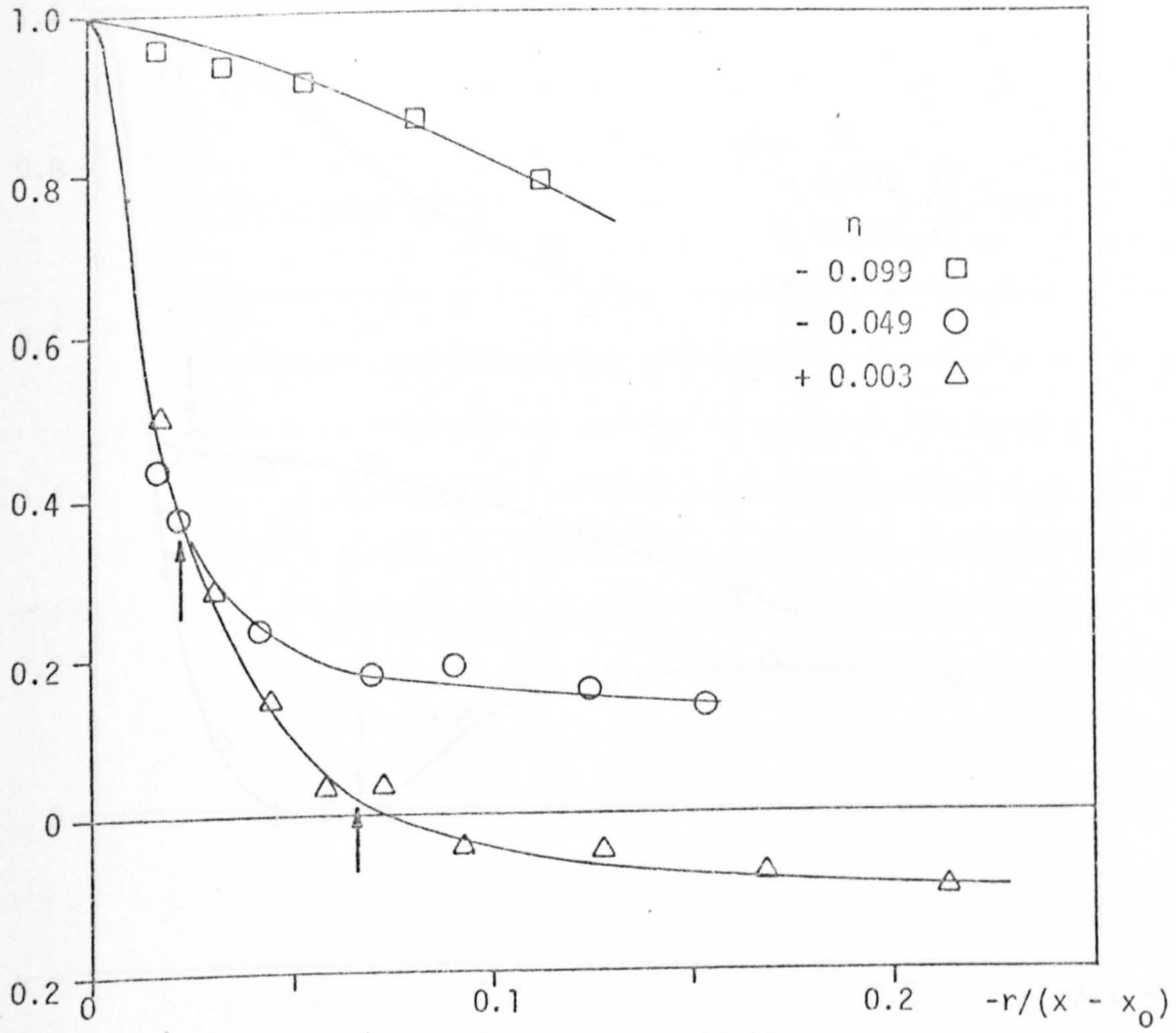


Fig. 5.24 $R_{11}(0, r, 0)$, $x - x_o$ = 36.89 cm

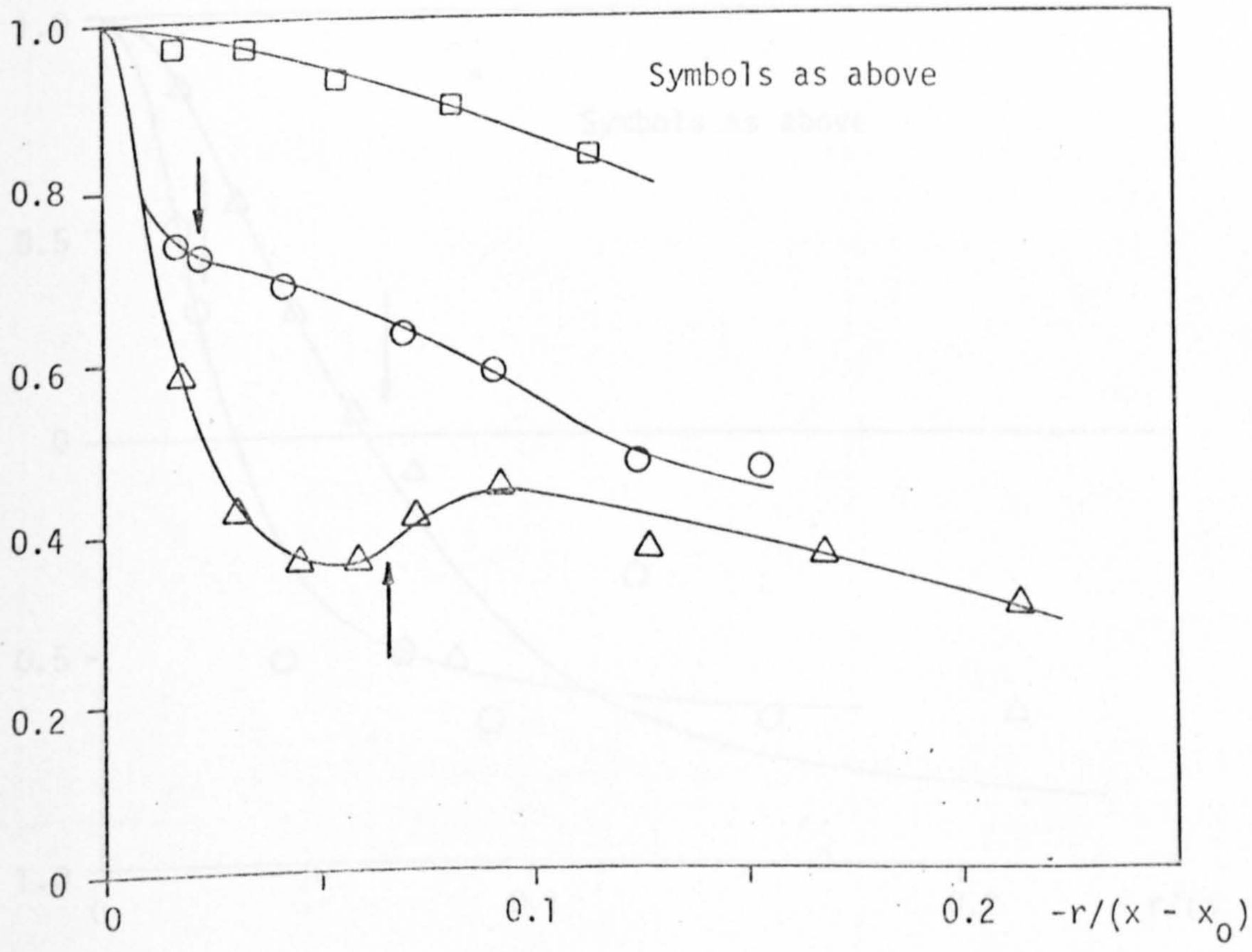


Fig. 5.25 $R_{22}(0, r, 0)$, $x - x_o$ = 36.89 cm

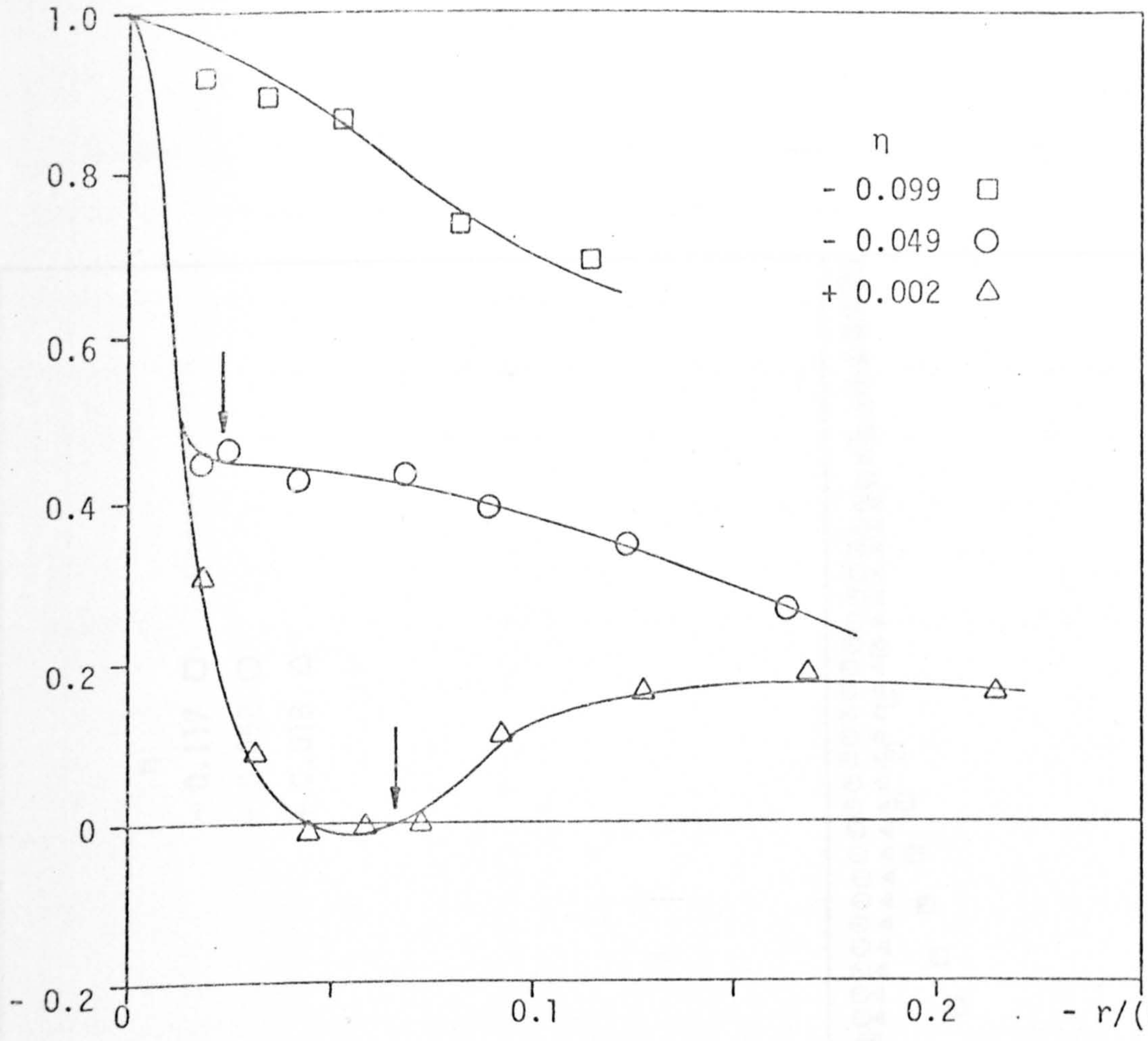


Fig. 5.26 $R_{33}(0, r, 0)$, $x - x_o = 36.89$ cm

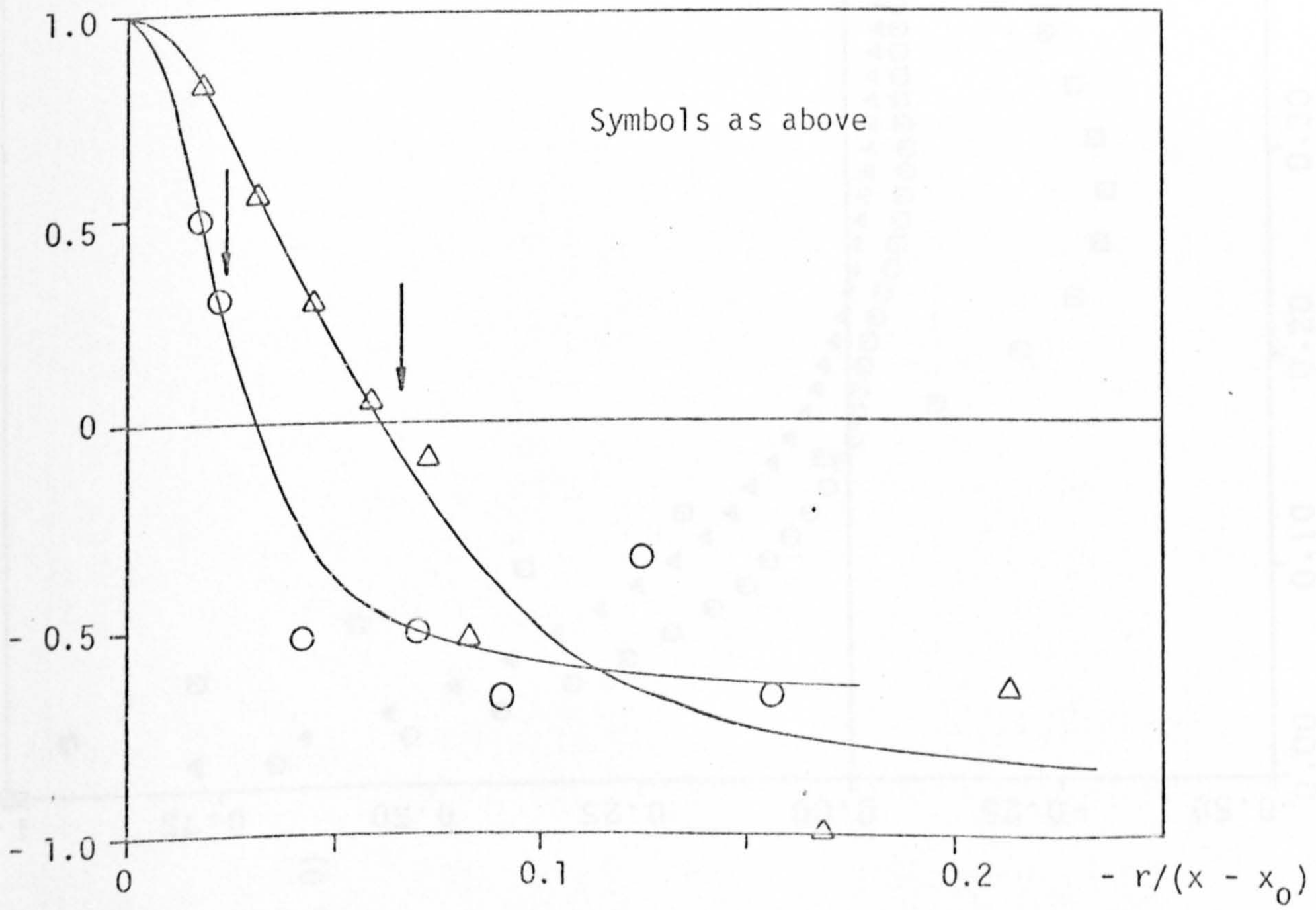


Fig. 5.27 $R_{21}(0, r, 0)$, $x - x_o = 36.89$ cm

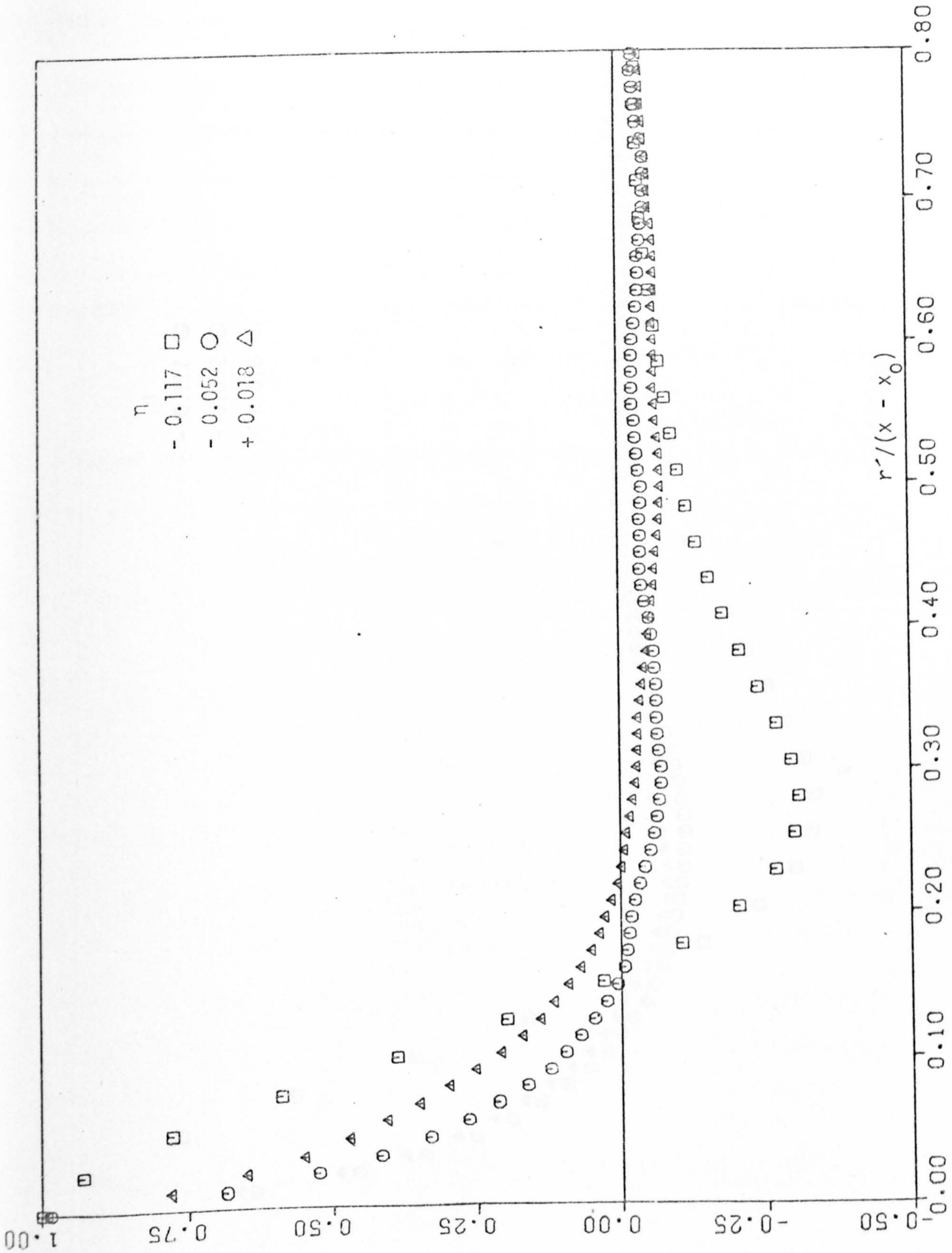


Fig. 5.23 Autocorrelation of u, x - x_o = 36.89 cm

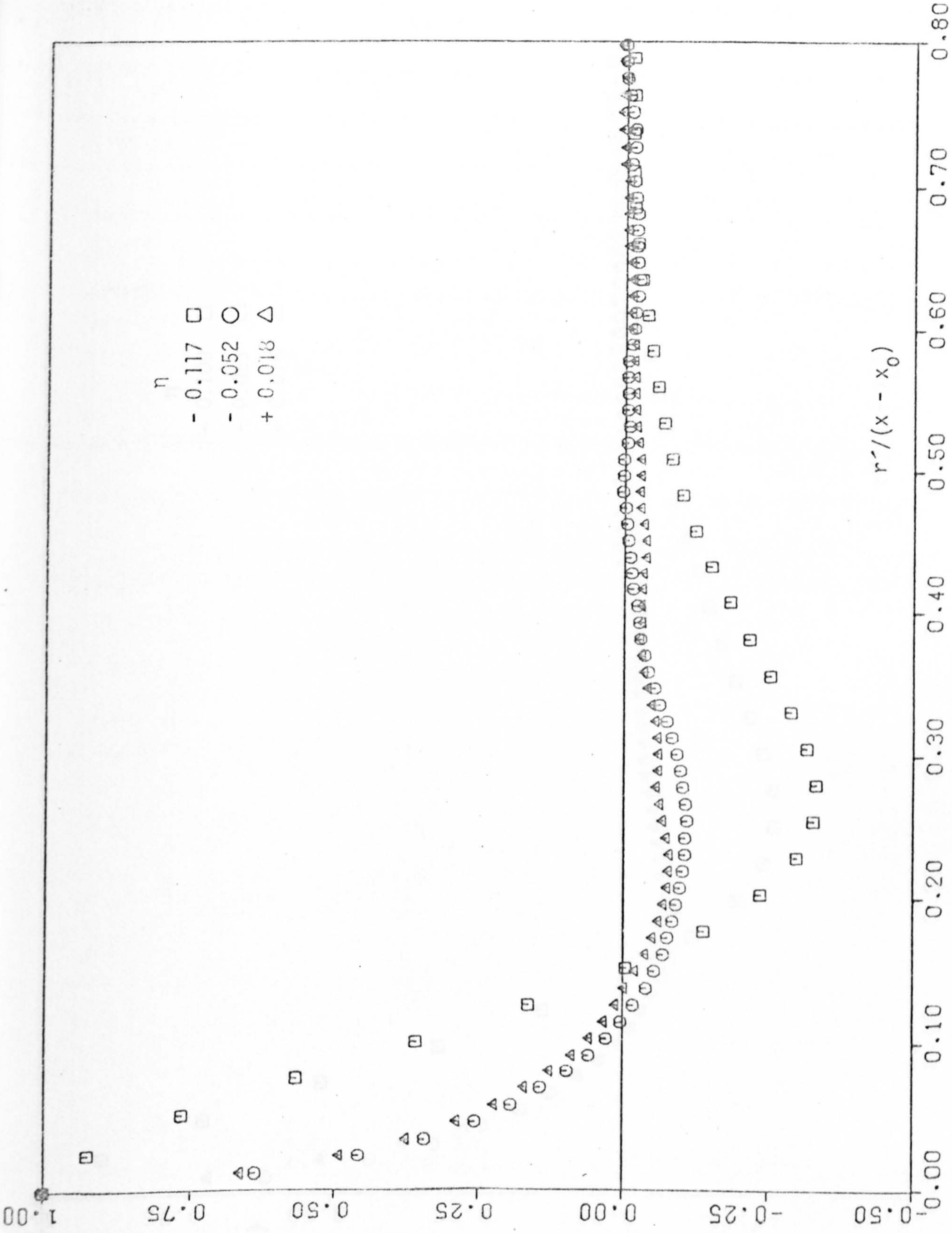


Fig. 5.29 Autocorrelation of v, x - x

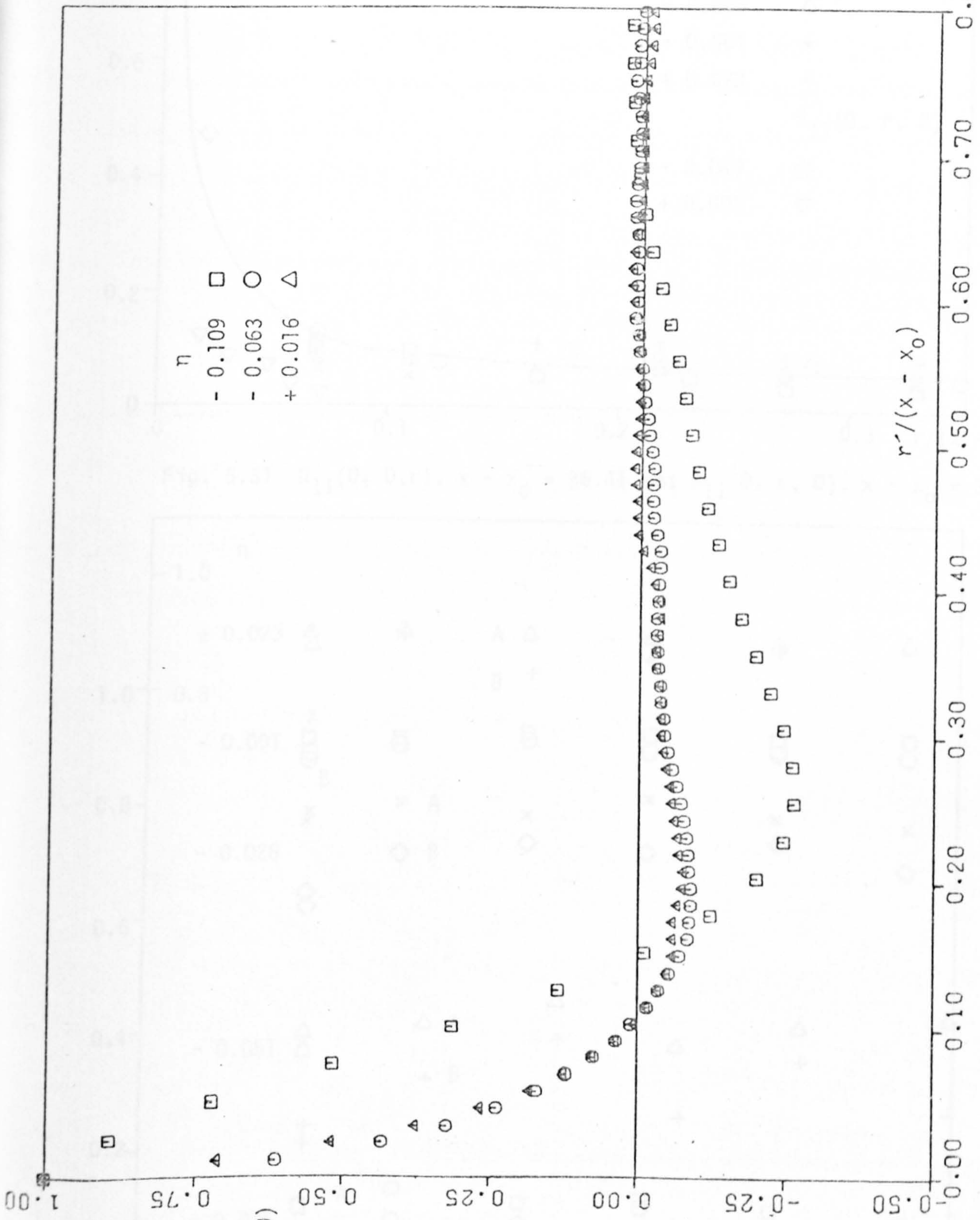


Fig. 5.30 Autocorrelation of w

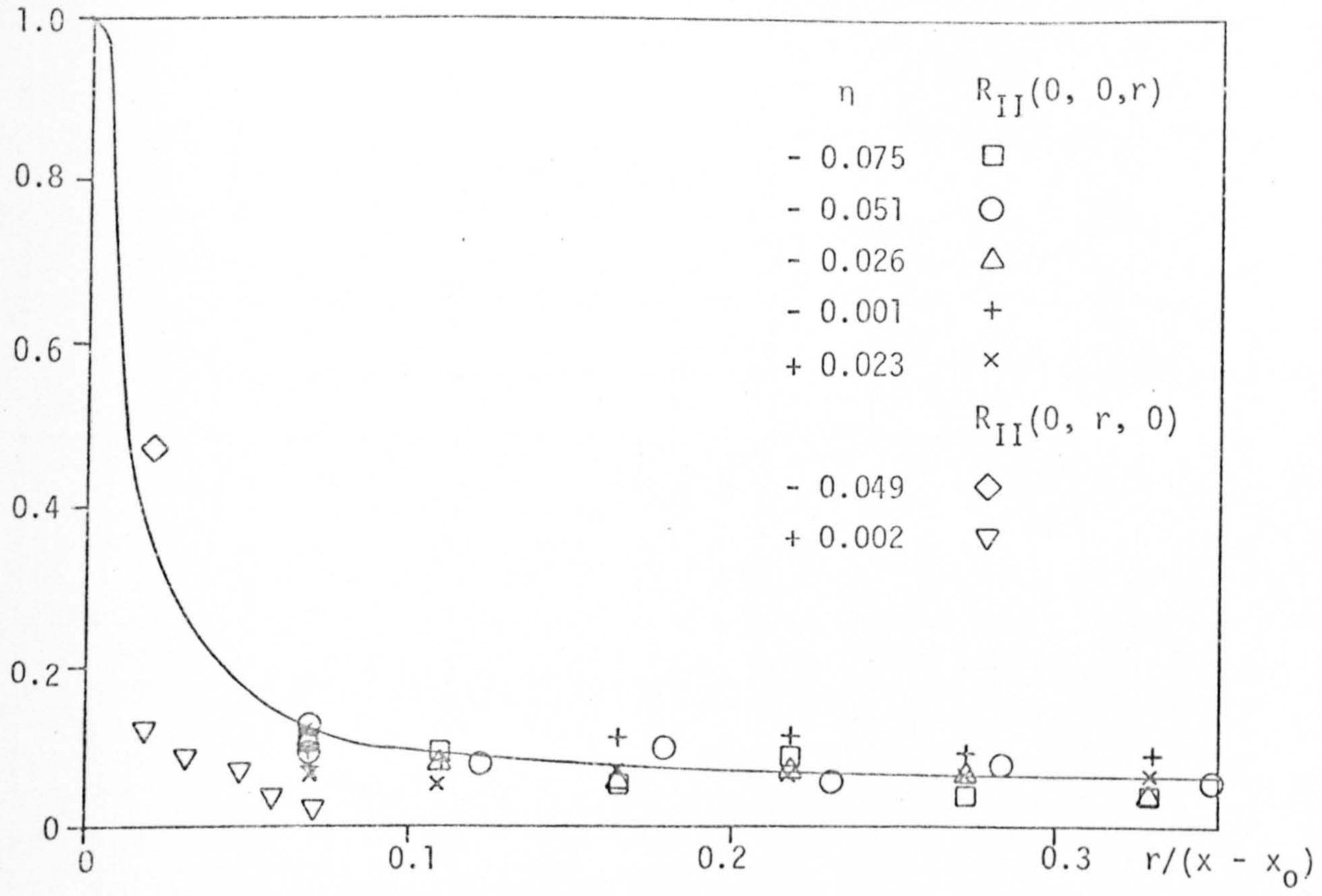


Fig. 5.31 $R_{II}(0, 0,r)$, $x - x_o$ = 36.41 cm; $R_{II}(0, r, 0)$, $x - x_o$ = 36.89 cm

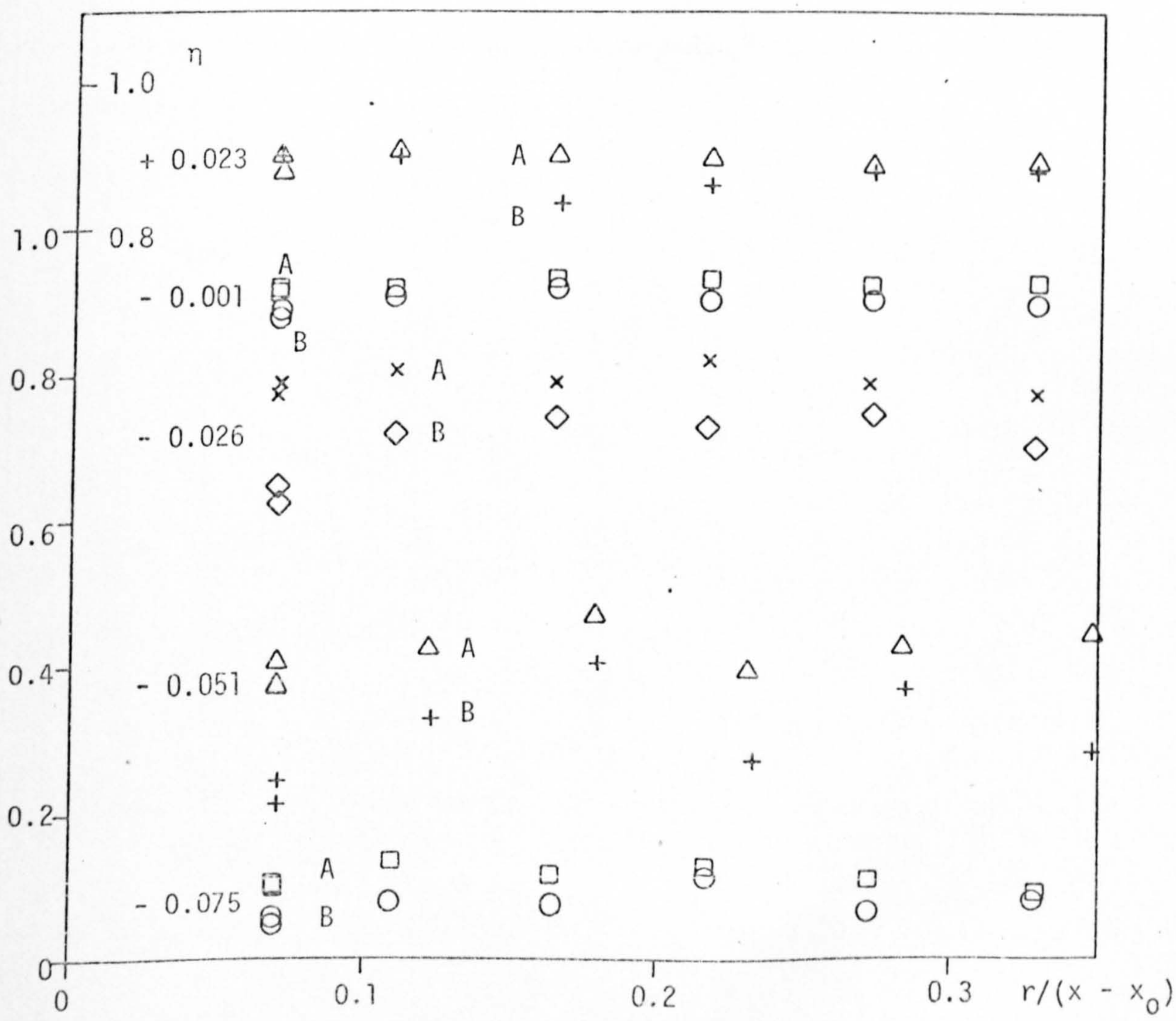


Fig. 5.32 Variation of γ_A and γ_B, $x - x_o$ = 36.41 cm

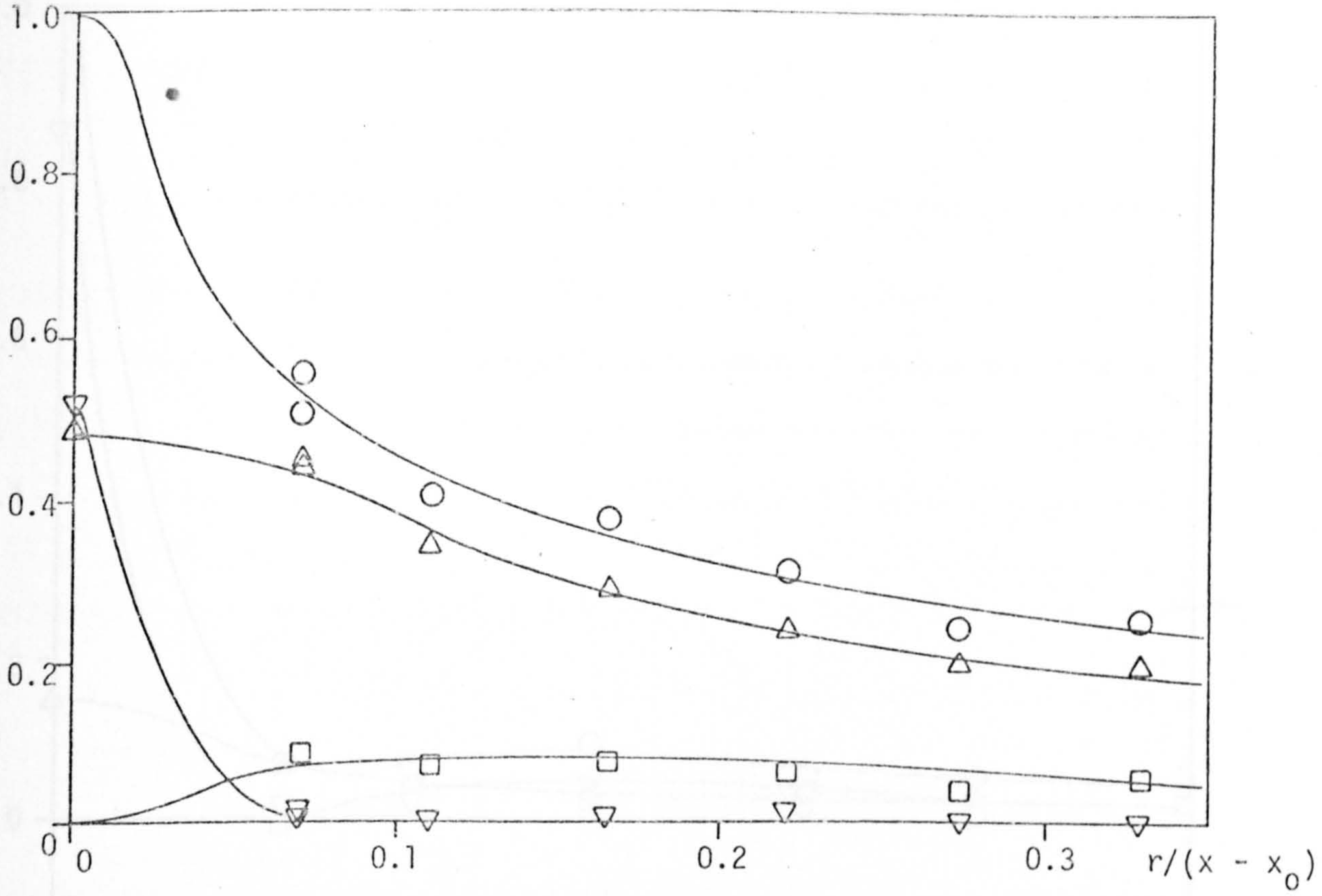


Fig. 5.33 Conditionally sampled $R_{11}(0, 0, r)$, $x - x_o = 36.41$ cm, $\eta = -0.075$

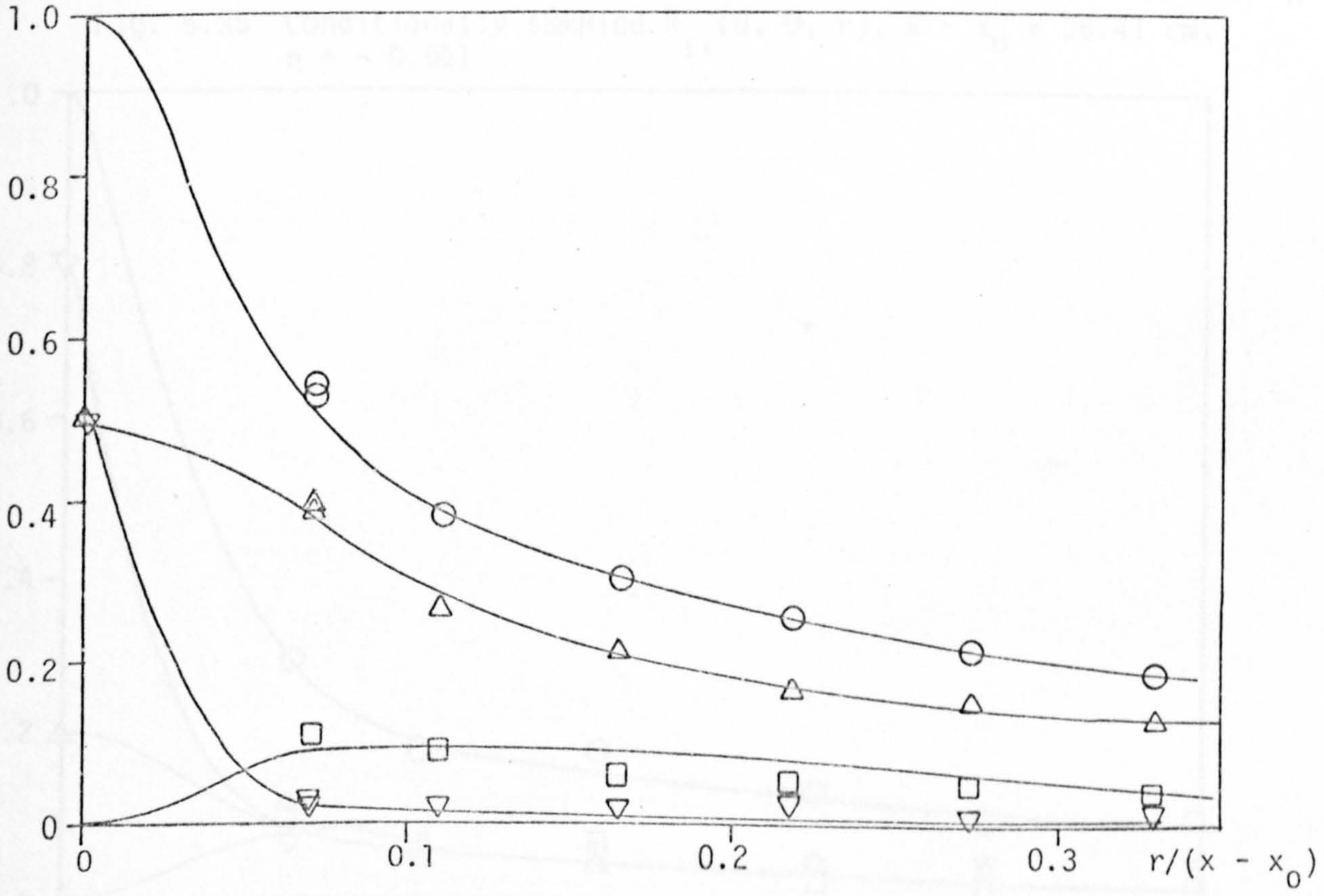


Fig. 5.34 Conditionally sampled $R_{22}(0, 0, r)$, $x - x_o = 36.41$ cm, $\eta = -0.075$

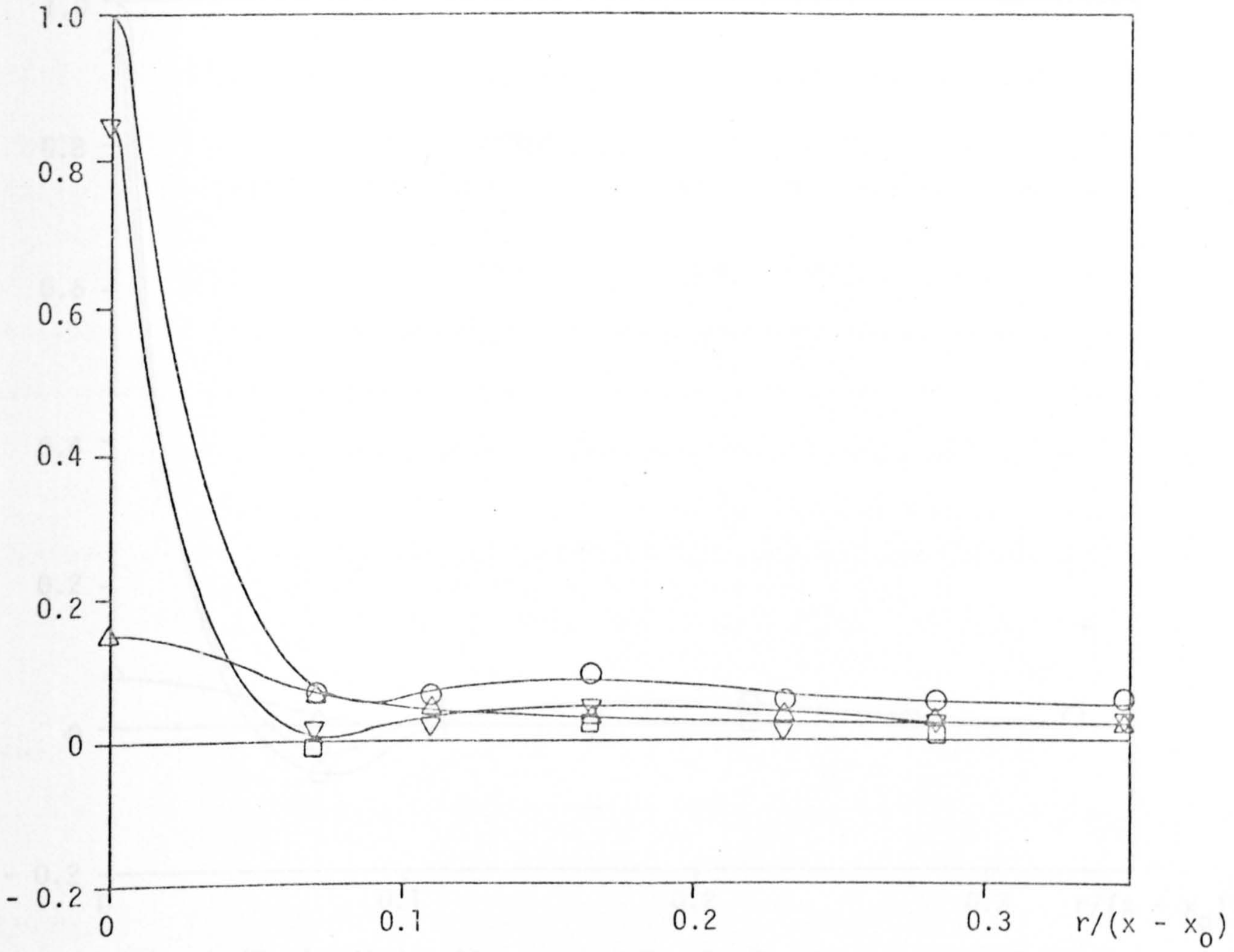


Fig. 5.35 Conditionally sampled $R_{11}(0, 0, r)$, $x - x_o = 36.41$ cm, $\eta = -0.051$

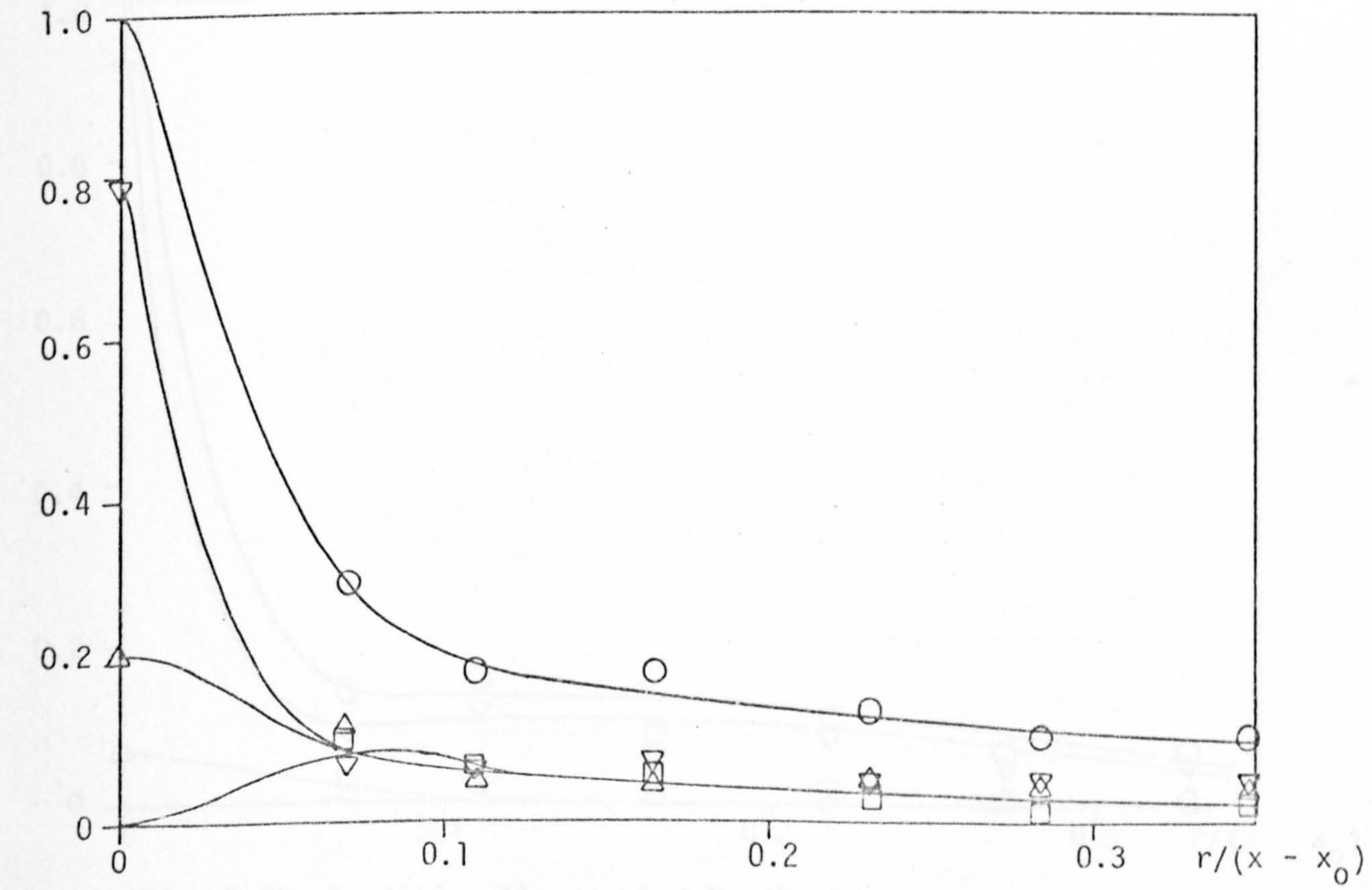


Fig. 5.36 Conditionally sampled $R_{22}(0, 0, r)$, $x - x_o = 36.41$ cm, $\eta = -0.051$

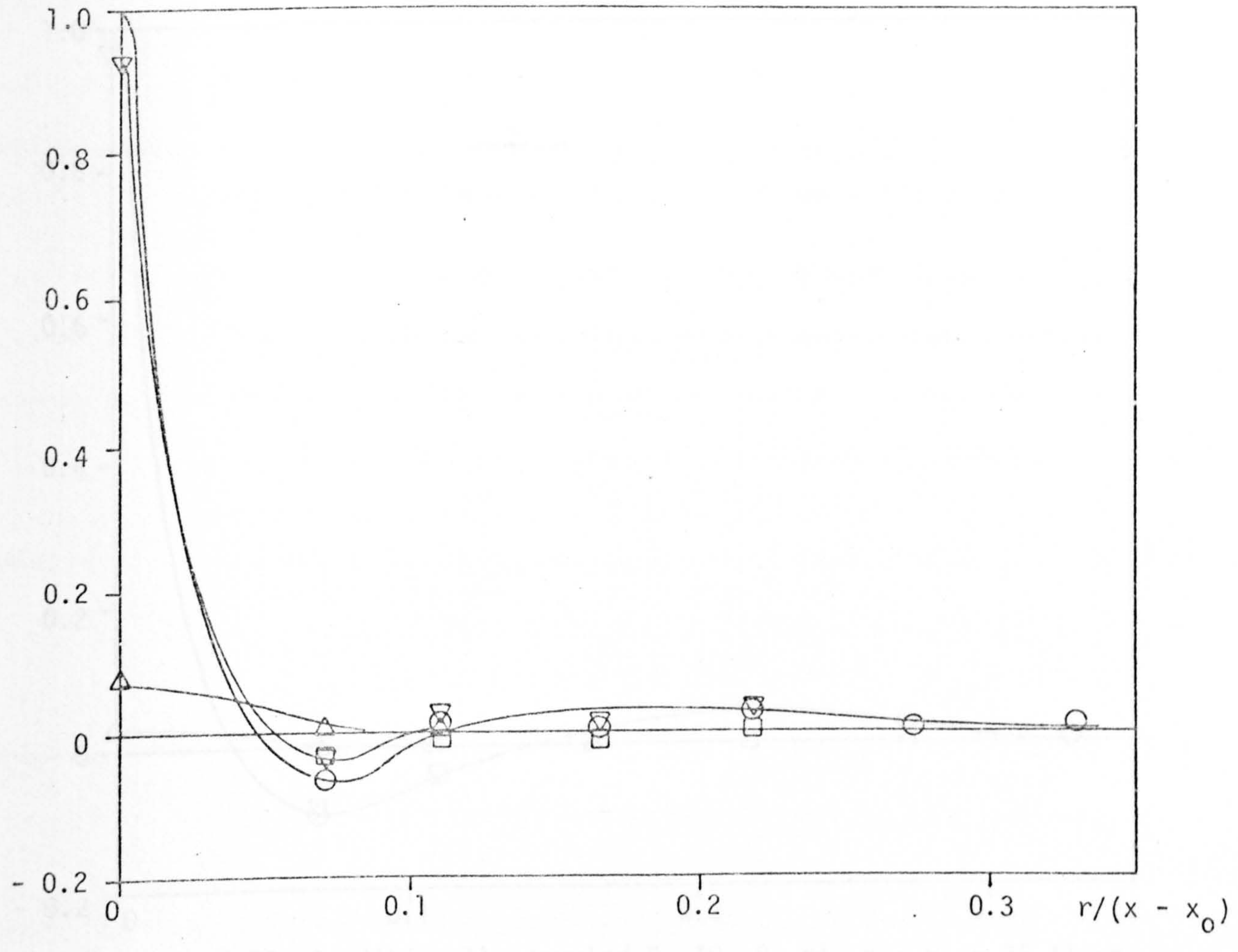


Fig. 5.37 Conditionally sampled $R_{11}(0, 0, r)$, $x - x_o = 36.41$ cm, $\eta = -0.026$

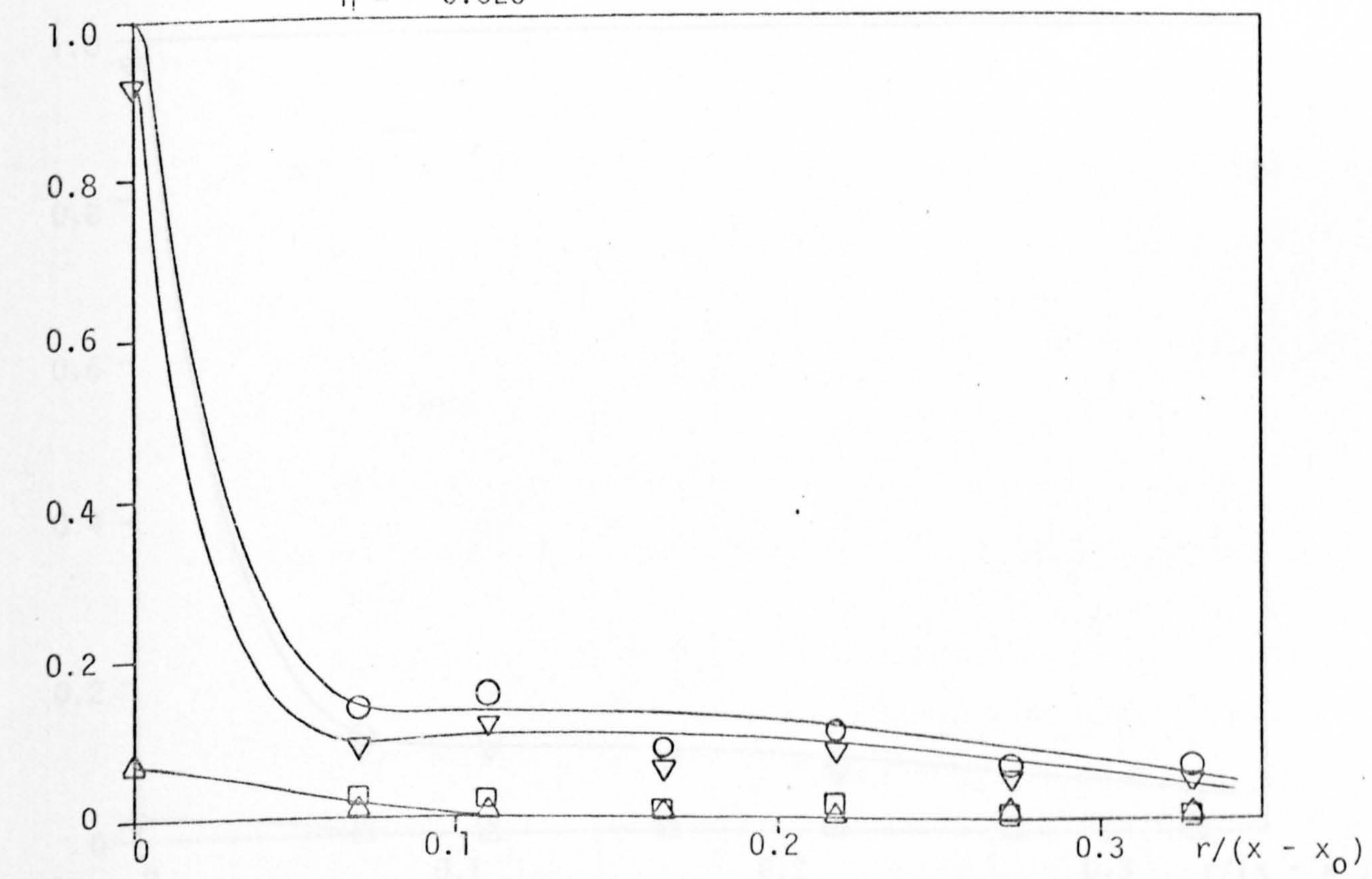


Fig. 5.38 Conditionally sampled $R_{22}(0, 0, r)$, $x - x_o = 36.41$ cm, $\eta = -0.026$

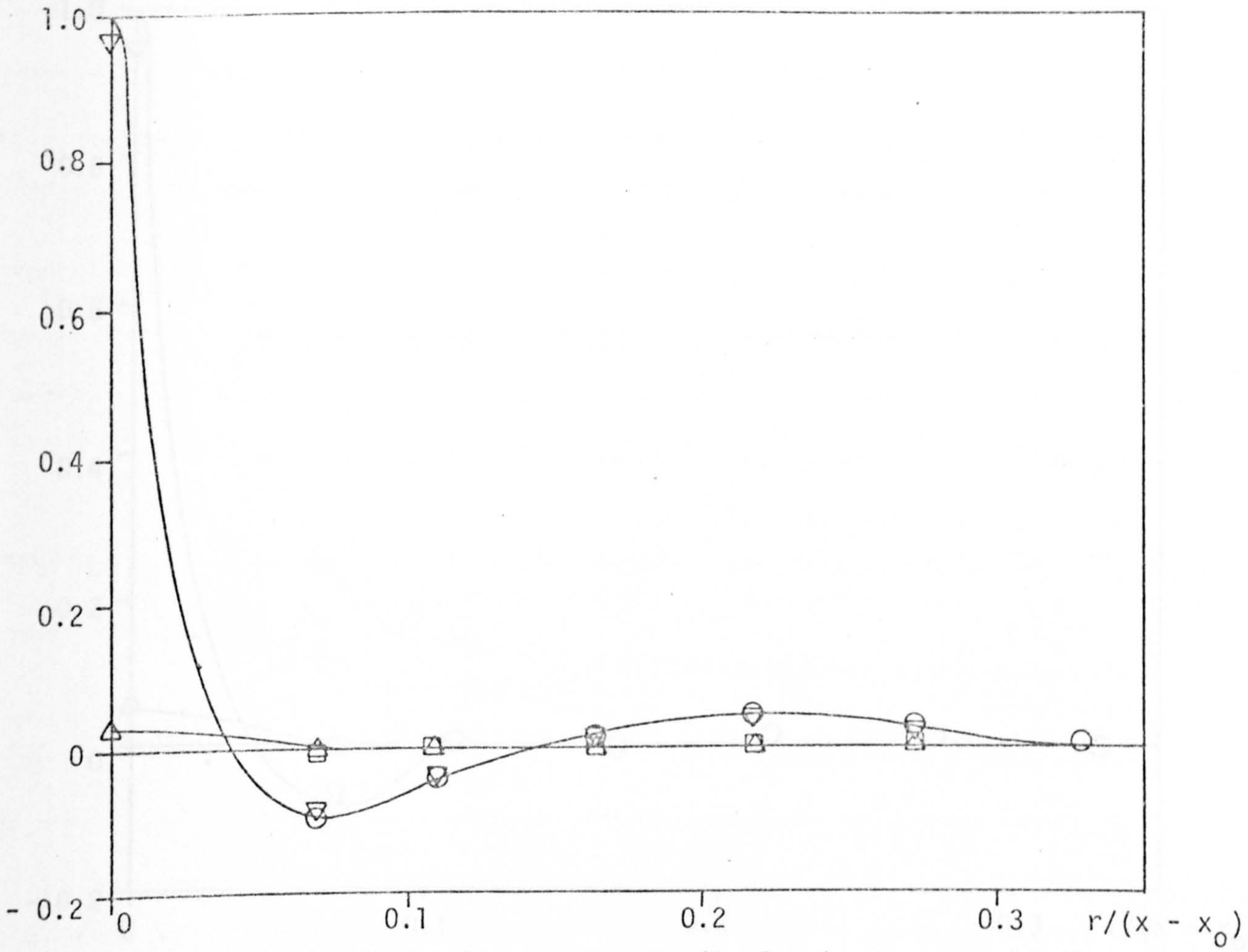


Fig. 5.39 Conditionally sampled $R_{11}(0, 0, r)$, $x - x_o = 36.41$ cm, $\eta = -0.001$

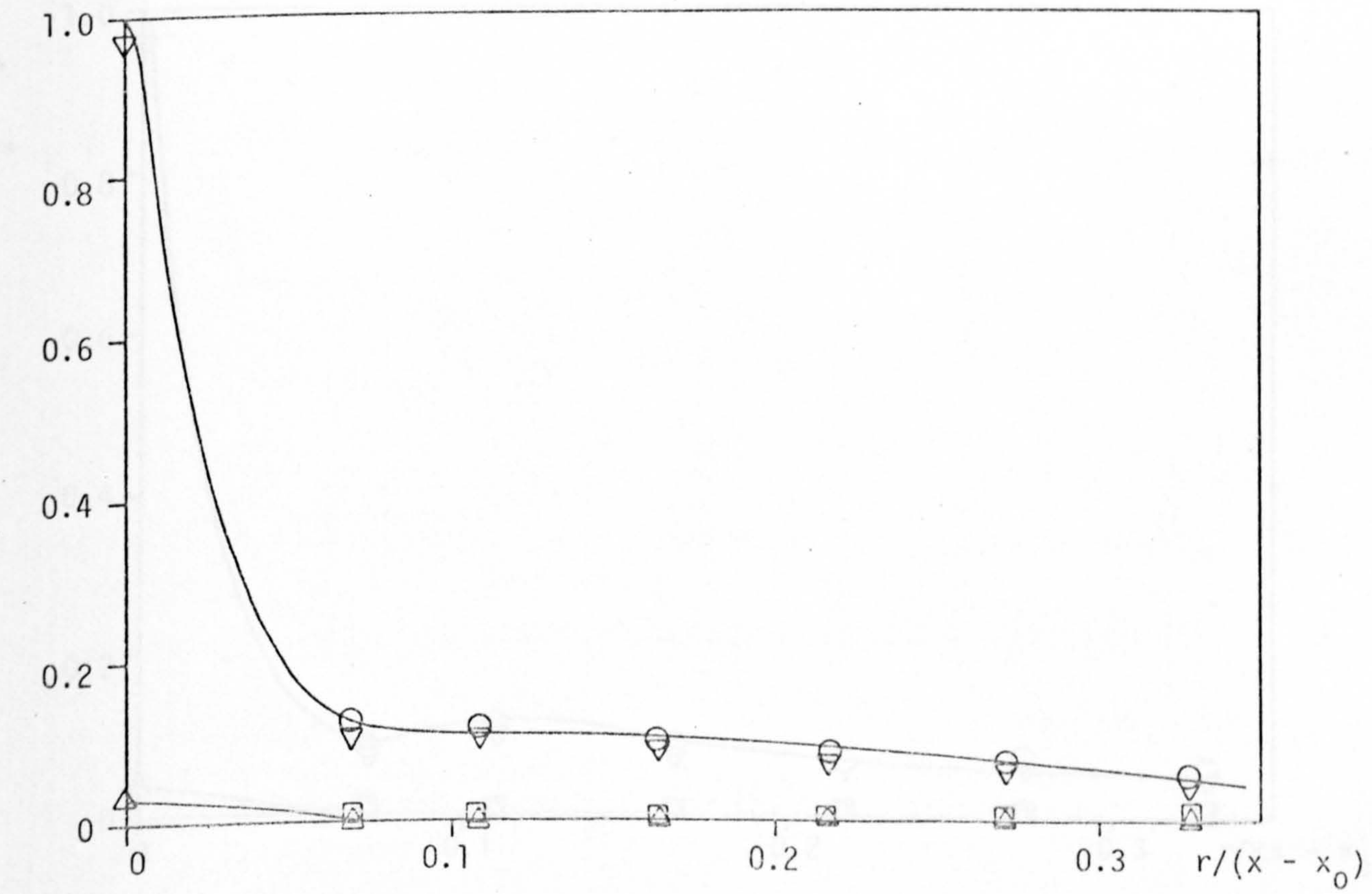


Fig. 5.40 Conditionally sampled $R_{22}(0, 0, r)$, $x - x_o = 36.41$ cm, $\eta = -0.001$

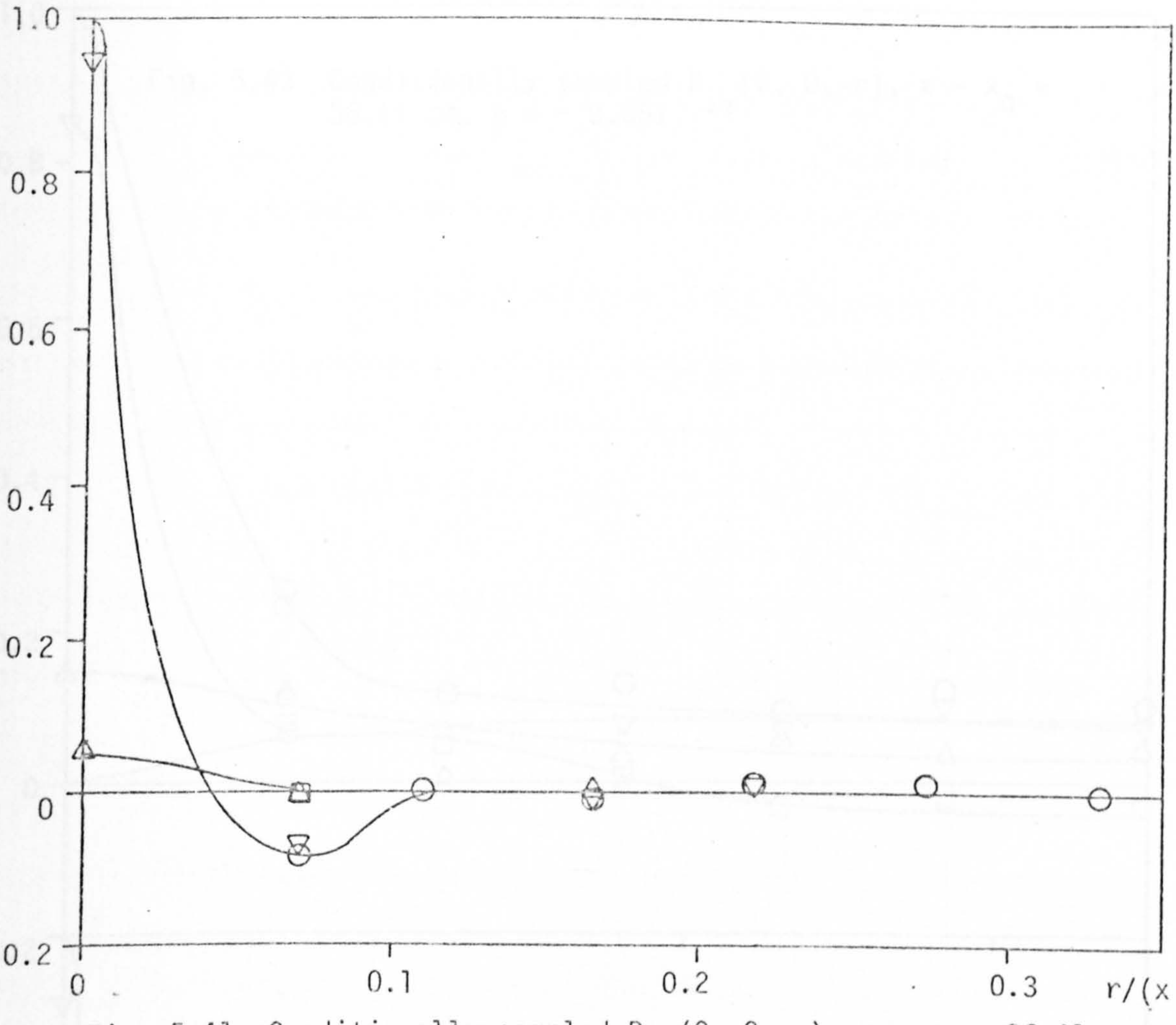


Fig. 5.41 Conditionally sampled $R_{11}(0, 0, r)$, $x - x_o = 36.41$ cm, $\eta = + 0.023$

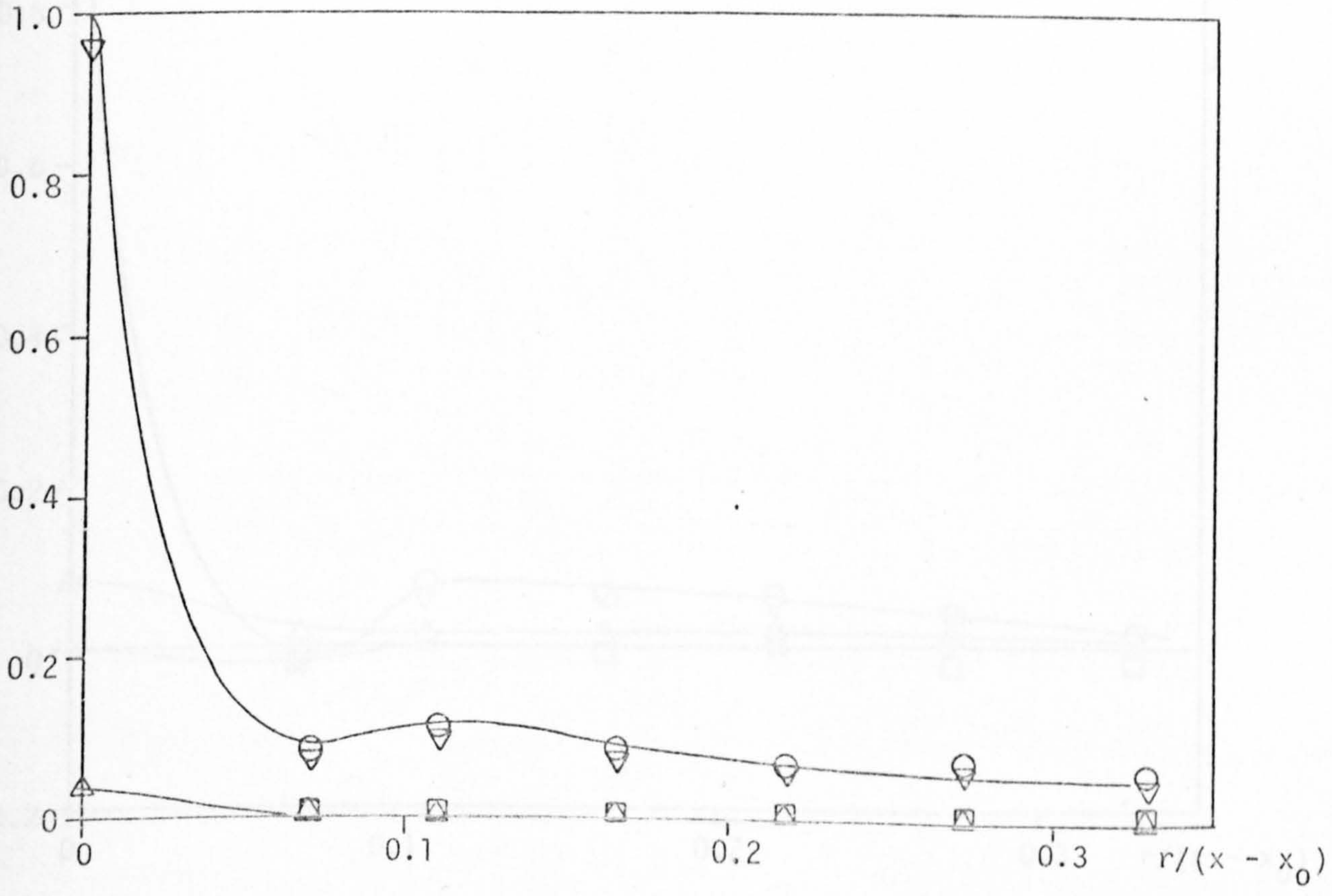


Fig. 5.42 Conditionally sampled $R_{22}(0, 0, r)$, $x - x_o = 36.41$ cm, $\eta = + 0.023$

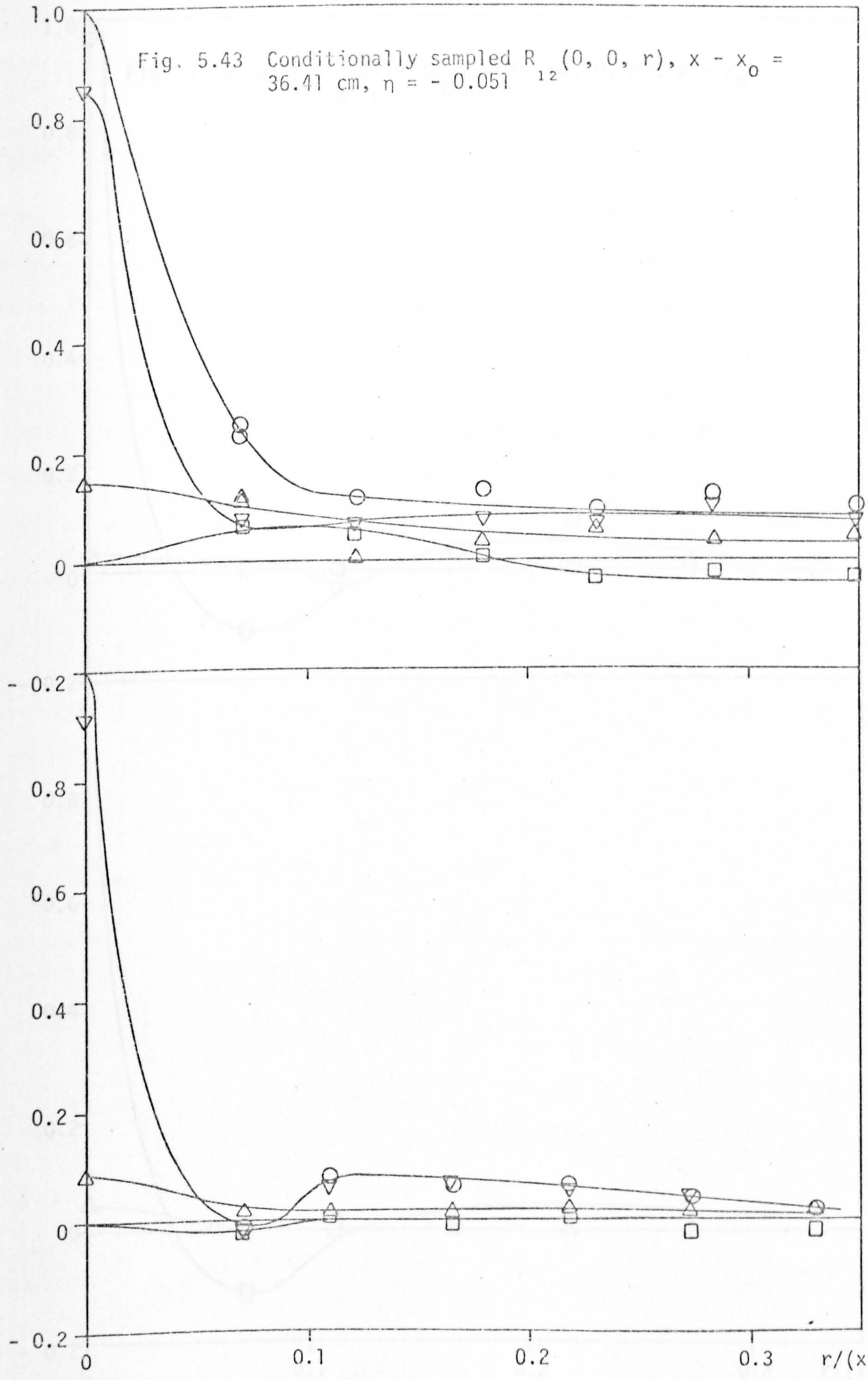


Fig. 5.43 Conditionally sampled $R_{12}(0, 0, r)$, $x - x_o$ = 36.41 cm, η = - 0.051

Fig. 5.44 Conditionally sampled $R_{12}(0, 0, r)$, $x - x_o$ = 36.41 cm, η = - 0.026

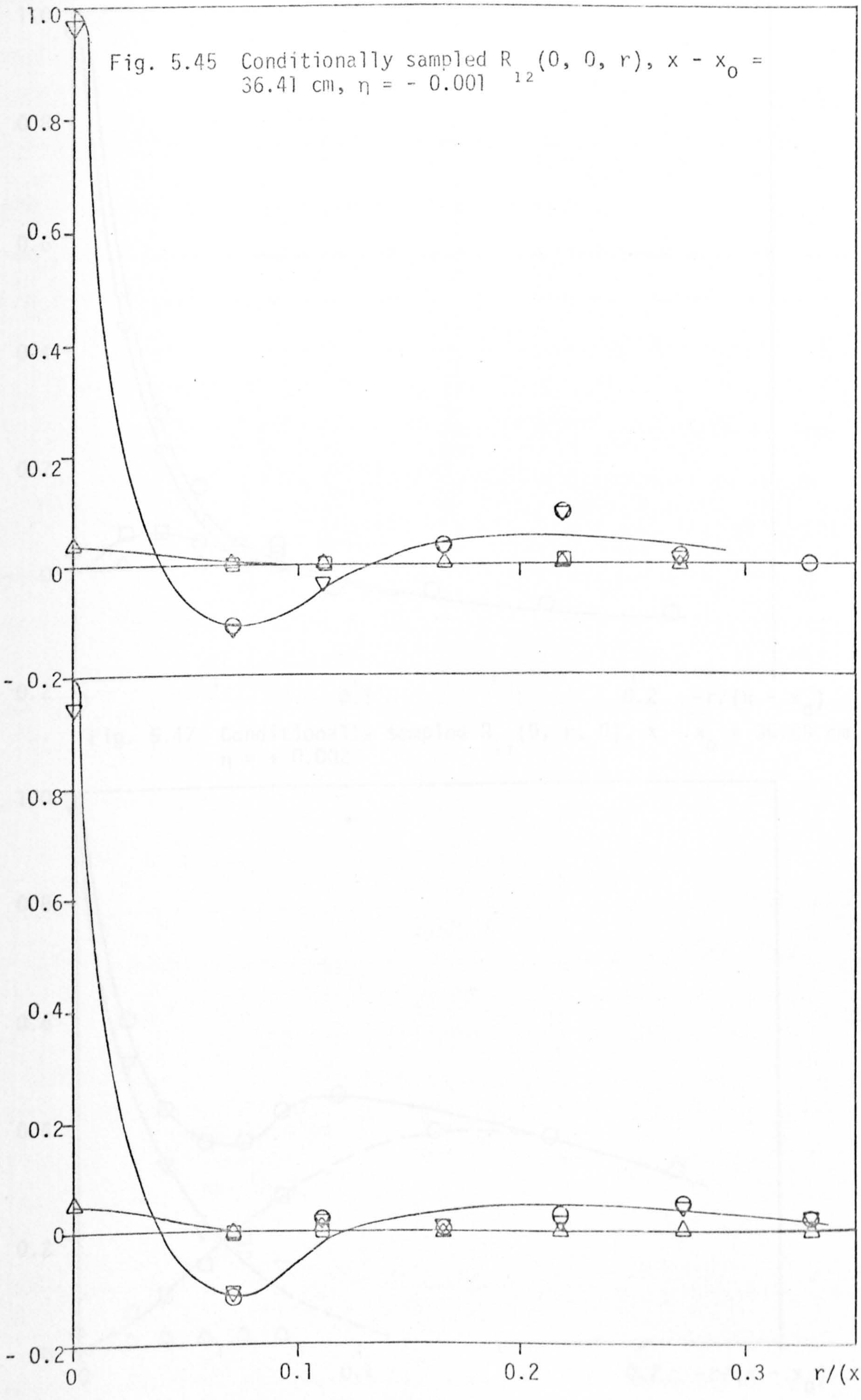


Fig. 5.45 Conditionally sampled $R_{12}(0, 0, r)$, $x - x_0$ = 36.41 cm, η = - 0.001

Fig. 5.46 Conditionally sampled $R_{12}(0, 0, r)$, $x - x_0$ = 36.41 cm, η = + 0.023

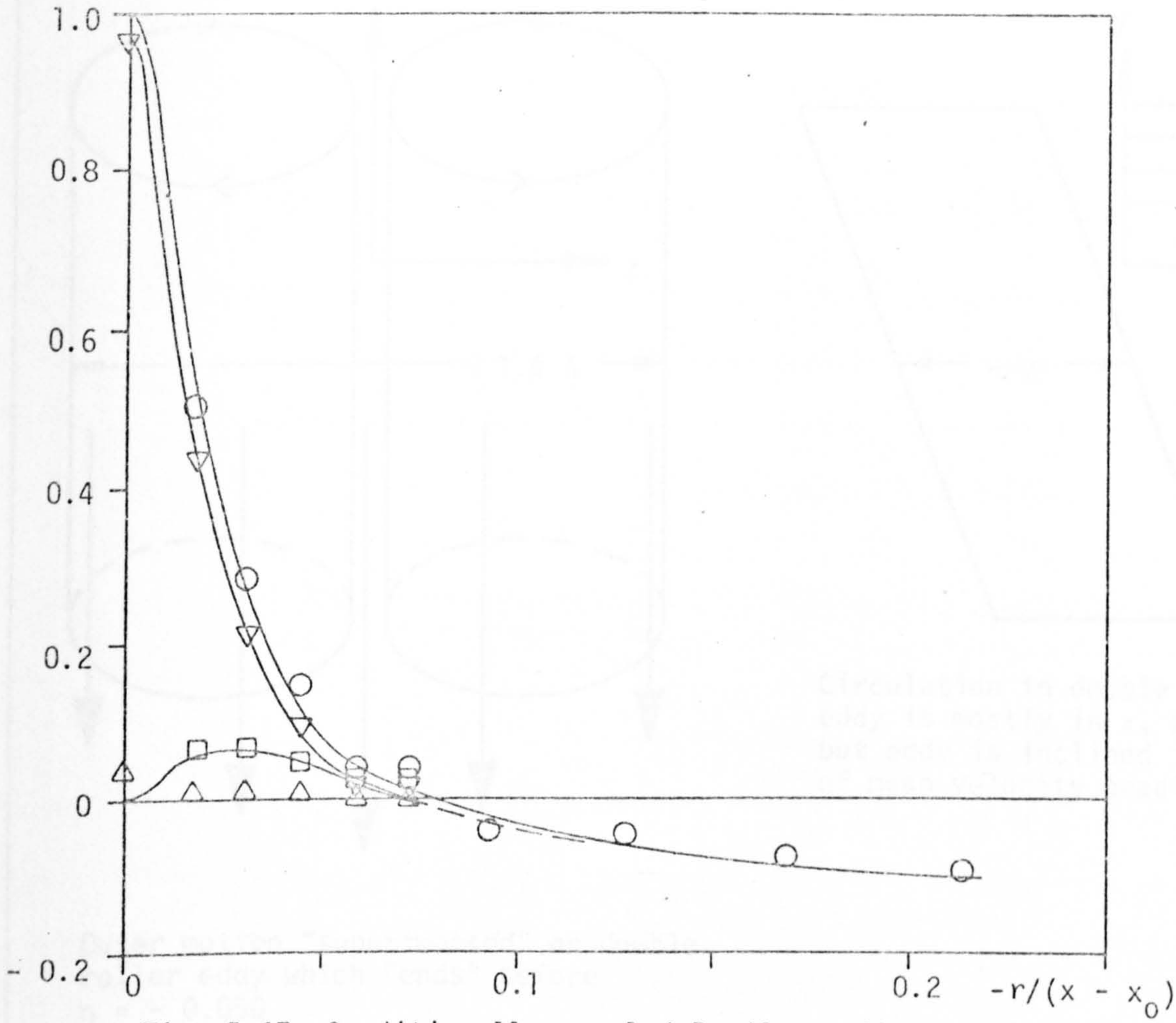


Fig. 5.47 Conditionally sampled $R_{11}(0, r, 0)$, $x - x_o = 36.89$ cm, $\eta = + 0.002$

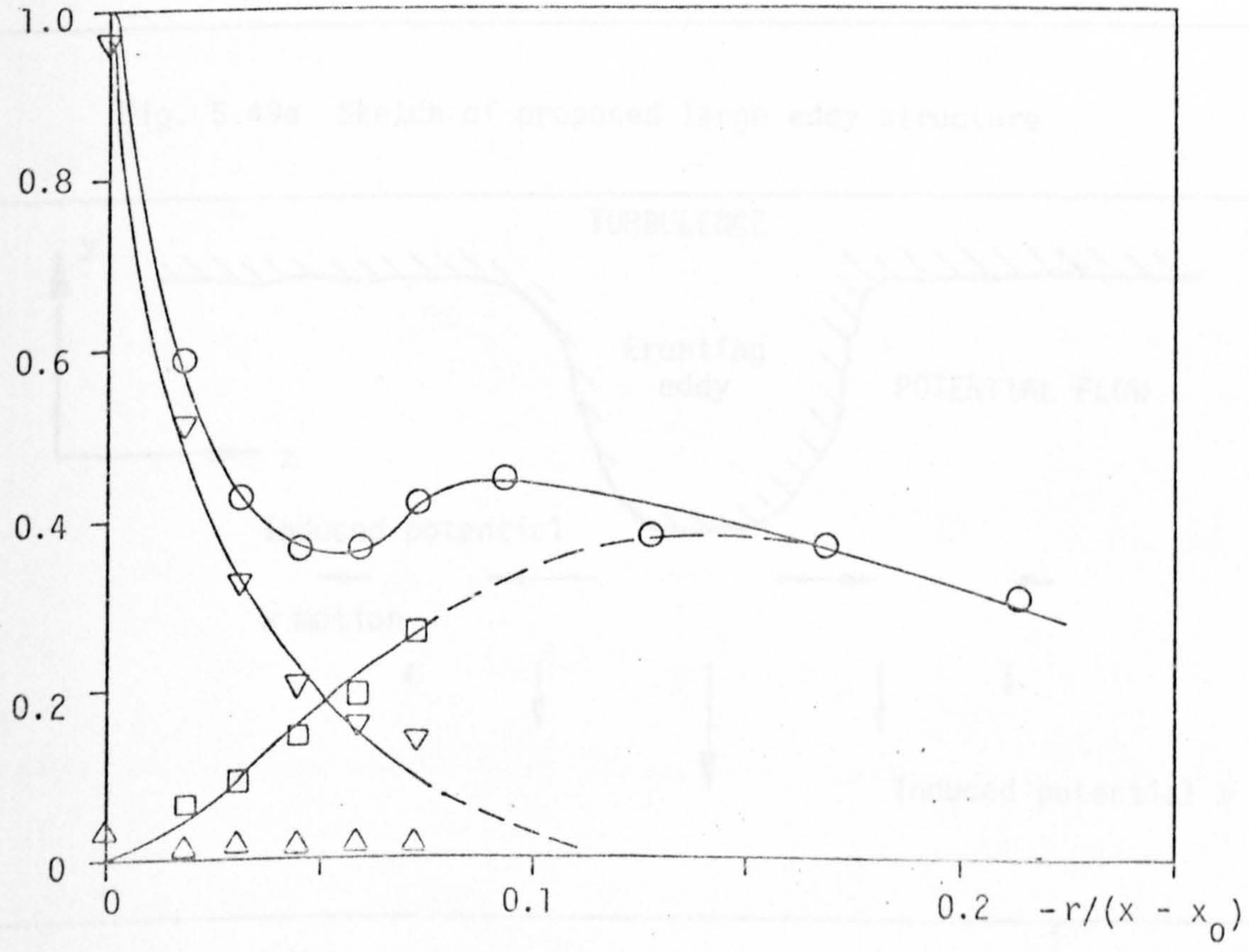
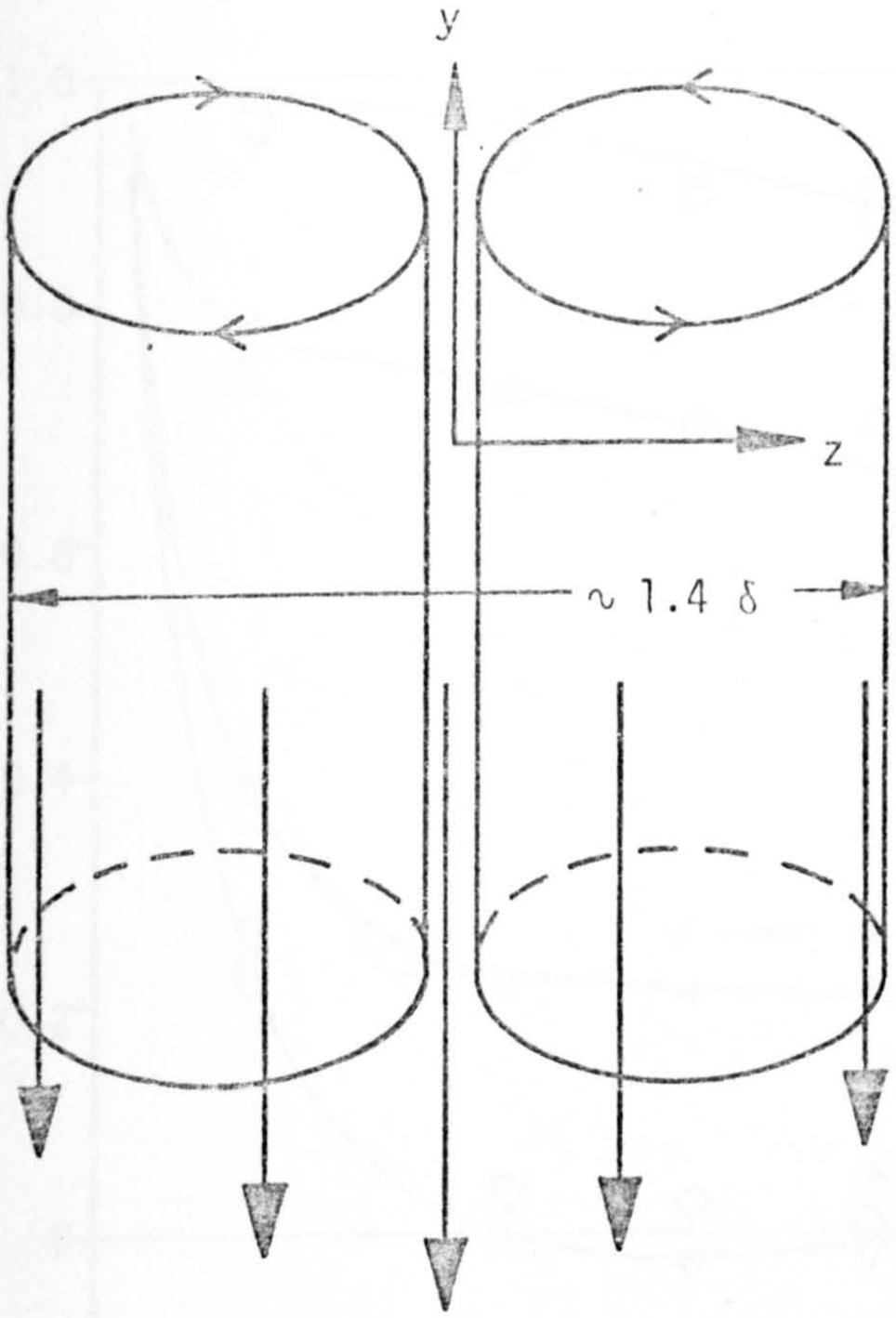
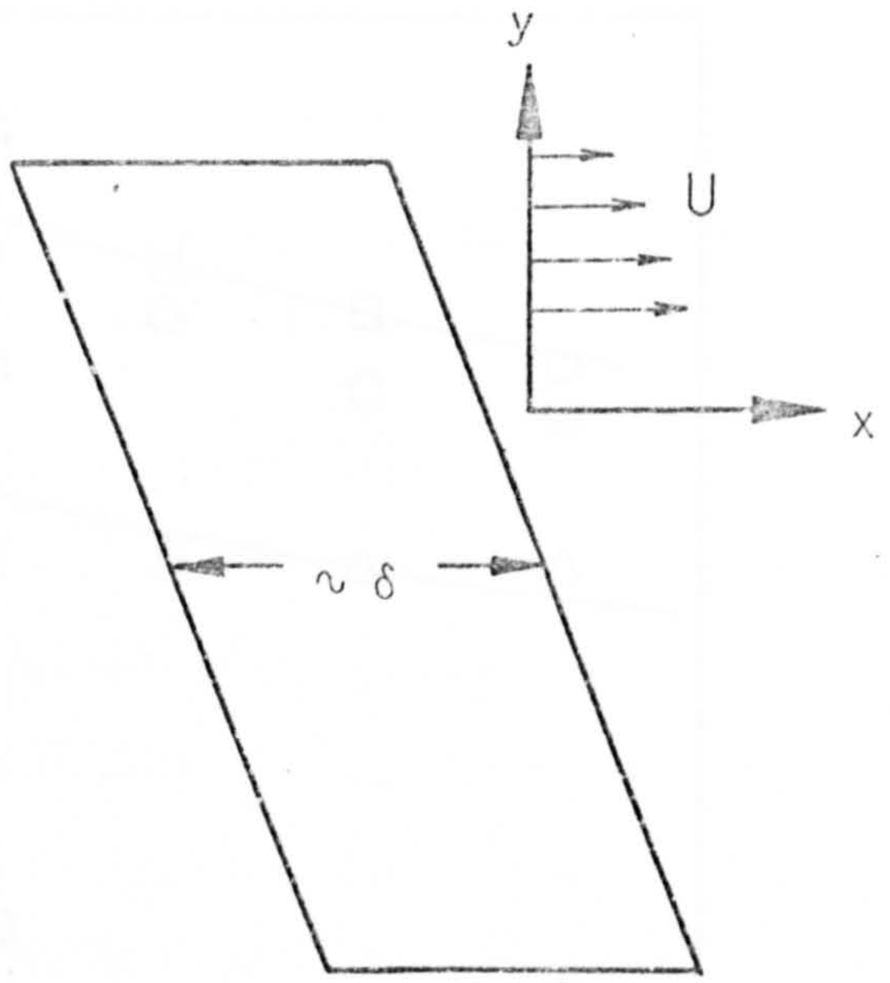


Fig. 5.48 Conditionally sampled $R_{22}(0, r, 0)$, $x - x_o = 36.89$ cm, $\eta = + 0.002$





Circulation in double roller eddy is mostly in x, z plane, but eddy is inclined in direction of mean velocity gradient

Outer motion "superimposed" on double roller eddy which "ends" before
$\eta = -0.050$

Fig. 5.49a Sketch of proposed large eddy structure

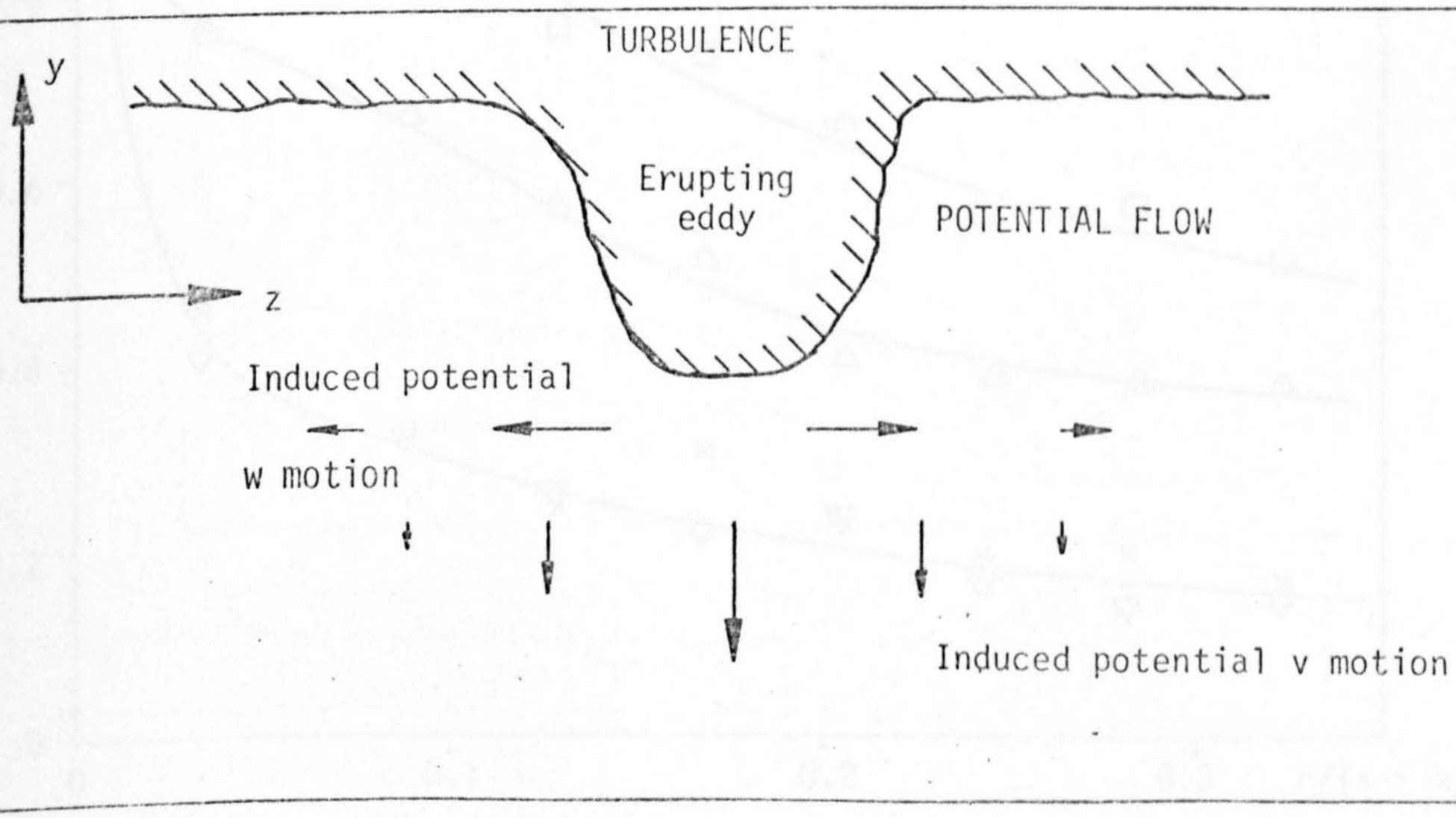


Fig. 5.49b Effect of large eddy on the potential flow

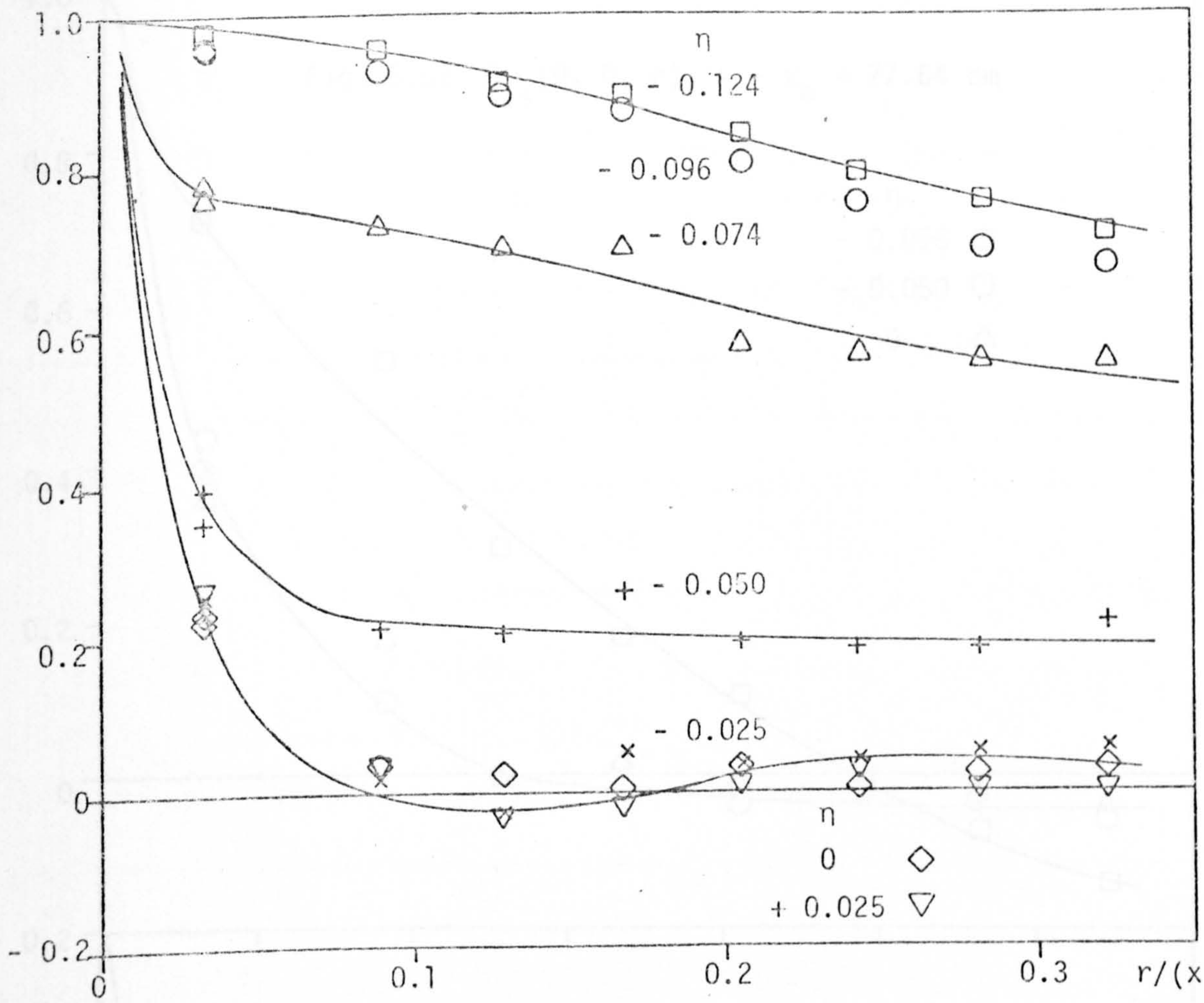


Fig. 5.50 $R_{11}(0, 0, r)$, $x - x_o = 77.64$ cm

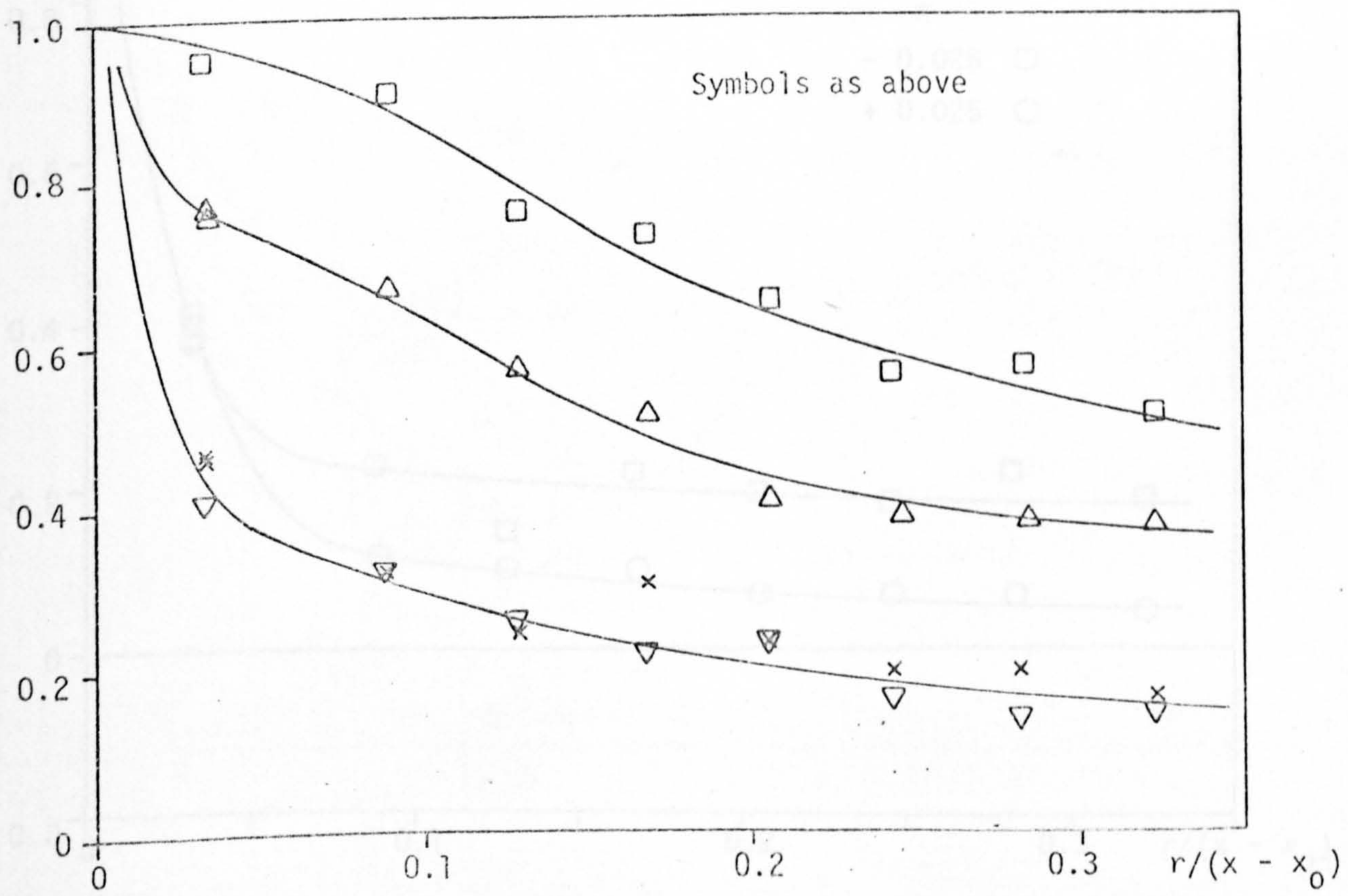


Fig. 5.51 $R_{22}(0, 0, r)$, $x - x_o = 77.64$ cm

Fig. 5.52 $R_{33}(0, 0, r)$, $x - x_o = 77.64$ cm

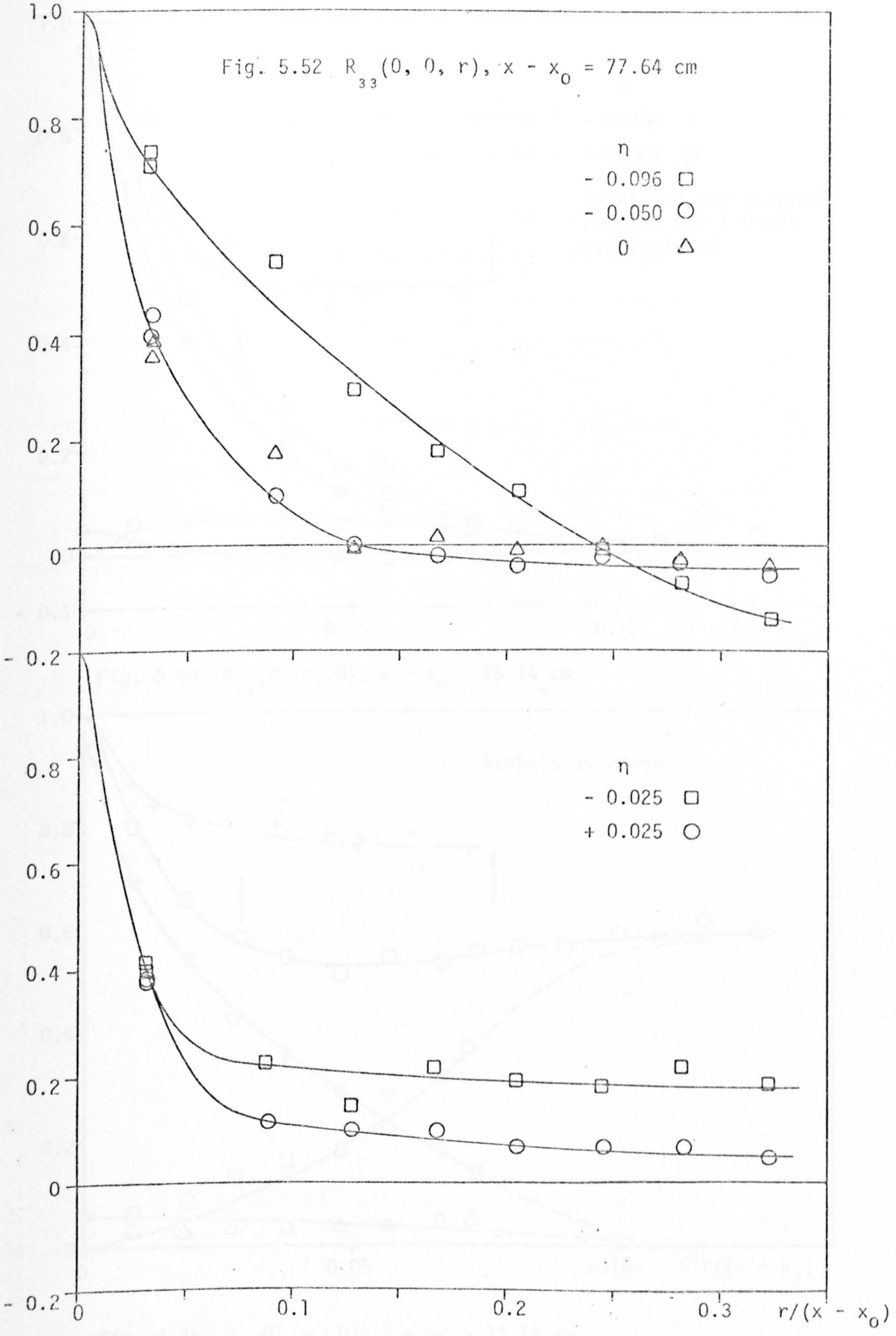


Fig. 5.53 $R_{12}(0, 0, r)$, $x - x_o = 77.64$ cm

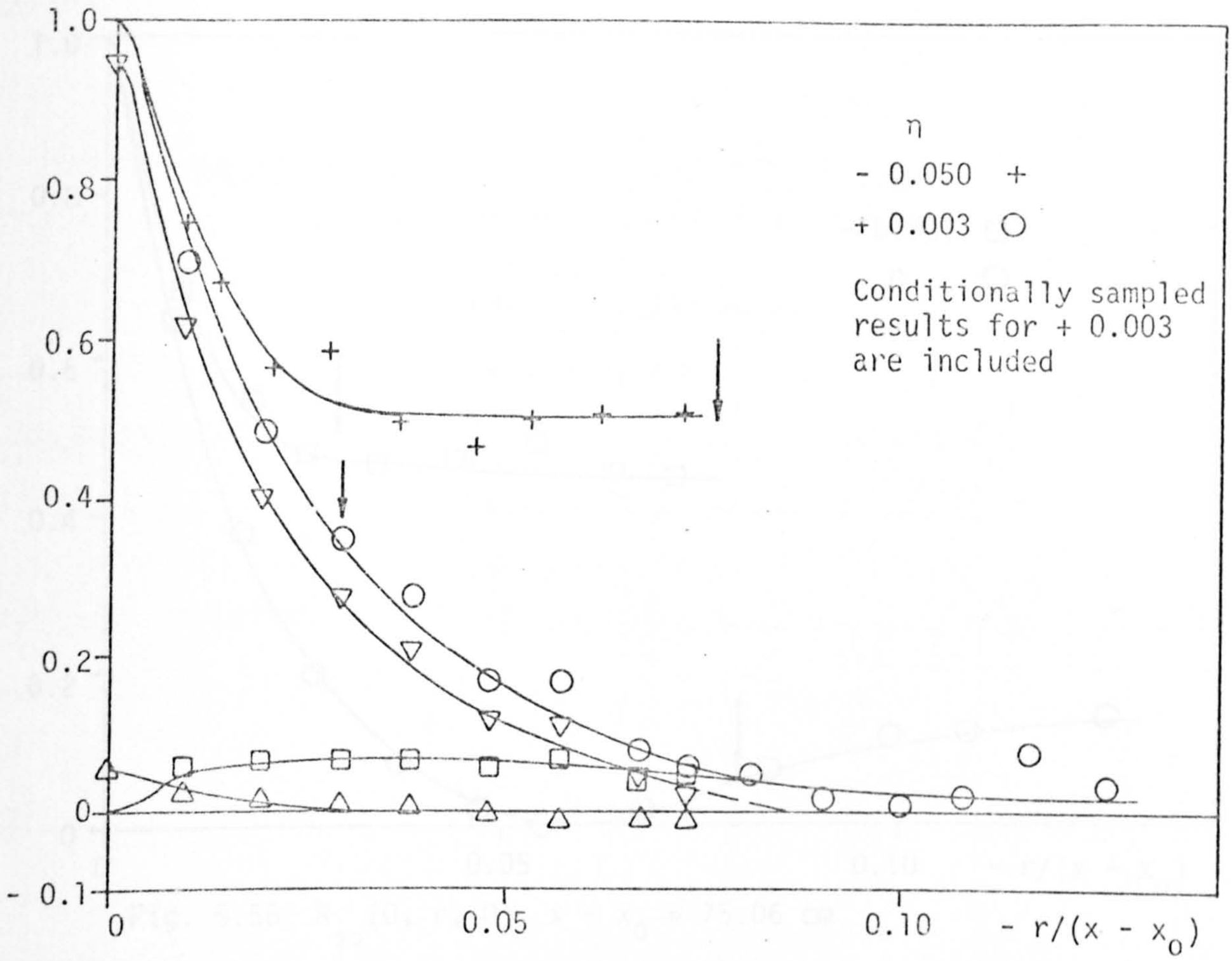


Fig. 5.54 $R_{11}(0, r, 0)$, $x - x_o = 75.14$ cm

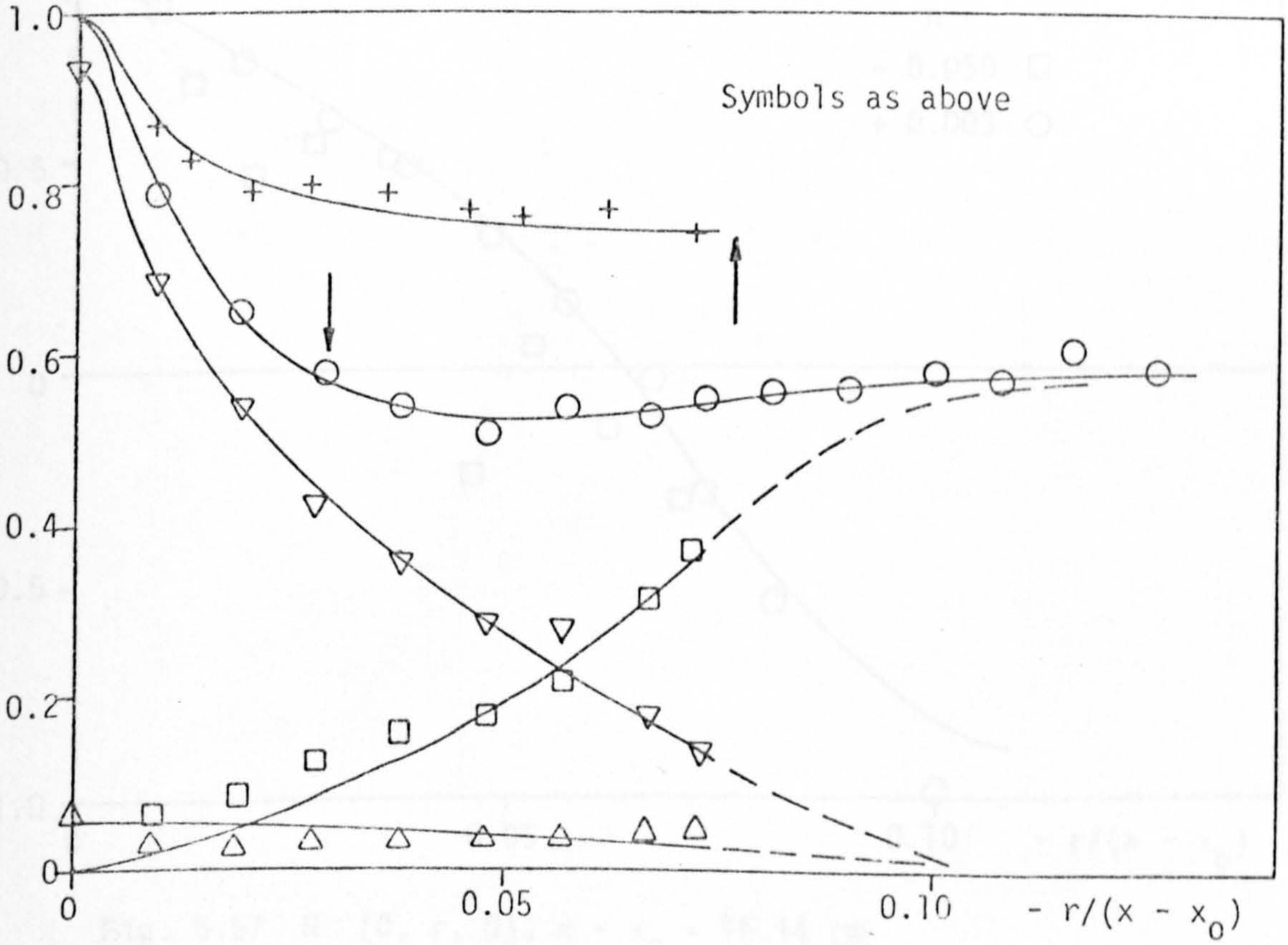


Fig. 5.55 $R_{22}(0, r, 0)$, $x - x_o = 75.14$ cm

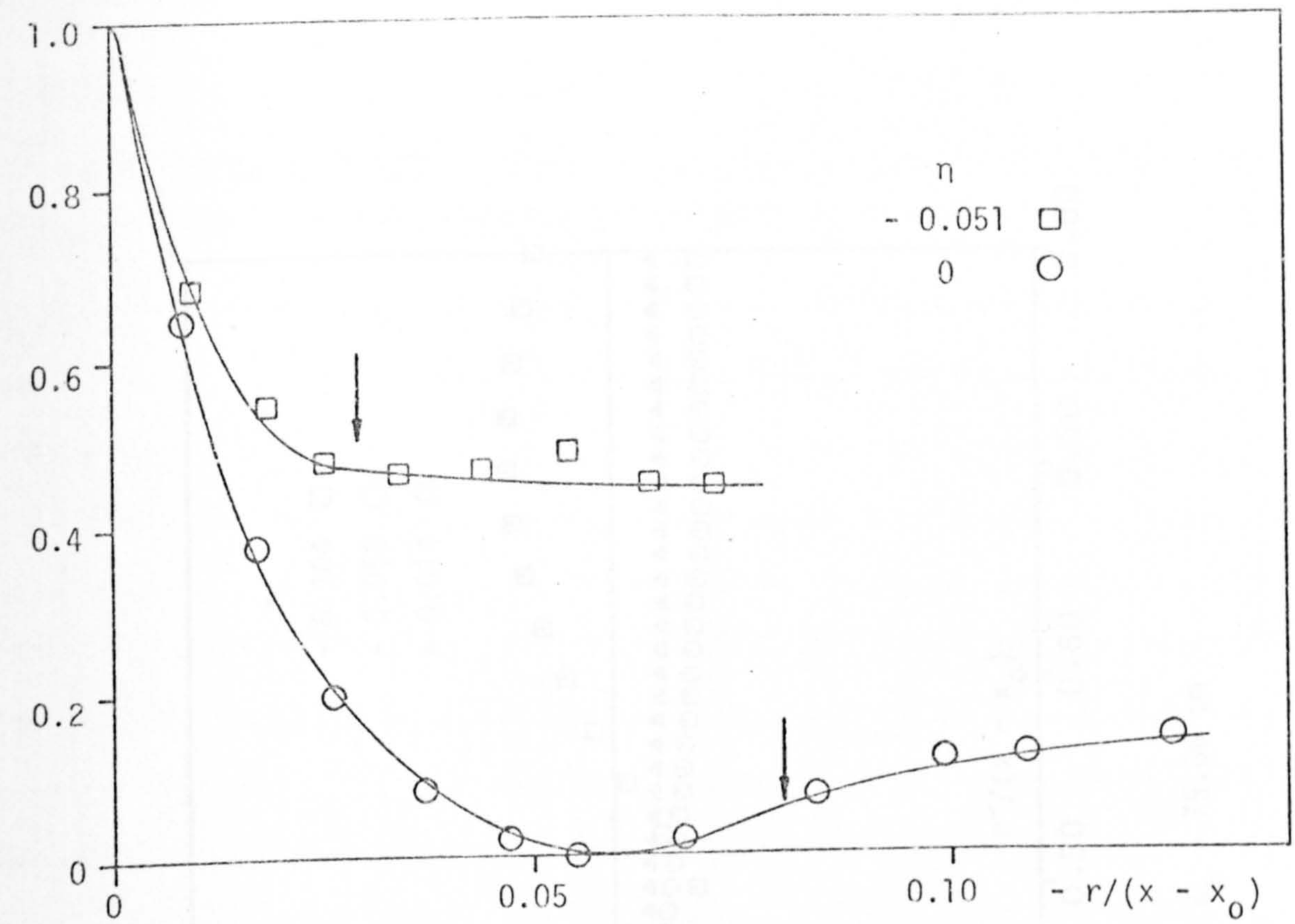


Fig. 5.56 $R_{33}(0, r, 0)$, $x - x_o = 75.06$ cm

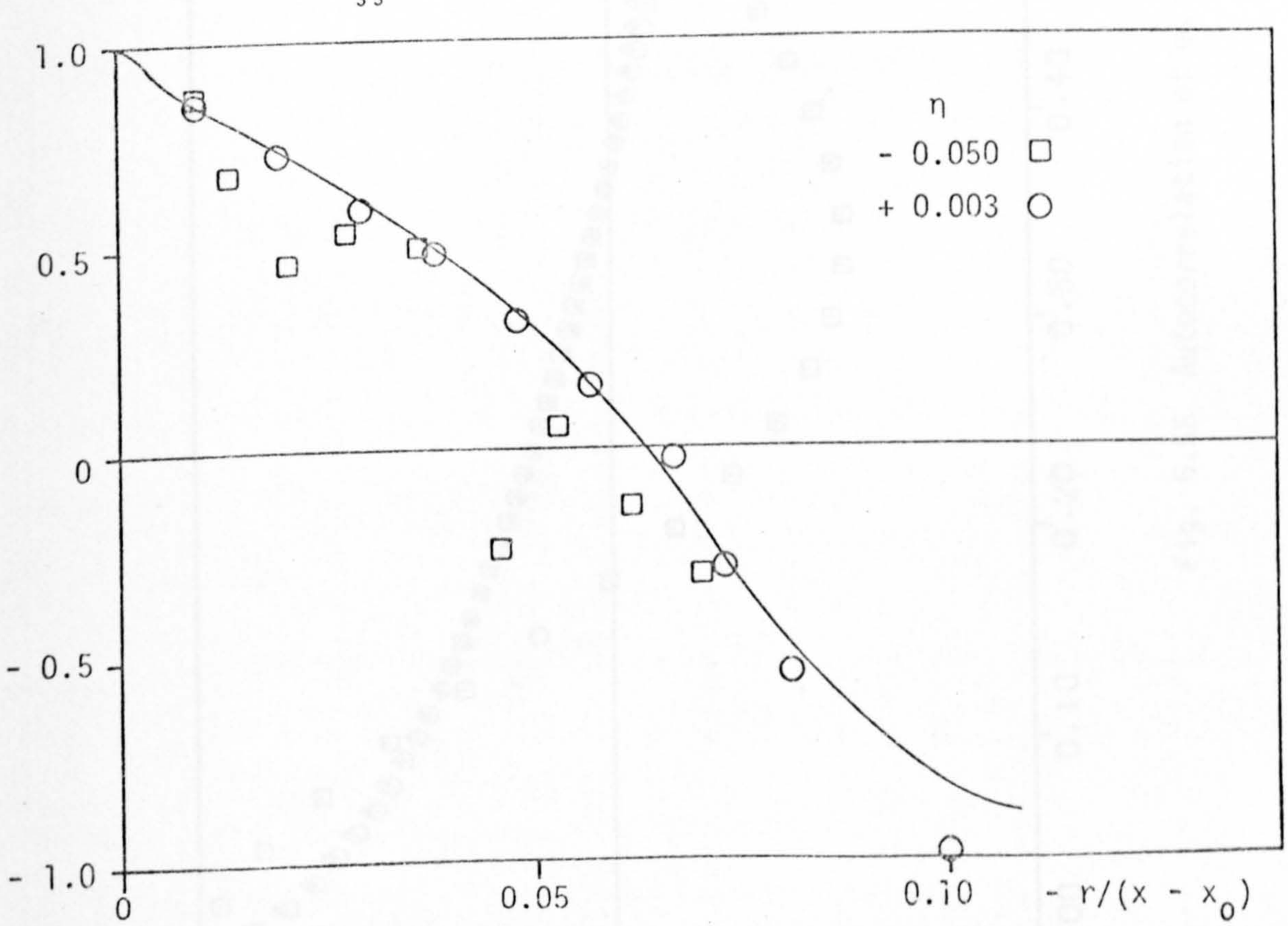


Fig. 5.57 $R_{21}(0, r, 0)$, $x - x_o = 75.14$ cm

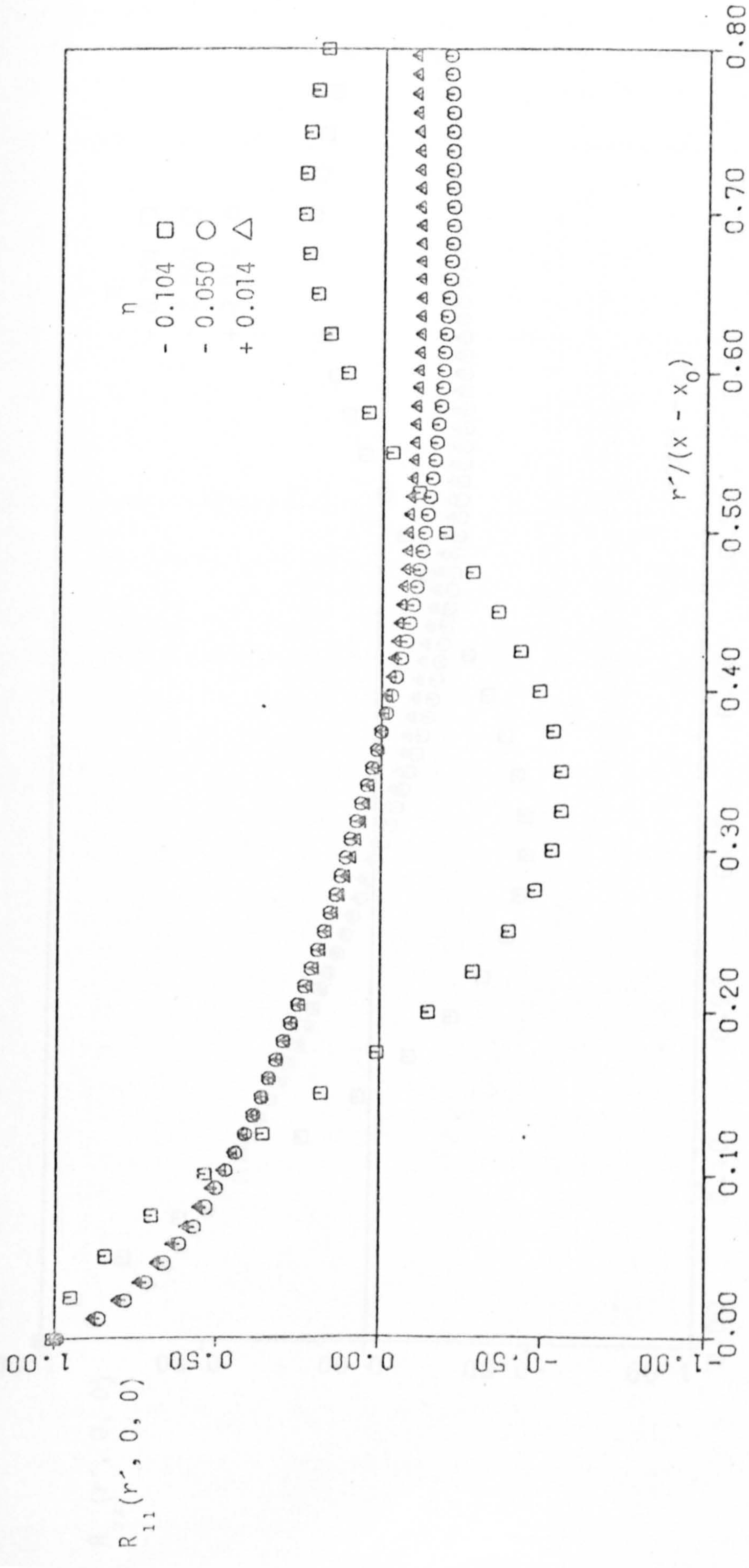


Fig. 5.58 Autocorrelation of u, $x - x_o$ = 75.06 cm

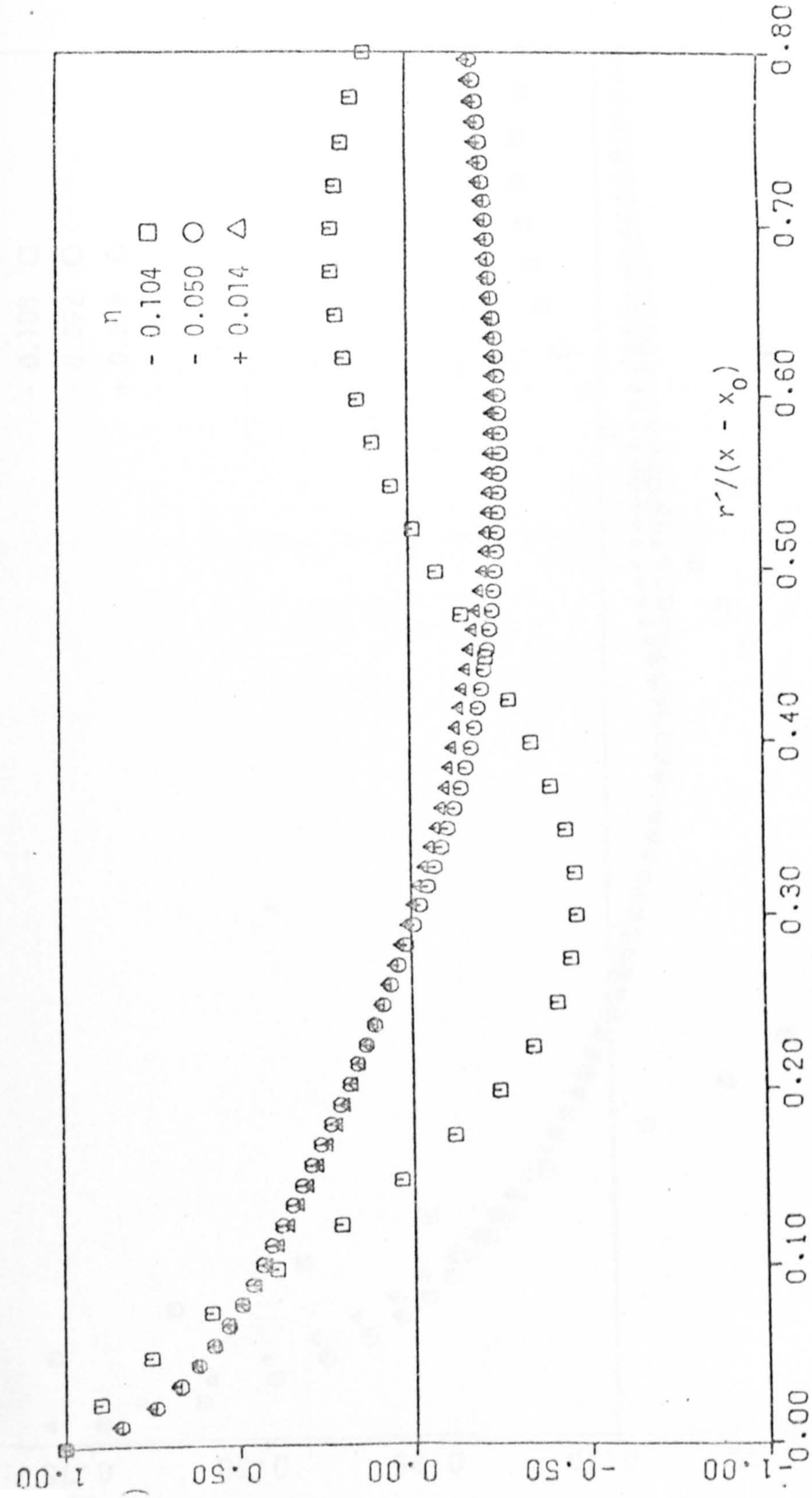


Fig. 5.59 Autocorrelation of v, $x - x_o$ = 75.06 cm

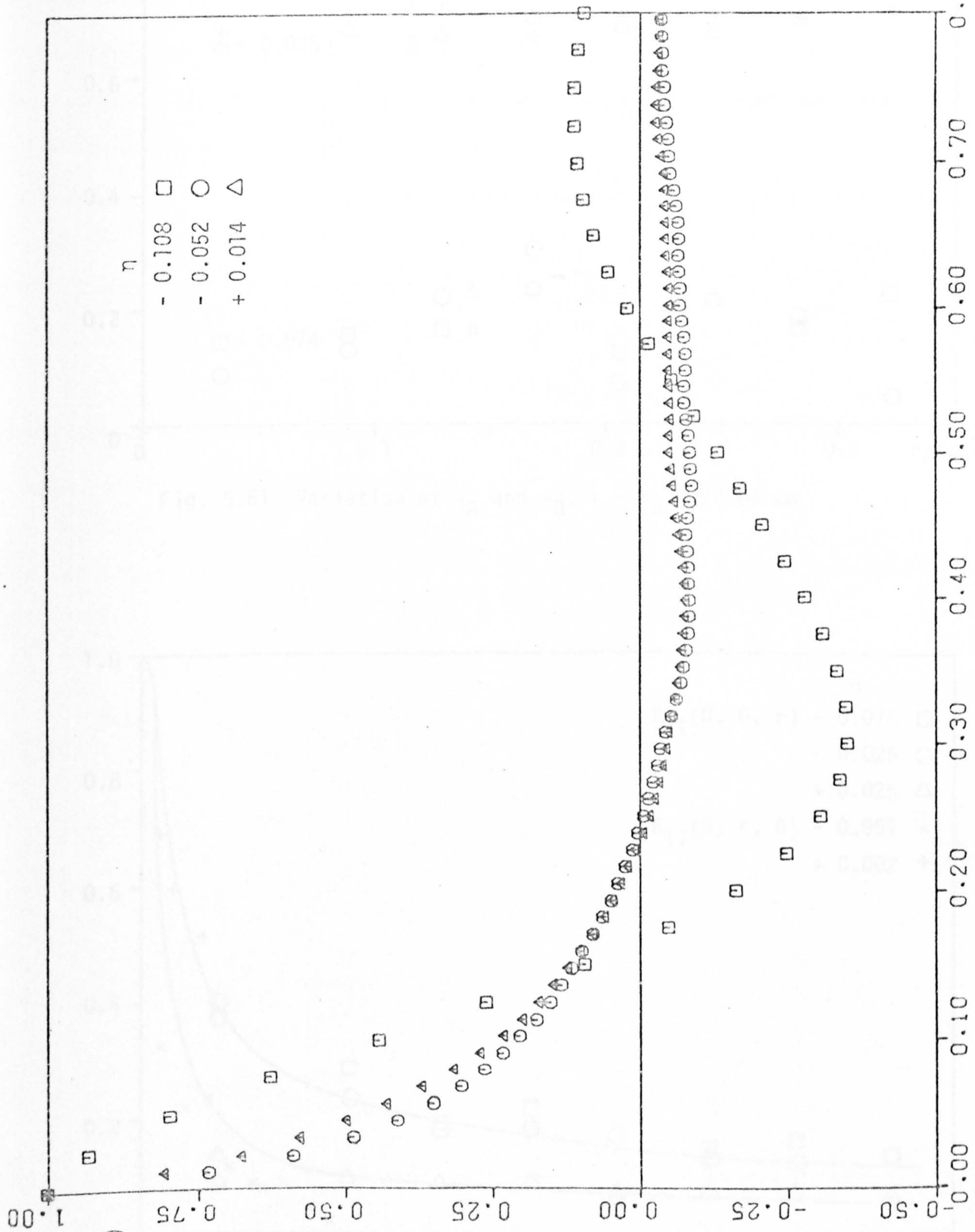


Fig. 5.60 Autocorrelation of w, $x - x_o = 75.06$ cm

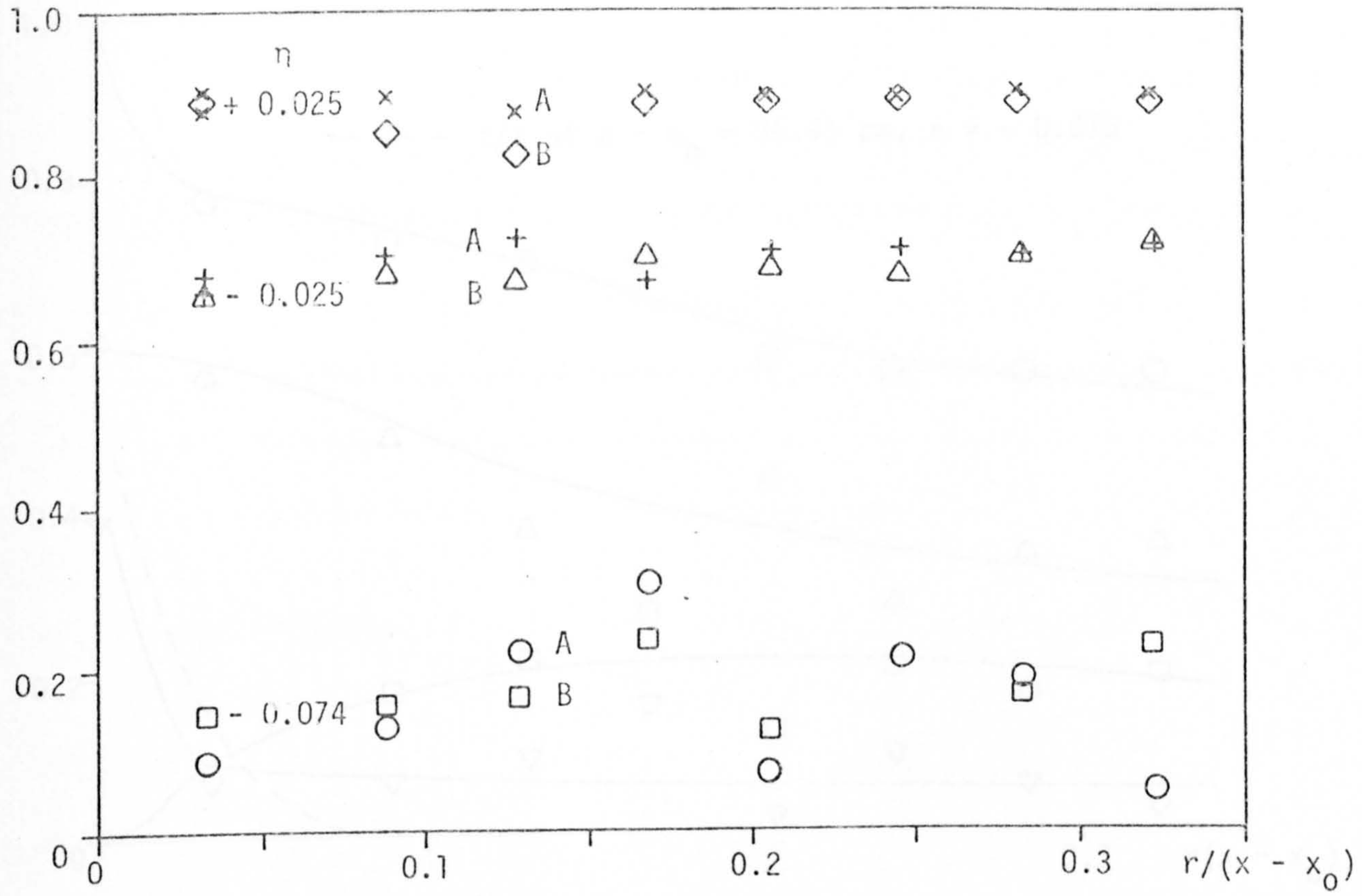


Fig. 5.61 Variation of γ_A and γ_B, $x - x_o = 77.64$ cm

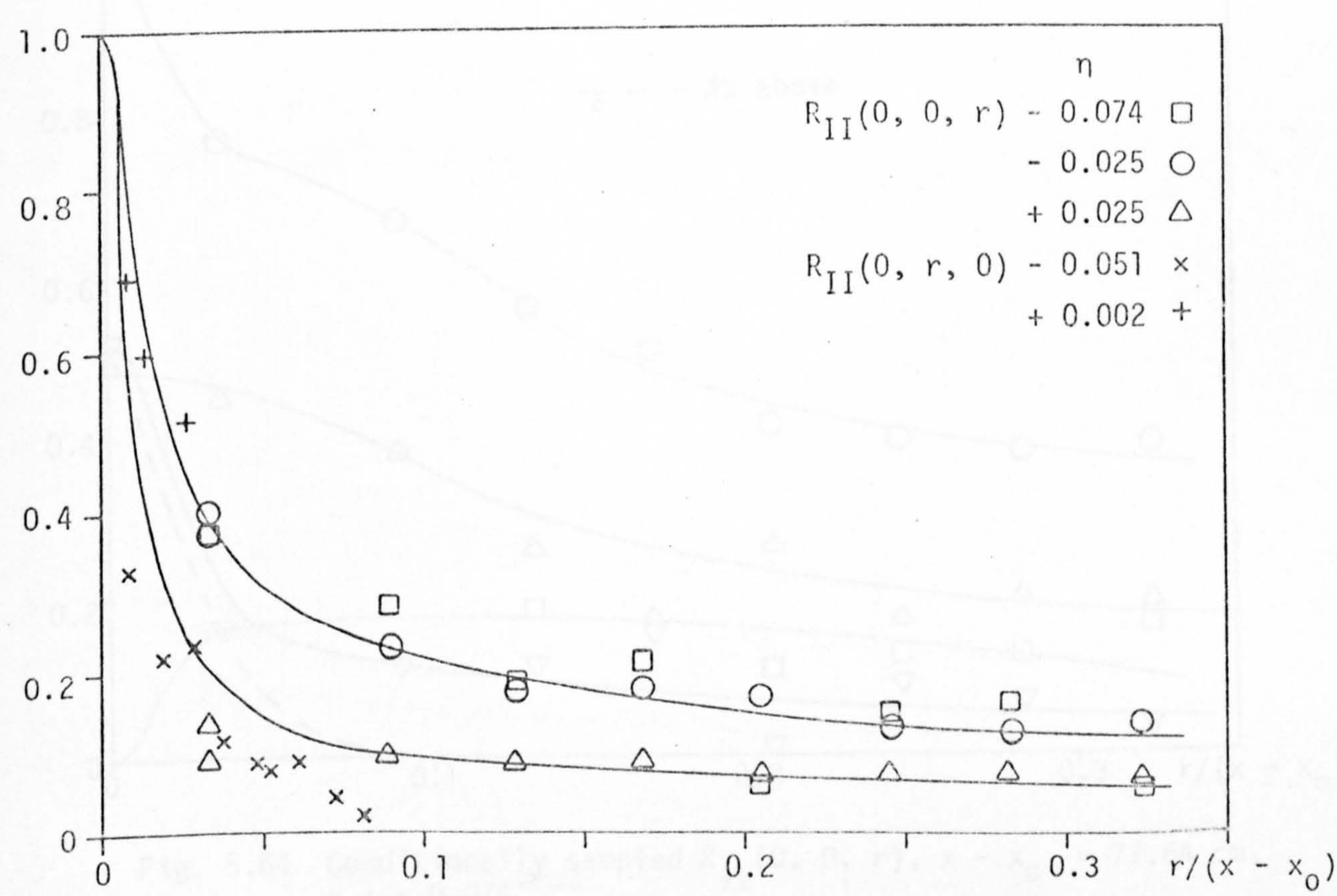


Fig. 5.62 $R_{II}(0, 0, r)$, $x - x_o = 77.64$ cm; $R_{II}(0, r, 0)$, $x - x_o = 75.14$ cm

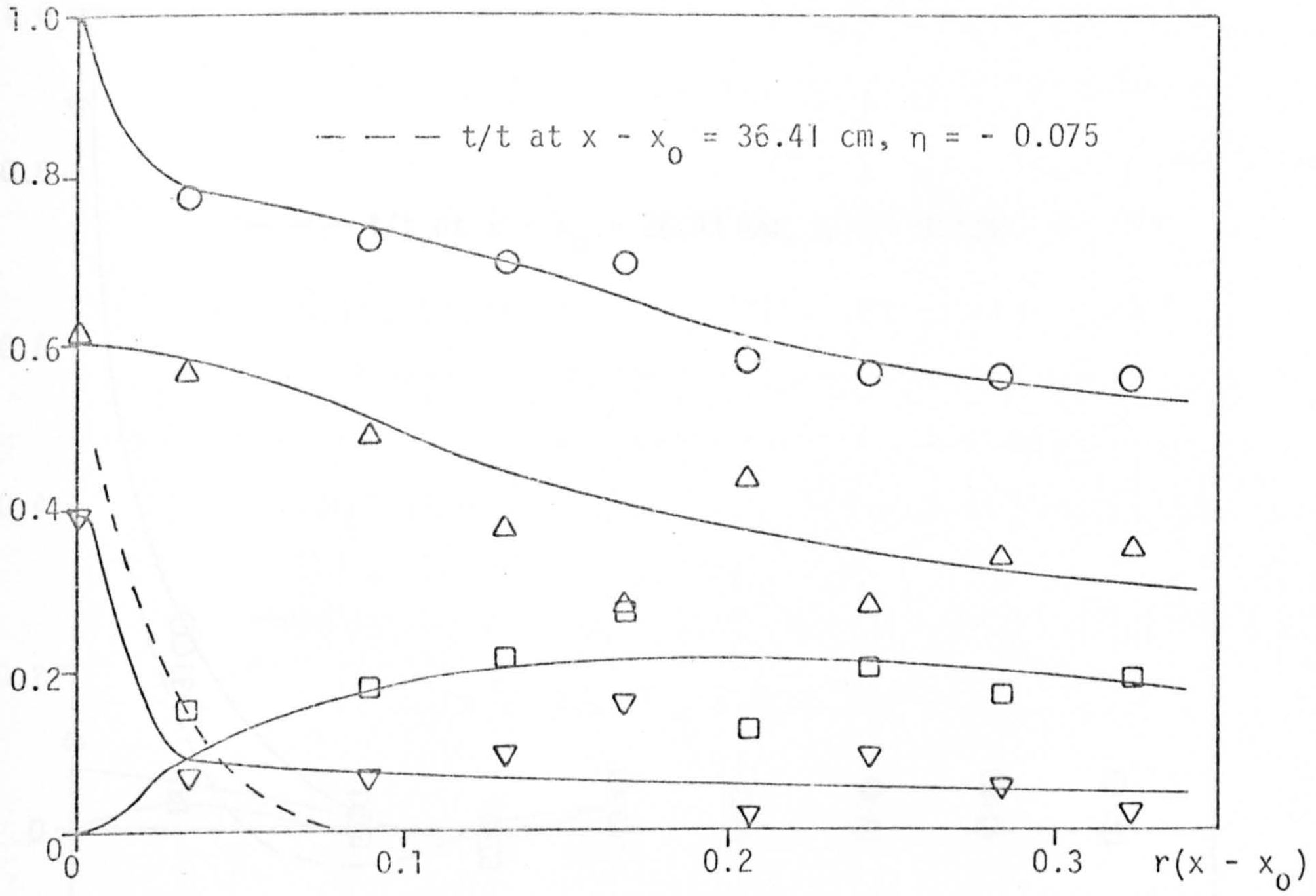


Fig. 5.63 Conditionally sampled $R_{11}(0, 0, r)$, $x - x_o = 77.64$ cm, $\eta = -0.074$

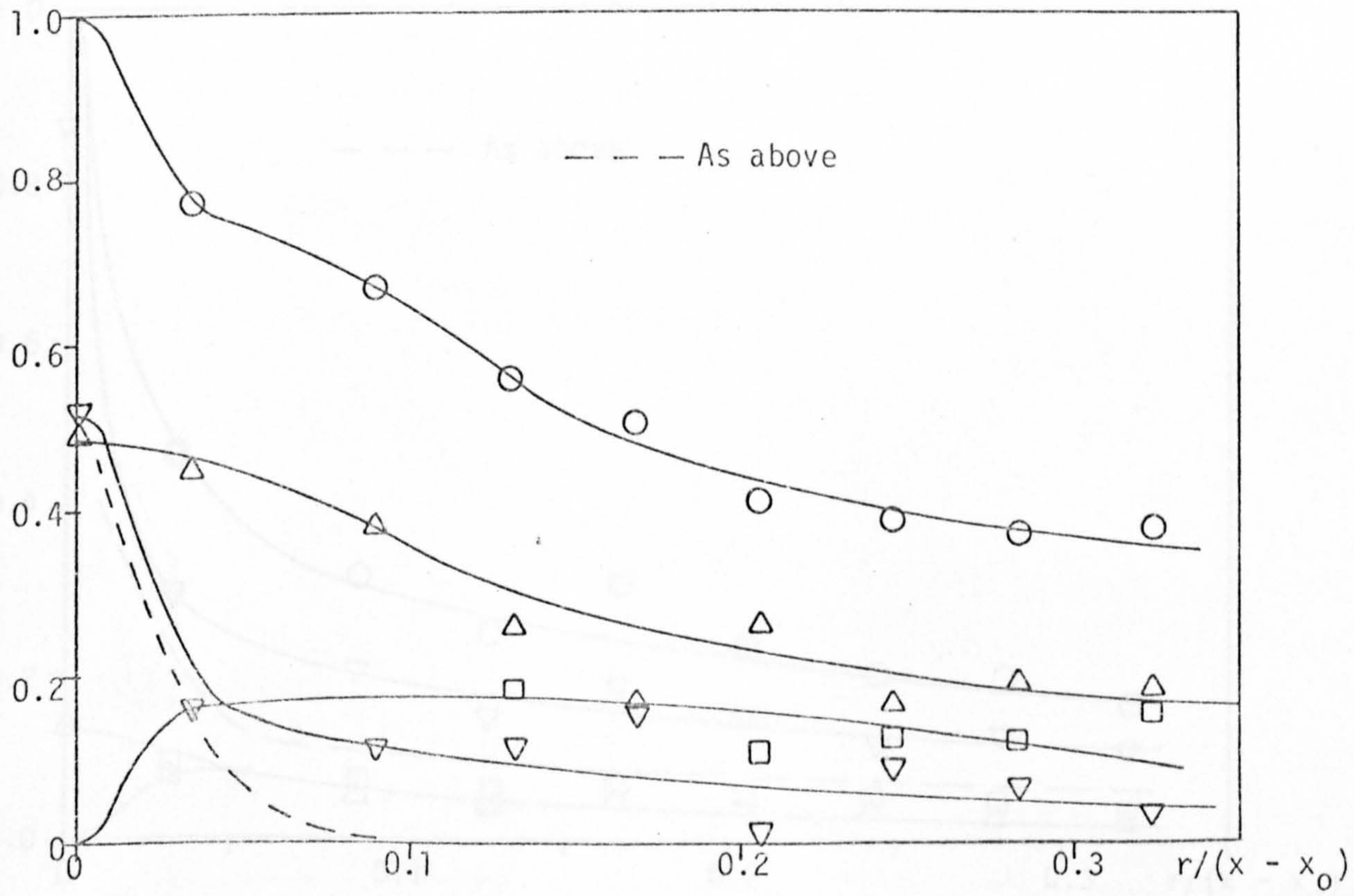


Fig. 5.64 Conditionally sampled $R_{22}(0, 0, r)$, $x - x_o = 77.64$ cm, $\eta = -0.074$

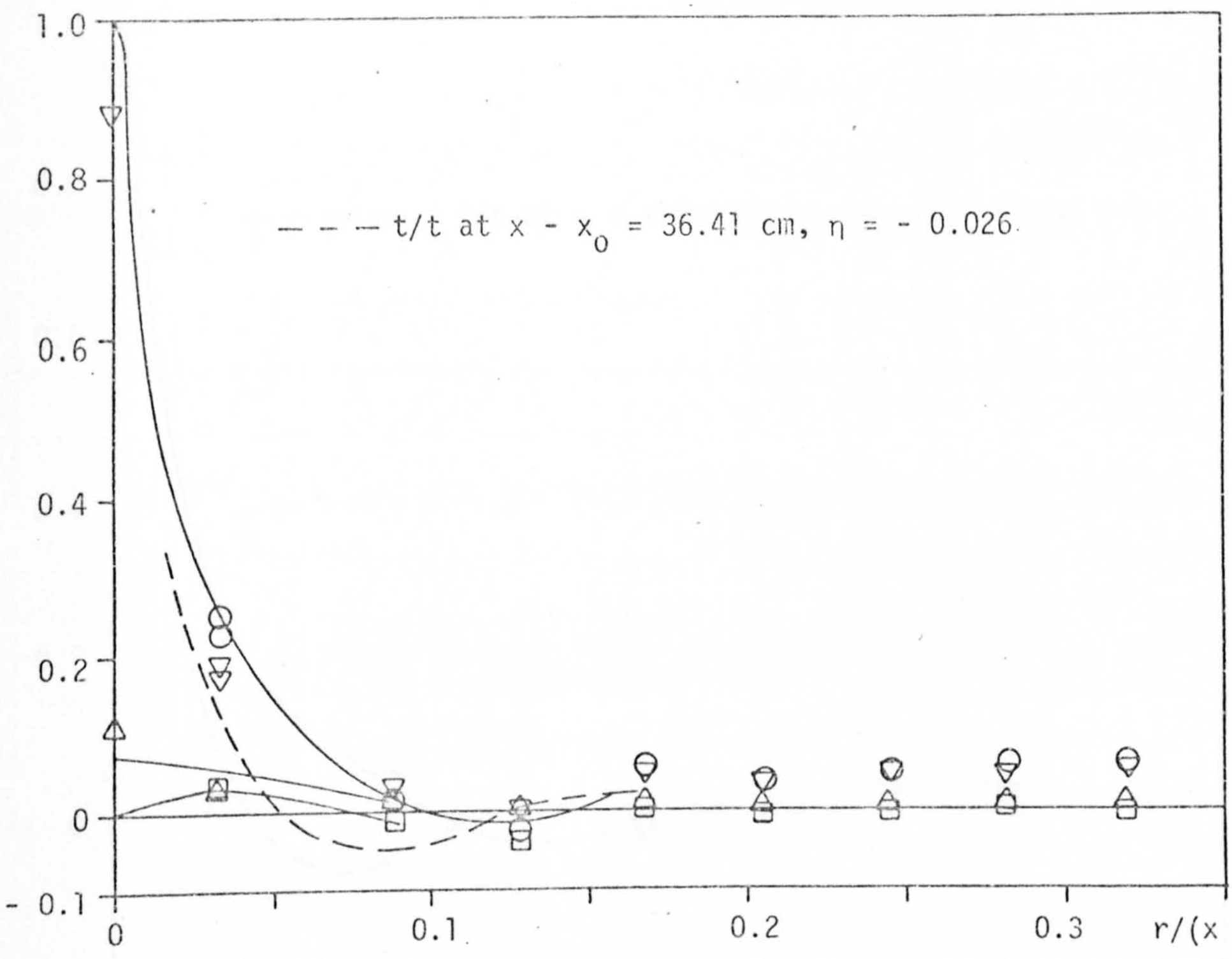


Fig. 5.65 Conditionally sampled $R_{11}(0, 0, r)$, $x - x_o = 77.64$ cm, $\eta = - 0.026$

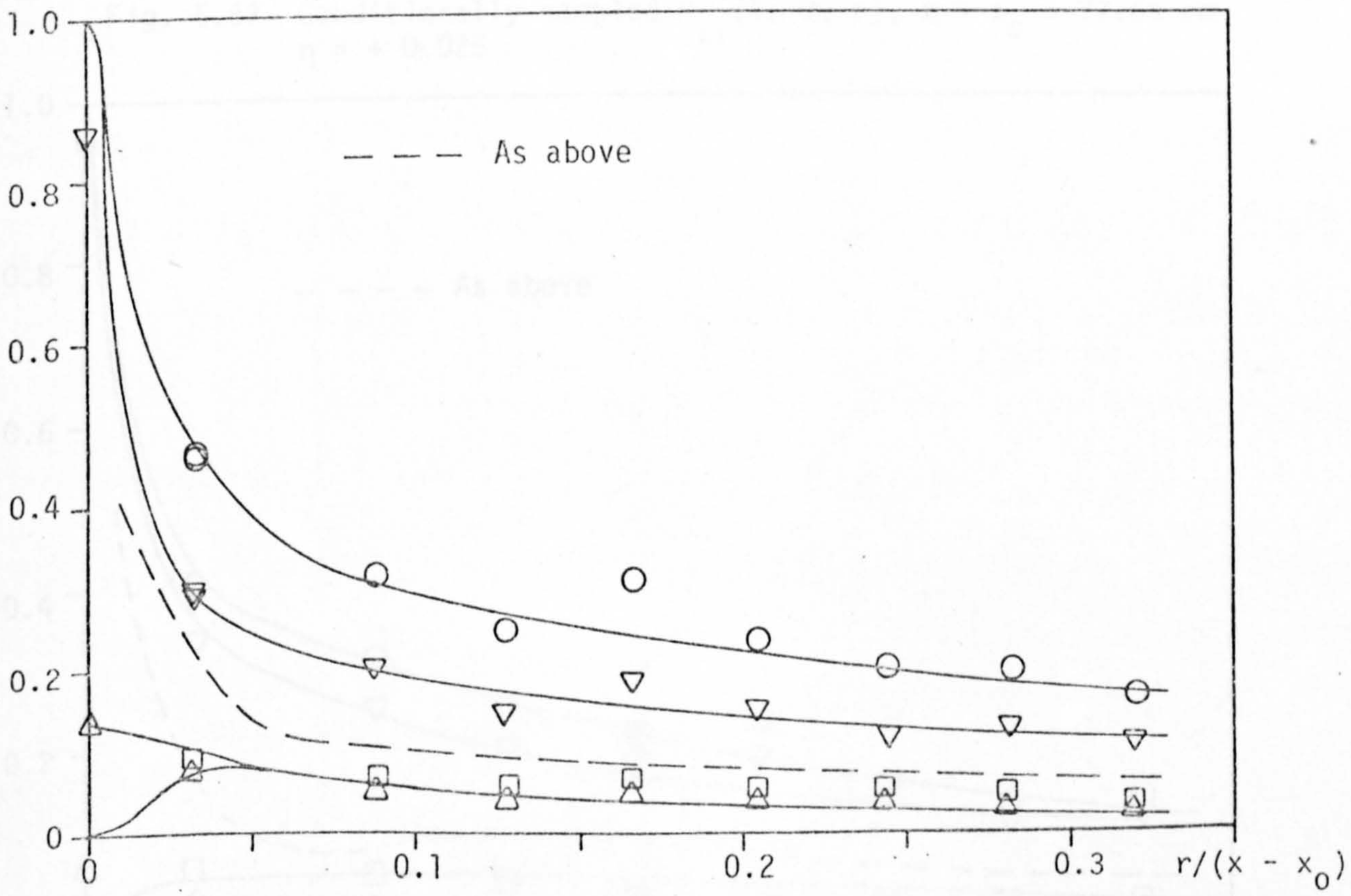


Fig. 5.66 Conditionally sampled $R_{22}(0, 0, r)$, $x - x_o = 77.64$ cm, $\eta = - 0.026$

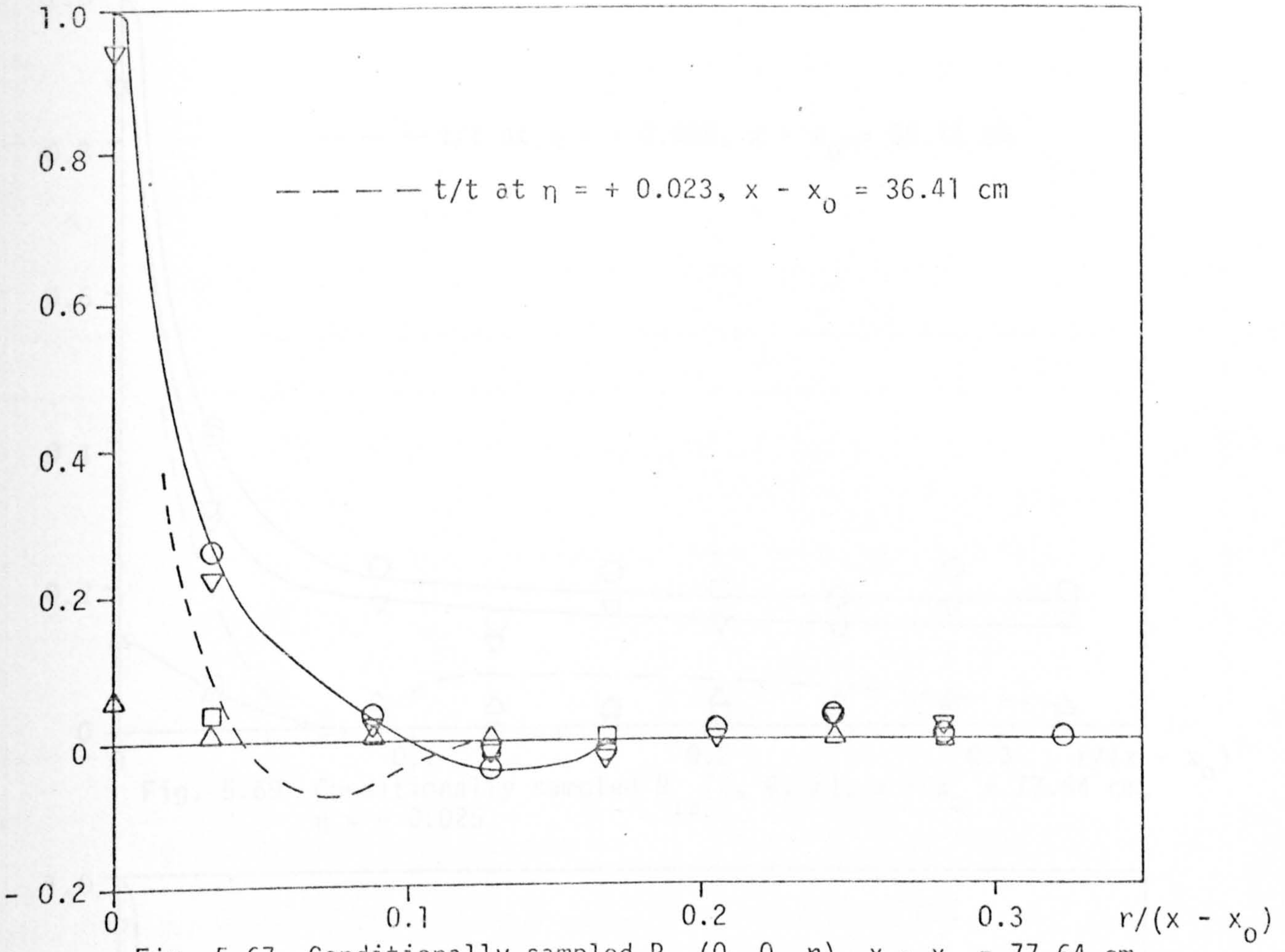


Fig. 5.67 Conditionally sampled $R_{11}(0, 0, r)$, $x - x_o = 77.64$ cm, $\eta = + 0.025$

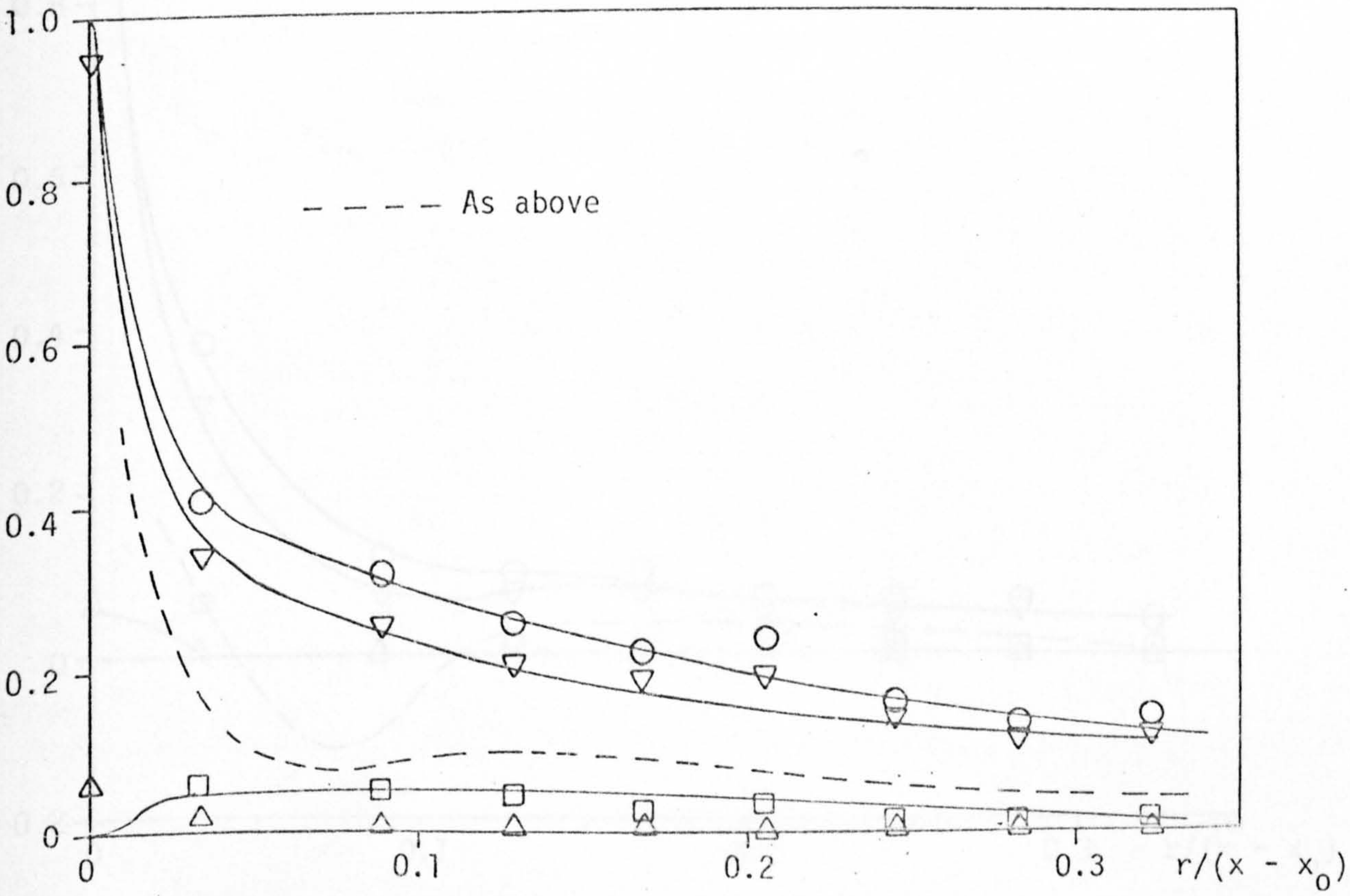


Fig. 5.68 Conditionally sampled $R_{22}(0, 0, r)$, $x - x_o = 77.64$ cm, $\eta = + 0.025$

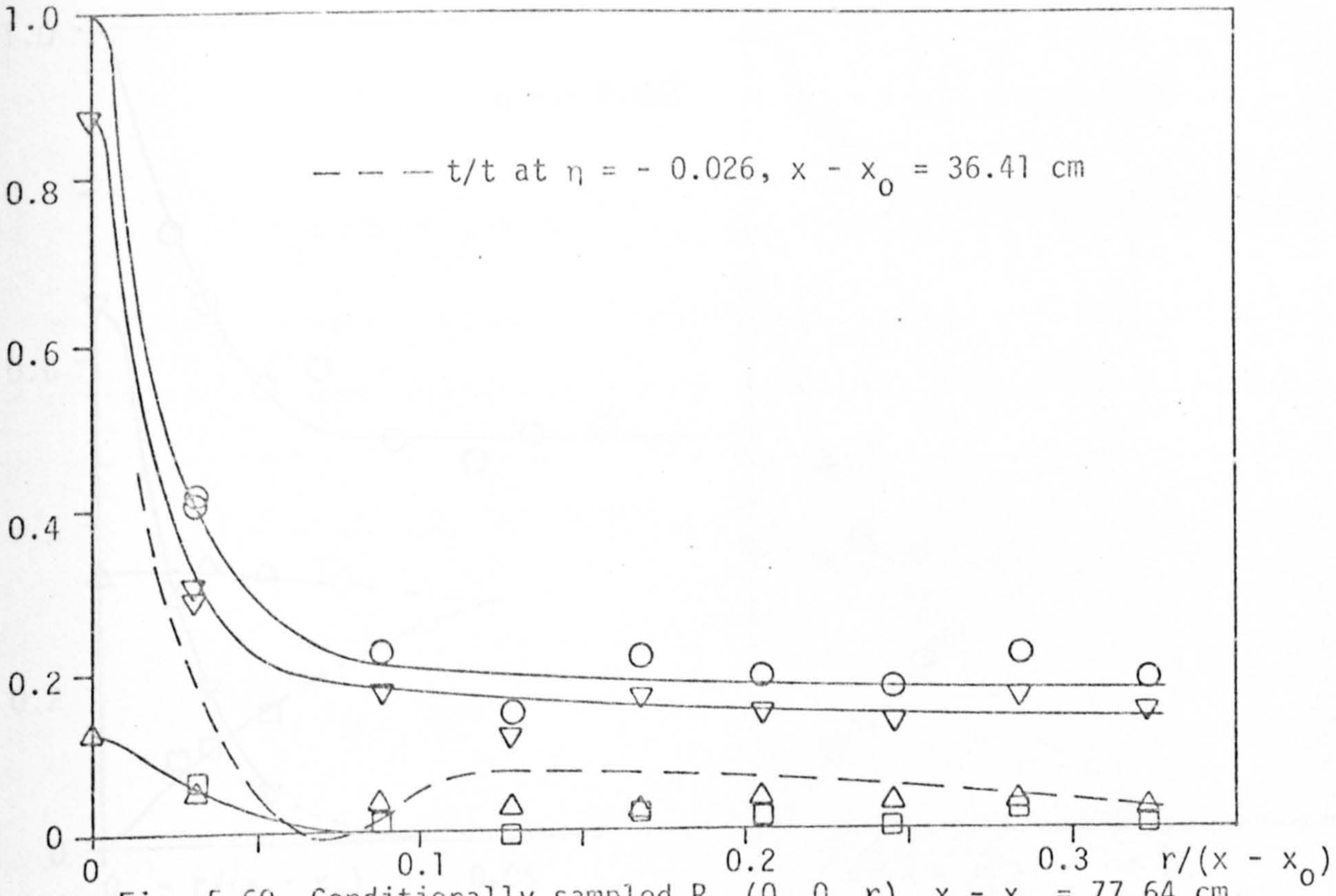


Fig. 5.69 Conditionally sampled $R_{12}(0, 0, r)$, $x - x_o = 77.64$ cm, $\eta = - 0.025$

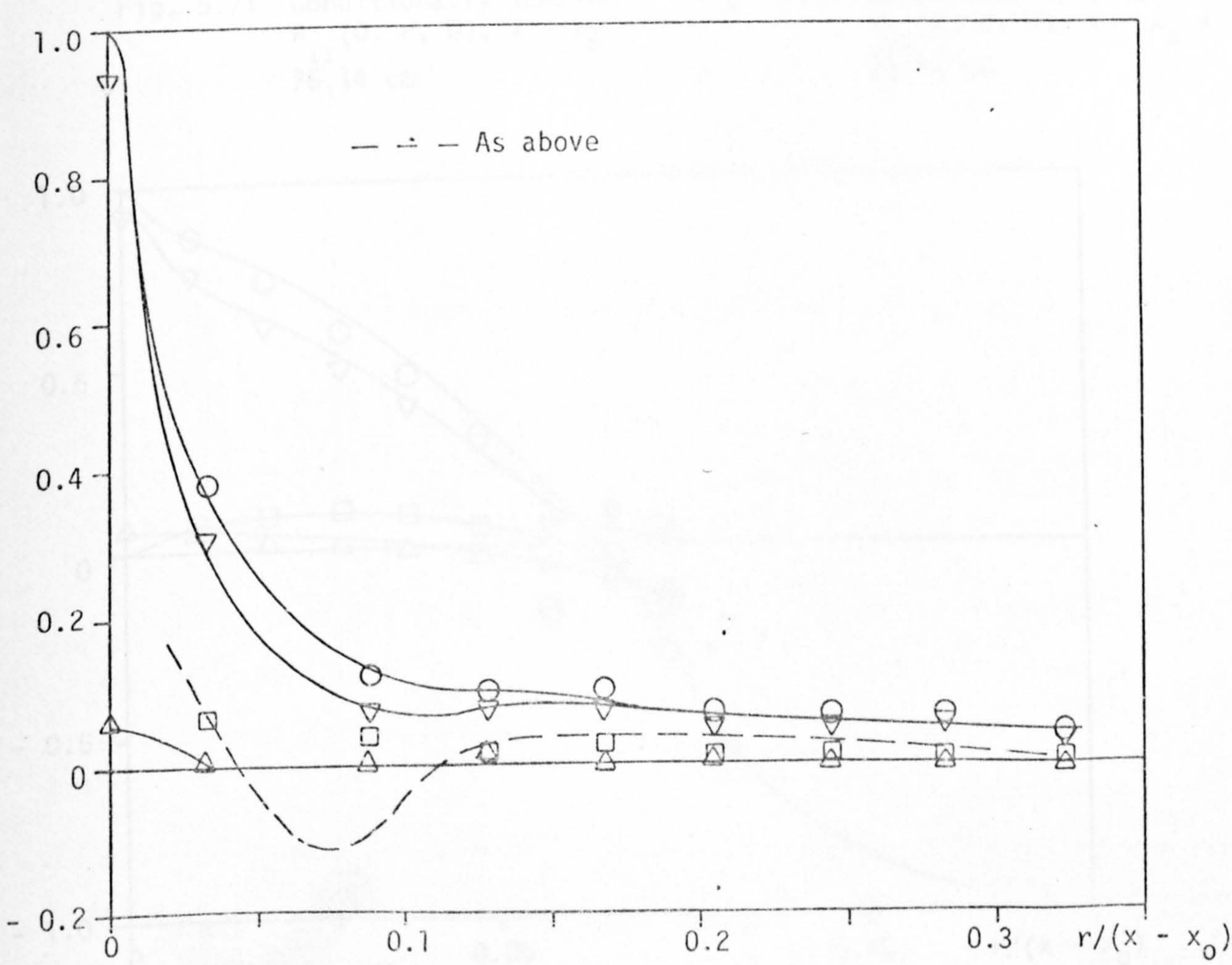


Fig. 5.70 Conditionally sampled $R_{12}(0, 0, r)$, $x - x_o = 77.64$ cm, $\eta = + 0.025$

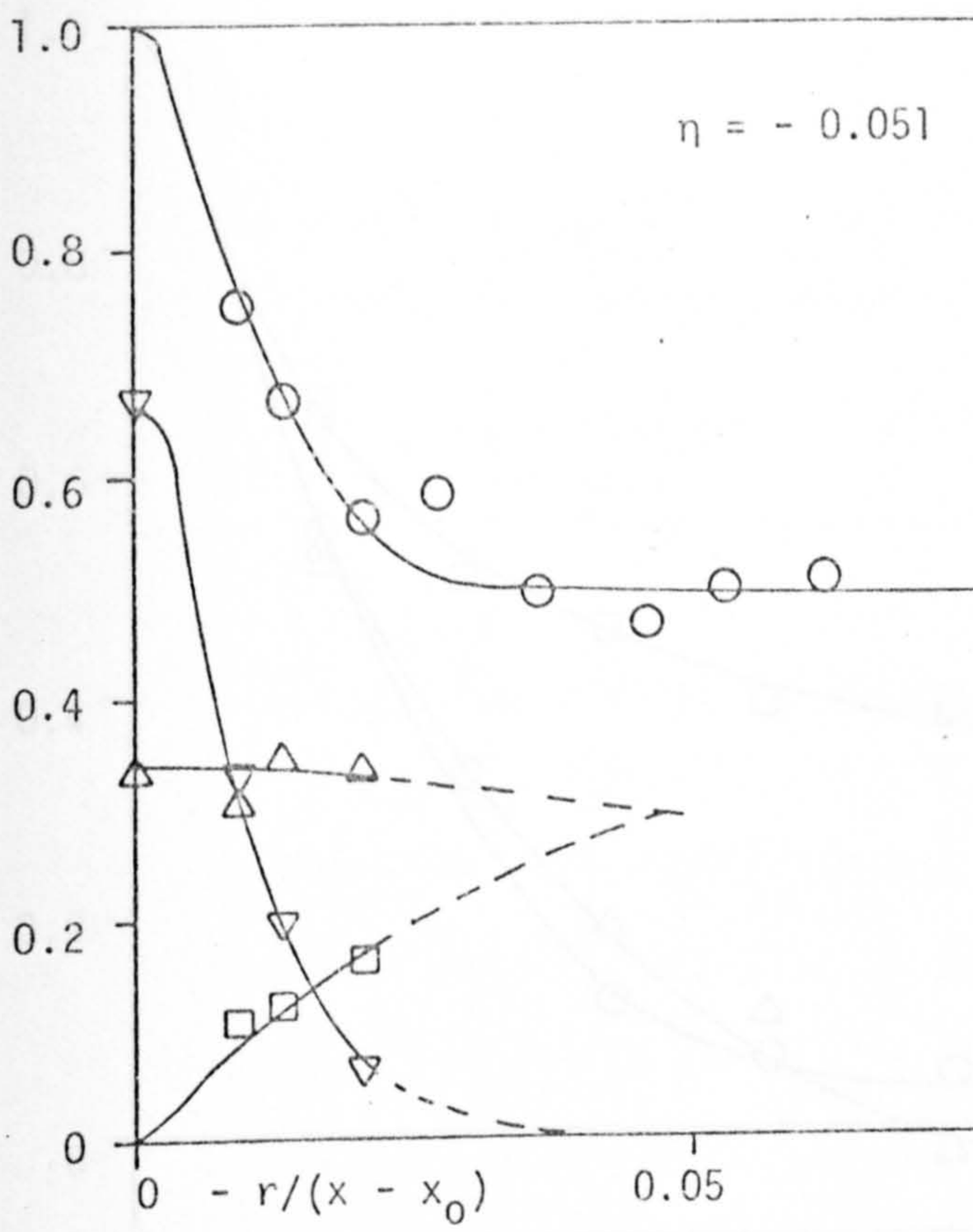


Fig. 5.71 Conditionally sampled $R_{11}(0, r, 0)$, $x - x_o$ = 75.14 cm

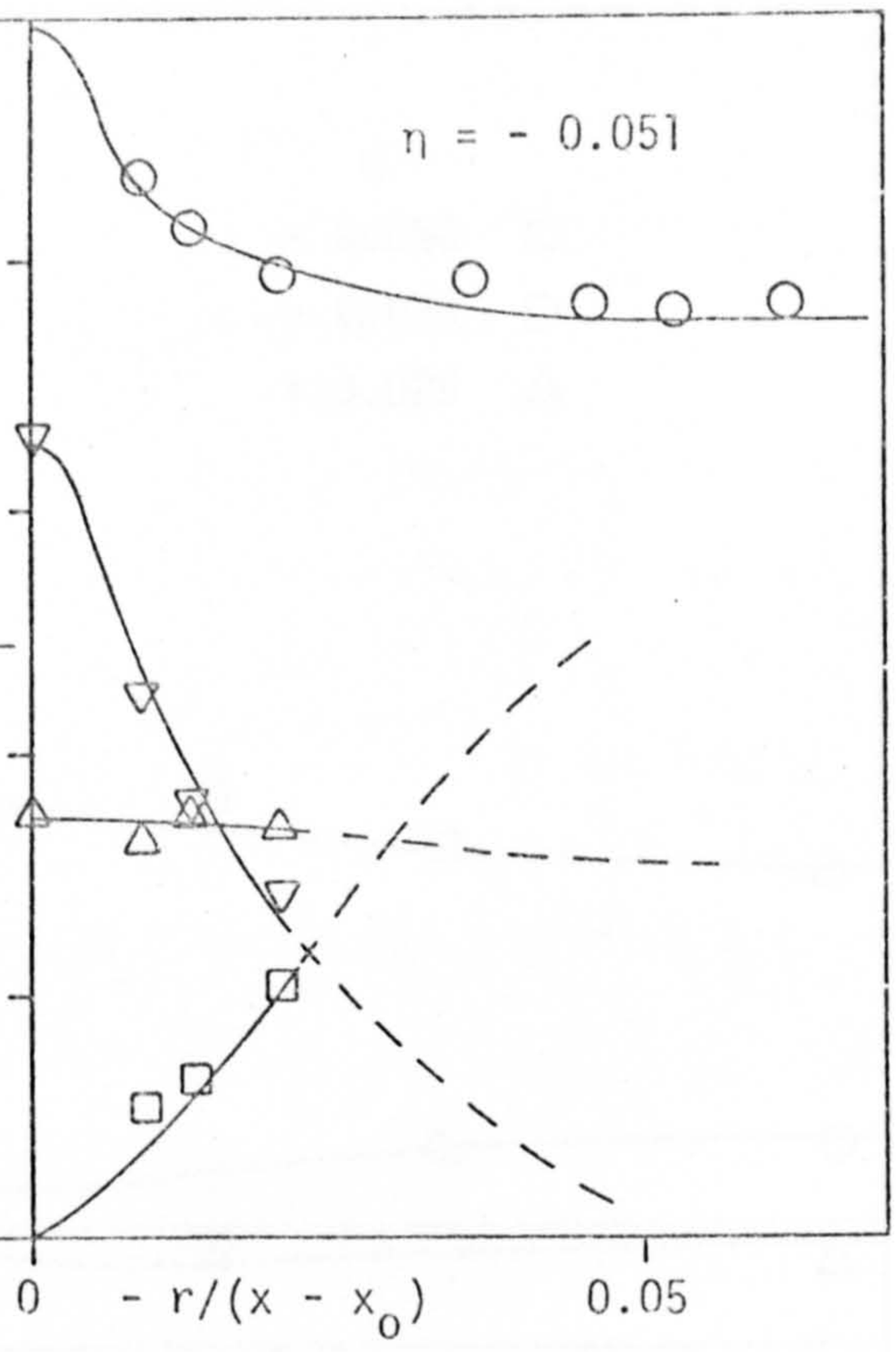


Fig. 5.72 Conditionally sampled $R_{22}(0, r, 0)$, $x - x_o$ = 75.14 cm

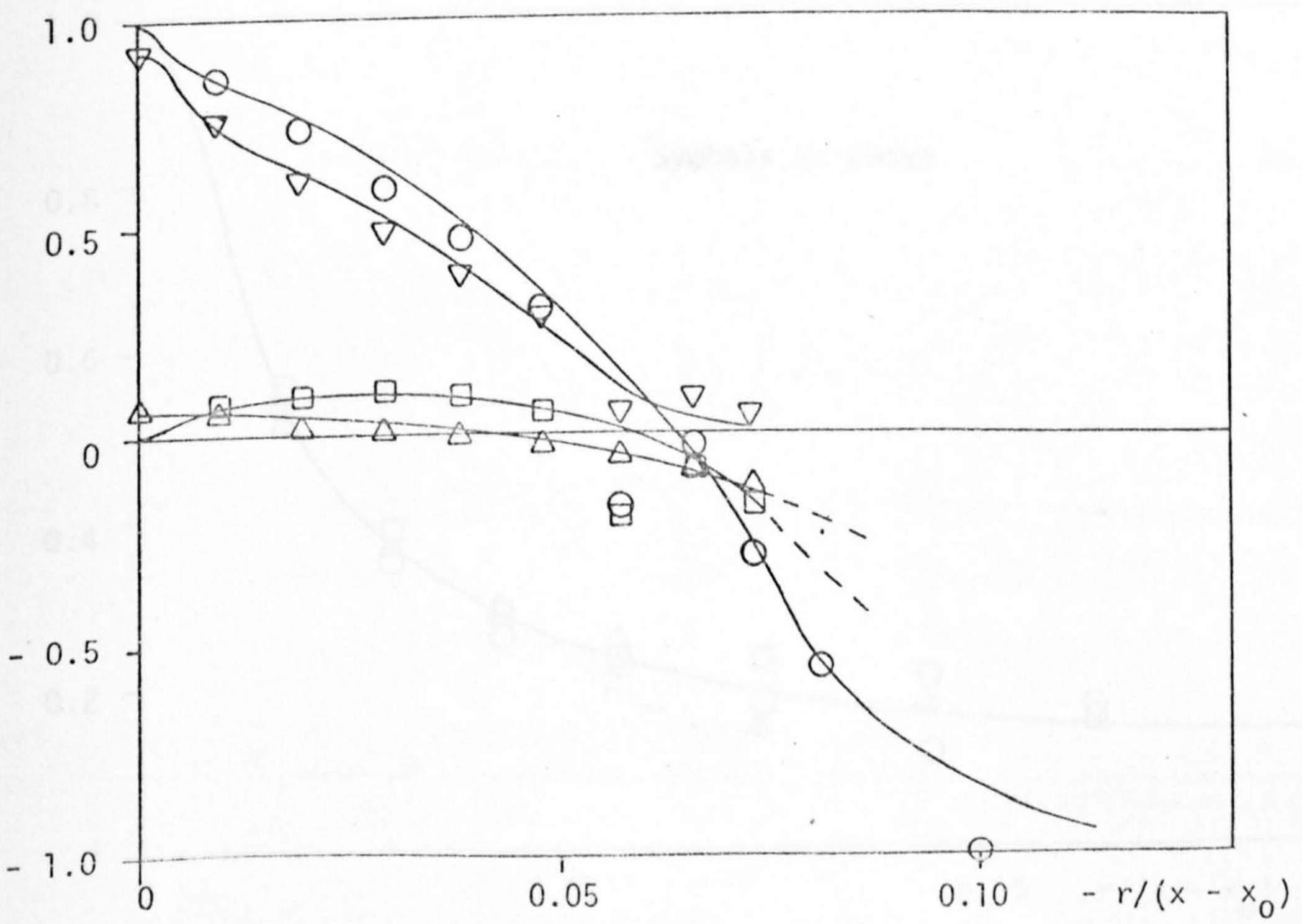


Fig. 5.73 Conditionally sampled $R_{21}(0, r, 0)$, $x - x_o$ = 75.14 cm, η = + 0.002

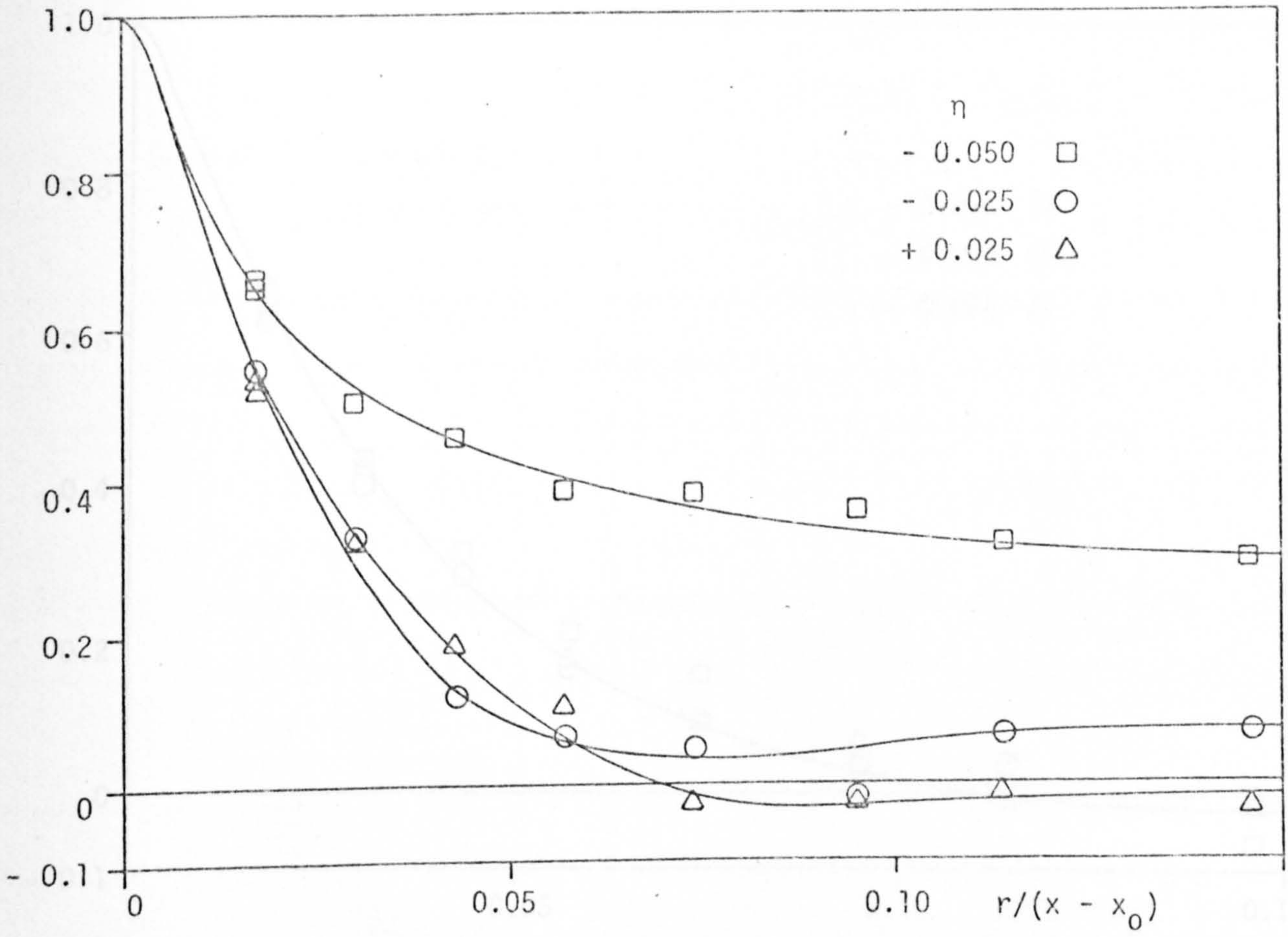


Fig. 5.74 $R_{11}(0, 0, r)$, $x - x_0 = 151.11$ cm

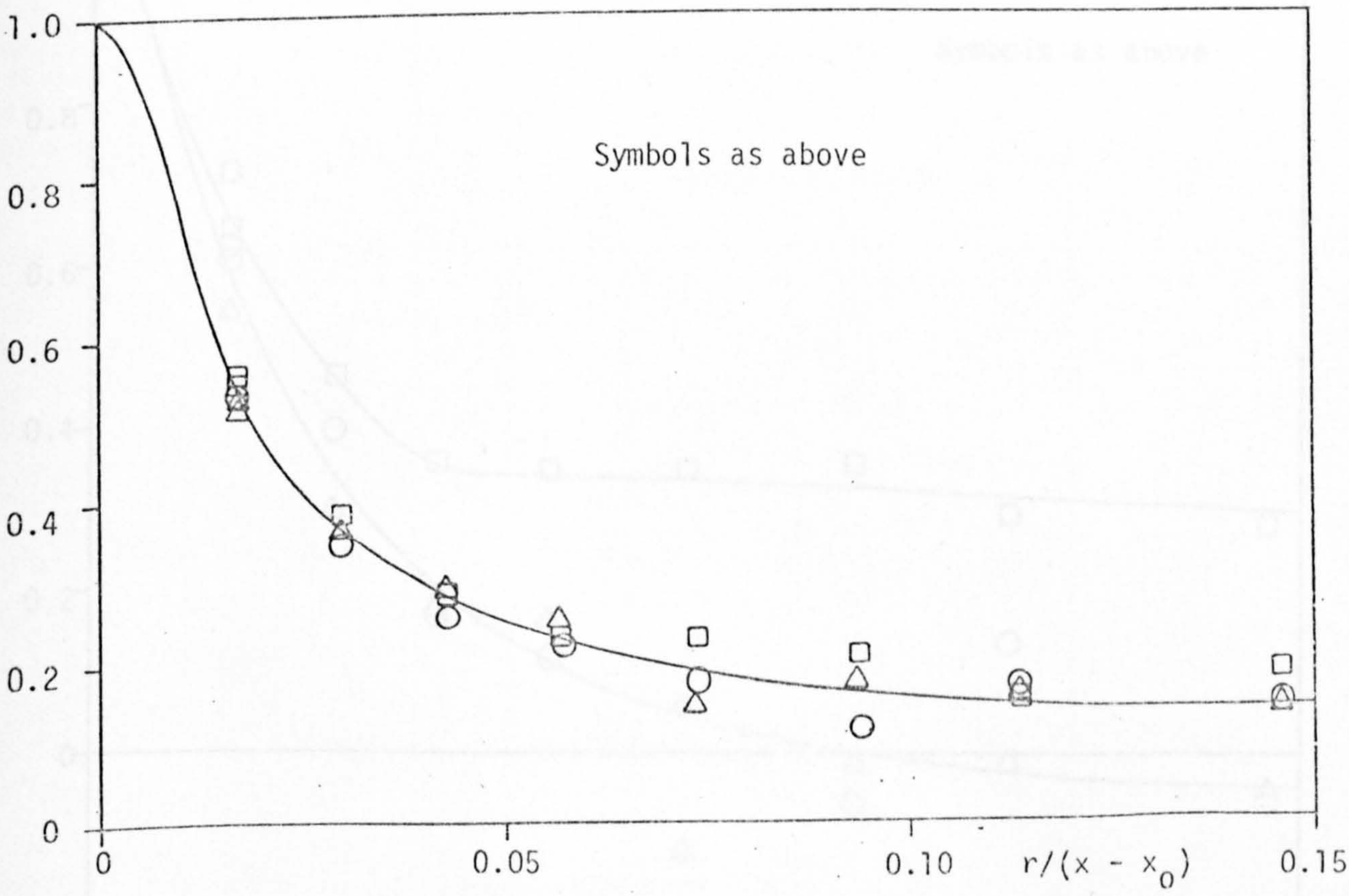


Fig. 5.75 $R_{22}(0, 0, r)$, $x - x_0 = 151.11$ cm

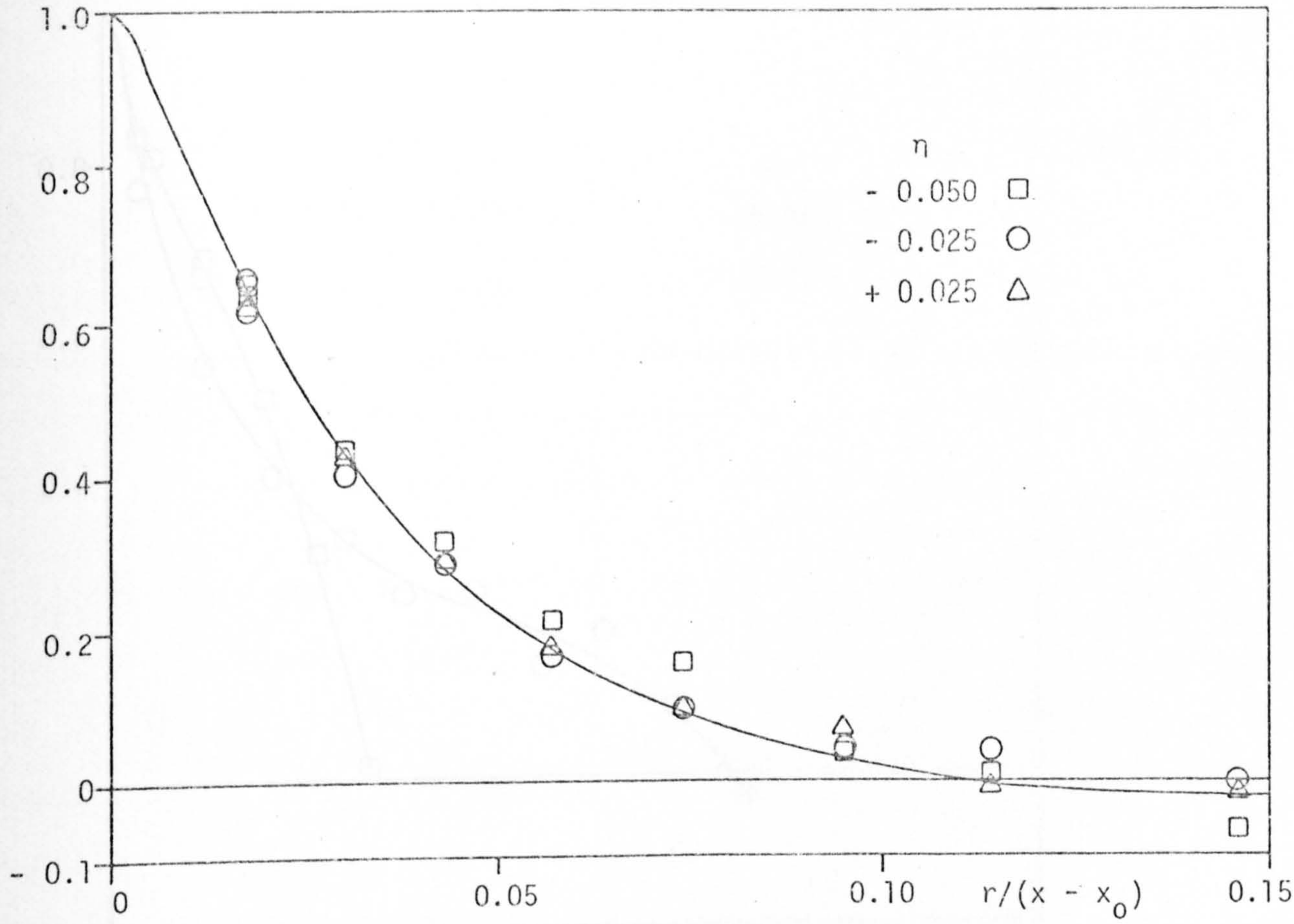


Fig. 5.76 $R_{33}(0, 0, r)$, $x - x_o$ = 151.11 cm

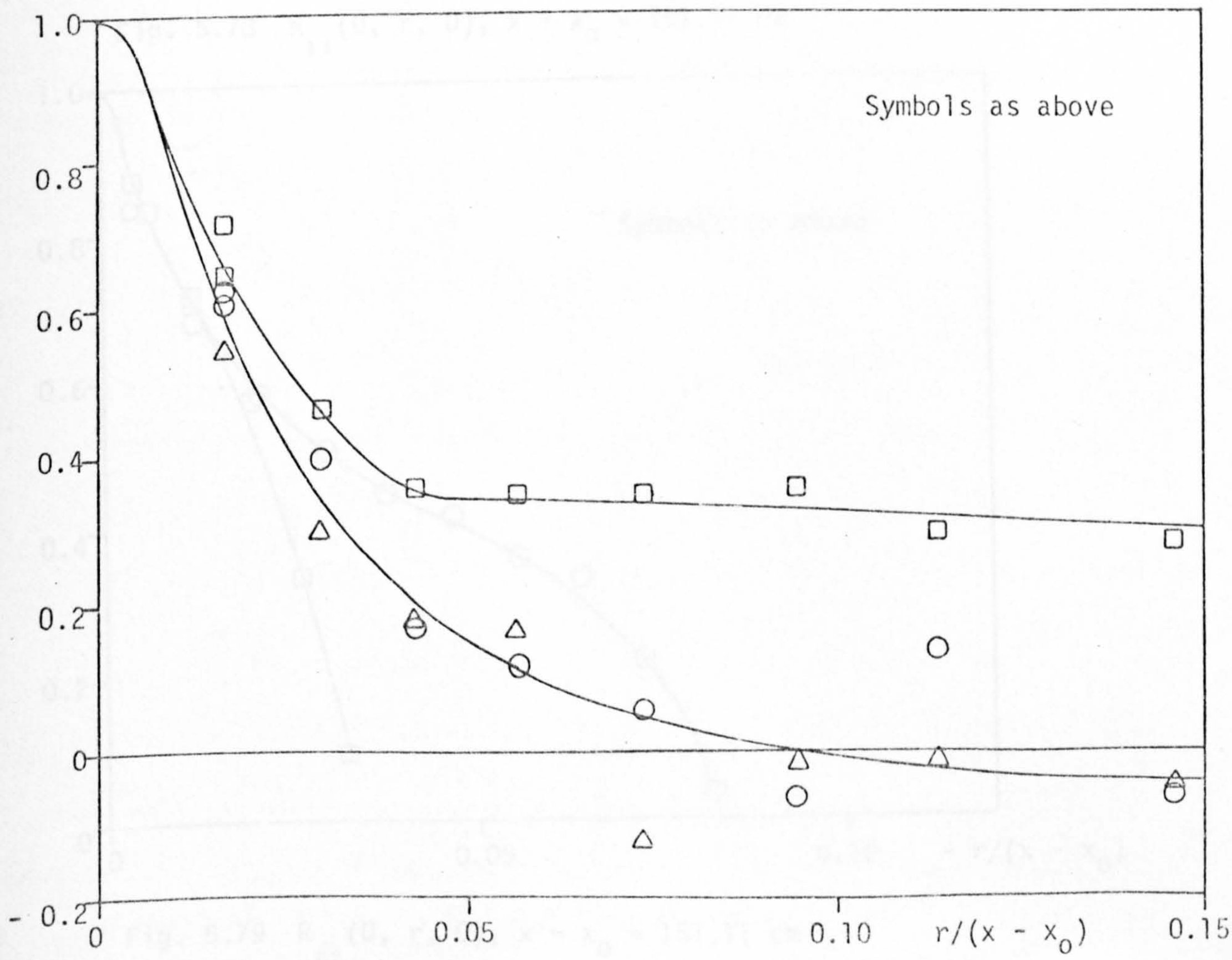


Fig. 5.77 $R_{12}(0, 0, r)$, $x - x_o$ = 151.11 cm

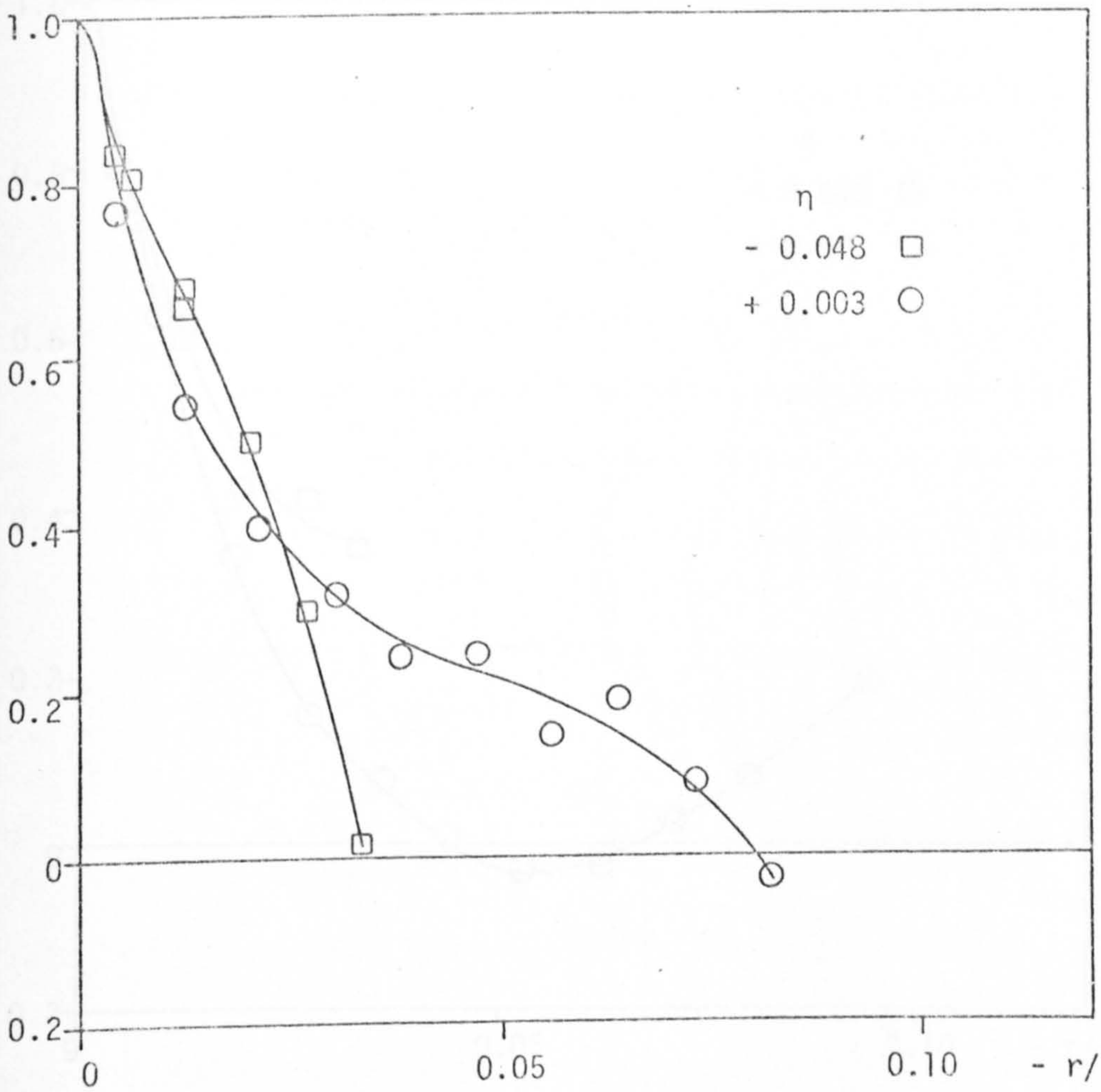


Fig. 5.78 $R_{11}(0, r, 0)$, $x - x_o$ = 151.11 cm

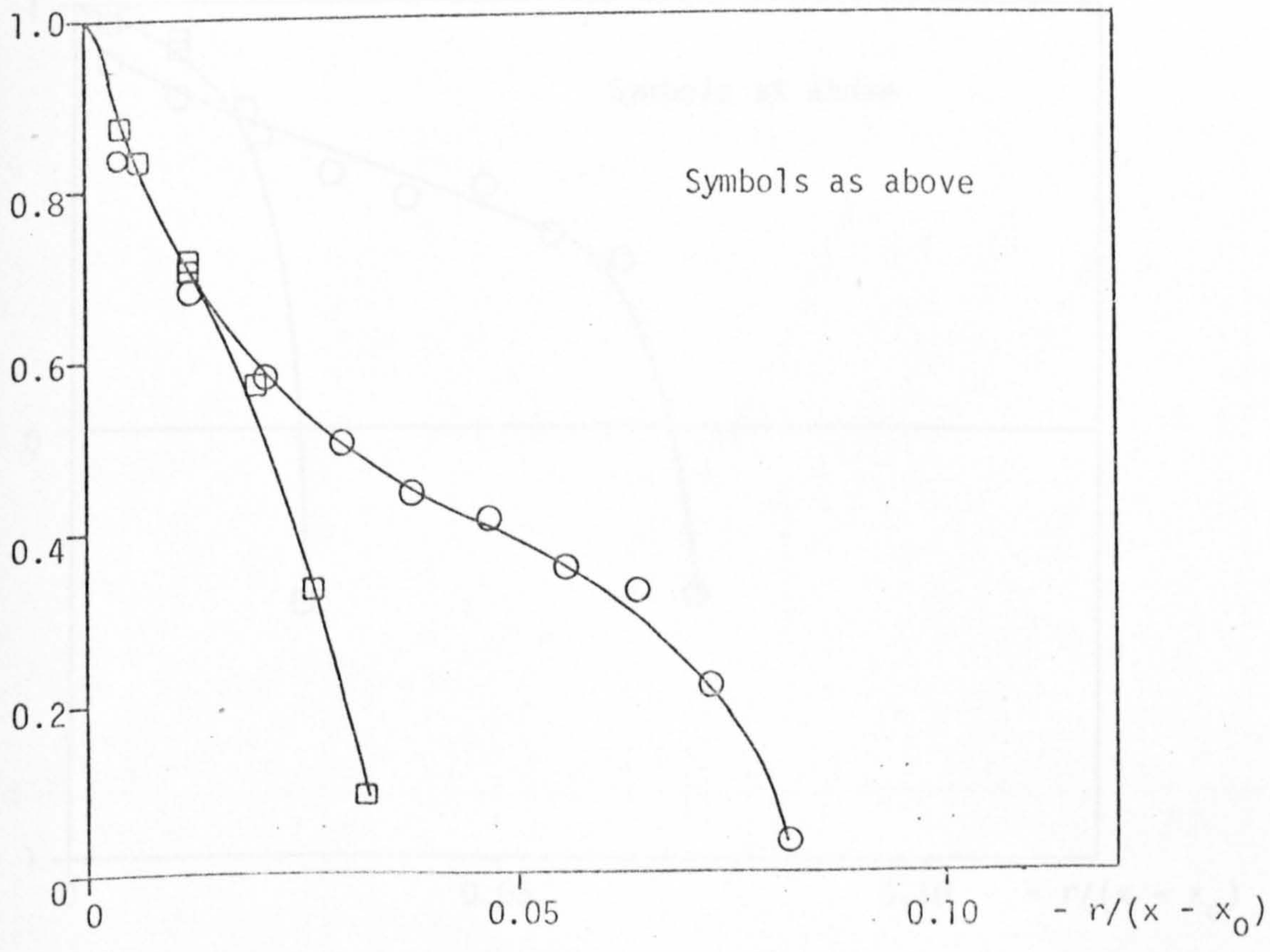


Fig. 5.79 $R_{22}(0, r, 0)$, $x - x_o$ = 151.11 cm

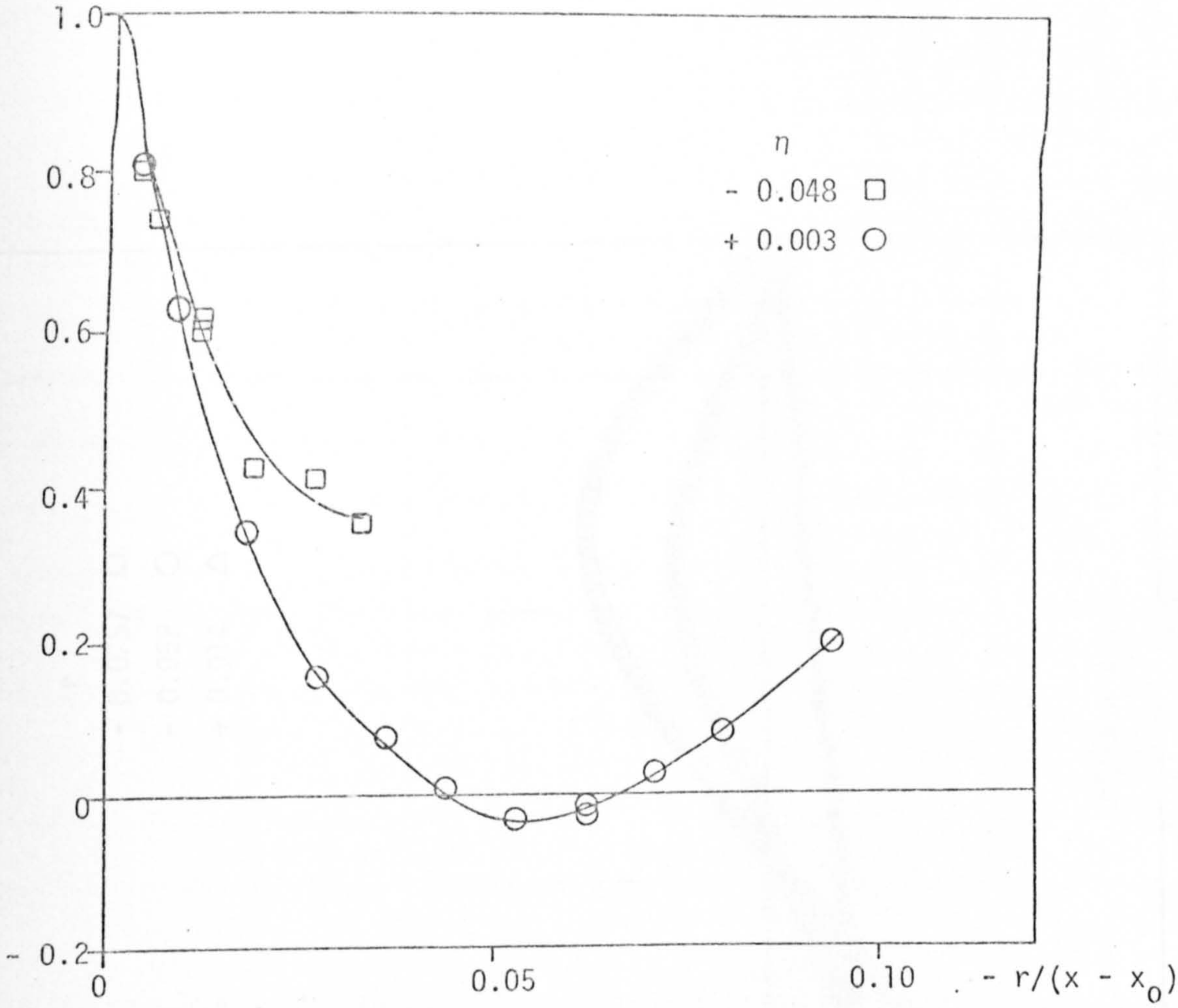


Fig. 5.80 $R_{33}(0, r, 0)$, $x - x_o = 151.11$ cm

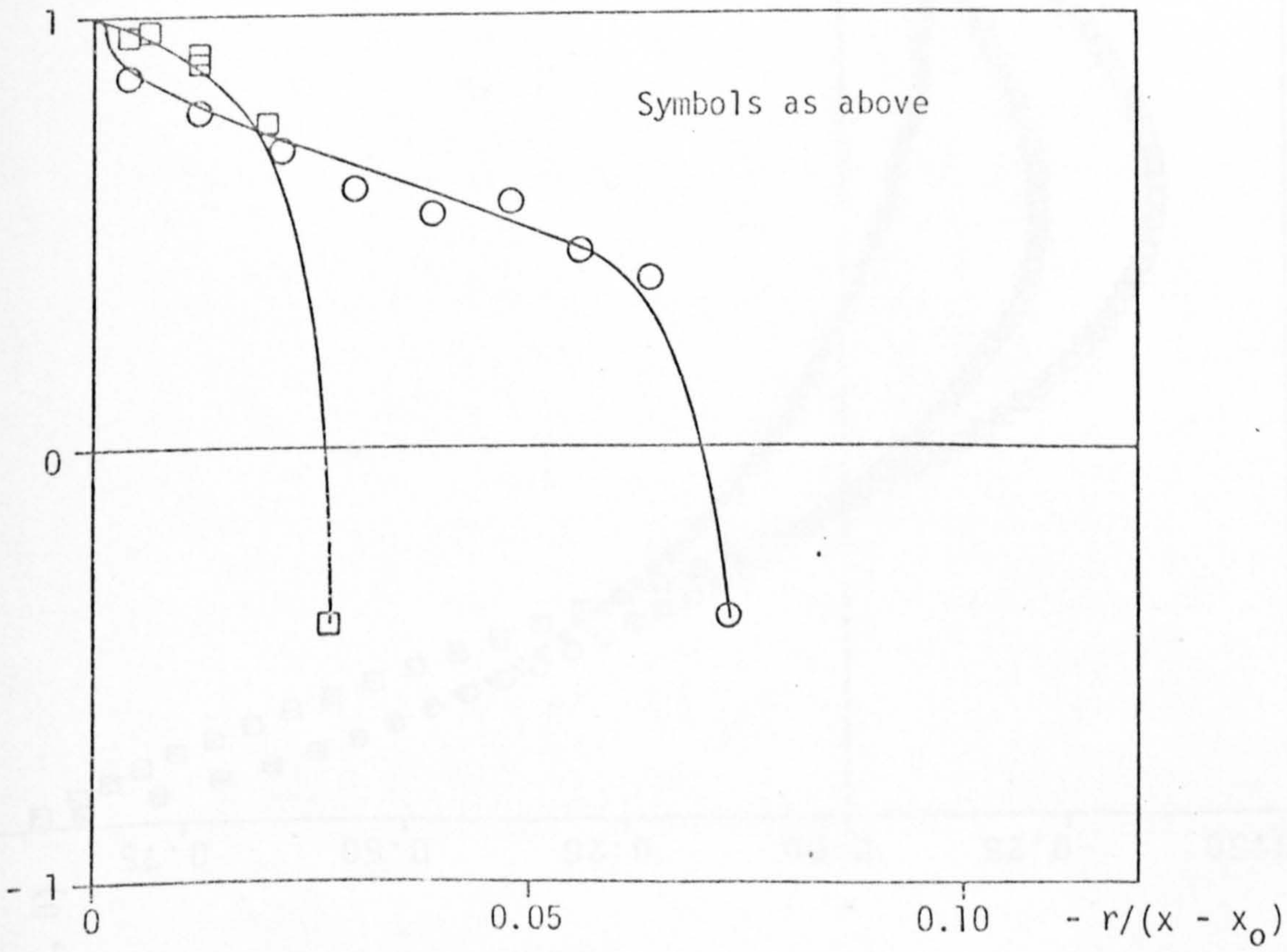


Fig. 5.81 $R_{21}(0, r, 0)$, $x - x_o = 151.11$ cm

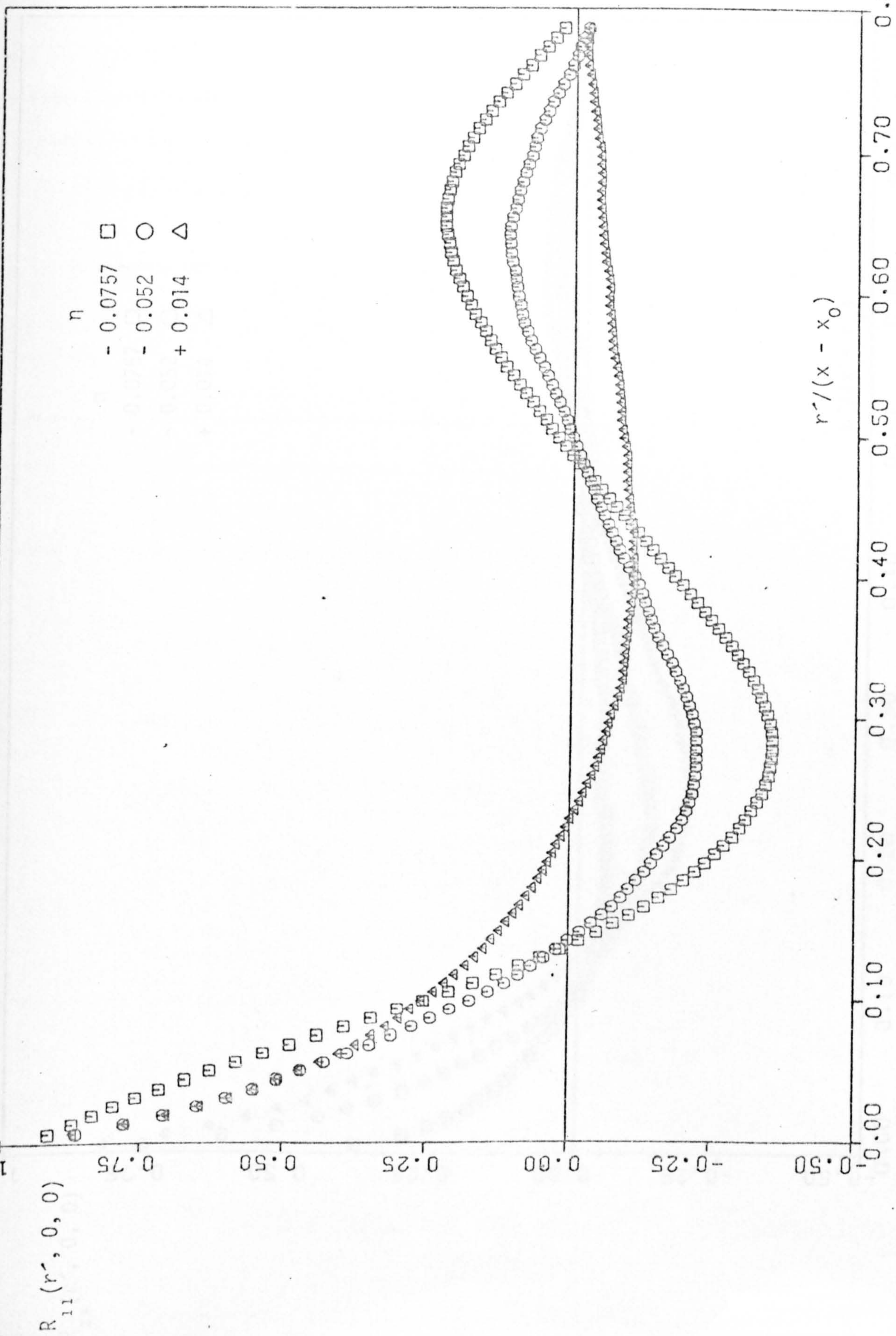


Fig. 5.82 Autocorrelation of u, x - x_o = 151.51 cm

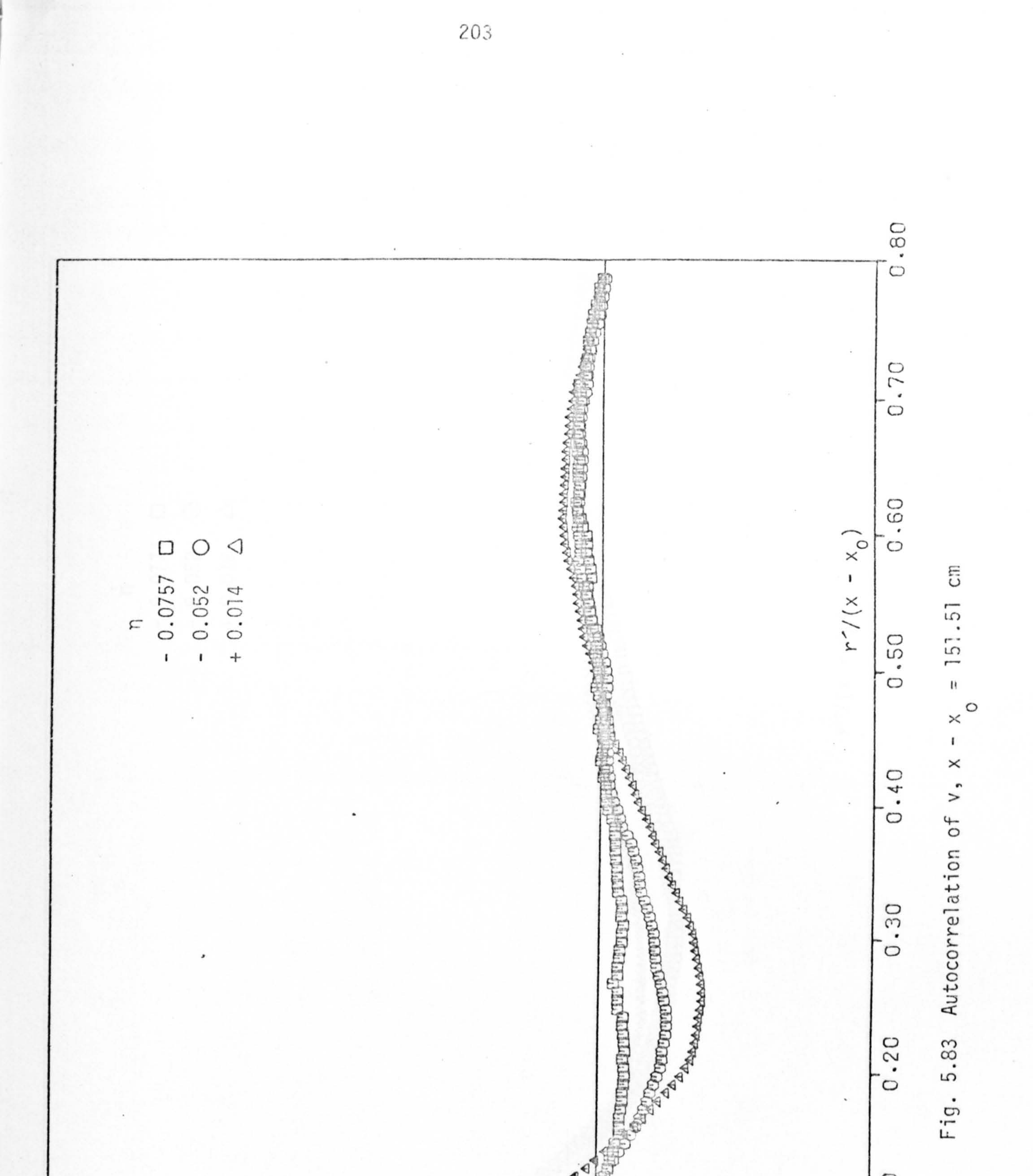


Fig. 5.83 Autocorrelation of v, x - x_o = 151.51 cm

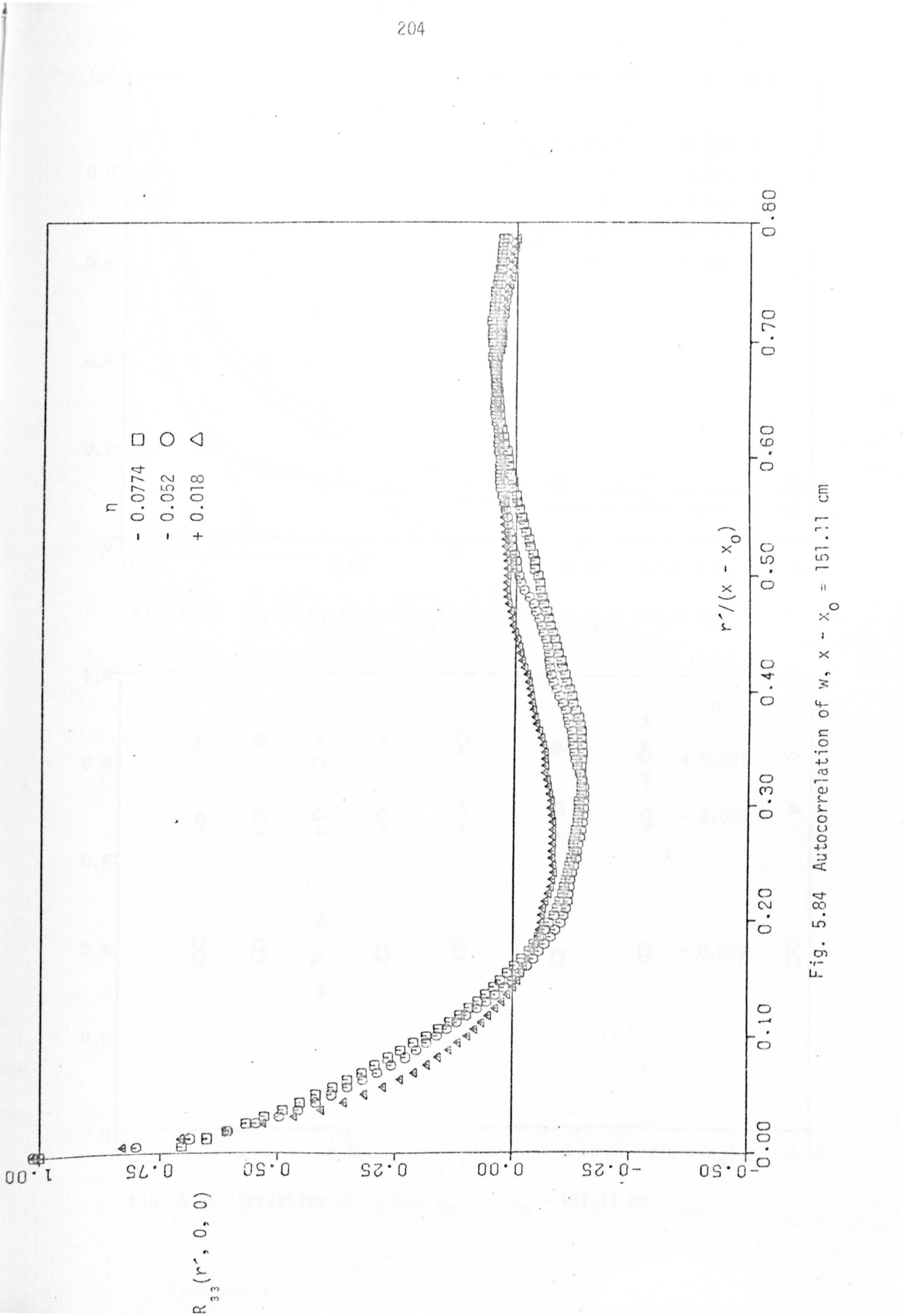


Fig. 5.84 Autocorrelation of w, x - x_0 = 151.11 cm

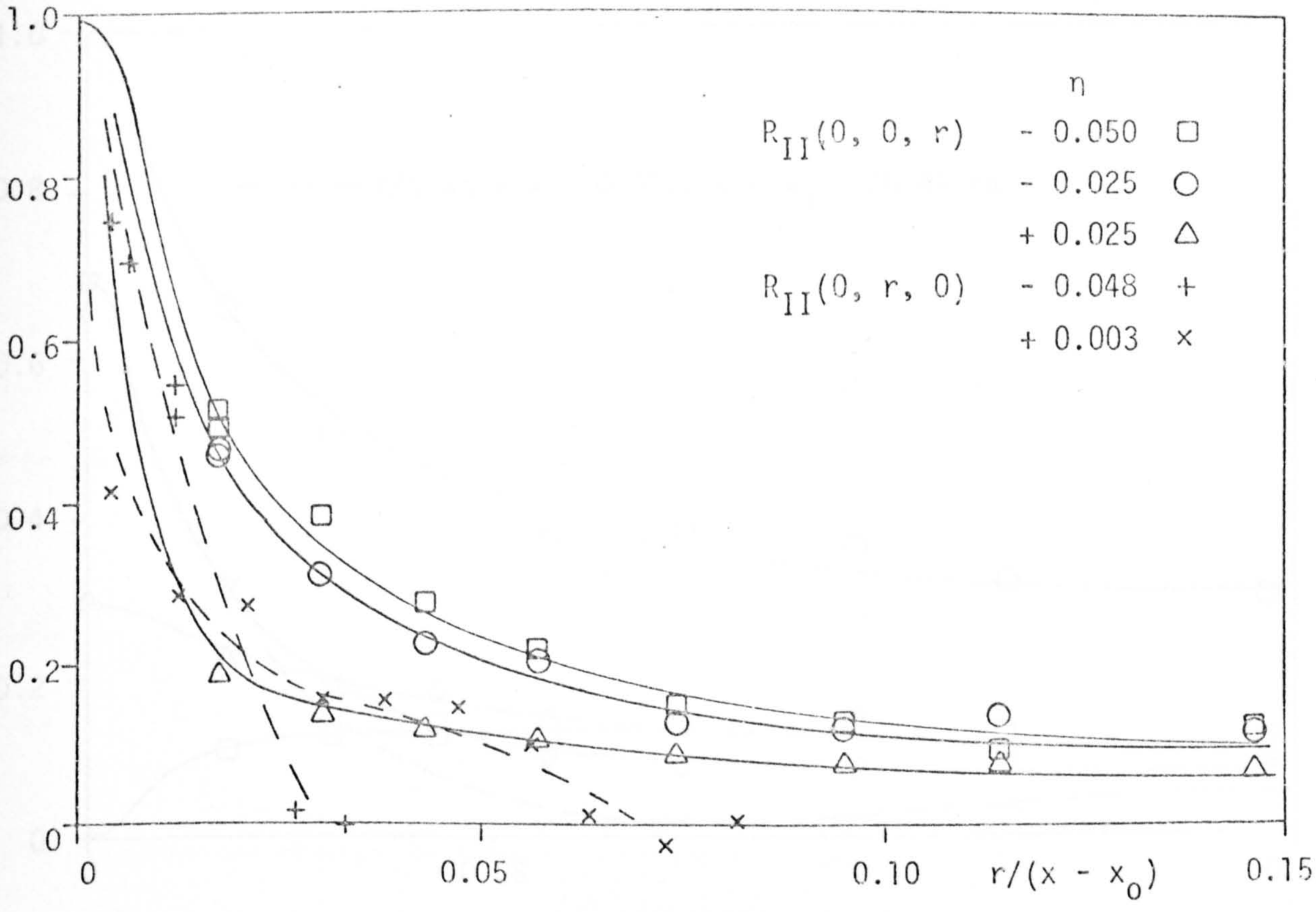


Fig. 5.85 $R_{II}(0, 0, r)$ and $R_{II}(0, r, 0)$, $x - x_o$ = 151.11 cm

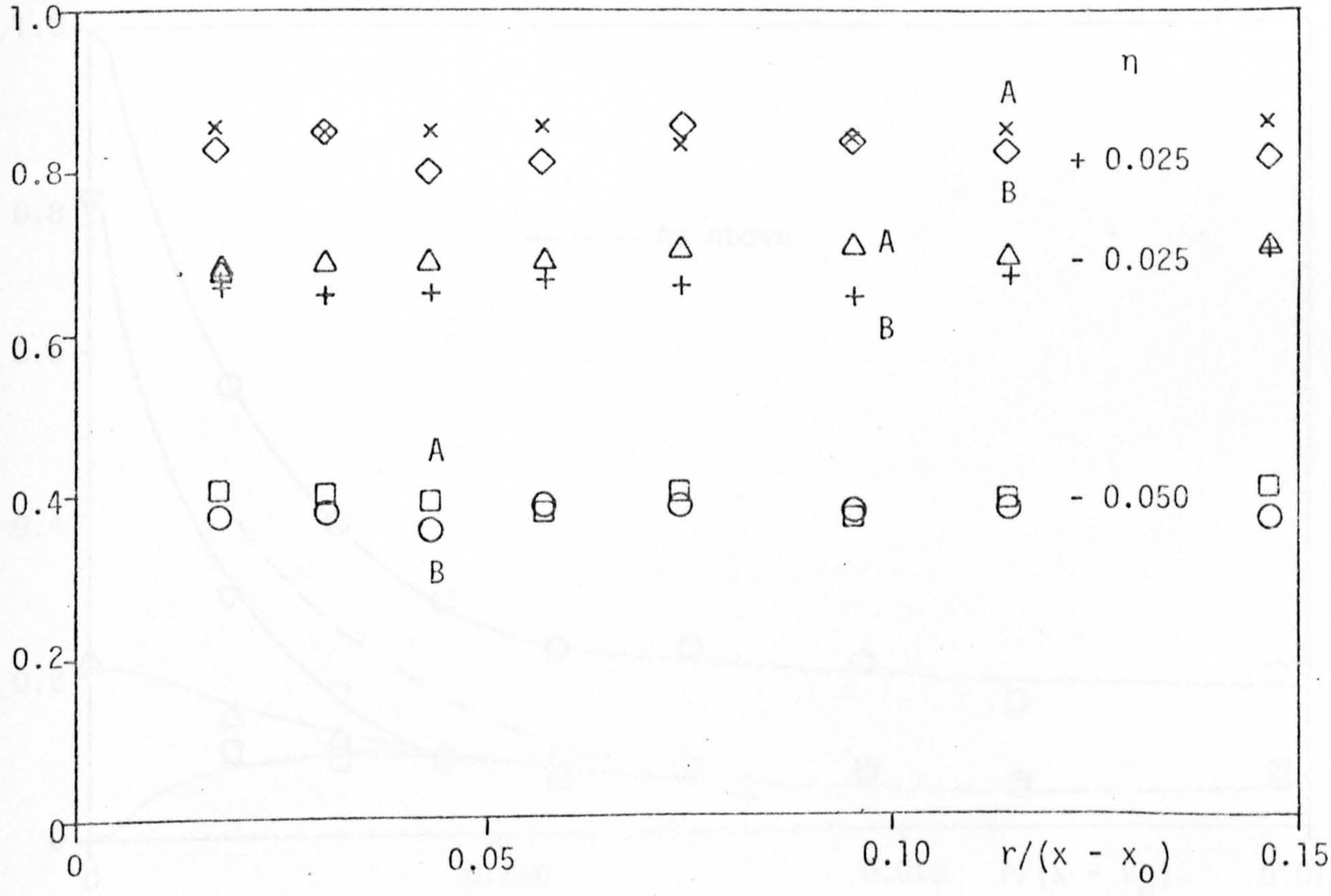


Fig. 5.86 Variation of γ_A and γ_B, $x - x_o$ = 151.11 cm

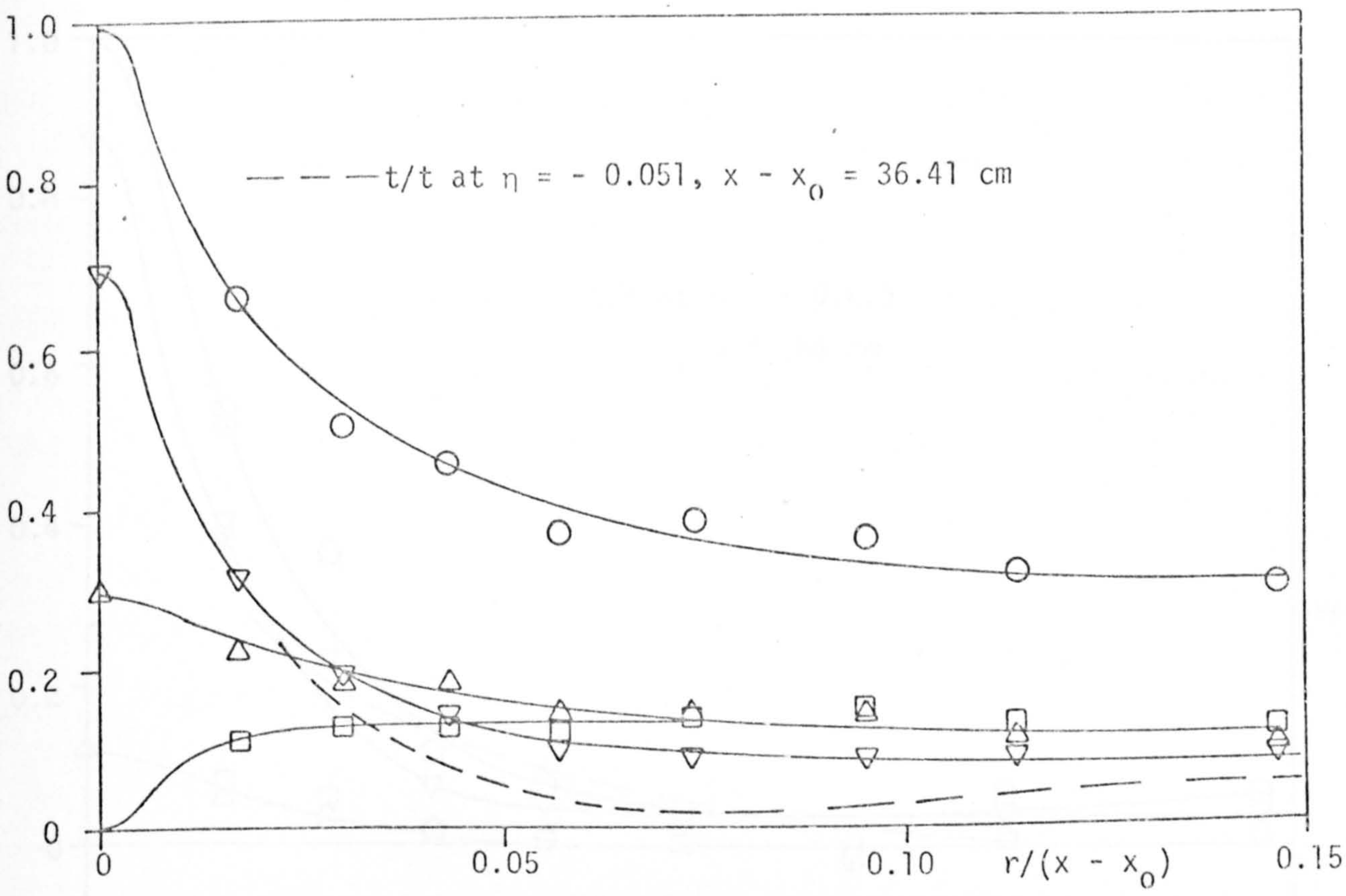


Fig. 5.87 Conditionally sampled $R_{11}(0, 0, r)$, $x - x_o = 151.11$ cm, $\eta = -0.050$

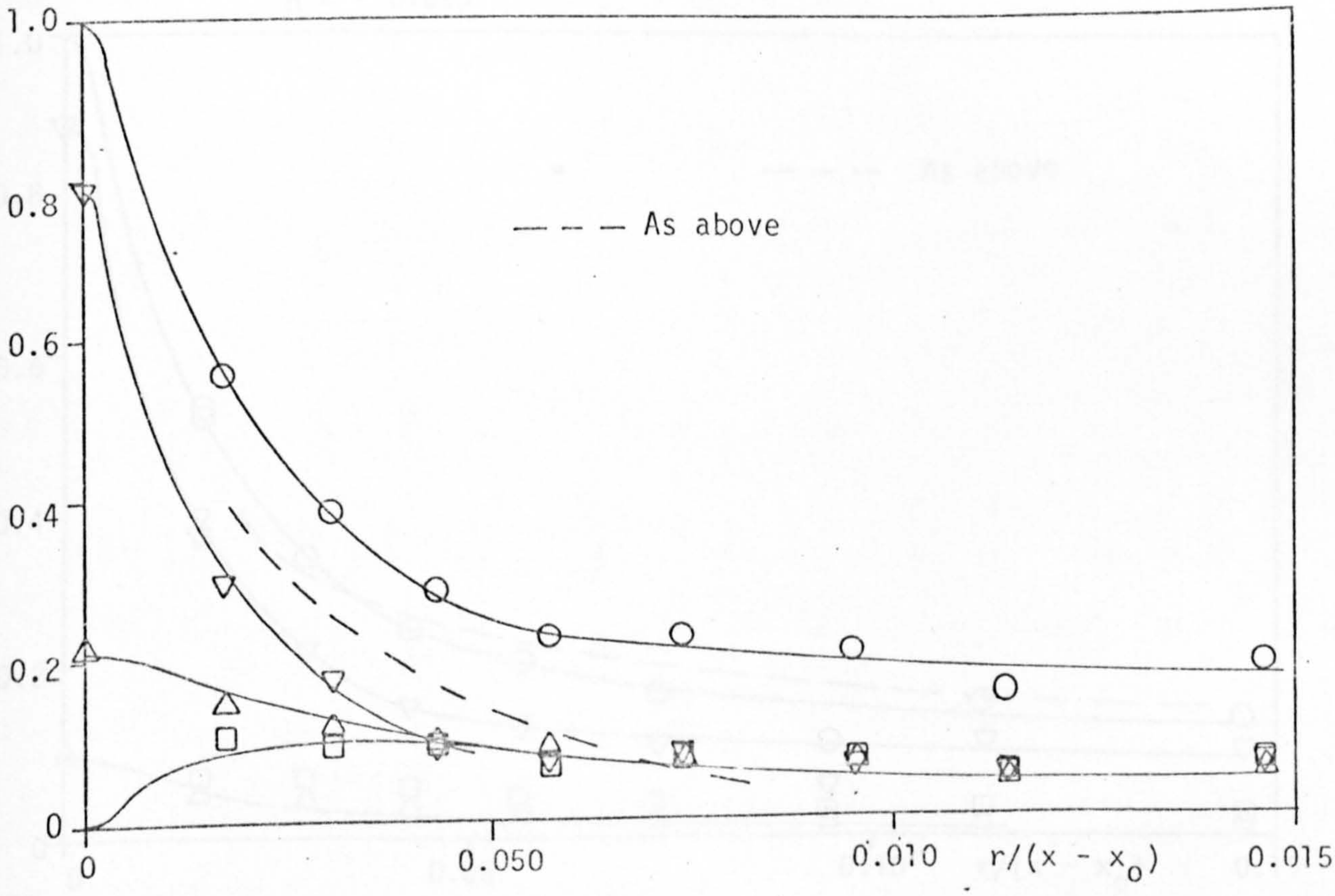


Fig. 5.88 Conditionally sampled $R_{22}(0, 0, r)$, $x - x_o = 151.11$ cm, $\eta = -0.050$

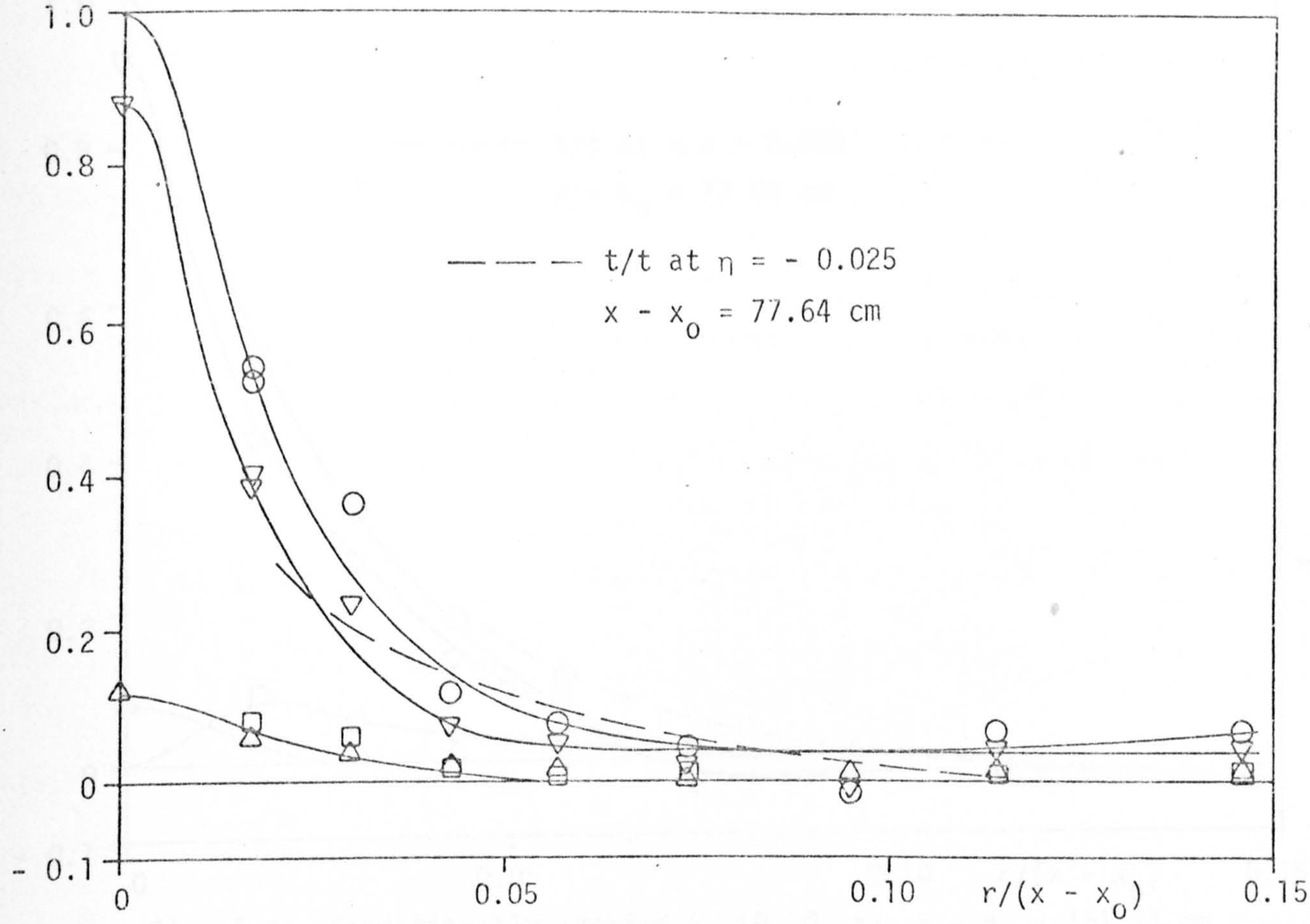


Fig. 5.89 Conditionally sampled $R_{11}(0, 0, r)$, $x - x_o = 151.11$ cm, $\eta = - 0.025$

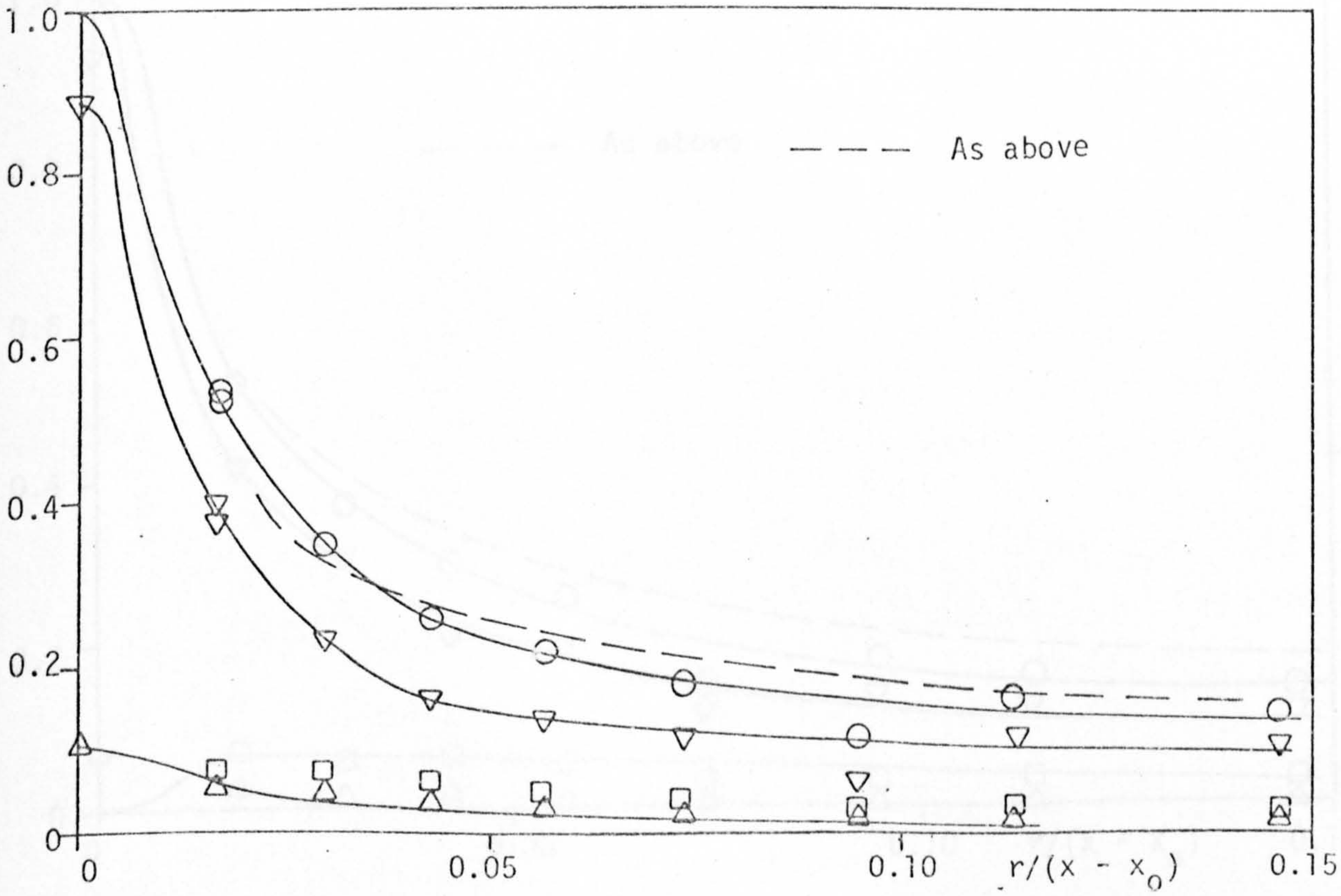


Fig. 5.90 Conditionally sampled $R_{22}(0, 0, r)$, $x - x_o = 151.11$ cm, $\eta = - 0.025$

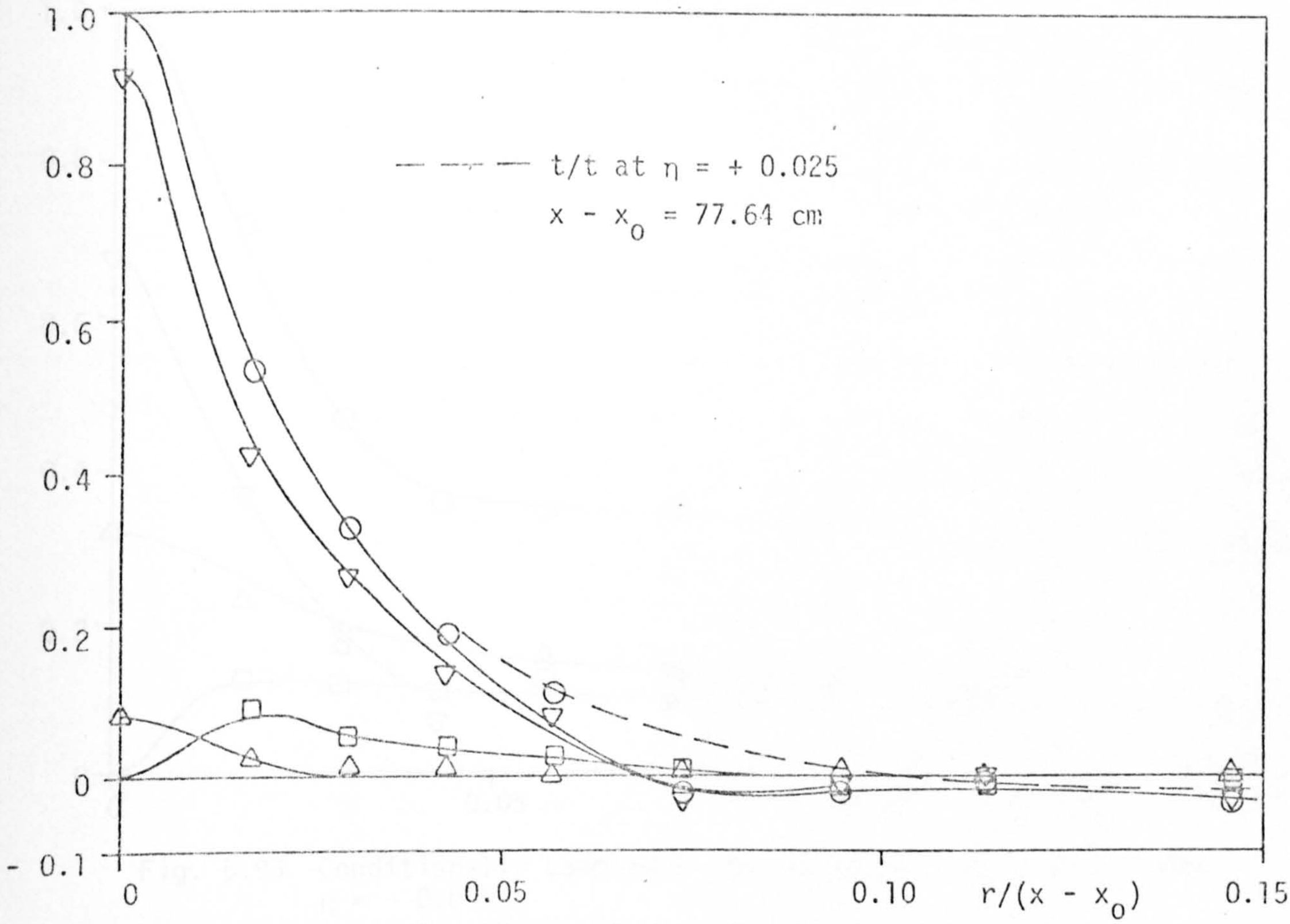


Fig. 5.91 Conditionally sampled $R_{11}(0, 0, r)$, $x - x_o = 151.11$ cm, $\eta = + 0.025$

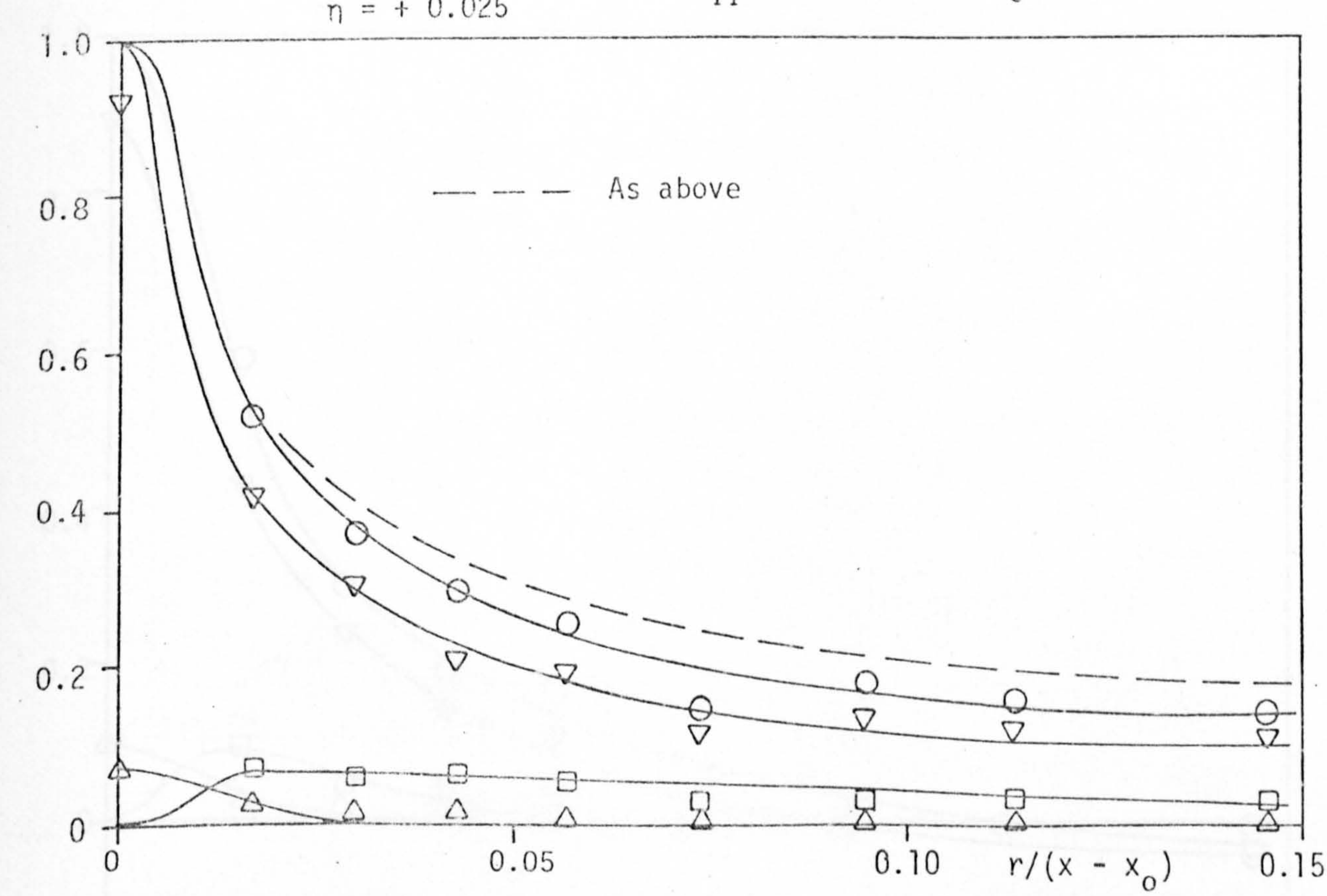


Fig. 5.92 Conditionally sampled $R_{22}(0, r, 0)$, $x - x_o = 151.11$ cm, $\eta = + 0.025$

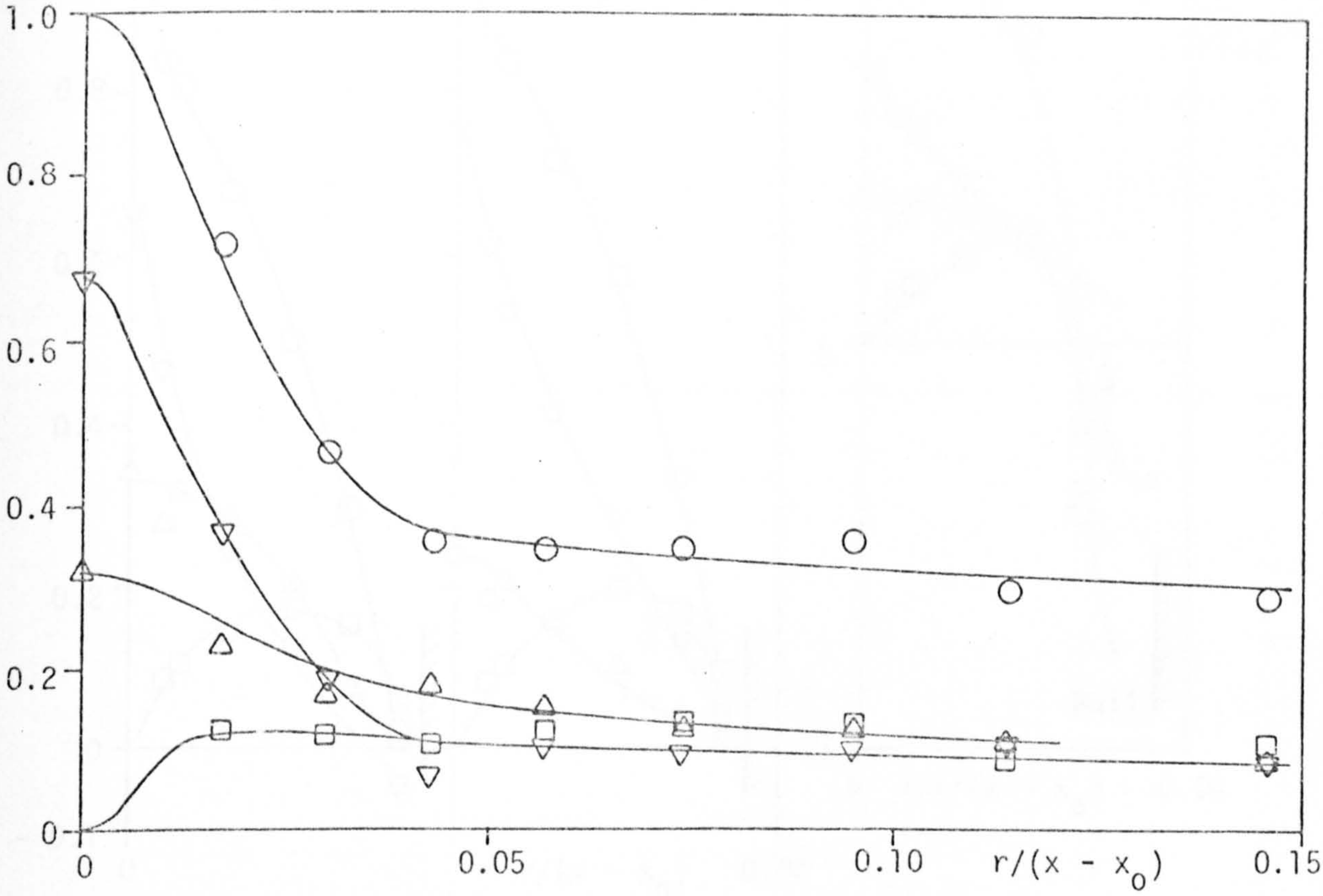


Fig. 5.93 Conditionally sampled $R_{12}(0, 0, r)$, $x - x_0 = 151.11$ cm, $\eta = -0.050$

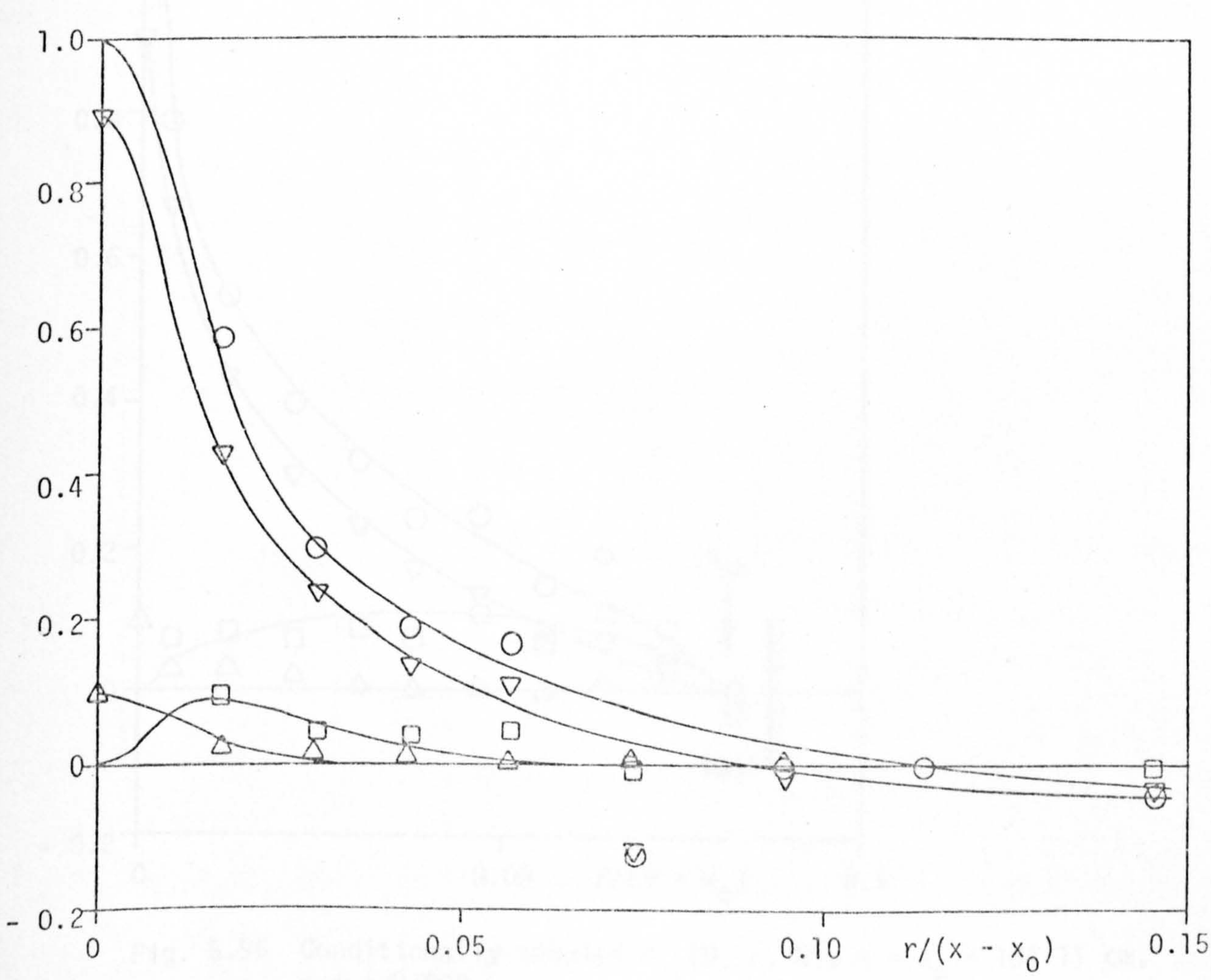


Fig. 5.94 Conditionally sampled $R_{12}(0, 0, r)$, $x - x_0 = 151.11$ cm, $\eta = +0.025$

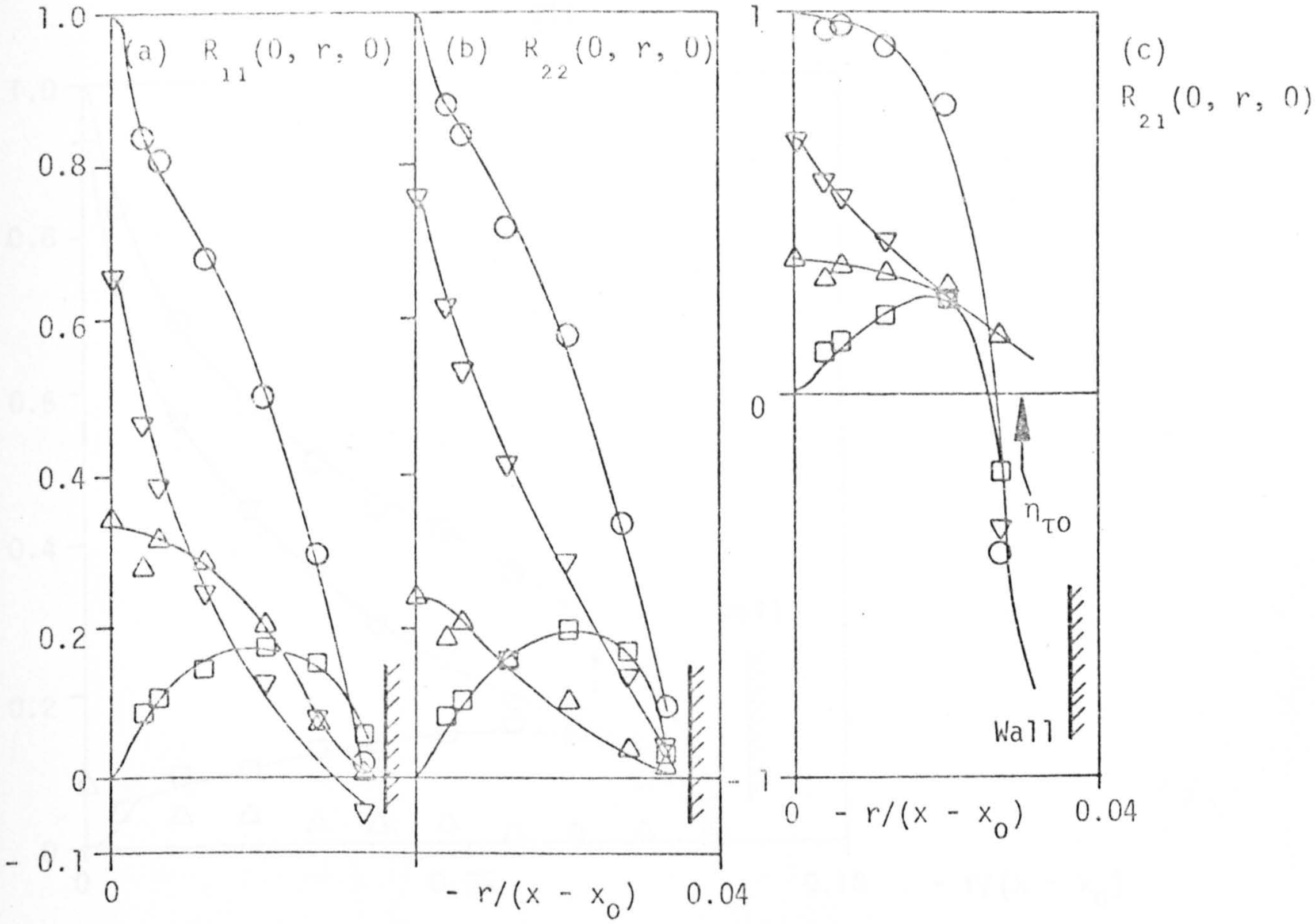


Fig. 5.95 Conditionally sampled normal correlations, $x - x_o$ = 151.11 cm, η = - 0.048

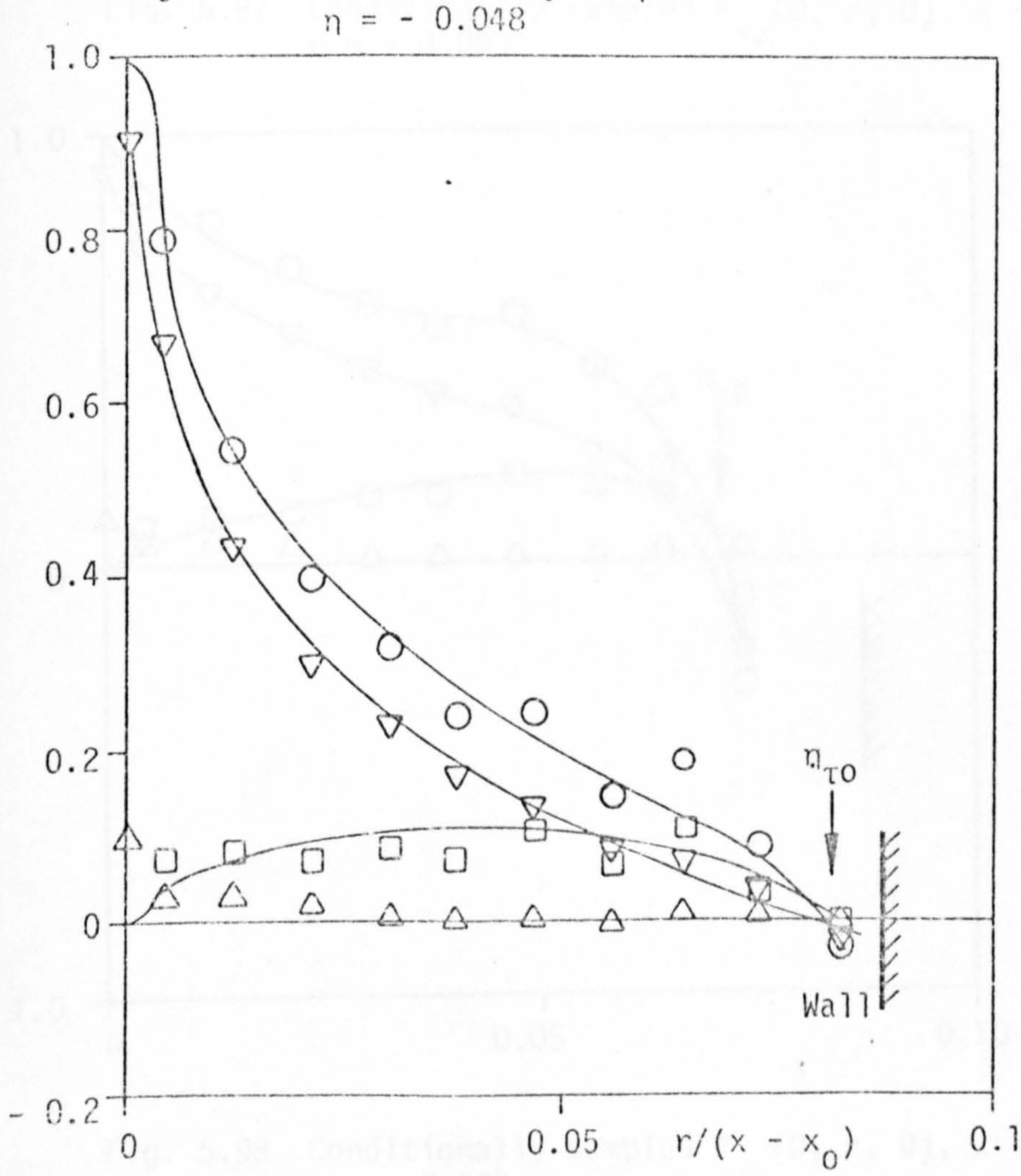


Fig. 5.96 Conditionally sampled $R_{11}(0, r, 0)$, $x - x_o$ = 151.11 cm, η = + 0.003

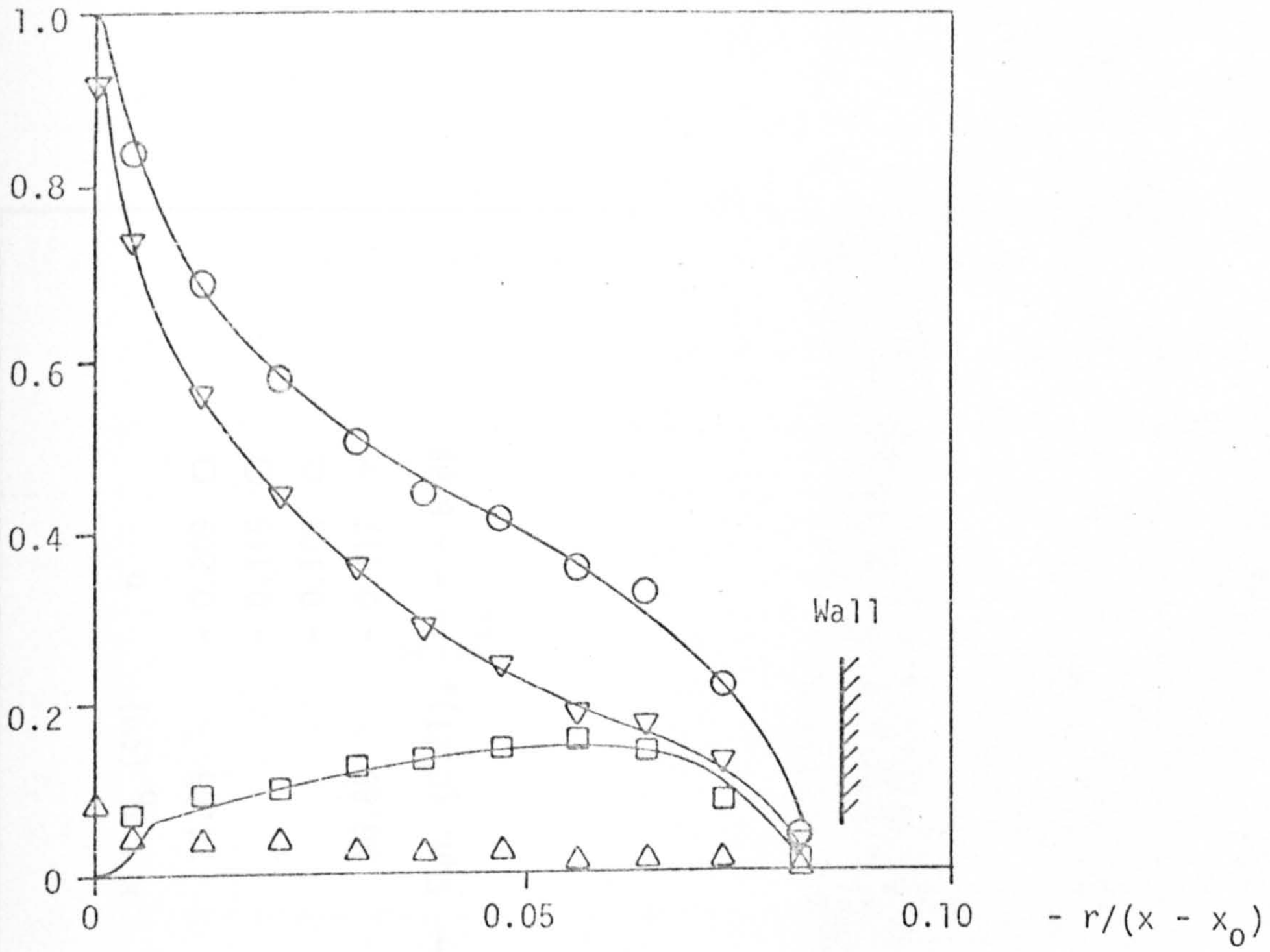


Fig. 5.97 Conditionally sampled $R_{22}(0, r, 0)$, $x - x_o = 151.51$ cm, $\eta = + 0.003$

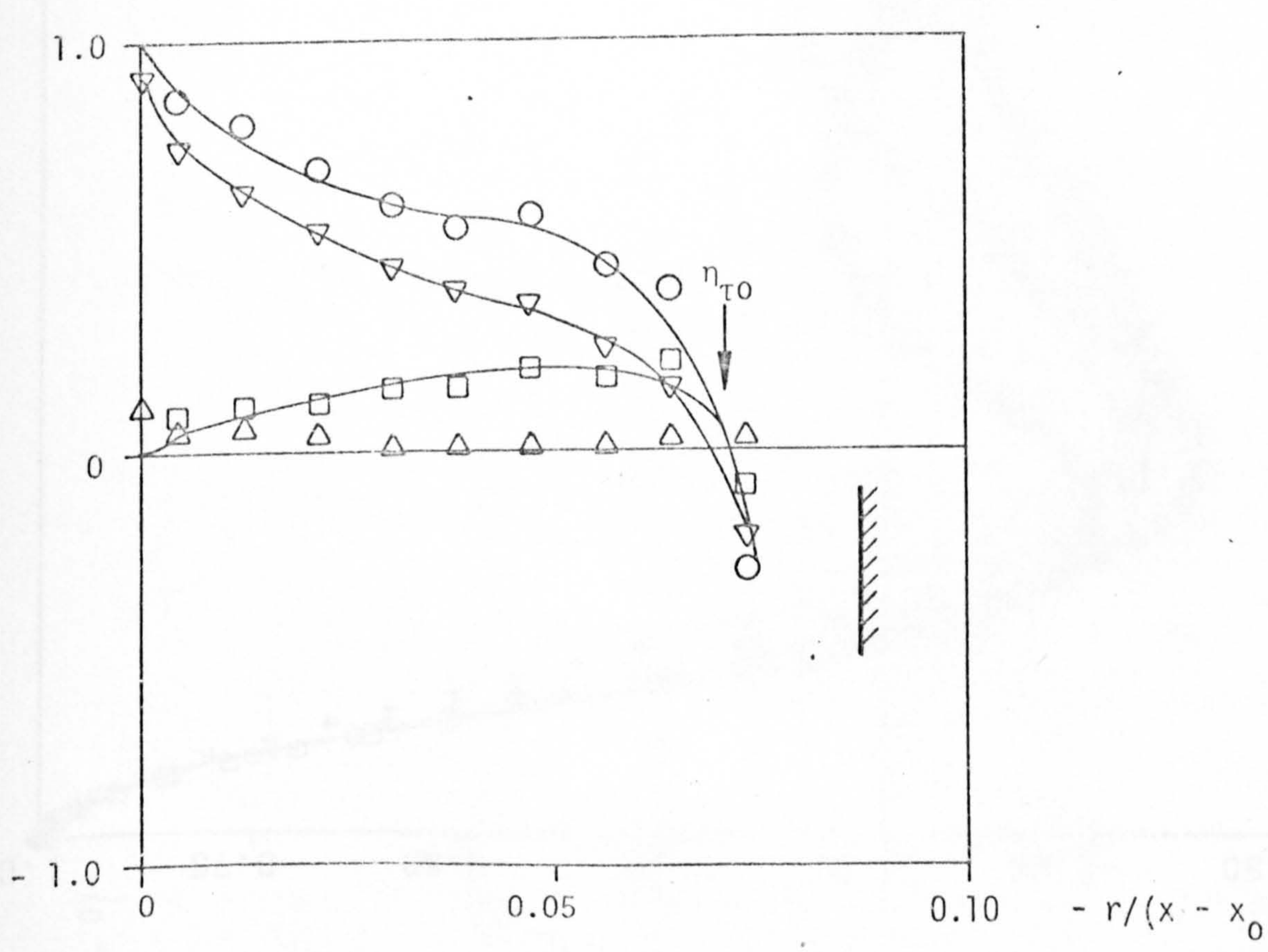


Fig. 5.98 Conditionally sampled $R_{21}(0, r, 0)$, $x - x_o = 151.51$ cm, $\eta = + 0.003$

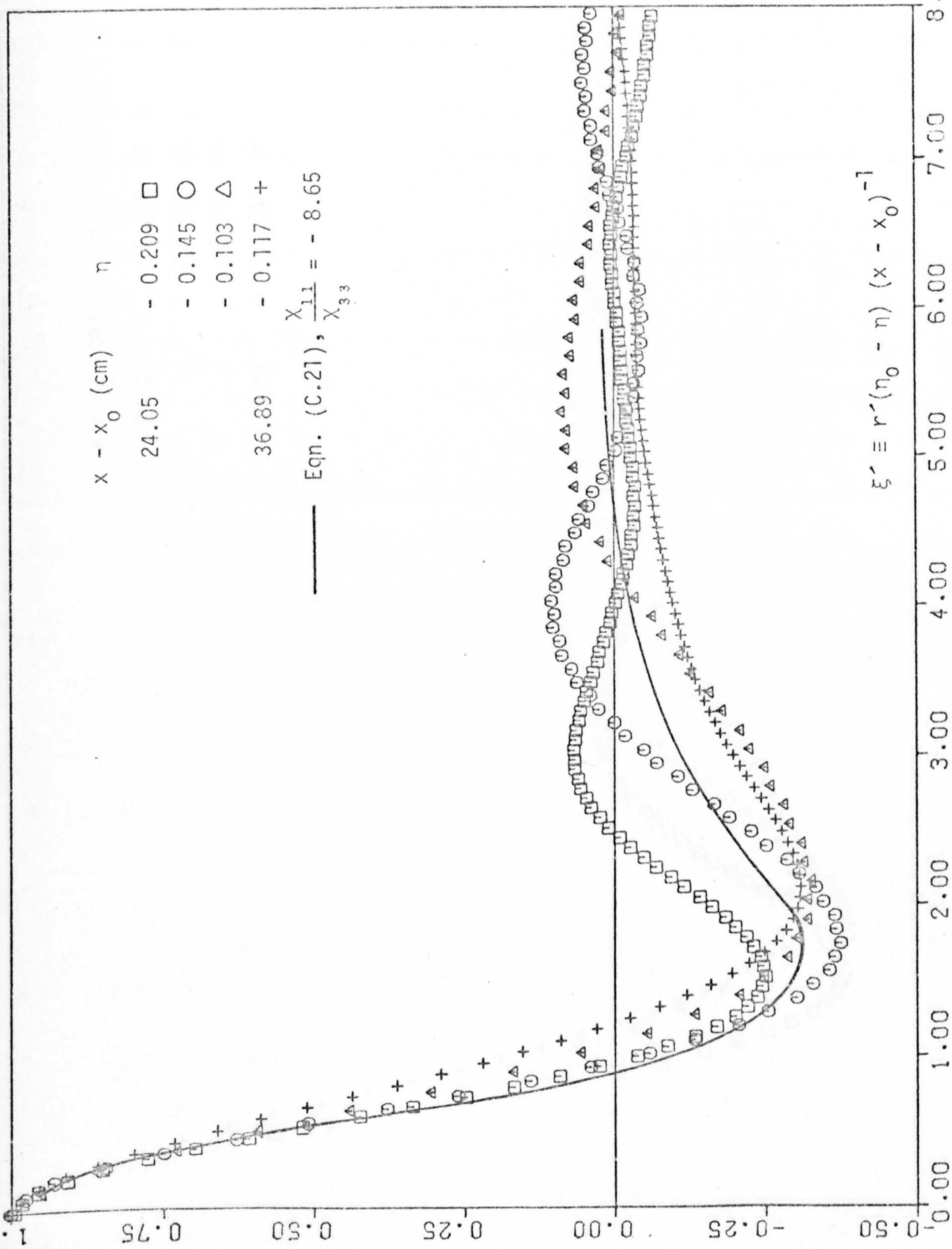


Fig. 5.99 Autocorrelation of u in the unaffected potential flow

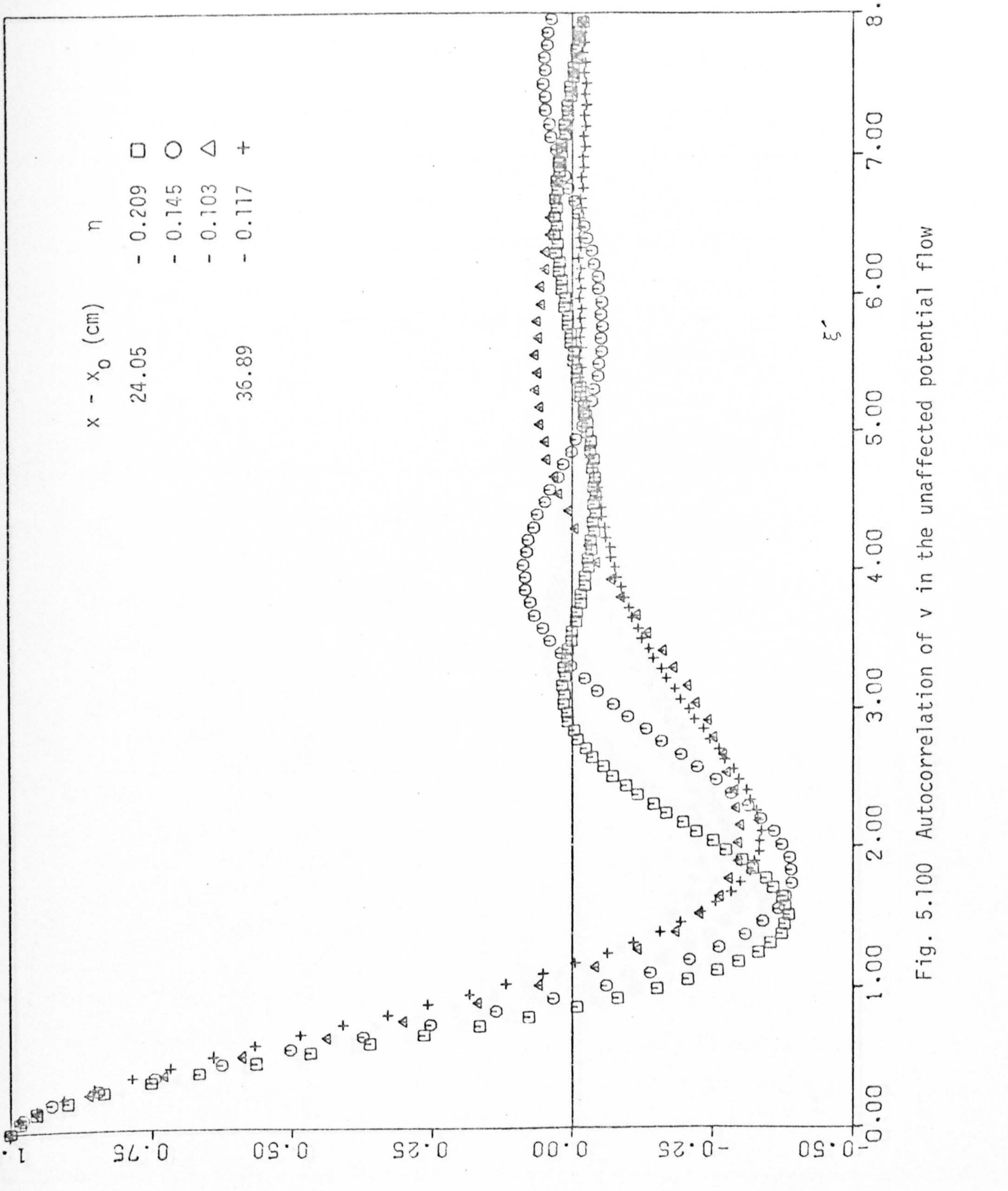


Fig. 5.100 Autocorrelation of v in the unaffected potential flow

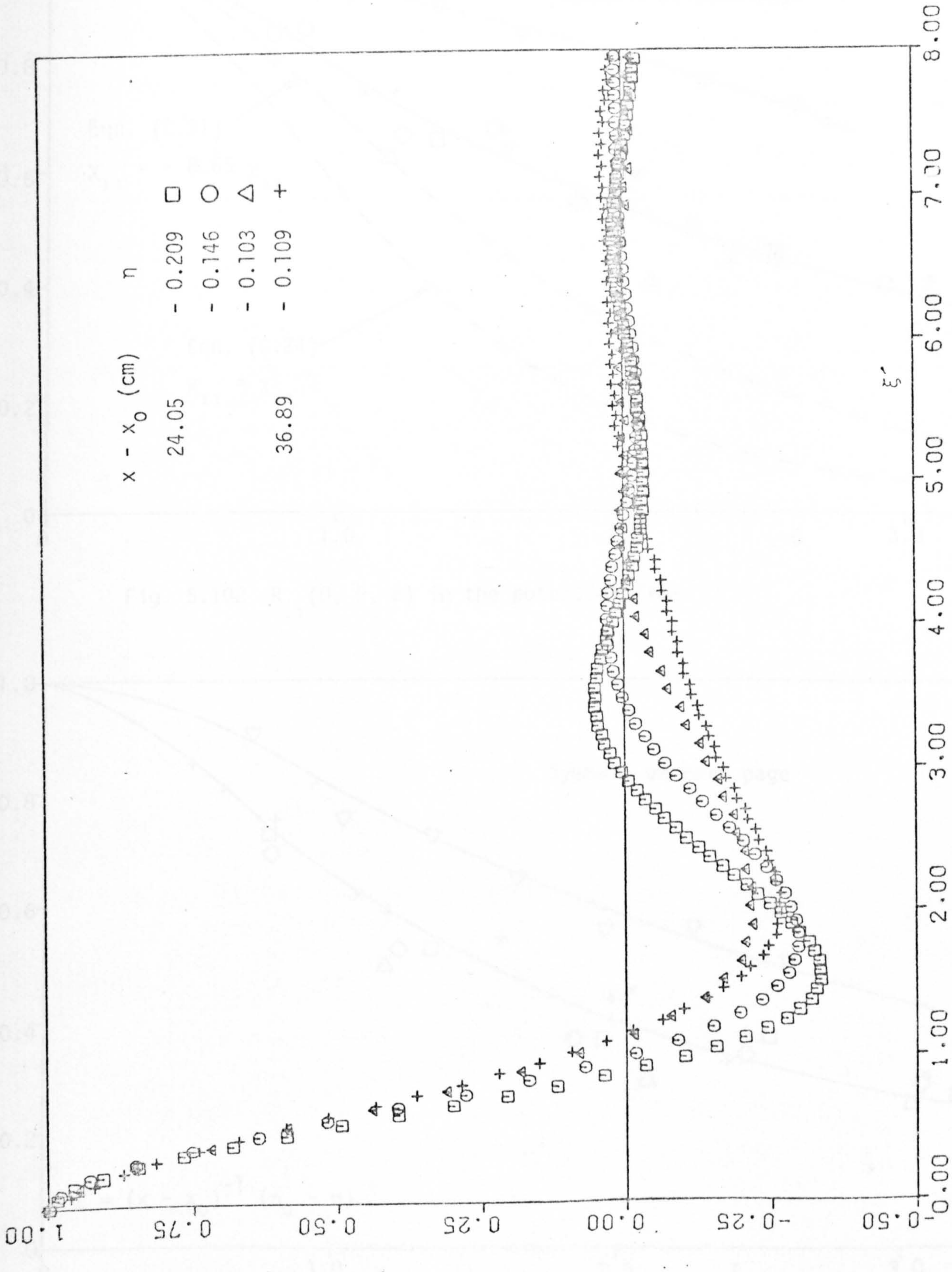


Fig. 5.101 Autocorrelation of w in the unaffected potential flow

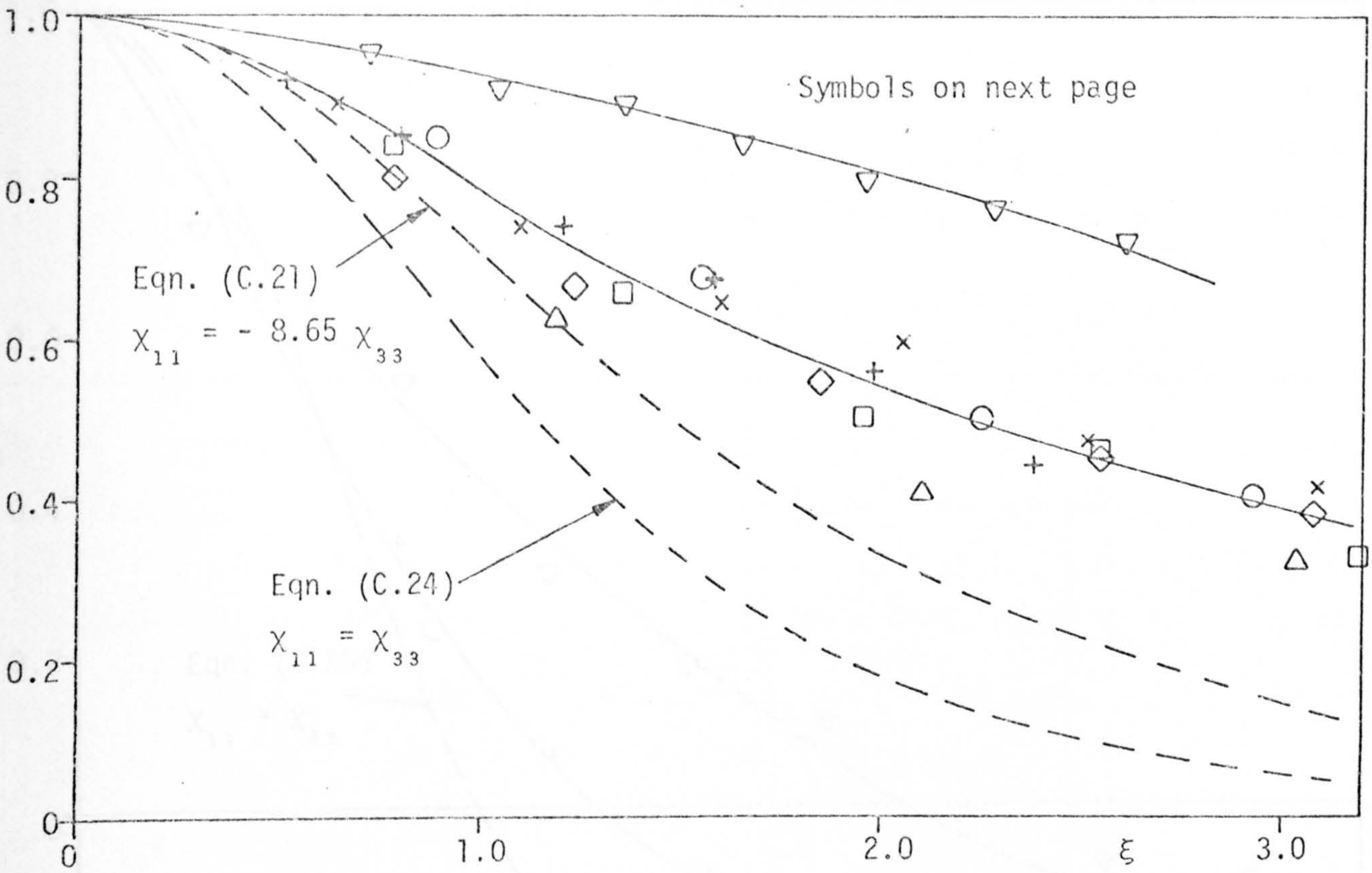


Fig. 5.102 $R_{11}(0, 0, r)$ in the potential flow

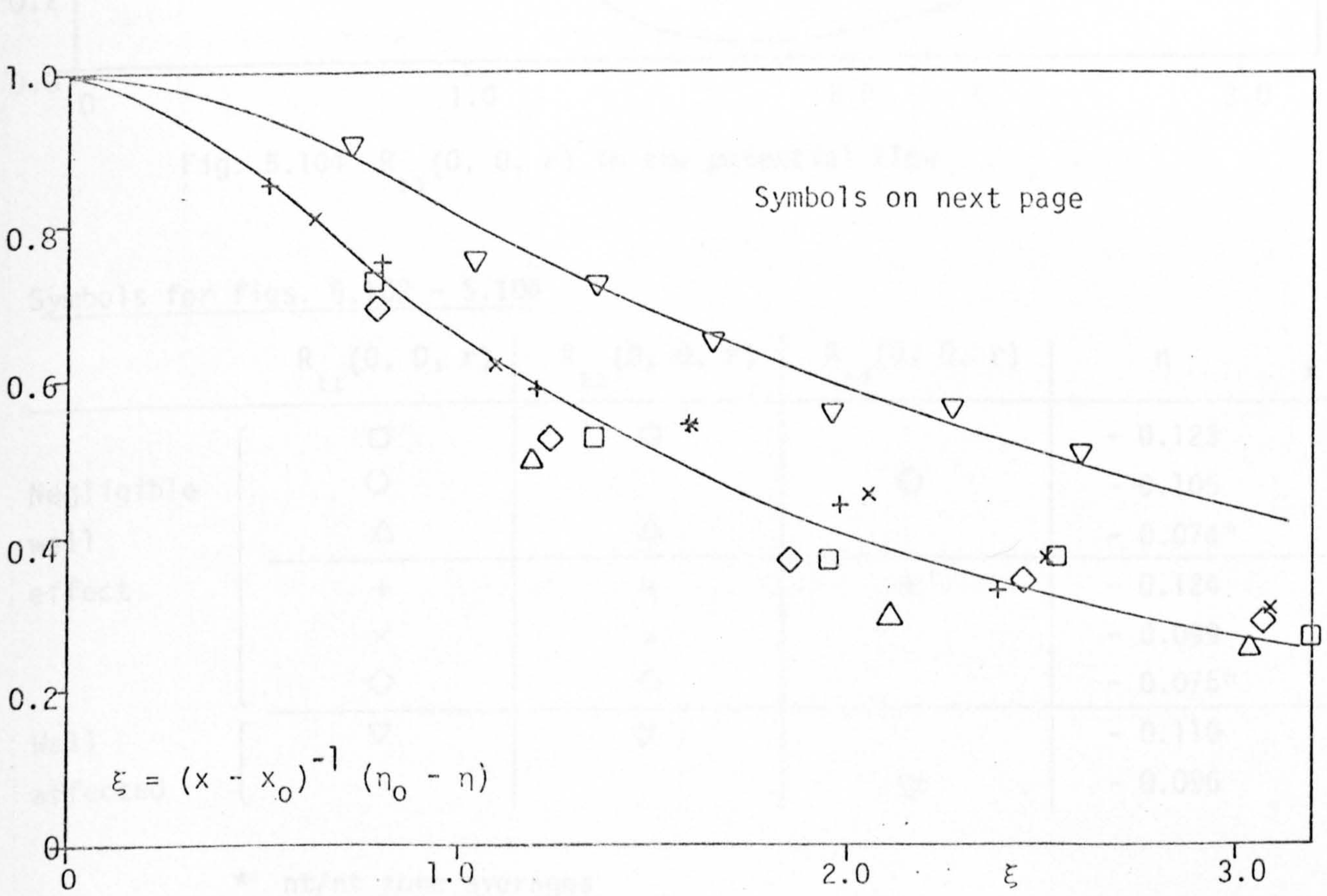


Fig. 5.103 $R_{22}(0, 0, r)$ in the potential flow

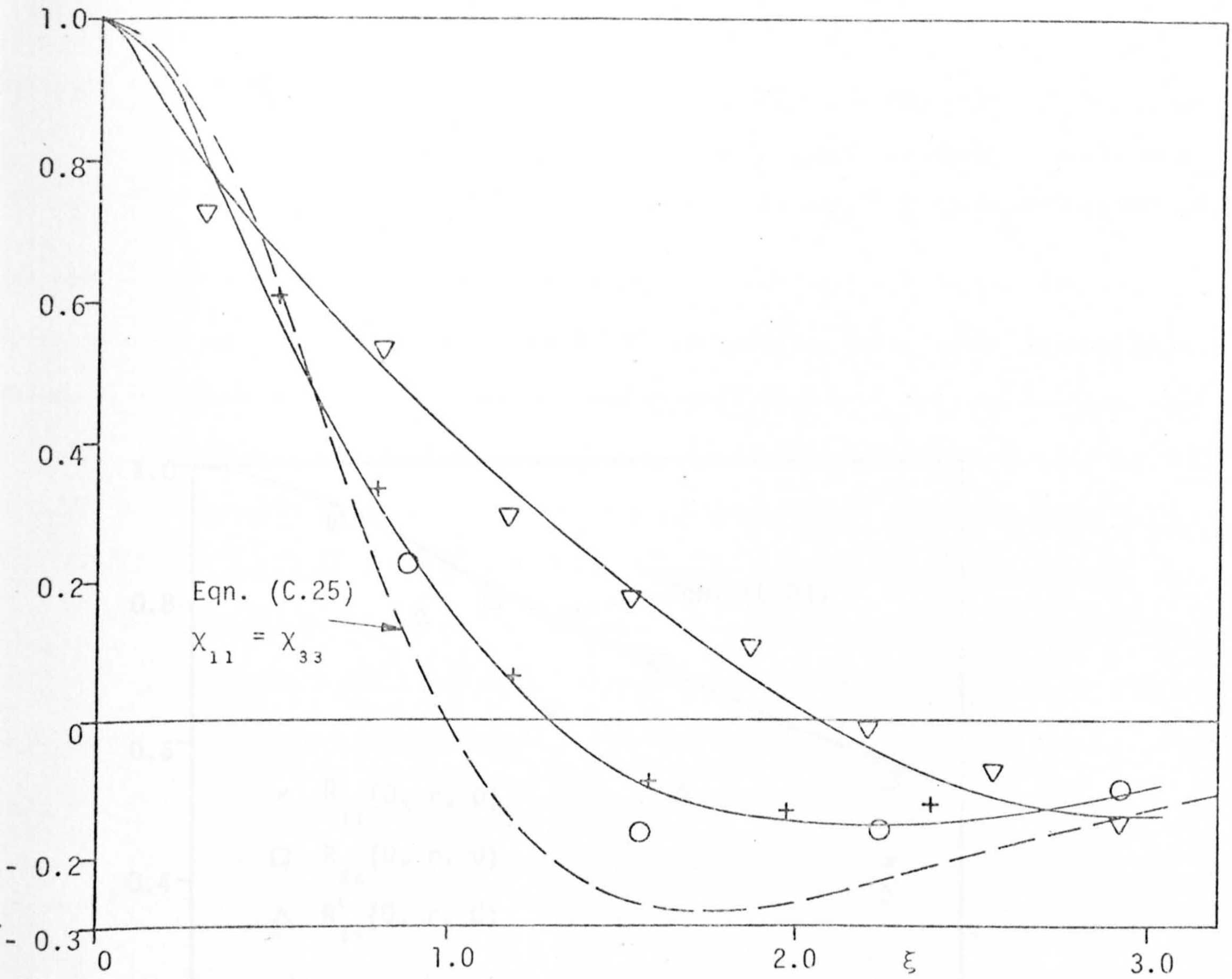


Fig. 5.104 $R_{33}(0, 0, r)$ in the potential flow

Symbols for figs. 5.102 - 5.104

	$R_{11}(0, 0, r)$	$R_{22}(0, 0, r)$	$R_{33}(0, 0, r)$	η	Nominal $x - x_o$ (cm)
Negligible wall effect	□	□		- 0.123	24
	○		○	- 0.105	
	△	△		- 0.074*	
	+	+	+	- 0.124	36
	×	×		- 0.099	
	◇	◇		- 0.075*	
Wall affected	▽	▽		- 0.110	75
			▽	- 0.096	

* nt/nt zone averages

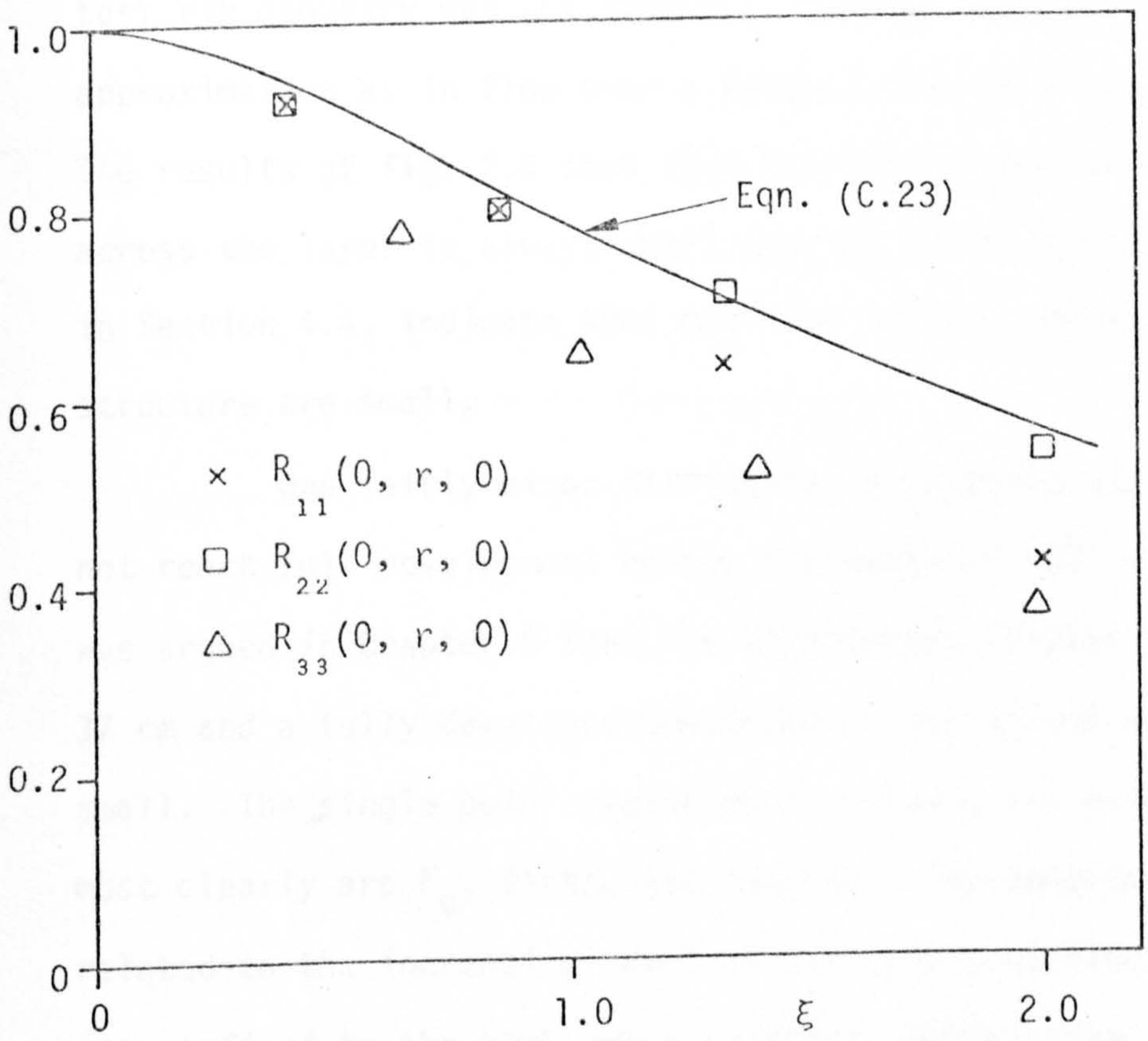


Fig. 5.105 Normal correlations in the unaffected potential flow.
$x - x_o$ = 24.05 cm, fixed probe at η = - 0.100

CHAPTER 6

FURTHER DISCUSSION AND CONCLUSIONS

6.1 Further Discussion

The present experiment is perhaps the simplest possible study of the effect of the wall on a free turbulent shear layer; the test rig geometry was not expected to break down the thin shear layer approximation as in flow over a backward facing step, for example. The results of fig. 2.4 show that the static pressure difference across the layer is always small and the discussion of the spectra in Section 4.4, indicate that upstream influences on the turbulence structure are small.

One fairly minor difficulty is that the mixing layer did not reach full development before the onset of wall effect, but it was argued in Chapter 5 that the differences between structure at 37 cm and a fully developed unbounded single stream mixing layer were small. The single point measurements showing the effect of the wall most clearly are F_u, first, and then $\overline{v^2}$. The behaviour of F_u was related to the increasing level of the potential fluctuations and so was confined to the high velocity side. Any scaling arguments, such as Eqn. (2.1) or the theoretical analyses of Appendix C and Hunt and Graham (1978) indicate that the distance to the wall is the important new parameter. However, $\overline{v^2}$ increases across the whole layer after 50 cm, indicating that wall effect on the pressure field is responsible, since only pressure disturbances can propagate vertically, even in a thin shear layer. At 50 cm, $\delta_{m\ell}/\delta_p \simeq 1.4$, fig. 3.4, or $\delta_{m\ell}/h \simeq 0.8$, so that measurements should be restricted to streamwise stations for which $\delta_{m\ell}/h < 0.8$ to avoid significant wall influence. The present author could find only one set of reliable, previous data on the streamwise development of $\overline{v^2}$ in a flow of similar geometry,

that of Wygnanski and Fiedler (1970). Their results do not show an increase with x, probably because their range of x was such that $\delta_{m\ell}/h < 0.8$ approximately. From the wind tunnel dimensions and spreading rates tabulated by Rodi (1973) it is likely that some previous mixing layer studies were influenced by the wall, including that of Brown and Roshko (1974), although it is not safe to extrapolate from the present results to flows involving two walls.

From Chapter 3, the wall does not influence the spreading rate and hence the shear stress distribution over the entire length of the free shear layer, while Chapter 5 shows important differences in the turbulence structure between 37 cm and 75 cm. This does not imply that the turbulence structure is unimportant because different structures will respond differently to imposed perturbations, and most flows of engineering interest are perturbed flows. In particular, it is difficult to see how the effect of the wall could increase the spanwise scales of the correlations if the large eddy structure of the unbounded flow was two-dimensional.

The measurements in both the potential core and the reattached flow show that $\overline{u^2}$ is amplified considerably more than $\overline{w^2}$ as in the grid turbulence measurements of Thomas and Hancock (1977). No satisfactory explanation can be offered, although it appears that the effect of the wall on the postulated outer motion is confined mostly to the x, y plane.

While the evidence for the presence of a double roller eddy in the inner region is fairly conclusive further work needs to be done on the outer layer structure. Correlations with separations oblique to the coordinate axes and the use of more sophisticated conditional sampling techniques would be worthwhile. The structure deduced from correlations is an average structure and it would be interesting to compare this structure with instantaneous measurements,

say from a hot wire rake.

Further work on the analysis of Appendix C is needed, to try to remove the physically implausible behaviour of χ_{33} and to reproduce the disparity in the amplification of $\overline{u^2}$ and $\overline{w^2}$. Related possibilities include the re-formulation of the low wave-number representation of $\theta(\underset{\sim}{k})$, Eqn. (C.9), and investigation of both the effects of streamwise inhomogeneity and of methods to incorporate structural changes within the shear layer into the analysis. The scaling law of Appendix C indicates that the scales of the potential correlations depend on the nature of the potential flow, independently of the ratio χ_{11}/χ_{33}. This result is in sufficiently good agreement with the measurements, Section 5.4, to conclude that the only relation between the scales of the turbulent motion and the scales of the potential motion is that the former set the lower bounds on the latter, fig. 5.49b.

The fact that the theory of Appendix C is an asymptotic theory has been passed over lightly in Sections 4.2 and 5.4, since the ratio $\overline{u^2}/\overline{w^2}$ shows no signs of either approaching a constant value, or of decreasing, with increasing negative η. This indicates that the difficulties with the theory are not related to the proximity of the measurements to the shear layer. In any case, the use of an effective origin is a correction for non-asymptotic effects.

The turbulence has only partially adjusted to the wall by the last measurement station and the correlations are still quite different from correlations in typical wall bounded flows (Townsend, 1976, pp. 156-162). The rise in $\overline{u^2}$ and $\overline{w^2}$ near the wall was attributed to mixing layer fluid, even though the behaviour of the flatness factors can only be due to the increasing level of the potential fluctuations. These two statements are not inconsistent. Assuming that the flatness factor of both the turbulent and the

potential motion is 3, Section 4.1, then F_u will be 3, independent of γ, if $\overline{u_T^2} = \overline{u_N^2}$. Near the wall, F_u is slightly greater than 3 so that $\overline{u_T^2}$ is slightly greater than $\overline{u_N^2}$ as is also shown by the ratio of $\overline{u_T^2}/\overline{u^2}$ (= 0.88 at η = - 0.0757, Section 4.3) being slightly higher than γ (= 0.60 at η = - 0.0757, fig. 5.1). The large increase in γ near the wall, fig. 5.1, increases the turbulent contribution to u^2 and the spectrum near the wall, fig. 4.64, shows that the dominant contributions to ϕ_{11} are from low wave-number, mixing layer motion. The theory of Hunt and Graham (1978) predicts that the effect of the wall on grid turbulence extends about one integral length scale from the wall, a distance corresponding to about the shear layer thickness. The huge rise in $\overline{u^2}$, and the smaller rise in $\overline{w^2}$ are confined to distances from the wall much less than this value. In Section 5.3 this was attributed to the difference between the inner and outer motion of the free shear layer. The initial effect of the wall on the double roller eddy is to stretch its spanwise and streamwise scales and so weaken its y direction vorticity, while the outer motion, responsible for the eruption of the large eddies into the potential flow, will be more strongly influenced by the wall. The huge increase in $\overline{u^2}$ is confined to the region where the outer motion dominated the unbounded mixing layer.

6.2 Conclusions

(i) Bradshaw's (1966) criterion that full development is not reached until after $10^3\ \theta_o$ is consistent with the present results.

(ii) The spanwise non-uniformity of the free shear layer is most pronounced at 37 cm (of the stations measured) and then decreases as $(x - x_o)^{-1}$. The mixing layer is bodily

wrinkled in the spanwise direction, and there are small changes in spreading rate with z. The associated secondary motion is probably a series of longitudinal vortices, that become increasingly weak relative to the turbulence structure. Even at 37 cm the secondary motion does not contribute to the correlations.

(iii) The effect of the wall does not alter the mean velocity profile or shear stress distribution until the flow has reattached.

(iv) The turbulent motion is significantly affected by the wall well before reattachment, with $\overline{v^2}$ increasing across the whole flow after 50 cm. This increase is largely confined to a narrow frequency band centred on $\omega' = 3.6$ at 75.06 cm. To avoid significant wall effect, measurements in similar rigs should be confined to a region where $\delta_{m\ell}/h < 0.8$.

(v) The correlations show the unbounded shear layer structure is essentially three-dimensional. In the inner region, $\eta > -0.050$, the large eddy structure appears to be a double roller eddy with a "superimposed" outer motion similar to Grant's (1958) mixing jets. The outer motion becomes dominant for $\eta \lesssim -0.050$.

(vi) The spanwise scales of the potential motion are <u>not</u> indicative of the spanwise scales of the turbulent motion.

(vii) The first effect of the wall is to stretch and weaken the double roller eddy and to increase the importance of the

outer motion. The nature of the outer motion is probably responsible for the unequal amplification of $\overline{u^2}$ and $\overline{w^2}$.

(viii) After reattachment, the large amplification of $\overline{u^2}$ and $\overline{w^2}$ near the wall is caused by wall effect on the mixing layer structure and is confined to the region where the outer motion dominates the unbounded shear layer.

(ix) Because of (iii), (iv), (viii) and the difference between the point where $\partial u/\partial y = 0$ and the crossover point in $\overline{uv}$ in the reattached flow, the present results will be a difficult test of calculation methods.

REFERENCES

BATCHELOR, G. K. (1956)
"The Theory of Homogeneous Turbulence".
C.U.P.

BATES, S. C. (1977)
"Luminescent Visualization of Molecular and Turbulent Transport in a Plane Shear Layer".
M.I.T., G.T.L. Rept. 134.

BATT, R. G. (1975)
"Some Measurements of the Effect of Tripping the Two-Dimensional Shear Layer".
A.I.A.A.J., 13, p. 245.

BATT, R. G. (1977)
"Turbulent Mixing of Passive and Chemically Reacting Species in a Low Speed Shear Layer".
J. Fluid Mech., 82, p. 53.

BERNAL, L. P., BREIDENTHAL, R. E., BROWN, G. L. and ROSHKO, A. (1979)
"On the Development of Three-Dimensional Small Scales in the Turbulent Mixing Layer".
Proc. 2nd Symp. Turb. Shear Flows, London.

BIRCH, S. F. (1977)
"On the Developing Region of a Plane Mixing Layer".
In Murthy (ed.), p. 89.

BIRINGEN, S., REYNOLDS, W. C., MOIN, P. and FERZIGER, J. H. (1979)
"Large Eddy Simulation of the Shear-Free Turbulent Boundary Layer".
Submitted to J. Fluid Mech.

BRADSHAW, P. (1965)
"The Effect of Wind-Tunnel Screens on Nominally Two-Dimensional Boundary Layers".
J. Fluid Mech., 22, p. 381.

BRADSHAW, P. (1966)
"The Effect of Initial Conditions on the Development of a Free Shear Layer".
J. Fluid Mech., 26, p. 225.

BRADSHAW, P. (1967a)
"Irrotational Fluctuations Near a Turbulent Boundary Layer".
J. Fluid Mech., 27, p. 209.

BRADSHAW, P. (1967b)
" 'Inactive' Motion and Pressure Fluctuations in Turbulent Boundary Layers".
J. Fluid Mech., 30, p. 241.

BRADSHAW, P. (1971)
"An Introduction to Turbulence and its Measurement".
Pergamon Press.

BRADSHAW, P. (1972)
"Two More Wind Tunnels Driven by Aerofoil-type Centrifugal Blowers".
Imperial College Aero Rept. 72-10.

BRADSHAW, P. (ed.) (1979)
"Aerodynamics Equipment Manual".
Imperial College Aero TN 73-101 (updated, September, 1979).

BRADSHAW, P. (1980)
"Introduction to the Section on 'Coherent Structures' ".
Proc. 2nd Symp. Turb. Shear Flows, London. To be published by Springer-Verlag.

BRADSHAW, P., DEAN, R. B. and McELIGOT, D. M. (1973)
"Calculation of Interacting Turbulent Shear Layers : Duct Flow".
Trans. A.S.M.E., J. Fluids Engng., 95I, p. 214.

BRADSHAW, P., FERRISS, D. H. and JOHNSON, R. F. (1964)
"Turbulence in the Noise Producing Region of a Circular Jet".
J. Fluid Mech., 19, p. 51.

BRADSHAW, P. and GEE, M. T. (1960)
"Turbulent Wall Jets With and Without an External Stream".
A.R.C. 22, 008, F.M. 2971.

BROWAND, F. K. (1966)
"An Experimental Investigation of the Instability of an Incompressible, Separated Shear Layer".
J. Fluid Mech., 26, p. 281.

BROWAND, F. K. and LATIGO, B. O. (1979)
"The Growth of the Two-Dimensional Mixing Layer from Turbulent and Non-Turbulent Boundary Layers".
Submitted to J. Fluid Mech.

BROWAND, F. K. and TROUTT, T. (1979)
"A Note on Spanwise Structure in the Two-Dimensional Mixing Layer".
Submitted to J. Fluid Mech.

BROWAND, F. K. and WIEDMANN, P. D. (1976)
"Large Structures in the Developing Mixing Layer".
J. Fluid Mech., 76, p. 127.

BROWN, G. L. and ROSHKO, A. (1974)
"On Density Effects and Large Structure in Turbulent Mixing Layers".
J. Fluid Mech., 64, p. 715.

BRUUN, H. H. (1979)
"A Time-Domain Evaluation of the Large-Scale Flow Structure in a Turbulent Jet".
Proc. Roy. Soc., Series A, 337, p. 193.

CASTRO, I. P. (1973)
"A Highly Distorted Turbulent Free Shear Layer".
Ph.D. Thesis, University of London.

CEBECI, T. and BRADSHAW, P. (1977)
"Momentum Transfer in Boundary Layers".
McGraw Hill - Hemisphere.

CHANDRSUDA, C. (1975)
"A Reattaching Turbulent Shear Layer in Incompressible Flow".
Ph.D Thesis, University of London.

CHANDRSUDA, C., MEHTA, R. D., WEIR, A. D. and BRADSHAW, P. (1978)
"Effect of Free-Stream Turbulence on Large Structure in Turbulent Mixing Layers".
J. Fluid Mech., 85, p. 693.

CLARK, J. A. and MARKLAND, E. (1973)
"Flow Visualizations in Free Shear Layers".
A.S.C.E. J. Hydr. Divn., HY11, p. 1897.

CORRSIN, S. and KISTLER, A. L. (1954)
"Free-Stream Boundaries of Turbulent Flows".
NACA Rep. 1244.

DIMOTAKIS, P. E. and BROWN, G. L. (1976)
"The Mixing Layer at High Reynolds Number : Large-Structure Dynamics and Entrainment".
J. Fluid Mech., 78, p. 535.

DEAN, R. B. and BRADSHAW, P. (1976)
"Measurements of Interacting Turbulent Shear Layers in a Duct".
J. Fluid Mech., 76, p. 241.

FABRIS, G. (1979)
"Conditional Sampling Study of the Turbulent Wake of a Cylinder. Part 1".
J. Fluid Mech., 94, p. 673.

FIEDLER, H. E. (1975)
"On Turbulence Structure and Mixing Mechanism in Free Turbulent Shear Flows".
In Murthy (ed.), p. 381.

FIEDLER, H. E. (ed.) (1977)
"Structure and Mechanisms of Turbulence".
Springer-Verlag, 2 Vols.

FIEDLER, H. E., KORSCHELT, D. and MENSING, P. (1978)
"On Transport Mechanism and Structure of Scalar Field in a Heated Plane Shear Layer".
In Fiedler (ed.), Vol. II, p. 58.

FIEDLER, H. E. and THIES, H. J. (1978)
"Some Observations in a Large Two-Dimensional Shear Layer".
In Fiedler (ed.), Vol. I, p. 108.

FOSS, J. F. (1977)
"The Effects of the Laminar/Turbulent Boundary Layer States on the Development of a Plane Mixing Layer".
Symp. Turb. Shear Flows, Penn State University, p. 11.33.

FREYMUTH, P. (1966)
"On Transition in a Separated Laminar Boundary Layer".
J. Fluid Mech., 25, p. 683.

GRANT, H. L. (1958)
"The Large Eddies of Turbulent Motion".
J. Fluid Mech., 4, p. 149.

GUITTON, D. E. (1968)
"Correction of Hot Wire Data for High Intensity Turbulence, Longitudinal Cooling and Probe Interference".
McGill University, Mech. Eng. Res. Lab., Rept. 68-6.

HAVERBEKE, A., WOOD, D. H. and SMITS, A. J. (1979)
"Uncertainties and Errors in Conditional Sampling".
Proc. 2nd Symp. Turb. Shear Flows, London, p.11.1.

HUNT, J. C. R. and GRAHAM, J. M. R. (1978)
"Free-Stream Turbulence Near Plane Boundaries".
J. Fluid Mech., 84, p. 209.

HUSAIN, Z. D. and HUSSAIN, A. K. M. F. (1978)
"Axisymmetric Mixing Layer : Influence of the Initial and Boundary Conditions".
A.I.A.A.J., 17, p. 48.

HUSSAIN, A. K. M. F. (1978)
"Initial Condition Effect on a Free Turbulent Shear Layer".
In Fiedler (ed.), Vol. I, p. 103.

HUSSAIN, A. K. M. F. and CLARK, A. R. (1977)
"Upstream Influence on the Near Field of a Plane Turbulent Jet".
Phys. Fluids, 20, p. 1416.

HUSSAIN, A. K. M. F. and ZAMAN, K. B. M. Q. (1978)
"Controlled Perturbation of Circular Jets".
In Fiedler (ed.), Vol. I, p. 31.

HUSSAIN, A. K. M. F. and ZEDAN, M. F. (1978a)
"Effects of the Initial Condition on the Axisymmetric Free Shear Layer : Effects of Initial Momentum Thickness".
Phys. Fluids, 21, p. 1100.

HUSSAIN, A. K. M. F. and ZEDAN, M. F. (1978b)
"Effects of the Initial Condition on the Axisymmetric Free Shear Layer : Effect of the Initial Fluctuation Level".
Phys. Fluids, 21, p. 1475.

JONES, B. G., PLANCHON, H. P. and HAMMERSLEY, R. J. (1973)
"Turbulent Correlation Measurements in a Two-Stream Mixing Layer".
A.I.A.A.J., 11, p. 1146.

KIBENS, V. and KOVASZNAY, L. S. G. (1969)
"The Intermittent Region of a Turbulent Boundary Layer".
Interim Tech. Rept. DA-31-124-ARO-D-313, Johns Hopkins University.

KOVASZNAY, L. S. G., KIBENS, V. and BLACKWELDER, R. F. (1970)
"Large-Scale Motion in the Intermittent Region of a Turbulent Boundary Layer".
J. Fluid Mech., 41, p. 283.

LAUNDER, B. E., REECE, G. J. and RODI, W. (1975)
"Progress in the Development of a Reynolds-Stress Closure".
J. Fluid Mech., 68, p. 537.

MICHALKE, A. (1972)
"The Instability of Free Shear Layers".
Prog. Aerospace Sc., 12, p. 213.

MIKSAD, R. W. (1970)
"Experiments on Free Shear Layer Transition".
Sc.D. Thesis, M.I.T.

MIKSAD, R. W. (1972)
"Experiments in the Non-Linear Stages of Free-Shear Layer Transition".
J. Fluid Mech., 56, p. 695.

MIKSAD, R. W. (1973)
"Experiments on Non-Linear Interaction in the Transition of a Free Shear Layer".
J. Fluid Mech., 59, p. 1.

MUCK KIN CHOONG, (1980)
"Comparison of Various Schemes for the Generation of the Intermittency Function".
To be published as an Imperial College Aero. Rept.

MURTHY, S. N. G. (ed.) (1975)
"Turbulent Mixing in Nonreactive and Reactive Flows".
Plenum Press.

OSTER, D., DZIOMBA, B., FIEDLER, H. and WYGNANSKI, I. (1978).
"On the Effect of Initial Conditions on the Two-Dimensional Turbulent Mixing Layer".
In Fiedler (ed.), Vol. I, p. 48.

PHILLIPS, O. M. (1955)
"The Irrotational Motion Outside a Free Turbulent Boundary".
Proc. Camb. Phil. Soc., 51, p. 220.

PUI, N. K. and GARTSHORE, I. S. (1979)
"Measurements of the Growth Rate and Structure in Plane Turbulent Mixing Layers".
J. Fluid Mech., 91, p. 111.

ROCKWELL, D. and NAUDASCHER, E. (1979)
"Self-Sustained Oscillations of Impinging Free Shear Layers".
Ann. Rev. Fluid Mech., 11, p. 67.

RODI, W. (1973)
"A Review of Experimental Data of Uniform Density Free Turbulent Boundary Layers".
In Launder, B. E. (ed.) "Studies in Convection", Vol. I, Academic Press, p. 79.

ROSHKO, A. (1976)
"Structure of Turbulent Shear Flows : A New Look".
A.I.A.A.J., 14, p. 1349.

SABIN, C. M. (1963)
"An Analytical and Experimental Study of the Plane, Incompressible, Turbulent Free Shear Layer with Arbitrary Velocity Ratio and Pressure Gradient".
Rept. MD-9, Mech. Engng. Dept., Stanford University.

SHABAKA, I. M. M. A. (1979)
"Turbulent Flow in an Idealized Wing-Body Junction".
Ph.D. Thesis, London University.

SHAW, R. (1960)
"The Influence of Hole Dimensions on Static Pressure Measurements".
J. Fluid Mech., 7, p. 550.

SMITS, A. J., YOUNG, S. T. B. and BRADSHAW, P. (1979)
"The Effect of Short Regions of High Surface Curvature on Turbulent Boundary Layers".
J. Fluid Mech., 94, p. 209.

SPENCER, B. W. and JONES, B. G. (1970)
"Statistical Investigation of Pressure and Velocity Fields in a Two Stream Mixing Layer".
A.I.A.A., Paper 71-613.

STEWART, R. W.
"Irrotational Motion Associated with Free Turbulent Flows".
J. Fluid Mech., 1, p. 593.

SUNYACH, M. (1971)
"Contribution a l'Etude des Frontières d'Écoulements Turbulents Libres".
Thèse Dr. ès Sciences, L'Université Claude Bernard de Lyon.

SUNYACH, M. and MATHIEU, J. (1969)
"Fluctuations de Vitesses Induites dan la Cône à Potential d'un Jet Plan".
C. R. Acad. Sc. Paris, Série A, Vol. 268, p. 742.

TENNEKES, H. and LUMLEY, J. L. (1972)
"A First Course in Turbulence".
M.I.T. Press.

THOMAS, N. H. and HANCOCK, P. E. (1977)
"Grid Turbulence Near a Moving Wall".
J. Fluid Mech., 82, p. 481.

TOWNSEND, A. A. (1961)
"Equilibrium Layers and Wall Turbulence".
J. Fluid Mech., 11, p. 97.

TOWNSEND, A. A. (1976)
"The Structure of Turbulent Shear Flow".
C.U.P. 2nd Edition.

TRITTON, D. J. (1967)
"Some New Correlation Measurements in a Turbulent Boundary Layer".
J. Fluid Mech., 28, p. 439.

UZKAN, T. and REYNOLDS, W. C. (1967)
"A Shear-Free Turbulent Boundary Layer".
J. Fluid Mech., 37, p. 95.

WEBER, D. P. (1974)
"Turbulent Velocity Field Structure of a Round Jet and its Relation to Fluctuating Pressure Fields".
Ph.D. Thesis, Nuclear Engineering Program, University of Illinois at Urbana Champaign.

WEIR, A. D. and BRADSHAW, P. (1974)
"Apparatus and Programs for Digital Analysis of Fluctuating Quantities in Turbulent Flow".
Imperial College Aero Rept., 74-09.

WEIR, A. D., WOOD, D. H. and BRADSHAW, P. (1980)
"Interacting Turbulent Shear Layers in a Plane Jet".
Submitted to J. Fluid Mech.

WINANT, C. D. and BROWAND, F. K. (1974)
"Vortex Pairing : The Mechanism of Turbulent Mixing-Layer Growth at Moderate Reynolds Number".
J. Fluid Mech., 63, p. 237.

WONG, F. Y. F. (1970)
"Shear Flow Over a Backward Facing Step".
M.Sc. Project Rept., Dept. Aeronautics, Imperial College.

WYGNANSKI, I. and FIEDLER, H. E. (1970)
"On the Two-Dimensional Mixing Region".
J. Fluid Mech., 41, p. 329.

WYGNANSKI, I., OSTER, D., FIEDLER, H. E. and DZIOMBA, B. (1979)
"On the Perserverance of a Quasi-Two-Dimensional Eddy-Structure in a Turbulent Mixing Layer".
J. Fluid Mech., 39, p. 325.

YU, J. C. and TAM, C. K. W. (1978)
"Experimental Investigation of the Trailing Edge Noise Mechanism".
A.I.A.A.J., 16, p. 1046.

YULE, A. J. (1978)
"Large Structure in the Mixing Layer of a Round Jet".
J. Fluid Mech., 89, p. 413.

YULE, A. J. (1979)
"Phase Scrambling Effects and Turbulence Data Analysis".
Proc. 2nd Symp. Turb. Shear Flows, London, p. 7.1.

APPENDIX A

SOME COMMENTS ON THE ACCURACY OF THE HOT WIRE RESULTS

Apart from the problems of probe misalignment discussed later in this Appendix, there are three major sources of measurement error in the present flow. Firstly, the mean velocity vector which is parallel to the x axis in the potential core changes direction across the shear layer to become normal to the x axis on the low speed edge. Since all the important measurements were made well away from the low velocity side the inclination of the mean velocity vector was not a serious problem. The high turbulence intensities may cause:-

(i) a possibly significant transverse component (normal to the measuring plane) contribution to the effective velocity seen by the wires, and,

(ii) the instantaneous flow in the measuring plane occasionally to be at an angle too large for the cosine law approximation to be valid.

Assuming the validity of the cosine law for the present and considering a wire measuring in the x, y plane, the effective velocity as defined in Chapter 2 becomes:-

$$U_{eff}^2 = (U \cos \psi + V \sin \psi)^2 + W^2 \qquad (A.1)$$

where the transverse component is included. A test of the validity of Eqn. (A.1) is shown in fig. A.1. A typical probe was calibrated

and then rotated by γ in the x, y plane. Since V = W = 0 in the potential core Eqn. (A.1) reduces to:-

$$\cos \psi_\gamma = \cos \psi_{\gamma=0} \left(\cos^2\gamma + \sin^2 \gamma \sec^2 \psi_{\gamma=0}\right)^{1/2} \qquad (A.2)$$

It can be seen that the response is not quite symmetric as required by Eqn. (A.2), perhaps because the wake of the upstream wire interferes with the downstream wire at large γ. However, for $|\gamma| < 5^o$ the change in U_{eff} is negligible which justifies neglecting γ changes in the calibration procedure outlined in Chapter 2, but does not justify neglecting W^2 in Eqn. (A.1). Even for a lincarized single inclined wire the expansion of Eqn. (A.1) is tedious (Guitton, 1968) while for the present, more difficult, case several attempts proved fruitless. By Eqn. (A.1) the resulting errors must be second order and so were ignored. Guitton (1968) indicates that transverse component corrections increase $\overline{u^2}$, $\overline{v^2}$ and $\overline{uv}$.

Several of the probes used were yaw calibrated over double the usual range of $\Delta\psi$ and ψ_{eff} was found using Eqn. (2.4). The results fig. A.2, show there is no repeatable trend with $\Delta\psi$ which implies that the cosine law is a remarkably good approximation for the probes used, at least to the accuracy with which ψ_{eff} can be determined.

Since the range of $\Delta\psi$ shown in fig. A.2 should cover nearly all the instantaneous flow angles (Castro, 1973, Appendix IV), the cosine law is adequate. The remaining source of significant error is misalignment of the probe axis with the x axis, if the probe had to be moved downstream or rotated 90° to measure in the x, y plane after the yaw calibration. Denoting the misalignment by $\Delta\psi_{cm}$ (see Chapter 2), the effective velocity (see Eqn. (2.6)) becomes:-

$$U_{eff} = U \left(\cos \Delta\psi_{cm} - \tan \psi_c \sin \Delta\psi_{cm}\right) + V \left(\tan \psi_c \cos \Delta\psi_{cm} + \sin \Delta\psi_{cm}\right)$$

where c denotes a calibration position value. Thus:-

$$\begin{pmatrix} U \\ V \end{pmatrix} = \frac{1}{\Delta} \begin{pmatrix} \alpha_{22} \tan \psi_{c_2} + \alpha_{12} \tan \psi_{c_1} \\ \alpha_{21} \qquad\qquad - \alpha_{11} \end{pmatrix} \begin{pmatrix} U_{eff_{c_1}} \\ U_{eff_{c_2}} \end{pmatrix}$$

where:-

$$\alpha_{i_1} = \cos \Delta\psi_{cm} - \tan \psi_{ci} \sin \Delta\psi_{cm} \qquad \text{for } i = 1, 2$$

$$\alpha_{12} = \cos \Delta\psi_{cm} + \sin \Delta\psi_{cm}/\tan \psi_{c_1}$$

$$\alpha_{22} = \cos \Delta\psi_{cm} - \sin \Delta\psi_{cm}/\tan \psi_{c_2}$$

$$\Delta = \tan \psi_{c_1} + \tan \psi_{c_2} + \sin 2\Delta\psi_{cm}$$

and $\Delta\psi$ is positive in the clockwise direction.

After a little algebra the resulting expressions for the correct total velocities are:-

$$\left.\begin{aligned} U &= \beta \, (U_m \cos \Delta\psi_{cm} - V_m \sin \Delta\psi_{cm}) \\ V &= \beta \, (V_m \cos \Delta\psi_{cm} + U_m \sin \Delta\psi_{cm}) \end{aligned}\right\} \qquad \text{(A.3)}$$

where:-

$$\beta = 1 + \frac{\sin 2\Delta\psi_{cm}}{\tan \psi_{c_2} + \tan \psi_{c_1}}$$

and the subscript m denotes values measured using the calibration plane values of A and B as defined in Chapter 2. Obviously the term inside the brackets in Eqn. (A.3) represents the effect of rotating the axes on U and V while β arises because of the angle dependence of the calibration constant B. The expressions for the corrected second

order quantities are:-

$$\overline{u^2} = \beta^2 \left[\overline{u_m^2} \cos^2 \Delta\psi_{cm} + \overline{v_m^2} \sin^2 \Delta\psi_{cm} - (\overline{uv})_m \sin 2\Delta\psi_{cm} \right] \qquad (A.4)$$

$$\overline{v^2} = \beta^2 \left[\overline{v_m^2} \cos^2 \Delta\psi_{cm} + \overline{u_m^2} \sin^2 \Delta\psi_{cm} + (\overline{uv})_m \sin 2\Delta\psi_{cm} \right] \qquad (A.5)$$

and:-

$$\overline{uv} = \beta^2 \left[(\overline{uv})_m \cos 2\Delta\psi_{cm} + (\overline{u_m^2} - \overline{v_m^2}) \frac{\sin 2\Delta\psi_{cm}}{2} \right] \qquad (A.6)$$

Again the terms inside the square brackets are the rotation terms. Using typical values for the region of maximum intensity Eqns. (A.4) - (A.6) give 2, 3.5 and 5% error for u^2, v^2 and $\overline{uv}$ respectively, per degree of $\Delta\psi_{cm}$ for $|\Delta\psi_{cm}| < 5^o$. Of course, these estimates are pessimistic since the calibrations were corrected for changes in ψ, but the importance of these corrections is clearly demonstrated.

The most scattered results in Chapter 5 are those containing u, which in turn has greater contributions from the low frequency component than has v or w. Since the Kolmogorov frequency goes as $x^{1/4}$ approximately (see Castro, 1973, pp. 38-39) while typical low frequencies scale on $U_1 \delta^{-1}$ typical high frequencies increase slightly with x while typical low frequencies decrease by nearly a factor of five over the range of x measured. The former meant that the effective real time digitizing rate could not be reduced with x while the latter required a big increase in averaging time with x. The large amount of data reduction precluded wholly satisfactory averaging times, even for the first station and the effects can be seen in the results presented in Chapter 5. To first order, averaging time errors

will cancel out of the correlations as defined by Eqn. (2.11) and the skewness and flatness factors. The repeatability of the correlations shcwn in Chapter 5 justified the use of shorter averaging times for these measurements.

The only direct test of the accuracy of the hot wire results is the comparison of $\overline{uv}$ measured in the self-preserving free shear layer with that calculated from the momentum equation, Appendix B. Fig. 4.4 shows that the agreement is generally within 10% which is about the repeatability of the $\overline{u^2}$ measurements, figs. 4.1a and 4.1b. Thus 10% is a reasonable estimate for the accuracy of the second order measurements. The $\overline{uv}$ measurements are generally lower than the calculated values, suggesting that transverse component effects may be responsible. From fig. 4.7 the repeatability of $\overline{u^3}$ is generally about 20%, so this value is the estimate for the accuracy of the third order measurements.

For $x - x_o$ greater than 100 cm the combination of uncertainty of probe positioning and the increasing effect of averaging time problems decreases the accuracy. From figs. 4.36 and 4.42 corresponding error estimates 15 and 30% appear reasonable.

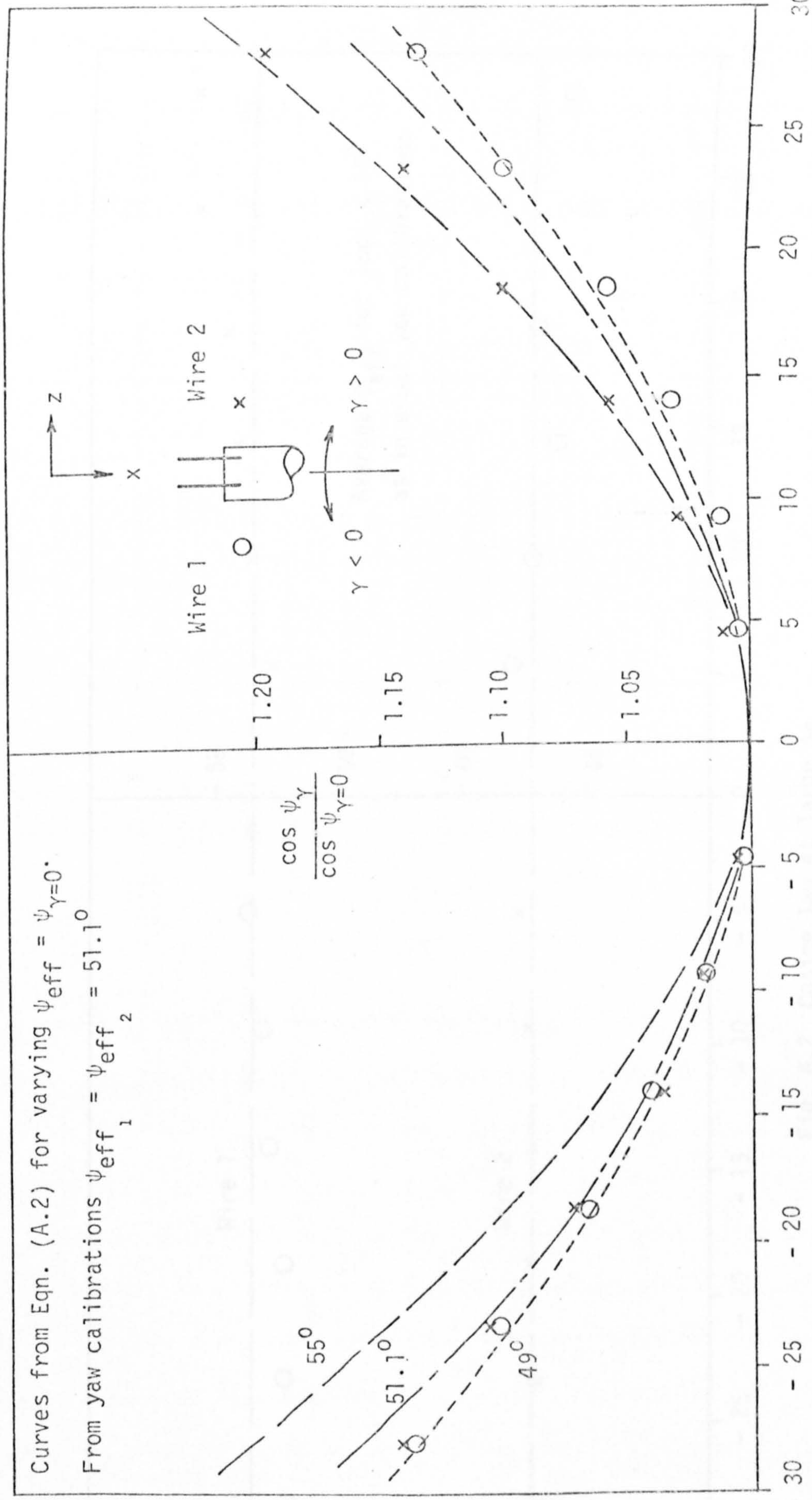
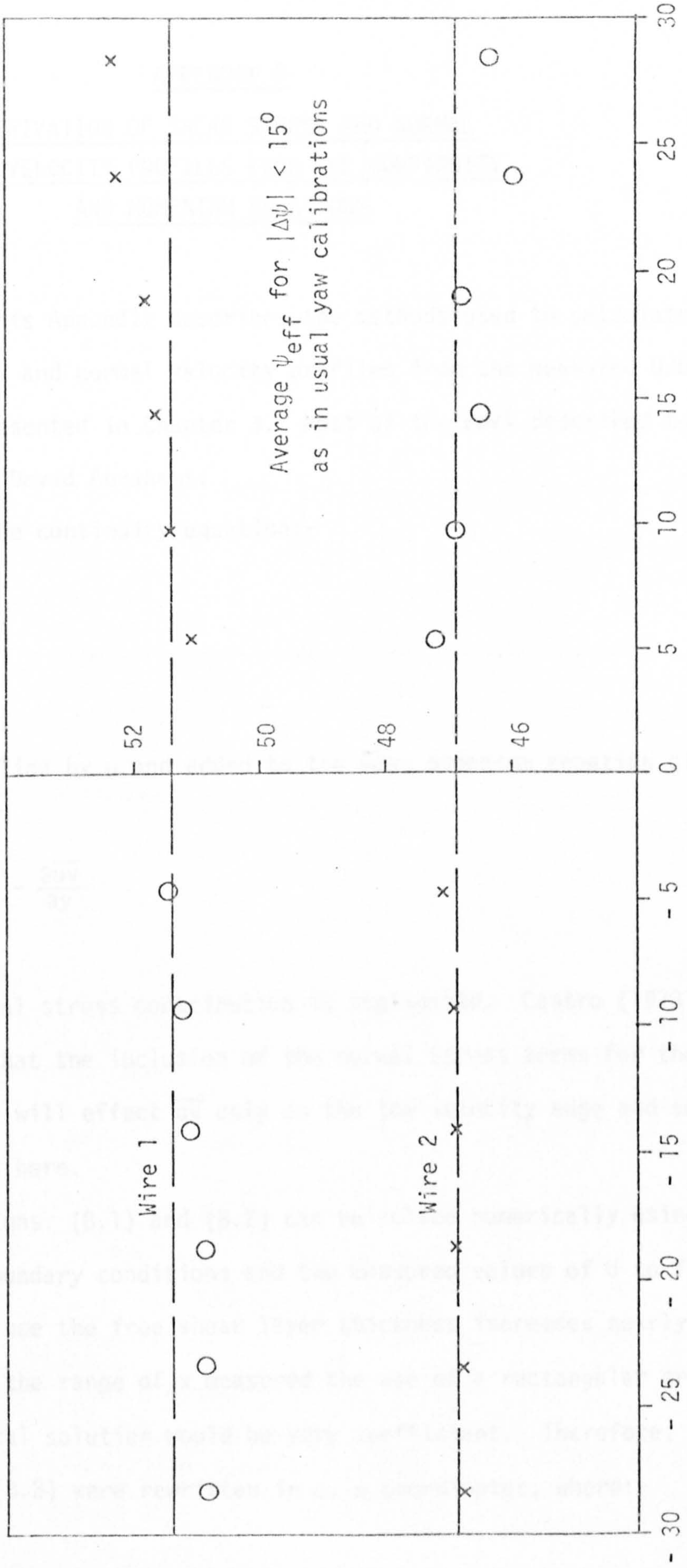


Fig. A.1 Transverse component effect on ψ_{eff}



NOTE : $\Delta\psi$ relative to probe axis. Circles denote wire tending to become at right angles to the flow.

Fig. A.2 Cosine law at large $\Delta\psi$

APPENDIX B

DERIVATION OF SHEAR STRESS AND NORMAL MEAN VELOCITY PROFILES FROM THE CONTINUITY AND MOMENTUM EQUATIONS

This Appendix describes the methods used to calculate the shear stress and normal velocity profiles from the measured U/U_1 profiles presented in Chapter 3. Most of the work described here was done by Mr. David Abrahams.

The continuity equation:-

$$\frac{\partial U}{\partial x} + \frac{\partial V}{\partial y} = 0 \qquad (B.1)$$

when multiplied by u and added to the mean momentum equation gives:-

$$\frac{\partial U^2}{\partial x} + \frac{\partial UV}{\partial y} = - \frac{\partial \overline{uv}}{\partial y} \qquad (B.2)$$

if the normal stress contribution is negligible. Castro (1973) indicates that the inclusion of the normal stress terms for the free shear layer will effect $\overline{uv}$ only on the low velocity edge and so they are ignored here.

Eqns. (B.1) and (B.2) can be solved numerically using the relevant boundary conditions and the measured values of U to find V and $\overline{uv}$. Since the free shear layer thickness increases nearly five times over the range of x measured the use of a rectangular grid for the numerical solution would be very inefficient. Therefore, Eqns. (B.1) and (B.2) were rewritten in ε, η coordinates, where:-

$$\varepsilon \equiv x - x_o \qquad \text{and} \qquad \eta \equiv y/(x - x_o)$$

as throughout this thesis. Using:-

$$\frac{\partial}{\partial x} = \frac{\partial}{\partial \varepsilon} - \frac{\eta}{\varepsilon} \frac{\partial}{\partial \eta} \qquad (B.3)$$

and:-

$$\frac{\partial}{\partial y} = \frac{1}{\varepsilon} \frac{\partial}{\partial \eta} \quad , \qquad (B.4)$$

Eqn. (B.1) becomes:-

$$\frac{\partial V}{\partial \eta} = - \varepsilon \frac{\partial U}{\partial \varepsilon} + \eta \frac{\partial U}{\partial \eta} \quad ,$$

while Eqn. (B.2) becomes:-

$$- \frac{\partial \overline{uv}}{\partial \eta} = \frac{\partial UV}{\partial \eta} - \eta \frac{\partial U^2}{\partial \eta} + \dot{\varepsilon} \frac{\partial U^2}{\partial \varepsilon} \quad .$$

From the results of Chapters 3 and 4, it appears reasonable to apply the boundary conditions:-

$$\frac{U}{U_1} = 1 \qquad , \qquad \frac{V}{U_1} = - \frac{\overline{uv}}{U_1^2} = 0$$

at $\eta = - 0.12$. Integrating the transformed equations from the potential core inwards gives:-

$$\frac{V(\eta)}{U_1} = \eta \frac{U(\eta)}{U_1} + 0.12 - \int_{-0.12}^{\eta} \frac{U}{U_1} d\eta - \dot{\varepsilon} \int_{-0.12}^{\eta} \frac{1}{U_1} \frac{\partial U}{\partial \varepsilon} d\eta \qquad (B.5)$$

and:-

$$-\frac{\overline{uv}}{U_1^2} = -\eta\left[\frac{U(\eta)}{U_1}\right]^2 + 0.12 + \int_{-0.12}^{\eta}\left[\frac{U(\eta)}{U_1}\right]^2 d\eta + \frac{U(\eta)\,V(\eta)}{U_1^2} +$$

$$+ 2\varepsilon \int_{-0.12}^{\eta} \frac{U}{U_1^2}\frac{\partial U}{\partial \varepsilon}\, d\eta \qquad \text{(B.6)}$$

The last term on the right hand side of Eqns. (B.5) and (B.6) will be zero (to within experimental scatter) in the self-preserving region, but must be included as the first three mean velocity profiles are not fully developed.

Eqns. (B.5) and (B.6) were solved as follows. The experimental U/U_1 profiles at each ε were interpolated using the NAG6F cubic spline routine E01ADF to form an equally spaced (in η) grid of 44 points. Very little smoothing of the measured profiles was done; at most it amounted to 0.5% of local U. The ε-dependent terms were evaluated at each η using the three point Lagrangian interpolation formula for unequally spaced intervals with special provision for the end points (Cebeci and Bradshaw, 1977, p. 261). Eqn. (B.5) was then integrated at each ε starting at 13.56 cm and once V/U_1 was known, so was Eqn. (B.6). The integration was done using the incremental form of Simpson's Rule:-

$$I_{2n+2} = I_{2n} + \frac{h}{3}\left(f_{2n+2} + 4f_{2n+1} + f_{2n}\right)$$

where:-

$$I_{2n} = \int_{-0.12}^{\eta(2n)} f(\eta)\, d\eta \qquad \text{and} \qquad h = \text{mesh width}$$

The calculations were done for two cases:-

(i) retaining the ε-dependent terms in Eqns. (B.5) and (B.6), and,

(ii) setting the ε-dependent terms to zero.

The respective results are shown in figs. B.1 and B.2. The mean velocity profile at ε = 77.29 cm was used to evaluate the ε-dependent terms for the last station shown in fig. B.1. Because of the uncertainty of determining ε derivatives at the end points the 13.56 cm results will not be very accurate, but $\overline{uv}$ was not measured there so this is not a problem. The agreement between the results for the last station in figs. B.1 and B.2 is encouraging. The case (i) results for 51.83 cm are presumably affected by the relatively large distance between the stations. From fig. 3.2 the mean velocity profile at 39.03 cm is not self-preserving while at 51.83 cm it is, so the V and $\overline{uv}$ distributions for the latter station should agree with those at 64.54 cm as they do in the case (ii) results. The fully developed case (ii) $\overline{uv}$ results are compared with the measured shear stress distributions in fig. 4.4. In the self-preserving region $\partial V/\partial \eta = 0$ at $\eta = 0$ in agreement with the results in figs. B.1 and B.2. In a fully developed free shear layer the maximum shear stress is proportional to the spreading rate. Since the effective origin for the present flow is upstream of the lip the spreading rate in the initial region is higher than the asymptotic value and so will be the maximum shear stress. Again the results of fig. B.2 are in agreement with expectation.

For the reattached flow calculations x, y coordinates were used, with the boundary conditions:-

$$\frac{U}{U_1} = \frac{V}{U_1} = 0 \qquad , \qquad -\frac{\overline{uv}}{U_1^2} = \tau_w \qquad \text{at } y = y_w$$

where the subscript w denotes a wall value and τ_w was taken as the Clauser Chart value, fig. 3.6. Two different mesh sizes were used. For the inner region, $y - y_w \leq 30$ mm, a twenty point mesh spaced at 1.5 mm was used, while for $y - y_w > 30$ mm an eighteen point mesh spaced at 10 mm was used. The x-dependent terms were evaluated in a manner similar to the ε-dependent terms described above, while the interpolation of the mean velocity results and the integration of the equations was done in the same way as for the free shear layer.

Only the mean velocity profiles for the three stations shown in figs. B.4 and B.5 were used to calculate V and $\overline{uv}$ which introduces large uncertainty in the determination of the streamwise derivatives at the first and last stations. This could have been partially avoided by starting the calculations from $x - x_o = 77.29$ cm but this would have given no indication of the likely errors for the last station.

From fig. B.3 the normal stress gradients are now important and so Eqn. (B.2) becomes:-

$$\frac{\partial U^2}{\partial x} + \frac{\partial UV}{\partial y} = -\frac{\partial \overline{uv}}{\partial y} - \frac{\partial}{\partial x}\left(\overline{u^2} - \overline{v^2}\right) . \qquad \text{(B.7)}$$

From fig. B.3 the normal stress gradients act to reduce the magnitude of $\overline{uv}$. Two calculations were done, the first without including the normal stress term and the second using Eqn. (B.7) for the last two stations only with the normal stress term evaluated from the interpolations shown as solid lines in fig. B.3. The results are shown in figs. B.4 and B.5 respectively. Since the free shear layer profile

at 104.59 cm is self-preserving the difference (about 20%) from the asymptotic result, fig. B.2, is an indication of the accuracy of the calculations. Fig. B.5 shows that inclusion of the normal stress term reduces $\overline{uv}$ at the more accurate middle station while the results for the last station are presumably affected by errors in evaluating the streamwise derivatives.

The importance of the normal stress terms degrades the accuracy of the calculations since it is only the fact that U/U_1 can be measured significantly more accurately than the turbulence quantities that justifies comparing the measured $\overline{uv}$ with the values calculated from the momentum equation. Furthermore, no hot wire measurements were made in the floor boundary layer at 100.38 cm so the extrapolation shown in fig. B.3 is conjectural and the difference between the x values for the hot wire measurements and the mean velocity measurements was ignored.

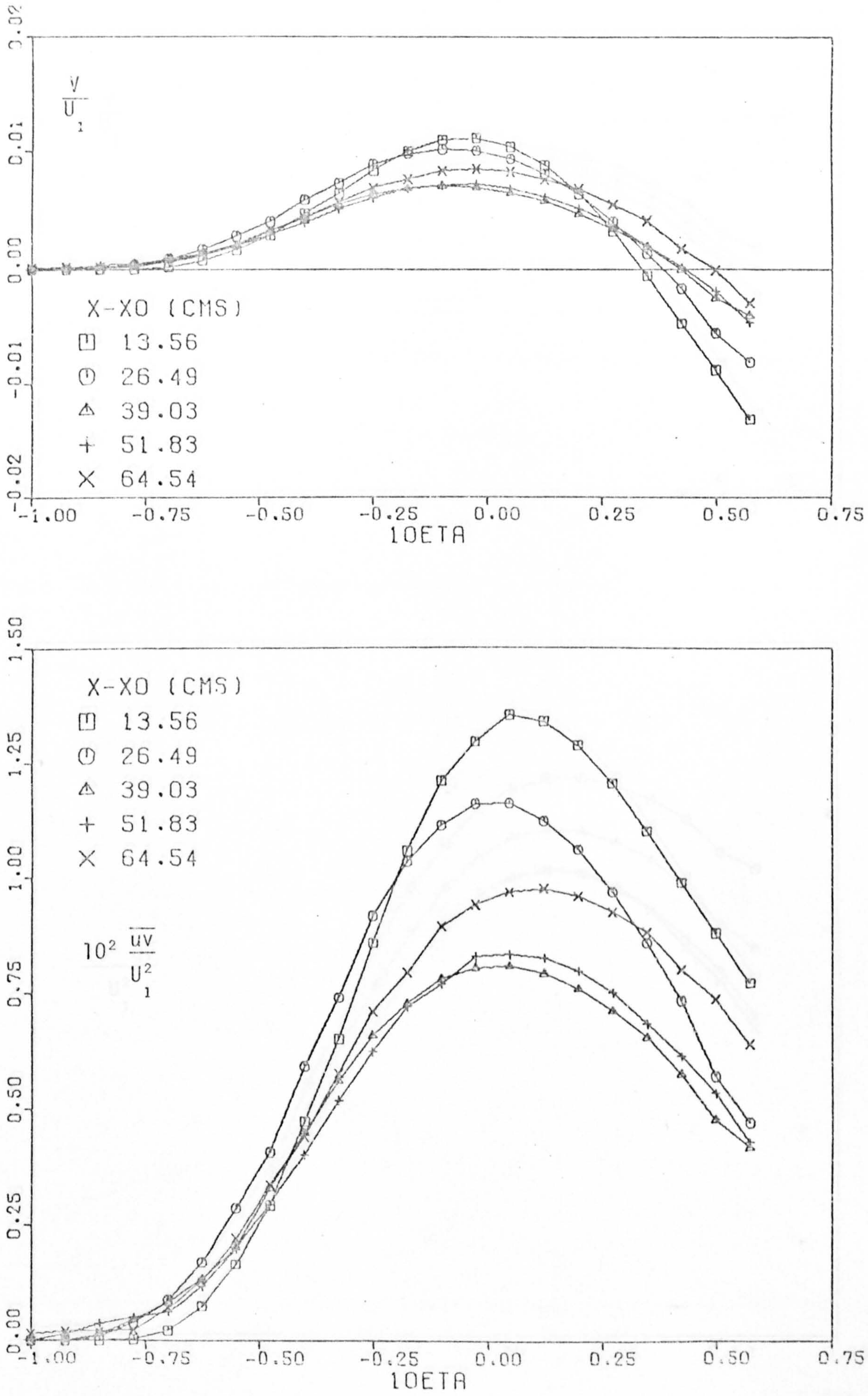


Fig. B.1 Calculated V and $\overline{uv}$ in the free shear layer, ε dependence included

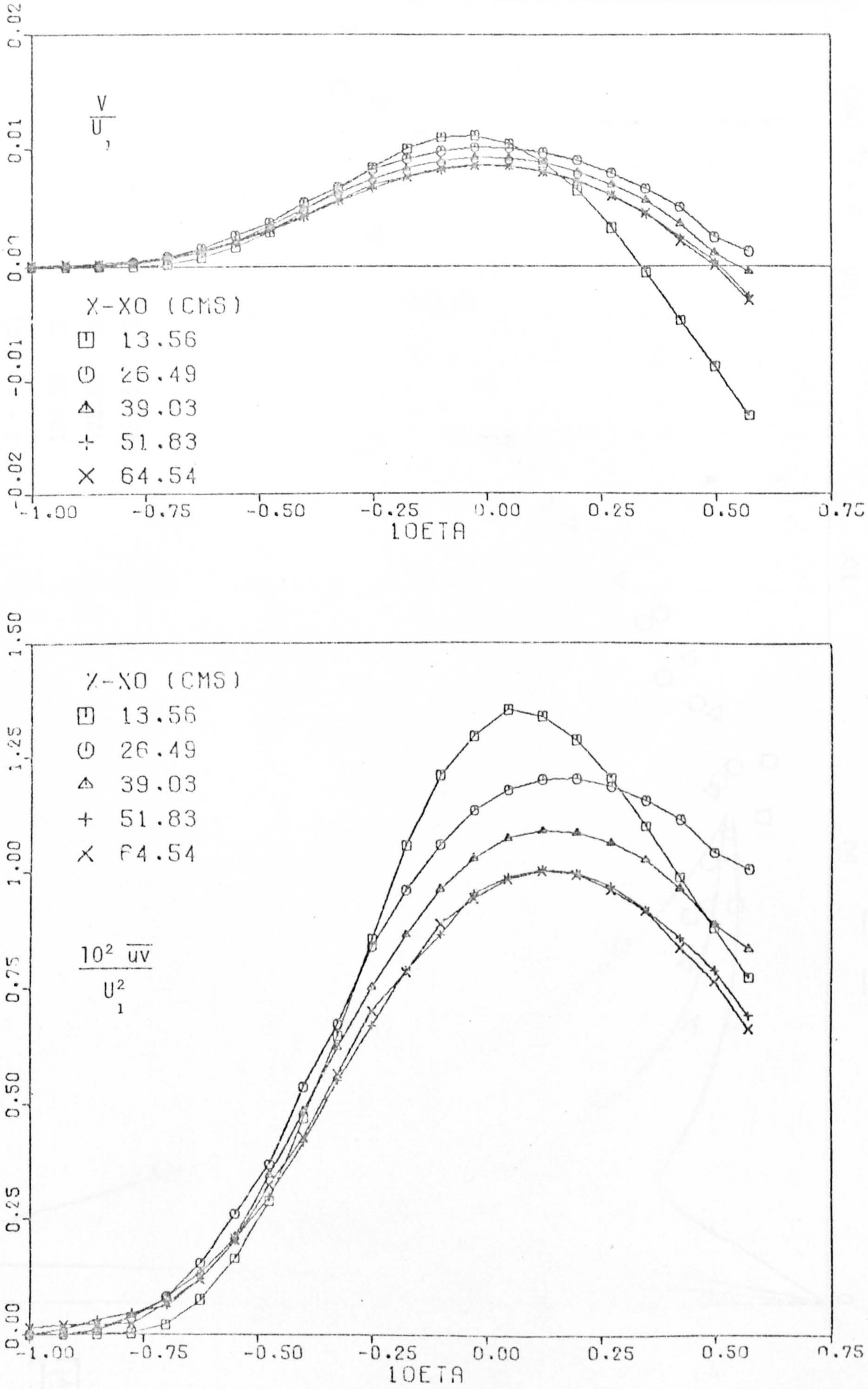
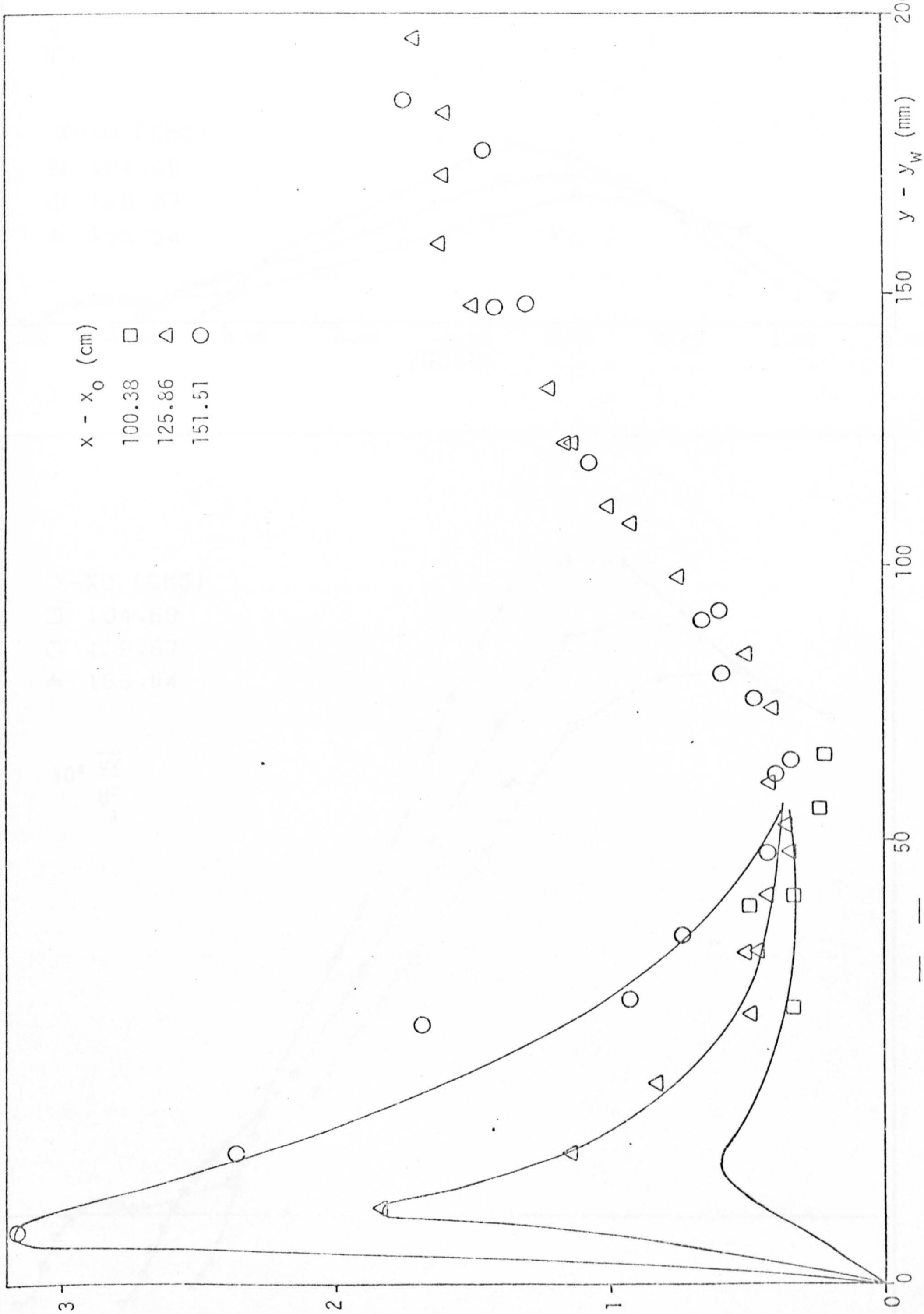


Fig. B.2 Calculated V and $\overline{uv}$ in the free shear layer, no ε dependence



B.3 $(\overline{u^2} - \overline{v^2})$ in the reattached flow

Fig. B

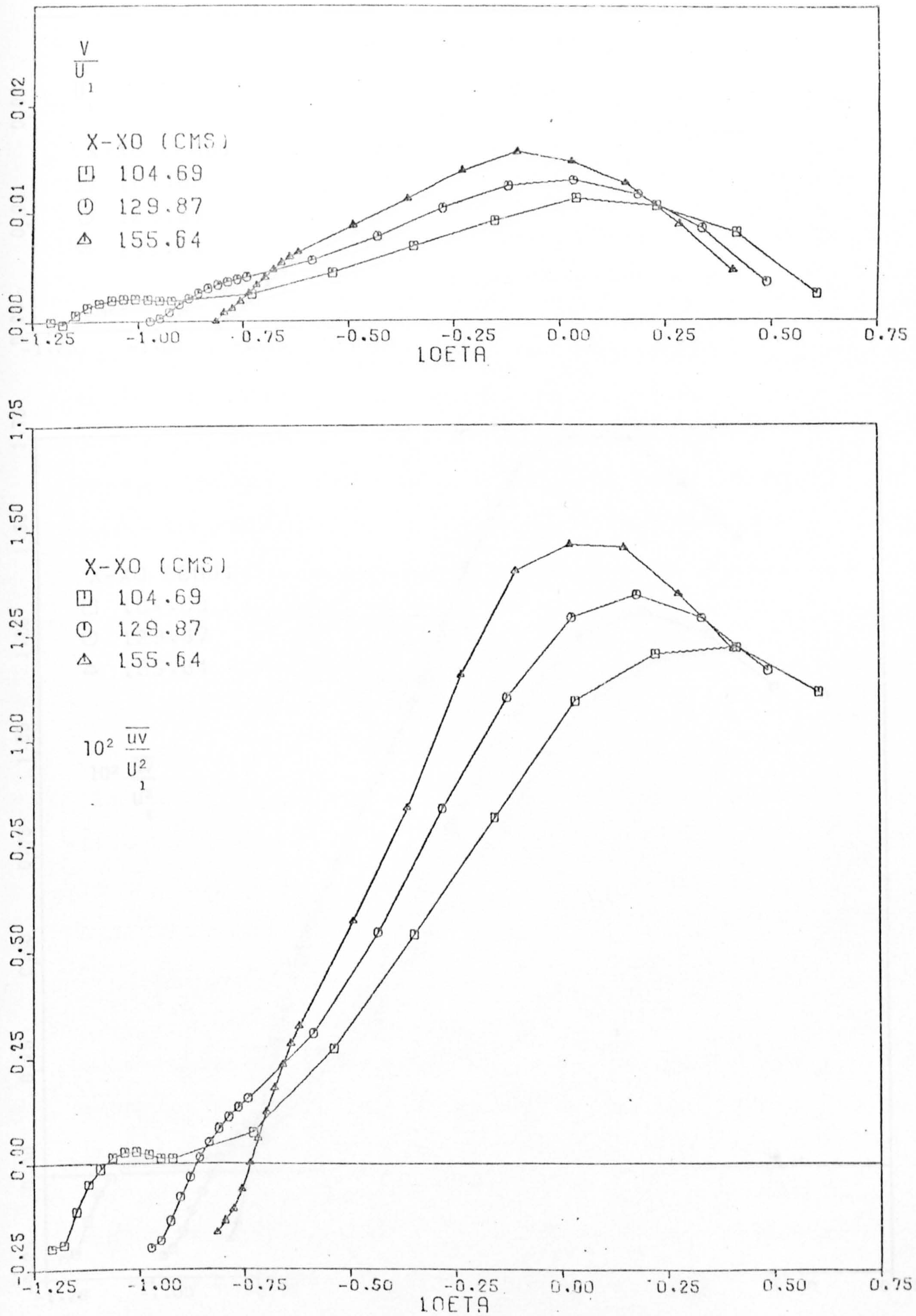


Fig. B.4 Calculated V and $\overline{uv}$ in the reattached flow without normal stress term

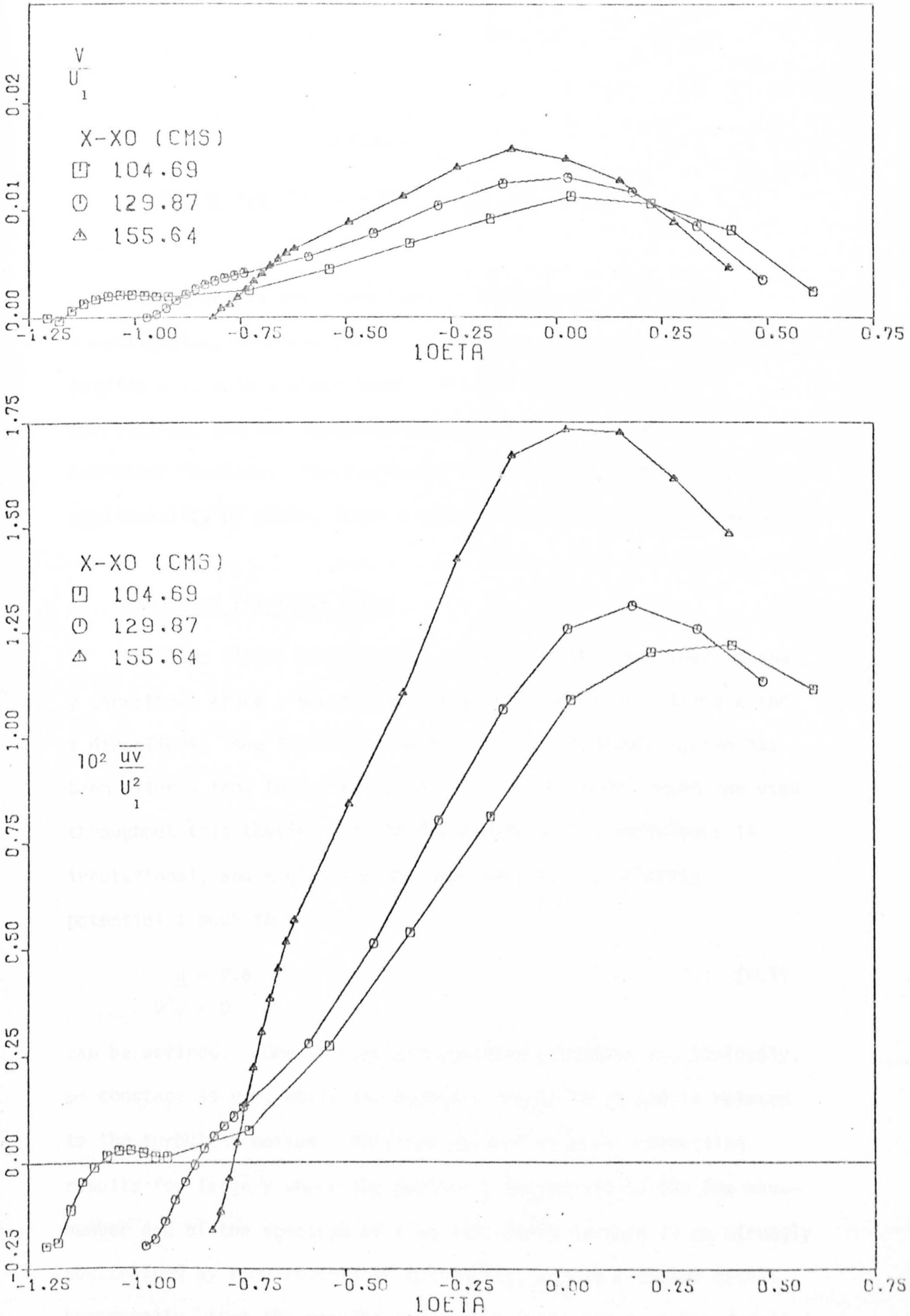


Fig. B.5 Calculated V and $\overline{uv}$ in the reattached flow, with normal stress term

APPENDIX C

AN ANALYSIS OF THE IRROTATIONAL NEAR-FIELD

This appendix describes some of the results of a joint investigation, with Professor J.H. Ferziger, of potential flow outside a turbulent shear layer. Most of the work on the correlations and the inclusion of wall effects was done by Professor Ferziger. The discussion of coordinate systems and the applicability of mixing layer scaling is due to the present author.

1. Unbounded Potential Flow

Phillips (1955) analysed the potential flow, unbounded in the y direction, above a homogeneous sheet of turbulence, in the x and z directions; see fig.C.1. Note that the coordinate system has been altered from that used by Phillips to the more common one used throughout this thesis. If the fluid outside the turbulence is irrotational, and neglecting the mean velocity, a velocity potential ϕ such that

$$\underset{\sim}{u} = \nabla.\phi \qquad (C.1)$$
$$\nabla^2\phi = 0$$

can be defined. One appropriate boundary condition is, obviously, $\phi \to$ constant as $y \to \infty$, while the boundary condition at y=0 is related to the turbulent motion. Phillips derived several interesting results for large y where the motion is determined by the low-wave-number end of the spectrum of v at y=0, which in turn is so strongly constrained by requirements of continuity, and to a lesser extent homogeneity, that the results are almost independent of the detailed turbulence structure. The boundary condition at y=0 can be written

as a Fourier integral

$$\left.\frac{\partial\phi}{\partial y}\right|_{y=0} = \int f(k_1,k_3)e^{i(k_1x + k_3z)}\, dk_1dk_3 \qquad (C.2)$$

where the integration is over all k_1 and k_3 (as it is in all the following integrals, unless otherwise stated). Since the flow is homogeneous in the x,y plane, $f(k_1,k_3)$ can be related to the two dimensional energy spectrum of the normal component v, and to the correlation of v in the (x, 0, z) plane which is the two-dimensional Fourier transform of the spectra, by

$$\hat{f}\,(k_1,k_3) = f(k_1,k_3)\, f^*(k_1,k_3)$$

$$= \frac{1}{(2\pi)^2}\int \left[\overline{v(\underset{\sim}{x}_1)\, v(\underset{\sim}{x}_2)}\right] e^{i\underset{\sim}{k}\cdot\underset{\sim}{r}}\, dr_1dr_3 \qquad (C.3)$$

$$= \theta(\underset{\sim}{k}) \text{ say}$$

where f* is the complex confugate of f and

$$\underset{\sim}{x}_1 = (x_1;y_1,z_1), \underset{\sim}{x}_2=(x_2,y_2,z_2)$$

$$\underset{\sim}{r} = (r_1, 0, r_3)=(x_2-x_1,0, z_2-z_1) \text{ and } \underset{\sim}{k}=(k_1,k_3).$$

Eqn.(C.3) can be derived by following Batchelor (1956,pp 28-32). The solution to Eqn.(C.1) is then

$$\phi(\underset{\sim}{x}) = -\int \frac{\theta(\underset{\sim}{k})}{k} e^{-ky}\, e^{\,i(k_1x\, +k_3z)}dk_1dk_3 \qquad (C.4)$$

where $k = |\underset{\sim}{k}| = (k_1^2+k_3^2)^{\frac{1}{2}}$, from which the velocity components can be found as

$$\begin{bmatrix} v(\underset{\sim}{x}) \\ u(\underset{\sim}{x}) \\ w(\underset{\sim}{x}) \end{bmatrix} = \int\int \begin{bmatrix} f(k) \\ -ik_1f(k)/k \\ -ik_3f(k)/k \end{bmatrix} e^{-ky}e^{i(k_1x\, +\, k_3y)}dk_1dk_3. \qquad (C.5)$$

and the velocity covariances are

$$\begin{bmatrix} \overline{v(\underset{\sim}{x}_1)v(\underset{\sim}{x}_2)} \\ \overline{u(\underset{\sim}{x}_1)u(\underset{\sim}{x}_2)} \\ \overline{w(\underset{\sim}{x}_1)w(\underset{\sim}{x}_2)} \end{bmatrix} = \int\int \begin{bmatrix} \theta(k) \\ k_1^2\theta(\underset{\sim}{k})/k^2 \\ k_3\theta(\underset{\sim}{k})/k^2 \end{bmatrix} e^{-k(y_1+\, y_2)}e^{i\underset{\sim}{k}\cdot\underset{\sim}{r}}\, dk_1dk_3. \qquad (C.6)$$

Thus immediately

$$\overline{v(\underset{\sim}{x}_1)v(\underset{\sim}{x}_2)} = \overline{u(\underset{\sim}{x}_1)u(\underset{\sim}{x}_2)} + \overline{w(\underset{\sim}{x}_1)w(\underset{\sim}{x}_2)} \qquad (C.7)$$

and in particular

$\overline{v^2} = \overline{u^2} + \overline{w^2}$ which is Eqn.(1.1).

Phillips also shows that the energy spectrum at distance y from the turbulence has the form

$$E(k,y) = E_{y=0}(k)\ e^{-2ky}. \qquad (C.8)$$

The exponential factor implies that the only contributions to the spectrum come from wave-numbers for which ky>>1 suggesting that a Taylor series expansion of $\theta(k)$ near k=0 would yield asymptotic results for $y\to\infty$. Following Batchelor (1956, pp 36-38) the appropriate expansion is

$$\theta(\underset{\sim}{k}) = k_i k_j\ \theta_{ij} + O(k^3) \qquad (C.9)$$

with summation over i,j=1,3 only. Inserting Eqn.(C.9) into Eqn. (C.6) and setting $\underset{\sim}{x}_1=\underset{\sim}{x}_2=y$ gives

$$\begin{bmatrix} \overline{v^2}(y) \\ \overline{u^2}(y) \\ \overline{w^2}(y) \end{bmatrix} = \frac{3\pi}{32} \begin{bmatrix} 4(\theta_{11}+\theta_{33}) \\ 3\theta_{11}+\theta_{33} \\ \theta_{11}+3\theta_{33} \end{bmatrix} y^{-4} = \begin{bmatrix} a_v \\ a_u \\ a_w \end{bmatrix} y^{-4} \qquad (C.10)$$

from which Eqn.(1.2) follows.

Stewart (1956) pointed out that Eqn.(1.1) follows from the irrotationality condition

$$\frac{\partial u_i}{\partial x_j} = \frac{\partial u_j}{\partial x_i} \qquad (C.11)$$

and it can be easily shown that Eqn.(C.7) does so as well. From Eqn.(C.11)

$$u_i(\underset{\sim}{x}_2)\frac{\partial u_i}{\partial y}(\underset{\sim}{x}_1) = u_i(\underset{\sim}{x}_2)\frac{\partial v}{\partial x_i}(\underset{\sim}{x}_1)$$

$$u_i(\underset{\sim}{x}_1)\frac{\partial u_i}{\partial y}(\underset{\sim}{x}_2) = u_i(\underset{\sim}{x}_1)\frac{\partial v}{\partial x_i}(\underset{\sim}{x}_2)$$

where u_i=u or w when x_i=x or z.

Thus

$$\overline{\frac{\partial u}{\partial y}(\underset{\sim}{x}_1)u(\underset{\sim}{x}_2)} = -\overline{v(\underset{\sim}{x}_1)\frac{\partial u}{\partial x}(\underset{\sim}{x}_2)} - \overline{v(\underset{\sim}{x}_1)\frac{\partial u}{\partial x}(\underset{\sim}{x}_2)}$$

$$+ \frac{\partial}{\partial x}\left[\overline{u(\underset{\sim}{x}_1)v(\underset{\sim}{x}_2)}+\overline{u(\underset{\sim}{x}_2)v(\underset{\sim}{x}_1)}\right] \qquad \text{(C.12)}$$

and similarly

$$\overline{\frac{\partial w}{\partial y}(\underset{\sim}{x}_1)w(\underset{\sim}{x}_2)} = -\overline{v(\underset{\sim}{x}_1)\frac{\partial w}{\partial z}(\underset{\sim}{x}_2)} - \overline{v(\underset{\sim}{x}_2)\frac{\partial w}{\partial z}(\underset{\sim}{x}_1)}$$

$$+ \frac{\partial}{\partial z}\left[\overline{v(\underset{\sim}{x}_2)w(\underset{\sim}{x}_1)} + \overline{v(\underset{\sim}{x}_1)w(\underset{\sim}{x}_2)}\right] \qquad \text{(C.13)}$$

where the derivatives of the covariances on the right hand sides of (C.12) and (C.13) are zero by homogeneity. Adding (C.12) and (C.13) and using the continuity equation gives

$$\frac{\partial}{\partial y}\left[\overline{u(\underset{\sim}{x}_1)u(\underset{\sim}{x}_2)} + \overline{w(\underset{\sim}{x}_1)w(\underset{\sim}{x}_2)} - \overline{v(\underset{\sim}{x}_1)v(\underset{\sim}{x}_2)}\right] = 0. \qquad \text{(C.14)}$$

Applying the boundary condition that $\overline{u_i(\underset{\sim}{x}_1)u_i(\underset{\sim}{x}_2)} \to 0$ as $y_1, y_2 \to \infty$ gives Eqn.(C.7).

Stewart also showed that, provided the basic assumptions of Phillips' analysis were not altered by the streamwise inhomogeneity of growing shear layers, Eqn.(C.10) could be rewritten in a form compatible with the self-preserving scaling for a turbulent wake. This can also be done for a mixing layer, but a different method is used since the argument in Stewart's Eqn.(3.1) is still dimensional. As mentioned in Chapter 1 in a self preserving mixing layer, all velocities must scale on the velocity difference across

the layer $\Delta U=U_1$, and all lengths on the distance from the effective origin $x-x_o$, which will be denoted by x for this Appendix. Then $\theta(\underset{\sim}{k})$ can be written as

$$\theta(\underset{\sim}{k}) = U_1^2 x^2 \chi(\underset{\sim}{k}x) = U_1^2 x^2 \chi(\underset{\sim}{k}^*).$$

Phillips (Eqn.17) gives the kinetic energy of the irrotational motion as

$$\tfrac{1}{2}\overline{q^2(y)} = \int \theta(k) e^{-2ky}\, dk_1 dk_3 \text{ which can be written as}$$

$$\tfrac{1}{2}\overline{q^2(y)} = \tfrac{1}{2}\overline{q^2(\eta)} = U_1^2 \int \chi(\underset{\sim}{k}^*) e^{-2k^*\eta}\, dk_1^* dk_3^*$$

where $k^*=kx$, $k_1^*=k_1x$, $k_3=k_3x$ and the integration is over all values of k_1^* and k_3^*. This shows that the fluctuation energy scales on U_1^2 only, as required by self preservation. Eqn.(C.9) has the nondimensional form

$$\theta(\underset{\sim}{k}) = U_i^2 x^2 \chi(\underset{\sim}{k}^*) = U_i^2 k_i^* k_j^* \chi_{ij}$$

so the equation for the mean square normal component from (C.6) is

$$\overline{v^2} = U_1^2 \int \chi_{ij} e^{-2k^*\eta}\, dk_1^*\, dk_3^* \text{ and similarly for } \overline{u^2} \text{ and } \overline{w^2}.$$

The asymptotic result for large y (C.10) can be rewritten as

$$\begin{bmatrix} \overline{v^2}(\eta) \\ \overline{u^2}(\eta) \\ \overline{w^2}(\eta) \end{bmatrix} = \frac{3\pi}{32} U_1^2 \begin{bmatrix} 4(\chi_{11}+\chi_{33}) \\ 3\chi_{11}+\chi_{33} \\ \chi_{11}+3\chi_{33} \end{bmatrix} (\eta-\eta_o)^{-4}. \qquad (C.15)$$

χ_{11} and χ_{33} are obviously related to θ_{11} and θ_{33}. In Eqn.(C.15) $\eta=\eta_o$ is the plane corresponding to y=0 in Phillips' analysis. This justifies the use of mixing layer scaling in presenting the potential flow measurements in Chapter 4.

Stewart also noted that the correct coordinate system for the application of Phillips' analysis to linearly growing shear layers is the cylindrical polar system shown in fig.C.2. However he was unable to find a suitable function analogous to Eqn.(C.2) to describe the boundary condition. Nevertheless some comments on the appropriate coordinate system can be made by deriving the equations analogous to (C.12) and (C.13) in cylindrical polar coordinates. Defining u_r, u_θ and u_z as the velocity components in the r, θ and z directions (see fig.C.2) and using homogeneity, the expression analogous to (C.14) is

$$\overline{\frac{\partial u_r}{\partial \theta}(\underset{\sim}{x}_1)u_r(\underset{\sim}{x}_2)}+\overline{\frac{\partial u_z}{\partial \theta}(\underset{\sim}{x}_1)u_z(\underset{\sim}{x}_2)}=\frac{r(\underset{\sim}{x}_1)}{r(\underset{\sim}{x}_2)}\,\overline{u_\theta(\underset{\sim}{x}_1)\frac{\partial u}{\partial \theta}(\underset{\sim}{x}_2)}$$

$$+\frac{r(\underset{\sim}{x}_2)}{r(\underset{\sim}{x}_1)}\overline{u_\theta(\underset{\sim}{x}_2)\frac{\partial u_\theta}{\partial \theta}(\underset{\sim}{x}_1)} \qquad (C.16)$$

where now $\underset{\sim}{x}_1=\underset{\sim}{x}_1(r,\theta,z)$, $\underset{\sim}{x}_2=\underset{\sim}{x}_2(r,\theta,z)$ and r is <u>not</u> related to the covariance separations used in Eqn.(C.3). From Eqn.(C.16)

$$\overline{u_r(x_1)u_r(x_2)} + \overline{u_z(x_1)u_z(x_2)} = \overline{u_\theta(x)u_\theta(x_2)}$$

if and only if $r(\underset{\sim}{x}_1)=r(\underset{\sim}{x}_2)$. A special case is

$$\overline{u_r^2}+ \overline{u_z^2}= \overline{u_\theta^2} \ .$$

Now u_z =w in the usual notation and q^2 is independent of the (orthogonal) coordinate used since it is a scalar. Thus

$$\overline{u_r^2}+ \overline{u_\theta^2} = \overline{u^2} + \overline{v^2} \qquad (C.17)$$

so the experimental result $\overline{u^2} + \overline{w^2} \simeq \overline{v^2}$ (fig 4.22) implies that $\overline{u^2} \simeq \overline{u_r^2}$, $\overline{v^2} \simeq \overline{u_\theta^2}$ by Eqn (1.1) and (C.17). This suggests that the errors incurred by using the Cartesian coordinate system in the

present analysis will be small, providing that the streamwise inhomogeneity does not seriously effect the basic assumptions used by Phillips.

2. The Effect of Wall Constraint

The simplest way to account for the presence of a solid wall bounding the potential flow (fig. C.3) is in terms of the image layer. With a wall at $y=y_w$, Eqn.(C.5) becomes

$$\begin{bmatrix} v(y) \\ u(y) \\ w(y) \end{bmatrix} = \int \begin{bmatrix} \theta(\underset{\sim}{k}) \\ k_1{}^2\theta(\underset{\sim}{k})/k^2 \\ k_3{}^2\theta(\underset{\sim}{k})/k^2 \end{bmatrix} \begin{bmatrix} e^{-ky} - e^{-k(2y_w-y)} \\ e^{-ky} + e^{-k(2y_w-y)} \\ e^{-ky} + e^{-k(2y_w-y)} \end{bmatrix} e^{i(k_1x+k_3z)} dk_1 dk_3 \qquad (C.18)$$

A B

where the terms in column A are the real shear layer contribution and those in column B the image layer contribution. The minus sign outside the term in column B for $v(y)$ arises because the image forcing function is of opposite sign to the real forcing function, which affects $v(y)$ only. In a form compatible with (C.15) the mean square intensities are given by

$$\begin{bmatrix} \overline{v^2}(\eta) \\ \overline{u^2}(\eta) \\ \overline{w^2}(\eta) \end{bmatrix} = \frac{3\pi}{32} U_1{}^2 \begin{bmatrix} 4(\chi_{11} + \chi_{33}) \\ 3\chi_{11} + \chi_{33} \\ \chi_{11} + 3\chi_{33} \end{bmatrix} \begin{bmatrix} \eta^{-4} + (2\eta_w - \eta)^{-4} - 2\eta_w{}^{-4} \\ \eta^{-4} + (2\eta_w - \eta)^{-4} + 2\eta_w{}^{-4} \\ \eta^{-4} + (2\eta_w - \eta)^{-4} + 2\eta_w{}^{-4} \end{bmatrix} \qquad (C.19)$$

where η and η_w are measured from the effective origin, η_0, for the potential flow. Note that from fig(C.3) the streamwise inhomogeneity of the shear layer is again ignored. Eqn.(C.19) reduces to (C.15) as $\eta_w \to \infty$. The qualitative behaviour is shown in fig(C.4) where it can be seen that there must be a small,

viscosity-dominated region next to the wall to accommodate the no-slip constraint on u and w. The trend of the mean-square intensities given by Eqn.(C.19) is very similar to the theoretical results of Hunt and Graham (1978) discussed in Chapter 1. In both analyses the components in the same plane as the wall, $\overline{u^2}$ and $\overline{w^2}$, are amplified equally while $\overline{v^2} \to 0$ as the wall is approached.

3. Calculation of the correlations

For unbounded potential flow the equations for the correlations as defined in Chapter 2 can be found from Eqn.(C.6) For separation in the x,z plane θ_{13} does not contribute to the correlations, which have the form

$$R_{11}(\underset{\sim}{x}(x,y,z);\ r_1,0,\ r_3) = \frac{\overline{u_i(x,y,z)u_i(x+r_1,y,z+r_3)}}{\left[\overline{u_i^2(x,y,z)u_i^2(x+r_1,y,z+r_3)}\right]^{\frac{1}{2}}}$$

$$= \frac{\overline{u_i(x,y,z)u_i(x+r_1,y,z+r_3)}}{\left[u_i{}^2(x,y,z)\right]^{\frac{1}{2}}}$$

$$= \begin{bmatrix} [\overline{v^2}(\underset{\sim}{x})]^{-1} \\ [\overline{u^2}(\underset{\sim}{x})]^{-1} \\ [\overline{w^2}(\underset{\sim}{x})]^{-1} \end{bmatrix} \iint \begin{bmatrix} k_1{}^2\theta_{11}+k_3{}^2\theta_{33} \\ (k_1{}^4\theta_{11}+k_1^2k_3^2\theta_{33})/k^2 \\ (k_3^2k_1\theta_{11}+k_3{}^4\theta_{33})/k^2 \end{bmatrix} e^{-2ky}\, e^{i(k_1r_1+k_3r_3)}\, dk_1dk_3 \quad (C.20)$$

where integration is over all k_1, k_3.

Eqn.(C.20) was integrated as follows using $R_{11}(x;r_1,0,r_3)$ as an example. Setting $k_1=k\cos\psi$, $k_3=k\sin\psi$ the integral in (C.20)

whose kernel is $k_1^2\theta_{11}+k_3^2\theta_{33}$ can be rewritten as

$$\int_0^{2\pi}\int k^3\cos^2\psi\left[\theta_{11}\cos^2\psi+\theta_{33}\sin^2\psi\right]e^{-2ky}e^{ik(r_1\cos\psi+r_3\sin\psi)}\,dk\,d\psi$$

$$\doteq \int_0^{2\pi}\frac{\left|\theta_{11}\cos^4\psi+\theta_{33}\sin^2\psi\cos^2\psi\right|d\psi}{\left[2y-i(r_1\cos\psi+r_3\sin\psi)\right]^4} = I, \text{ say}$$

Thus

$$\left.\begin{aligned} R_{11}\left(\frac{r}{2y},0,0\right) &= \frac{\theta_{11}I_1\left(\frac{r}{2y}\right)+\theta_{33}I_2\left(\frac{r}{2y}\right)}{\theta_{11}I_1(0)+\theta_{33}I_2(0)} \\ R_{11}\left(0,0,\frac{r}{2y}\right) &= \frac{\theta_{11}I_3\left(\frac{r}{2y}\right)+\theta_{33}I_4\left(\frac{r}{2y}\right)}{\theta_{11}I_3(0)+\theta_{33}I_4(0)} \end{aligned}\right] \qquad (C.21)$$

where y is measured from the effective origin for the potential fluctuations (as are y, η and η_w as used in the rest of this appendix) and

$$\left.\begin{aligned} I_1\left(\frac{r}{2y}\right) &= \int_0^{2\pi}\frac{\cos^4\psi}{\left(1-\frac{ir}{2y}\cos\psi\right)^4}\,d\psi, \quad I_2\left(\frac{r}{2y}\right) = \int_0^{2\pi}\frac{\sin^2\psi\cos^2\psi}{\left(1-\frac{ir}{2y}\cos\psi\right)^4}\,d\psi \\ I_3\left(\frac{r}{2y}\right) &= \int_0^{2\pi}\frac{\cos^4\psi}{\left(1-\frac{ir}{2y}\sin\psi\right)^4}\,d\psi, \quad I_4\left(\frac{r}{2y}\right) = \int_0^{2\pi}\frac{\sin^2\psi\cos^2\psi}{\left(1-\frac{ir}{2y}\sin\psi\right)^4}\,d\psi \end{aligned}\right] \qquad (C.22)$$

and $\quad I_1(0)=I_3(0)=\frac{3\pi}{4}$, $I_2(0)=I_4(0)=\frac{\pi}{4}$

and $\quad I=I_1\theta_{11}+I_2\theta_{33}+I_3\theta_{11}+I_4\theta_{33}$.

Similar equations to (C.21) and (C.22) can be derived for the

spanwise component correlations, and the normal component correlations can then be found using Eqn.(C.7). All the integrals in (C.22) and the similar integrals for the spanwise component are real, and can be solved, tediously, by contour integration. Because of the difficulties in applying this analysis to the real inhomogeneous flow in the present experiment, principally the unphysical result that $\chi_{33}<0$ (see Chapter 4), a simpler approach was adopted. Professor Ferziger numerically integrated the equations for the correlations and the results are compared to the experimental values in Chapter 5.

Because $\underset{\sim}{k}.\underset{\sim}{r}=0$ if the separation is in the y direction only, the normal correlations are very easy to compute. The result is

$$R_{ii}(\underset{\sim}{x}(x,y,z);\ 0,r,0)=(1+\frac{r}{y})^2(1+\frac{r}{2y})^{-4},\ i=1,2,3 \qquad (C.23)$$

The interesting aspect of Eqns.(C.21) and (C.23) is that the potential flow correlations scale on $\frac{r}{y}$, or $\xi\equiv r\eta(x-x_o)^{-1}$ in mixing layer similarity form, showing that the correlation scales in the potential flow, when plotted against $r/(x-x_o)$ can be made arbitrarily large simply by increasing the distance of the fixed probe from the shear layer.

The inclusion of image effects in Eqn.(C.21) is extremely tedious and was not seriously attempted. The effects of the solid wall on the spanwise correlations can be estimated using the homogeneity assumption $\theta_{11}=\theta_{33}$. This should give some idea of changes induced by the wall. Under this assumption the

correlations in the unbounded flow have the simple form

$$R_{11}(0,0,r) \quad [=R_{33}(r,0,0) \text{ by homogeneity}]$$

$$= \left[1+\left(\frac{r}{2y}\right)^2\right]^{-5/2} = \left[1+\left(\frac{\xi}{2}\right)^2\right]^{-5/2} \tag{C.24}$$

and

$$R_{33}(0,0,r) \quad [=R_{11}(r,0,0) \text{ by homogeneity}]$$

$$= (1-\xi^2)\left[1+\left(\frac{\xi}{2}\right)^2\right]^{-7/2} \tag{C.25}$$

By writing the integrals in the equations for the correlations in a form analogous to Eqn.(C.18) the corresponding results for the wall effected flow are

$$R_{11}(0,0,r) = \frac{\left[1+\left(\frac{\xi}{2}\right)^2\right]^{-5/2} + \alpha\left[\alpha^2+\left(\frac{\xi}{2}\right)^2\right]^{-5/2} + 2\beta\left[\beta^2+\left(\frac{\xi}{2}\right)^2\right]^{-5/2}}{1 + \alpha^{-4} + 2\beta^{-4}} \tag{C.26}$$

$$R_{11}(r,0,0) = \frac{\frac{\beta(\beta^2-\xi^2)}{(\beta^2+\xi^2)^{7/2}} + \frac{(1-\xi^2)}{\left[1+\left(\frac{\xi}{2}\right)^2\right]^{7/2}} + \frac{2\beta(\beta^2-\xi^2)}{\left[\left(\frac{\xi}{2}\right)^2+\beta^2\right]^{7/2}}}{1 + \alpha^{-4} + 2\beta^{-4}} \tag{C.27}$$

where $\alpha = \frac{2\eta_w}{\eta} - 1, \beta = \frac{\eta_w}{\eta}$.

Eqns. (C.26) and (C.27) were solved for values of ξ, η and η_w typical of the experimental range and some of the calculated results are shown in fig.C.5. The changes induced by the wall are in qualitative agreement with the experimental changes shown in Chapter 5.



Turbulence

Fig. C.1 Homogeneous unbounded potential flow

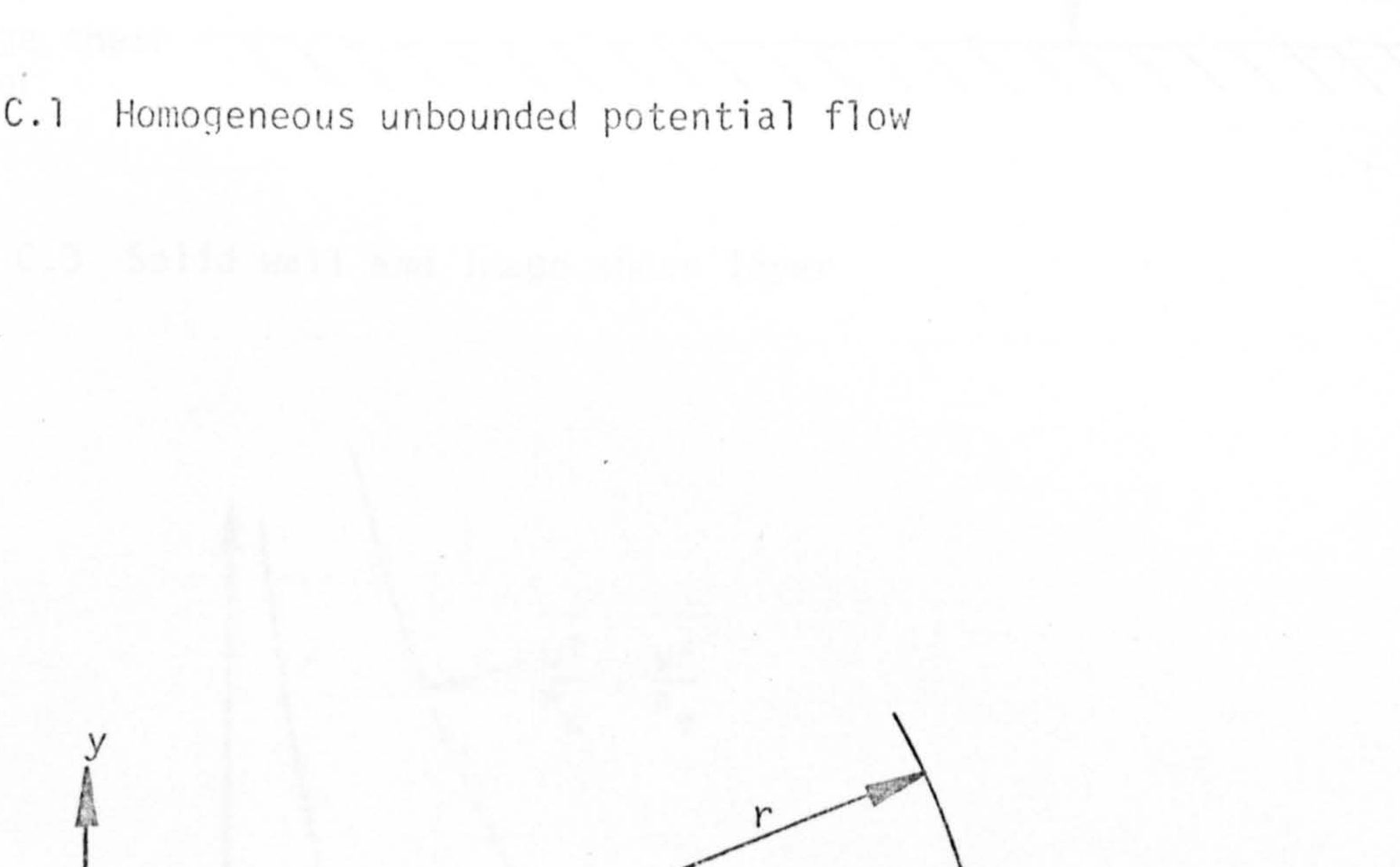


Fig. C.2 Coordinates for potential flow outside linearly growing shear layers

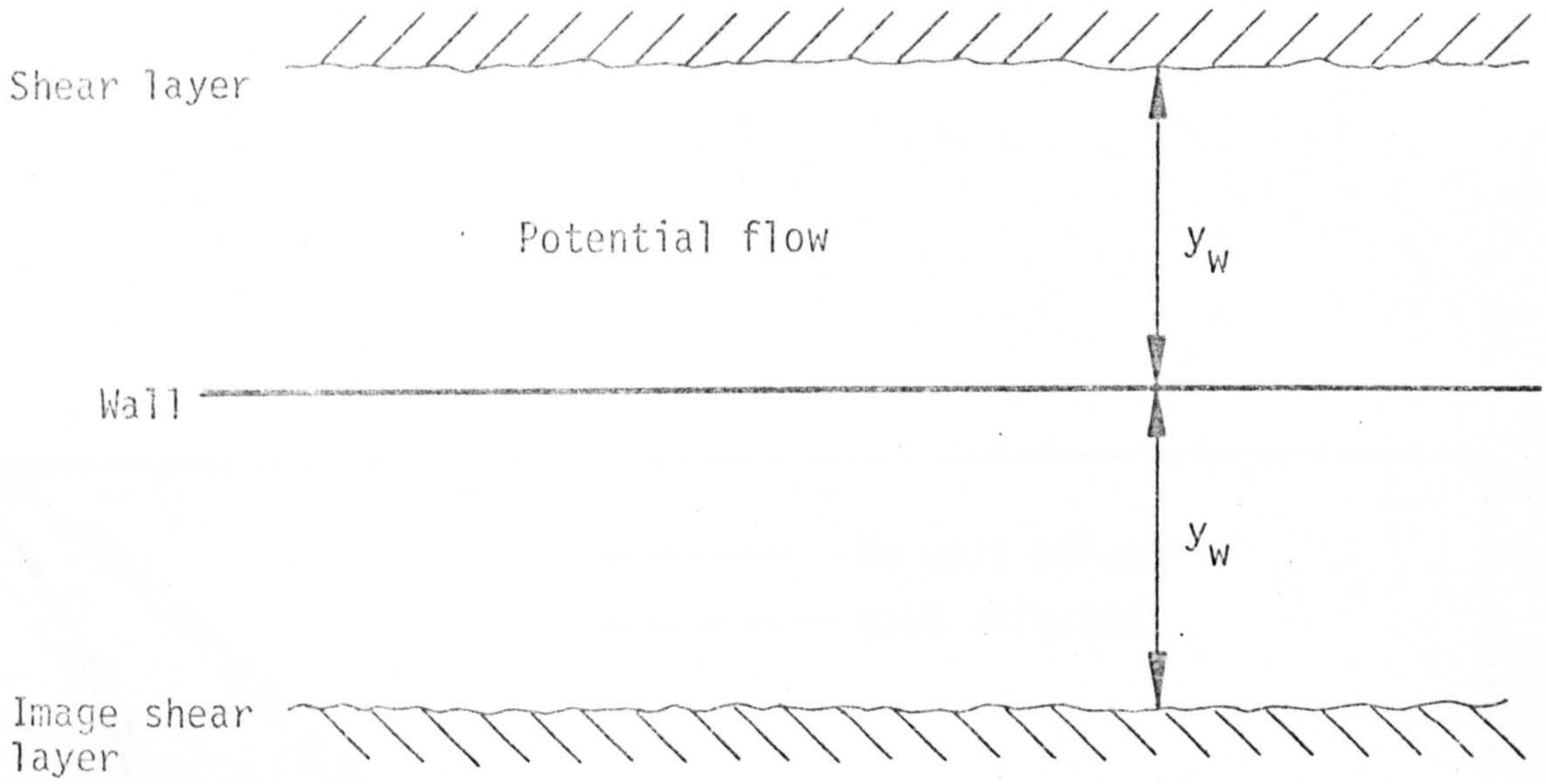


Fig. C.3 Solid wall and image shear layer

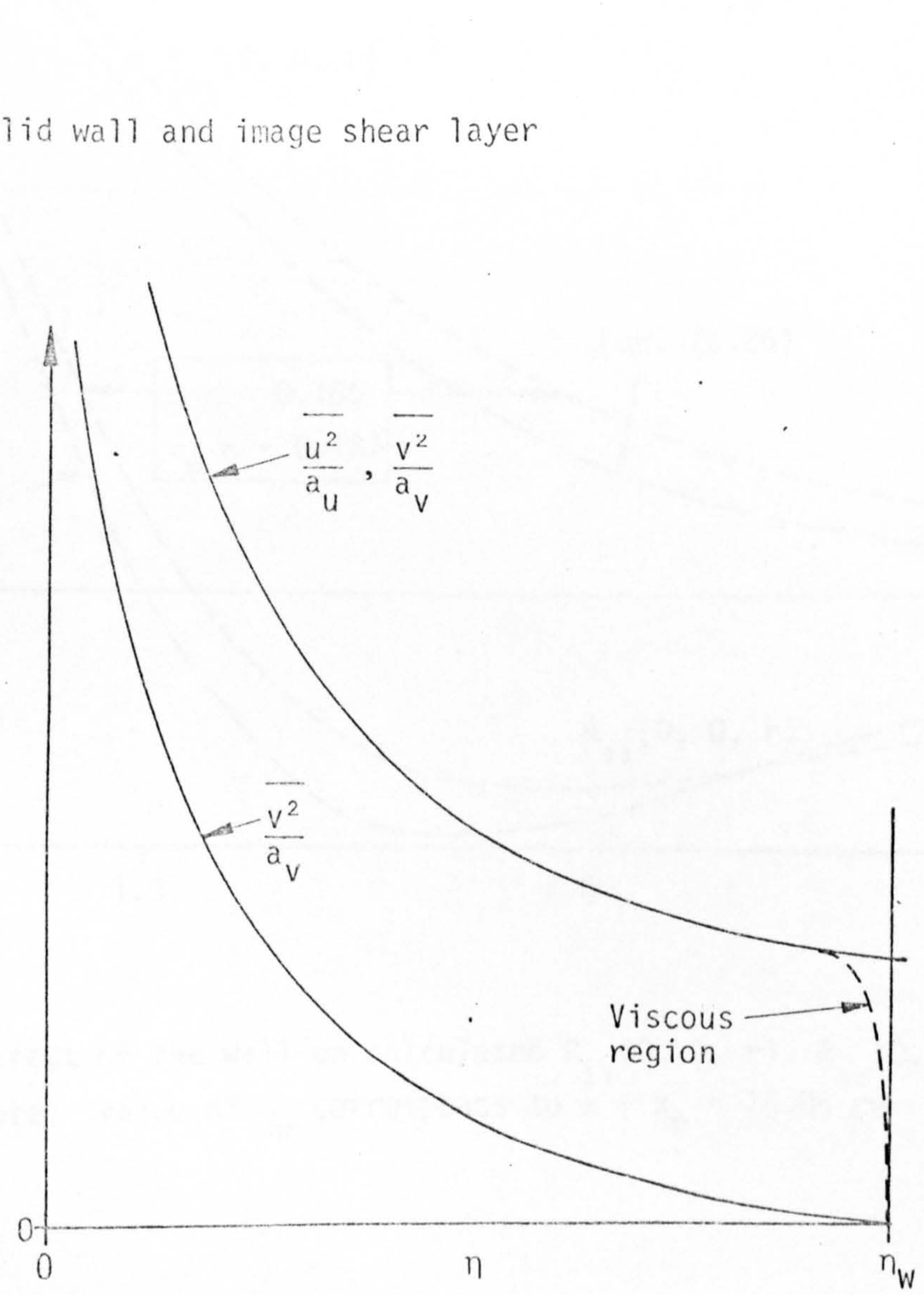


Fig. C.4 Effect of the wall on $\overline{v^2}$, $\overline{u^2}$ and $\overline{w^2}$

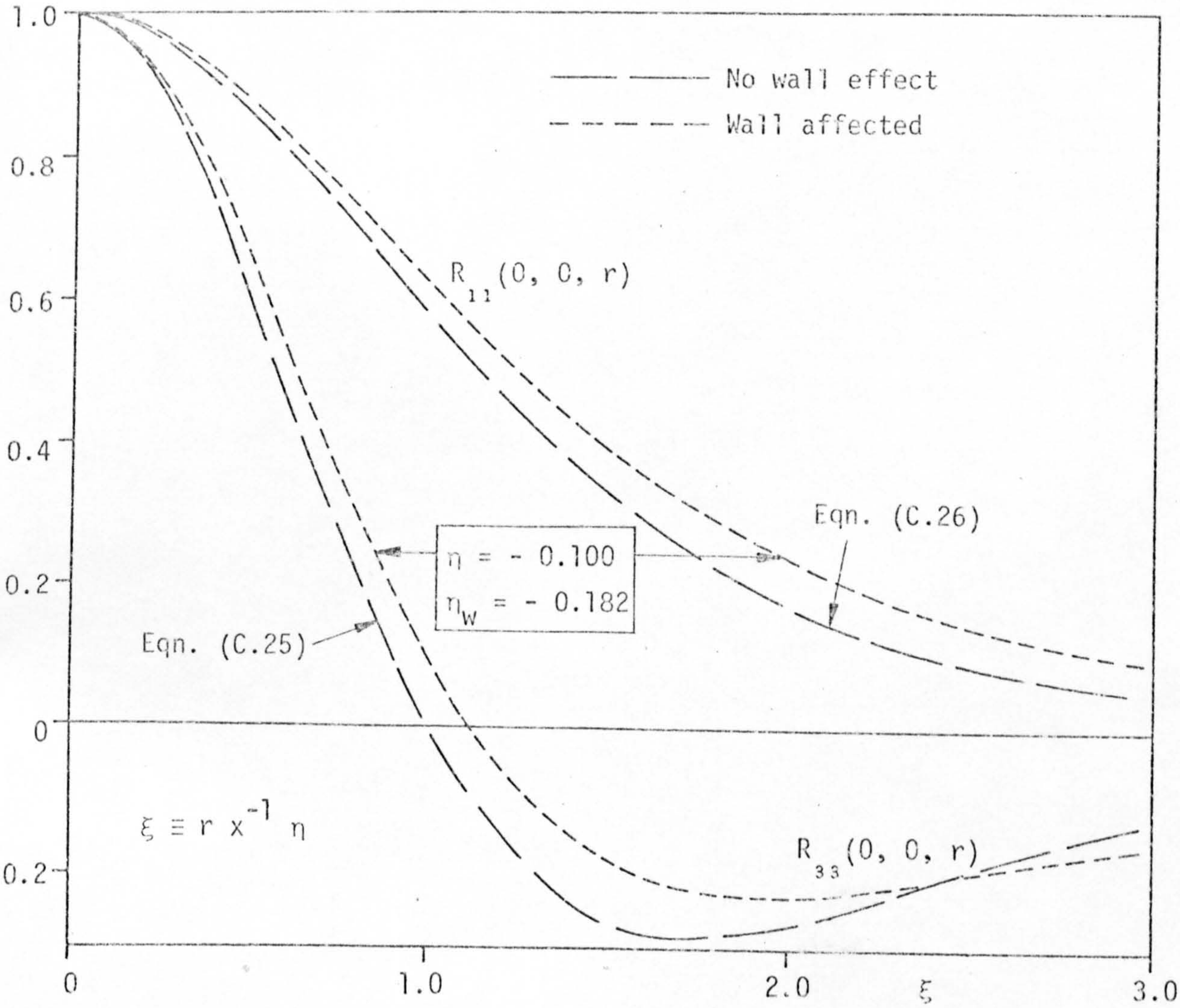


Fig. C.5 Effect of the wall on calculated $R_{11}(0, 0, r)$, $R_{33}(0, 0, r)$.
Note: value of η_w corresponds to $x - x_o = 75.06$ cm.